



**HAL**  
open science

# Definition at the atomic-scale of the external surface of ZSM-5 zeolite and its interactions with binder using molecular modeling

Laureline Treps

► **To cite this version:**

Laureline Treps. Definition at the atomic-scale of the external surface of ZSM-5 zeolite and its interactions with binder using molecular modeling. Material chemistry. Université de Lyon, 2020. English. NNT : 2020LYSEN040 . tel-03352173

**HAL Id: tel-03352173**

**<https://theses.hal.science/tel-03352173>**

Submitted on 23 Sep 2021

**HAL** is a multi-disciplinary open access archive for the deposit and dissemination of scientific research documents, whether they are published or not. The documents may come from teaching and research institutions in France or abroad, or from public or private research centers.

L'archive ouverte pluridisciplinaire **HAL**, est destinée au dépôt et à la diffusion de documents scientifiques de niveau recherche, publiés ou non, émanant des établissements d'enseignement et de recherche français ou étrangers, des laboratoires publics ou privés.



Numéro National de Thèse : 2020LYSEN040

**THESE de DOCTORAT DE L'UNIVERSITE DE LYON**  
opérée par  
**l'Ecole Normale Supérieure de Lyon**

**Ecole Doctorale N° 206**  
**Ecole Doctorale de Chimie** (Chimie, Procédés, Environnement)  
**Spécialité de doctorat** : Chimie Théorique et des Matériaux  
**Discipline** : Chimie

Soutenue publiquement le 22/09/2020, par :  
**Laureline TREPS**

---

**Définition à l'échelle atomique de la  
surface externe de la zéolithe ZSM-5 et  
de son interface avec le liant**

---

Devant le jury composé de :

COSTA, Dominique  
PAUL, Jean-François  
MAUGE, Françoise  
VERSTRAELEN, Toon  
CHIZALLET, Céline  
DE BRUIN, Théodoros

Directrice de recherche, IRCP  
Professeur, Université de Lille  
Directrice de recherche, ENSICAEN  
Assistant Professor, Ghent University  
Ingénieure de recherche, IFPEN  
Ingénieur de recherche, IFPEN

Rapporteure  
Rapporteur  
Examinatrice  
Examineur  
Directrice de thèse  
Co-encadrant



## Acknowledgements

First of all, this PhD work has been conducted at IFP Energies Nouvelles. I would like to thank Luc Nougier, director of the Catalysis, Biocatalysis, and Separation direction, and Tivadar Cseri and Emmanuelle Guillon, the two successive department chiefs of the department Catalyse par les Métaux et les solides Acido-Basiques.

My second point is to thank my PhD director, Céline Chizallet, and my PhD promoter, Theodorus De Bruin, for all their advices, their kindness, and their support. And to thank all the experimental teams we cooperate closely with, including Coralie Demaret, and Mickael Rivallan.

My third point is to thank all my fellow doctoral students and interns who shared the adventure: Elsy, Hanane, Jérôme, Amit, Sharmin, Axel, Thomas.

My last point is to thank my family and my friend who are so much supportive. I am embraced by your love and I can reach any goal with you. Jean-Marie I will say “yes” with all my heart.



## Abstract

Zeolites are nanoporous aluminosilicates crystals of prominent fundamental and industrial importance. Among these, ZSM-5 is one of the most investigated solid, with paramount industrial use, that can be obtained in various forms. Some of these (hierarchical forms, nanoslabs, nanosheets and nanocrystals) exhibit a very high surface over volume ratio which make them useful for multiple industrial processes. The shaping is used to adapt ZSM-5 (and zeolites in general) to the needs of the industrial reactors. Empirically, preparing a technical zeolite is a strong industrial know-how, but with limited physic-chemical understanding of the zeolite-binder interface. Periodic Density Functional Theory (DFT, VASP, PAW, PBE dDsC) calculations of the relative stability of relevant surface orientations for silicalite and ZSM-5 crystals ((100), (010) and (101)) were performed at different hydration levels thanks to ab initio thermodynamics. Their relative acidities (pyridine and di-tertbutylpyridine adsorption) and spectral features (vibration modes, NMR chemical shifts) are determined. The interaction of the most relevant ones with binders (alumina, silica) is simulated ab initio, and an empirical reactive force field (ReaxFF) is built on purpose to model larger scales. Several kinds of surface sites have been identified. Bridging Al-OH-Si are present at the pore mouth, of similar or higher stability with respect to bulk sites. These are not stable at the outermost surface, where the following groups prevail: Si-OH, Al-OH and most importantly water adsorbed on aluminum Al-(H<sub>2</sub>O)(OH)<sub>n</sub>. Models of pyridine and 2,6-ditertbutylpyridine adsorption show that the acidity of the bridging groups is stronger than the other, and more particularly with a strong confinement. Al-(H<sub>2</sub>O)(OH)<sub>n</sub> surface site are shown to be the most stable at the external surface of ZSM-5 and are studied upon the hydration and dehydration of the ZSM-5 external surfaces. The results issue from these DFT simulations are compared to FT-IR, <sup>1</sup>H NMR, and pyridine/2,6-ditertbutylpyridine adsorption experiments conducted at IFPEN. The interaction between zeolite and binders (silica, alumina) is first modeled by the interaction of the zeolite with small components like Si(OH)<sub>4</sub>, Na<sup>+</sup> - present in some silica sources - and Al(OH)<sub>3</sub>(H<sub>2</sub>O). The results show that alumina components are more strongly attracted by the aluminum of the zeolitic network than silicic species. Na<sup>+</sup> binds more strongly with the zeolite rather than silica and these results are once more compared to experimental data. The reactive force field parameters optimization is allowing to model larger external zeolite surfaces that are in contact with more realistic binder surfaces. All these results provide a rational understanding of a large set of experimental observations from the literature, that remained so far poorly understood. These findings are likely not limited to the case of the MFI framework (some of them already appeared to be valid for zeolite Beta), as our conclusions are mainly dictated by local topology aspects. The zeolite we investigate and the reactive sites we reveal are of both fundamental and industrial importance.

# Table of content

## Introduction and Objectives

## Chapter 1. State of the art

1.1. Zeolites .....	10
1.1.1. Definition and structural features .....	10
1.1.2. Applications of Zeolites .....	11
1.1.3. Acidity .....	12
1.1.4. Catalytic activity.....	14
1.1.5. ZSM-5 .....	15
1.1.6. Diffusion paths and localization of active sites at the particles scale.....	19
1.1.7. Characterization of the active sites.....	22
1.2. Shaping.....	25
1.2.1. Zeolite shaping .....	25
1.2.2. Textural changes.....	27
1.2.3. Effects on acid sites environment.....	29
1.2.4. Evolution of the acid properties .....	32
1.2.5. Evolution of the catalytic properties.....	33
1.3. Molecular Modeling .....	34
1.3.1. Nature and strength of the acid sites.....	35
1.3.2. Ab initio studies of external surface models .....	38
1.3.3. Surface hydration .....	40
1.3.4. ZSM-5 external surface models.....	41
1.3.5. Simulation of the zeolite-binder interface .....	43
1.4. Conclusion and strategy of the thesis .....	46
References .....	47
Chapter 2. Methodology	
2.1. Quantum mechanics basics .....	57
2.1.1. Born-Oppenheimer approximation.....	57
2.1.2. Electronic density.....	58
2.2. Density Functional Theory (DFT).....	58
2.2.1. Hohenberg, Kohn and Sham first theorems and approximations .....	58
2.2.2. Exchange-correlation energy.....	61
2.2.3. DFT-based dispersion method.....	62
2.2.4. Basis sets .....	63
2.3. Calculations types.....	64
2.3.1. Search of geometry optimized-structures.....	64
2.3.2. Vibrational frequencies calculations .....	65

## Table of content

2.3.3. Thermodynamic calculations.....	67
2.3.4. Linear Response Approach for the calculation of NMR chemical shifts.....	69
2.3.5. Code and methods employed in this work.....	70
2.4. Reactive Force Fields approach.....	71
2.4.1. The ReaxFF model.....	71
2.4.2. Reactive Force Field optimization.....	73
2.4.3. Covariance Matrix Adaptation Evolutionary Strategy.....	74
References.....	75
Chapter 3. External surface models of ZSM-5	
3.1. Introduction.....	77
3.2. Computational details.....	81
3.3. Stability Ranking of Silicalite-1 Surfaces: The Bulk Cleavage Approach.....	83
3.4. Stability Ranking of Silicalite-1 Surfaces: The Precursor Growth Approach.....	85
3.5. Stability of Aluminum Containing Surfaces: Diversity of Sites.....	88
3.5.1. Preliminary Investigation: Thermodynamic Sitting of Aluminum for Bulk Framework Sites.....	88
3.5.2. Nature and Stability of Surface Aluminium Sites.....	89
3.5.3. Effect of the Si/Al Ratio.....	90
3.6. Thermal Stability: Hydration and Dehydration Properties.....	91
3.7. Brønsted and Lewis Acidity of Surface Sites.....	94
3.8. Conclusions.....	97
References.....	99
Chapter 4. Spectroscopic Expression of the External Sites of H-ZSM-5	
4.1. Introduction.....	108
4.2. Experimental Methods and Computational Section.....	111
4.2.1. DFT calculations.....	111
4.2.2. Samples and general characterization.....	112
4.2.3. Infrared spectroscopy.....	113
4.2.4. Nuclear Magnetic Resonance.....	113
4.3. Results and Discussion.....	114
4.3.1. Surface OH groups calculated by DFT.....	114
4.3.2. Main characteristics of the two zeolite samples.....	115
4.3.3. Infrared feature of surface groups.....	117
4.3.3.1. General features.....	117
4.3.3.2. Contributions close to $3610\text{ cm}^{-1}$ .....	120
4.3.3.3. Contributions between $3750$ and $3720\text{ cm}^{-1}$ .....	120
4.3.3.4. Contributions in the $3700 - 3660\text{ cm}^{-1}$ range.....	122

## Table of content

4.3.3.5. Signal at 3780 cm <sup>-1</sup> .....	122
4.3.3.6. Broad contribution between 3700 and 2800 cm <sup>-1</sup> .....	122
4.3.3.7. Combination modes and bending zone.....	123
4.3.3.8. Quantitative analysis: impact of crystal size and of temperature .....	123
4.3.4. <sup>1</sup> H NMR feature of surface groups .....	125
4.3.4.1. General feature .....	125
4.3.4.2. Signal close to 4 ppm .....	127
4.3.4.3. Signal close to 2.6 ppm .....	128
4.3.4.4. Signals below 2.5 ppm .....	129
4.3.4.5. Broad signal at higher chemical shifts.....	130
4.3.4.6. Decomposition of the spectra, analysis of crystal size effects.....	130
4.3.4.7. 2D NMR: assessing proximities .....	130
4.4. Conclusion.....	134
References .....	135
Chapter 5. Interaction of the acid sites with probe molecules and simple models of binder components	
5.1. Acidity of the aluminated sites .....	143
5.1.1. Brønsted Acid Sites .....	144
5.1.1.1. Pyridine adsorption.....	144
5.1.1.2. 2,6-ditertbutylpyridine adsorption .....	147
5.1.2. Lewis Acid Sites.....	148
5.1.2.1. Pyridine adsorption.....	148
5.1.2.2. 2,6-ditertbutylpyridine adsorption.....	150
5.1.3. Vibrational analysis of Brønsted and Lewis acid sites.....	150
5.1.4. Comparison of calculated feature with respect to experiments from Demaret et al.....	151
5.2. Sodium poisoning.....	154
5.3. Interaction with monomers representative of the binders .....	157
5.3.1. Monomer adsorption in bulk .....	158
5.3.2. Monomer adsorption on the external surface of H-ZSM-5 .....	160
5.4. Conclusion.....	161
References .....	163
Chapter 6. Optimization of Reactive Force fields for models of Interaction between ZSM-5 and binder	
6.1. Introduction .....	165
6.2. Methodology .....	166
6.2.1. Reactive force field .....	166
6.2.2. Parameterization of ReaxFF .....	166
6.2.3. Parameters optimized .....	167

## Table of content

6.2.4. Training set.....	168
6.2.5. Validation set.....	170
6.3. Results .....	171
6.3.1. H-ZSM-5 cleavage 1 along (100) orientation.....	171
6.3.2. Selection of the initial reactive force field .....	172
6.3.3. Objective function convergence and water desorption.....	173
6.3.4. Error distribution on the training sets for the two best force fields .....	175
6.3.4.1. Distance and angle errors .....	175
6.3.4.2. Hirshfeld charge errors .....	178
6.3.4.1. Energy errors .....	179
6.3.5. Performance of the two optimized force fields on the validation set .....	182
6.3.5.1. Purely silicic surfaces and aluminated zeolite surfaces .....	182
6.3.5.2. $\gamma$ -alumina surfaces and edges .....	183
6.3.5.3. Boehmite surfaces .....	186
6.3.5.4. Various alumino-silicate structures .....	188
6.4. Conclusion.....	189
References .....	190
General Conclusions and Perspectives	
Chapter 3: Supplementary Information	
SI. Variation of the cleavage height for each surface orientation .....	S1
SII. Convergence of the calculated properties as a function of the slab thickness .....	S4
SIII. Surface free energies for the various surfaces as a function of temperature .....	S6
SIII.1. (100) orientation.....	S6
SIII.2. (010) orientation.....	S6
SIII.3. (101) orientation.....	S7
SIII.4. Comparison of surface free energies for the various surfaces as a function of temperature..	S7
SIV. Morphology constructions and comparison with experiments .....	S8
SV. Construction of surface model from the $\text{Si}_{133}$ precursor species .....	S9
SVI. Aluminations energies .....	S10
SVI.1. Aluminations of the bulk sites .....	S10
SVI.2. Aluminations of the surface sites.....	S11
SVII. Surface hydration/dehydration reactions .....	S26
References .....	S33
Chapter 4: Supplementary Information	
SI. Additional structural DFT data .....	S34
SI.1. Surface orientations considered .....	S34

## Table of content

SII. Main characteristics of the two zeolite samples .....	S35
SIII. Additional Infrared data .....	S36
S4. Additional <sup>1</sup> H NMR data.....	S37
SV. Correlation between IR and NMR computational data .....	S42
References .....	S43
Chapter 5: Supplementary Information	
SI. Pyridine adsorption .....	S44
SI.1. Pyridine adsorption on Brønsted Acid Sites .....	S44
SI.2. Experimental results of pyridine adsorption .....	S45
SII. Exchange energy of sodium .....	S46
SIII. Monomer adsorption .....	S47
SIII.1. Monomer adsorption in bulk .....	S47
SIII.2. Monomer adsorption at the external surface .....	S49
References .....	S52
Chapter 6: Supplementary Information	
SI. Inputs for ReaxFF optimization with CMA-ES optimizer.....	S53
SI.1. Starting force fields.....	S53
SI.2. Cma-es.run for CMA-ES optimizers .....	S53
SI.3. Tests on MAXIT criteria.....	S54
SI.4. Params for CMA-ES optimizers .....	S54
SI.5. Trainset.in for CMA-ES optimizers.....	S55
SI.6. Geo file for Tr.1 and Tr2 CMA-ES optimizers.....	S56
SII. Inputs for Validation Sets with CMA-ES optimizer .....	S56
SIII. Analysis of H-ZSM-5 pores' area .....	S56
SIV. Rff1 and Rff2 compositions.....	S56
SIV.1. Rff1 .....	S56
SIV.2. Rff2 .....	S56
SV. Error distribution on the training sets for the two best force fields.....	S57
SV.1. $\gamma$ -alumina edges.....	S57
SV.2. (110) $\gamma$ -alumina surface.....	S58
SV.3. Water molecule desorption on alumina and silicon cluster $\text{Al}(\text{H}_2\text{O})[\text{Si}(\text{OH})_3]_3$ .....	S59
SV.4. Water molecule desorption on aluminated site no. 77 on cleavage 6 of (100) orientation ...	S60
SVI. Error distribution $\gamma$ -alumina edges of the alumina validation sets for the two best force fields. S61	
References .....	S62

## Introduction and Objectives

Zeolites are microporous aluminosilicates crystals which can be used for various industrial processes. They are used in refining and petrochemistry for numerous processes like hydrocracking, hydro isomerization, oligocracking, etc.<sup>1,2</sup> due to their exceptional properties.<sup>3</sup> They are also used for pollution abatement<sup>4-6</sup> and are very promising candidates for biomass conversion.<sup>7</sup> But the zeolites can generally not be used in their powder form. The latter indeed induces technical problems in the catalytic units: an acidity which is too important, the loss of charge for example and issues of mechanical resistances. To overcome these technical problems and to improve the practical use of zeolites in catalytic processes, they are therefore mixed with other components to form bigger objects (millimeter size), which is called shaping. Binders are the main compounds involved in zeolite shaping.

Shaping was not closely looked at so far in academic studies until recently.<sup>8-10</sup> The shaping was considered to play only a role of dilution of acidity and to increase the mechanical resistance. Importantly, some authors revealed that the shaping is not just a linear combination of the properties of the zeolite and the binder, suggesting an interaction between the zeolite and the binder at the origin of new properties. The experimental studies indeed reveal physical impacts (loss of microporosity) and chemical impacts (realumination, sodium poisoning). However, until now no theoretical models have been established to understand these phenomena, nor to propose a atomistic structure for the zeolite/binder interface.

**The objectives of this study is to improve our understanding of the impact of the shaping on the properties of the zeolite and the binders at the atomic scale, thanks to a theoretical approach, combining *ab initio* calculations and reactive force-field simulations.** To this end, we focus on the case of the HZSM-5 zeolite, which was the object of several experimental investigations with respect to shaping, in particular in the context of the thesis of Coralie Demaret (2016-2019).<sup>11</sup>

A first step towards the elucidation of the interaction between the binder and the zeolite is the understanding of the structure and acidity of the external surface of zeolites, which was also poorly investigated in the past from a computational point of view.<sup>12</sup> Experimental information is however available. In this work, such models are developed and their spectroscopic features (infrared - IR, Nuclear Magnetic Resonance - NMR) are compared with experiments. The strength of their interaction with basic probe molecules is then simulated. Then, interaction with compounds representative of binders, at increasing levels of complexity, will be addressed.

Chapter 1 reviews previous studies conducted on zeolites (more particularly ZSM-5 - MFI type zeolite) and their external surface. Also, the zeolite shaping and its impact on zeolite properties are detailed. The bibliography on the theoretical models of zeolites and zeolite surfaces will be also explored.

Chapter 2 concerns the theoretical methodology and the computational tools which will be used to establish our model. In a first place, Density Functional Theory (DFT) which is an *ab initio* calculation method is detailed. DFT allows to conduct different kind of calculations

to highlight crucial information about the studied systems: geometry optimizations (to find the geometries of minima on the potential energy surface), vibrational frequencies calculations (to highlight the the vibrational frequencies of part of the structures), and linear response approach (for the calculation of NMR chemical shifts). In a second place, reactive force field model will be used with the objective to describe larger models of zeolite/binder interactions than what DFT allows. The application of such reactive force fields is described in comparison with DFT. The reactive force field optimization method with Covariance Matrix Adaptation Evolutionary Strategy (CMA-ES) is described.

Chapter 3 describes the periodic DFT simulation on the ZSM-5 external surface through an article written and published in the context of this PhD and entitled: “Environment, Stability, and Acidity of External Surface Sites of Silicalite-1 and ZSM-5 Micro and Nano Slabs, Sheets, and Crystals” (doi: 10.1021/acscatal.9b05103 and written by L. Treps, A. Gomez, T. de Bruin, and C. Chizallet).

Chapter 4 analyzes the spectroscopic features calculated with ab initio methods in comparison with experimental data which were obtained in the context of the thesis of C. Demaret.<sup>11</sup> This chapter is composed of an article that will be submitted soon about the spectroscopy description (FT-IR and NMR) of surface groups with hydrogen atoms entitled: “Spectroscopic Expression of the External Surface Sites of H-ZSM-5” (written by L. Treps, C. Demaret, D. Wissler, B. Harbuzaru, A. Méthivier, E. Guillon, D. Benedis, A. Gomez, T. de Bruin, M. Rivallan, L. Catita, A. Lesage, and C. Chizallet).

Chapter 5 is composed of different sections describing the interaction of H-ZSM-5 (bulk and external surfaces) with molecules. First, the interaction with pyridine and 2,6-ditertbutylpyridine which are also the experimental acid sites probe molecules is studied and analyzed with DFT models. Second, sodium adsorption on various surfaces of binders and H-ZSM-5 are compared to understand the origin of the experimental observation of zeolite poisoning with sodium. Third, the interaction of H-ZSM-5 surface and bulk with monomers of binders,  $\text{Al}(\text{OH})_3\text{H}_2\text{O}$  and  $\text{Si}(\text{OH})_4$ , are studied in detail.

And finally, Chapter 6 describes the optimization of reactive force fields. There is currently no reactive force fields adapted to describe systems including H-ZSM-5 and binders. Using the CMA-ES optimization method, initial reactive force fields developed by different groups,<sup>13–15</sup> are reoptimized against our reference DFT data, and validated on a set of complementary geometries to enhance and understand their performance. The use of these new generated force fields builds on the results reported in chapter 3 and 5 and opens short- and long-term perspectives for the simulation of binder/zeolite interfaces using larger and more representative models.



## References

- (1) Marcilly, C.; Decroocq, D. *Catalyse acido-basique: Application au raffinage et à la pétrochimie*; Publications de l'Institut français du pétrole; Ed. Technip: Paris, 2003.
- (2) Vermeiren, W.; Gilson, J.-P. Impact of Zeolites on the Petroleum and Petrochemical Industry. *Top. Catal.* **2009**, *52*, 1131–1161.
- (3) Vogt, E. T. C.; Weckhuysen, B. M. Fluid catalytic cracking: Recent developments on the grand old lady of zeolite catalysis. *Chem. Soc. Rev.* **2015**, *44*, 7342–7370.
- (4) Deka, U.; Lezcano-Gonzalez, I.; Weckhuysen, B. M.; Beale, A. M. Local Environment and Nature of Cu Active Sites in Zeolite-Based Catalysts for the Selective Catalytic Reduction of NO<sub>x</sub>. *ACS Catal.* **2013**, *3*, 413–427.
- (5) Borfecchia, E.; Beato, P.; Svelle, S.; Olsbye, U.; Lamberti, C.; Bordiga, S. Cu-CHA - a model system for applied selective redox catalysis. *Chem. Soc. Rev.* **2018**, *47*, 8097–8133.
- (6) Paolucci, C.; Khurana, I.; Parekh, A. A.; Li, S.; Shih, A. J.; Li, H.; Di Iorio, J. R.; Albarracin-Caballero, J. D.; Yezerets, A.; Miller, J. T. *et al.* Dynamic multinuclear sites formed by mobilized copper ions in NO<sub>x</sub> selective catalytic reduction. *Science* **2017**, *357*, 898–903.
- (7) Ennaert, T.; van Aelst, J.; Dijkmans, J.; Clercq, R. de; Schutyser, W.; Dusselier, M.; Verboekend, D.; Sels, B. F. Potential and challenges of zeolite chemistry in the catalytic conversion of biomass. *Chem. Soc. Rev.* **2016**, *45*, 584–611.
- (8) Hargreaves, J. S. J.; Munnoch, A. L. A survey of the influence of binders in zeolite catalysis. *Catal. Sci. Technol.* **2013**, *3*, 1165.
- (9) Michels, N.-L.; Mitchell, S.; Pérez-Ramírez, J. Effects of Binders on the Performance of Shaped Hierarchical MFI Zeolites in Methanol-to-Hydrocarbons. *ACS Catal.* **2014**, *4*, 2409–2417.
- (10) Mitchell, S.; Michels, N.-L.; Pérez-Ramírez, J. From powder to technical body: the undervalued science of catalyst scale up. *Chem. Soc. Rev.* **2013**, *42*, 6094–6112.
- (11) Demaret, C. Mise en forme de zéolithes : Contrôle des propriétés acides des zéolithes et description de l'interface zéolithe / liant, Thèse de doctorat, IFPEN, 2019.
- (12) Chizallet, C. Toward the Atomic Scale Simulation of Intricate Acidic Aluminosilicate Catalysts. *ACS Catal.* **2020**, *10*, 5579–5601.
- (13) Bai, C.; Liu, L.; Sun, H. Molecular Dynamics Simulations of Methanol to Olefin Reactions in HZSM-5 Zeolite Using a ReaxFF Force Field. *J. Phys. Chem. C* **2012**, *116*, 7029–7039.
- (14) Pitman, M. C.; Duin, A. C. T. van. Dynamics of confined reactive water in smectite clay-zeolite composites. *Journal of the American Chemical Society* **2012**, *134*, 3042–3053.
- (15) Joshi, K. L.; van Duin, A. C. T. Molecular Dynamics Study on the Influence of Additives on the High-Temperature Structural and Acidic Properties of ZSM-5 Zeolite. *Energy Fuels* **2013**, *27*, 4481–4488.

# Chapter 1. State of the art

## 1.1. Zeolites

### 1.1.1. Definition and structural features

Zeolites are microporous aluminosilicates with a well-defined crystalline structure. They are generally composed of numerous cavities which are connected one to another with channels of various dimensions. They also can be described as a rigid three-dimensional network of  $TO_4$  tetrahedra (where T is mostly Si or Al, and sometimes B, Ge, Ga, Ti or Fe) as presented in Figure 1. These tetrahedra are linked at their corner via a common oxygen atom to form a secondary building unit (SBU) for example sodalite unit or pentasil unit. Following this building rule it comes that the net formula for the tetrahedral units in a common zeolite are  $SiO_2$  and  $AlO_2^-$ . There is a negative charge residue in each tetrahedron which has aluminum in the center. These charges are compensated by the presence of various cation.<sup>1</sup> In general the chaining of  $SiO_4$  and  $AlO_4$  tetrahedra follows the empiric law of Loewenstein.<sup>2</sup> This law says that two  $AlO_4$  tetrahedra cannot be linked inside the structure. It comes that the chemical composition of a zeolite can be represented by the Equation 1.

$$M_{x/m}^{m+} [(AlO_2^-)_x (SiO_2)_y] \quad \text{Equation 1}$$

where M is a cation with the charge  $m$ ,  $(x + y)$  is the number of tetrahedra per crystallographic unit cell. The  $y/x$  is the so-called silicon/aluminum ratio (Si/Al).  $y/x \geq 1$  is a consequence of the Loewenstein's rule which forbids Al-O-Al linkages.

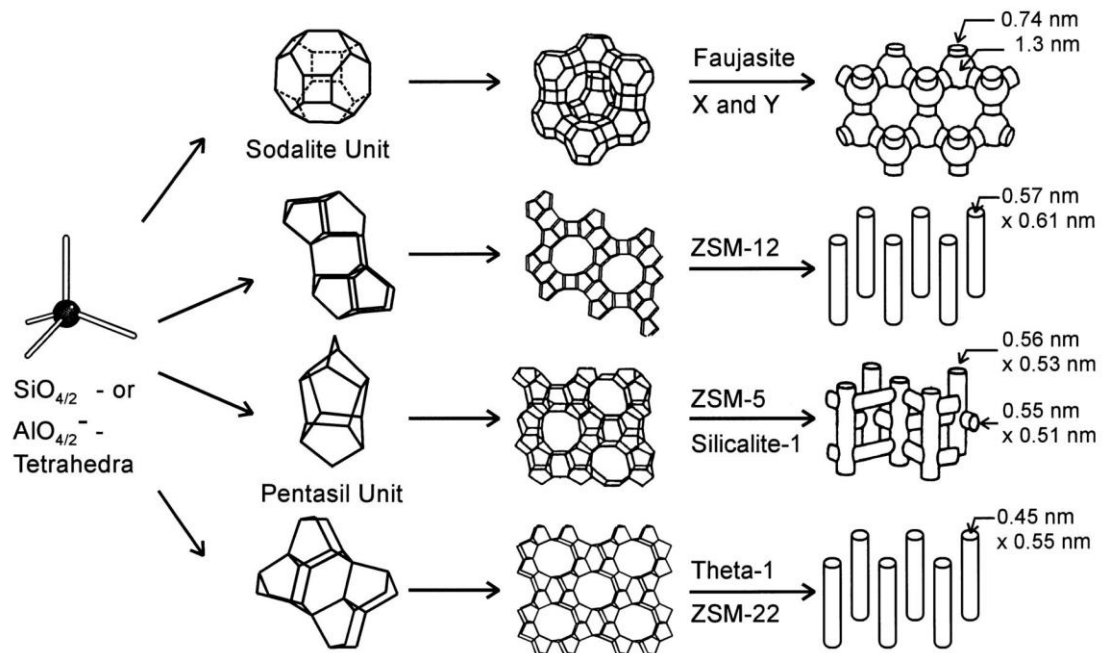


**Figure 1.** Structures of four selected zeolites (from top to bottom: faujasite or zeolites X, Y; zeolite ZSM-12; zeolite ZSM-5 or silicalite-1; zeolite Theta-1 or ZSM-22) and their micropore systems and dimensions.<sup>3</sup>

The SBUs, composed by a definite number of tetrahedra, are combined with a precise symmetry for each zeolite and generate a regular microporous network. Zeolites are classified according to their pore sizes and some representative example are presented in Figure 1: zeolites with small pores have 8 membered ring (8MR) pores which is equivalent to a diameter in between 0.30 and 0.45 nm like Theta-1 or ZSM-22; zeolites with medium pores have 10 membered ring (10MR) pores which is equivalent to a diameter in between 0.45 and 0.60 nm like ZSM-2, ZSM-5 and Silicalite-1 and zeolites with large pores have 12 membered ring (12MR) or more pores which is equivalent to a diameter larger than 0.65 nm like faujasite X and Y.

These are non-exhaustive examples: more than 230 structure of zeolite (natural and synthetic) have been identified and listed on the International Zeolite Association (IZA) website.<sup>4</sup> IZA attributes to each structure a code composed of three letters like FAU for faujasite X and Y or MFI for ZSM-5. All of these species offer a wide range of zeolite typical characteristics, Si/Al ratio, specific surface, pore size, nature of compensating cations which allow the use of zeolites for numerous and various applications.

### 1.1.2. Applications of Zeolites

The intrinsic property of ion-exchange is due to the substitution of silica in the zeolite structure by divalent or trivalent elements.<sup>5</sup> Consequently the induced negative charge arises on the framework of the zeolite. The presence of cations within the pores allows the neutralization of the zeolite. This property can be indirectly used in catalysis for example but can also be directly exploited in several applications. These include water softening in detergents; zeolites can selectively adsorb  $\text{Ca}^{2+}$  and  $\text{Mg}^{2+}$ , which are both represented in Figure 2 c by cation 1 which is maintained in the zeolite structure contrary to cation 2 which represents all the initial compensating cation inside the zeolite structure. Zeolites are more environment friendly than phosphated detergents and their usage allowed to reduce the pollution and the phosphorus concentration in Lake Biwa in Japan for example.<sup>6,7</sup> Another application is the removal of certain radio-nuclei from low and medium level nuclear waste. The principal radioactive components of nuclear waste, typically  $^{90}\text{Sr}^{2+}$  and  $^{137}\text{Cs}^{+}$ , can be encapsulated by mordenite (MOR) or clinoptilolite (HEU).<sup>8,9</sup> Zeolites are also commonly used to remove ammonia and ammonium ions from municipal and agricultural wastewater and as animal food supplementation. Choosing properly the nature and the quantity of cations can change the diameter and the shape of the pores which could modify the adsorption properties of zeolites.

The confinement is a major effect that enhances the interactions with adsorbed molecules. These properties qualify zeolite into microporous adsorbents and are used for various application in everyday life; dehydration and purification of liquids and gas. One major domain of zeolite adsorption is the  $\text{H}_2\text{S}$  sorption where Na-X (FAU), Na-A(LTA) and Ca-A(LTA) are efficient.<sup>10</sup> For example FAU are used for desulfurization of biogas.<sup>11-14</sup>

Zeolite are also powerful molecular sieve; they are useful for the separation of molecules in gaseous or liquid phases. The porosity of zeolite is almost constant witch is a

criterion of selectivity at the entrance of the pores or within the pores. When molecules enter the zeolite network, the interaction between the zeolite framework and the molecules is also selective. Zeolites exhibiting the CHA framework can separate both  $\text{H}_2\text{S}$  and  $\text{CO}_2$  acid gases from methane<sup>15</sup> and zeolites exhibiting the LTA framework are well-known for the processes of separation of n-paraffins.<sup>10</sup> It is also possible to separate meta-xylene from para-xylene with H-ZSM-5 (MFI framework) as represented in Figure 2 b.<sup>16,17</sup>

Zeolites are also active as catalysts. A catalyst is defined as a substance added in a process to increase the rate of the reaction but which is not consumed in the catalyzed reaction and can continue to act repeatedly. Zeolite are more precisely heterogeneous catalysts and act in a different phase than the reactant. Petroleum refining makes use of zeolites for separation processes and chemical transformation as represented in Figure 2 a.<sup>1</sup> The reactions occur on the active sites on the internal (microporosity surface) and external surface of zeolites (pore mouth catalysis concept). We will be focusing on the case of catalysis by protonic zeolites (proton as exchange cation) in this work.

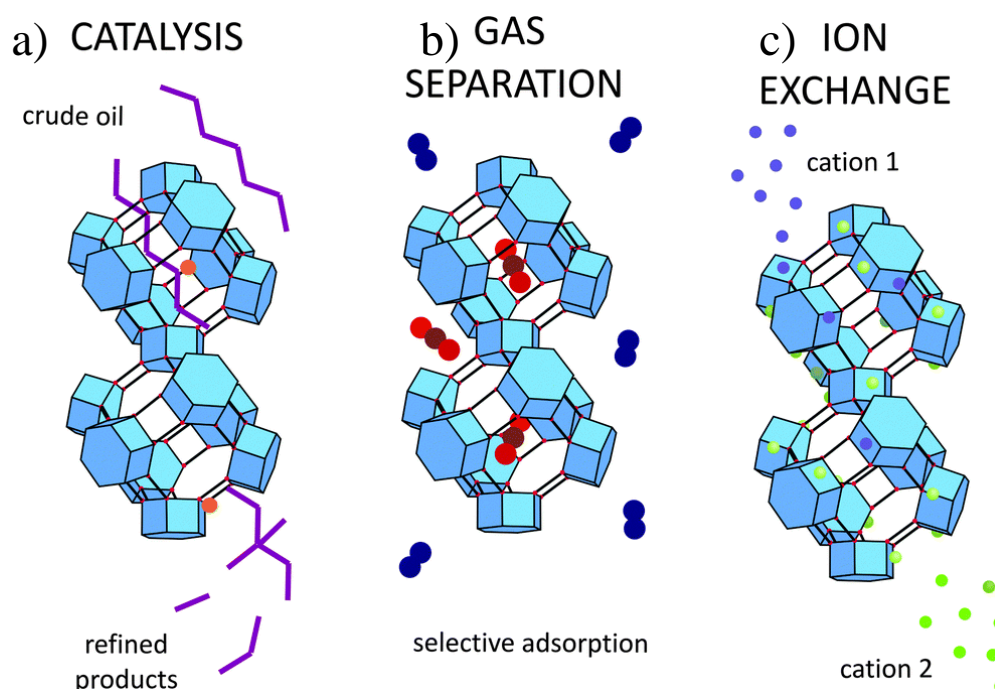


**Figure 2.** Main applications of zeolites<sup>18</sup>

### 1.1.3. Acidity

The acidity of zeolites is generally explained with the two most famous theories, by Brønsted-Lowry<sup>19–22</sup> and Lewis.<sup>23</sup> A Brønsted-Lowry acid is a proton donor whereas a base is a proton acceptor. In the second theory, an acid is an electron-pair acceptor and a base is an electron base donor. A Lewis acid tends to complete its valence band to get the noble gas electronic configuration. Some hydroxyls groups which tend to enhance the acidity in zeolite and on the surface of zeolite are represented on Figure 3. They can be directly responsible of the Brønsted acidity and but are not directly involved in Lewis acidity.

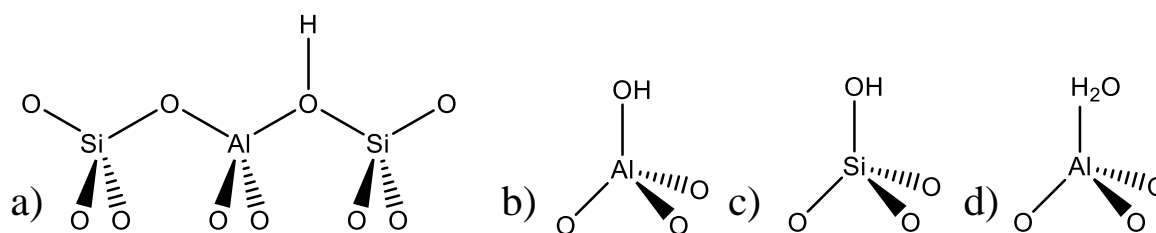


**Figure 3.** Brønsted acid sites in zeolites a) Al-OH-Si ; b) Al-OH ; c) Si-OH ; d) Al-(H<sub>2</sub>O)<sup>24,25</sup>

The Brønsted strength of these acid sites are not equal. The presence of tetrahedral aluminum instead of tetrahedral silica creates a negative charge which is compensated by a compensating hydrogen. The main Brønsted acid sites (BAS) are the bridging OH groups (Figure 3 a) formed by the proton acting as compensation cation. The silanol Si-OH (Figure 3 c) are generally non considered as a Brønsted acid site<sup>24</sup> and are considered to exhibit a similar acidity as the Al-OH sites (Figure 3 b) which are weak acid sites and present few or no catalytic activity.<sup>26</sup> Molecular ab initio modelling reveals that Al-(H<sub>2</sub>O) sites may exist at the external surface of zeolite Beta (Figure 3 d), and have a weak acidity<sup>25</sup> also compared to the bridging Al-OH-Si which are the most acidic sites and often the only ones to have an sufficient catalytic activity for chemical reactions.<sup>26</sup>

The sites considered in the literature as Lewis acid site (LAS) are the aluminum atoms tri-coordinated in the bulk of the zeolite (defects) or at the zeolite surface<sup>24,25</sup> as shown on Figure 4, a. The latter are expected to be formed upon Al-(H<sub>2</sub>O) Brønsted acid sites (Figure 3, d) dehydration or ion exchange. On the surface, aluminum oxides (AlO<sup>+</sup> or Al<sub>x</sub>O<sub>y</sub><sup>n+</sup>) in extra framework positions are electrons acceptors, Figure 4, b.<sup>27,28</sup> The compensating cations can also be electrons acceptors Figure 4, c but their strength is not very important and the subject is still debated.<sup>24</sup> Most of the acid catalysis performed with zeolite have been attributed to the Brønsted acid sites.<sup>29-32</sup> However, it has been showed that the Lewis acid sites can also play an active role in the catalytic activity of zeolites. The Lewis acid sites allow to increase the strength of Brønsted acid sites in zeolites, this phenomenon is called the synergic effect.<sup>33</sup> The study of their own reactivity has most recently been the subject of a considerable interest.<sup>34-37</sup>

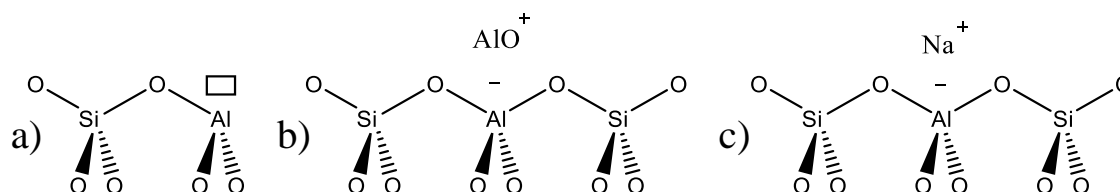


**Figure 4.** Lewis acid sites in zeolites a) Tri-coordinated Al ; b) aluminum oxides extra framework ; c) compensating cation<sup>24</sup>

The strength of the different sites in zeolite and at their surface depends on their nature and their environment. It is defined as the equilibrium constant of the acid/base reaction. Following the Lowenstein rule, two tetrahedral aluminum cannot be first neighbors but they can be second neighbors if they are separated by a tetrahedral silicon. This proximity is considered to be an important impact factor on the acid strength.<sup>38</sup> The more tetrahedral aluminum there are in the structure, the weaker the electronegativity of the structure and the

weaker the expected charge of the proton. It induces that the strength of the Brønsted acid sites increase with an important Si/Al ratio.<sup>39</sup> This ratio is a key factor but is also an average on all the zeolite structure. The distribution of aluminum can be heterogeneous and this cannot be easily predicted and controlled for any framework, despite intensive studies devoted to the identification of the location of sites occupied by aluminum in the framework.<sup>40–47</sup>

#### 1.1.4. Catalytic activity

The activity of the zeolite is widely studied and the comparison can be made between the activity of the internal surface, surface of the pores inside the zeolite framework, and the activity of the external surface. The internal activity depends on the confinement effects in zeolite. This confinement can induce a shape selectivity as it was shown for hydrocracking reactions (demonstrated with force field simulations).<sup>48</sup> The diffusion of the reactants, the sterical hindrance of the transition states and the diffusion of products depend highly of this shape selectivity.<sup>49</sup>

The external surface activity is expected to be different from the internal surface activity because of changes in the topology between the both surface. The catalysis of long-alkane reactions by acid sites located at the external surface of small pore zeolites (like ZSM-22) is called “pore-mouth catalysis” or “key-lock catalysis”.<sup>50,51</sup> The name depends on the number of acid sites involved into the reaction (Figure 5).

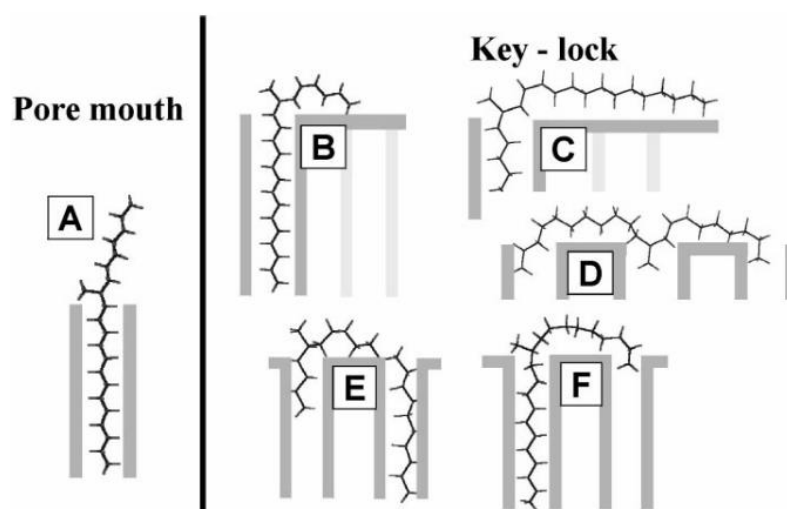


**Figure 5.** Favorable adsorption configurations of multibranched C<sub>21</sub> hydrocarbons molecules on ZSM-22.<sup>51</sup>

The ratio of external surface over internal surface increase with small zeolite particles (below 100 nm). The activity of the external surface is supposed to take an important role in the general activity of small zeolite particles. Mintova *et al.* prepared nanocrystals of faujasite (around 10 pm) where the activity was mainly located at the external surface.<sup>52</sup> At the external surface the nature of the acid site and the confinement effect is necessarily changed. The understanding of the pore mouth activity and the nature of its acid sites is crucial to

understand the activity of the external surface of zeolites. More particularly for the zeolite of our interest, the ZSM-5 (MFI type zeolite), which can be concerned by this phenomenon.<sup>53</sup>

### 1.1.5. ZSM-5

ZSM-5 (Zeolite Socony Mobil-5) is a zeolite that was discovered and multi-patented by Mobil Oil Corporation in 1969.<sup>54-56</sup> It is a very well-known and used catalyst in the petrochemical industry and more particularly for the xylene isomerization reaction, aromatic alkylation reaction and dewaxing reaction.

The first synthesis proposed led to only small particles (around 20  $\mu\text{m}$ ) which induced difficulties to use X-ray diffraction method to describe them.<sup>57,58</sup> The classical morphology presented by these groups of these particles is the rounded-boat, Figure 6 a, but deeper and more recent investigations show that the small particle can have other forms: the coffin-shaped crystals, Figure 6 b, and the octagon-shaped crystals, Figure 6 c.<sup>59</sup>

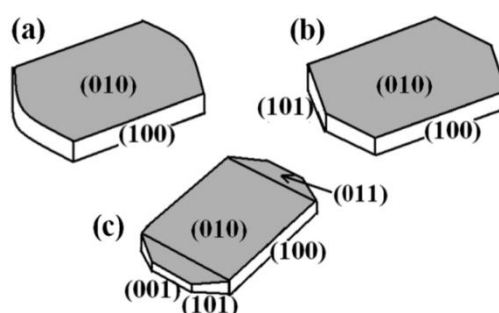


**Figure 6.** Schematic representation of MFI zeolite crystal shape for small particles: (a) rounded-boat crystal, (b) coffin-shaped crystal, (c) octagon-shaped crystal.<sup>59</sup>

Price *et al.* suggested the presence of a complex overgrown structure of MFI-type zeolite.<sup>60</sup> They studied the crystallization of a fluoride silicalite precursor which has the same topology as ZSM-5 zeolite. On the basis of X-ray diffraction results, they suggested that larger crystals of ZSM-5 could be synthesized with a non mono crystalline intergrowth structure. With a synthesis based on previous studies,<sup>61,62</sup> Lermer *et al* were the first to synthesize suitably large crystals of ZSM-5 (up to 280  $\mu\text{m}$ ).<sup>63</sup> They found two kinds of ZSM-5 crystals: an unusual one with a pyramidal-shape, and the more classical coffin-shape crystals. The first one exposes five different surfaces (analyzed with energy dispersive spectroscopy EDS) that can be seen in Figure 7: 100 (base of the pyramid),  $\bar{1}\bar{2}0$ ,  $\bar{1}20$ ,  $\bar{3}02$  and  $30\bar{2}$ . The description of the coffin-shape crystal was not clear at that stage, Figure 8. Koegler *et al* used optical and electron microscopy to illustrate and to confirm that the coffin-shape crystal is the result of the crystallization of ZSM-5 from its primary form (small rounded-boat crystals) and has a non mono crystalline intergrowth structure as predicted by Price *et al.*<sup>64</sup>



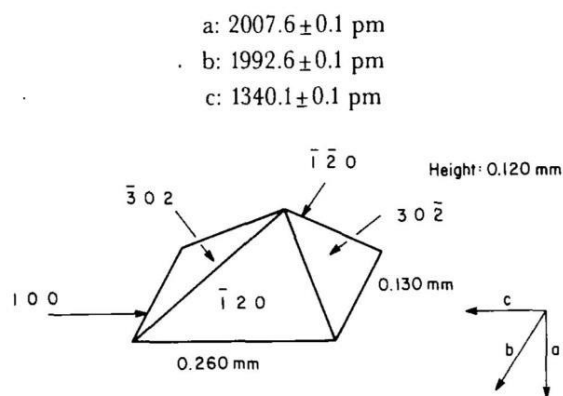


**Figure 7.** Measurements of the pyramidal-shaped crystal studied showing the indexed faces.<sup>63</sup>

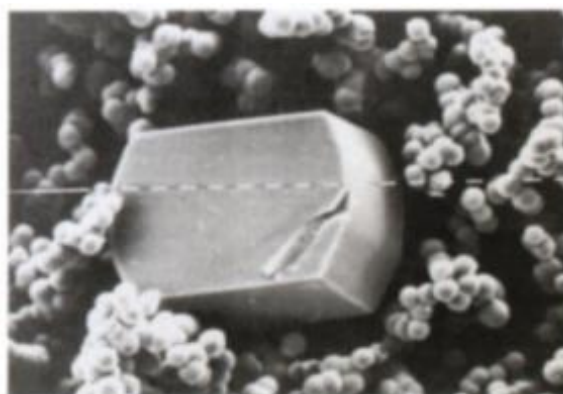


**Figure 8.** Coffin particle of ZSM-5, surrounded by analcime and alpha-quartz. Scale - bar =  $10\mu\text{m}$ .<sup>63</sup>

From these observations, many studies were performed to determine the decomposition of large coffin-shape crystals of ZSM-5. A first group of studies promotes the 2 component coffin-shape crystal, presented on Figure 9 b, based on polarized optic microscopy (where an hourglass pattern can be discerned especially when polarized light is used).<sup>65</sup> This work is the first clearly indicating the nature of the surfaces of the coffin-shapes large crystal surfaces as presented in Figure 8. But the 2 component model has been challenged by various analysis methods suggesting a 3 component model for coffin-shape crystals of ZSM-5. AFM,<sup>66</sup>  $\text{I}_2$  adsorption,<sup>67</sup> interference microscopy<sup>68</sup> and polarized infrared microscopy<sup>69</sup> did not allow for unambiguous choice between the two models. Even then when Weckhuysen *et al* followed the inside activity via the formation of styrene oligomer with polarized light optical microscopy,<sup>70,71</sup> it seems obvious that the model depends on the molecular dimensions and the selected reagents. Roeffaers *et al.* tried to differentiate the two models by using previous characterizations (AFM, SEM, ...) and fluorescent probes on different batches of large ZSM-5.<sup>72</sup> In terms of external surfaces, the DAMPI (4-(4-diethylaminostyryl)-1-methylpyridinium iodide, is a probe which is able to “show” the (010) faces (where the straight pores are perpendicular to the surface). The fluorescence experiments showed different results on the samples. Some coffins expose (010) surfaces on two sides and (100) (perpendicular to the sinusoidal channels) on the two others. Some other coffins exposed two (100) surfaces, whereas (010) surfaces are partially recovered by another crystal. This surface expose a (100) surface, which thus dominates around the crystal. The presence of (100) and (010) surfaces is



most in favor of the 3 component model as presented in Figure 9 b. But the presence of multiples default induces interrogation about the reliability of this model.

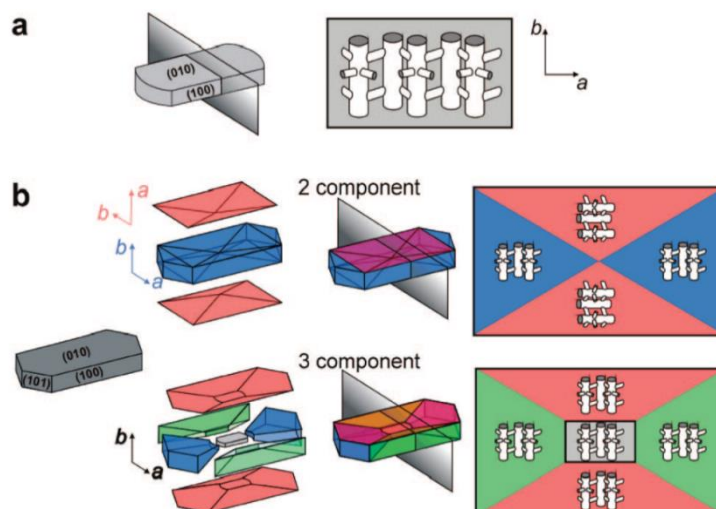


**Figure 9.** Schematic representation of MFI zeolite crystallography: (a) pore organization in rounded-boat crystals; (b) the 2- and 3-component models for coffin-shaped crystals.<sup>72</sup>

Weckhuysen *et al.* proposed another model of the internal structure of the coffins; they recorded confocal fluorescence images and SEM and diffraction patterns after ion-beam milling halfway through the crystals' thickness and measured two diffraction patterns (orange and green on Figure 10).<sup>73</sup> The proposed structure seems more complex than the previous ones (the crystals are composed of 6 to 11 different elements), but a common feature of that the most exposed surface is the (100) on the long sides and (101) on the top and bottom of coffins. This model proposed a decomposition into multiple crystals of all the different shape of large H-ZSM-5 crystals. The bigger crystals C and D up to  $280 \times 130 \times 130 \mu\text{m}^3$ , possess supplementary elements (in orange in the diagonals) which are responsible of great defects in the crystals. The smaller crystals which are the most common and studied ones do not present such important defects. These defect were revealed to be important between all the components which can be very important for the diffusion of molecules into the zeolite framework.

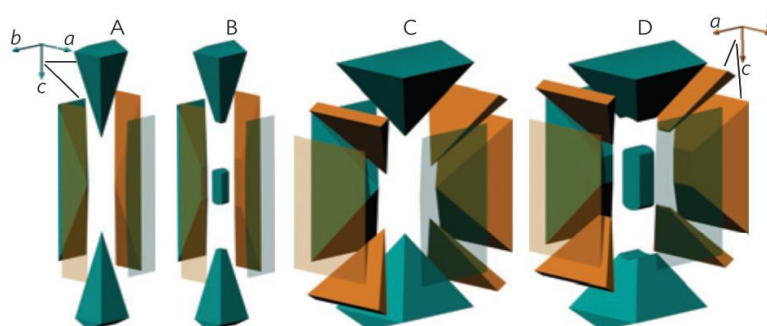


**Figure 10.** Exploded representation of the MFI-type crystals with distinct morphologies and intergrowth structures for crystals A, B, C and D. Subunits differing in their crystallographic orientation, that is, pore geometry, are color coded in green and orange, indicating a  $90^\circ$  rotation over the common crystallographic c axis. The orientation of the crystallographic a, b and c axes is indicated for the different subunits.<sup>73</sup>

The results of Roeffaers *et al.* and Weckhuysen *et al.* seem to be incompatible at first glance, but become interestingly related in the following papers of both groups. Roeffaers *et al.* could show as a surface defects, Figure 11, and use for catalytic activity,<sup>74,75</sup> that the defects are actually more deeply anchored in the coffin, Figure 12.<sup>76</sup> This new model implies that that the major surface exposed is the (100) due to defects (ramp, central defects) growing on the (010) surfaces and exposing a (100) surface. This consideration tends to correspond to the Weckhuysen model (of 3 components), Figure 9 for A and B crystals, but with a interrupt growth of the defect of the surface. This induces that the (010) surface is more present on Roeffaers crystals than on the Weckhuysen ones but these studies finally tend to the same intergrowth crystal structure.<sup>77</sup>

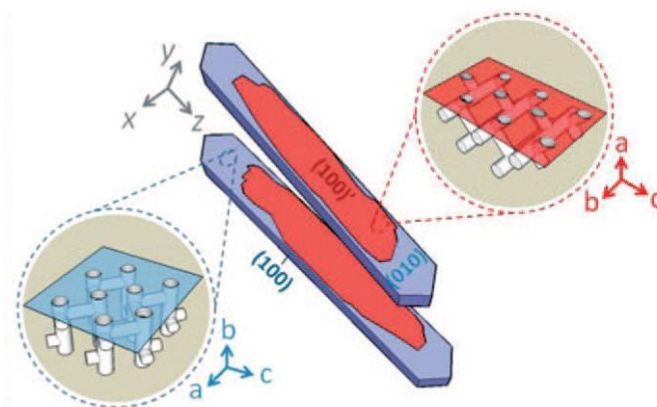


**Figure 11.** Roeffaers representation of the "growth" of a (100) surface over the (010) surface.<sup>74</sup>

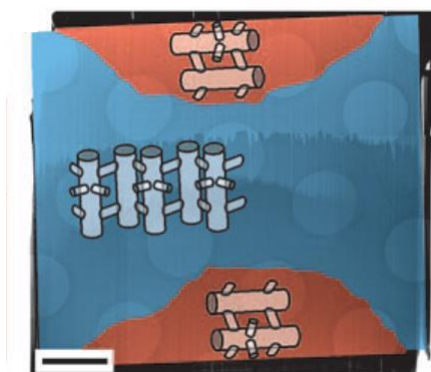


**Figure 12.** Summary of the FIB-TEM observations, with the crystal orientation indicated by color and by a schematic representation of the channel system. Scale bar: 2  $\mu\text{m}$ .<sup>76</sup>

Weckhuysen and Roeffaers groups validate the model A with six subunits presented in Figure 9. The detailed crystallographic structure is represented in Figure 14 along the gable and roof view. The black and blue subunits have the same orientation whereas the red subunits are 90° rotated. They continued to study this model with similar goals: the localization of acid sites, the accessibility of the acid sites and the influence of high temperature treatment on the structure.

These nanocrystal syntheses aim at improving the catalytic activity of ZSM-5 zeolite. First, the particular activity of the pore-mouth has to be enhanced. As it has been shown in section 1.1.4., the reactivity of smaller particles is often more interesting than larger ones. Second, the residence time of molecules inside the zeolite crystal needs to be limited to decrease the mass transfer limitations. These goals can be reached with an increase of the (external surface)/(internal surface) ratio or the (mesoporous surface)/(microporous surface) ratio. Different strategy from the nanocrystals of zeolites are: (i) preparing hierarchical zeolite by introducing meso(macro)porosity in the microporous crystals<sup>78–80</sup> (ii) or preparing hollow zeolite structures,<sup>81</sup> (iii) or obtaining nanosheets of zeolites (thickness less than 10 nm), delaminated and 2D zeolites.<sup>82–84</sup> The different kinds of nanosheets (MFI nanosheets,<sup>83,85</sup> Self-Pillared nanosheets,<sup>86</sup> and thin films grown from nanosheets<sup>87,88</sup> shown on Figure 13), expose mostly (010) surfaces. In some case, seeds are used and are aligned with the (100) surface.<sup>88</sup>

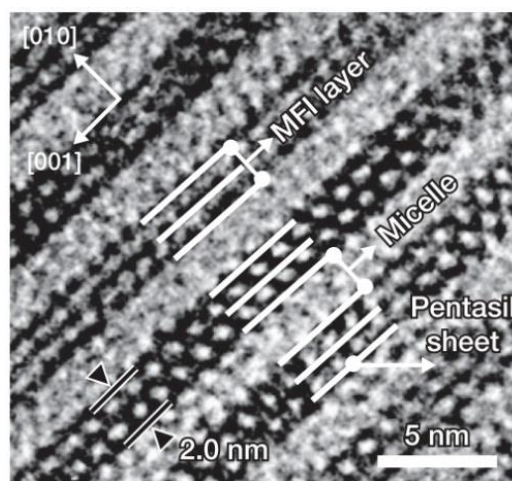


**Figure 13.** TEM of MFI nanosheets from ref <sup>83</sup>

### 1.1.6. Diffusion paths and localization of active sites at the particles scale

The fluorescence microscopy is a major technique to determine the active sites and the pore disposition of zeolite. A review of Roeflaers *et al.* gave a first overview of the different results obtained with this technique.<sup>75</sup> The probe molecule named DAMPI (4-(4-diethylaminostyryl)-1-methylpyridinium iodide) was previously mentioned to selectively visualizes the straight pores, which mostly established the difference between the 2-component and the 3-component particles.<sup>72</sup> The accessibility of probe molecules in the zeolite pore network and structural imperfections, such as cracks, of these two types of large zeolite crystals was evaluated using a series of fluorescent DAMPI-based probe molecules with increasingly bulky alkyl substituents.<sup>89</sup> It showed that the rotated subunits are prone to develop imperfections during crystal growth. The results of the adsorption of the distinct DAMPI-type probes can be quantified by CFM and provide a quantitative measurement of the accessibility of the channel of the crystal depending on the size of the molecules. The results of adsorption for a small DAMPI type molecule is shown in Figure 14.<sup>90</sup> The molecule emits light when its position is parallel to the polarization orientation. The straight pore should be

the most accessible pore. In the roof view, the black component should be full of probe molecule. But it is not the case so the diffusion must be slow event in straight pores. Polarization-dependent CFM measurements suggest that although the cracks and imperfections are responsible for the macro-distribution, the probes are still aligned to the pore system of the crystal. The larger probes tested have the same kind of spectra but with a less important intensity. They are presumably inserted end-on into the zeolite pore mouth, in a “stopcock” fashion.

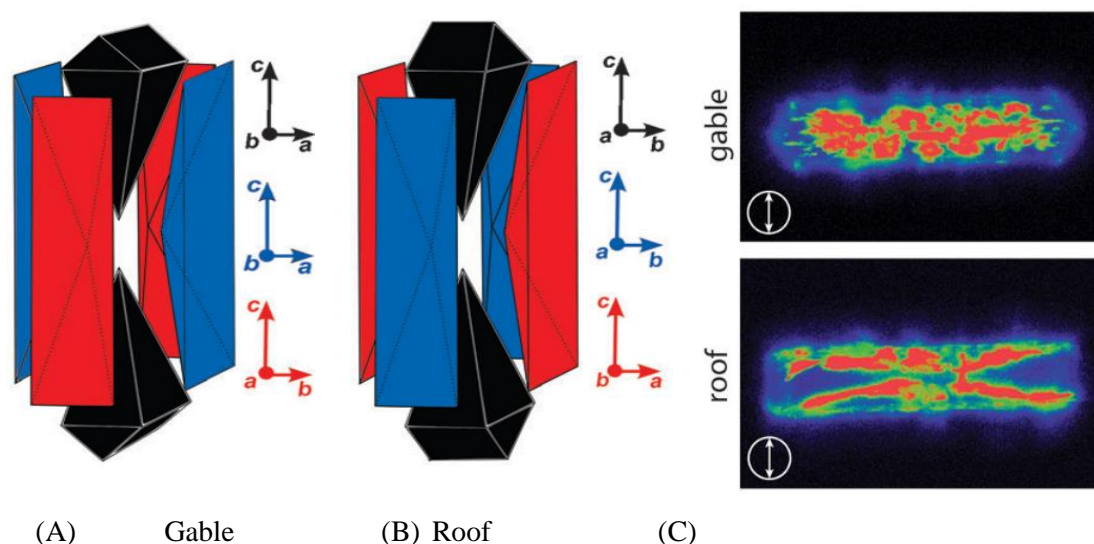


**Figure 14.** Crystallographic structure of the admitted most common H-ZSM-5 crystals as 3-components crystals with components of the same orientation (black and blue) and 90° rotated components (red): (A) gable view; (B) roof view (adapted image from<sup>91</sup>); (C) Fluorescence location of a DAMPI type probe (small) in zeolite MFI crystals in the two possible orientation of zeolite crystals.<sup>90</sup>

The experimental analysis techniques are combined to visualize the complex inside organization of ZSM-5. The fluorescence and the optical transmission microscopy were combined to probe the formation of colored species during the heat-induced template removal process.<sup>92</sup> The decomposition of amine and quaternary ammonium compounds creates products which adsorb visible light but also exhibit a strong light emission. The authors were able to show an interesting overview of the inside structure of many zeolite and more particularly ZSM-5 as presented in Figure 15 a. Fluorescence can be combined to UV-Vis micro spectroscopy to visualize the difference in coke precursor formation during the methanol to olefin (MTO) reaction.<sup>93</sup> It is possible to discriminate the fluorescent aromatic compounds formed inside the micropore and the non-fluorescent graphitic compounds at the outer surface as presented in Figure 15 b.



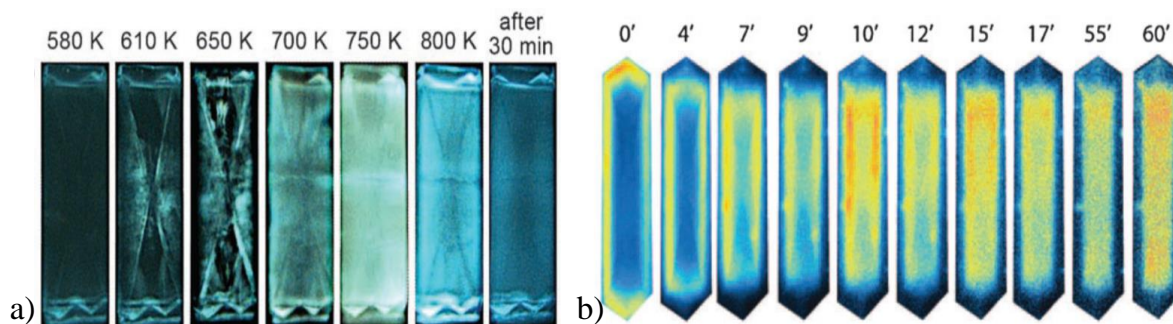


**Figure 15.** a) Fluorescence micrographs of ZSM-5 crystals taken during template removal<sup>92</sup>; b) Fluorescence intensity profiles of H-ZSM-5 crystal during MTO reaction at 660K.<sup>93</sup>

The fluorescence of amine functionalized fluorescent probe (PDI-TEA according to its two main functionalities a perylene diimide core and a trimethylamine-like side chain) reveals the active sites of the zeolite on surfaces.<sup>72</sup> When the probe reacts with the acid site, the fluorescence appears. Whereas when the probe is free the tertiary amine functions quench the fluorescence of the perylene diimide chromophores through photo induced electron transfer.<sup>94</sup> The acid sites of the ZSM-5 are present on all the surfaces of the coffins-shaped crystals. The catalytic activity of the zeolite can also be observed through the acid-catalyzed oligomerization of 4-fluorostyrene. In a first time it is used as a time and space resolver for the catalytic reaction in and over the ZSM-5 crystals. Roeffaers *et al.* highlight the presence of diffusional barriers for the catalytic activity of the ZSM-5.<sup>95</sup> Figure 16 A shows that initially the reaction takes place at the outer surface of the zeolite, on the (100) surfaces of ZSM-5 blue components, Figure 14. The products' emission of light, which is showed here as an intensity, highlights that reaction mainly takes place in the black components of zeolite, Figure 14. As presented in Figure 16 B, the products of the reaction can emit in different part of the visible light. The length of the product determines in which part of the visible light they emit, an increase of the length is associated to a red-shift. The longest products are located into the black components of ZSM-5, which are the most accessible ones due to the straight pores perpendicular to the surface, whereas smaller products can be found in the all structure. Weckhuysen *et al.* use the same reaction and distinguish two products: the linear dimer and the cyclic dimer, which are specific to straight and sinusoidal pores respectively.<sup>77</sup> This work comfort the crystallinity established of the ZSM-5 crystals. The authors also studied the degradation of the zeolite framework upon post synthesis steam treatment.

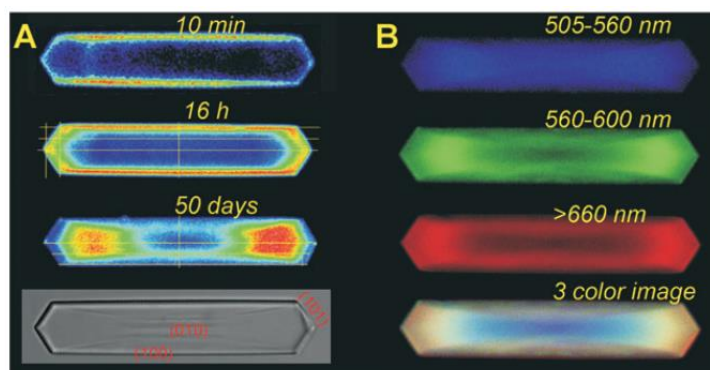


**Figure 16.** Confocal microscopic imaging of furfuryl alcohol condensation catalysed by individual ZSM-5 zeolite crystals. (A) Fluorescence intensity (false color) in ZSM-5 crystals after 10 min, 16 h and 50 days of reaction with corresponding optical transmission image (gray scale). (B) Multicolor imaging of reaction products from furfuryl alcohol in ZSM-5 after prolonged exposure: blue channel, 488 nm excitation and emission from 505 to 560 nm; green channel, 543 nm excitation and emission from 560 to 660 nm; red channel, 633 nm excitation and emission higher than 660 nm. The different colors refer to different furfuryl alcohol oligomers; the longer the oligomer, the more red-shifted its emission spectrum.<sup>95</sup>

### 1.1.7. Characterization of the active sites

All the previous characterizations are used to study the catalytic activity of the ZSM-5. A recent study was able to distinguish the activity of different member of the population of zeolite crystals.<sup>96</sup> It proves that the ZSM-5 sample can be heterogeneously dispersed in their catalytic activity through the distribution of their active sites. In the same spirit, a previous study focusses on the catalytic activity in the presence of sodium. The sodium poison the active sites of the zeolites and this study highlight the proportion need to deactivate zeolite including ZSM-5.<sup>97</sup> The study of the impact on catalytic activity is a main subject for zeolite and even more in this work where the zeolite is considered in contact with the binders which are used for industrial reactors. The catalytic activity is multi-factorial dependent and the impact on each characteristics of the zeolites can be crucial.

The acid site localization is made, in the previous paragraph, at the crystals scale. At the atomic scale, identifying the location of the acid sites requires the knowledge of the crystallographic location of aluminum atoms. The previous sections locate the active sites depending on the reaction and their accessibility. An 80's study of the ZSM-5 structure, locate the aluminum at the particle scale with X-ray micrograph.<sup>62</sup> The particles have a Si/Al ratio between 50 and 100 and the study highlights that the aluminum are located at the external surface (or close to it) and in the rim (which corresponds to the black compounds of the structure as established latter and presented in Figure 14. The high reactivity of these two positions does not only depends on the accessibility of the acid sites but is also due to the heterogeneous distribution of the acid site in the zeolite particles. The specific localization of the aluminum in the particle is confirmed by a more recent study of Weckhuysen *et al.* who used synchrotron-based micro X-ray diffraction imaging.<sup>91</sup> These data describe the aluminum gradient revealing insight into the crystalline structure of ZSM-5.

The experimentalists make a point to localize more precisely the aluminum in the zeolite framework, which is still a challenge today. The basic crystalline cell of ZSM-5 is composed of 192 oxygen atoms and 96 silica and/or aluminums (Figure 17). This conventional cell, also called “bulk” of ZSM-5, exposes 12 non-equivalent positions of silicon or aluminum, which are represented in blue on the same figure. All the other positions, represented in yellow, are replicable by symmetry from one of these 12. The same remark can be done on oxygen atom. Knowing the localization of the aluminum atom is not strictly sufficient to know the acid site localization. The acidity is determined by the position of the compensating proton around the aluminum. The proton is generally bonded to an oxygen of the zeolite framework which is directly bonded to aluminum. For each aluminum position there are four possible localization of acid sites. To conclude, there are 48 possibilities of acid site location in ZSM-5 bulk conventional cell.

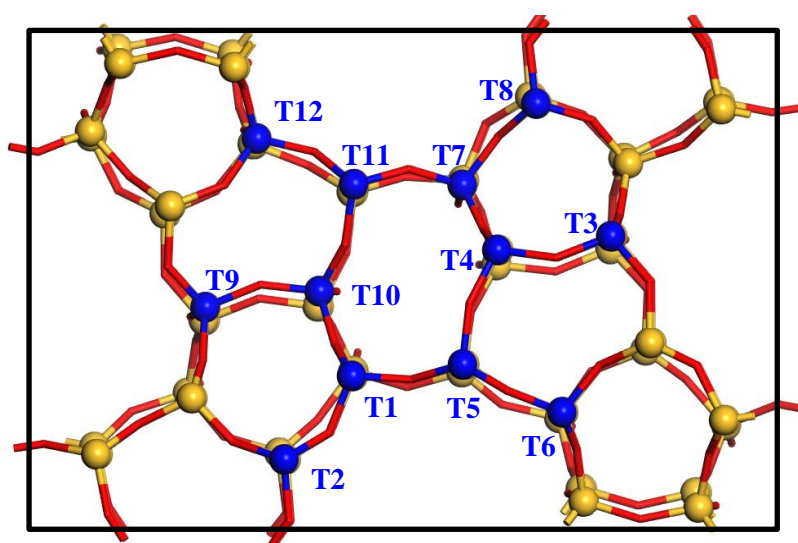


**Figure 17.** Conventional crystalline cell of ZSM-5, the positions of oxygen atoms are represented in red, the positions of the silica are in yellow. The blue atoms represent the 12 non-equivalent positions of silica atoms named from T1 to T12.

The distinction between aluminum can also be established with  $^{27}\text{Al}$  MAS NMR spectra. The spectra of the ZSM-5 spectra shows a line at 55 ppm which is attributed to four-coordinated framework aluminum.<sup>98</sup> The steaming of the zeolite induce the apparition of two other peaks at 35 and 6 ppm. These two peaks are attributed to distorted tetrahedral and higher coordination states. Some more recent studies showed that the aluminum are mainly located at the intersection between the straight and the sinusoidal channel, regardless of the conditions of synthesis.<sup>99</sup> The equivalent position on Figure 17 are the T2, T6, T9 and T11. The intersection is shown to be composed of more than 55% of framework Al atoms. More details will be given in the following sections. The attribution of the  $^{27}\text{Al}$  MAS NMR spectra and the 2D  $^{27}\text{Al}$  MAS NMR spectra are generally associated to theoretical researches which are more detailed later (Section 1.3).<sup>40</sup>

The study of the external surface site is an important aspect of the study of ZSM-5 activity. The main goals of these studies is to determine the nature of the surface site. The nature can be the structure nature but also the nature of the acidity of the site and their strength. The hydroxyl groups on the activated zeolite surface are often examined by Fourier

Transform InfraRed spectroscopy (FTIR). The adsorption of probe molecules such as pyridine and 2,6-ditertbutylpyridine (DTBPy) is also a way of quantifying the acidity.<sup>100</sup> One example of use these techniques on ZSM-5 was performed by Maijanen *et al.* and the spectra were measured between 4000 and 400  $\text{cm}^{-1}$ .<sup>98</sup>

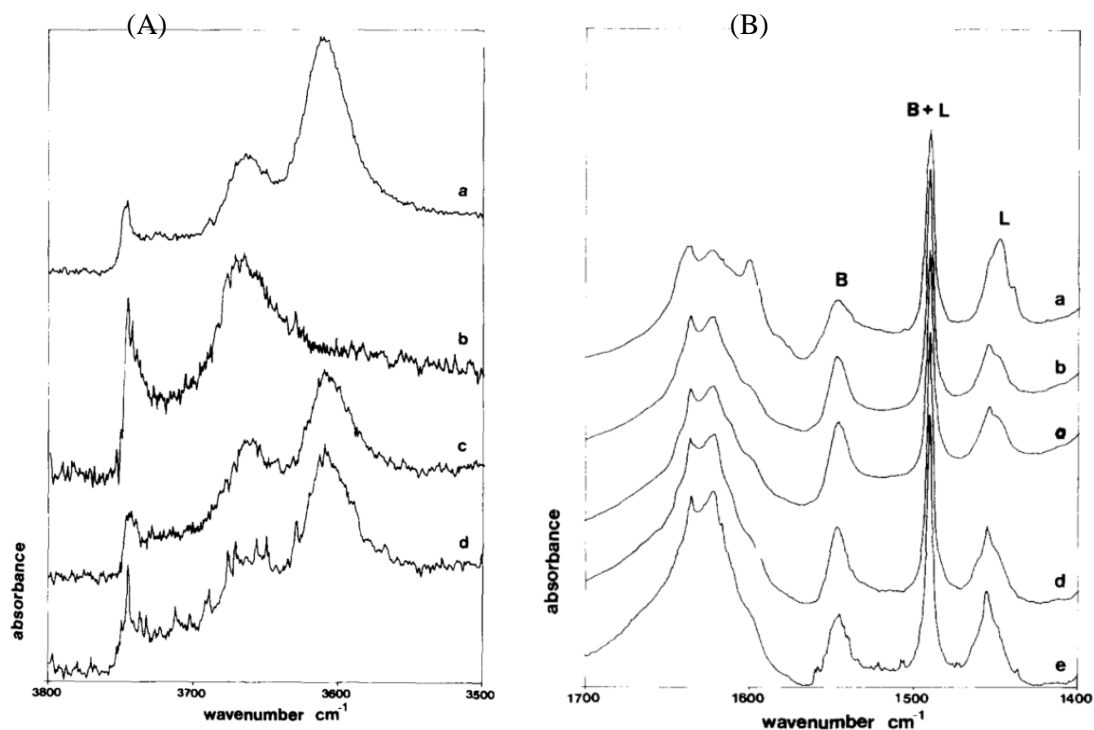


**Figure 18.** FT-IR spectra of ZSM-5 steamed for 25h of the O-H stretching region between 3500 and 3800  $\text{cm}^{-1}$  (A) and in the pyridine region between 1700 and 1400  $\text{cm}^{-1}$  (B). Spectra after dehydration treatment at 500°C (A,a), after desorption of pyridine at 150°C (B,a), 250°C (A,b) (B,b), 350°C (B,c), 450°C (A,c) (B,d) and 550°C (A,d) (B,e). Each spectrum is shown on a normalized absorbance scale. B and L stand for Brønsted and Lewis site, respectively.<sup>98</sup>

It appears that three peaks are representative of the ZSM-5 surface and are presented in Figure 18 (A,a). The weak bands at 3745 and 3664  $\text{cm}^{-1}$  are assigned to terminal SiOH and AlOH groups respectively.<sup>101</sup> The acidic bridged hydroxyls Si-OH-Al show a band at 3610  $\text{cm}^{-1}$ . This band disappears when pyridine is adsorbed, Figure 18 (A,b), and reappears when pyridine start to desorbs around 450°C, Figure 18 (A,c,d). The adsorption of the pyridine can be detected with typical bands. The wavenumber of these bands are indicators if the acid sites are Brønsted or Lewis acid sites. On Figure 18 (B), the band at 1545  $\text{cm}^{-1}$  is attributed to the pyridinium ions formed on Brønsted acid site whereas the band at 1450  $\text{cm}^{-1}$  is assigned to the pyridine coordinately bonded to Lewis acid sites. Increasing the temperature reduces the number of pyridine adsorbed on the surface, Figure 18 (B), but some pyridine molecules remain adsorbed even after the temperature of pyridine desorption on the ZSM-5 surface of 550°C.

FT-IR spectroscopy is also used to study the interactions of ZSM-5 with aromatic molecules and other non-aromatic molecules (alkenes and nitriles). The characterizations allowed to distinguish the adsorption of the different molecules on the internal OHs and on the external OHs.<sup>102</sup> The FT-IR spectroscopy is combined with temperature programmed



desorption (TPD) examination to determine the strength of the surface and intern acid sites. They are classified considering their desorption activation energy (DEA) of pyridine.<sup>103</sup> The acid sites are divided between four sets of different strength of DEA: 70, 90, 120 and 150 kJ.mol<sup>-1</sup>. The implication of the different kind of acid sites, Brønsted or Lewis, in each group is evaluated. The Brønsted acid sites take a major part in the group with the highest strength (150 kJ.mol<sup>-1</sup>) whereas the Lewis acid site are majority in the second group of 120 kJ.mol<sup>-1</sup>. In the two lower groups there is no predominance of one kind of acid site. These two groups were associated to the hydroxyl surface groups on silicon Si-OH, on extra-framework aluminum and bridged between aluminum and silicon Si-OH-Al at the surface. These techniques are used also to study the impact of various treatment applied on the zeolite. It is crucial to understand the factors which have an important impact on the acidity of ZSM-5 and the structural changes implied.<sup>104</sup> FT-IR spectroscopy can also be used with the adsorption of the 2,6-ditertbutylpyridine (DTBPy). This molecule is specific to the external acid sites of the zeolite. The two trimethyl which are present on the molecule stop the introduction in the zeolite pores.<sup>105-107</sup>

## 1.2. Shaping

### 1.2.1. Zeolite shaping

The appearance of pure zeolite as studied by experimentalist in laboratories is a white (it can be colored if metallic transition cations are inside the zeolite framework) and thin powder. The powder form of zeolite is unsuitable for industrial reactor because of its weak mechanical resistance and a phenomenon of charges loss. Most of the time the acidity of the zeolite must also be reduced for a better efficiency of the processes. To face these problems the zeolite is diluted and shaped with numerous additives including binders.

The zeolite shaping is the change of the powder into millimetric particles which enhance the resistance of the particles to abrasion and crushing and minimize the loss of charges. But the size of particles themselves can influence the diffusion of molecules in the grains, the activity and the external and internal mass transfer. A compromise must be found between the size of the particles and the properties chosen to be enhanced.<sup>108</sup>

Figure 19 describes the development of a zeolitic catalyst from the active site to its industrial use.<sup>109</sup> The shaping of zeolite intervenes at the key step of changing a catalyst of research into a technical catalyst which can be used at high scale and important quantities.<sup>110</sup> A good catalyst will deliver interesting performance along all the steps at all length scale, from the active site to the millimetric sized catalyst. These development step by step can take around ten year when it is successful. The development of the research catalyst includes the active phase and the support. But the technical catalyst development starting at the scale up includes many additives to conform to quality standards of the reactors.

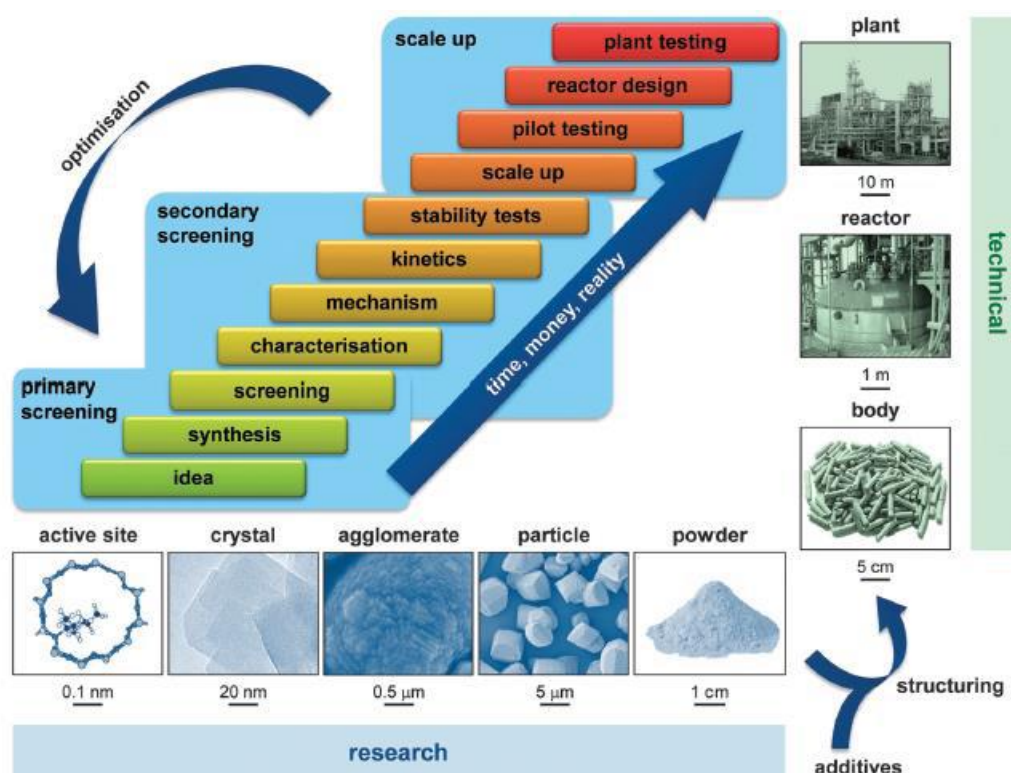


**Figure 19.** Typical sequence of interactive tasks followed in a catalyst development program.<sup>109</sup>

The binders and the matrix used have to be chosen with care because they influence significantly the future performances of the catalyst.<sup>111,112</sup> They change the catalyst coking characteristics, the entrapment of poisons, the transfer of chemical species to and from the active phase, the porosity characteristics, the heat transfer and thermal characteristic, the physical durability and the acidity of zeolites. The nature of these additives and the changes associated are detailed by Mitchell *et al.*<sup>109</sup>

- the binders increase the mechanical strength and dilute the acidity of the zeolite (alumina, silica, zirconia, ...)
- the lubricants reduce friction during mixing and shaping operations (ethylene glycol, graphite, glycerin, ...)
- the modifiers enhance performance of the catalyst (zeolite, metal or metal oxide, ...)
- the peptisers disperse particles to improve the homogeneity of the catalyst (acetic, citric, formic, nitric, sulphuric, phosphoric or hydrochloric acids)
- the plasticizers decrease the viscosity (water, sugars, polyethylene glycol, ...)
- the porogens increase the interparticles porosity (carbon black, flax, ...)

The preparation of a fixed-bed catalyst is mostly done by the mixing and extrusion method. This method allows to keep a control on the geometry of the technical catalyst. The first step of this method is the mixing step to obtain a pasty and homogeneous mixture, it is the first contact between the zeolite powder and the liquid composed of the additives. Depending on the size of the grains and the size of the liquid drop, the contact between the two phases and the good distribution of these engender or not an homogeneous phase.<sup>113</sup> Most of the time the particles have a micrometric size, and when the quantity of liquid has to be

adapted to obtain a paste as the homogeneous phase which will have the good consistence for the next step: extrusion.<sup>114</sup>

The extrusion is the molding of the paste. After mixing the paste is passed through a mold of a particular shape with a pressure applied on it. The ideal behavior of the paste is a shear-thinning one. The viscosity of the paste must be low enough so during the mixing the dispersion of the particles will be good but it also should be high enough so that during the extrusion the paste will conserve the form given by the mold.<sup>115</sup> If the viscosity of the extrudates is not correct, they could present defaults on their surfaces. The choices of the components are again essential to obtain an homogeneous paste with an adapted rheological behavior to avoid the formation of defaults on the surface. However the knowledge of this step is mostly empirical and needs a well-established expertise.<sup>116</sup>

The extrudates then undergo a thermal treatment to obtain the final structure of the catalyst and to get rid of all the volatile molecules which were used for the shaping. The thermal treatment starts by a drying between 80 and 200°C. This step is an exchange of heat and molecules between the zeolite and the air. The air molecules take the other volatile gas out of the zeolite passing by the inside surface of the zeolite which is the surface in the pores.<sup>117</sup> The removal of many molecules from the zeolitic network can engender deformation or framework defects which depends on the mechanical properties of the support.<sup>118</sup> The catalyst is then calcinated at an higher temperature. The organic additives of the mixing step are evacuated to free the spaces in micro and macroporosity.

At the end of the calcination, the catalyst produced is different from the initial powder of zeolite and is available to be used in industrial reactors. The changes between the initial catalyst and the technical catalyst is mastered in industry without any clear understanding of the chemical and physical phenomenon engender by the shaping. A knowledge on the subject should allow scientist and manufacturers to optimize the catalyst to their need and to foresee changes in their properties.

### 1.2.2. Textural changes

The study of the textural properties of the shaped zeolites is very important to understand the catalytic phenomena which intervene in refineries and petro chemistry industry. The diffusion of reactants, the reactivity of the surface, the products of reaction and the shape selectivity are directly influenced by measurable characteristics as the specific surface, the pore size and the pore volume. Moreover, there are two types of pore in shaped zeolite: the intracrystalline pores which correspond to the vacuum created by the structure and the layout of the atoms of the zeolite and the intragranular pores which are the vacuum between the binder and the zeolite created by shaping. The principal techniques to characterize the pores are nitrogen or argon sorption and desorption isotherms and mercury porosimetry. They give information about typical values like the specific surface area (in  $\text{m}^2 \text{g}^{-1}$ ) and the pore volume (in  $\text{cm}^3 \text{g}^{-1}$ ).<sup>119</sup>

The binder effect on ZSM-5 extrudate from a textural point of view is studied by Whiting *et al.* for a ZSM-5 crystal with Si/Al=32 and silica and alumina binders.<sup>112</sup> The authors changed the binder proportion in the extrudates from 0% (zeolite alone) to 100% (binder alone) and measured the porous volume of the extrudates. The results obtained by nitrogen adsorption and desorption are given in Figure 20. The BET surface area is higher for the zeolite as compared to the binder. In consequence, when the proportion of binder increases the BET decreases. The same tendency is observed for the pore volume, it is higher for the silica binder (mainly corresponding to mesopores) so when the proportion of binder increases, the pore volume also increases. But the pore volume of extrudates is lower than what is expected by the theoretical calculation depending on the proportions of the two components, and even more in the case of the silica binder. The conclusion relative to this difference is attributed to pore blockage of the binder by ZSM-5 and by morphological modification of the binder. Some other studies proposed that the zeolite pore are blocked by binder sheets (silica and alumina).<sup>120,121</sup> Whiting *et al.* also show that extrudates based on silica have a larger distribution of pore diameters than alumina-based extrudates.<sup>115</sup>

Sample	ZSM-5:binder [wt.%]	Binder	Na content [ppm]	BET surface area [m <sup>2</sup> g <sup>-1</sup> ]	t-plot micropore area [m <sup>2</sup> g <sup>-1</sup> ]	Pore volume [cm <sup>3</sup> g <sup>-1</sup> ]	t-plot micropore volume [cm <sup>3</sup> gm <sup>-1</sup> ]
ZSM-5	100:0	–	–	356	261	0.21	0.13
Z80-Si	80:20	SiO <sub>2</sub>	5600	347 (336) <sup>[a]</sup>	213 (211)	0.35 (0.38)	0.11 <sup>[b]</sup>
Z50-Si	50:50	SiO <sub>2</sub>	3690	313 (306)	137 (136)	0.54 (0.64)	0.07
Z20-Si	20:80	SiO <sub>2</sub>	1490	255 (275)	59 (61)	0.70 (0.89)	0.03
SiO <sub>2</sub>	0:100	SiO <sub>2</sub>	–	255	11	1.06	0
Z80-Al	80:20	Al <sub>2</sub> O <sub>3</sub>	5690	349 (340)	217 (213)	0.28 (0.33)	0.11
Z50-Al	50:50	Al <sub>2</sub> O <sub>3</sub>	3510	322 (315)	148 (141)	0.45 (0.5)	0.07
Z20-Al	20:80	Al <sub>2</sub> O <sub>3</sub>	1210	288 (289)	74 (68)	0.60 (0.67)	0.03
Al <sub>2</sub> O <sub>3</sub>	0:100	Al <sub>2</sub> O <sub>3</sub>	–	273	20	0.79	0

[a] Predicted values calculated from the extrudate composition and the experimental values of the pure binder and pure zeolite. [b] Predicted micropore volume identical to experimental values.

**Figure 20.** Physicochemical properties of the two series of ZSM-5-containing SiO<sub>2</sub> and Al<sub>2</sub>O<sub>3</sub>-bound extrudates under investigation.<sup>112</sup>

A study from Michels *et al.* focuses on the impact of the shaping by granulation (G) with an attapulgite binder compared to the powder form of the zeolite (P).<sup>122</sup> This shaping is applied on a classical ZSM-5 (C) (Si/Al=39) and a hierarchical and mesoporous ZSM-5 (M) (Si/Al=28). The zeolite:binder ratio is equal to 80:20. The results given in Figure 21 show a reduction of the microporous volume for shaped zeolites. For example, the classical ZSM-5 has an initial microporous volume of 0.16 cm<sup>3</sup> g<sup>-1</sup> and the expected theoretical volume in the granules of the zeolite is evaluated to 0.13 cm<sup>3</sup> g<sup>-1</sup>. This reduction is associated to the dilution of the zeolite in the binder. No pore blockage is observed in this study.

Sample code	Si/Al <sup>a)</sup> [-]	V <sub>pore</sub> <sup>b)</sup> [cm <sup>3</sup> g <sup>-1</sup> ]	V <sub>micro</sub> <sup>c)</sup> [cm <sup>3</sup> g <sup>-1</sup> ]	S <sub>meso</sub> <sup>c)</sup> [m <sup>2</sup> g <sup>-1</sup> ]	S <sub>BET</sub> <sup>d)</sup> [m <sup>2</sup> g <sup>-1</sup> ]	V <sub>meso</sub> <sup>e)</sup> [cm <sup>3</sup> g <sup>-1</sup> ]	V <sub>macro</sub> <sup>f)</sup> [cm <sup>3</sup> g <sup>-1</sup> ]	Crush strength [N]
APc	–	0.43	0.00	125	125	0.29	–	–
CPc	39	0.27	0.16	77	449	0.04	–	–
CGc	32	0.32 (0.30) <sup>g)</sup>	0.13 (0.13)	91 (87)	394 (384)	0.13	0.27	12
MPc	28	0.61	0.12	207	496	0.35	–	–
MGc	23	0.56 (0.57)	0.09 (0.10)	197 (191)	428 (422)	0.37	0.32	12

<sup>a)</sup>Molar ratio in the solid, determined by AAS; <sup>b)</sup>Volume of N<sub>2</sub> adsorbed at  $p/p_0 = 0.99$ ; <sup>c)</sup> $t$ -plot method; <sup>d)</sup>BET (Brunauer-Emmett-Teller) method; <sup>e)</sup>Volume of Hg intruded into pores of 3.7–50 nm diameter; <sup>f)</sup>Volume of Hg intruded into pores of >50 nm diameter; <sup>g)</sup>In parenthesis, calculated values based on the proportional contribution of component species (20 wt% attapulgite and 80 wt% zeolite).

**Figure 21.** Characterization data of the zeolite granules and their powder constituents.<sup>122</sup>

### 1.2.3. Effects on acid sites environment

In the previous sections, it has been shown that the FT-IR spectroscopy is widely used to determine the position of the hydroxyl groups on the surface of ZSM-5 after dehydration. The different possible hydroxyl groups at the surface, Si-OH, Al-OH and Si-OH-Al have been associated to the IR spectroscopy signals at 3745, 3665 and 3610 cm<sup>-1</sup> respectively. The effect of the shaping on the acid properties of zeolite was studied by Michels *et al.* on one conventional ZSM-5 (CPc) and on a mesoporous ZSM-5 (MPc).<sup>122</sup> These zeolite are shaped with attapulgite as a binder in a mixture of 80% of zeolite and 20% of binder. The hydroxyl groups IR spectrum are presented on Figure 22 a, for the pure zeolite and for the shaped zeolite.

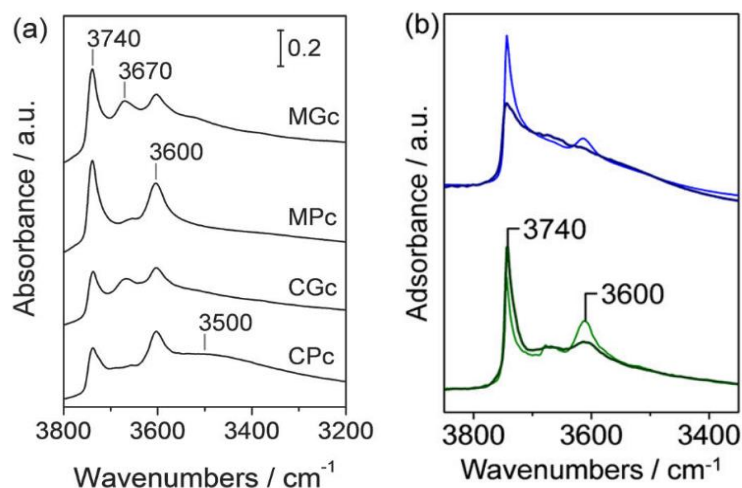


**Figure 22.** Infrared spectra in the hydroxyl stretching region (a) of conventional (C) and mesoporous (M) ZSM-5 powders (P) and granules (G) (80% of zeolite and 20% of attapulgite)<sup>122</sup> (b) of hierarchical ZSM-5 (Si/Al=40) shaped with silica (blue) and attapulgite (green) with a ratio 1:1; clear lines physical mixture of zeolite and binder, thick lines crushed extrudates of zeolite and binder.<sup>112</sup>

The comparison of the infrared spectrum before shaping (MPc and CPc) and after shaping (MGc and CGc) shows a decrease of the signal at 3600 cm<sup>-1</sup> when the samples are

shaped. This signal which is attributed to the bridging hydroxyls on Si-OH-Al are also associated to the Brønsted acid sites. Attapulgite has no contribution at  $3600\text{ cm}^{-1}$ , the decrease in intensity of the signal can be due to their dilution. The authors detected no evidence of dealumination but as the comparison of the expected spectrum of the binder and zeolite mixture with the real spectrum of the material is not given, quantification of the effects of the shaping is not straight forward.

Michels *et al.* also compared the FT-IR spectra of hierarchical ZSM-5 shaped with attapulgite and with silica.<sup>112</sup> The results of the mixture of zeolite with binders are presented on Figure 22 (b). The ratio between the two is 1:1 and the clear lines represent the mixture of powders whereas the thick lines are crushed extrudates. The authors do not present the initial spectra of zeolite so the effects of binder on zeolite can not be determined. But in the two cases the intensity of the bands associated to Si-OH and Al-OH-Si ( $3740$  and  $3600\text{ cm}^{-1}$  respectively) decreases between the mixture of powder and the extrudates. One more time we cannot conclude about dealumination. The IR spectra allow to follow the effect of the shaping on the hydroxyl groups on the external surface of zeolite but the study must be completed with other analyses.

The NMR spectra of  $^{27}\text{Al}$  have also been reported for the analysis of the zeolite and the mixtures of zeolite and binders. The NMR allow the distinction between the coordination of the aluminum atoms. As previously seen in this work, the NMR spectra of ZSM-5 is essentially composed of one signal at  $55\text{ ppm}$ , corresponding to the framework  $\text{Al}_{\text{IV}}$ . But the NMR spectra can reveal penta coordinated aluminum  $\text{Al}_{\text{V}}$  between  $20$  and  $40\text{ ppm}$  and hexa coordinated aluminum  $\text{Al}_{\text{VI}}$  between  $-20$  and  $10\text{ ppm}$ . In the two previous studies presented by Michels *et al.*, the authors completed their approach with the NMR spectra of the shaped zeolites.

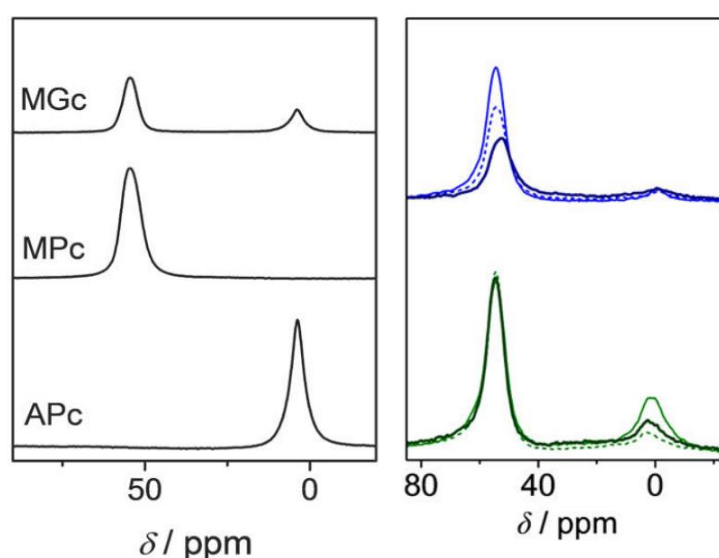


**Figure 23.**  $^{27}\text{Al}$  MAS NMR spectra of (Left) mesoporous ZSM-5 powder (MPc), or granule (MGc) and the attapulgite alone (APc)<sup>122</sup> (Right) of hierarchical ZSM-5 (Si/Al=40) shaped with silica (blue) and attapulgite (green) with a ratio 1:1; clear lines physical mixture of zeolite and binder, thick lines crushed extrudates of zeolite and binder, dashed line milled zeolite and binder.<sup>112</sup>



In the first study,<sup>122</sup> Michel *et al.* obtained the  $^{27}\text{Al}$  NMR spectra presented on the left of Figure 23 which correspond to the samples of Figure 22 (a). For the pure zeolite (MPC), we observe, as previously announced, one peak at 55 ppm which stands for Al(IV). The binder alone spectra (attapulgite) presents one peak around 5 ppm which stands for Al(VI). The spectra for the granule composed of both zeolite and binder presents the two peaks. The authors conclude that the peaks of Al(VI) is only here because of the binder and the shaping has only a dilution effect. But again, the expected spectrum (linear combination of that of the binder and that of the zeolite) is compared to the real spectrum.

In the second study,<sup>112</sup> the authors recorded the  $^{27}\text{Al}$  MAS NMR spectra for a hierarchical ZSM-5 of Si/Al=40 which are shown on Figure 23 (right) which correspond to the same samples as the Figure 22 (b). The author highlight the fact that for the blue curves (zeolite shaped with silica) there is a significant decrease of Al(IV) between the physical mixture of zeolite and binder and the extrudates of the same components. Combined with the IR spectra conclude that the zeolite framework is dealuminated. But for the extrudates based on zeolite and attapulgite, their conclusions are different (and similar to their previous study). They highlight the decrease of the bridging OH on the IR spectra but there is no decrease of Al(IV) in the NMR spectra (green curves). So, there is no dealumination but only dilution effect. Note however that the spectra were likely normalized which renders the discussion of the evolutions difficult, but do not indicate how.

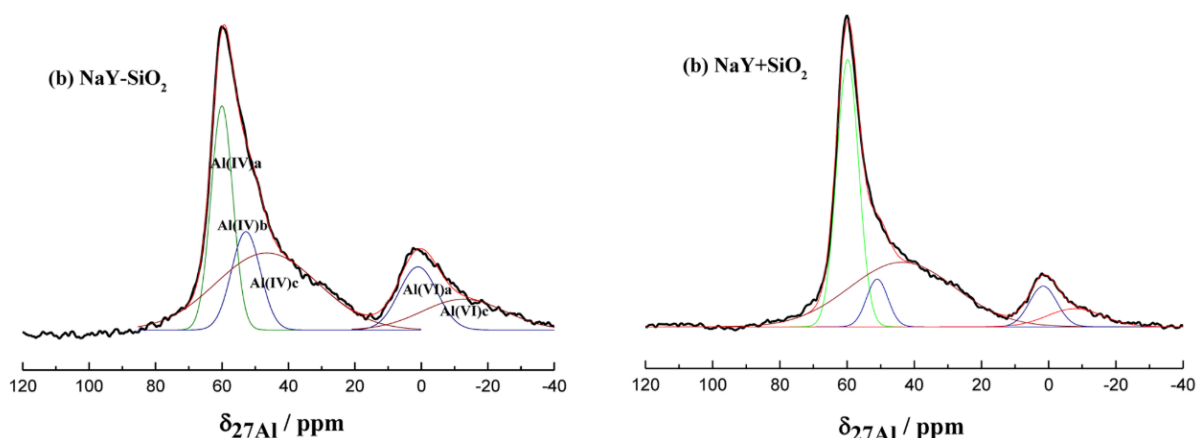


**Figure 24.**  $^{27}\text{Al}$  NMR spectra with deconvoluted peaks of NaY-SiO<sub>2</sub> and NaY+SiO<sub>2</sub>.<sup>123</sup>

$^{27}\text{Al}$  NMR spectra have also been done on extrudates of NaY zeolite and silicate by Chen *et al.*<sup>123</sup> They focus on the interactions between the zeolite and the binder thanks to the comparison of the spectrum of a physical mixture of zeolite and binder (NaY+SiO<sub>2</sub>) and that of an extrudates of zeolite and binder (NaY-SiO<sub>2</sub>) as shown on Figure 24. They deconvolute the Al(IV) signal into 3 components: Al(IV)a which are attributed to the aluminum of the zeolite framework, Al(IV)b assigned to the aluminum close to the framework defects of the zeolite and Al(IV)c which are associated to the extra framework aluminum. The results show a decreasing Al(IV)a peak and an increase of the Al(IV)b peak with the shaping. According to the author these results are the proof of the NaY dealumination with shaping and of a migration of the Al from the zeolite framework to the extra framework sites close to the defects of the framework.

Chen and Michels works show with IR spectroscopy and  $^{27}\text{Al}$  MAS NMR spectra that the shaping with silica induce a dealumination of the zeolite framework. To complete these observation it could be very interesting to investigate the expected spectra of various zeolite and binder interfaces compared to the zeolite and binder separated spectra.

#### 1.2.4. Evolution of the acid properties

The influence of the shaping on zeolite can be measured by the differences in the acid properties. They are usually determined by combining pyridine adsorption and IR spectroscopy. Michels studied the shaping of ZSM-5 with various binders: silica (si), boehmite (bo), attapugite (at) and kaolin (ka) in extrudates composed of 50% of zeolite and 50% of binder.<sup>112</sup> The adsorption of pyridine on these shaped zeolite gives access to the acid site concentration which are reported in Table 1.

	ZSM-5	ZSM-5-si	ZSM-5-bo	ZSM-5-ka	ZSM-5-at
$C_B$ ( $\mu\text{mol}/\text{g}_{\text{zeolite}}$ )	212	50	96	190	113

**Table 1.** Brønsted acid sites concentration ( $C_B$ ) of a ZSM-5 zeolite shaped with different binder: silica (si), boehmite (bo), attapugite (at) and kaolin (ka).<sup>112</sup>

Pyridine desorption has been performed at 200°C and the molar extinction coefficients to quantify the acid sites were taken equal to 1.67  $\mu\text{mol g}^{-1}$  for Brønsted acid sites and 2.94  $\mu\text{mol g}^{-1}$  for Lewis acid sites. The binders have also been analyzed separately and revealed no Brønsted acid sites. In theory, 50% of the Brønsted acid sites should be maintained in the extrudates. The number of these acid sites are maintained only with the kaolin binder. But the authors could observe a decrease in the number of Brønsted acid site when the zeolite is shaped with other binders. The explanation could be a dealumination, which has been shown for silica binders previously, or a neutralization of these acid sites by ionic exchange. The sodium in the attapugite for example can neutralize the Brønsted acid sites of ZSM-5. But for the boehmite the explanation is more complicated. The authors suppose that the Brønsted acid site are neutralized by aluminum migration.

The same tendency can be found in the same study for the variation of the number of Brønsted acid sites with or without shaping and for different Si/Al ratio. The first ZSM-5 has a ratio of 15 and the second of 140. They are shaped with attapulgite. The Brønsted acid sites number goes below what was expected ( $<304 \mu\text{mol}/\text{g}_{\text{zeolite}}$ ), as shown in Table 2.

	at	ZSM-5	ZSM-5-at	ZSM-5	ZSM-5-at
Si/Al	-	15	15	140	140
$C_B$ ( $\mu\text{mol}/\text{g}_{\text{zeolite}}$ )	0	304	189	36	24

**Table 2.** Brønsted acid sites concentration ( $C_B$ ) of two ZSM-5 with different Si/Al ratio shaped or not with attapulgite binder.<sup>112</sup>

The decreasing number of acid site which is induced by the shaping is not totally explained by the authors who have been working on the subject. But the molecule adsorption can drive us to the nature, the number, the strength and the accessibility of the acid sites. These results are important for this work and the resulting theoretical study, because the same tools could be used.



### 1.2.5. Evolution of the catalytic properties

The analysis presented so far have operating conditions which are not similar to the real catalytic conditions in industrial processes. A characterization with a model reaction can quantify the catalytic activity of the catalysts but also their stability and their selectivity in similar reaction conditions.

In one of their study Michels *et al.* evaluated the impact of the shaping of conventional and hierarchical ZSM-5 with different binders on the catalytic properties.<sup>122</sup> The methanol-to-olefins (MTO) reaction is tested to evaluate their properties at two different temperatures (350 and 400°C). They proved that the choice of binder has an impact on the life time of a catalyst (with an conversion higher than 90%) and the selectivity of the reaction. The results shown on Figure 25 highlight that silica reduces the life time of the catalyst. Whereas the attapugite induce a life time around 70h when the zeolite has 40h and the silica 10h. The same results have been shown for the different temperatures. These results are in concordance with the previous ones about Brønsted acid sites. There is a higher concentration of these acid sites with the attapugite binder than with the silica. But this difference does not explain the difference of life time.

In a review by Hargreaves and Munnoch,<sup>111</sup> the authors reported that alumina enhances the activity of the ZSM-5 in n-hexane cracking. The original study of Shihabi *et al.*,<sup>124</sup> the results (Figure 26 (Left)) shows that for zeolite with the same Si/Al=13000 with or without binder, the activity changes from 0.02 to 1.4 with the addition of binder. The authors suppose an alumination of the zeolite by the alumina. The zeolite was initially composed of a very low number of aluminums.

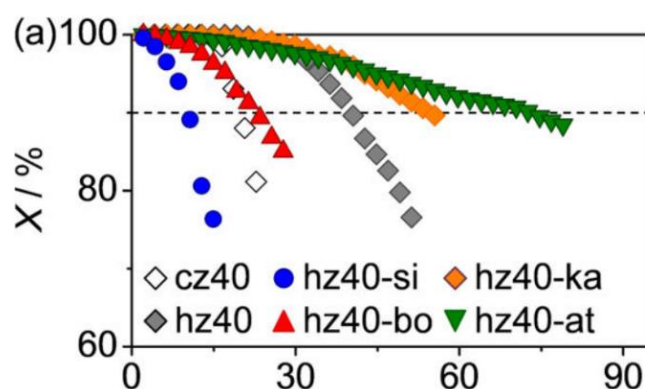


**Figure 25.** MTO test: conversion versus time at 450°C, P=1bar and PPH=9.5g<sub>methanol</sub>.g<sub>zeolite</sub><sup>-1</sup>.h<sup>-1</sup>.<sup>112</sup>

In a study of the reaction of dimethylether (DME) into light olefins (DTO), a ZSM-5 zeolite with a Si/Al=140 ratio, shaped with boehmite and bentonite was used as a catalyst. The effects of the binders on the conversion and the yield are reported in Figure 26 (Right). The catalyst prepared with boehmite exhibits a higher conversion (39%) than the catalysts shaped with bentonite (25%). Furthermore, the selectivity is as high as 64% into olefins with more than 30% into propylene whereas the selectivity in olefins with bentonite is 57%. The

authors explain the difference by the mesoporous volume and the acidity of boehmite which are more important.

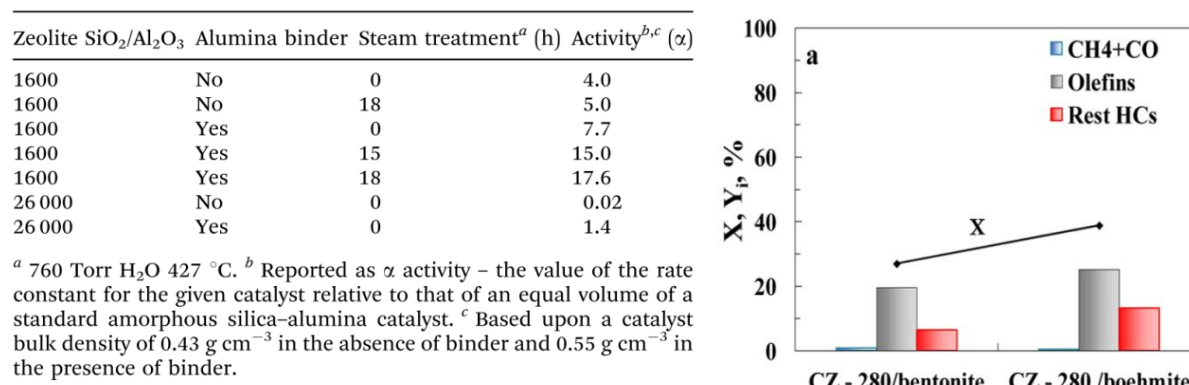


**Figure 26.** Effects of binders on ZSM-5 (Left) binder as alumina for n-hexane cracking at 538°C in He<sup>111,124</sup> (Right) effect in the DTO reaction on the conversion at t=0(X) and the product yields (Y) at 350°C for pph=0.4g<sub>zeolite</sub>.h.mol<sub>c</sub><sup>-1</sup>.<sup>125</sup>

The evolution of the catalytic properties into zeolite materials after the shaping with different binders are well represented in these examples. Many observation and explanation about the changes in the conversion, the activity and the selectivity are given by the authors but a theoretical model to clarify the situation and the explanation should be welcome.

### 1.3. Molecular Modeling

The improvement of the computing technologies allows since the 70's to develop zeolite models to complete the experimental data. Thousands of studies evaluating the properties of silicate and aluminosilicates with quantum mechanics methods are reviewed.<sup>18,126-128</sup> The main goal of these studies is to establish a relevant model of the solids which could be representative of its properties. The solid phase studies were using cluster models which are models of this solid phase with a finite number of atoms. But more recently the periodic calculations of zeolite bulk are the most used. The size of this model is important, a large model will allow to be more representative but the cost (in computational resources) will also increase.

The studies of the properties of ZSM-5 crystals are numerous.<sup>129-134</sup> These studies focus mostly on the bulk of zeolite and the properties of the insight structure of the zeolite. Understanding these aspects is essential but the understanding about the behavior of external surfaces are also important, in particular for the investigation of the effects of shaping. As it has been shown in the previous sections, the acidity and reactivity of the surface play a massive role in many cases. Creating external surface models of ZSM-5 and its properties is one of the important steps of this work and is essential to study the interaction between two surfaces.

### 1.3.1. Nature and strength of the acid sites

In a recent study Li *et al.* investigated the preferential position of aluminum in the T-sites of the bulk of ZSM-5.<sup>47</sup> They aluminated the 12 possible T-sites and calculated the relative energies of these sites to determine which one is the most stable. They differentiate the T-sites in the straight pores (T8 and T11) from the T-site in the sinusoidal pores (T4 and T10) and from the T-sites at the intersection of the two kind of pores (T1-3, T5-7, T9 and T12). According to previous quantum chemical calculation the interval of energy of all these site is not larger than 4 kcal.mol<sup>-1</sup> for high Si/Al ratio and 8 kcal.mol<sup>-1</sup> for lower ratios.<sup>135-137</sup> Some results for Si/Al=95 and for Si/Al=23 extracted from their work are presented in Figure 27. The intervals of energy are respected and the distinction of the T-site at high Si/Al ratio is complicated because of the low difference between the energies. But with higher contents of Al, six different positions have a difference lower than 3 kcal.mol<sup>-1</sup> in energy: T1-3 and T12 (intersection), T4 (sinusoidal) and T11 (straight). Only the T7 site is totally unstable compared to the others for Si/Al=23.

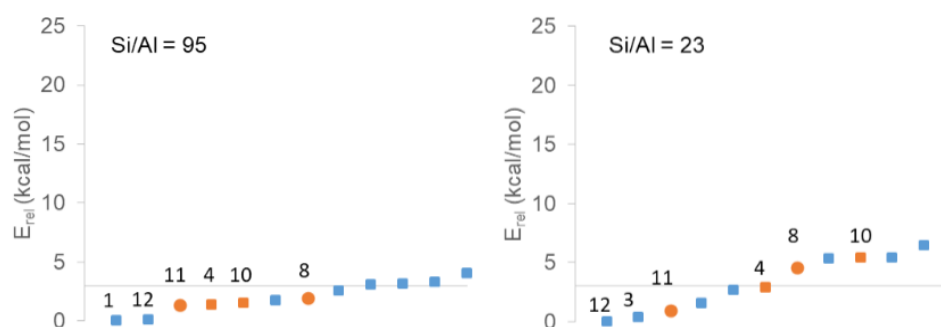


**Figure 27.** Relative energy (in kcal/mol) with respect to the most stable distribution in Al-ZSM-5 (Left) with Si/Al=95 (Right) with Si/Al=23. T-sites at channel intersections are plotted in blue and orange square and circles correspond to T-sites within the sinusoidal and the straight channels respectively. Some T-sites are indicated by numbers.<sup>47</sup>

The aluminated theoretical models are essential to refine the models and to tie in the experimental results. To be representative, the model should respect the experimental Si/Al ratio, which dictates the number of Al to put in the unit cell of the model. The <sup>27</sup>Al NMR was insufficient until recent years to determine precisely the positions of Al in the zeolite framework, but recent breakthroughs were recently obtained from the combination of MQMAS. <sup>27</sup>Al NMR with DFT calculations. DFT can provide calculated chemical shifts with very high precision and allows to attribute the different participation of the plots.<sup>40,47,138</sup> Holzinger *et al.* used <sup>27</sup>Al QMAS NMR, using ultrahigh field at 22.3T, and found a signal which can be deconvoluted into 10 distinct tetrahedral framework resonances of Al(IV), as presented on Figure 28.<sup>40</sup> This 2D spectrum is the spectrum of one sample of the study. The same spectrum is made for all the samples and the participation of each resonance is evaluated. XRD is applied on the same samples of ZSM-5 and allows the atoms identification by the average of T-O-T angles. Whereas DFT gives the theoretical chemical shifts corresponding to the different atoms positions of the bulk structure.<sup>139,140</sup> The theoretical analysis distinguishes 24 different T-sites instead of the 12 different possible positions of silicon. The NMR and XRD

analysis are then combined to the theoretical results to associate signals to aluminum positions and determine which ones are the major ones. The results tend to give an average of which site will be the most aluminated in the zeolite structure but the differences do not allow to distinguish one site in particular.

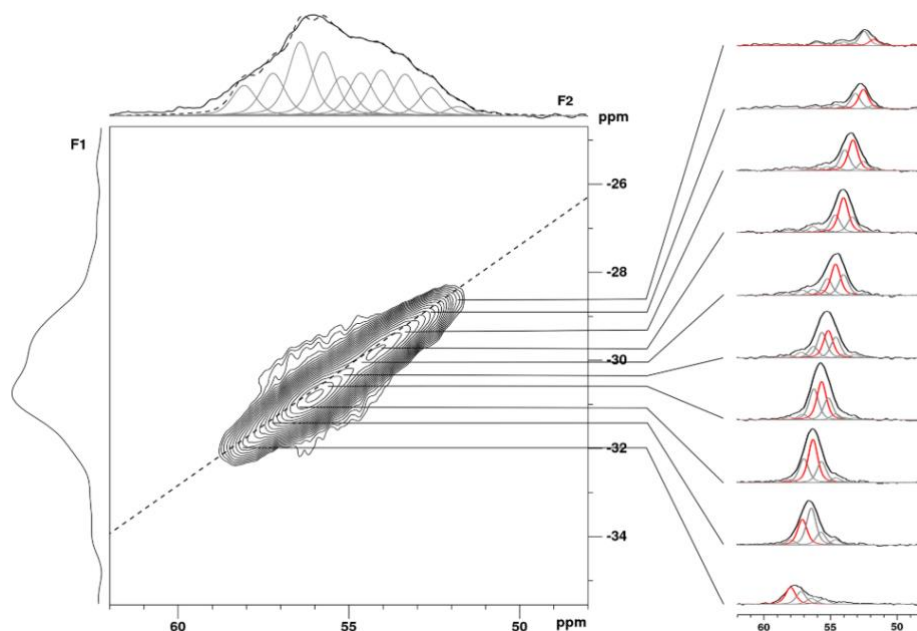


**Figure 28.** Two-dimensional  $^{27}\text{Al}$  MQM;AS NMR spectrum ( $B_0=22.3\text{T}$ ,  $\nu_R=30.0\text{kHz}$ ) of ZSM-5 sample with summed projections in both dimensions. The right-hand side illustrates 1D slices taken out at the resonances of the distinct tetrahedral sites along with their deconvolution. The dominating site for each slice is shown in red. The deconvolution of the  $F_2$  projection employs the distinct Al(IV) resonances identified in the 1D slices from the contour plot. The dashed line represents pure chemical shift.<sup>40</sup>

But important results are extracted from this study. They show that the incorporation of the aluminum depends on the Si/Al ratio. This study also quantified the number of Al in the different T-sites upon dealumination by steam treatment on each ZSM-5 samples. The aluminum at the intersection of the pores is shown to be most prone to dealumination whereas the aluminum in straight and sinusoidal pores more stable upon steam treatment, in line with previous theoretical findings.<sup>80,141</sup> The combination of experiments and theory allows to access a detailed structural insight into the distribution of the aluminum. It also gives access to the redistribution of aluminum which occurs during dealumination and steam treatment.

The strength of the Brønsted and Lewis acid sites are studied experimentally with the adsorption of pyridine on these acid sites. The vibrational analysis with infrared spectroscopy reveals in the experiment a peak at  $1450\text{ cm}^{-1}$  for pyridine adsorbed on Lewis acid sites and a peak at  $1545\text{ cm}^{-1}$  for an adsorption on Brønsted acid sites. These two peaks are associated to the 8a and 19b vibration modes of pyridine which are different when the pyridine is not adsorbed. The adsorption of pyridine on a Brønsted acid site modifies the vibration modes 8a from  $1590$  to  $1614\text{ cm}^{-1}$  and 19b around from  $1445$  to  $1540\text{ cm}^{-1}$ .<sup>98,142</sup> However, for the pyridine coordinately bonded on Lewis acid site the 19b and 8a vibration modes are only

slightly shifted. The frequency shifts between the both cases are mostly due to the pyridine ring stretching and the CH bending with ring stretching. A theoretical study of pyridine adsorption in faujasite zeolite has emphasized the variation of IR bands of these vibration modes.<sup>143</sup> The calculated shifts and the absolute frequencies calculated are in good agreement with the experimental results as shown on Figure 29 and Figure 30.

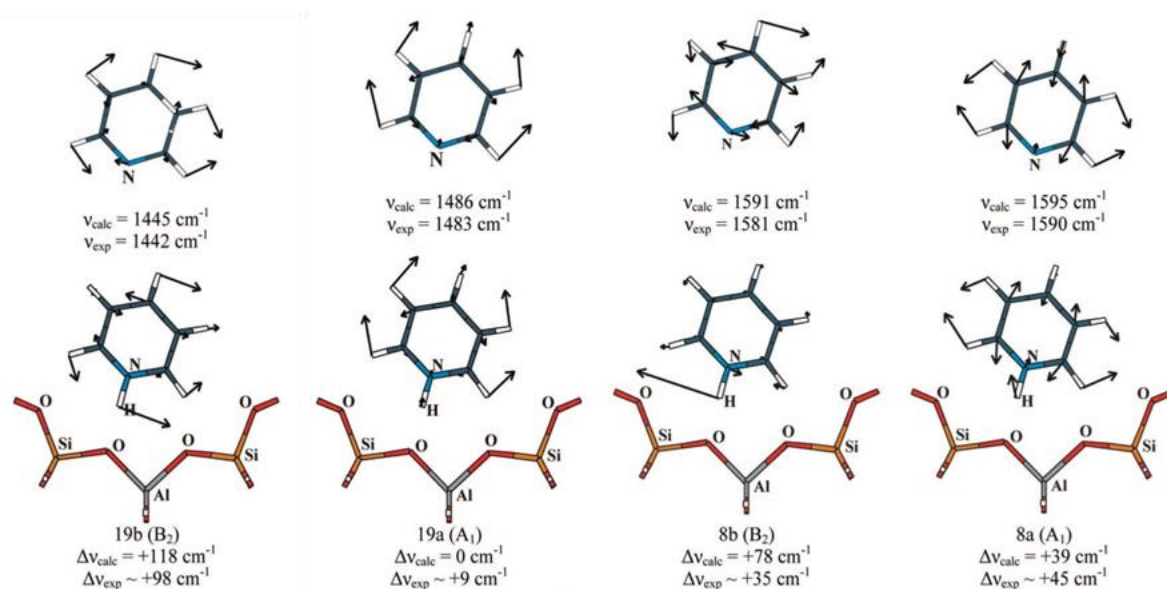


**Figure 29.** Calculated vibrational patterns of some in-plane normal modes of free and adsorbed pyridine on 12T<sub>OH</sub> within the ion-pair complex in the 1400-1700  $\text{cm}^{-1}$  spectral region. Numbers indicate the calculated and mean observed frequencies and frequency shifts. The scale for the arrows is arbitrary but common to all the normal modes. Only a part of the 12T<sub>OH</sub> of faujasite is shown.<sup>143</sup>

The vibrational analysis for the study of the adsorption of pyridine is essential and presented in most of the works. The pyridine is adsorbed on the Brønsted acid sites to determine their strength. The reactivity of the acid sites is then studied for different reactions which take place in the bulk of various zeolites.<sup>144,145</sup> The pyridine is not the only probe molecule for the acid site, ammonia can be used experimentally and theoretically.

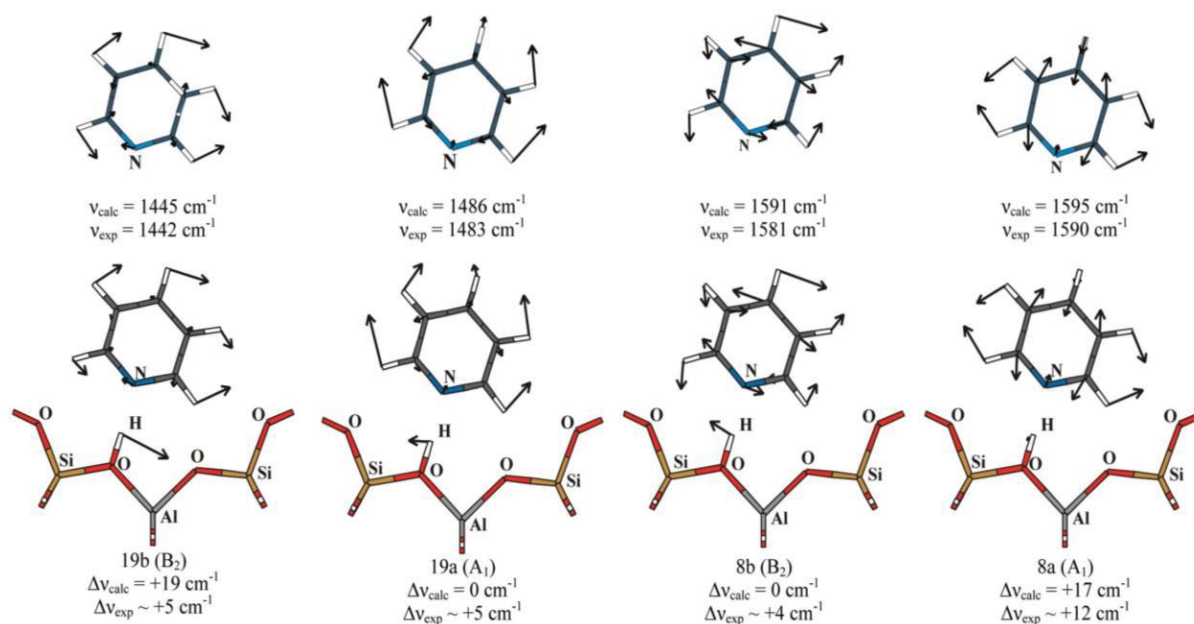


**Figure 30.** Calculated vibrational patterns of some in-plane normal modes of free and adsorbed PY on 12TOH within the hydrogen-bonded complex in the 1400-1700 cm<sup>-1</sup> spectral region. Numbers indicate the calculated and mean observed frequencies and frequency shifts. The scale for the arrows is arbitrary but common to all the normal modes. Only a part of the 12TOH of faujasite is shown.<sup>143</sup>

The theoretical analysis of the vibrational modes on a pyridine adsorbed on zeolite can confirm the nature of the acid sites. The frequencies indicate if the acid sites are a strong or weak Brønsted acid site or a Lewis acid site as a confirmation of the geometry of the model. A parallel can be done between the stability of pyridine on the acid sites and the experimental TPD.<sup>146,147</sup> The vibrational analysis should allow us to link the desorption of pyridine from the acid sites, Brønsted and Lewis, to the desorption groups enhanced in the previous section<sup>103</sup> and the experimental data we should access. The link could allow us to determine the preferential adsorption sites of pyridine.

### 1.3.2. Ab initio studies of external surface models

The first periodic DFT studies on the external surfaces of zeolites were performed by Bucko *et al* on mordenite.<sup>148-151</sup> Stoyanov *et al.* continued on this momentum and proposed a periodic external surface models for chabazite.<sup>152</sup> Both studies showed the absence of strong reconstruction and the stability of Brønsted acid sites close to the surface. Other surfaces models of purely silicic crystal were proposed for BEC,<sup>153</sup> LTL<sup>154</sup> and LTA zeolite.<sup>155-157</sup> The most recent external surface study is a study on zeolite Beta written by Rey *et al.*<sup>25</sup> This study is a DFT study which enhanced the nature of the acid surface sites and highlights the local structure of the aluminums at the surface depending on the temperature and water partial pressure.

The present work is about describing the interface between two surfaces including the external surface of zeolite. The description of the external surface of ZSM-5 is essential and the description of the acid site needs to be explored in depth. The main paper for the



description of the external surface of zeolite and its acids sites with DFT is the study of Rey *et al.*<sup>25</sup> They studied the external surface of zeolite Beta. The first step of this study is the construction of the external surface model. The choice of the thickness must be representative of the zeolite properties. A thick cell would be allowed to have a more precise model but the cost in computing resources would be too expensive. Rey *et al.* studied the (001) termination of external surface with two bulk height, with two different height named Cleavage 1 and Cleavage 2 presented on Figure 31.

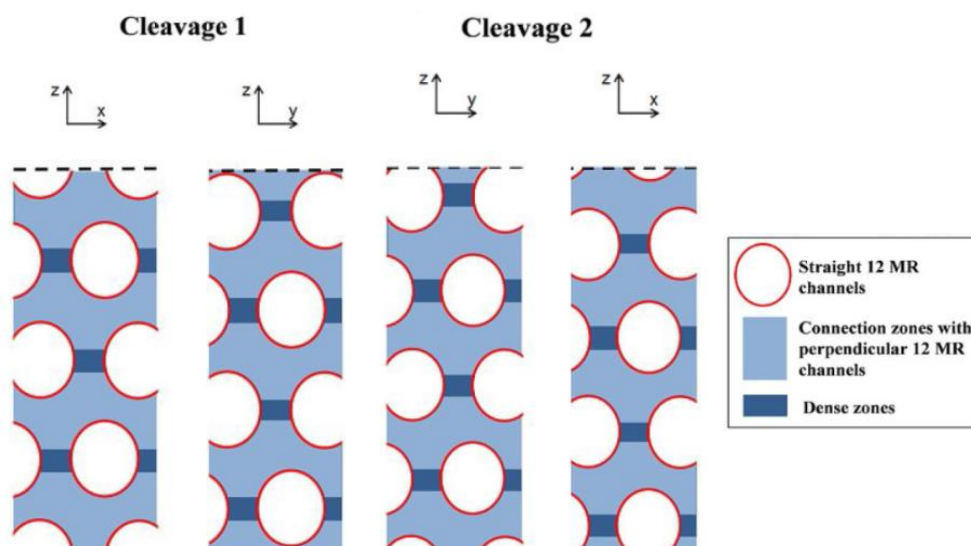


**Figure 31.** Schematic view of the slabs employed for the simulation of the (001) termination of BEA (polymorph A), cleavage 1 and cleavage 2, side views perpendicular to the  $y$  (left) and  $x$  axes (right).<sup>25</sup>

The second step of this study is the substitution of silicon T-sites on these surfaces by aluminum atom to highlight the difference of stability depending of the structure of the sites. The aluminations energies were calculated for a large set of surface sites and compared one to another and to bulk aluminated sites. The different sites proposed in this work are presented in Figure 32. The bridging Al-OH-Si are present in the zeolite bulk but also at the external surface as described in this figure. The open micropores are the pores open on the surface whereas the outermost surface is the plane zone at the external surface as shown in Figure 31. At the outermost surface, two different sites are presented: the water molecule adsorbed on the aluminum with or without an other hydroxyl adsorbed on the aluminum. The results show that the aluminated sites at the surface are thermodynamically more stable than in the bulk and moreover when the sites are located at the outermost surface in the form of a water molecule adsorbed on Al atoms.



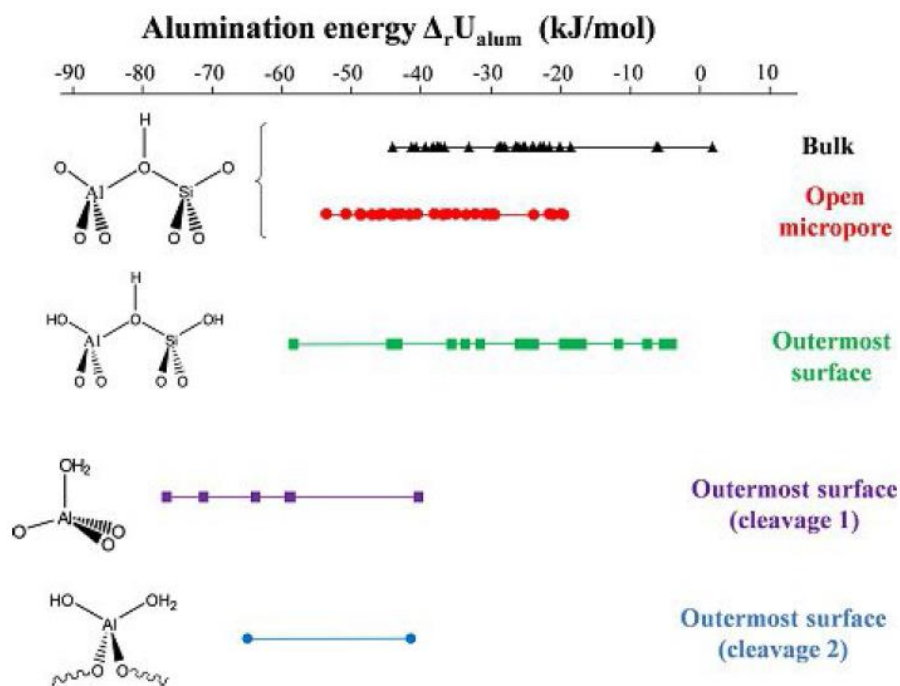


**Figure 32.** Aluminium energy (substitution of one Si by an Al-H pair) of the various sites investigated in the bulk and at the external surface of zeolite Beta (both cleavages). Left: structure of the site obtained after aluminium.<sup>25</sup>

### 1.3.3. Surface hydration

The analysis of the external surface of zeolite concern also the thermal stability of this surface. The DFT study of Rey *et al.* is a good representation of a theoretical investigation of the hydration level of the zeolite Beta external surface.<sup>25</sup> On the cleavage 1 of their study, which has been presented on Figure 31, the most favorable configuration at  $3.8 \text{ OH nm}^{-2}$  for an aluminated site on the external surface is a Al-(H<sub>2</sub>O) specie. The stability of this surface is studied depending on the temperature and the water partial pressure, its existence domain is represented by the clear blue part on Figure 33. This diagram has been constructed through the calculation of the hydration free energies. The surface is hydrated and dehydrated and the results reveal the most stable surface for the conditions of temperature and pressure (Figure 33). Several configurations have been studied for each hydration and dehydration levels. For the dehydration, the water molecule is desorbed from the aluminum. But instead of forming Al(III), the aluminum is coordinated to an oxygen lower in the zeolite structure. The adsorption energy of this water molecule is evaluated to  $-188 \text{ kJ mol}^{-1}$  which is quite similar to previous studies on the same subject but with mordenite ( $-117 \text{ kJ mol}^{-1}$ ).<sup>149</sup> Regarding hydration, it first breaks the Si-O-Si bridge to generate two silanols. Then another water molecule coordinates on the aluminum.

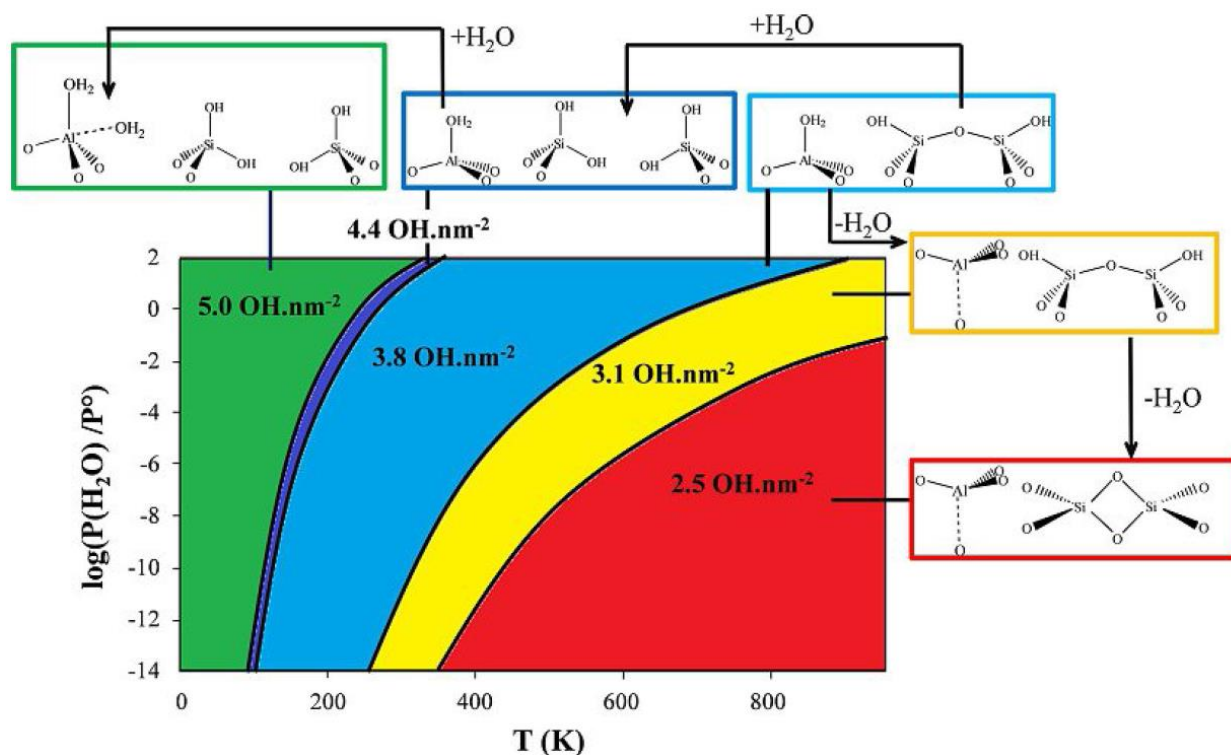


**Figure 33.** Thermodynamic diagram that depicts the evolution of the OH coverage and the nature of external surface groups for BEA.<sup>25</sup>

### 1.3.4. ZSM-5 external surface models

Cluster models of ZSM-5 external surface were already built to study their reactivity. The isomerization reaction of *trans*-but-2-ene to *cis*-but-2-ene for example was studied with density functional theory (DFT).<sup>158</sup> The choice of the surface orientation in this study is not justified. The bulk model is multiplied into the three direction of space and hydroxyl groups are exposed on the surface of interest. The surface of interest in this work is the (001) which is parallel to both kinds of pores (straight and sinusoidal). This choice may be surprising from the experimental point of view because it is not exposed on ZSM-5 particles. But the main interest of this study is the comparison of the acidity of the aluminated sites on the surface and in the bulk of zeolite crystals. By comparing one surface site and one bulk site, they showed that the reaction is more favorable inside the crystal than at the outer surface. Another DFT study focused on the propan-2-ol dehydration.<sup>159</sup> They compared the reaction path of the reaction. They apparently used the same surface model of (001) with hydroxyl groups on the surface. But only bridging OH groups were considered contrary to the previous study where Al-OH and Si-OH groups were considered on the surface. Both studies are using surface models but without any systematic study of the surface nature and surface sites.

One other DFT models have been built relatively to a different experimental model system. The self-pillared pentasil (SPP) are hierarchically-structured zeolites. They are composed of zeolite nanosheets with a thickness composed between two and three pentasil units which are arranged into a “house of card” structure. This structure, presented on Figure 34, is obtained from the modification of layered zeolite precursors or direct synthesis.<sup>85,160</sup>

There are eleven zeolite framework which are known to have these 2D structures, including MFI type zeolite like ZSM-5.<sup>84</sup> The thermal, hydrothermal and mechanical stability of the MFI nanosheets were shown to be remarkable. The acid strength of the SPP ZSM-5 is similar to the bulk acid strength. The reactivity of the ZSM-5 is enhanced upon larger molecules which normally do not fit inside the pores.<sup>161,162</sup> The structure is very thin (~2nm) layers which expose the entrance of the straight pore. The straight pores are perpendicular to the surfaces whereas the sinusoidal pores are parallel to the surfaces.<sup>163</sup>

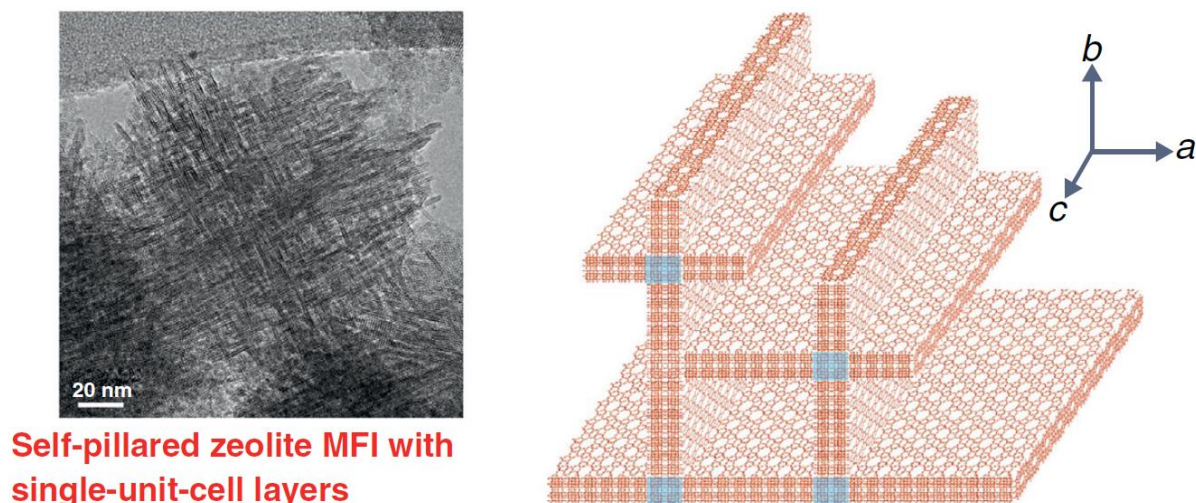


**Figure 34.** TEM image and schematic of idealized structure of self-pillared single-unit-cell thick zeolite layers prepared by repetitive branching.<sup>161,162</sup>

The properties of layered ZSM-5 remain very interesting from an experimental and fundamental point of view.<sup>164,165</sup> Based on these experiments, a DFT and IP (Interatomic Potential) study has been conducted to examine the properties of the ZSM-5 nanosheets.<sup>134</sup> The study focused on the substitution of silicon into aluminum in each independent T-sites. It also provides a complete vibrational analysis for both silanols and bridging oxygen binding a proton as counter ion. The study is composed of two different models based on the possibility to change the thickness of the nanosheets from three pentasil units to two pentasil units as shown experimentally by Ryoo *et al.*<sup>83</sup> The models do not concern the intersection of the nanosheets represented by the blue square on Figure 34. They both expose nanosheets models with (010) surface with eight hydroxyl groups per unit cell as presented on Figure 35. The two models (a) and (b) have the same nature of surface at the top but also at the bottom. The height of the cleavage is the same for every surface, no other height of cleavage was tested.

In this study, the focus is made on the localization of the acid sites and their impact on the general zeolite framework. The different T-sites are replaced by aluminum atoms on the surface and in the bulk. The substitution of the aluminum influences the vibrational response of the zeolite structure. The H-bonds between the surface silanols induces a red shift of 500  $\text{cm}^{-1}$  as soon as a silicon is replaced by an aluminum. They studied only the case of the H-bond between the Al-substituted silanols O atom and the silanol H atom. This bond is slightly stronger than with its equivalent without aluminum.

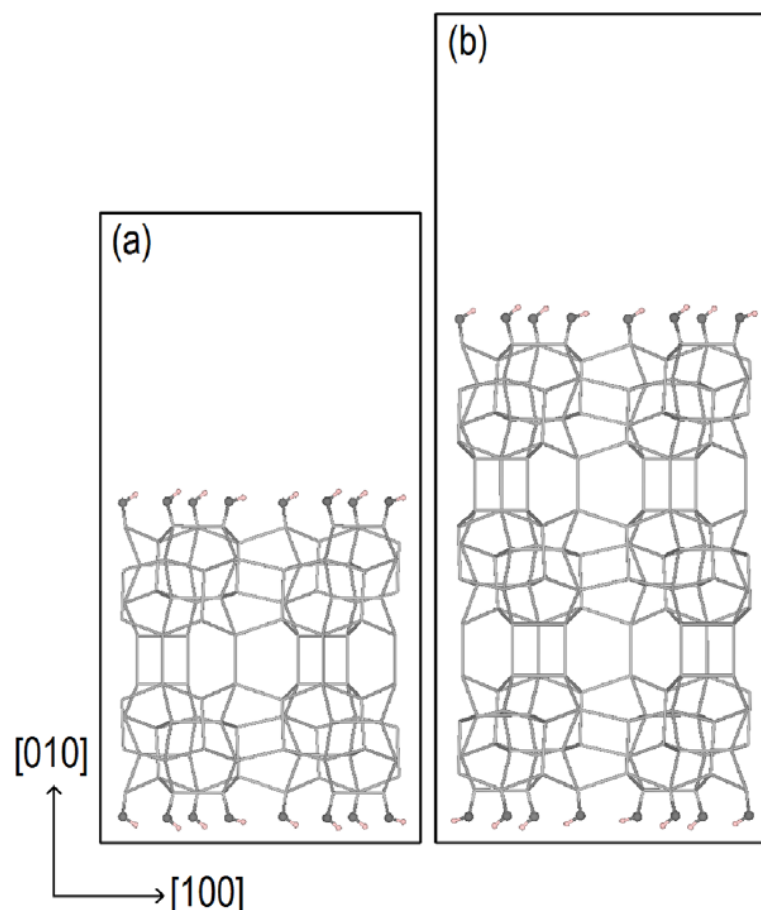


**Figure 35.** Pure-silica slabs formed by two (a) and three (b) pentasil layers; the black lines denote the supercell box. The silanols hydrogen atoms are oriented towards their nearest silanols groups. The silicon atoms are located at the interception of the grey sticks and the framework oxygen were eliminated for a better view. The silanols oxygen are represented with dark grey balls and the hydrogens with light pink balls.<sup>134</sup>

The Al-substituted silanol and Al-substituted tetrahedron inside the bulk are studied according to their accessibility, the O-H stretching frequency and their dehydration. The kinetics of dehydration of the various surface sites showed that the energy difference between the Al-substituted silanol and the silanol dehydration have a  $10 \text{ kJ.mol}^{-1}$  difference. But the Al-substituted silanols are less stable with one water molecule adsorbed on the Lewis center, it makes the dehydration of Brønsted acids sites a natural process on the external surface of ZSM-5 nanosheets. These results give us a first idea of the data researched about the external surface of ZSM-5. But the approach of our work will be different. It will focus on the most prominent surface of ZSM-5 crystals, the (100) surfaces, and is meant to be more precise on the description of the nature of the surface and bulk acid sites.

### 1.3.5. Simulation of the zeolite-binder interface

The properties of the zeolite and binder interface has been studied into multiples aspect as it has been shown in Section 1.2. However, until now, no theoretical studies have been conducted on the interface of zeolite and binder and its properties. However, a relevant molecular dynamics study was recently published investigating a system containing both MFI



and pyrophyllite smectite sheets. Since the applied methodology could be employed in this study, we will further detail it.

Indeed, Pitman and van Duin studied the dynamics of water confined in mesoporous regions, and more particularly between pyrophyllite smectite sheets in a cage of pure silicate MFI zeolite using molecular dynamics simulations with an empirical reactive force field. Contrary to DFT, the reactive force field calculations are computationally far less expensive and thus allows to be applied to much larger models.<sup>166</sup> For example, the size of the model is presented in Figure 36.

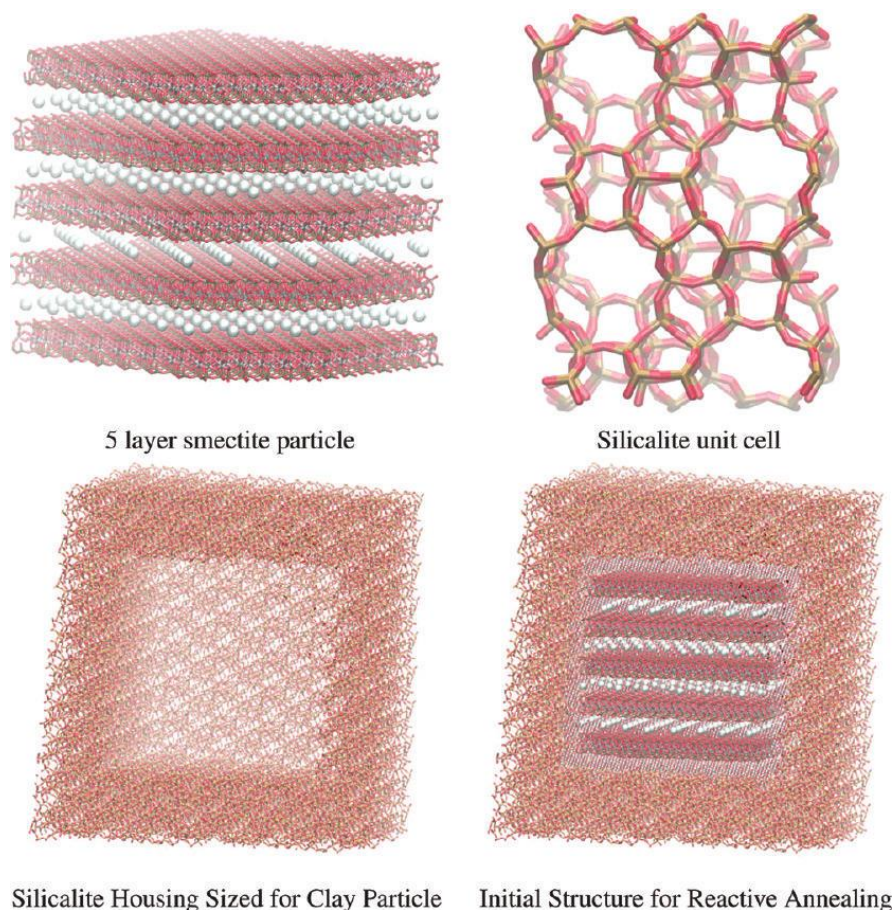


**Figure 36.** Stages of construction for clay-zeolite composite system. (Top left) A five-layer particle constructed from  $11 \times 9 \times 5$  units cells of smectite, where each clay stack is rotated  $60^\circ$ . (Top right) Unit cell of the all-siliceous zeolite ZSM-5-silicalite. (Bottom left) Silicalite unit cells are stacked in a shell to create a housing that can accommodate the clay particles with room for a thin layer of water across the clay-zeolite interface. (Bottom right) The trimmed clay particle placed in the silicalite housing with water placed on a lattice throughout the clay calcium interlayer and clay-silicalite interface.<sup>166</sup>

The main objective of the study was to study the dynamics of water as a function of the composition of the structure of the clay, the counter ion, the Mg isomorph and the number of water molecules are varied to study their influence (Figure 37). Although the interaction between the zeolite and the clay particle was not explicitly studied, the used force field would allow to do so. Therefore, this approach could be transferred to study the interaction of ZSM-5 with the binders studied in this PhD thesis.

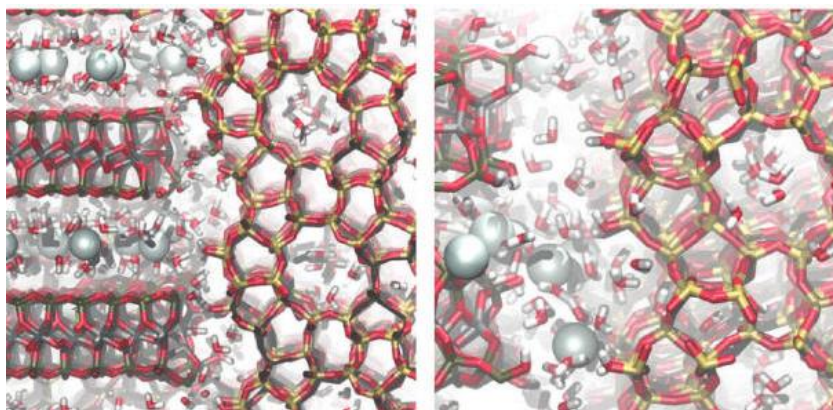


**Figure 37.** Selected views of the clay particle in silicalite housing after annealing at  $T = 500$  K and re-equilibration at  $T = 300$  K. Color scheme: aluminum, gray; clay silicon, dark green; zeolite silicon, tan; oxygen, red; hydrogen, white; calcium, light spheres. (Left) Surface of clay (left) interacting with silicalite (right). (Right) Exchangeable calcium ions which have diffused into the clay-zeolite interface after being expelled from the calcium interlayer during a transition from bilayer to monolayer hydration.

## 1.4. Conclusion and strategy of the thesis

The state of the art shows that if zeolites of high interest for many industrial processes, the understanding of the structure and properties at the atomic scale of its active site, in particular at the external surface and after shaping, remain unknown to date. The ZSM-5 zeolite in particular has been studied experimentally and theoretically very widely but only a few experimental data are available for the shaped zeolite, whereas almost no theoretical investigation has ever been performed.

The main goal of the present PhD project is to construct a representative model of the interface between ZSM-5 and binders. ZSM-5 was chosen due to the numerous available data on this system. Experimentally this zeolite is very easily tunable in terms of crystal size and Si/Al ratio, by changing the synthesis parameters. The theoretical tools which will be used are density functional theory (DFT) and a Reactive force field approach. The two techniques need to be combined to maximize the accuracy of the model while having a large and representative model.

In a first step, we will establish a DFT model of external surfaces of ZSM-5. The stability of the surfaces will be calculated and compared. The behavior of these surface will be analyzed with aluminated T-sites but also by considering the hydration and dehydration of the surface hydroxyl groups. We will reproduce with our theoretical tools several kinds of experimental spectroscopic features to compare our models and find the most accurate one. In particular, the experimental results obtained in the course of another PhD project at IFPEN (Coralie Demaret, PhD 2016-2019) will be taken as reference.<sup>167</sup> In a second step, the acidity of the ZSM-5 will be established and compared between the surface and the bulk of the zeolite. The experimental adsorption of probe molecules will be reproduced to establish the location, the number and the strength of the acid sites. And in a third and last step, the external surface of zeolite will be studied in interaction with compounds representative of two binders (silica and alumina): cations which can be found in binders' framework or binder monomers. In the last part of the thesis, a reactive force field will be optimized, that will open perspectives for establishing more relevant models of the zeolite/binder interface, beyond the consideration of monomers of the binders.



## References

- (1) Martínez, C.; Pérez-Ramírez, J. *Zeolite and ordered porous solids: fundamentals and applications*; Universitat Politecnica de Valencia, 2011.
- (2) Loewenstein, W. The Distribution of aluminum in the Tetrahedra of Silicates and Aluminates. *Am. Miner.* **1954**, *39*, 92–96.
- (3) Weitkamp, J. Zeolites and catalysis. *Solid State Ion.* **2000**, *131*, 175–188.
- (4) Baerlocher, C.; McCusker, J. K. *Database of Zeolite Structures*. <http://www.iza-structure.org/databases/> (accessed 2018).
- (5) Townsend, R.; Coker, E. *Studies in Surface Science and Catalysis: Chapitre 11 : Ion exchange in zeolites*, Elsevier Science; Royal Society of Chemistry, 2001.
- (6) Yamane, I.; Nakazawa, T. Development of zeolite for non-phosphated detergents in Japan. *Pure & Appl. Chem.* **1986**, *58*, 1397–1404.
- (7) Upadck, H.; Krings, P.; Karge, H. G.; Weitkamp, J. *Zeolites as Catalysts, Sorbents and Detergent Builders* p.701; Elsevier: London, 1989.
- (8) Sand, L.; Mumpton, F. *Natural Zeolites: Occurrence, Properties, Use*; Pergamon Press, 1978.
- (9) Dyer, A. *An Introduction to Zeolite Molecular Sieves*; John Wiley and Sons, 1988.
- (10) Nagy, J. B. *Synthesis, characterization and use of zeolitic microporous materials*, DecaGen, 1998.
- (11) Xiao, C.; Ma, Y.; Ji, D.; Zang, L. Review of desulfurization process for biogas purification. *IOP Conf. Ser.: Earth Environ. Sci.* **2017**, *100*, 12177.
- (12) Peluso, A.; Gargiulo, N.; Aprea, P.; Pepe, F.; Caputo, D. Nanoporous Materials as H<sub>2</sub>S Adsorbents for Biogas Purification: A Review. *Separation & Purification Reviews* **2018**, *48*, 78–89.
- (13) Liu, C.; Zhang, R.; Wei, S.; Wang, J.; Liu, Y.; Li, M.; Liu, R. Selective removal of H<sub>2</sub>S from biogas using a regenerable hybrid TiO<sub>2</sub>/zeolite composite. *Fuel* **2015**, *157*, 183–190.
- (14) Liu, X.; Wang, R. Effective removal of hydrogen sulfide using 4A molecular sieve zeolite synthesized from attapulgite. *J. Hazard. Mater.* **2017**, *326*, 157–164.
- (15) Maghsoudi, H.; Soltanieh, M. Simultaneous separation of H<sub>2</sub>S and CO<sub>2</sub> from CH<sub>4</sub> by a high silica CHA-type zeolite membrane. *J. Memb. Sci.* **2014**, *470*, 159–165.
- (16) Guillon, E.; Leflaive, P. Traitement des essences aromatiques pour la pétrochimie. *Techniques de l'ingénieur* **2011**, *J5920v2*, 1–18.
- (17) Dyer, A. *An introduction to zeolite molecular sieves*, J. Wiley, 1988.
- (18) Speybroeck, V. van; Hemelsoet, K.; Joos, L.; Waroquier, M.; Bell, R. G.; Catlow, C. R. A. Advances in theory and their application within the field of zeolite chemistry. *Chem. Soc. Rev.* **2015**, *44*, 7044–7111.
- (19) Brønsted, J. N. Einige Bemerkungen über den Begriff der Säuren und Basen. *Recueil des Travaux Chimiques* **1923**, *48*, 718–728.
- (20) Lowry, T. M. The uniqueness of hydrogen. *J. Chem. and Ind.* **1923**, *42*, 43–47.
- (21) Brønsted, J. N. The Acid-Basic Function of Molecules and its Dependency on the Electric Charge Type. *J. Phys. Chem.* **1926**, *30*, 777–790.
- (22) Brønsted, J. N. Acid and Basic Catalysis. *Chem. Rev.* **1928**, *5*, 231–338.
- (23) Lewis, G. N. *Valence and the Structure of Atoms and Molecules*; Chemical Catalog: New York, 1923.

- (24) Santos, V. Caractérisation et modification de l'acidité résiduelle en zéolithes cationiques: Thèse de doctorat, 2008.
- (25) Rey, J.; Raybaud, P.; Chizallet, C. Ab Initio Simulation of the Acid Sites at the External Surface of Zeolite Beta. *ChemCatChem* **2017**, *9*, 2176–2185.
- (26) Gorte, R. J. *Handbook of Porous Solids: Surface Acidity*; Wiley-VCH Verlag GmbH, 2002.
- (27) Szostak, R. Chapter 5 Modified Zeolites. *Introduction to Zeolite Science and Practice*; Studies in Surface Science and Catalysis; Elsevier, 1991; pp 153–199.
- (28) Sonnemans, M. H. W.; Den Heijer, C.; Crocker, M. Studies on the acidity of mordenite and ZSM 5. 2. Loss of Brønsted acidity by dehydroxylation and dealumination. *J. Phys. Chem.* **1993**, *97*, 440–445.
- (29) Poutsma, M. L. *Zeolite Chemistry and Catalysis- ACS Monograph*. 437-551; Elsevier, Amsterdam, 1976.
- (30) Karge, H. G. *J. Phys. Chem.* **1971**, *76*, 133.
- (31) Venuto, P. *Adv. Catal.* **1968**, *18*, 259.
- (32) Becker, K.; Karge, H. G.; Streubel, W. D. *J. Catal.* **1973**, *28*.
- (33) Makarova, M. A.; Bates, S. P.; Dwyer, J. In Situ Modeling of the Enhanced Brønsted Acidity in Zeolites. *J. Am. Chem. Soc.* **1995**, *117*, 11309–11313.
- (34) Boronat, M.; Corma, A.; Renz, M.; Viruela, P. M. Predicting the activity of single isolated Lewis acid sites in solid catalysts. *Chem.* **2006**, *12*, 7067–7077.
- (35) Bates, J. S.; Gounder, R. Influence of confining environment polarity on ethanol dehydration catalysis by Lewis acid zeolites. *J. Catal.* **2018**, *365*, 213–226.
- (36) Josephson, T. R.; DeJaco, R. F.; Pahari, S.; Ren, L.; Guo, Q.; Tsapatsis, M.; Siepmann, J. I.; Vlachos, D. G.; Caratzoulas, S. Cooperative Catalysis by Surface Lewis Acid/Silanol for Selective Fructose Etherification on Sn-SPP Zeolite. *ACS Catal.* **2018**, *8*, 9056–9065.
- (37) Koehle, M.; Zhang, Z.; Goulas, K. A.; Caratzoulas, S.; Vlachos, D. G.; Lobo, R. F. Acylation of methylfuran with Brønsted and Lewis acid zeolites. *Appl. Catal. A* **2018**, *564*, 90–101.
- (38) Auroux, A. Microcalorimetry Methods to Study the Acidity and Reactivity of Zeolites, Pillared Clays and Mesoporous Materials. *Top. Catal.* **2002**, *19*, 205–213.
- (39) Jia, C.; Massiani, P.; Barthomeuf, D. Characterization by infrared and nuclear magnetic resonance spectroscopies of calcined beta zeolite. *Faraday Trans.* **1993**, *89*, 3659.
- (40) Holzinger, J.; Beato, P.; Lundegaard, L. F.; Skibsted, J. Distribution of Aluminum over the Tetrahedral Sites in ZSM-5 Zeolites and Their Evolution after Steam Treatment. *J. Phys. Chem. C* **2018**, *122*, 15595–15613.
- (41) Bokhoven, J. A. van; Koningsberger, D. C.; Kunkeler, P.; Bekkum, H. van; Kentgens, A. P. M. Stepwise Dealumination of Zeolite Beta at Specific T-Sites Observed with <sup>27</sup>Al MAS and <sup>27</sup>Al MQ MAS NMR. *J. Am. Chem. Soc.* **2000**, *122*, 12842–12847.
- (42) Sklenak, S.; Dědeček, J.; Li, C.; Wichterlová, B.; Gábová, V.; Sierka, M.; Sauer, J. Aluminum siting in silicon-rich zeolite frameworks: a combined high-resolution (<sup>27</sup>Al) NMR spectroscopy and quantum mechanics / molecular mechanics study of ZSM-5. *Angew. Chem. Int. Ed.* **2007**, *46*, 7286–7289.

- (43) Pinar, A. B.; Gómez-Hortigüela, L.; McCusker, L. B.; Pérez-Ramírez, J. Controlling the Aluminum Distribution in the Zeolite Ferrierite via the Organic Structure Directing Agent. *Chem. Mater.* **2013**, *25*, 3654–3661.
- (44) Vjunov, A.; Fulton, J. L.; Huthwelker, T.; Pin, S.; Mei, D.; Schenter, G. K.; Govind, N.; Camaioni, D. M.; Hu, J. Z.; Lercher, J. A. Quantitatively probing the Al distribution in zeolites. *J. Am. Chem. Soc.* **2014**, *136*, 8296–8306.
- (45) Brus, J.; Kobera, L.; Schoefberger, W.; Urbanova, M.; Klein, P.; Sazama, P.; Tabor, E.; Sklenak, S.; Fishchuk, A. V.; Dědeček, J. Structure of framework aluminum Lewis sites and perturbed aluminum atoms in zeolites as determined by  $^{27}\text{Al}\{1\text{H}\}$  REDOR (3Q) MAS NMR spectroscopy and DFT/molecular mechanics. *Angew. Chem. Int. Ed.* **2015**, *54*, 541–545.
- (46) Perea, D. E.; Arslan, I.; Liu, J.; Ristanović, Z.; Kovarik, L.; Arey, B. W.; Lercher, J. A.; Bare, S. R.; Weckhuysen, B. M. Determining the location and nearest neighbours of aluminium in zeolites with atom probe tomography. *Nat. Commun.* **2015**, *6*, 7589.
- (47) Li, C.; Vidal-Moya, A.; Miguel, P. J.; Dědeček, J.; Boronat, M.; Corma, A. Selective Introduction of Acid Sites in Different Confined Positions in ZSM-5 and Its Catalytic Implications. *ACS Catal.* **2018**, *8*, 7688–7697.
- (48) Toulhoat, H.; Raybaud, P.; Benazzi, E. Effect of confinement on the selectivity of hydrocracking. *J. Catal.* **2004**, *221*, 500–509.
- (49) Smit, B.; Maesen, T. L. M. Molecular simulations of zeolites: Adsorption, diffusion, and shape selectivity. *Chem. Rev.* **2008**, *108*, 4125–4184.
- (50) Martens, J. A.; Souverijns, W.; Verrelst, W.; Parton, R.; Froment, G. F.; Jacobs, P. A. Selective Isomerization of Hydrocarbon Chains on External Surfaces of Zeolite Crystals. *Angew. Chem. Int. Ed.* **1995**, *34*, 2528–2531.
- (51) Martens, J. A.; Vanbutsele, G.; Jacobs, P. A.; Denayer, J.; Ocakoglu, R.; Baron, G.; Muñoz Arroyo, J. A.; Thybaut, J.; Marin, G. B. Evidences for pore mouth and key–lock catalysis in hydroisomerization of long n-alkanes over 10-ring tubular pore bifunctional zeolites. *Catal. Today* **2001**, *65*, 111–116.
- (52) Awala, H.; Gilson, J.-P.; Retoux, R.; Boullay, P.; Goupil, J.-M.; Valtchev, V.; Mintova, S. Template-free nanosized faujasite-type zeolites. *Nat. Mater.* **2015**, *14*, 447–451.
- (53) Wu, Z.; Wang, Y. Catalytic Application of Mesoporous ZSM-5 Zeolite. *Curr. Org. Chem.* **2014**, *18*, 1305–1322.
- (54) Argauer, R. J.; Landolt, G. R. Crystalline zeolite ZSM-5 and method of preparing the same. 865,472, Oct 10, 1969.
- (55) Pelrine, B. P. Synthesis of zeolite ZSM-5. 824,379, Aug 15, 1978.
- (56) Rollmann, L. D.; Valyocsik, E. W. Synthesis of large crystal zeolite ZSM-5 and zeolite so made - European Patent Office - EP 0021674 A1. EP19800301895, Jun 6, 1980.
- (57) Kokotailo, G. T.; Lawton, S. L.; Olson, D. H.; Meier, W. M. Structure of synthetic zeolite ZSM-5. *Nature* **1978**, *272*, 437–438.
- (58) Olson, D. H.; Kokotailo, G. T.; Lawton, S. L.; Meier, W. M. Crystal structure and structure-related properties of ZSM-5. *J. Phys. Chem.* **1981**, *85*, 2238–2243.
- (59) Zeng, G.; Chen, C.; Li, D.; Hou, B.; Sun, Y. Exposure of (001) planes and (011) planes in MFI zeolite. *Cryst. Eng. Comm.* **2013**, *15*, 3521.

- (60) Price, G. D.; Pluth, J. J.; Smith, J. V.; Bennett, J. M.; Patton, R. L. Crystal structure of tetrapropylammonium fluoride-containing precursor to fluoride silicalite. *J. Am. Chem. Soc.* **1982**, *104*, 5971–5977.
- (61) Ballmoos, R. von. Thesis ETH Zurich, 1981.
- (62) Ballmoos, R. von; Meier, W. M. Zoned aluminium distribution in synthetic zeolite ZSM-5. *Nature* **1981**, 289.
- (63) Lermer, H.; Draeger, M.; Steffen, J.; Unger, K. K. Synthesis and structure refinement of ZSM—5 single crystals. *Zeolites* **1985**, *5*, 131–134.
- (64) Koegler, J. H.; Bekkum, H. van; Jansen, J. C. Growth model of oriented crystals of zeolite Si-ZSM-5. *Zeolites* **1997**, *19*, 262–269.
- (65) Weidenthaler, C.; Fischer, R. X.; Shannon, R. D.; Medenbach, O. Optical Investigations of Intergrowth Effects in the Zeolite Catalysts ZSM-5 and ZSM-8. *J. Phys. Chem.* **1994**, *98*, 12687–12694.
- (66) Agger, J. R.; Hanif, N.; Cundy, C. S.; Wade, A. P.; Dennison, S.; Rawlinson, P. A.; Anderson, M. W. Silicalite crystal growth investigated by atomic force microscopy. *J. Am. Chem. Soc.* **2003**, *125*, 830–839.
- (67) Kocirik, M.; Kornatowski, J.; Masařík, V.; Novák, P.; Zikánová, A.; Maixner, J. Investigation of sorption and transport of sorbate molecules in crystals of MFI structure type by iodine indicator technique. *Micropor. Mesopor. Mat.* **1998**, *23*, 295–308.
- (68) Geier, O.; Vasenkov, S.; Lehmann, E.; Kärger, J.; Schemmert, U.; Rakoczy, R. A.; Weitkamp, J. Interference Microscopy Investigation of the Influence of Regular Intergrowth Effects in MFI-Type Zeolites on Molecular Uptake. *J. Phys. Chem. B* **2001**, *105*, 10217–10222.
- (69) Schuth, F. Polarized Fourier transform infrared microscopy as a tool for structural analysis of adsorbates in molecular sieves. *J. Phys. Chem.* **1992**, *96*, 7493–7496.
- (70) Stavitski, E.; Kox, M. H. F.; Weckhuysen, B. M. Revealing shape selectivity and catalytic activity trends within the pores of H-ZSM-5 crystals by time- and space-resolved optical and fluorescence microspectroscopy. *Chem.* **2007**, *13*, 7057–7065.
- (71) Kox, M. H. F.; Stavitski, E.; Weckhuysen, B. M. Nonuniform catalytic behavior of zeolite crystals as revealed by in situ optical microspectroscopy. *Angew. Chem. Int. Ed.* **2007**, *46*, 3652–3655.
- (72) Roeffaers, M. B. J.; Ameloot, R.; Baruah, M.; Uji-I, H.; Bulut, M.; Cremer, G. de; Müller, U.; Jacobs, P. A.; Hofkens, J.; Sels, B. F. *et al.* Morphology of large ZSM-5 crystals unraveled by fluorescence microscopy. *J. Am. Chem. Soc.* **2008**, *130*, 5763–5772.
- (73) Karwacki, L.; Kox, M. H. F.; Winter, D. A. M. de; Drury, M. R.; Meeldijk, J. D.; Stavitski, E.; Schmidt, W.; Mertens, M.; Cubillas, P.; John, N. *et al.* Morphology-dependent zeolite intergrowth structures leading to distinct internal and outer-surface molecular diffusion barriers. *Nat. Mater.* **2009**, *8*, 959–965.
- (74) Roeffaers, M. B. J.; Ameloot, R.; Bons, A.-J.; Mortier, W.; Cremer, G. de; Kloe, R. de; Hofkens, J.; Vos, D. E. de; Sels, B. F. Relating pore structure to activity at the subcrystal level for ZSM-5: an electron backscattering diffraction and fluorescence microscopy study. *J. Am. Chem. Soc.* **2008**, *130*, 13516–13517.

- (75) Cremer, G. de; Sels, B. F.; Vos, D. E. de; Hofkens, J.; Roeffaers, M. B. J. Fluorescence micro(spectro)scopy as a tool to study catalytic materials in action. *Chem. Soc. Rev.* **2010**, *39*, 4703–4717.
- (76) Roeffaers, M. B. J.; Cremer, G. de; Libeert, J.; Ameloot, R.; Dedecker, P.; Bons, A.-J.; Bückins, M.; Martens, J. A.; Sels, B. F.; Vos, D. E. de *et al.* Super-resolution reactivity mapping of nanostructured catalyst particles. *Angew. Chem. Int. Ed.* **2009**, *48*, 9285–9289.
- (77) Sprung, C.; Weckhuysen, B. M. Differences in the location of guest molecules within zeolite pores as revealed by multilaser excitation confocal fluorescence microscopy: which molecule is where? *J. Am. Chem. Soc.* **2015**, *137*, 1916–1928.
- (78) Valtchev, V.; Majano, G.; Mintova, S.; Pérez-Ramírez, J. Tailored crystalline microporous materials by post-synthesis modification. *Chem. Soc. Rev.* **2013**, *42*, 263–290.
- (79) Pérez-Ramírez, J.; Egeblad, K.; Christensen, C. H.; Groen, J. C. Hierarchical zeolites: Enhanced utilisation of microporous crystals in catalysis by advances in materials design. *Chem. Soc. Rev.* **2008**, *37*, 2530–2542.
- (80) Silaghi, M.-C.; Chizallet, C.; Petracovschi, E.; Kerber, T.; Sauer, J.; Raybaud, P. Regioselectivity of Al–O Bond Hydrolysis during Zeolites Dealumination Unified by Brønsted–Evans–Polanyi Relationship. *ACS Catal.* **2014**, *5*, 11–15.
- (81) Pagis, C.; Morgado Prates, A. R.; Farrusseng, D.; Bats, N.; Tuel, A. Hollow Zeolite Structures: An Overview of Synthesis Methods. *Chem. Mater.* **2016**, *28*, 5205–5223.
- (82) Corma, A.; Fornés, V.; Pergher, S. B.; Maesen, T. L. M.; Buglass, J. G. Delaminated zeolite precursors as selective acidic catalysts. *Nature* **1998**, *396*, 353–356.
- (83) Choi, M.; Na, K.; Kim, J.; Sakamoto, Y.; Terasaki, O.; Ryoo, R. Stable single-unit-cell nanosheets of zeolite MFI as active and long-lived catalysts. *Nature* **2009**, *461*, 246–249.
- (84) Roth, W. J.; Nachtigall, P.; Morris, R. E.; Čejka, J. Two-dimensional zeolites: Current status and perspectives. *Chem. Rev.* **2014**, *114*, 4807–4837.
- (85) Varoon K.; Zhang, X.; Elyassi B.; Brewer D.; Gettel M.; Kumar S.; Lee A.; Maheshwari S.; Mittal A.; Sung, C. *et al.* Dispersible Exfoliated Zeolite Nanosheets and Their Application as a Selective Membrane. *Science* **2011**, *334*, 72–75.
- (86) Zhang, X.; Liu, D.; Xu, D.; Asahina, S.; Cychosz, K. A.; Agrawal, K. V.; Al Wahedi, Y.; Bhan, A.; Al Hashimi, S.; Terasaki, O. *et al.* Synthesis of self-pillared zeolite nanosheets by repetitive branching. *Science* **2012**, *336*, 1684–1687.
- (87) Shete, M.; Kumar, M.; Kim, D.; Rangnekar, N.; Xu, D.; Topuz, B.; Agrawal, K. V.; Karapetrova, E.; Stottrup, B.; Al-Thabaiti, S. *et al.* Nanoscale Control of Homoepitaxial Growth on a Two-Dimensional Zeolite. *Angew. Chem. Int. Ed.* **2017**, *56*, 535–539.
- (88) Jeon, M. Y.; Kim, D.; Kumar, P.; Lee, P. S.; Rangnekar, N.; Bai, P.; Shete, M.; Elyassi B.; Lee, H. S.; Narasimharao, K. *et al.* Ultra-selective high-flux membranes from directly synthesized zeolite nanosheets. *Nature* **2017**, *543*, 690–694.
- (89) Hendriks, F. C.; Valencia, D.; Bruijninx, P. C. A.; Weckhuysen, B. M. Zeolite molecular accessibility and host-guest interactions studied by adsorption of organic probes of tunable size. *Phys. Chem. Chem. Phys.* **2017**, *19*, 1857–1867.
- (90) Hendriks, F. C.; Schmidt, J. E.; Rombouts, J. A.; Lammertsma, K.; Bruijninx, P. C. A.; Weckhuysen, B. M. Probing Zeolite Crystal Architecture and Structural Imperfections using Differently Sized Fluorescent Organic Probe Molecules. *Chem.* **2017**, *23*, 6305–6314.

- (91) Ristanović, Z.; Hofmann, J. P.; Deka, U.; Schüllli, T. U.; Rohnke, M.; Beale, A. M.; Weckhuysen, B. M. Intergrowth structure and aluminium zoning of a zeolite ZSM-5 crystal as resolved by synchrotron-based micro X-ray diffraction imaging. *Angew. Chem. Int. Ed.* **2013**, *52*, 13382–13386.
- (92) Karwacki, L.; Stavitski, E.; Kox, M. H. F.; Kornatowski, J.; Weckhuysen, B. M. Intergrowth structure of zeolite crystals as determined by optical and fluorescence microscopy of the template-removal process. *Angew. Chem. Int. Ed.* **2007**, *46*, 7228–7231.
- (93) Mores, D.; Stavitski, E.; Kox, M. H. F.; Kornatowski, J.; Olsbye, U.; Weckhuysen, B. M. Space- and time-resolved in-situ spectroscopy on the coke formation in molecular sieves: methanol-to-olefin conversion over H-ZSM-5 and H-SAPO-34. *Chem.* **2008**, *14*, 11320–11327.
- (94) Daffy, L. M.; Silva, A. P. de; Gunaratne, H. Q. N.; Huber, C.; Lynch, P. L. M.; Werner, T.; Wolfbeis, O. S. Arededicarboximide Building Blocks for Fluorescent Photoinduced Electron Transfer pH Sensors Applicable with Different Media and Communication Wavelengths. *Chem. Eur. J.* **1998**, *4*, 1810–1815.
- (95) Roeffaers, M. B. J.; Sels, B. F.; Uji-I, H.; Blanpain, B.; L'hoëst, P.; Jacobs, P. A.; Schryver, F. C. de; Hofkens, J.; Vos, D. E. de. Space- and time-resolved visualization of acid catalysis in ZSM-5 crystals by fluorescence microscopy. *Angew. Chem. Int. Ed.* **2007**, *46*, 1706–1709.
- (96) Kennes, K.; Demaret, C.; Loon, J. van; Kubarev, A. V.; Fleury, G.; Sliwa, M.; Delpoux, O.; Maury, S.; Harbuzaru, B.; Roeffaers, M. B. J. Assessing Inter and Intra-particle Heterogeneity in Alumina-poor H-ZSM-5 Zeolites. *ChemCatChem* **2017**, *9*, 3440–3445.
- (97) Kotrel, S.; Rosynek, M. P.; Lunsford, J. H. Quantification of Acid Sites in H-ZSM-5, H-b, and H-Y Zeolites. *J. Catal.* **1998**, *182*, 278–281.
- (98) Maijanen, A.; Derouane, E. G.; Nagy, J. B. FT-IR and solid-state NMR investigation of surface hydroxyl groups on dealuminated ZSM-5. *Appl. Surf. Sci.* **1994**, *75*, 204–212.
- (99) Pashkova, V.; Sklenak, S.; Klein, P.; Urbanova, M.; Dědeček, J. Location of Framework Al Atoms in the Channels of ZSM-5: Effect of the (Hydrothermal) Synthesis. *Chem.* **2016**, *22*, 3937–3941.
- (100) Bordiga, S.; Lamberti, C.; Bonino, F.; Travert, A.; Thibault-Starzyk, F. Probing zeolites by vibrational spectroscopies. *Chem. Soc. Rev.* **2015**, *44*, 7262–7341.
- (101) Hoffmann, P.; Lobo, J. A. Identification of diverse silanols on protonated ZSM-5 zeolites by means of FTIR spectroscopy. *Micropor. Mesopor. Mat.* **2007**, *106*, 122–128.
- (102) Trombetta, M.; Armaroli, T.; Gutiérrez Alejandro, A.; Ramirez Solis, J.; Busca, G. An FT-IR study of the internal and external surfaces of HZSM5 zeolite. *Appl. Catal. A* **2000**, *192*, 125–136.
- (103) Jin, F.; Li, Y. A FTIR and TPD examination of the distributive properties of acid sites on ZSM-5 zeolite with pyridine as a probe molecule. *Catal. Today* **2009**, *145*, 101–107.
- (104) Isernia, L. F. FTIR study of the relation, between extra-framework aluminum species and the adsorbed molecular water, and its effect on the acidity in ZSM-5 steamed zeolite. *Mat. Res.* **2013**, *16*, 792–802.
- (105) Weitkamp, J. Zeolites and related microporous materials: State of the art 1994 / proceedings of the 10th International Zeolite Conference, Garmisch-Partenkirchen, Germany, July 17-22, 1994 **1994**.

- (106) Corma, A.; Fornés, V.; Forni, L.; Márquez, F.; Martínez-Triguero, J.; Moscotti, D. 2,6-Di-Tert-Butyl-Pyridine as a Probe Molecule to Measure External Acidity of Zeolites. *J. Catal.* **1998**, *179*, 451–458.
- (107) Góra-Marek, K.; Tarach, K.; Choi, M. 2,6-Di- tert- butylpyridine Sorption Approach to Quantify the External Acidity in Hierarchical Zeolites. *J. Phys. Chem. C* **2014**, *118*, 12266–12274.
- (108) Devyatkov S.; Kuzichkin N. V.; Murzin D. Y. *Chimica oggi: On comprehensive understanding of catalyst shaping by extrusion*; (p. 57), 2015.
- (109) Mitchell, S.; Michels, N.-L.; Pérez-Ramírez, J. From powder to technical body: the undervalued science of catalyst scale up. *Chem. Soc. Rev.* **2013**, *42*, 6094–6112.
- (110) Mitchell, S.; Michels, N.-L.; Kunze, K.; Pérez-Ramírez, J. Visualization of hierarchically structured zeolite bodies from macro to nano length scales. *Nat. Chem.* **2012**, *4*, 825–831.
- (111) Hargreaves, J. S. J.; Munnoch, A. L. A survey of the influence of binders in zeolite catalysis. *Catal. Sci. Technol.* **2013**, *3*, 1165.
- (112) Michels, N.-L.; Mitchell, S.; Pérez-Ramírez, J. Effects of Binders on the Performance of Shaped Hierarchical MFI Zeolites in Methanol-to-Hydrocarbons. *ACS Catal.* **2014**, *4*, 2409–2417.
- (113) Iveson, S. M.; Litster, J. D.; Hapgood, K.; Ennis, B. J. Nucleation, growth and breakage phenomena in agitated wet granulation processes: A review. *Powder Technol.* **2001**, *117*, 3–39.
- (114) Wildeboer, W. J.; Litster, J. D.; Cameron, I. T. Modelling nucleation in wet granulation. *Chem. Eng. Sci.* **2005**, *60*, 3751–3761.
- (115) Whiting, G. T.; Meirer, F.; Mertens, M.; Bons, A.-J.; Weiss, B. M.; Stevens, P. A.; Smit, E. de; Weckhuysen, B. M. Binder Effects in SiO<sub>2</sub>- and Al<sub>2</sub>O<sub>3</sub>-Bound Zeolite ZSM-5-Based Extrudates as Studied by Microspectroscopy. *ChemCatChem* **2015**, *7*, 1312–1321.
- (116) Benbow, J. J.; Bridgwater, J. The cutting of paste extrudates. *Chem. Eng. Sci.* **1993**, *48*, 3088–3091.
- (117) Scherer, W. Theory of Drying. *J. Am. Ceram. Soc.* **1990**, *73*, 3–14.
- (118) Chemkhi, S. Séchage d'un milieu déformable non saturé Modélisation du couplage hygromécanique: Thèse de doctorat, 2008.
- (119) Lynch, J. *Analyse physico-chimique des catalyseurs industriels Manuel pratique de caractérisation*, 2001.
- (120) Nakhaei Pour, A.; Housaindokht, M. R. Study of activity, products selectivity and physico-chemical properties of bifunctional Fe/HZSM-5 Fischer–Tropsch catalyst: Effect of catalyst shaping. *J. Nat. Gas Sci. Eng.* **2013**, *14*, 29–33.
- (121) Michels, N.-L. From powder to Technical Body: Structured Zeolite Catalysts with Enhanced Functionality: Thèse de doctorat, 2014.
- (122) Michels, N.-L.; Mitchell, S.; Milina, M.; Kunze, K.; Krumeich, F.; Marone, F.; Erdmann, M.; Marti, N.; Pérez-Ramírez, J. Hierarchically Structured Zeolite Bodies: Assembling Micro-, Meso-, and Macroporosity Levels in Complex Materials with Enhanced Properties. *Adv. Funct. Mater.* **2012**, *22*, 2509–2518.



- (123) Chen, N.-Y.; Liu, M.-C.; Yang, S.-C.; Sheu, H.-S.; Chang, J.-R. Impacts of Binder-Zeolite Interactions on the Structure and Surface Properties of NaY–SiO<sub>2</sub> Extrudates. *Ind. Eng. Chem. Res.* **2015**, *54*, 8456–8468.
- (124) Shihabi, D. S.; Garwood, W. E.; Chu, P.; Miale, J. N.; Lago, R. M.; Chu, C. T.-W.; Chang, C. D. Aluminum insertion into high-silica zeolite frameworks II. Binder activation of high-silica ZSM-5. *J. Catal.* **1985**, *93*, 471–474.
- (125) Pérez-Uriarte, P.; Gamero, M.; Ateka, A.; Díaz, M.; Aguayo, A. T.; Bilbao, J. Effect of the Acidity of HZSM-5 Zeolite and the Binder in the DME Transformation to Olefins. *Ind. Eng. Chem. Res.* **2016**, *55*, 1513–1521.
- (126) Sauer, J. Molecular models in ab initio studies of solids and surfaces: from ionic crystals and semiconductors to catalysts.
- (127) Santen, R. A. van; Kramer, G. J. Reactivity Theory of Zeolitic Brønsted Acidic Sites.
- (128) Speybroeck, V. van; Wispelaere, K. de; Mynsbrugge, J. van der; Vandichel, M.; Hemelsoet, K.; Waroquier, M. First principle chemical kinetics in zeolites: The methanol-to-olefin process as a case study. *Chem. Soc. Rev.* **2014**, *43*, 7326–7357.
- (129) Kassab, E.; Castellà-Ventura, M.; Akacem, Y. Theoretical Study of 4,4'-Bipyridine Adsorption on the Brønsted Acid Sites of H-ZSM-5 Zeolite. *J. Phys. Chem. C* **2009**, *113*, 20388–20395.
- (130) Akacem, Y.; Castellà-Ventura, M.; Kassab, E. Theoretical study of the aluminum distribution effects on the double proton transfer mechanisms upon adsorption of 4,4'-bipyridine on H-ZSM-5. *J. Phys. Chem. A* **2012**, *116*, 1261–1271.
- (131) Schnell, S. K.; Wu, L.; Koekkoek, A. J. J.; Kjelstrup, S.; Hensen, E. J. M.; Vlugt, T. J. H. Adsorption of Argon on MFI Nanosheets: Experiments and Simulations. *J. Phys. Chem. C* **2013**, *117*, 24503–24510.
- (132) Byun, Y.; Jo, D.; Shin, D. N.; Hong, S. B. Theoretical Investigation of the Isomerization and Disproportionation of m-Xylene over Medium-Pore Zeolites with Different Framework Topologies. *ACS Catal.* **2014**, *4*, 1764–1776.
- (133) Zhang, Y.; Yu, J.; Yeh, Y.-H.; Gorte, R. J.; Rangarajan, S.; Mavrikakis, M. An Adsorption Study of CH<sub>4</sub> on ZSM-5, MOR, and ZSM-12 Zeolites. *J. Phys. Chem. C* **2015**, *119*, 28970–28978.
- (134) Hernandez-Tamargo, C. E.; Roldan, A.; Leeuw, N. H. de. A density functional theory study of the structure of pure-silica and aluminium-substituted MFI nanosheets. *J. Solid State Chem.* **2016**, *237*, 192–203.
- (135) Schröder, K.-P.; Sauer, J.; Leslie, M.; Richard, C.; Catlow, A. Siting of Al and bridging hydroxyl groups in ZSM-5: A computer simulation study **1992**, *12*, 20–23.
- (136) Nchtigallova, D.; Nchtigall, P.; Sierka, M.; Sauer, J. Coordination and siting of Cu<sup>+</sup> ions in ZSM-5: A combined quantum mechanics/interatomic potential function study **1999**, *1*, 2019–2026.
- (137) Ghorbanpour, A.; Rimer, J. D.; Grabow, L. C. Periodic, vdW-corrected density functional theory investigation of the effect of Al siting in H-ZSM-5 on chemisorption properties and site-specific acidity. *Catal. Commun.* **2014**, *52*, 98–102.
- (138) Knott, B. C.; Nimlos, C. T.; Robichaud, D. J.; Nimlos, M. R.; Kim, S.; Gounder, R. Consideration of the Aluminum Distribution in Zeolites in Theoretical and Experimental Catalysis Research. *ACS Catal.* **2018**, *8*, 770–784.

- (139) Sklenak, S.; Dědeček, J.; Li, C.; Wichterlová, B.; Gábová, V.; Sierka, M.; Sauer, J. Aluminium siting in the ZSM-5 framework by combination of high resolution  $^{27}\text{Al}$  NMR and DFT/MM calculations. *Phys. Chem. Chem. Phys.* **2009**, *11*, 1237–1247.
- (140) Dib, E.; Mineva, T.; Veron, E.; Sarou-Kanian, V.; Fayon, F.; Alonso, B. ZSM-5 Zeolite: Complete Al Bond Connectivity and Implications on Structure Formation from Solid-State NMR and Quantum Chemistry Calculations. *J. Phys. Chem.* **2018**, *9*, 19–24.
- (141) Silaghi, M.-C.; Chizallet, C.; Sauer, J.; Raybaud, P. Dealumination mechanisms of zeolites and extra-framework aluminum confinement. *J. Catal.* **2016**, *339*, 242–255.
- (142) Vedrine, J.; Auroux, A.; Bolis, V.; Dejaifve, P.; Naccache, C.; Wierzchowski, P.; Derouane, E. G.; Nagy, J. B.; Gilson, J.-P.; Vanhooff, J. Infrared, microcalorimetric, and electron spin resonance investigations of the acidic properties of the H-ZSM-5 zeolite. *J. Catal.* **1979**, *59*, 248–262.
- (143) Akacem, Y.; Kassab, E. Vibrational Analysis of Pyridine Adsorption on the Brønsted Acid Sites of Zeolites Based on Density Functional Cluster Calculations. *J. Phys. Chem. C* **2008**, *112*, 19045–19054.
- (144) Liu, C.; Li, G.; Hensen, E. J. M.; Pidko, E. A. Relationship between acidity and catalytic reactivity of faujasite zeolite: A periodic DFT study. *J. Catal.* **2016**, *344*, 570–577.
- (145) Josephson, T. R.; Jenness, G. R.; Vlachos, D. G.; Caratzoulas, S. Distribution of open sites in Sn-Beta zeolite. *Micropor. Mesopor. Mat.* **2017**, *245*, 45–50.
- (146) Manoilova, O. V.; Podkolzin, S. G.; Tope, B.; Lercher, J. A.; Stangland, E. E.; Goupil, J.-M.; Weckhuysen, B. M. Surface Acidity and Basicity of  $\text{La}_2\text{O}_3$ ,  $\text{LaOCl}$ , and  $\text{LaCl}_3$  Characterized by IR Spectroscopy, TPD, and DFT Calculations. *J. Phys. Chem. B* **2004**, *108*, 15770–15781.
- (147) Gafurov, M. R.; Mukhambetov, I. N.; Yavkin, B. V.; Mamin, G. V.; Lamberov, A. A.; Orlinkii, S. B. Quantitative Analysis of Lewis Acid Centers of  $\gamma$ -Alumina by Using EPR of the Adsorbed Anthraquinone as a Probe Molecule: Comparison with the Pyridine, Carbon Monoxide IR, and TPD of Ammonia. *J. Phys. Chem. C* **2015**, *119*, 27410–27415.
- (148) Bučko, T.; Benco, L.; Demuth, T.; Hafner, J. Ab initio density functional investigation of the (001) surface of mordenite. *J. Chem. Phys.* **2002**, *117*, 7295–7305.
- (149) Bučko, T.; Benco, L.; Hafner, J. Defect sites at the (001) surface of mordenite: An ab initio study. *J. Chem. Phys.* **2003**, *118*, 8437–8445.
- (150) Benco, L.; Bučko, T.; Hafner, J.; Toulhoat, H. Ab Initio Simulation of Lewis Sites in Mordenite and Comparative Study of the Strength of Active Sites via CO Adsorption. *J. Phys. Chem. B* **2004**, *108*, 13656–13666.
- (151) Bučko, T.; Hafner, J.; Benco, L. Adsorption and vibrational spectroscopy of CO on mordenite: Ab initio density-functional study. *J. Phys. Chem. B* **2005**, *109*, 7345–7357.
- (152) Stoyanov, S. R.; Gusarov, S.; Kuznicki, S. M.; Kovalenko, A. Theoretical Modeling of Zeolite Nanoparticle Surface Acidity for Heavy Oil Upgrading. *J. Phys. Chem. C* **2008**, *112*, 6794–6810.
- (153) Slater, B.; Catlow, C. R. A.; Liu, Z.; Ohsuna, T.; Terasaki, O.; Cambor, M. A. Surface structure and crystal growth of zeolite Beta C. *Angew. Chem. Int. Ed.* **2002**, *41*, 1235–1237.
- (154) Ohsuna, T.; Slater, B.; Gao, F.; Yu, J.; Sakamoto, Y.; Zhu, G.; Terasaki, O.; Vaughan, D. E. W.; Qiu, S.; Catlow, C. R. A. Fine structures of zeolite-Linde-L (LTL): Surface structures, growth unit and defects. *Chem.* **2004**, *10*, 5031–5040.

- (155) Slater, B.; Titiloye, J. O.; Higgins, F. M.; Parker, S. C. Atomistic simulation of zeolite surfaces. *Curr. Opin. Solid St. M.* **2001**, *5*, 417–424.
- (156) Abril, D. M.; Slater, B.; Blanco, C. Modeling dynamics of the external surface of zeolite LTA. *Micropor. Mesopor. Mat.* **2009**, *123*, 268–273.
- (157) Greń, W.; Parker, S. C.; Slater, B.; Lewis, D. W. Structure of Zeolite A (LTA) Surfaces and the Zeolite A/Water Interface. *J. Phys. Chem. C* **2010**, *114*, 9739–9747.
- (158) Ferrante, F.; Rubino, T.; Duca, D. Butene Isomerization and Double-Bond Migration on the H-ZSM-5 Outer Surface: A Density Functional Theory Study. *J. Phys. Chem. C* **2011**, *115*, 14862–14868.
- (159) Prestianni, A.; Cortese, R.; Duca, D. Propan-2-ol dehydration on H-ZSM-5 and H-Y zeolite: A DFT study. *Reac. Kinet. Mech. Cat.* **2013**, *108*, 565–582.
- (160) Na, K.; Park, W.; Seo, Y.; Ryoo, R. Disordered Assembly of MFI Zeolite Nanosheets with a Large Volume of Intersheet Mesopores. *Chem. Mater.* **2011**, *23*, 1273–1279.
- (161) Na, K.; Jo, C.; Kim, J.; Ahn, W.-S.; Ryoo, R. MFI Titanosilicate Nanosheets with Single-Unit-Cell Thickness as an Oxidation Catalyst Using Peroxides. *ACS Catal.* **2011**, *1*, 901–907.
- (162) Jung, J.; Jo, C.; Cho, K.; Ryoo, R. Zeolite nanosheet of a single-pore thickness generated by a zeolite-structure-directing surfactant. *J. Mater. Chem.* **2012**, *22*, 4637.
- (163) Liu, D.; Zhang, X.; Bhan, A.; Tsapatsis, M. Activity and selectivity differences of external Brønsted acid sites of single-unit-cell thick and conventional MFI and MWW zeolites. *Micropor. Mesopor. Mat.* **2014**, *200*, 287–290.
- (164) Swindlehurst, G. R.; Kumar, P.; Xu, D.; Alhassan, S. M.; Mkhoyan, A.; Tsapatsis, M. Nucleation, Growth, and Robust Synthesis of SPP Zeolite: Effect of Ethanol, Sodium, and Potassium. *Top. Catal.* **2015**, *58*, 545–558.
- (165) Josephson, T. R.; DeJaco, R. F.; Pahari, S.; Ren, L.; Guo, Q.; Tsapatsis, M.; Siepmann, J. I.; Vlachos, D. G.; Caratzoulas, S. Cooperative Catalysis by Surface Lewis Acid/Silanol for Selective Fructose Etherification on Sn-SPP Zeolite. *ACS Catal.* **2018**, *8*, 9056–9065.
- (166) Pitman, M. C.; Duin, A. C. T. van. Dynamics of confined reactive water in smectite clay-zeolite composites. *J. Am. Chem. Soc.* **2012**, *134*, 3042–3053.
- (167) Demaret, C. Mise en forme de zéolithes : Contrôle des propriétés acides des zéolithes et description de l'interface zéolithe / liant: Thèse de doctorat, IFPEN, 2019.

## Chapter 2. Methodology

### 2.1. Quantum mechanics basics

Quantum mechanics aims at the description of the stationary states of a system at the atomic scale which can be determined by an approximate solution of the non-relativistic time-independent Schrödinger equation presented in Equation 1.

$$\mathbf{H}\psi = E\psi \quad \text{Equation 1}$$

With  $\mathbf{H}$  the Hamiltonian operator,  $\psi$  the wave function and  $E$  the energy of the system. Molecular properties can be deduced from the solution of this equation: geometry, relative stability, vibration spectrum, dipolar and quadrupolar moments, electronic spectrum and functions which describe reactivity like atomic charges or Fukui functions. This equation cannot be solved exactly for all the systems and approximation will be necessary. For a system of  $N$  electrons and  $M$  nuclei, the Hamiltonian is given by Equation 2.

$$\mathbf{H} = \mathbf{H}(\{i = 1, \dots, N\}, \{k = 1, \dots, M\}) \quad \text{Equation 2}$$

$$\mathbf{H} = \underbrace{-\sum_{i=1}^N \frac{\hbar}{2m_e} \cdot \nabla_i^2}_{\text{kinetic energy of electrons}} - \underbrace{\sum_{i=1}^N \sum_{k=1}^M \frac{e^2}{4\pi\epsilon_0} \cdot \frac{Z_k}{R_{ik}}}_{\text{Coulomb attraction between electrons and nuclei}} + \underbrace{\sum_{i=1}^N \sum_{j>i}^N \frac{e^2}{4\pi\epsilon_0 \cdot r_{ij}}}_{\text{electrostatic repulsion energy between electrons}} - \underbrace{\sum_{k=1}^M \frac{\hbar}{2 \cdot M_k} \cdot \nabla_k^2}_{\text{kinetic energy of nuclei}} + \underbrace{\sum_{k=1}^M \sum_{l>k}^M \frac{e^2}{4\pi\epsilon_0} \cdot \frac{Z_k Z_l}{R_{kl}}}_{\text{electrostatic repulsion energy between nuclei}}$$

With  $\hbar$  the Planck constant  $h$  divided by  $2\pi$ ,  $m_e$  the electronic mass,  $e$  the electronic charge,  $M_k$  the masse of the nucleus  $k$ ,  $r_{ij}$  is the distance between the electrons  $i$  and  $j$ ,  $R_{ik}$  is the distance between the electron  $i$  and the nucleus  $k$  and  $\nabla_i^2$  is the Laplacian of the  $i^{\text{th}}$  electron.

#### 2.1.1. Born-Oppenheimer approximation

The Born-Oppenheimer approximation first distinguishes the two types of particles, the nuclei and the electrons which possess an important difference of mass. The mass of the nuclei is more than 2000 times higher than the electron mass which allows this approximation to consider the nuclear position  $\mathbf{R}_k$  as fixed. Considering the atomic unit system where  $m_e = 1$ ,  $\hbar = 1$ ,  $e = 1$  and  $4\pi\epsilon_0 = 1$ , the Hamiltonian becomes like in Equation 3.

$$\mathbf{H} = \sum_{i=1}^N -\frac{1}{2} \nabla_i^2 - \sum_{i=1}^N \sum_{k=1}^M \frac{Z_k}{R_{ik}} + \sum_{i>j>1}^N \frac{1}{r_{ij}} + \sum_{k=1}^M \sum_{l>k}^M \frac{Z_k Z_l}{R_{kl}}$$

$$\text{Equation 3}$$

The repulsion between nuclei can be considered as constant when all the nuclei are considered as fixed. Only the electronic contributions have to be solved then and are included in the electronic Hamiltonian  $\mathbf{H}_{el}$  presented in Equation 4.

$$\mathbf{H}_{el}\psi_{el} = E_{el}\psi_{el} \quad \text{Equation 4}$$

$$\mathbf{H}_{el} = \sum_{i=1}^N -\frac{1}{2}\nabla_i^2 - \sum_{i=1}^N \sum_{k=1}^M \frac{Z_k}{R_{ik}} + \sum_{i>j>1}^N \frac{1}{r_{ij}}$$

$$\mathbf{H}_{el} = \hat{\mathbf{T}} + \hat{\mathbf{V}}_{ext} + \hat{\mathbf{V}}_{ee}$$

When the nuclei are fixed, the total energy is calculated by the sum of the electronic energy and the repulsion energy of the nuclei like in Equation 5.

$$E_{tot} = E_{el} + \sum_{k=1}^M \sum_{l>k}^M \frac{Z_k Z_l}{R_{kl}}$$

**Equation 5**

### 2.1.2. Electronic density

The sought wave function  $\psi_{el}(r_1\sigma_1, \dots, r_i\sigma_i, \dots, r_j\sigma_j, \dots, r_N\sigma_N)$  is an electronic wave function which depends on the positions and the spin of each electron and validates Equation 6, which describes the density of probability function as equal to one.

$$\sum_{\sigma_1, \dots, \sigma_N} \int_{\mathbb{R}^3} \dots \int_{\mathbb{R}^3} |\psi_{el}(r_1\sigma_1, \dots, r_i\sigma_i, \dots, r_j\sigma_j, \dots, r_N\sigma_N)|^2 d^3r_1, \dots, d^3r_i, \dots, d^3r_j, \dots, d^3r_N = 1$$

**Equation 6**

With  $|\psi_{el}(r_1\sigma_1, \dots, r_i\sigma_i, \dots, r_j\sigma_j, \dots, r_N\sigma_N)|^2 d^3r_1, \dots, d^3r_i, \dots, d^3r_j, \dots, d^3r_N$  the probability to find the electron 1 at the position  $r_1$  in the spin state  $\sigma_1$ , the electron 2 at the position  $r_2$  in the spin state  $\sigma_2$ , etc... The spin state can be described for each spin by two values  $\frac{1}{2}$  or  $-\frac{1}{2}$ . And so the total electronic density can be written like Equation 7.

$$\rho(r) = N \int \dots \int |\psi(r, r_2, \dots, r_N, \sigma_1, \dots, \sigma_N)|^2 dr_2, \dots, dr_N, d\sigma_1, \dots, d\sigma_N$$

**Equation 7**

## 2.2. Density Functional Theory (DFT)

### 2.2.1. Hohenberg, Kohn and Sham first theorems and approximations

The density functional theory is based on the model of Thomas and Fermi, stating that all the electronic properties can be described with functional of the electronic density  $\rho(r)$ . The density functional theory was born in 1964 with Hohenberg, Kohn and Sham publications.<sup>1,2</sup> Their first theorem states that for a system in its ground state, the external potential  $\hat{\mathbf{V}}_{ext}$  is determined by the electronic density. The second one states that the energy can be written as a density functional and the density for which the functional is at its

minimum is the ground state of the system. Thus, the electronic energy  $E_{el}$  can be written as a functional of the electron density in Equation 8 and Equation 9.

$$E_{el}[\rho] = \hat{T}[\rho] + \hat{V}_{ee}[\rho] + \hat{V}_{ext}[\rho] \quad \text{Equation 8}$$

$$E_{el}[\rho] = F_{HK}[\rho] + \int v_{ext}(r)\rho(r)d^3r \quad \text{Equation 9}$$

With:

$$F_{HK}[\rho] = \hat{T}[\rho] + \hat{V}_{ee}[\rho] \quad \text{Equation 10}$$

With  $F_{HK}$  the universal functional of Hohenberg and Kohn. Considering the new form of the energy, the second theorem can be written like Equation 11.

$$E_{el}[\rho_0] = F_{HK}[\rho_0] + \int v_{ext}(r)\rho_0(r)d^3r = E_0 \quad \text{Equation 11}$$

With  $E_0$  the energy of the system at the ground state and  $\rho_0$  the density of this state. And the first theorem can be written like Equation 12.

$$E_{el}[\tilde{\rho}] \geq E_0 \quad \text{Equation 12}$$

With  $\tilde{\rho}$  a trial density which determines the external potential and Hamiltonian.

The universal functional of Hohenberg and Kohn could provide an exact equation for the ground state electronic density using this last equation if there was a known, exact and explicit form for  $F_{HK}[\rho]$ . But the theorems do not provide it and theoreticians must build approximations to solve it. In 1965, Kohn and Sham proposed a new approach of the issue. Considering that the kinetic energy of an electron gas is known they changed the interacting electron of the problem into independent electron evolving into an external potential. Orbitals  $\psi_i$  are associated to each non-interacting electrons determining the general wave function  $\psi$  and the electronic density  $\rho(r)$  which are written in Equation 13.

$$\psi = \frac{1}{\sqrt{N!}} \det [\psi_1, \psi_2, \dots, \psi_N] \quad \text{Equation 13}$$

$$\rho(r) = \sum_{i=1}^{occ} |\psi_i(r)|^2$$

The fictitious system they created with the N independent electrons is associated to the real system by the same ground state electron density. The electronic energy can be rewritten like in Equation 14.

$$E_{el}[\rho(r)] = T_S[\psi_i(r)] + E_{ext}[\rho(r)] + E_H[\rho(r)] + E_{xc}[\rho(r)]$$

$$\text{Equation 14}$$

$T_S$  is a functional which represents the kinetic energy of the Kohn-Sham system of independent electrons,  $E_H$  is the classical Hartree functional of electronic repulsion,  $E_{ext}$  is the functional associated to the external potential.  $E_{xc}$  is the functional of exchange and correlation which contains the difference between the kinetic energy of the model and the true

and the non-classical part of the electronic repulsion. These functionals can be written as in Equation 15.

$$T_s[\psi_i(r)] = \sum_{i=1}^N \langle \psi_i | \nabla_i^2 | \psi_i \rangle$$

$$E_H[\rho(r)] = \frac{1}{2} \iint \frac{\rho(r)\rho(r')}{|r-r'|} dr dr'$$

$$E_{ext}[\rho(r)] = \int \rho(r)v_{ext}(r)dr$$

**Equation 15**

The energy functional can be rewritten as in Equation 16.

$$E_{el}[\rho(r)] = \int v_{eff}(r)\rho(r) + T_s[\rho(r)]$$

**Equation 16**

With:

$$v_{xc}(r) = \frac{\delta E_{xc}[\rho(r)]}{\delta \rho(r)}$$

$$v_{eff}(r) = v(r) + \int \frac{\rho(r')}{|r-r'|} dr' + v_{xc}(r)$$

This leads to the Hamiltonian form of the Kohn-Sham equations of Equation 17.

$$H = \sum_{i=1}^N \left[ -\frac{1}{2} \nabla_i^2 + v_{eff}(r_i) \right]$$

**Equation 17**

These equations are similar to the Hartree-Fock equations which use another approximation level for the resolution of Schrödinger equation. The main difference is the presence of the correlation energy. For the other term, they are solved with a self-consistent field as for the Hartree-Fock method. A trial density is chosen and can give access to the wave function thanks to Kohn-Sham equation, which allows to calculate a new electronic density, etc. The main goal is to minimize the electronic energy which was defined in Equation 14. But one more time, the exact and analytical expression of the exchange and correlation energy are still unknown. Some functional are commonly used to approximate this energy.



### 2.2.2. Exchange-correlation energy

The approximations of the exchange-correlation energy as a functional have been developed since the beginning of the DFT. They all have the same expression presented in Equation 18.

$$E_{xc}[\rho(r)] = \int \varepsilon_{xc}(r, \rho(r)) \rho(r) dr$$

**Equation 18**

where  $\varepsilon_{xc}$  is the volume density of the exchange-correlation energy with  $x$  the term of exchange and  $c$  the term of correlation.

These approximations have been classified by Perdew in 2001 using the metaphor of “Jacob DFT ladder” represented on Figure 1.<sup>3,4</sup> The bottom of the ladder represents the Hartree world and the top represents the chemical accuracy.

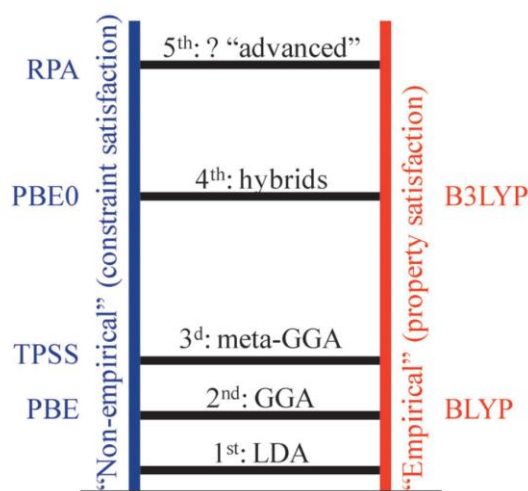


**Figure 1.** Jacob’s ladder of density-functional approximations (after Perdew).<sup>4</sup>

On the first rung of the ladder, the Local Density Approximation (LDA) is the simpler functional form. The exchange and correlation functional is equivalent to the functional of homogeneous electron gas of a density  $\rho$ , it depends solely upon the value of the electronic density at each point in space. The correlation functional was calculated by Bloch before the development of the DFT.<sup>5</sup> The correlation functional can be evaluated by quantic Monte Carlo simulations (for example the Vosko, Wilk and Nusair VWN functional).<sup>6</sup> The main weakness of this approximation is the fact that the electronic density is usually not uniform in most of the molecular system and even more in crystals.

The second rung is composed of the Generalized Gradient Approximation (GGA) which was built to be representative of the non-uniformity of the electronic density. To reach this goal the functionals depend on the electronic density but also on the gradient of the electronic density. They can be constructed with parameters from Monte Carlo simulations, for example the exchange functional PW91,<sup>7</sup> or by using quantum mechanics principles, for example the

PBE functional<sup>8</sup> or the Lee-Yang-Parr functional.<sup>9</sup> The general performances of these functionals are better but they overestimate the bond length and not performing well to evaluate the intermolecular interactions (Van der Waals, hydrogen bonds).

The third rung are the meta-GGA functionals. These are improved GGA functionals which were proposed by Becke in 1995.<sup>10</sup> The correlation energy of these functionals are completed by dynamic correction on depends on the density, the density gradient and the kinetic energy density.

The fourth rung, which can also be subdivided, is composed of hybrid functionals. The exchange energy is partially determined by GGA and the other part by Hartree-Fock exchange, the exchange being exactly described with Hartree-Fock methods. The weight of each contribution is empirically determined which induce that DFT with hybrid functional is not considered as an *ab initio* method. The most well-known is B3LYP for “Beck with 3 parameters – LYP” which uses the exchange GGA B88 and a correlation functional LYP.<sup>9,11,12</sup> The molecular interaction are better described than with GGA. But for many properties, post-Hartree-Fock remains more accurate (for example the simulation of electronic spectra).

### 2.2.3. DFT-based dispersion method

The short range electrostatic interactions are correctly described by DFT. But the long range dispersion interactions are not well described by standard exchange correlation functionals. These interactions are included in Van der Waals forces in particular in the London term. The electronic density at an instant  $t$  is not homogeneous, this induces a small dipolar moment. The London force is the result of the interaction between all the small induced dipolar moment. The London instantaneous induced-dipole interactions has a  $-1/r^6$  decay of the energy with the distance.<sup>13,14</sup>

Several methods were proposed to better take into account this contribution to the energy.<sup>14</sup> In the one we chose here, a dispersion term,  $E_{disp}$ , is added to the energy calculated in DFT,  $E_{el}$ , as presented in Equation 19. The dispersion term is added to provide the correct  $-1/r^6$  dependence of the dispersion interaction energy on the interatomic distance  $r$ . Most of the dispersion corrections in DFT include in various way empirical components. They are particularly important for the equilibrium of van der Waals complexes and the thermodynamic properties of large molecules.<sup>13</sup>

$$E_{tot} = E_{el} + E_{disp} \quad \text{Equation 19}$$

The dispersion correction used in this work is a correction based on the electron density. It is a quite recent dispersion correction and has application in very various domains.<sup>15</sup>

### 2.2.4. Basis sets

The spin orbitals which intervene in the calculation are associated to linear combinations of basis functions. The kind of basis functions is chosen depending on the system. The linear combination of atomic orbital (LCAO) is mostly employed for finite-size systems like molecules. In this method the (spin) molecular orbitals  $\chi$  are described as a linear combination of atom-centered atomic (spin) orbitals  $\varphi$  which are themselves linear combinations of basis functions (generally Gaussians or Slater functions), also centered on atoms. Their form is presented in Equation 20.

$$\chi_{M,i}(r) = \sum_j a_{ij} \varphi_j(r) = \sum_j \sum_k a_{ij} b_{jk} u_{jk}(r)$$

**Equation 20**

where  $\varphi_j(r)$  are atomic orbitals and  $u_{jk}(r)$  are the basis functions to describe the atomic orbitals  $j$ . These functions must give a good description of the system by integrating the inhomogeneity of the electronic density in atoms. The core and the valence electrons are described by different functions. For valence electrons the basis functions are diffuse to be representative of the interactions with the environment. In theory an infinite number of basis functions is mandatory to describe perfectly the systems (in the limit of the complete basis set). But in practice they must be limited to a finite number which could be calculated by a calculator. There is a great variety of basis set types today.

In contrast to molecular systems, solids or surfaces can be described as periodic systems. The calculations can be simplified by using the translation symmetry. The Bloch theorem states that for an Hamiltonian of the form as in Equation 21, the wave functions are of the form presented in Equation 22.

$$H = -\frac{1}{2} \nabla^2 + U(r) \quad \text{Equation 21}$$

$$\chi_{i,k}(r) = u_{ik}(r) e^{i\vec{k}\cdot\vec{r}} \quad \text{Equation 22}$$

where  $U(r)$  is a periodic functional with a period  $R$ ,  $\vec{k}$  is a reciprocal network vector and  $u_{ik}(r)$  is a periodic functional which can be expressed as a Fourier serie,  $\chi_{i,k}(r)$  can be considered as a linear combination of plane waves presented in Equation 23.

$$\chi_{i,k}(r) = u_{ik}(r) e^{i\vec{k}\cdot\vec{r}} = e^{i\vec{k}\cdot\vec{r}} \sum_{\vec{g}} c_{ik,g} e^{-i\vec{g}\cdot\vec{r}}$$

**Equation 23**

The energy is calculated by relaxing the different coefficients  $c_{ik,g}$ . An infinity of wave vectors  $\vec{g}$  should be necessary to describe the wave function. In practice there is only a limited number and the name of the highest plane wave kinetic energy is called “cutoff energy” (Equation 24).

$$\frac{1}{2}|\vec{k} + \vec{g}| < E_{cutoff} \quad \text{Equation 24}$$

To be correctly defined, the band energy density needs the exact calculation of the vectors  $\vec{k}$  (which are designed as the k points associated to the vectors at the origin) which are included in the primary zone of Brillouin (PZB). In practice the k points of the PZB are sampled to obtain a converged energy. The number of required k point to get a converged energy decreases as the size of the PZB increases. The dimensions of the PZB itself decrease when the dimensions of the unit cell increase. The basis functions can be described also with a localized approach (LCAO) but the long distance interactions are better described with plane waves.

The considered systems may include an important number of electrons thereby requiring significant computational need to solve the Schrödinger equation. To alleviate the calculations, the core electrons, as opposed to the valence electrons, are considered differently, because they are located close to the nuclei and have a very low participation in the chemical bonds. In a first approximation their states can be considered independent of the environment. The interaction between core and valence electrons can be modeled by a potential which is equivalent to a screen of the potentials generated by the nuclei. They are called “pseudo-potentials” and then only the valence electrons are calculated with quantum mechanics.

## 2.3. Calculations types

### 2.3.1. Search of geometry optimized-structures

The previous methodologies are made to calculate the electronic part of the total energy. The total energy includes the Coulomb interaction between nuclei. Considering the same system of M nuclei and N electrons, the potential energy surface depends on the coordinates of the M nuclei as presented in Equation 25.

$$E_{tot}(R_A) = E_{elec}(R_A) + \sum_{A=1}^M \sum_{B=A}^M \frac{Z_A Z_B}{R_{AB}}$$

Equation 25

The solution sought is the structure with the lowest energy among all the possible configurations. This solution is equivalent to a global minimum on the potential energy surface. Each geometry corresponds to the coordinates of each atom and the dual  $\{\mathbf{R}_A, E_{tot}(\mathbf{R}_A)\}$  represents the coordinates of one point on the surface.

The difficulty of this research is to find the global and absolute minimum because the potential energy surface is not known a priori and can be composed of many local minima. The whole surface cannot be calculated for a reasonable computational cost and more particularly with a high number of atoms.

The geometry optimization starts from an initial geometry from which the total energy is calculated. A point on the surface can be associated to this energy, this is named a “single point energy” calculation. This geometry is likely not optimal. From the initial geometry and the first calculation of the energy, the forces applied on the atoms are calculated. The atoms are moved accordingly and the energy of the new configuration is calculated, by calculating the first derivatives of the energy with respect to the positions of the nuclei. The same process is repeated until the energy variation or the force on each atom is under an arbitrary (threshold) value chosen by the user. The final geometry is said “optimized”. The geometry optimization allows to move the atoms to obtain a geometry which corresponds to a local minimum on the energy surface but not necessarily to the global minimum. The temperature is not included, the energy obtained is the internal energy at 0 K of the system. This kind of calculations may not allow to get out a potential well in which the initial configuration is. The initial structure should be chosen wisely to get a relevant result.

A calculation of molecular dynamic takes into account thermal motion. In this kind of calculations, the atoms have also an initial velocity in a Maxwell-Boltzmann distribution which will simulate molecular motions at a given temperature. The time step is chosen by the user (of the order of 1 fs). The calculation is made over a chosen number of time steps. The velocity of the atoms can allow to jump from a potential well to another one. The analysis of the energy as a function of time allows to highlight the lowest energy structures then an geometry optimization is made on these structures, and local energy minimum are found. The results are compared to determine their relevance depending on their stability. This method is named the “quench” method.

### 2.3.2. Vibrational frequencies calculations

Molecular modelling allows to calculate the vibrational frequencies of the optimized structures. A system composed of  $N$  atoms has a total of  $3N$  coordinates  $q_i$  (for  $i=1$  to  $3N$ ). A small move from the position is written  $dq_i$  in one of the three directions of space. The total energy and the forces applied on each atom are calculated. The intensity of the force  $F_j(q_1, \dots, q_i + dq_i, \dots, q_{3N})$  applied on the coordinate  $j$  can be written as in Equation 26.

$$F_j(q_1, \dots, q_i + dq_i, \dots, q_{3N}) = F_j(q_1, \dots, q_i, \dots, q_{3N}) + dq_i \frac{\partial F_j}{\partial q_i}(q_1, \dots, q_i, \dots, q_{3N})$$

**Equation 26**

Thus, the force on the  $j$  coordinate can be also defined by Equation 27.

$$F_j(q_1, \dots, q_{3N}) = -\frac{\partial E}{\partial q_j}$$

**Equation 27**

If the structure is optimized, the force acting on each atom is close to zero. The force can be written as in Equation 28.

$$F_j(q_1, \dots, q_i + dq_i, \dots, q_{3N}) = -dq_i \frac{\partial}{\partial q_i} \left( \frac{\partial E}{\partial q_j} \right) (q_1, \dots, q_i, \dots, q_{3N}) = -q_i \frac{\partial^2 E}{\partial q_i \partial q_j}$$

**Equation 28**

The second derivative of the energy can be obtained in relation to the different coordinates of the system as presented in Equation 29.

$$\frac{\partial^2 E}{\partial q_i \partial q_j} = - \frac{F_j(q_1, \dots, q_i + dq_i, \dots, q_{3N})}{dq_i}$$

**Equation 29**

This operation is made for all the coordinates  $q_i$  which allows to write the Hessian matrix as in Equation 30.

$$H = \begin{pmatrix} \frac{\partial^2 E}{\partial q_1^2} & \dots & \frac{\partial^2 E}{\partial q_1 \partial q_{3N}} \\ \vdots & \ddots & \vdots \\ \frac{\partial^2 E}{\partial q_{3N} \partial q_1} & \dots & \frac{\partial^2 E}{\partial q_{3N}^2} \end{pmatrix}$$

**Equation 30**

The diagonalization of the matrix gives the vibration frequencies which are the eigenvalues of the matrix and the resonance modes which are the eigenvectors of the matrix.

In this work, to avoid any residual strength in the optimized structure each coordinate  $q_i$  is moved in the two directions ( $+dq_i$  and  $-dq_i$ ) which makes a total of  $6N$  moves for the all system. For each movement the energies and the strength on the atoms are calculated. The difference can be calculated as in Equation 31.

$$\begin{aligned} & F_j(q_1, \dots, q_i + dq_i, \dots, q_{3N}) - F_j(q_1, \dots, q_i - dq_i, \dots, q_{3N}) \\ &= \left[ F_j(q_1, \dots, q_i, \dots, q_{3N}) - dq_i \frac{\partial^2 E}{\partial q_i \partial q_j} \right] - \left[ F_j(q_1, \dots, q_i, \dots, q_{3N}) + dq_i \frac{\partial^2 E}{\partial q_i \partial q_j} \right] \\ &= 2dq_i \frac{\partial^2 E}{\partial q_i \partial q_j} \end{aligned}$$

**Equation 31**

More moves can be done in each direction but for a more expensive calculation.  $dq_i$  must be as small as possible so the development in Equation 31 could have a meaning but as high as possible so the variations of the energy can be important enough to be considered numerically.

This kind of calculation cannot take into account the anharmonicity of molecular vibrations so a no negligible difference between the calculated frequencies and those observed experimentally is highly possible.

### 2.3.3. Thermodynamic calculations

All calculations mentioned at this point are performed on the system considered at 0K, whereas all the reactions and chemistry presented in this work take place at finite temperature. To take into account the effect of temperature and pressure the calculations can be completed by statistic thermodynamic calculations which allows to obtain a more realistic description of the experimental system.

The Gibbs free energy  $G$  is the main descriptor for reactions which take place at constant temperature and pressure. It can be decomposed into the enthalpy  $H$  and the entropy  $S$  of the system as presented in Equation 32.

$$G = H - T \times S \quad \text{Equation 32}$$

In practice, the molar values ( $X_m$ ) of these terms are used because they are intensive and depend explicitly of the temperature. The enthalpy can also be decomposed into the free energy  $U$  and the product of the pressure and molecular volume like in Equation 33.

$$H_m = U_m + P \times V_m \quad \text{Equation 33}$$

$$H_m = U_{elec,m} + U_{vib,m} + U_{trans,m} + U_{rot,m} + P \times V_m$$

$U_{elec,m}$ ,  $U_{vib,m}$ ,  $U_{trans,m}$ ,  $U_{rot,m}$  and  $V_m$  are respectively the internal electronic energy, vibrational energy, translational energy, rotational energy and the molar volume. This molar volume can be neglected in the case of adsorbed chemical species (which are condensed phase, contrary to gas phase species), which means that the enthalpy and the internal energy are approximately equal. The first term is the result given by DFT calculations as described before, whereas the other terms can be calculated by using statistical thermodynamics.

The vibrational term of the free energy can be calculated by knowing the natural vibration modes  $\nu_i$  of the system (which can be calculated with VASP as presented before) with Equation 34.

$$U_{vib,m}(T) = N_A \left[ \sum_i \frac{1}{2} h\nu_i + \sum_i \frac{h\nu_i \times \exp\left(-\frac{h\nu_i}{k_B T}\right)}{1 - \exp\left(-\frac{h\nu_i}{k_B T}\right)} \right]$$

**Equation 34**

where  $h$  is the constant of Planck,  $k_B$  is the constant of Boltzmann and  $T$  the absolute temperature. The first term of this formula corresponds to the vibrational term at 0K of the system and is called “Zero Point Energy” or ZPE which can be sometimes separated of the vibrational term in the following work.



The rotational and translational terms of the free energy have an analytical expression in the case of an ideal gas as presented in Equation 35.

$$U_{trans,m}(T) = U_{rot,m}(T) = \frac{3}{2} N_A k_B T \quad \text{Equation 35}$$

In the case of a molecule adsorbed on a surface, diffusion phenomenon can take place on the surface, but are not straightforward to model. In a first approximation, it is considered that the translation and rotation modes are converted into vibration modes and are included in the vibrational term.

Similarly, the entropy can be decomposed as in Equation 36.

$$S_m = S_{vib,m} + S_{trans,m} + S_{rot,m} \quad \text{Equation 36}$$

With  $S_{vib,m}$ ,  $S_{trans,m}$  and  $S_{rot,m}$  which are respectively the molecular vibrational entropy, translational entropy and rotational entropy. Once more statistical thermodynamics helps in decomposing the vibrational term with the vibration modes presented in Equation 37.

$$S_{vib,m}(T) = N_A k \left[ \sum_i \frac{\frac{h\nu_i}{k_B T} \times \exp\left(-\frac{h\nu_i}{k_B T}\right)}{1 - \exp\left(-\frac{h\nu_i}{k_B T}\right)} - \sum_i \ln\left(1 - \exp\left(-\frac{h\nu_i}{k_B T}\right)\right) \right]$$

$$\text{Equation 37}$$

The translational and rotational term can be associated to the formula of an ideal gas are presented in Equation 38.

$$S_{trans,m}(T) = N k_B \left( \frac{5}{2} \ln(T) - \ln(P) + \frac{5}{2} \ln(M) - 1,165 \right)$$

$$S_{rot,m}(T) = N k_B \left[ \frac{\sqrt{\pi}}{\sigma} \left( \frac{8\pi^2 k_B}{h^2} \right)^{\frac{3}{2}} \sqrt{A_e \times B_e \times C_e} \right]$$

$$\text{Equation 38}$$

Where P is the partial pressure in this ideal gas, M is the molar weight,  $\sigma$  is the number of symmetry and  $A_e$ ,  $B_e$  and  $C_e$  are rotational constants of the molecule. Here it is also considered that for an adsorbed molecule on a surface rotation and translation modes are converted into vibration modes of the molecule and that only the vibrational term defines the entropy. The website <http://www.colby.edu/chemistry/PChem/scripts/ABC.html> was used to calculate the translational and rotational terms for the entropy of any compound in its gaseous phase.

Considering a chemical reaction  $\sum a_i A_i = 0$ , with  $a_i$  the stoichiometric coefficient of the  $A_i$  compound. The enthalpy, entropy and Gibb's free energy at the temperature T are defined as in Equation 39.

$$\begin{aligned}\Delta_r H^o(T) &= \sum_i a_i H_{i,m}^o(T) \\ \Delta_r S^o(T) &= \sum_i a_i S_{i,m}^o(T) \\ \Delta_r G^o(T) &= \sum_i a_i G_{i,m}^o(T) = \sum_i a_i [H_{i,m}^o(T) - TS_{i,m}^o(T)]\end{aligned}$$

**Equation 39**

where the terms  $X_{i,m}^o(T)$  are the molar values of the compound  $i$  in its standard state at the temperature  $T$  (generally the compound is in gaseous phase with a partial pressure equal to 1 bar).

### 2.3.4. Linear Response Approach for the calculation of NMR chemical shifts

The linear response approach applies a uniform magnetic field  $B$  on the samples which induce a current  $j^{(1)}(r)$ . In the following study, the systems contain no magnetic atoms, so the induced current is only due to the orbital motions of electrons. A non-uniform magnetic field,  $B_{ind}$ , is induced from this current, and its expression is presented in Equation 40.

$$B_{ind}^{(1)}(\vec{r}) = \int_{\mathbb{R}^3} \frac{\vec{r} - \vec{r}'}{|\vec{r} - \vec{r}'|^3} j^{(1)}(\vec{r}') d^3 \vec{r}'$$

**Equation 40**

The chemical shift, which is in reality a tensor, is defined as the ratio of the induced magnetic field and the initial magnetic field  $B$ , as presented in Equation 41.

$$B_{ind}^{(1)}(\vec{r}) = -\vec{\sigma}(r)B$$

**Equation 41**

The isotopic chemical shift can be deduced from the chemical shift tensor as shown in Equation 42.

$$\delta_{iso} = \frac{Tr(\vec{\sigma}(r))}{3}$$

**Equation 42**

Experimentally, the chemical shifts are measured through the magnetic field at the nuclei position, which can be associated to the chemical shift proposed by the linear response method. More details are given in the work of Pickard and Mauri<sup>16</sup> for the whole calculation method which explain how the induced current is calculated by means of perturbation theory and then allows to deduce the induced magnetic field and the chemical shift of atoms.

### 2.3.5. Code and methods employed in this work

Periodic DFT calculations were performed with the PBE (Perdew, Burke, and Ernzerhof) exchange-correlation functional<sup>8</sup> as implemented in VASP 5.4.1.<sup>17,18</sup> The projected augmented wave (PAW) method<sup>19</sup> was used to describe the core-electron interactions, and the plane wave basis set was limited to a kinetic cutoff energy of 400-800 eV (which depended on the kind of calculation performed, see below). The density dependent dispersion correction, dDsC,<sup>15</sup> was applied. The convergence criterion for the electronic self-consistent field relaxation was fixed to  $10^{-5}$  eV. Even for nonsymmetric slabs, no dipolar correction was applied to remove the spurious interactions in the direction perpendicular to the surface, as it has a minor impact on the electronic energy (less than  $2 \cdot 10^{-3}$  eV). All calculations were performed at the gamma point (origin of the reciprocal space). Full geometry optimizations were performed using a conjugate-gradient algorithm, with a convergence criterion on forces of  $0.02 \text{ eV} \cdot \text{\AA}^{-1}$ .

Harmonic frequency calculations (Chapter 3, 4, and 5) were performed with an energy cutoff of 400 eV on optimized structures under the same conditions with displacements of  $\pm 0.005 \text{ \AA}$  around the equilibrium atomic positions. For aluminated slabs, the atoms allowed to vibrate were the OH group containing the compensation cation, the Al/Si first neighbor, all O second neighbors, Si third neighbors, and O fourth neighbors. For pyridine and 2,6-ditertbutylpyridine (DTBPy) adsorptions, the C, N and H atoms of these molecules were allowed to vibrate in addition to the previous ones. Reaction Free energies were determined thanks to the evaluation of the vibrational partition function of reactants and products (which include the condensed phase), as explained in the previous Section 0. For each of these species, the Gibbs free energy is calculated by considering the rotational, translational, and vibrational degrees of freedom for isolated (gas-phase) molecules and only the vibrational degrees of freedom for the surface models with adsorbed molecules.

Chemical shifts were calculated with the linear response approach, using the gauge including projector augmented wave (GIPAW) formalism.<sup>16,20</sup> The step size for the finite difference k-space derivative was set to 0.003. First order of the finite difference stencil was used to calculate the magnetic susceptibility. The average of the isotropic chemical shielding ( $\sigma_{\text{TMS}}$ ) of each proton of a single tetramethylsilane in vacuum ( $20 \text{ \AA}^3$  box) was used as a reference to calculate the isotropic chemical shift  $\delta_{\text{iso}}$  of the various protons at the surface of ZSM-5, from their isotropic chemical shielding ( $\sigma_{\text{iso}}$ ):

$$\delta_{\text{iso}} = \sigma_{\text{iso}} - \sigma_{\text{TMS}}$$

**Equation 43**

## 2.4. Reactive Force Fields approach

### 2.4.1. The ReaxFF model

The computational cost of the quantum mechanics methods limits the simulation scale, both in time and size (number of atoms). Empirical force field methods use far less computational resources, but classical empirical force fields are not able to describe reactivity. However, the reactive force fields, like ReaxFF can model dynamically the atomic interactions and describe bond breaking and formation.<sup>21</sup> Hence, ReaxFF is a potential complement to full DFT calculations to study our systems. The ReaxFF force field will therefore be described more precisely in the following paragraphs.

ReaxFF employs both a polarizable charge description and uses bond orders to describe the interactions between atoms. The energy contributions to the ReaxFF potential are described by Equation 44.

$$E_{system} = E_{bond} + E_{over} + E_{angle} + E_{tors} + E_{vdWaals} + E_{Coulomb} + E_{Specific}$$

**Equation 44**

$E_{bond}$  is a continuous function of the bond order, which in turn is a function of the interatomic distance, which describes the energy released by forming a bonds between two given atoms, or the energy required to break an existing bond, i.e. the bond dissociation energy.  $E_{angle}$  and  $E_{tors}$  are the energies associated with three-body valence angle strain and four-body torsional angle strain.  $E_{over}$  is an energy penalty for over coordination, for example a carbon atom with more than four bonds induces a stiff energy penalty.  $E_{vdWaals}$  and  $E_{Coulomb}$  are the dispersive and electrostatic interactions energies calculated between all atoms without considering the connectivity and the bond-order.  $E_{Specific}$  represents all the specific term which are included in very specific cases, for example the lone-pair energy, the hydrogen binding energy, the C<sub>2</sub> corrections energy and the conjugation energy. These energetic terms can be divided into two families: the bond-order-dependent and the bond-order-independent. The bond order is the most important variable of ReaxFF. It is a continuous variable which is independent of the atom bonds. The bond order can be calculated from interatomic distance  $r_{ij}$  using the empirical formula in Equation 45.

$$\begin{aligned} \mathbf{BO}_{ij} &= \mathbf{BO}_{ij}^{\sigma} + \mathbf{BO}_{ij}^{\pi} + \mathbf{BO}_{ij}^{\pi\pi} \\ &= \exp\left[\mathbf{p}_{bo,1} \left(\frac{r_{ij}}{r_0^{\sigma}}\right)^{p_{bo,2}}\right] + \exp\left[\mathbf{p}_{bo,3} \left(\frac{r_{ij}}{r_0^{\sigma}}\right)^{p_{bo,4}}\right] + \exp\left[\mathbf{p}_{bo,5} \left(\frac{r_{ij}}{r_0^{\sigma}}\right)^{p_{bo,6}}\right] \end{aligned}$$

**Equation 45**

The corrected bond order  $\mathbf{BO}_{ij}$  is composed of three exponential terms, one for the  $\sigma$ -bond (with the  $\mathbf{p}_{bo,1}$  and  $\mathbf{p}_{bo,2}$  parameters), the second for the first  $\pi$ -bond ( $\mathbf{p}_{bo,3}$  and  $\mathbf{p}_{bo,4}$ ) and the last for the double  $\pi$ -bond ( $\mathbf{p}_{bo,5}$  and  $\mathbf{p}_{bo,6}$ ) between two atoms. The bonding terms  $\mathbf{p}_{bo,i}$  and the equilibrium distance  $r_0$  are parameterized so that the bond strengths and distances correspond at best with the *ab initio* calculations. Over coordination and 1-3 bond

order in valence angles need to be corrected into the calculated bond order.<sup>22</sup> An example is given by Van Duin *et al.* for the participation of each contribution to the carbon-carbon bond as a function of the distance as presented in Figure 2. There is a smooth transition from the single, double and triple bonded systems when the distance between atoms decrease. To be representative, ReaxFF employs a bond length and bond order relationship which are updated every iteration. All the interactions which are connectivity dependent (valence and torsion angles) are made bond-order dependent, ensuring that their energy contributions disappear upon bond dissociation. These are examples of corrections which are included in ReaxFF to be as representative as possible of the bond-order interaction.

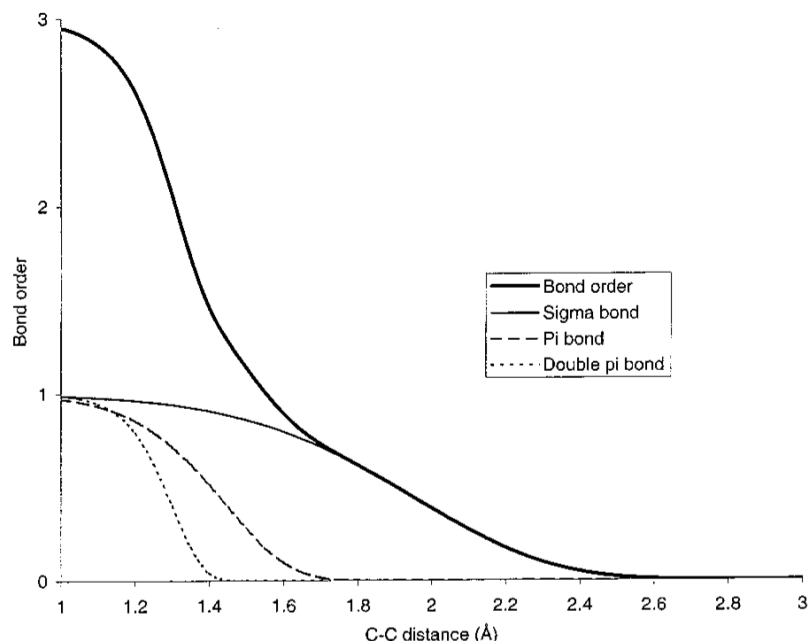


**Figure 2.** Interatomic distance dependency of the carbon-carbon bond order.<sup>22</sup>

In the ReaxFF approach, the bonded and non-bonded terms are calculated independently for each atom pair. This avoids the alterations during bond dissociation. Non-bonded interactions (van der Waals and Coulomb) are calculated between each atom pair, irrespective of the connectivity. A too important close-range non-bonded interaction value is avoided by shielding which is another kind of correction.

While the partial atomic charges are most often fixed in classical force field, in ReaxFF the charge is calculated at each  $x$  step ( $x$  is chosen by the user). The partial charges are regularly recalculated because they depend widely on their environment. ReaxFF uses a geometry dependent charge calculation scheme that accounts for polarization effects. An electronegativity and a hardness is attributed to each element. These parameters are optimized against QM-charge distribution. The geometry of the system is used in every iteration to solve the electronegativity equilibration. This is the most expensive part of the reactive force field, because it needs to be updated at each step.

### 2.4.2. Reactive Force Field optimization

All the ReaxFF results presented in the following work are obtained with ReaxAMS in ADF2019. This implementation is widely inspired from the original “Stand-alone ReaxFF” code.<sup>21–23</sup> The expression of the energy depends on multiple empirical parameter, they must be optimized before ReaxFF can be used to simulate a system in an appropriate way. Even if many reactive force fields have been developed to correspond to chemistry of interest in the literature, one have to work individually to find the correct reactive force field to fit to a precise database of systems. To find the best parameters of these reactive force field, a training set must be constructed to “train” the reactive force field to be adapted to chosen systems. To challenge a reactive force field, reference properties,  $x_{i,ref}$ , are chosen (bond, angle, dihedral, charge, energy, ...) and compared to the ReaxFF predictions of these properties,  $x_{i,calc}\{p_j\}$ , for a set of parameters  $p_j$  implemented at the  $j$  step of ReaxFF optimization. Previous studies allow to constrain the variation of some parameters with historical values, and less than 100 parameters must be estimated according to Verstraelen *et al.*<sup>24</sup> The quality of a set of parameter  $p_j$  is quantified with the objective function also called the error and presented in Equation 46.<sup>24,25</sup>

$$\text{error}(\{p_j\}) = \sum_{i=1}^n \left( \frac{x_{i,calc}(\{p_j\}) - x_{i,ref}}{\sigma_i} \right)^2$$

**Equation 46**

where the sum concern all the training data properties and for each term  $\sigma_i$  is an estimate acceptable deviation between the reference value and the ReaxFF value.

Historically, the successive one-parameter extrapolations (SOPPE) method is the first one to optimize the parameters of a reactive force field,<sup>25</sup> but SOPPE is very laborious due to numerical noises and numerous local minima.<sup>26</sup> Brute-force global optimizers are not relevant for the optimization of the ReaxFF parameter sets because they are computationally very expensive. The genetic algorithms (GAs) have also a good global optimization efficiency for ReaxFF parametrization,<sup>27</sup> and was shown to minimize the objective function as well or even better than the SOPPE method. The automatization of the optimization is also an important advantage to get rid of the human error and intervention. The multi-objective evolutionary strategy,<sup>28</sup> the parallel local search algorithm,<sup>29</sup> the Taguchi method-based optimization,<sup>30</sup> and the Monte-Carlo FF (MCFF) optimizer<sup>31</sup> are some other techniques which were developed for the parametrization or reparametrization of ReaxFF force fields. Finally a last method, named covariance matrix adaptation evolutionary strategy (CMA-ES), was shown to be more performing than GAs and MCFF by Verstraelen *et al.*<sup>31</sup> They compared the three optimization methods for the same computational cost over three different training sets. The CMA-ES method finds the minimum error value for two training sets over the three. But it is highly depending on the initial guess of the reactive force field, and cannot easily avoid local minimum and escape them. Multiple runs are needed to be sure to fall in the global minimum. The MCFF method combines the same disadvantages and furthermore does not find the main minimum for the three training sets. Conversely, the GAs method is more reproducible and

can easily avoid local minima, but for the same cost the convergence is considerably slow compared to CMA-ES or converge to higher error values. Based on these conclusions, the ReaxFF force field parametrization of the following work will use the CMA-ES method.

### 2.4.3. Covariance Matrix Adaptation Evolutionary Strategy

The CMA-ES method is a gradient-free optimization algorithm established by Hansen *et al.*<sup>32</sup> The CMA-ES has also been used for force field parametrizations.<sup>33</sup> The user gives an initial guess of the force field parameters, which the CMA-ES algorithm tries to optimize by minimizing the objective function, i.e. the total error with respect to a reference (training) set. The optimization is a multi-iterative process, Hansen<sup>32</sup>. where at each iteration the algorithm tries to improve the multi-variant normal distribution in the parameter space

The user selects a set of force field parameters to be optimized, where is  $N_{par}$  is the number of parameters. Next, a population ( $\lambda$ ) is randomly drawn such as that  $\lambda = 4 + \lceil 3 \ln N_{par} \rceil$ . Secondly, the error function is calculated for all these trial parameters, yielding a population with  $\lambda$  errors. Then, the population is sorted by ranking the error in increasing order and only the first (best)  $\lambda/2$  points of the population are retained. These points (or individuals) become the “parents” in the next generation. As in biological evolution, in evolution strategy, there is a repeated interplay of variation (via recombination and mutation) and selection. The recombination is accomplished by reweighting the “parent” individuals such as that the mean value shifts to a value closer to the minimum (here, the lowest total error), but this minimum is, of course, unknown in the beginning. However, by setting up the covariance matrix, this shift is not completely random, but becomes more and more “directed” as the number of generations (or iteration) increases. Mutations are taken care of by adding new random parameters (from  $N_{par}$ ). Note that the parent population makes up only 50% ( $\lambda/2$ ) of the total population ( $\lambda$ ).

The optimization calculation is, practically speaking, stopped when the step size (shift of the mean value) has fallen below a certain value and there is no significant improvement in the covariance matrix with respect to the previous generations. Alternatively, one can stop the optimization when a user-defined maximum number of iterations has been reached.

## References

- (1) Hohenberg, P.; Kohn, W. Inhomogeneous Electron Gas. *Phys. Rev.* **1964**, *136*, B864–B871.
- (2) Kohn, W.; Sham, L. J. Self-Consistent Equations Including Exchange and Correlation Effects. *Phys. Rev.* **1965**, *140*, A1133–A1138.
- (3) Doren, V. E. van; Alsenoy, C. van; Geerlings, P. *Density functional theory and its application to materials: Antwerp, Belgium, 8-10 June 2000*; AIP conference proceedings 577; American Institute of Physics: Melville N.Y., 2001.
- (4) Sabbe, M. K.; Reyniers, M.-F.; Reuter, K. First-principles kinetic modeling in heterogeneous catalysis: An industrial perspective on best-practice, gaps and needs. *Catal. Sci. Technol.* **2012**, *2*, 2010.
- (5) Bloch, F. Bemerkung zur Elektronentheorie des Ferromagnetismus und der elektrischen Leitfähigkeit. *Z. Physik (Zeitschrift für Physik)* **1929**, *57*, 545–555.
- (6) Vosko, S. H.; Wilk, L.; Nusais, M. *Can. J. Phys.* **1980**, *58*, 1200–1211.
- (7) Perdew, J. P.; Wang, Y. *Phys. Rev. B* **1992**, *45*, 13244.
- (8) Perdew, J. P.; Burke, K.; Ernzerhof, M. *Phys. Rev. Lett.* **1996**, *77*.
- (9) Lee, C. T.; Yang, W.; Parr, R. G. Development of the Colle-Salvetti correlation-energy formula into a functional of the electron density. *Phys. Rev. B* **1988**, *37*, 785.
- (10) Becke, A. D. *J. Chem. Phys.* **1996**, *104*, 1040.
- (11) Becke, A. D. *J. Chem. Phys.* **1993**, *98*, 5648.
- (12) Stephens, P. J.; Devlin, F. J.; Chabalowki, C. F.; Frisch, M. J. *J. Phys. Chem.* **1994**, *98*.
- (13) Grimme, S. Density functional theory with London dispersion corrections. *WIREs Comput Mol Sci* **2011**, *1*, 211–228.
- (14) Klimeš, J.; Michaelides, A. Perspective: Advances and challenges in treating van der Waals dispersion forces in density functional theory. *The Journal of Chemical Physics* **2012**, *137*, 120901.
- (15) Steinmann, S. N.; Corminboeuf, C. Comprehensive Benchmarking of a Density-Dependent Dispersion Correction. *Journal of chemical theory and computation* **2011**, *7*, 3567–3577.
- (16) Pickard, C. J.; Mauri, F. All-electron magnetic response with pseudopotentials: NMR chemical shifts. *Phys. Rev. B* **2001**, *63*, 70.
- (17) Kresse, G.; Hafner, J. Ab initio molecular-dynamics simulation of the liquid-metal–amorphous-semiconductor transition in germanium. *Phys. Rev. B* **1994**, *49*, 14251–14269.
- (18) Kresse, G.; Furthmüller, J. Efficient iterative schemes for ab initio total-energy calculations using a plane-wave basis set. *Phys. Rev. B* **1996**, *54*, 11169–11186.
- (19) Kresse, G.; Joubert, D. From ultrasoft pseudopotentials to the projector augmented-wave method. *Phys. Rev. B* **1999**, *59*, 1758–1775.
- (20) Yates, J. R.; Pickard, C. J.; Mauri, F. Calculation of NMR chemical shifts for extended systems using ultrasoft pseudopotentials. *Phys. Rev. B* **2007**, *76*, 293.
- (21) Senftle, T. P.; Hong, S.; Islam, M. M.; Kylasa, S. B.; Zheng, Y.; Shin, Y. K.; Junkermeier, C.; Engel-Herbert, R.; Janik, M. J.; Aktulga, H. M. *et al.* The ReaxFF reactive force-field: Development, applications and future directions. *npj Comput Mater* **2016**, *2*, 9396.



- (22) Duin, A. C. T. van; Dasgupta, S.; Lorant, F.; Goddard, W. A. ReaxFF: A Reactive Force Field for Hydrocarbons. *J. Phys. Chem. A* **2001**, *105*, 9396–9409.
- (23) Chenoweth, K.; van Duin, A. C. T.; Goddard, W. A. ReaxFF reactive force field for molecular dynamics simulations of hydrocarbon oxidation. *The journal of physical chemistry. A* **2008**, *112*, 1040–1053.
- (24) Shchygol, G.; Yakovlev, A.; Trnka, T.; van Duin, A. C. T.; Verstraelen, T. ReaxFF Parameter Optimization with Monte-Carlo and Evolutionary Algorithms: Guidelines and Insights. *Journal of chemical theory and computation* **2019**, *15*, 6799–6812.
- (25) Duin, A. C. T. van; Baas, J. M. A.; van de Graaf, B. Delft Molecular Mechanics: A New Approach to Hydrocarbon Force Fields: Inclusion of a Geometry-dependent Charge Calculation. *J. Am. Chem. Soc.* **1994**, *90*, 2881–2895.
- (26) Iype, E.; Hütter, M.; Jansen, A. P. J.; Nedea, S. V.; Rindt, C. C. M. Parameterization of a reactive force field using a Monte Carlo algorithm. *Journal of computational chemistry* **2013**, *34*, 1143–1154.
- (27) Dittner, M.; Müller, J.; Aktulga, H. M.; Hartke, B. Efficient global optimization of reactive force-field parameters. *Journal of computational chemistry* **2015**, *36*, 1550–1561.
- (28) Rice, B. M.; Larentzos, J. P.; Byrd, E. F. C.; Weingarten, N. S. Parameterizing complex reactive force fields using multiple objective evolutionary strategies (MOES): Part 2: transferability of ReaxFF models to C-H-N-O energetic materials. *Journal of chemical theory and computation* **2015**, *11*, 392–405.
- (29) Deetz, J. D.; Faller, R. Parallel optimization of a reactive force field for polycondensation of alkoxy silanes. *The journal of physical chemistry. B* **2014**, *118*, 10966–10978.
- (30) Hu, X.; Schuster, J.; Schulz, S. E. Multiparameter and Parallel Optimization of ReaxFF Reactive Force Field for Modeling the Atomic Layer Deposition of Copper. *J. Phys. Chem. C* **2017**, *121*, 28077–28089.
- (31) Kirkpatrick, S.; Gelatt, C. D., JR.; Vecchi, M. P. Optimization by Simulated Annealing. *Science* **1983**, *220*, 671–680.
- (32) Hansen, N. The CMA Evolution Strategy: A Comparing Review. Towards a New Evolutionary Computation. Advances in the Estimation of Distribution. *Springer: Berlin Heidelberg* **2005**, *192*, 75–102.
- (33) Trnka, T.; Tvaroška, I.; Koča, J. Automated Training of ReaxFF Reactive Force Fields for Energetics of Enzymatic Reactions. *Journal of chemical theory and computation* **2018**, *14*, 291–302.

## Chapter 3. External surface models of ZSM-5

As enhanced in chapter 2, the main goal of this work is to determine what happens at the interface between zeolite and binders at the atomic scale. If studies focused already on the surfaces of alumina binders like boehmite or  $\gamma$ -alumina, there are only a very few dealing with the external surface of zeolites, in particular ZSM-5, which this study is focused on. This first chapter of results will consist on the study of the environment, the stability and the acidity of these surfaces. It consists in an article written in the context of this PhD and entitled: “Environment, Stability, and Acidity of External Surface Sites of Silicalite-1 and ZSM-5 Micro and Nano Slabs, Sheets, and Crystals” (doi: 10.1021/acscatal.9b05103 and written by L. Treps, A. Gomez, T. de Bruin, and C. Chizallet).

The first step of this study is the construction of a set of realistic models of the external surface of H-ZSM-5 zeolite. The analysis of the literature confirms that three orientation stand out of the numerous possibilities: (100), (010), and (101). These surfaces are compared one to another to find the most stable ones. Silanol surface sites are revealed contrary to previous molecular modeling studies of ZSM-5 bulk. These are also aluminated by the formal exchange of a silicon by an aluminum atom and a compensating proton. The nature of these so called active sites are various, from the well-known bridging group Si-OH-Al, which can be already found in the bulk, to  $\text{Al}(\text{OH})_n(\text{H}_2\text{O})$  surface groups (for  $n = 0$  to 2), which were barely studied in previous work. The nature of the surface sites is deduced from the study of their alumination, hydration and dehydration reactions, their thermal and local stabilities are also discussed at length. This article gives a solid knowledge about on the surfaces of ZSM-5 which will be completed in the next chapters which address their reactivity and the interaction with molecules, particles, and other surfaces (pyridine, 2,6-ditertbutylpyridine, sodium,  $\gamma$ -alumina, boehmite).

### 3.1. Introduction

Zeolites are nanoporous (historically called “microporous”) aluminosilicates with a well-defined crystalline structure. They can be described as a rigid three-dimensional network of  $\text{TO}_4$  tetrahedra (where T is mostly Si). These tetrahedra are linked at their corner via a common oxygen atom to form a secondary building unit (SBU). The presence of  $\text{Al}^{3+}$  cations in crystallographic positions otherwise occupied by  $\text{Si}^{4+}$  is compensated in terms of charge by extraframework cations, conferring a large array of properties such as ion exchange, gas separation and catalysis.<sup>1-2</sup> In particular, zeolites are widely employed in refining and petrochemical processes, due to their particular properties, such as high adsorption capacity, hydrothermal stability, shape selectivity, and intrinsic (Brønsted and Lewis) acidity.<sup>3-5</sup> They are also used in pollution abatement,<sup>6-8</sup> and are promising candidates for biomass conversion.<sup>9</sup>

The well-defined crystalline structure of zeolites and the large diversity of pore architectures, at the origin of tunable confinement effects,<sup>10</sup> allow the design of catalysts and adsorbents from structural considerations.<sup>8,11-12</sup> Indeed, more than 230 zeolite structures (natural and synthetic) have been identified and are listed on the International Zeolite Association (IZA) Web site.<sup>13</sup> Moreover, in the case of a proton as a compensation cation that we will consider further, it has been known for decades that bridging  $\text{Si}_{\text{IV}}\text{-OH-Al}_{\text{IV}}$  hydroxyls

are the Brønsted acid sites in the microporosity.<sup>14-16</sup> Much less information is available on the nature of the sites accessible at the external surface of the crystallites. This is, however, a crucial information in several contexts. First, the “pore-mouth catalysis” was invoked to take place with a specific reactivity at the external surface for zeolites whose pores are smaller than the bulky molecules to be converted.<sup>17-18</sup> Second, some recent developments aim at reducing mass transfer limitations and thus the residence time of molecules in the zeolite crystal. Several strategies can be found in the literature to reach this goal, all leading to an increase of the (external surface)/(internal surface) or (mesoporous surface)/(microporous surface) ratios: (i) obtaining nanocrystals of zeolites (several tens of nanometers)<sup>19-20</sup> or even embryonic zeolites,<sup>21-22</sup> (ii) preparing hierarchical zeolites, by introducing meso(macro)porosity in the microporous crystals<sup>23-25</sup> or by preparing hollow zeolite structures,<sup>26</sup> and (iii) obtaining nanosheets of zeolites (thickness less than 10 nm), delaminated and 2D zeolites.<sup>27-29</sup> Thus, advanced knowledge of the environment of surface sites at the external surface is required.

ZSM-5 (Zeolite Socony Mobil-5) is a zeolite that was discovered and multipatented by Mobil Oil Corporation in 1969.<sup>30-32</sup> It is a very well known and used catalyst in the petrochemical industry.<sup>4</sup> The structure type of ZSM-5 is MFI,<sup>33</sup> also corresponding to the silicalite-1 zeolite.<sup>34</sup> In addition to its industrial impact, this system is used as a prototype to investigate crystal growth mechanisms.<sup>35</sup> A large range of crystal sizes (from a few nanometers to several hundreds of micrometers) and Si/Al ratios (currently from 8<sup>36</sup> to infinity in the case of silicalite-1<sup>34</sup>) are accessible with the same structure type. For all of these reasons, we will focus on this zeolite type in the following.

The MFI structure (Figure 1a) is composed of two 10-membered ring (MR) interconnected channel system: a sinusoidal and a straight one system along the directions of the *a* and *b* axes, respectively.<sup>13</sup> MFI exhibits a monoclinic structure, undergoing a phase transition toward an orthorhombic symmetry (*Pnma*), depending on the temperature (orthorhombic above ~330 K for silicalite-1), the Si/Al ratio (the transition temperature decreases as the Al content increases), and the presence of adsorbed molecules in the pores.<sup>37-39</sup>

A large set of experimental investigations has been devoted to identify the exposed surface orientations on silicalite-1 and ZSM-5, which is complex due to the existence of intergrowth phenomena that lead to poly-crystalline particles. The morphology of the crystals appears to strongly depend on the crystal size, the synthesis procedure, and the choice of the structure directing agent (SDA). The formation of nanoslabs with dominant (100) expositions was observed in the very first stage of silicalite-1 crystallization.<sup>40</sup> A formation mechanism was proposed for these nanoslabs, as a result of a combination of <sup>29</sup>Si NMR, X-Ray Scattering, and gel permeation chromatography.<sup>41</sup> Clathrate-like silicate units, where the SDA (tetrapropyl-ammonium hydroxide, TPAOH) is hosted in a silica matrix forming the intersection of the zeolite, were invoked.<sup>21</sup> In particular, a Si<sub>33</sub> species (Figure 1b,c) was proposed,<sup>41</sup> being an elementary portion of the straight channel, which – assembled along the *b* direction – makes this channel grow, and thus the (100) orientation develops. Such proposal was later debated,<sup>42-44</sup> due to the multistep nature of the formation mechanism of zeolites,<sup>45</sup> making the level of self-organization of the systems strongly dependent on many operating

parameters. More recent investigations confirmed that the  $\text{Si}_{33}$  precursor is relevant to explain part of the crystal growth.<sup>46</sup>

Monocrystalline MFI nanocrystals in the range of 100-200 nm could be obtained,<sup>19,44,47-49</sup> where the smaller crystals may have a rounded shape preventing the identification of a well-defined surface orientation,<sup>19,44,47</sup> while the larger nanocrystals may have rather well-defined facets, which were, however, not indexed.<sup>48-49</sup> The parallelepiped shape of some of the nanocrystals suggests the existence of (100), (010), and (001) orientations, whereas the hexagonal morphology of others could be compatible with the additional presence of (101) cuts. A clear proof of the monocrystalline nature of some silicalite-1 and ZSM-5 nanocrystals (50-200 nm) was given recently.<sup>49</sup>

At more advanced growth regimes,<sup>50</sup> seeds evolve into rounded-boats crystals, themselves giving rise to coffin-shaped crystals. Rounded-boat crystals were found to be monocrystalline with dominant (010) facets, and rectangular lateral (100) facets<sup>50-51</sup> (Figure 1d). In contrast, the complexity of the intergrowth structures of the coffin-shaped crystals was inferred from X-Ray diffraction in the 1980s.<sup>52</sup> Since then, several sets of models have been proposed, on the basis of optical, electronic, and atomic force microscopy and X-Ray and electron diffraction.<sup>52-56</sup> These models invoked the presence or absence of 90° intergrowth, of MEL (Mobil Eleven)-type defects, and various numbers of components for the coffin-shaped crystals. The nature of the exposed orientations thus has been subjected to debate. About 10 years ago, a consensus was obtained thanks to the use of a set of characterization techniques: in particular, confocal fluorescence microscopy with various fluorescent probes, scanning electron microscopy, and electron diffraction after ion-beam milling.<sup>51,57-59</sup>

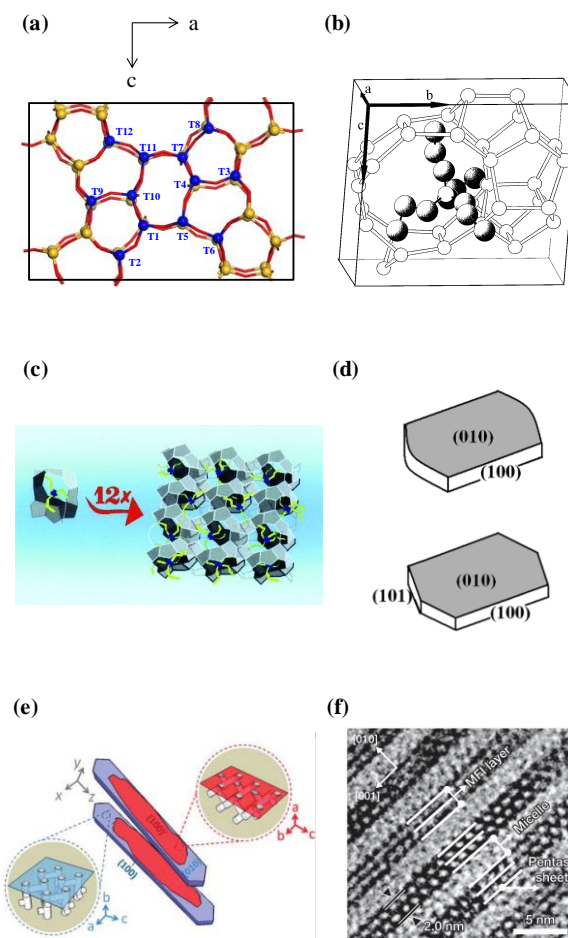


**Figure 1.** (a) Conventional crystalline cell of ZSM-5, the Oxygen atoms are represented in red and the silicon atoms in yellow. The blue atoms represent the 12 nonequivalent silicon atoms denoted T1-T12. (b)  $\text{Si}_{33}$  entity identified as the precursor of MFI nanoslabs surrounding TPAOH as SDA,<sup>41</sup> (c) Formation of nanoslabs by the assembly of the  $\text{Si}_{33}$  elementary units,<sup>40</sup> (d) Schematic representation of rounded-boat (top) and coffin-shaped (bottom) crystals,<sup>60</sup> (e) Relationship between the crystallographic  $abc$  axes and the morphological  $xyz$  axes for coffin-shaped crystals,<sup>59</sup> (f) TEM of MFI nanosheets.<sup>28</sup> Reprinted from refs 28,40-41,59-60. with permission from The Royal Society of Chemistry, American Chemical Society (Copyright 1999 and 2008), Wiley (Copyright 2001), Nature (Copyright 2009).

These studies demonstrated the existence of several kinds of crystals, but with a common feature: that is, a  $90^\circ$  rotation of the subunits exposed on the “(010)” facets. These intergrowths make the (100) surface (intersecting the sinusoidal pores) largely exposed on all lateral faces of the polycrystalline crystals (Figure 1e). Only perfectly monocrystalline coffins expose both the (100) and (010) orientations.<sup>51</sup> Tips of the coffins mainly expose (101) and (10-1) surface orientations.<sup>60</sup> Octagonal variants of the coffin-shaped crystals exhibit (001) and (011) orientations at their tip.<sup>60</sup> HRTEM (High-Resolution Transmission Electron Microscopy) was also performed on silicalite-1 crystals,<sup>61</sup> where (100) and (101) surface terminations have clearly been observed.

Unambiguously, the (010) orientation (perpendicular to the straight channels) appears to be exposed on MFI nanosheets<sup>28,62</sup> on Self-Pillared nanosheets,<sup>63</sup> and on thin films grown from nanosheets (Figure 1f).<sup>64-65</sup> In some studies, seeds were employed to grow the sheets, the

(010) orientation of the sheets growth aligned with the (100) plane of the seeds,<sup>65</sup> revealing an orthogonal rotational intergrowth relationship between the two objects.

The respective stabilities of these many surface orientations are unknown, however, and the structure of the surface sites is supposed to be equivalent to that of the bulk crystal (bridging Si-(OH)-Al groups), but with improved accessibility. The nature and stability of the active sites at these different external surface orientations need to be unraveled. To address these key questions, several studies based on theoretical calculations have been undertaken. Car-Parrinello molecular dynamics simulations have been reported for (010) nanosheets silicalite-1 models, revealing a significant stability of the atomic arrangement at the surface.<sup>62</sup> Hernandez-Tamargo *et al.* proposed the first detailed density functional theory (DFT) investigation of bridging OH groups located at the (010) surface, in the vicinity of silanols terminating the surface, but they excluded the possible formation of other types of groups.<sup>66</sup> Other DFT studies with different purposes were undertaken for this surface orientation.<sup>67-70</sup> The (001) surface was chosen by Duca *et al.* to build a cluster model.<sup>71-72</sup> To the best of our knowledge, the most relevant (100) surface was only modeled once,<sup>67</sup> with small slabs saturated by Si-H groups at the bottom.

In the present work, we propose a general DFT investigation of the stability of the three dominant orientations for silicalite-1 and ZSM-5 crystals and nanosheets: consistent models are constructed for the (100), (010), and (101) surface orientations, with an in-depth analysis of the influence of the nature of the terminating structures (varied here by changing the height of the cleavage of the bulk structure) on the thermodynamic stability. For technical reasons, the surface models are constructed by cleaving the bulk structure. Although such a process does not faithfully represent the experimental conditions, with growth mechanisms in solution at non-neutral pH and in the presence of the SDA, we manage to make a link between the simulated structures and some building blocks invoked experimentally, for all surface orientations. The consequences of the exchange of silicon by aluminum and their positions will be discussed with respect to the surface stability and the chemical nature of surface species (Si-OH, Si-OH-Al, Al-OH but more importantly Al-(H<sub>2</sub>O)(OH)<sub>n</sub> with n=0-2) has been systematically quantified in comparison with that of bulk Si<sub>IV</sub>-OH-Al<sub>IV</sub> groups as a function of temperature and partial water pressure to investigate their hydration/dehydration properties as well. General rules connecting the thermal stability of surface sites and the local topology will be discussed in relation to the expected equilibrium morphologies, helping to unravel the much debated question<sup>73-77</sup> on the framework Lewis acid sites in zeolites.

### 3.2. Computational details

Periodic DFT calculations were performed with the PBE (Perdew, Burke, and Ernzerhof) exchange-correlation functional<sup>78</sup> as implemented in VASP 5.4.1.<sup>79-80</sup> The projected augmented wave (PAW) method<sup>81</sup> was used to describe the core-electron interactions, and the plane wave basis set was limited to a kinetic cutoff energy of 400-800 eV (depending on the kind of calculation performed, see below). A density-dependent dispersion correction, dDsC,<sup>82</sup> was applied. The convergence criterion for the electronic self-consistent field relaxation was fixed at 10<sup>-5</sup> eV. Even for nonsymmetric slabs, no dipolar correction was

applied to remove the spurious interactions in the direction perpendicular to the surface, as it has a minor effect on the electronic energy (less than  $2.10^{-3}$  eV; see table S1 in section SI in the Supporting Information of Chapter 3). All calculations were performed at the  $\Gamma$ -point. Full geometry optimizations were performed using the implemented conjugate-gradient algorithm, with a convergence criterion on forces of  $0.02$  eV  $\text{\AA}^{-1}$ .

We considered the orthorhombic cell of MFI for the calculations, as it is experimentally the most stable cell after thermal treatment. The bulk cell parameters and initial ionic positions were obtained from the International Zeolite Association database<sup>13</sup> and then reoptimized in the purely siliceous form with an increased energy cutoff of 800 eV. The final values are (almost orthorhombic:  $\alpha=89.99^\circ$ ,  $\beta=90.00^\circ$ ,  $\gamma=90.00^\circ$ ):  $a=19.901$   $\text{\AA}$ ,  $b=20.009$   $\text{\AA}$ , and  $c=13.364$   $\text{\AA}$ , in good agreement with the experimental values<sup>83-84</sup> (orthorhombic:  $a=20.07\pm 0.01$   $\text{\AA}$ ,  $b=19.92\pm 0.01$   $\text{\AA}$  and  $c=13.42\pm 0.01$   $\text{\AA}$ ). These values were then kept constant throughout the study. The bulk configuration exhibits 12 nonequivalent T sites in the structure (Figure 1a). The alumination of the bulk structure was modeled by the replacement of one silicon by an aluminum atom. A proton was added as a compensation cation on one of the neighboring oxygens of the aluminum, which induced four possibilities of bridging OH group as Al-(OH)-Si for one aluminum position. The silicic structure was cleaved along the (100), (010), or (101) surface orientations, to mimic the relevant surface orientations identified experimentally (see 0). For each investigated cleavage direction, a set of cleavage heights was investigated as illustrated in section SI in the Supporting Information of Chapter 3. The thickness of the slab was initially set at two bulk units, which appeared to provide satisfactory convergence of structural properties (see section SII in the Supporting Information of Chapter 3). The wish to simulate a symmetric slab led us in some cases to slightly deviate from this thickness (see section SI in the Supporting Information of Chapter 3). A 25  $\text{\AA}$  vacuum layer was added on top of the surfaces. The dimensions of the cells were  $60.83\times 20.01\times 13.36$   $\text{\AA}^3$ ,  $19.90\times 60.77\times 13.36$   $\text{\AA}^3$ , and  $23.97\times 20.01\times 50.17$   $\text{\AA}^3$  for the (100), (010), and (101) directions, respectively. Finally, the surface was saturated with OH groups, hydrogen atoms were added to monocoordinated O atoms, and OH moieties saturated  $\text{Si}_{\text{III}}/\text{Si}_{\text{II}}/\text{Si}_{\text{I}}$  atoms. The total numbers of atoms are in the 516-642, 528-648 and 414-678 intervals for the (100), (010), and (101) surface models, respectively.

The alumination energy  $\Delta_r U_{al}$  is calculated with eq 1 using the energy of the aluminated surface (or bulk)  $U_{slab\_Al}$ , the energy of the surface (or the bulk) without aluminum  $U_{slab}$ , and the energies  $U_{Al(OH)_3H_2O}$  and  $U_{Si(OH)_4}$  of tetrahedral components of zeolites  $\text{Al(OH)}_3\text{H}_2\text{O}$  and  $\text{Si(OH)}_4$  respectively. The energy of these last two species has been calculated in a cubic cell of 30  $\text{\AA}$  side lengths.

$$\Delta_r U_{al} = (U_{slab\_Al} + U_{Si(OH)_4} - U_{slab} - U_{Al(OH)_3H_2O}) \quad (1)$$

The choice of the references is rather arbitrary; other choices could have been made with other Al/Si components. The goal of the introduction of the alumination energy is to report a straightforward comparison of the stability of various aluminated slabs, instead of total energies.



The thermodynamic stabilities of the surfaces are determined by calculating the temperature- and pressure -dependent surface free energy  $\gamma_{surf}$ .<sup>85</sup> It was calculated through the formation reaction of the hydrated zeolite surface relative to the zeolite bulk and gaseous water, as indicated by eq (2).

$$\gamma_{surf}(T, P_{H_2O}) = \frac{1}{2A} (G_{surf}(T, P_{H_2O}) - N_{H_2O}G_{H_2O}(T, P_{H_2O}) - N_{Al}G_{zeo\_AlH\_bulk} - N_{SiO_2}G_{zeo\_Si\_bulk}) \quad (2)$$

where  $G_{surf}$ ,  $G_{H_2O}$ ,  $G_{zeo\_AlH\_bulk}$ , and  $G_{zeo\_Si\_bulk}$  are respectively the Gibbs free energy of the surface (which depends on the number of Si and O in the zeolite structure), the Gibbs free energy of water, the Gibbs free energy of one aluminated site in the zeolite bulk and the average Gibbs free energy of one  $SiO_2$  units of the bulk zeolite. The vibrational contributions to the Gibbs free energy in the bulk and surface systems are considered to be equal. Therefore, we only considered their electronic energies.  $N_{H_2O}$ ,  $N_{Al}$ , and  $N_{SiO_2}$  are respectively the number of water molecules adsorbed on the surface, the number of Al atoms in the cell, and the number of  $SiO_2$  units in the zeolite surface model.  $\gamma_{surf}$  is normalized to the energy per unit area by dividing by the surface area  $A$ . The equilibrium morphologies were built thanks to the Morphology module of Materials Studio (Dassault Systèmes).

Hydration/dehydration reactions were simulated on one surface on the investigated slabs. Hydration free energies were determined by evaluating the vibrational partition function of water,<sup>86</sup> here considered as an ideal gas. The vibrational partition function of the surface OH groups was considered as unchanged with respect to that of water, for the sake of calculation resources. The same method was applied to evaluate the adsorption energies and free energies for the adsorption of pyridine. For a limited number of cases mentioned in the following, we have explicitly evaluated the vibration free energy for condensed phases, thanks to finite difference frequency calculations, with a displacement of  $\pm 0.005$  Å for the atoms allowed to vibrate (all atoms of the silicic bulk cell, half of the slab for the silicic hydroxylated surfaces, the aluminum atoms and their first, second, third and fourth neighbors for aluminated surfaces).

### 3.3. Stability Ranking of Silicalite-1 Surfaces: The Bulk Cleavage Approach

A large set of surface models was constructed according to the method described in section 0 They differ in their surface orientation and cleavage height, which in turn results in various  $H_2O$  (in the form of Si-OH pairs) coverages: from 1.50 to 4.51  $H_2O$   $nm^{-2}$ . The surface energies calculated at 0 K are all presented in Table S1. Consistent with previous simulations of the external surface of zeolite beta<sup>87</sup> and with that of hydroxylated quartz surfaces,<sup>88</sup> the energies are very low and have a first-order dependence on the hydroxylation level (Figure S2), even though the local arrangement of the OH groups also influences the stability. Taking into account the effect of temperature and water partial pressure on the thermodynamic stability of the surfaces, phase diagrams have been built which include surfaces that do not appear in the final diagrams (Figure 2, and section SIII in the Supporting Information of Chapter 3). In section SIII.3 in the Supporting Information of Chapter 3, we also report an estimation of the variation of the frontier between two cleavages, depending on the method

that is used for the estimation of the vibration free energy of the condensed phases (either calculating it explicitly or assuming that it compensates among the various forms of water gas phase, adsorbed and silica-bulk, slab). At a typical water pressure of  $10^{-4}$  bar, the frontier appears at a temperature lower by 29 K, which does not affect the conclusions drawn in the following.

For each surface orientation, above 300 K, the stability diagram is dominated by a single cleavage height, which in all cases leads to the exposition of a minimal number of Si-OH groups at the surface ( $\theta_{H_2O} = 1.50 \text{ nm}^{-2}$  for the (100) and (010) surfaces and  $1.88 \text{ nm}^{-2}$  for the (101) surface). This means that, from a thermodynamic point of view, conserving most siloxane bridges, also present in the bulk, is a strong thermodynamic driving force, giving a substance to the minimum cut hypothesis made previously,<sup>89</sup> although this does not appear from the consideration of surface energies at 0 K. For the (100) surface, the preferred model exhibits a straight pore cut at the half, as represented in Figure 2a (and Figure S2), exhibiting pairs of vicinal and nonvicinal silanol groups, connected one to another by hydrogen bonds. The two other models exhibiting a (narrow) stability domain in Figure 2a are cut at the border of the straight channel (model no. 6) or make the straight channel flush (model no. 10) (Figure S2). In these cases, geminal silanols are exposed and groups of three silanols are connected to the same Si, respectively.

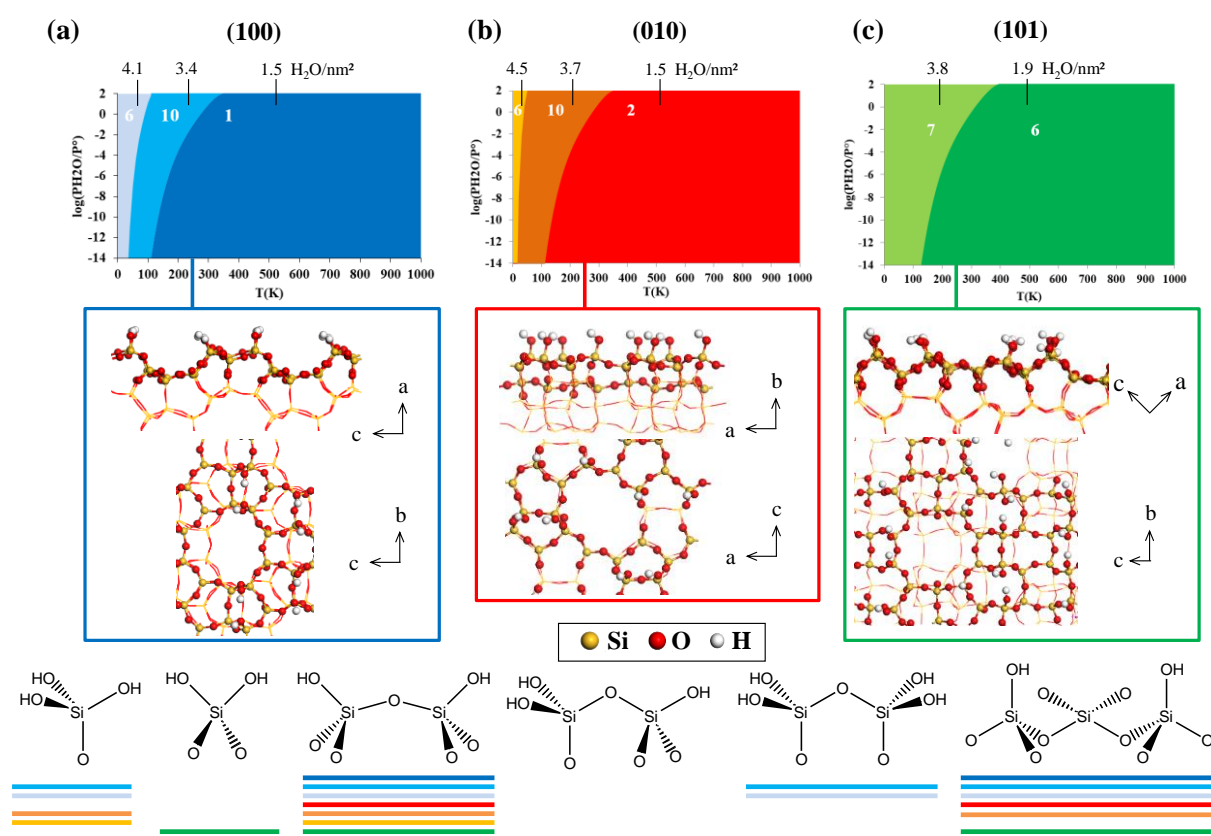


**Figure 2.** Stability diagrams (top) and most surface models (side and top views) for the siliceous (a) (100), (b) (010), and (c) (101) surface orientations. The numbers in the diagrams correspond to the thermodynamically most stable heights for the cleavages (in section SI in the Supporting Information of Chapter 3 for details). The typical surface groups that are present at the surface cleavage are depicted at the bottom of the figure; they are underlined with the colors used in the stability diagrams to show under which conditions these groups are present.

For the (010) orientation, the preferred cleavage corresponds to height no. 2, with full pentasil layers (in contrast to the other cleavage height, which cut a part of the pentasil layer), consistent with previous computational works<sup>66</sup> and with experimental knowledge of nanosheets.<sup>28,90</sup>

Finally, for the (101) orientation, the termination of the most stable cleavage 6 exhibits terminal and geminal silanols. It also corresponds to the case where all the units connected to the straight channels are uncut.

Next, we compare the stabilities of the various surface orientations with each other (Table 1 and section SIII.2 in the Supporting Information of Chapter 3). At 400 K (a typical temperature for zeolite synthesis<sup>35,45</sup>) and  $P_{H_2O} = 1$  bar, the surface free energy of the (100) surface is slightly lower ( $12.7 \text{ mJ m}^{-2}$ ) than that of the (010) surface ( $13.1 \text{ mJ m}^{-2}$ ). The (101) surface is less stable than the two other surfaces ( $14.2 \text{ mJ m}^{-2}$ ). Following the Gibbs-Curie-Wulff law,<sup>91-92</sup> the equilibrium morphology corresponds to those depicted in Figure 3a,b.

An hexagonal prism is predicted, but it is shorter than the experimental coffins along the  $c$  direction. The projections show that we should expect rectangular and almost regular hexagonal shapes in microscopy, which compare very well with some studies dealing with well-defined silicalite-1 nanocrystals.<sup>48-49,93</sup> Gruene *et al.*<sup>49</sup> measured the dimensions of their silicalite-1 monocrystals. The hexagonal projection of the model exhibits a ratio of the longest to shortest dimension of  $1.29d/0.96d = 1.34$  ( $d$  being the height of the coffin, Figure 3a), in very good agreement with the experimental measurement value of  $1.20$ <sup>49</sup> (section SIV in the Supporting Information of Chapter 3). However, TEM also shows that the height /width ratio of the particles ( $125 \text{ nm} / 210 \text{ nm} = 0.60$ ) is smaller than the one we predict by our thermodynamic approach ( $d/0.96d = 1.04$ ), suggesting that the growth of (100) facets is somewhat slower than the one of the (010) in this range of size.

**Table 1.** Surface Energies  $\gamma_{surf}$  ( $\text{mJ m}^{-2}$ ) at 400 K and  $P(H_2O) = 1$  bar of Purely Silicic Cleavages (CLV) for the (100), (010), and (101) Surface Orientations and the Same Cleavages for Similar Aluminum Contents.

		(100) CLV1	(010) CLV2	(101) CLV6	(101) CLV9
purely silicic	$\gamma_{surf}$	12.7	13.1	14.2	17.4
aluminated	$\text{Al nm}^{-2}$	0.37	0.38	0.41	0.41
surface	$\gamma_{surf}$	11.0	11.5	12.8	14.7

### 3.4. Stability Ranking of Silicalite-1 Surfaces: The Precursor Growth Approach

While the approach detailed in section 0. essentially considers thermodynamic conditions, the exposed surfaces are also dictated by crystal growth conditions in solution. A  $\text{Si}_{33}$  precursor structure has been proposed from a set of experiments by Kirschhock *et al.*<sup>41</sup> in the presence of TPA as SDA (Figure 1b,c). The analyses of the terminations that can be obtained from this  $\text{Si}_{33}$  precursor (Figure 4a) reveal a strong similarity with the termination modeled upon cleavage of the crystal structure. Following the mechanism proposed in Figure 1c,<sup>40</sup> the (100) surface orientation is developed in the first stages of the crystal growth. As the

$\text{Si}_{33}$  species is not symmetric, two surfaces are formed, which appeared to be similar to cleavages no. 1 and 2 (Figure 4b, see also section SV in the Supporting Information of Chapter 3). Cleavage no. 1 is the dominant one from the thermodynamic cleavage approach (Figure 2a), meaning that in this case, thermodynamic and kinetic driving forces for crystal growth are converging. Cleavage no. 2 is thermodynamically significantly less stable than cleavage no. 1 (SIII.1 in the Supporting Information of Chapter 3). We shall next consider the stacking of two nanoslabs one with the other to make the crystal grow in the  $a$  direction (one of the possibilities suggested in ref. 94). Two scenarios may be followed to form a double nanoslab: exclusively exposing cleavage no. 1 (type 1, Figure 4c) or exclusively exposing no. 2 (type 2, Figure 4d). Cleavage no. 1 being the more stable, type 1 thus becomes the most favorable type. On the other hand, if an odd number of nanoslabs is stacked along the  $a$  direction during the crystal growth, both surfaces will be exposed.

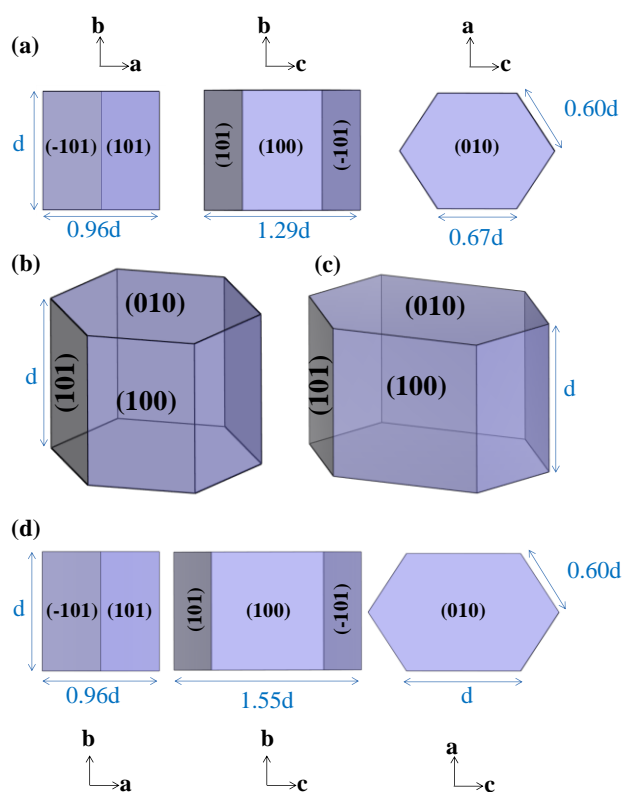


**Figure 3.** Equilibrium morphology of silicalite-1 and ZSM-5 crystals predicted by a Gibbs-Curie-Wulff approach, from the surface free energies calculated at 400 K and 1 bar, considering the  $(100)$ ,  $(010)$ , and  $(101)$  orientations: (a, b): most stable morphology predicted by the bulk cleavage approach; (c, d): approximation of the morphology predicted upon construction of the surface models with the  $\text{Si}_{33}$  precursor building block approach (see also Figure 4). (a) and (d) are projections along specific axes.

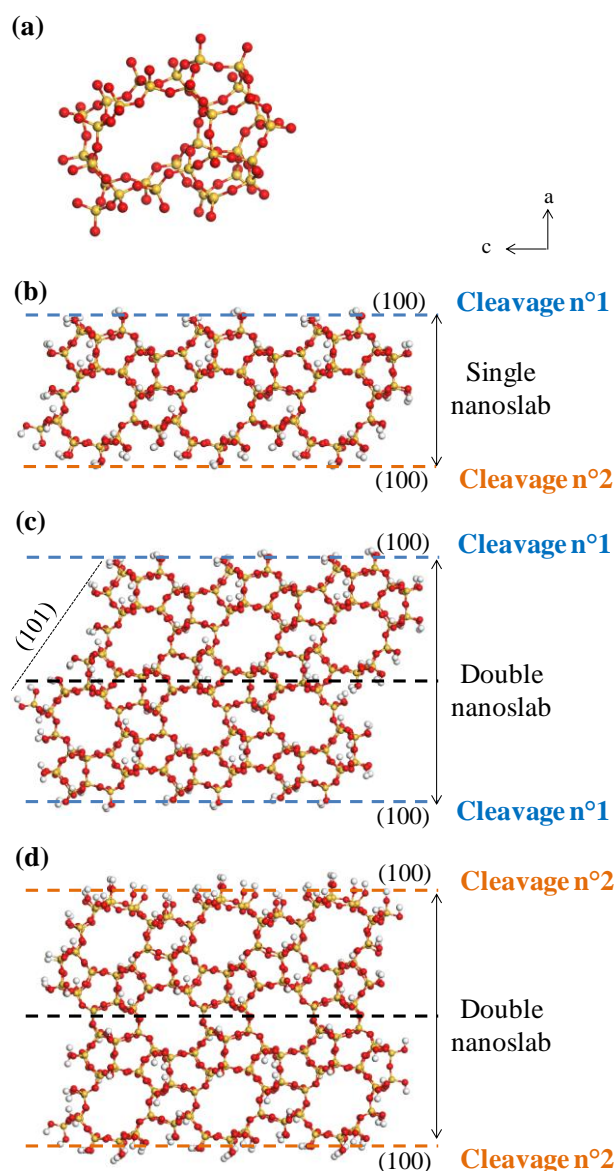


**Figure 4.** (a)  $\text{Si}_{33}$  precursor species constructed in the spirit of Kirshhock *et al.*<sup>41</sup> from the optimized bulk MFI structure, (b) Lateral view of the structure of a nanoslab, exhibiting (100) surfaces, constructed in the spirit of ref 40. The nature of the equivalent cleavages along the (100) surface is depicted. Stacking of two nanoslabs along the *a* axis, making cleavage no. 1 (c) or no. 2 (d) being solely exposed. Note that the structure of the isolated nanoslabs was not relaxed. The color code is the same as in Figure 2.

Note that as by construction we find a perfect correspondence between the surfaces exposed by this growth approach and the systems obtained by the cleavage approach (section 0.), the energies of the systems obtained by the growth approach were not evaluated.

A similar construction approach for the (010) and (101) orientations with the  $\text{Si}_{33}$  precursor was undertaken (section SV in the Supporting Information of Chapter 3). According to Figure 4c,d the (010) orientation is actually one of the surfaces that grows most importantly, when double nanoslabs are constructed by extension along the *a* axis. From this construction method, cleavage no. 2 of the (010) orientation appears on both sides, in full agreement with the bulk cleavage approach (Figure 2b) and with previous structural considerations.<sup>95</sup> With regard to the (101) orientation, construction with the  $\text{Si}_{33}$  precursors

leads to a surface that is very similar (but not strictly identical) to cleavage no. 9, obtained using the bulk cleavage approach. At 400 K and  $P_{H_2O} = 1$  bar, this surface cleavage is less stable ( $\gamma_{surf} = 17.4$  mJ m<sup>-2</sup>) than cleavage no. 6 (14.2 mJ m<sup>-2</sup>). Thus, the equilibrium morphology predicted by such a crystal growth approach does not differ much from that deduced from the bulk cleavage approach, as the (100) and (010) models do not change. The change in the (101) cleavage to be considered leads to a destabilization of the latter surface with respect to the (100) and the (010) surfaces, thus resulting in longer coffin like geometries (Figure 3c,d).

In the following, we consider the introduction of aluminum in the ZSM-5 models. We start with the silicalite-1 models established in sections 0. and 0., where in the first place we investigate the cleavages no. 1 and 2 for respectively the (100) and (010) surfaces, as result of their large thermodynamic stability domain and their relevance in the crystal growth with the Si<sub>33</sub> building block approach. However, the other models are not excluded for further investigations, as they may also be relevant in kinetically controlled growth conditions,<sup>96-97</sup> where a diversity of precursors may play a role.<sup>44</sup>

### 3.5. Stability of Aluminum Containing Surfaces: Diversity of Sites

#### 3.5.1. Preliminary Investigation: Thermodynamic Sitting of Aluminum for Bulk Framework Sites

The alumination of the bulk structure has been simulated by replacing one silicon by an aluminum atom, in one of the T site positions. To compensate the charge, a proton was added on one of the neighboring oxygen atoms of the aluminum, which gives rise to four possibilities of Al-(OH)-Si bridging OH groups for one aluminum position. The aluminations energies  $\Delta_r U_{al}$  were calculated using eq (1) and are reported in Figure 5. The detailed value of each point is presented in SVI.1 in the Supporting Information. The lower (more negative) the value, the more stable the site.  $\Delta_r U_{al}$  values range between  $-8$  and  $-44$  kJ mol<sup>-1</sup>, which is similar to the previous results for zeolite beta<sup>87</sup> (domain between  $-45$  and  $5$  kJ mol<sup>-1</sup>). The domains also correspond to the  $50-60$  kJ mol<sup>-1</sup> range previously found for many zeolites,<sup>98-99</sup> including bulk ZSM-5,<sup>67,100-103</sup> mordenite<sup>104-105</sup> and EU-1,<sup>106</sup> to cite a few.

On the basis of thermodynamic stability, our calculations indicate that the T3 sites are the most likely ones to be occupied by Al, in close competition with T8 (SVI in the Supporting Information). However, not all computational investigations agree on this point,<sup>67,101,107</sup> suggesting that the difference in stability of these sites is not sufficiently pronounced to draw conclusions and that other (kinetic) factors may also play an important role. Similar to other studies, however,<sup>101,107-108</sup> some sites located at the intersection of both kinds of channels are the most stable ones, despite also being the ones that are most easily dislodged upon steaming.<sup>109-111</sup> Furthermore, the position of the Al atom can experimentally be tuned by changing the synthesis conditions.<sup>111-114</sup> Therefore, considering all possible positions is required to get a complete view of the stability of the systems.



### 3.5.2. Nature and Stability of Surface Aluminium Sites

Whereas bridging OH groups are the only possibility in the bulk, the aluminium of silicon atoms located at the surface (Si-OH) generates new sites. The structure and stability of these sites were sampled on several cleavages of the surface orientations considered, and are depicted in Figure 5. Details are given in section SVI.2 in the Supporting Information of Chapter 3. Generally speaking, the reaction energy interval of surface species is larger than that in the bulk, suggesting the importance of numerous local effects playing a role in the preferential location of {Al,H} pairs. For each family of surface groups, the configurations leading to the most negative aluminium energies are those where the introduced proton becomes a hydrogen bond donor toward a pre-existing Si-OH group, explaining why the most negative aluminium energies are found for silanol-rich surfaces. We did not find a direct relation between the stability of the corresponding bulk site (Table S13) and  $\Delta_r U_{al}$ .

“Classical” bridging OH groups appear to be distributed according to a similar aluminium energy range at the surface and in the bulk. At the surface, a larger variety of bridging OH groups is moreover obtained, where an additional terminal OH group is connected to the Al and/or Si atom. Some of these groups exhibit a significantly more negative aluminium energy with respect to bulk bridging OH groups, resulting from the extra hydrogen bond as mentioned above.

In the case where the aluminum is situated at the surface, i.e. it is connected to at least one surface OH oxygen, the compensation proton can also bind to the surface Al-OH groups and generate an adsorbed H<sub>2</sub>O molecule, yielding an Al-(H<sub>2</sub>O) species, as already has been shown for zeolite beta.<sup>87</sup> Some silicon atoms at the surface are linked to the bulk of the zeolite by one or two Si-O-Si bridges and are connected to three or two OH groups. The aluminium of these silicon atoms generates Al-(H<sub>2</sub>O)(OH)<sub>n</sub> species with n = 1 or 2. It appears from Figure 5 that Al-(H<sub>2</sub>O)(OH)<sub>n</sub> species (with n = 0-2) are the most stable ones, whatever the surface orientation under consideration. The stability domains are lying in a very large range (between - 140 and - 30 kJ mol<sup>-1</sup>) even though the majority fall in the range between - 100 and - 50 kJ mol<sup>-1</sup>. For all of the surface orientations, the closer the aluminated sites are to the outermost surface, the more stable they are. Note that in the previous DFT simulations of MFI surfaces, these most stable configurations were often omitted.<sup>66-67</sup> In some cases, they were considered as precursor states for the dehydration of the surface,<sup>66,115</sup> which we further investigate in section 0.

Thus, the bridging Si-OH-Al groups can exist at the pore mouth, strengthening the pore mouth catalysis concept.<sup>17-18</sup> However, they do not exist at the outermost surface, confirming the idea that the existence of the cavity is needed to stabilize such bridging groups.<sup>116-117</sup>



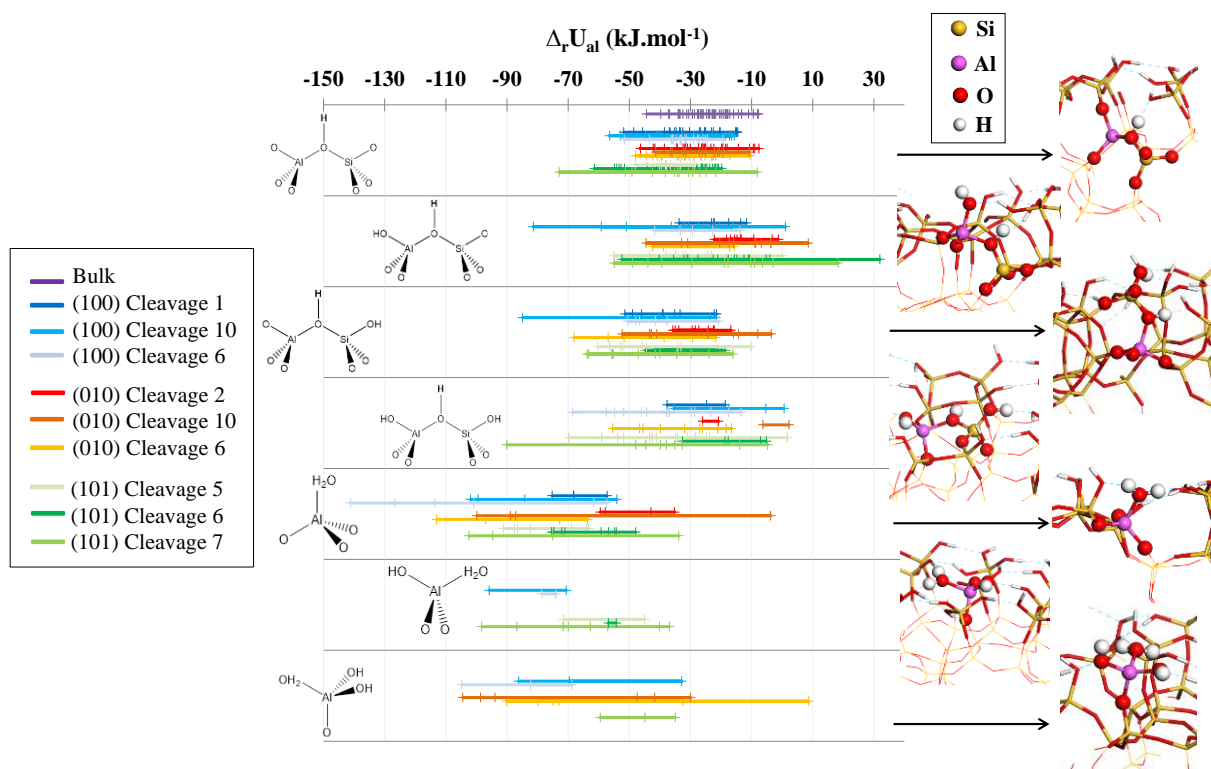


**Figure 5.** Alumination energy along the various considered cleavages and in the bulk of ZSM-5 for the large variety of considered aluminated sites. On the right, the site corresponding to the lowest alumination energy for a given kind of site is shown.

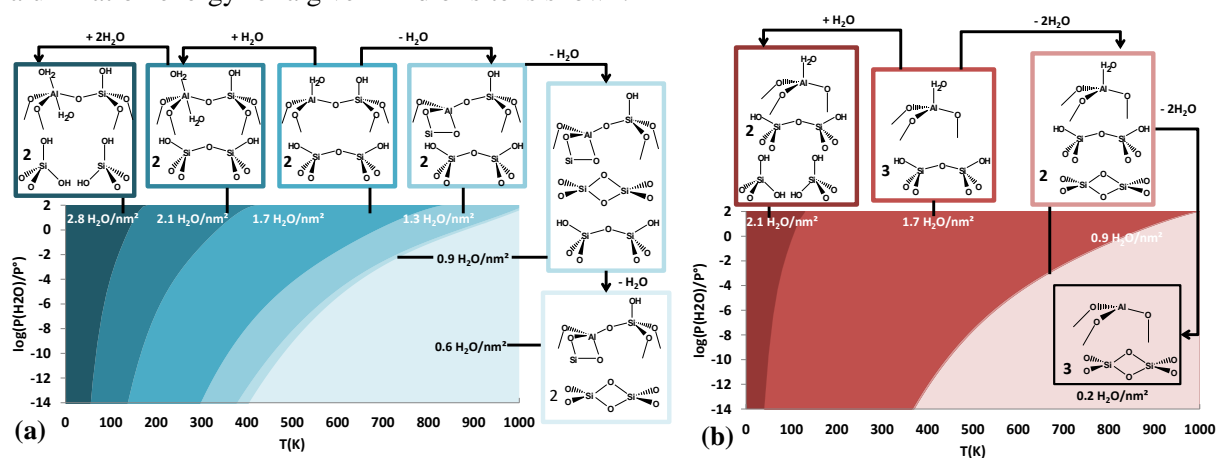


**Figure 6.** Surface hydration thermodynamic diagram for two types of Al-(H<sub>2</sub>O) sites belonging to the cleavage 1 of the(100) surface of ZSM-5: (a) site no. 59 and (b) site no. 75. The terminology of the surface sites is given in Figure S14.

### 3.5.3. Effect of the Si/Al Ratio

The influence of the Si/Al ratio on the stability of the system was investigated for cleavage 1 along the (100) surface orientation and cleavages 6 and 9 along the (101) surface orientation. Instead of one, four T and two T sites per unit cell were substituted by Al for, respectively, the (100) and (101) orientations. These Al atoms were introduced at the surface, similar to what would have taken place in the case of zoned Al distribution.<sup>118</sup> For the

calculation of the local Si/Al ratio, we may consider the surface layer corresponding to one bulk unit. This leads to variation intervals between 23 and 95 for the (100) orientation and between 43 and 102 for the (101) orientation. This is representative of most experimental investigations: the Si/Al ratio of ZSM-5 varies from 8<sup>36</sup> to infinity<sup>34</sup> (silicalite-1), with a predominance of investigations dealing with Si/Al > 15. The results are reported in Table S14. In this range of Si/Al variation, the lateral interaction between the acid sites themselves is negligible. Also in the case of zoning, bulk calculations suggest that the average alumination energy may not strongly depend on the Si/Al ratio down to local values of 8.<sup>119</sup>

In the end, the presence of aluminum affects the stability of the surface terminations, and thanks to DFT we can quantify this effect. Whereas the alumination energy quantifies the respective stabilities of silicon *versus* aluminum sites at a given position, the equilibrium morphology is given by the nature of the most stable aluminated surface termination. For similar surface aluminum contents (0.37, 0.38, and 0.41 Al nm<sup>-2</sup> for the (100), (010), and (101) surface orientations, respectively), the surface energies are the following: 11.0, 11.5, 12.8, and 14.7 mJ m<sup>-2</sup> for the (100) (cleavage 1), (010) (cleavage 2), (101) surface orientations (cleavages 6 and 9), respectively (Table 1). These values lead essentially to the same equilibrium morphology in comparison to silicalite (Figure 3). Experimentally, some differences were observed in some studies between silicalite and ZSM-5,<sup>49</sup> suggesting that kinetic limitations may take place for the growth in some directions, which depend on the Al concentration in the medium, and/or that the Al content is not the same on any surface orientation.<sup>118</sup>

### 3.6. Thermal Stability: Hydration and Dehydration Properties

Considering the presence of nondissociated water molecules at the external surface of zeolites also requires studying the thermal stability as a function of temperature and partial water pressure. We therefore undertook a systematic investigation of the hydration/dehydration reactions that are likely to take place on a selection of relevant surface systems. Al-(H<sub>2</sub>O) species at the (100) surface are first studied and compared to what we call the reference state representing the surface obtained after cleavage, saturation by Si-OH groups, and alumination as described in the previous sections. Three sites were selected: on cleavage 1, the least (Figure 6a) and the most (Figure 6b) stable Al-(H<sub>2</sub>O) group and the most stable site for cleavage 6 (Figure S17), which is also the most stable site simulated for all (100) investigated configurations. Several kinds of reactions give rise to stable products on the phase diagram: desorption / adsorption of water from / to Al-(H<sub>2</sub>O) sites, hydrolysis of siloxane bridges, and condensation of silanol pairs (vicinal or not) to generate new siloxane bridges. An example of such a detailed study is provided in the section SVII in the Supporting Information of Chapter 3. Several configurations were studied for each hydration or dehydration level, and the most stable configurations were selected. Phase diagrams were then constructed (Figure 6 and Figure S17), where the evolution of the surface free energy is plotted with respect to temperature and water partial pressure. Here again, the effect of the consideration of the vibrational free energies of surfaces was taken into account in a few cases, which demonstrate a moderate variation of the transition temperatures (Figure S9).

The coordination number of Al, initially modeled at 4, was shown to increase upon water adsorption to 5, as shown in Figure 6 and Figure S17. This is in agreement with the spectroscopic data obtained by Al K-Edge XAS and  $^{27}\text{Al}$  NMR, where the coordination number even reaches 6.<sup>75,120</sup> In fact, we could simulate  $\text{Al}_{\text{VI}}$  species with two  $\text{H}_2\text{O}$  molecules coordinated onto the surface Al atom, whose stability appeared to be similar to that of hydrolyzed siloxane bridges, which in turn is expected to be stable below room temperature. For the three investigated cases, depending on the local environment, two typical behaviors of the aluminum sites above room temperature were encountered upon heating (Figure 6, Figure 7 and Figure S17):

- The water desorbs, leading to the formation on an undercoordinated  $\text{Al}_{\text{III}}$ .

- In those cases where a framework oxygen atom from a siloxane bridge is accessible below this  $\text{Al}_{\text{III}}$  atom, a new Al-O bond is formed, leading to (distorted)  $\text{Al}_{\text{IV}}$  instead of  $\text{Al}_{\text{III}}$ . This situation has also been encountered for the beta zeolite.<sup>87</sup>

In the second case, the desorption of water from the aluminum atom represents the most favorable dehydration reaction, starting from the reference system. Conversely, for the configuration where Al remains  $\text{Al}_{\text{III}}$ , the closure of siloxane bridges takes place at lower temperature. It gives rise to 2MR rings as for cleavage 1, site no. 75 (Figure 6b) or to form larger surface rings upon temperature increase and water desorption, like for cleavage 6, site no. 77 (Figure S17).

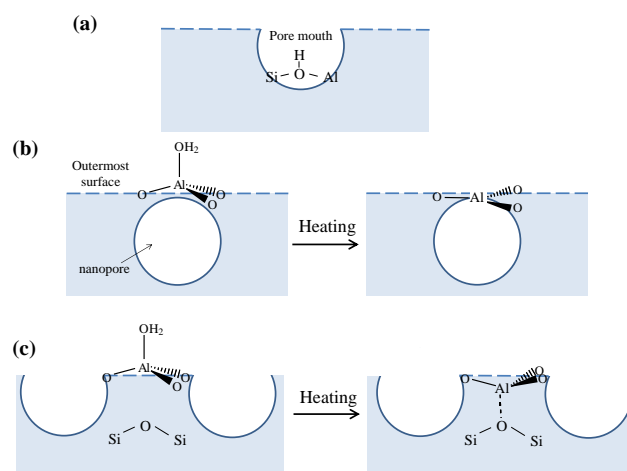


**Figure 7.** Dehydration of  $\text{Al}-(\text{H}_2\text{O})(\text{OH})_n$  groups (exemplified in the case of  $n = 0$ ) depending on the presence of a nanopore (b) or a siloxane bridge (c) below the Al atom, while bridging OH groups at the pore mouth (a) are stable upon dehydration.

To elucidate the general rules explaining the thermal stability of  $\text{Al}-(\text{H}_2\text{O})$  and the nature ( $\text{Al}_{\text{III}}$  versus  $\text{Al}_{\text{IV}}$ ) of the aluminum atom obtained upon dehydration, we systematically calculated and compared the desorption structures and temperature at  $P(\text{H}_2\text{O})=10^{-4}$  bar of the water molecule adsorbed on the Al atom, omitting the other kinds of dehydration reactions that also take place (e.g., the condensation of silanol groups into siloxane bridges).

surface orientation	cleavage	site no.	$T_{\text{des}}$ (K)	$d(\text{Al}\cdots\text{O})$ (Å)	$N_{\text{LH}}$	state of Al after desorption
(100)	1	59	507	3.003	1	Al <sub>IV</sub>
		71	536	3.155	1	Al <sub>IV</sub>
		87	576	3.467	1	Al <sub>III</sub>
		75	622	3.330	1	Al <sub>III</sub>
		6	77	684	-	2
(010)	2	121	492	3.612	0	Al <sub>III</sub>
		111	558	3.416	1	Al <sub>III</sub>
		45	592	3.557	1	Al <sub>III</sub>
		43	530	3.394	1	Al <sub>III</sub>
		6	19	671	3.669	1
(101)	6	84	538	-	1	Al <sub>III</sub>
		132	640	3.822	1	Al <sub>III</sub>
		37	556	3.485	1	Al <sub>III</sub>
	9	8	636	3.433	2	Al <sub>IV</sub>
		51	600	-	2	Al <sub>III</sub>
		59	691	3.418	2	Al <sub>III</sub>
		57	671	3.874	1	Al <sub>III</sub>

**Table 2.** Dehydration Temperature  $T_{\text{des}}$  at  $P(\text{H}_2\text{O})=10^{-4}$  bar for Various Al-(H<sub>2</sub>O) Surface Sites. See Figures S14 and S15 for the terminology of the sites. The shortest non covalent Al $\cdots$ O bond length  $d(\text{Al}\cdots\text{O})$  between the Al of Al-(H<sub>2</sub>O) and the closest siloxane bridge underneath (if any), before desorption, is also given, as well as the number of hydrogen bond  $N_{\text{LH}}$  (2.5 Å cutoff) between the water molecule and neighboring OH groups before desorption and the coordination state of aluminum after water desorption.

The results are shown in Table 2. This simplified approach gives results comparable to the more detailed approach (Figure 6 and S17) for sites no. 59 and 75, but a shift is seen for site no. 77, showing that trends are well reproduced, but the precise desorption temperatures obtained by the simplified approach have to be considered with care. It appears that the critical distance allowing the formation of the new Al-O bond between the dehydrated Al site and the siloxane bridge underneath is between  $\sim 3.2$  and  $\sim 3.4$  Å. The dehydration temperature is most of the time higher when an Al<sub>III</sub> is formed than when an Al<sub>IV</sub> is formed, which translates into a higher reactivity of Al<sub>III</sub>. However, exceptions exist, in particular on the (010) orientation where Al<sub>III</sub> species are formed at moderate heating temperatures (below 500K for site no. 121, for example). This can be linked to the smaller number of hydrogen bonds that stabilize the adsorbed water molecule (zero or one), due to a lower OH content (1.5 OH nm<sup>-2</sup>). Thereby, this makes the desorption easier than in the case of the (101) orientation at cleavage 9 (the more relevant model for the tips of the coffin-shaped crystal, according to the “crystal growth” approach), where several configurations of the water molecule are stabilized by two hydrogen bonds, thanks to a higher OH coverage (2.71 OH nm<sup>-2</sup>).

Experimentally, Al<sub>III</sub> atoms were observed or suggested by X-ray absorption near edge structure spectroscopy and nuclear magnetic resonance above 623-723 K in the case of mordenite, beta, ferrierite and chabazite.<sup>73-75</sup> Although the role of the external surface was not invoked in these works to explain the Al<sub>III</sub> presence, the reactions we simulate in the present work are able to rationalize it. Also, we give here a better understanding of why water desorbs more easily from nanosheets, essentially represented by the (010) surface having the lowest desorption temperature, in comparison to more classical samples seen experimentally.<sup>121</sup>

One thus observes a strong dependence of the surface reactivity toward water, depending on the local topology of the surface sites, already for a given zeolite (here with the MFI framework), but also likely from one zeolite framework to another. In practice, many

gas-phase catalytic reactions using zeolites and ZSM-5 take place between 500 and 800 K.<sup>3-5,116</sup> For a typical water pressure of  $10^{-4}$  bar, this means that, on the same sample, Al-(H<sub>2</sub>O) and dehydrated Al<sub>IV</sub> and Al<sub>III</sub> species will be present at the same time. Note that the bridging OH groups present at the pore mouth are expected to be thermally stable, with respect to hydration/dehydration reactions.

### 3.7. Brønsted and Lewis Acidity of Surface Sites

Transposing the aforementioned results in terms of acidity means that several families of Brønsted (BAS) and Lewis acid sites (LAS) can potentially exist under experimental conditions, depending on the operating conditions. To check this in practice, we quantified the interaction of a very popular probe molecule,<sup>122</sup> pyridine,<sup>123</sup> with the possible acid sites of the external surface (focusing here on typical sites of the (100) surface sites). Our results are reported in Table 3 and Table 4, together with the adsorption geometries. For the sake of comparison, we also considered the BAS/LAS nature of one bulk site.

Consistently with previous theoretical and experimental reports,<sup>124-125</sup> the adsorption of pyridine at the bulk BAS leads to proton transfer, thus forming pyridinium, stabilized by an adsorption energy of  $-213$  kJ mol<sup>-1</sup>. For a partial pressure of pyridine of  $10^{-4}$  bar, this corresponds to a desorption temperature of pyridine of 638 K, in line with temperature-programmed desorption experiments.<sup>126</sup> All surface sites under consideration in our computational study are able to transfer their proton to pyridine, suggesting that they are all BAS. At the bridging OH group of the pore mouth, the lowest adsorption energy found ( $-215$  kJ mol<sup>-1</sup>) is comparable to the “bulk”, proving that these sites are as acidic as the bulk sites.

Interestingly, the contribution of the dispersion energy to the overall adsorption energy is even more negative at the pore mouth ( $-91$  kJ mol<sup>-1</sup>) than in the bulk ( $-69$  kJ mol<sup>-1</sup>), showing that confinement effects play an important role at the pore mouth, resulting in a stabilization of the pyridinium ion by the sinusoidal channel. Some other sites at the pore mouth provide lower adsorption energies (between  $-167$  and  $-185$  kJ mol<sup>-1</sup>), corresponding to lower desorption temperatures (between 549 and 562 K), due to a slightly more external location of the pyridinium ion or to its location in the surface straight channel only. The relatively large variations in the dispersion (between  $-45$  and  $-91$  kJ mol<sup>-1</sup>) and nondispersive ( $-96$  to  $-144$  kJ mol<sup>-1</sup>) energy components suggest that the differences in stabilization have both van der Waals and electrostatic origins. Al-(H<sub>2</sub>O) species exhibit lower (between  $-150$  and  $-122$  kJ mol<sup>-1</sup>) adsorption energies. This can be assigned again to both van der Waals and electrostatic factors. In particular, considering the most stable Al-(H<sub>2</sub>O) group on the (100) surface orientation (no. 75 in Table 3) both the dispersion and the nondispersive terms are weaker than for the bulk or pore mouth sites. One can conclude that Al-(H<sub>2</sub>O) sites are mild BAS. Note that these adsorption configurations of pyridinium are very similar to that obtained after proton transfer from bridging OH groups. Pyridinium is in both cases better stabilized at the pore mouth than at the outermost surface. Thus, the origin of the lower acidity of Al-(H<sub>2</sub>O) can at least in part be assigned to the higher stability of Al-(H<sub>2</sub>O) with respect to the pore mouth bridging OH group. This is at variance with the observations made by comparing bulk zeolites and amorphous silica-alumina (ASA),<sup>127</sup> as in the last case the cavity effect is

absent, making the lower stabilization of the protonated probe molecule the main factor to explain the milder acidity of ASA.

Sites (number)	Bulk	57	69	79	89	91	59	75
Nature of the reaction								
$\Delta_{\text{ads}}U_{\text{py}}$ (kJ mol <sup>-1</sup> )	-213	-180	-185	-184	-167	-215	-150	-122
$\Delta_{\text{disp}}U_{\text{py}}$ (kJ mol <sup>-1</sup> )	-69	-73	-45	-88	-51	-91	-78	-47
$\Delta_{\text{non\_disp}}U_{\text{py}}$ (kJ mol <sup>-1</sup> )	-144	-107	-140	-96	-116	-124	-72	-75
$T_{\text{des-py}}$ (K)	638	549	562	560	513	645	465	385
Structure of adsorbed pyridinium								

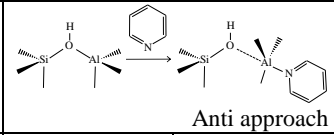
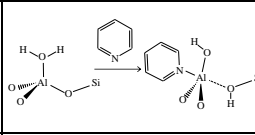
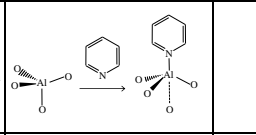
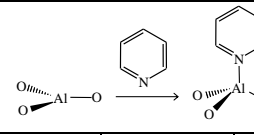
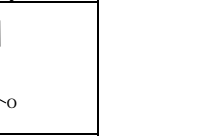
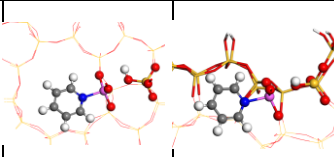
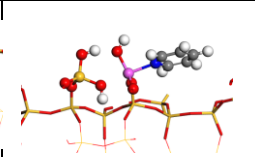
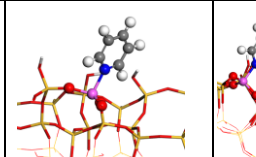
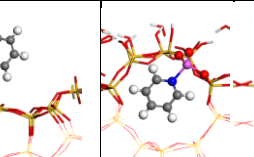
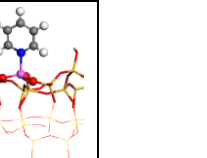
**Table 3.** Brønsted Acidity As Measured by the Pyridine Adsorption on a Selected Number of Protonic Sites of the (100) surface (Cleavage 1). See Figure S14 for the terminology of the sites. The adsorption energy  $\Delta_{\text{ads}}U_{\text{py}}$  is given, as well as the corresponding dispersion ( $\Delta_{\text{disp}}U_{\text{py}}$ ) and the non-dispersive ( $\Delta_{\text{non\_disp}}U_{\text{py}}$ ) components of  $\Delta_{\text{ads}}U_{\text{py}}$ , the estimated pyridine desorption temperature  $T_{\text{des-py}}$  for  $P(\text{pyridine}) = 10^{-4}$  bar, and the structure of adsorbed pyridine. Color code for the structures: oxygen: red, silicon: yellow, aluminum: purple, hydrogen: white, nitrogen: blue, carbon: grey. The same properties for the bulk site T5 are also given for comparison.

With respect to the Lewis acidity, we could obtain as an energy minimum a specific approach of the Al bulk site by pyridine that makes the formation of a Al-N bond possible. The approach making this possible is in anti with respect to the bridging OH group, see illustration in Table 4. This is consistent with our previous findings for water adsorption,<sup>109-110</sup> and with previous proposals by Busca *et al.* to explain the existence of LAS in high Si/Al faujasite samples that exhibit LAS without any EFAL.<sup>76</sup> After adsorption, the anti Al-OH bond is broken, forming a pseudo-bridging silanol,<sup>128</sup> and maintaining the coordination number of Al at 4. However the adsorption energy is lower than that for the bulk BAS, so that bulk sites will express their Brønsted acidity rather than their Lewis acidity, in line with the absence of experimental detection of LAS in the bulk of ZSM-5.<sup>76</sup>

A similar conclusion is reached for aluminum belonging to pore mouth bridging OH groups. Surface Al-(H<sub>2</sub>O) also behave as poor Lewis acids ( $-110$  kJ mol<sup>-1</sup>). In the most stable configuration found after adsorption of pyridine on the Al atom, one of the proton of the water molecule jumps onto the Si-O-Al bridge in anti to pyridine, to allow the formation of a pseudo-bridging silanol.

In contrast, sites obtained after their dehydration (Al<sub>III</sub> and Al<sub>IV</sub>) interact more strongly with pyridine (with a nondispersive term between  $-160$  and  $-180$  kJ mol<sup>-1</sup>). The strongest expression of Lewis acidity ( $-256$  kJ mol<sup>-1</sup>) was found for a Al<sub>III</sub> site at cleavage 6 of the (100) surface, when pyridine is able to access to the LAS by the pore underneath, with a bulklike dispersion contribution ( $-83$  kJ mol<sup>-1</sup>).



Sites	Bulk	(100) cleavage 1, n°91	(100) cleavage 1, n°59, hydrated	(100) cleavage 1, n°59, dehydrated	(100) cleavage 1, n°75, dehydrated	(100) cleavage 6, n°77, dehydrated	(010) cleavage 2, n°121, dehydrated
Nature of the reaction							
$\Delta_{\text{ads}}U_{\text{py}}$ (kJ mol <sup>-1</sup> )	-141	-122	-110	-179	-212	-256	-194
$\Delta_{\text{disp}}U_{\text{py}}$ (kJ mol <sup>-1</sup> )	-81	-95	-47	-14	-33	-83	-33
$\Delta_{\text{non\_disp}}U_{\text{py}}$ (kJ mol <sup>-1</sup> )	-60	-27	-63	-165	-179	-173	-161
$T_{\text{des-py}}$ (K)	440	385	350	545	638	754	589
Structure of adsorbed pyridine							

**Table 4.** Lewis Acidity Measured by Adsorption of Pyridine on Selected Al Sites of the (100) and (010) surfaces. See Figure S14 for the terminology of the sites. The adsorption energy  $\Delta_{\text{ads}}U_{\text{py}}$  is given, as well as the corresponding dispersion ( $\Delta_{\text{disp}}U_{\text{py}}$ ) and the nondispersive ( $\Delta_{\text{non\_disp}}U_{\text{py}}$ ) components of the adsorption energy, the estimated pyridine desorption temperature  $T_{\text{des-py}}$  for  $P(\text{pyridine}) = 10^{-4}$  bar, and the structure of adsorbed pyridine. Color code for the structures: oxygen: red, silicon: yellow, aluminum: purple, hydrogen: white, nitrogen: blue, carbon: grey. The same properties for the bulk site T5 are also given for comparison.

For other cases, Al<sub>III</sub> appears to be a stronger LAS ( $-194$  to  $-212$  kJ mol<sup>-1</sup>, desorption temperatures between 589 and 638 K) than the probed Al<sub>IV</sub> ( $-179$  kJ mol<sup>-1</sup>, 545 K), for which pyridine induces the breaking of the underneath Al<sub>IV</sub>-O bond. In particular, the Al<sub>III</sub> site no. 121, which is easily formed upon dehydration of the (010) surface and is representative of nanosheets, exhibits a strong Lewis acidity.

Our calculations give an atomistic interpretation for the existence of BAS and LAS detected at the external surface of ZSM-5 crystals<sup>129</sup> and nanosheets.<sup>90,121</sup> In particular for nanosheets, it was found<sup>121</sup> that the strength of the BAS at the pore mouth is similar to that of the bulk, which is in agreement with our calculations. In ref 121, a very intense band at 1450 cm<sup>-1</sup> was observed upon pyridine adsorption on the nanosheets, which the author did not comment upon but can be assigned to a LAS. Opanasenko *et al.* also report a significant Lewis acidity of nanosheets.<sup>130</sup> This is in full agreement with the very easy formation of Al<sub>III</sub> at the (010) surface that we calculate (Table 2) and the strong LAS character of the corresponding dehydrated sites (Table 4). This is expected to be specific for nanosheets, as for large coffin-shaped crystals, this orientation is no longer exposed, due to intergrowths leading to the dominant (100) surface (see section 3.3).

Our results also explain the interconversion of BAS into LAS upon thermal treatment,<sup>77</sup> but without invoking severe dehydroxylation of the framework.<sup>131</sup> We also understand the higher number of LAS and lower number of strong BAS, observed upon pyridine adsorption for ZSM-5 as the particle size decreases<sup>132</sup> or as the mesoporous volume increases,<sup>133</sup> even if the amount of extraframework species can also affect this feature. In the case of mordenite, it has recently been shown that the number of overcoordinated Al atoms under a wet atmosphere is directly correlated to the number of LAS (detected by pyridine adsorption) after treatment



under vacuum at 723 K.<sup>75</sup> These sites were shown to belong to the zeolite framework, and their number is directly linked to the Si/Al ratio of the zeolite. These observations can be fully rationalized by the presently proposed calculations, considering that the LAS are Al<sub>III</sub> and Al<sub>IV</sub> obtained after water desorption from a Al<sub>IV</sub>-(H<sub>2</sub>O) species, which can adsorb additional water molecules on exposure to high water pressures.

Interestingly, for ordered surfaces such as those considered here, the structure of the sites and their acidity are different from what DFT calculations predict in the case of amorphous silica-alumina.<sup>127-128,134-136</sup> In particular, no pseudobridging OH group can be observed in the present simulation of the external surfaces of crystalline H-ZSM-5, except after adsorption of pyridine. Also, we see here that the cavity effects still play a huge role in the expression of the acidity of the external zeolite surface, whereas they are absent in the case of ASA.

This means that the optimal expression of the acidity at the pore mouth needs to control the degree of crystallinity of the external surface of the zeolite in a very cautious way. Should an amorphous surface be obtained instead, dramatic consequences in terms of depletion of the acidity should be expected.

### 3.8. Conclusions

Thanks to DFT calculations, we propose a detailed model for relevant surface orientations ((100), (010), and (101)) of silicalite-1 and ZSM-5 zeolites (MFI framework), contributing to the unraveling of the nature, stability, and reactivity of surface sites, as well as equilibrium morphologies of the crystallites.

A crystallography approach, consisting of the cleavage of the silicic bulk structure, is compared to a crystal growth approach, using a Si<sub>33</sub> building block to elaborate surface models. Both approaches lead to very similar results in terms of preferred surfaces, except for the (101) surface, suggesting a convergence of thermodynamic and kinetic factors to qualitatively describe crystal growth for the (100) and (010) orientations. The calculated equilibrium morphologies are in qualitative agreement with microscopy pictures, although the calculated surface ratios differ to some extent, demonstrating that the experimental morphology is not fully determined by thermodynamics; apparently kinetic aspects need to be taken into account to further improve the description of the surface models. However, both surface model approaches describe the nature of the surface sites for nano- to microcrystals, as well as nanoslabs and nanosheets.

The exchange of silicon by aluminum atoms at the surface was then examined, as well as the corresponding thermal stability of the sites, by considering the hydration and dehydration reactions and calculating the Lewis and/or Brønsted acidity, probed by the simulation of pyridine adsorption. A diversity of surface sites in terms of nature, stability, and strength has been identified thanks to this approach.

Bridging Al-OH-Si groups are present at the pore mouth, where the effect of the cavity is present. They have stability similar to or higher than that of bulk sites. They are also thermally stable and exhibit similarly (strong) Brønsted acidity with respect to bulk sites.

They can be considered to be responsible for what is called “pore mouth catalysis”. They are, however, not the most stable groups at the outermost surface, where the effect of the cavity is absent.

At the outermost surface, the following groups prevail: Si-OH and Al-OH groups and most importantly water adsorbed on aluminum  $\text{Al}(\text{H}_2\text{O})(\text{OH})_n$ . They behave as milder Brønsted acid sites with respect to bridging OH groups, mainly because of their intrinsically higher stability. Whatever the starting OH group, the pyridinium cation will stabilize at the pore mouth.

However, the adsorbed water molecule is shown to desorb upon heating, revealing a surface aluminum, which behaves as a Lewis acid site. The desorption of water is calculated to occur at temperatures that strongly depend on the local topology of the surface site and on the surface orientation. Factors that enhance the desorption of water are (i) the presence of a siloxane bridge below the surface Al atom and (ii) low OH content on the surface orientation, making the adsorbed water molecule less stable. The second factor dominates in the specific behavior of the (010) orientation, being a representative for nanosheets, thus holding easily formed  $\text{Al}_{\text{III}}$  ions that behave as strong Lewis acid sites. Conversely, the OH-rich (101) surface (at the tips of the coffin-shaped crystals) leads to more stable  $\text{Al}(\text{H}_2\text{O})$  groups, which are mild Brønsted acid sites.

These results provide a rational understanding of a large set of experimental observations from the literature, which have so far remained poorly understood. They also show that under typical industrial operating conditions (between 500 and 700 K, water pressure on the order of  $10^{-4}$  mbar), several kinds of sites coexist: strong BAS in the pore mouth and mild BAS and LAS at the outermost surface.

These findings are likely not limited to the case of the MFI framework (some of them already appeared to be valid for zeolite beta), as our conclusions are mainly dictated by local topology aspects. Controlling the global topology of the network may tune not only the respective concentration of the different acid sites, but also the confinement effects for bulky molecules that cannot access the bulk sites. All of these aspects, together with transport limitations within the framework, contribute to the final properties of the system.

## References

- (1) Davis, M. E., Ordered Porous Materials for Emerging Applications, *Nature* **2002**, *417*, 813.
- (2) Corma, A., Inorganic Solid Acids and their Use in Acid-Catalyzed Hydrocarbon Reactions, *Chem. Rev.* **1995**, *95*, 559-614.
- (3) Marcilly, C. *Acido-Basic Catalysis*; Technip: Paris, 2005.
- (4) Vermeiren, W.; Gilson, J. P., Impact of Zeolites on the Petroleum and Petrochemical Industry, *Topics Catal.* **2009**, *52*, 1131-1161.
- (5) Vogt, E. T. C.; Weckhuysen, B. M., Fluid Catalytic Cracking: Recent Developments on the Grand Old Lady of Zeolite Catalysis, *Chem. Soc. Rev.* **2015**, *44*, 7342-7370.
- (6) Deka, U.; Lezcano-Gonzalez, I.; Weckhuysen, B. M.; Beale, A. M., Local Environment and Nature of Cu Active Sites in Zeolite-Based Catalysts for the Selective Catalytic Reduction of NO<sub>x</sub>, *ACS Catal.* **2013**, *3*, 413-427.
- (7) Borfecchia, E.; Beato, P.; Svelle, S.; Olsbye, U.; Lamberti, C.; Bordiga, S., Cu-CHA – a model system for applied selective redox catalysis, *Chem. Soc. Rev.* **2018**, *47*, 8097-8133.
- (8) Paolucci, C.; Khurana, I.; Parekh, A. A.; Li, S.; Shih, A. J.; Li, H.; Di Iorio, J. R.; Albarracin-Caballero, J. D.; Yezerets, A.; Miller, J. T.; Delgass, W. N.; Ribeiro, F. H.; Schneider, W. F.; Gounder, R., Dynamic Multinuclear Sites Formed by Mobilized Copper Ions in NO<sub>x</sub> Selective Catalytic Reduction, *Science* **2017**, *357*, 898-903.
- (9) Ennaert, T.; Van Aelst, J.; Dijkmans, J.; De Clercq, R.; Schutyser, W.; Dusselier, M.; Verboekend, D.; Sels, B. F., Potential and Challenges of Zeolite Chemistry in the Catalytic Conversion of Biomass, *Chem. Soc. Rev.* **2016**, *45*, 584-611.
- (10) Derouane, E. G.; André, J. M.; Lucas, A. A., Surface Curvature Effects in Physisorption and Catalysis by Microporous Solids and Molecular Sieves, *J. Catal.* **1988**, *110*, 58-73.
- (11) Gallego, E. M.; Portilla, M. T.; Paris, C.; León-Escamilla, A.; Boronat, M.; Moliner, M.; Corma, A., “Ab initio” Synthesis of Zeolites for Preestablished Catalytic Reactions, *Science* **2017**, *355*, 1051–1054.
- (12) Yarulina, I.; De Wispelaere, K.; Bailleul, S.; Goetze, J.; Radersma, M.; Abou-Hamad, E.; Vollmer, I.; Goesten, M.; Mezari, B.; Hensen, E. J. M.; Martínez-Espín, J. S.; Morten, M.; Mitchell, S.; Perez-Ramirez, J.; Olsbye, U.; Weckhuysen, B. M.; Van Speybroeck, V.; Kapteijn, F.; Gascon, J., Structure–Performance Descriptors and the Role of Lewis Acidity in the Methanol-to-Propylene Process, *Nature Chem.* **2018**, *10*, 804-812.
- (13) Baerlocher, C.; McCusker, J. K., *Database of Zeolite Structures*: <http://www.iza-structure.org/databases/>.
- (14) Uytterhoeven, J. B.; Christner, L. G.; Hall, W. K., Studies of the Hydrogen Held by Solids. VIII. The Decationated Zeolites, *J. Phys. Chem.* **1965**, *69*, 2117-2126.
- (15) Haag, W. O.; Lago, R. M.; Weisz, P. B., The Active Site of Acidic Aluminosilicate Catalysts, *Nature* **1984**, *309*, 589-591.
- (16) Mortier, W. J.; Sauer, J.; Lercher, J. A.; Noller, H., Bridging and Terminal Hydroxyls. A Structural Chemical and Quantum Chemical Discussion, *J. Phys. Chem.* **1984**, *88*, 905-912.
- (17) Martens, J. A.; Souverijns, W.; Verrelst, W.; Parton, R.; Froment, G. F.; Jacobs, P. A., Selective Isomerization of Hydrocarbon Chains on External Surfaces of Zeolite Crystals, *Angew. Chem. Int. Ed.* **1995**, *34*, 2528-2530.

- (18) Martens, G. G.; Marin, G. B.; Martens, J. A.; Jacobs, P. A.; Baron, G. V., A Fundamental Kinetic Model for Hydrocracking of C8 to C12 Alkanes on Pt/US–Y Zeolites, *J. Catal.* **2000**, *195*, 253-267.
- (19) Grand, J.; Talapaneni, S. N.; Vicente, A.; Fernandez, C.; Dib, E.; Aleksandrov, H. A.; Vayssilov, G. N.; Retoux, R.; Boullay, P.; Gilson, J.-P.; Valtchev, V.; Mintova, S., One-Pot Synthesis of Silanol-Free Nanosized MFI Zeolite, *Nat. Mater.* **2017**, *16*, 1010-1015.
- (20) Mintova, S.; Jaber, M.; Valtchev, V., Nanosized Microporous Crystals: Emerging Applications, *Chem. Soc. Rev.* **2015**, *44*, 7207-7233.
- (21) Chang, C. D.; Bell, A. T., Studies on the mechanism of ZSM-5 formation, *Catal. Lett.* **1991**, *8*, 305-316.
- (22) Haw, K.-G.; Gilson, J.-P.; Nesterenko, N.; Akouche, M.; El Siblani, H.; Goupil, J.-M.; Rigaud, B.; Minoux, D.; Dath, J.-P.; Valtchev, V., Supported Embryonic Zeolites and their Use to Process Bulky Molecules, *ACS Catal.* **2018**, *8*, 8199-8212.
- (23) Valtchev, V.; Majano, G.; Mintova, S.; Perez-Ramirez, J., Tailored Crystalline Microporous Materials by Post-Synthesis Modification, *Chem. Soc. Rev.* **2013**, *42*, 263-290.
- (24) Perez-Ramirez, J.; Christensen, C. H.; Egeblad, K.; Christensen, C. H.; Groen, J. C., Hierarchical Zeolites: Enhanced Utilisation of Microporous Crystals in Catalysis by Advances in Materials Design, *Chem. Soc. Rev.* **2008**, *37*, 2530-2542.
- (25) Silaghi, M.-C.; Chizallet, C.; Raybaud, P., Challenges on Molecular Aspects of Dealumination and Desilication of Zeolites, *Microporous Mesoporous Mater.* **2014**, *191*, 82-96.
- (26) Pagis, C.; Morgado Prates, A. R.; Farrusseng, D.; Bats, N.; Tuel, A., Hollow Zeolite Structures: An Overview of Synthesis Methods, *Chem. Mater.* **2016**, *28*, 5205-5223.
- (27) Corma, A.; Fornes, V.; Pergher, S. B.; Maesen, T. L. M.; Buglass, J. G., Delaminated Zeolite Precursors as Selective Acidic Catalysts, *Nature* **1998**, *396*, 353.
- (28) Choi, M.; Na, K.; Kim, J.; Sakamoto, Y.; Terasaki, O.; Ryoo, R., Stable Single-Unit-Cell Nanosheets of Zeolite MFI as Active and Long-Lived Catalysts, *Nature* **2009**, *461*, 246-249.
- (29) Roth, W. J.; Nachtigall, P.; Morris, R. E.; Čejka, J., Two-Dimensional Zeolites: Current Status and Perspectives, *Chem. Rev.* **2014**, *114*, 4807-4837.
- (30) Argauer, R. J.; Landolt, G. R.; Mobil Oil Corporation: US 3702886, 1972.
- (31) Pelrine, B. P.; Mobil Oil Corporation: US 4100262, 1978.
- (32) Rollman, L. D.; Valyocsik, E. W.; Corporation, M. O., Ed. EP 0021674, 1980.
- (33) Kokotailo, G. T.; Lawton, S. L.; Olson, D. H.; Meier, W. M., Structure of Synthetic Zeolite ZSM-5, *Nature* **1978**, *272*, 437.
- (34) Flanigen, E. M.; Bennett, J. M.; Grose, R. W.; Cohen, J. P.; Patton, R. L.; Kirchner, R. M.; Smith, J. V., Silicalite, a New Hydrophobic Crystalline Silica Molecular Sieve, *Nature* **1978**, *271*, 512-516.
- (35) Cundy, C. S.; Cox, P. A., The Hydrothermal Synthesis of Zeolites: History and Development from the Earliest Days to the Present Time, *Chem. Rev.* **2003**, *103*, 663-702.
- (36) Pereira, M. M.; Gomes, E. S.; Silva, A. V.; Pinar, A. B.; Willinger, M.-G.; Shanmugam, S.; Chizallet, C.; Laugel, G.; Losch, P.; Louis, B., Biomass-Mediated ZSM-5 Zeolite Synthesis: When Self-Assembly Allows to Cross the Si/Al Lower Limit, *Chem. Sci.* **2018**, *9*, 6532-6539.

- (37) Lermer, H.; Draeger, M.; Steffen, J.; Unger, K. K., Synthesis and Structure Refinement of ZSM-5 Single Crystals, *Zeolites* **1985**, *5*, 131-134.
- (38) Fyfe, C. A.; Kennedy, G. J.; De Schutter, C. T.; Kokotailo, G. T., Sorbate-Induced Structural Changes in ZSM-5 (Silicalite), *J. Chem. Soc., Chem. Commun.* **1984**, 541-542.
- (39) Hay, D. G.; Jaeger, H., Orthorhombic-Monoclinic Phase Changes in ZSM-5 Zeolite/Silicalite, *J. Chem. Soc., Chem. Commun.* **1984**, 1433-1433.
- (40) Kirschhock, C. E. A.; Buschmann, V.; Kremer, S.; Ravishankar, R.; Houssin, C. J. Y.; Mojet, B. L.; van Santen, R. A.; Grobet, P. J.; Jacobs, P. A.; Martens, J. A., Zeosil Nanoslabs: Building Blocks in  $n\text{Pr}_4\text{N}^+$ -Mediated Synthesis of MFI Zeolite, *Angew. Chem. Int. Ed.* **2001**, *40*, 2637-2640.
- (41) Kirschhock, C. E. A.; Ravishankar, R.; Looveren, L. V.; Jacobs, P. A.; Martens, J. A., Mechanism of Transformation of Precursors into Nanoslabs in the Early Stages of MFI and MEL Zeolite Formation from TPAOH-TEOS-H<sub>2</sub>O and TBAOH-TEOS-H<sub>2</sub>O Mixtures, *J. Phys. Chem. B* **1999**, *103*, 4972-4978.
- (42) Knight, C. T. G.; Kinrade, S. D., Comment on "Identification of Precursor Species in the Formation of MFI Zeolite in the TPAOH-TEOS-H<sub>2</sub>O System", *J. Phys. Chem. B* **2002**, *106*, 3329-3332.
- (43) Kirschhock, C. E. A.; Ravishankar, R.; Verspeurt, F.; Grobet, P. J.; Jacobs, P. A.; Martens, J. A., Reply to the Comment on "Identification of Precursor Species in the Formation of MFI Zeolite in the TPAOH-TEOS-H<sub>2</sub>O System", *J. Phys. Chem. B* **2002**, *106*, 3333-3334.
- (44) Davis, T. M.; Drews, T. O.; Ramanan, H.; He, C.; Dong, J.; Schnablegger, H.; Katsoulakis, M. A.; Kokkoli, E.; McCormick, A. V.; Penn, R. L.; Tsapatsis, M., Mechanistic Principles of Nanoparticle Evolution to Zeolite Crystals, *Nat. Mater.* **2006**, *5*, 400.
- (45) Cundy, C. S.; Cox, P. A., The Hydrothermal Synthesis of Zeolites: Precursors, Intermediates and Reaction Mechanism, *Microporous Mesoporous Mater.* **2005**, *82*, 1-78.
- (46) Lupulescu, A. I.; Rimer, J. D., In Situ Imaging of Silicalite-1 Surface Growth Reveals the Mechanism of Crystallization, *Science* **2014**, *344*, 729.
- (47) Kumar, S.; Wang, Z.; Penn, R. L.; Tsapatsis, M., A Structural Resolution Cryo-TEM Study of the Early Stages of MFI Growth, *J. Am. Chem. Soc.* **2008**, *130*, 17284-17286.
- (48) Burel, L.; Tuel, A., Nanozeolites: New Strategies for Designing Ultra Small Silicalite Crystals with Very Few Framework Defects, *Microporous Mesoporous Mater.* **2013**, *174*, 90-99.
- (49) Gruene, T.; Li, T.; van Genderen, E.; Pinar, A. B.; van Bokhoven, J. A., Characterization at the Level of Individual Crystals: Single-Crystal MFI Type Zeolite Grains, *Chem. Eur. J.* **2018**, *24*, 2384-2388.
- (50) Koegler, J. H.; van Bekkum, H.; Jansen, J. C., Growth Model of Oriented Crystals of Zeolite Si-ZSM-5, *Zeolites* **1997**, *19*, 262-269.
- (51) Roeffaers, M. B. J.; Ameloot, R.; Baruah, M.; Uji-i, H.; Bulut, M.; De Cremer, G.; Müller, U.; Jacobs, P. A.; Hofkens, J.; Sels, B. F.; De Vos, D. E., Morphology of Large ZSM-5 Crystals Unraveled by Fluorescence Microscopy, *J. Am. Chem. Soc.* **2008**, *130*, 5763-5772.
- (52) Price, G. D.; Pluth, J. J.; Smith, J. V.; Bennett, J. M.; Patton, R. L., Crystal Structure of Tetrapropylammonium Fluoride-Containing Precursor to Fluoride Silicalite, *J. Am. Chem. Soc.* **1982**, *104*, 5971-5977.

- (53) Millward, G. R.; Ramdas, S.; Thomas, J. M.; Barlow, M. T., Evidence for Semi-Regularly Ordered Sequences of Mirror and Inversion Symmetry Planes in ZSM-5/ZSM-11 Shape-Selective Zeolitic Catalysts, *J. Chem. Soc., Faraday Trans. 2* **1983**, *79*, 1075-1082.
- (54) Hay, D. G.; Jaeger, H.; Wilshier, K. G., Systematic Intergrowth in Crystals of ZSM-5 Zeolite, *Zeolites* **1990**, *10*, 571-576.
- (55) Weidenthaler, C.; Fischer, R. X.; Shannon, R. D.; Medenbach, O., Optical Investigations of Intergrowth Effects in the Zeolite Catalysts ZSM-5 and ZSM-8, *J. Phys. Chem.* **1994**, *98*, 12687-12694.
- (56) Agger, J. R.; Hanif, N.; Cundy, C. S.; Wade, A. P.; Dennison, S.; Rawlinson, P. A.; Anderson, M. W., Silicalite Crystal Growth Investigated by Atomic Force Microscopy, *J. Am. Chem. Soc.* **2003**, *125*, 830-839.
- (57) Karwacki, L.; Kox, M. H. F.; Matthijs de Winter, D. A.; Drury, M. R.; Meeldijk, J. D.; Stavitski, E.; Schmidt, W.; Mertens, M.; Cubillas, P.; John, N.; Chan, A.; Kahn, N.; Bare, S. R.; Anderson, M.; Kornatowski, J.; Weckhuysen, B. M., Morphology-Dependent Zeolite Intergrowth Structures Leading to Distinct Internal and Outer-Surface Molecular Diffusion Barriers, *Nat. Mater.* **2009**, *8*, 959.
- (58) Stavitski, E.; Drury, M. R.; de Winter, D. A. M.; Kox, M. H. F.; Weckhuysen, B. M., Intergrowth Structure of Zeolite Crystals and Pore Orientation of Individual Subunits Revealed by Electron Backscatter Diffraction/Focused Ion Beam Experiments, *Angew. Chem. Int. Ed.* **2008**, *47*, 5637-5640.
- (59) Roeffaers, M. B. J.; Ameloot, R.; Bons, A.-J.; Mortier, W.; De Cremer, G.; de Kloe, R.; Hofkens, J.; De Vos, D. E.; Sels, B. F., Relating Pore Structure to Activity at the Subcrystal Level for ZSM-5: An Electron Backscattering Diffraction and Fluorescence Microscopy Study, *J. Am. Chem. Soc.* **2008**, *130*, 13516-13517.
- (60) Zeng, G.; Chen, C.; Li, D.; Hou, B.; Sun, Y., Exposure of (001) Planes and (011) Planes in MFI Zeolite, *CrystEngComm* **2013**, *15*, 3521-3524.
- (61) Díaz, I.; Kokkoli, E.; Terasaki, O.; Tsapatsis, M., Surface Structure of Zeolite (MFI) Crystals, *Chem. Mater.* **2004**, *16*, 5226-5232.
- (62) Varoon, K.; Zhang, X.; Elyassi, B.; Brewer, D. D.; Gettel, M.; Kumar, S.; Lee, J. A.; Maheshwari, S.; Mittal, A.; Sung, C.-Y.; Cococcioni, M.; Francis, L. F.; McCormick, A. V.; Mkhoyan, K. A.; Tsapatsis, M., Dispersible Exfoliated Zeolite Nanosheets and Their Application as a Selective Membrane, *Science* **2011**, *334*, 72.
- (63) Zhang, X.; Liu, D.; Xu, D.; Asahina, S.; Cychoz, K. A.; Agrawal, K. V.; Al Wahedi, Y.; Bhan, A.; Al Hashimi, S.; Terasaki, O.; Thommes, M.; Tsapatsis, M., Synthesis of Self-Pillared Zeolite Nanosheets by Repetitive Branching, *Science* **2012**, *336*, 1684.
- (64) Shete, M.; Kumar, M.; Kim, D.; Rangnekar, N.; Xu, D.; Topuz, B.; Agrawal, K. V.; Karapetrova, E.; Stottrup, B.; Al-Thabaiti, S.; Basahel, S.; Narasimharao, K.; Rimer, J. D.; Tsapatsis, M., Nanoscale Control of Homoepitaxial Growth on a Two-Dimensional Zeolite, *Angew. Chem. Int. Ed.* **2017**, *56*, 535-539.
- (65) Jeon, M. Y.; Kim, D.; Kumar, P.; Lee, P. S.; Rangnekar, N.; Bai, P.; Shete, M.; Elyassi, B.; Lee, H. S.; Narasimharao, K.; Basahel, S. N.; Al-Thabaiti, S.; Xu, W.; Cho, H. J.; Fetisov, E. O.; Thyagarajan, R.; DeJaco, R. F.; Fan, W.; Mkhoyan, K. A.; Siepmann, J. I.; Tsapatsis, M., Ultra-Selective High-Flux Membranes from Directly Synthesized Zeolite Nanosheets, *Nature* **2017**, *543*, 690-694.

- (66) Hernandez-Tamargo, C. E.; Roldan, A.; de Leeuw, N. H., A Density Functional Theory Study of the Structure of Pure-Silica and Aluminium-Substituted MFI Nanosheets, *J. Solid State Chem.* **2016**, *237*, 192-203.
- (67) Zhai, D.; Liu, Y.; Zheng, H.; Zhao, L.; Gao, J.; Xu, C.; Shen, B., A First-Principles Evaluation of the Stability, Accessibility, and Strength of Brønsted Acid Sites in Zeolites, *J. Catal.* **2017**, *352*, 627-637.
- (68) Rybicki, M.; Sauer, J., Acid strength of zeolitic Brønsted sites—Dependence on dielectric properties, *Catal. Today* **2019**, *323*, 86-93.
- (69) Ho, T. V.; Nachtigall, P.; Grajciar, L., The Lewis acidity of three- and two-dimensional zeolites: The effect of framework topology, *Catal. Today* **2018**, *304*, 12-21.
- (70) Thang, H. V.; Vaculík, J.; Přeč, J.; Kubů, M.; Čejka, J.; Nachtigall, P.; Bulánek, R.; Grajciar, L., The Brønsted acidity of three- and two-dimensional zeolites, *Microporous Mesoporous Mater.* **2019**, *282*, 121-132.
- (71) Prestianni, A.; Cortese, R.; Duca, D., Propan-2-ol dehydration on H-ZSM-5 and H-Y zeolite: a DFT study, *React. Kinet. Catal.* **2013**, *108*, 565-582.
- (72) Ferrante, F.; Rubino, T.; Duca, D., Butene Isomerization and Double-Bond Migration on the H-ZSM-5 Outer Surface: A Density Functional Theory Study, *J. Phys. Chem. C* **2011**, *115*, 14862-14868.
- (73) van Bokhoven, J. A.; van der Eerden, A. M. J.; Koningsberger, D. C., Three-Coordinate Aluminum in Zeolites Observed with In situ X-ray Absorption Near-Edge Spectroscopy at the Al K-Edge: Flexibility of Aluminum Coordinations in Zeolites, *J. Am. Chem. Soc.* **2003**, *125*, 7435-7442.
- (74) Brus, J.; Kobera, L.; Schoefberger, W.; Urbanova, M.; Klein, P.; Sazama, P.; Tabor, E.; Sklenak, S.; Fishchuk, A. V.; Dedecek, J., Structure of Framework Aluminum Lewis sites and Perturbed Aluminum atoms in Zeolites as Determined by  $^{27}\text{Al}\{^1\text{H}\}$  REDOR (3Q) MAS NMR Spectroscopy and DFT/Molecular Mechanics, *Angew. Chem. Int. Ed.* **2015**, *54*, 541-545.
- (75) Ravi, M.; Sushkevich, V. L.; van Bokhoven, J. A., Lewis Acidity Inherent to the Framework of Zeolite Mordenite, *J. Phys. Chem. C* **2019**, *123*, 15139-15144.
- (76) Phung, T. K.; Busca, G., On the Lewis Acidity of Protonic Zeolites, *Appl. Catal. A* **2015**, *504*, 151-157.
- (77) Derouane, E. G.; Védrine, J. C.; Pinto, R. R.; Borges, P. M.; Costa, L.; Lemos, M. A. N. D. A.; Lemos, F.; Ribeiro, F. R., The Acidity of Zeolites: Concepts, Measurements and Relation to Catalysis: A Review on Experimental and Theoretical Methods for the Study of Zeolite Acidity, *Catal. Rev.* **2013**, *55*, 454-515.
- (78) Perdew, J.; Burke, K.; Ernzerhof, M., Generalized Gradient Approximation Made Simple, *Phys. Rev. Lett.* **1996**, *77*, 3865-3868.
- (79) Kresse, G.; Hafner, J., Ab Initio Molecular-Dynamics Simulation of the Liquid-Metal-Amorphous-Semiconductor Transition in Germanium, *Phys. Rev. B* **1994**, *49*, 14251-14269.
- (80) Kresse, G.; Furthmüller, J., Efficiency of Ab-Initio Total Energy Calculations for Metals and Semiconductors using a Plane-Wave Basis Set, *Comput. Mat. Sci.* **1996**, *6*, 15-50.
- (81) Kresse, G.; Joubert, D., From Ultrasoft Pseudopotentials to the Projector Augmented-Wave Method, *Phys. Rev. B* **1999**, *59*, 1758-1775.
- (82) Steinmann, S. N.; Corminboeuf, C., Comprehensive Benchmarking of a Density-Dependent Dispersion Correction, *J Chem Theory Comput* **2011**, *7*, 3567-3577.



- (83) Wu, E. L.; Lawton, S. L.; Olson, D. H.; Rohrman, A. C.; Kokotailo, G. T., ZSM-5-Type Materials. Factors Affecting Crystal Symmetry, *J. Phys. Chem.* **1979**, *83*, 2777-2781.
- (84) Olson, D. H.; Kokotailo, G. T.; Lawton, S. L.; Meier, W. M., Crystal Structure and Structure-Related Properties of ZSM-5, *J. Phys. Chem.* **1981**, *85*, 2238-2243.
- (85) Reuter, K.; Scheffler, M., Composition, Structure, and Stability of RuO<sub>2</sub>(110) as a Function of Oxygen Pressure, *Phys. Rev. B* **2001**, *65*, 035406.
- (86) Larmier, K.; Chizallet, C.; Cadran, N.; Maury, S.; Abboud, J.; Lamic-Humblot, A.-F.; Marceau, E.; Lauron-Pernot, H., Mechanistic Investigation of Isopropanol Conversion on Alumina Catalysts: Location of Active Sites for Alkene/Ether Production, *ACS Catal.* **2015**, *5*, 4423-4437.
- (87) Rey, J.; Raybaud, P.; Chizallet, C., Ab Initio Simulation of the Acid Sites at the External Surface of Zeolite Beta, *ChemCatChem* **2017**, *9*, 2176-2185.
- (88) Musso, F.; Sodupe, M.; Corno, M.; Ugliengo, P., H-Bond Features of Fully Hydroxylated Surfaces of Crystalline Silica Polymorphs: A Periodic B3LYP Study, *J. Phys. Chem. C* **2009**, *113*, 17876-17884.
- (89) Witman, M.; Ling, S.; Boyd, P.; Barthel, S.; Haranczyk, M.; Slater, B.; Smit, B., Cutting Materials in Half: A Graph Theory Approach for Generating Crystal Surfaces and Its Prediction of 2D Zeolites, *ACS central science* **2018**, *4*, 235-245.
- (90) Seo, Y.; Cho, K.; Jung, Y.; Ryoo, R., Characterization of the Surface Acidity of MFI Zeolite Nanosheets by <sup>31</sup>P NMR of Adsorbed Phosphine Oxides and Catalytic Cracking of Decalin, *ACS Catal.* **2013**, *3*, 713-720.
- (91) Curie, P., Sur la Formation des Cristaux et sur les Constantes Capillaires de leurs Différentes Faces, *Bulletin de Minéralogie* **1885**, 145-150.
- (92) Wulff, G., Zur Frage der Geschwindigkeit des Wachstums und der Auflösung der Krystallflächen, *Zeitschrift f. Krystallogr.* **1901**, *34*, 449-530.
- (93) Baumgärtl, M.; Jentys, A.; Lercher, J. A., Understanding Elementary Steps of Transport of Xylene Mixtures in ZSM-5 Zeolites, *J. Phys. Chem. C* **2018**, *123*, 8092-8100.
- (94) Liang, D.; Follens, L. R. A.; Aerts, A.; Martens, J. A.; Van Tendeloo, G.; Kirschhock, C. E. A., TEM Observation of Aggregation Steps in Room-Temperature Silicalite-1 Zeolite Formation, *J. Phys. Chem. C* **2007**, *111*, 14283-14285.
- (95) Rohling, R. Y.; Szyja, B. M.; Hensen, E. J. M., Insight into the Formation of Nanostructured MFI Sheets and MEL Needles Driven by Molecular Recognition, *The journal of physical chemistry. C, Nanomaterials and interfaces* **2019**, *123*, 5326-5335.
- (96) Piccione, P. M.; Yang, S.; Navrotsky, A.; Davis, M. E., Thermodynamics of Pure-Silica Molecular Sieve Synthesis, *J. Phys. Chem. B* **2002**, *106*, 3629-3638.
- (97) Corma, A.; Davis, M. E., Issues in the Synthesis of Crystalline Molecular Sieves: Towards the Crystallization of Low Framework-Density Structures, *ChemPhysChem* **2004**, *5*, 304-313.
- (98) Wang, S.; He, Y.; Jiao, W.; Wang, J.; Fan, W., Recent Experimental and Theoretical Studies on Al Siting/Acid Site Distribution in Zeolite Framework, *Curr. Opin. Chem. Eng.* **2019**, *23*, 146-154.
- (99) Muraoka, K.; Chaikittisilp, W.; Okubo, T., Energy Analysis of Aluminosilicate Zeolites with Comprehensive Ranges of Framework Topologies, Chemical Compositions, and Aluminum Distributions, *J. Am. Chem. Soc.* **2016**, *138*, 6184-6193.

- (100) Schröder, K.-P.; Sauer, J.; Leslie, M.; Catlow, C. R., Siting of Al and Bridging Hydroxyl Groups in ZSM-5: A Computer Simulation Study, *Zeolites* **1992**, *12*, 20-23.
- (101) Li, C.; Vidal-Moya, A.; Miguel, P. J.; Dedecek, J.; Boronat, M.; Corma, A., Selective Introduction of Acid Sites in Different Confined Positions in ZSM-5 and Its Catalytic Implications, *ACS Catal.* **2018**, *8*, 7688-7697.
- (102) Dib, E.; Mineva, T.; Gaveau, P.; Véron, E.; Sarou-Kanian, V.; Fayon, F.; Alonso, B., Probing Disorder in Al-ZSM-5 Zeolites by <sup>14</sup>N NMR Spectroscopy, *J. Phys. Chem. C* **2017**, *121*, 15831-15841.
- (103) Knott, B. C.; Nimlos, C. T.; Robichaud, D. J.; Nimlos, M. R.; Kim, S.; Gounder, R., Consideration of the Aluminum Distribution in Zeolites in Theoretical and Experimental Catalysis Research, *ACS Catal.* **2017**, *8*, 770-784.
- (104) Bucko, T.; Benco, L.; Demuth, T.; Hafner, J., Ab Initio Density Functional Investigation of the (001) Surface of Mordenite, *J. Chem. Phys.* **2002**, *117*, 7295-7305.
- (105) Demuth, T.; Hafner, J.; Benco, L.; Toulhoat, H., Structural and Acidic Properties of Mordenite. An ab Initio Density-Functional Study, *J. Phys. Chem. B* **2000**, *104*, 4593-4607.
- (106) Gutierrez-Acebo, E.; Rey, J.; Bouchy, C.; Schuurman, Y.; Chizallet, C., Location of the Active Sites for Ethylcyclohexane Hydroisomerization by Ring Contraction and Expansion in the EUO Zeolitic Framework, *ACS Catal.* **2019**, *9*, 1692-1704.
- (107) Ghorbanpour, A.; Rimer, J. D.; Grabow, L. C., Periodic, vdW-Corrected Density Functional Theory Investigation of the Effect of Al Siting in H-ZSM-5 on Chemisorption Properties and Site-Specific Acidity, *Catal. Comm.* **2014**, *52*, 98-102.
- (108) Dib, E.; Mineva, T.; Veron, E.; Sarou-Kanian, V.; Fayon, F.; Alonso, B., ZSM-5 Zeolite: Complete Al Bond Connectivity and Implications on Structure Formation from Solid-State NMR and Quantum Chemistry Calculations, *J Phys Chem Lett* **2018**, *9*, 19-24.
- (109) Silaghi, M.-C.; Chizallet, C.; Petracovschi, E.; Kerber, T.; Sauer, J.; Raybaud, P., Regioselectivity of Al-O Bond Hydrolysis During Zeolites Dealumination Unified by Brønsted-Evans-Polanyi Relationship, *ACS Catal.* **2015**, *5*, 11-15.
- (110) Silaghi, M.-C.; Chizallet, C.; Sauer, J.; Raybaud, P., Dealumination Mechanisms of Zeolites and Extra-Framework Aluminum Confinement, *J. Catal.* **2016**, *339*, 242-255.
- (111) Holzinger, J.; Beato, P.; Lundegaard, L. F.; Skibsted, J., Distribution of Aluminum over the Tetrahedral Sites in ZSM-5 Zeolites and Their Evolution after Steam Treatment, *J. Phys. Chem. C* **2018**, *122*, 15595-15613.
- (112) Han, O. H.; Kim, C. S.; Hong, S. B., Direct Evidence for the Nonrandom Nature of Al Substitution in Zeolite ZSM-5: An Investigation by <sup>27</sup>Al MAS and MQ MAS NMR, *Angew. Chem. Int. Ed.* **2002**, *41*, 469-472.
- (113) Sklenak, S.; Dedecek, J.; Li, C.; Wichterlova, B.; Gabova, V.; Sierka, M.; Sauer, J., Aluminum Siting in Silicon-Rich Zeolite Frameworks: A Combined High-Resolution <sup>27</sup>Al NMR Spectroscopy and Quantum Mechanics/Molecular Mechanics Study of ZSM-5, *Angew. Chem., Int. Ed* **2007**, *46*, 7286-7289.
- (114) Dědeček, J.; Sobalík, Z.; Wichterlová, B., Siting and Distribution of Framework Aluminium Atoms in Silicon-Rich Zeolites and Impact on Catalysis, *Catal. Rev.* **2012**, *54*, 135-223.
- (115) Bucko, T.; Benco, L.; Hafner, J., Defect Sites at the .001. Surface of Mordenite: An Ab Initio Study, *J. Chem. Phys.* **2003**, *118*, 8437-8445.

- (116) Busca, G., Catalytic Materials Based on Silica and Alumina: Structural Features and Generation of Surface Acidity, *Prog. Mater. Sci.* **2019**, *104*, 215-249.
- (117) Bevilacqua, M.; Montanari, T.; Finocchio, E.; Busca, G., Are the Active Sites of Protonic Zeolites Generated by the Cavities?, *Catal. Today* **2006**, *116*, 132-142.
- (118) von Ballmoos, R.; Meier, W. M., Zoned Aluminium Distribution in Synthetic Zeolite ZSM-5, *Nature* **1981**, *289*, 782-783.
- (119) Maciel, G. E.; Sindorf, D. W., Silicon-29 NMR study of the surface of silica gel by cross polarization and magic-angle spinning, *J. Am. Chem. Soc.* **1980**, *102*, 7606-7607.
- (120) Drake, I. J.; Zhang, Y.; Gilles, M. K.; Teris Liu, C. N.; Nachimuthu, P.; Perera, R. C. C.; Wakita, H.; Bell, A. T., An In Situ Al K-Edge XAS Investigation of the Local Environment of H<sup>+</sup>- and Cu<sup>+</sup>-Exchanged USY and ZSM-5 Zeolites, *J. Phys. Chem. B* **2006**, *110*, 11665-11676.
- (121) Lonstad Bleken, B.-T.; Mino, L.; Giordanino, F.; Beato, P.; Svelle, S.; Lillerud, K. P.; Bordiga, S., Probing the surface of nanosheet H-ZSM-5 with FTIR spectroscopy, *Phys. Chem. Chem. Phys.* **2013**, *15*, 13363-13370.
- (122) Knözinger, H., Infrared Spectroscopy for the Characterization of Surface Acidity and Basicity, In *Handbook of Heterogeneous Catalysis*; Ertl, G., Knözinger, H., Weitkamp, J., Eds.; Wiley: Weinheim, 1997; Vol. 2, p 707-732.
- (123) Bordiga, S.; Lamberti, C.; Bonino, F.; Travert, A.; Thibault-Starzyk, F., Probing zeolites by vibrational spectroscopies, *Chem. Soc. Rev.* **2015**, *44*, 7262-7341.
- (124) Zhang, N.; Liu, C.; Ma, J.; Li, R.; Jiao, H., Determining the structures, acidity and adsorption properties of Al substituted HZSM-5, *Phys. Chem. Chem. Phys.* **2019**, *21*, 18758-18768.
- (125) Lee, C.; Parrillo, D. J.; Gorte, R. J.; Farneth, W. E., Relationship between Differential Heats of Adsorption and Brønsted Acid Strengths of Acidic Zeolites: H-ZSM-5 and H-Mordenite, *J. Am. Chem. Soc.* **1996**, *118*, 3262-3268.
- (126) Jin, F.; Li, Y., A FTIR and TPD examination of the distributive properties of acid sites on ZSM-5 zeolite with pyridine as a probe molecule, *Catal. Today* **2009**, *145*, 101-107.
- (127) Leydier, F.; Chizallet, C.; Chaumonnot, A.; Digne, M.; Soyer, E.; Quoineaud, A. A.; Costa, D.; Raybaud, P., Brønsted acidity of amorphous silica–alumina: The molecular rules of proton transfer, *J. Catal.* **2011**, *284*, 215-229.
- (128) Chizallet, C.; Raybaud, P., Pseudo-bridging silanols as versatile Brønsted acid sites of amorphous aluminosilicates surfaces, *Angew. Chem. Int. Ed.* **2009**, *48*, 2891-2893.
- (129) Trombetta, M.; Armaroli, T.; Gutiérrez Alejandro, A. d.; Ramirez Solis, J.; Busca, G., An FT-IR study of the Internal and External Surfaces of HZSM5 Zeolite, *Appl. Catal. A* **2000**, *192*, 125-136.
- (130) Opanasenko, M. V.; Shamzhy, M. V.; Jo, C.; Ryoo, R.; Čejka, J., Annulation of Phenols: Catalytic Behavior of Conventional and 2 D Zeolites, *ChemCatChem* **2014**, *6*, 1919-1927.
- (131) Bolton, A. P.; Lanewala, M. A., Thermochemical Reactions of Ammonium-Exchanged Y Zeolite and its Derivatives, *J. Catal.* **1970**, *18*, 154-163.
- (132) Louis, B.; Vicente, A. I.; Fernandez, C.; Valtchev, V., Crystal Size–Acid Sites Relationship Study of Nano- and Micrometer-Sized Zeolite Crystals, *J. Phys. Chem. C* **2011**, *115*, 18603-18610.

- (133) Thibault-Starzyk, F.; Stan, I.; Abello, S.; Bonilla, A.; Thomas, K.; Fernandez, C.; Gilson, J. P.; Perez-Ramirez, J., Quantification of Enhanced Acid Site Accessibility in Hierarchical Zeolites – The Accessibility Index, *J. Catal.* **2009**, *264*, 11-14.
- (134) Leydier, F.; Chizallet, C.; Costa, D.; Raybaud, P., Revisiting Carbenium Chemistry on Amorphous Silica-Alumina: Unraveling their Milder Acidity as Compared to Zeolites, *J. Catal.* **2015**, *325*, 35-47.
- (135) Valla, M.; Rossini, A. J.; Caillot, M.; Chizallet, C.; Raybaud, P.; Digne, M.; Chaumonnot, A.; Lesage, A.; Emsley, L.; van Bokhoven, J. A.; Coperet, C., Atomic Description of the Interface between Silica and Alumina in Aluminosilicates through Dynamic Nuclear Polarization Surface-Enhanced NMR Spectroscopy and First-Principles Calculations, *J. Am. Chem. Soc.* **2015**, *137*, 10710-10719.
- (136) Larmier, K.; Chizallet, C.; Maury, S.; Cadran, N.; Abboud, J.; Lamic-Humblot, A. F.; Marceau, E.; Lauron-Pernot, H., Isopropanol Dehydration on Amorphous Silica-Alumina: Synergy of Bronsted and Lewis Acidities at Pseudo-Bridging Silanols, *Angew. Chem. Int. Ed.* **2017**, *56*, 230-234.

## Chapter 4. Spectroscopic Expression of the External Surface Sites of H-ZSM-5

Chapter 3 described theoretical models aiming at understanding the structure of the external surface of H-ZSM-5. This study gave multiple details about the structure of H-ZSM-5 external surface and the nature of its surface sites. To get additional information and afford a full comparison with experiments, spectroscopic theoretical calculations are made and compared to experimental spectroscopic features. The ultimate aims of such an approach are i) the experimental validation of the proposed models, ii) the proposal of new assignments for experimental spectra, at the light of theoretical results. This chapter consist in a theoretical/experimental article which is about to be submitted and entitled: “Spectroscopic Expression of the External Surface Sites of H-ZSM-5” (written by L. Treps, C. Demaret, D. Wisser, B. Harbuzaru, A. Méthivier, E. Guillon, D. Benedis, A. Gomez, T. de Bruin, M. Rivallan, L. Catita, A. Lesage, C. Chizallet).

Here, the external surface of two H-ZSM-5 samples is studied using three cutting-edge experimental and computational techniques (FTIR with Fourier self-deconvolution,  $^1\text{H}$  MAS NMR at 800 MHz – DEPTH and DQ-BABA, periodic DFT calculations of external surface models). My contribution concerns all the theoretical aspects. The combination with the experiments obtained in the course of the thesis of Coralie Demaret gives a unequaled description of the various kinds of hydroxyl surface groups and their proximity.

### 4.1. Introduction

Zeolites are nanoporous – called microporous - (pore diameter < 2 nm) aluminosilicate materials, described as 3D frameworks of  $\text{SiO}_4$  tetrahedra.  $\text{Al}^{3+}$  cations occupy  $\text{Si}^{4+}$  crystallographic positions, requiring charge compensation cations that give birth to chemical reactivity of zeolites. This is why these solids are widely employed in refining, petrochemistry, pollution abatement and biomass conversion, among other applications.<sup>1-6</sup> In the case where the compensation cation is a proton ( $\text{H}^+$ ), it gives rise to a hydroxyl group, bridging between a silicon and an aluminium atom (Figure 1-a). These sites are considered as the Brønsted acid sites of the protonic zeolite. ZSM-5 (Zeolite Socony Mobil-5<sup>7</sup>) is one of the most used and studied zeolites, both from fundamental and industrial points of view. Many model studies have been proposed to better understand the structure and reactivity of ZSM-5, based on the consideration of very big zeolite particles (several  $\mu\text{m}$ ), thanks to their well-defined shape that makes the understanding of their inner structure possible.<sup>8-12</sup> However, zeolite particles that are used in practice exhibit much smaller crystal sizes, knowing that zeolite nano-sheets,<sup>13-15</sup> nano-crystals<sup>16-17</sup> (~100 nm) and even embryonic zeolites<sup>18-19</sup> (so small that they do not induce any X-Ray Diffraction signature) currently attract a lot of attention. The main motivation for the small crystallite size is the expected reduction of diffusion time to reach the acid sites located at their center. However, for such systems with increased surface/volume ratio, the role of the external surface of the crystallites cannot be neglected. For bulky reactants, it is even considered that catalysis takes place at the pore mouth only,<sup>20-23</sup> or that the pore mouth exhibits specific selectivity.<sup>24</sup> The structure of the acid sites located at the external surface remains a matter of debate.<sup>25</sup>

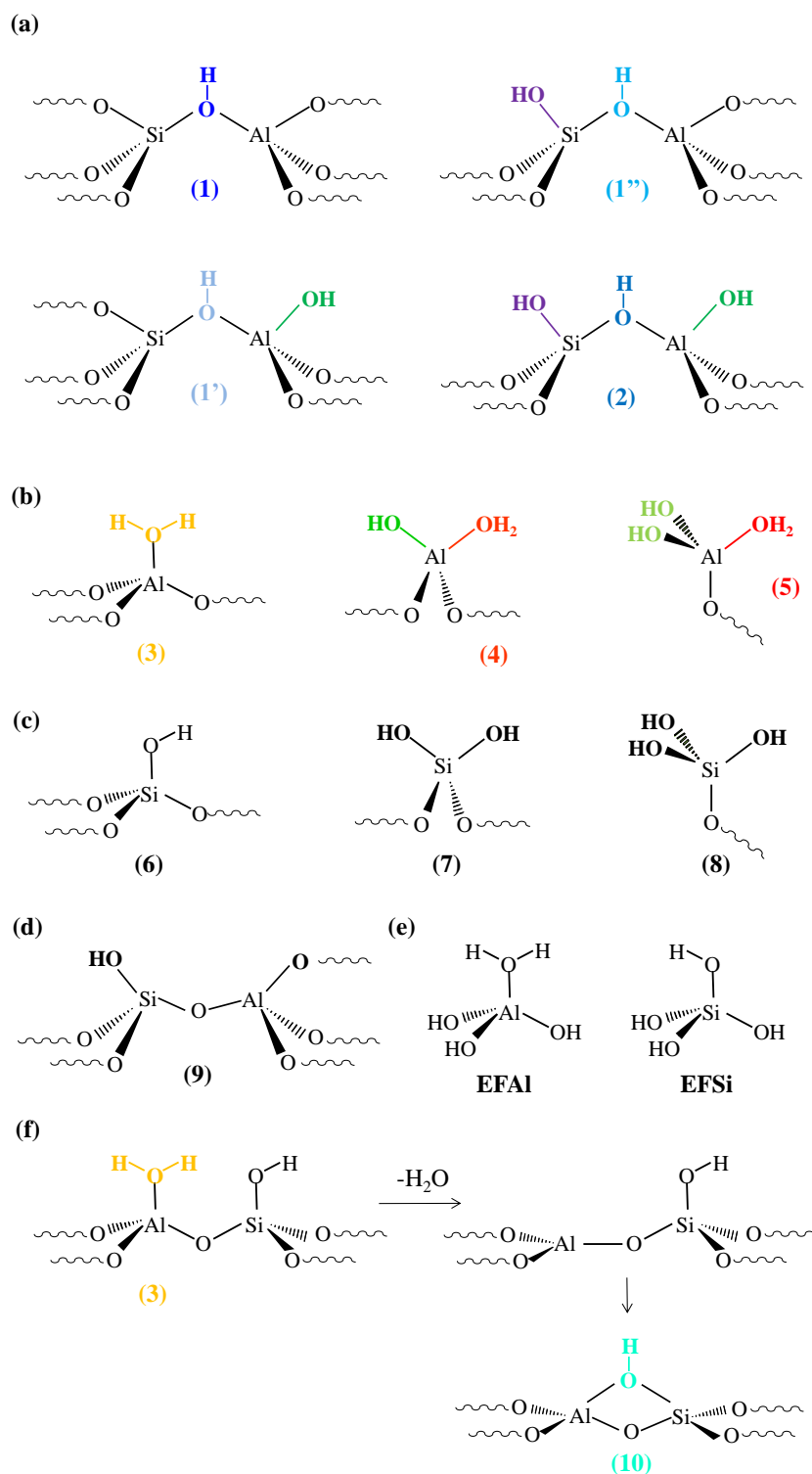


**Figure 1.** Environment and terminology of the various hydroxyl groups modeled by DFT in this work. (a) bridging Si-(OH)-Al group, known to be present in the bulk and at the external surface, with various possible second neighbors. (b) water molecules adsorbed at surface aluminum, at the external surface,<sup>26-27</sup> with possible Al-OH neighbors. (c) Silanols. (d) Silanol-Al.<sup>28-29</sup> (e) Mononuclear model extra-framework species, hosted in the zeolite porosity. (f) Dehydration of a Al-(H<sub>2</sub>O) site giving a Al<sub>III</sub> close to a silanol, that then forms a 2MR upon Si-(OH)-Al bridge closure.

Infrared spectroscopy is a relevant and frequently used method to analyze hydroxyl groups, as the stretching frequency of the O-H bond is sensitive to the environment of the hydroxyl, in terms of coordination number of the oxygen, of nature of the cation to which it is bonded, and to the hydrogen-bond network.<sup>30-31</sup> Infrared spectra of ZSM-5 exhibit features that are usually assigned from empirical considerations to several kinds of bridging OH groups ( $\sim 3610\text{ cm}^{-1}$ ), silanols ( $\sim 3740\text{ cm}^{-1}$ , Figure 1-c), and various kinds of poorly defined framework and extra-framework species and defects ( $\sim 3700\text{-}3650\text{ cm}^{-1}$ , Figure 1-e).<sup>31-42</sup> In some cases a broad absorption band is observed between  $3400\text{ and }3700\text{ cm}^{-1}$ , linked to silanol nests and adsorbed water.<sup>43-44</sup> Hoffmann et al.<sup>43</sup> proposed a more detailed assignment for the  $3740\text{ cm}^{-1}$  region assigned to silanols, on the basis of the intensity and width of the bands. They expect external silanols to vibrate at high frequency: free or terminal silanols are proposed to appear at  $3747\text{ cm}^{-1}$ , geminal silanols at  $3742\text{ cm}^{-1}$ . Internal silanols are expected at lower frequencies ( $3730\text{-}3700\text{ cm}^{-1}$ ), with a possible influence of aluminum atoms (sometimes hypothesized to be tricoordinated) connected to these silanols (then vibrating at  $3730\text{ cm}^{-1}$ ) via Si-O-Al bridges.<sup>43</sup> The sites were called Silanol-Al<sup>28-29</sup> (Figure 1-d) and also invoked for amorphous silica-alumina previously.<sup>45</sup> A drawback of the technique is the need to get knowledge of the extinction coefficient for each kind of surface OH group to quantify them. The determination of these coefficients is not straightforward and their values differ a lot from one study to another.<sup>30,46</sup> Issues related to the choice of the baseline before deconvolution also render the integration operator-dependent.

<sup>1</sup>H Magic angle Spinning Nuclear Magnetic Resonance (<sup>1</sup>H MAS NMR) has been less frequently used than Infrared for H-ZSM-5, but gave interesting insight on the present OH groups.<sup>47-57</sup> Three main regions are usually observed in <sup>1</sup>H spectra of dehydrated H-ZSM-5 zeolite:<sup>58-63</sup> bridging OH group are expected close to 4 ppm, isolated or hydrogen-bond acceptor silanols between 1.3 and 2.2 ppm, whereas Al-OH groups associated with extraframework aluminum (EFAl) are assumed to give rise to an intermediate signal close to 2.6 ppm. Large signals at 5-6 ppm are usually assigned to adsorbed water molecules. Besides the nature of the acidic OH groups, <sup>1</sup>H MAS NMR also gives information about the concentration of hydroxyl groups, which can be derived from the <sup>1</sup>H MAS NMR intensities. This is an advantage with respect to infrared spectroscopy. Additionally, <sup>1</sup>H double-quantum magic angle spinning (DQ MAS NMR) has been applied for probing spatial H-H proximities of hydroxyl groups.<sup>64</sup> Recently, this technique was used to reveal spatial proximities between Brønsted and Lewis acid sites in dealuminated H-ZSM-5 zeolites, which resulted in a remarkable enhancement of the Brønsted acid strength.<sup>65-66</sup>

For both types of spectroscopy, removing physisorbed water is required to get a well-resolved spectrum, so as to minimize the hydrogen-bond network, hence revealing sharper signals that can be more specifically assigned to the various kinds of OH groups. Despite these efforts, a strong uncertainty remains for the assignment of signals corresponding to non-ideal sites (i.e., different from bulk bridging OH groups), as the structure and environment of these sites is still poorly defined.



First principles calculations have proven helpful for the assignment of infrared and  $^1\text{H}$  MAS NMR spectra of various hydroxylated inorganic systems,<sup>29,67-78</sup> including H-ZSM-5 bulk sites.<sup>41-42,79-80</sup> The investigation of intricate zeolites is, however, much scarcer than that of the bulk bridging OH groups.<sup>25</sup> Recently, some of us have established models of the external surface of the ZSM-5 zeolite thanks to Density Functional Theory (DFT) calculations that comprehensively consider the effect of the surface orientation ((100), (010) and (101)), and that of the location of the {Al, H} pairs<sup>27</sup> on the structure of hydroxyl groups. Several kinds of surface sites have been identified. Bridging Al-OH-Si groups (Figure 1-a) were shown to be present at the pore mouth with similar or higher stability with respect to those in bulk sites. However, at the outermost surface, the following groups prevail: Si-OH, Al-OH groups, and most importantly water adsorbed on aluminum Al-(H<sub>2</sub>O)(OH)<sub>n</sub> (n=0-2) (Figure 1-b). Some of these groups are not clearly invoked in current spectroscopic assignments.

The aim of the present work is to unambiguously identify, thanks to a combination of DFT calculations and dedicated experiments, the spectroscopic expression of surface OH groups on zeolites, in the case where the zeolite is free from physisorbed water, but still hydroxylated. DFT predicts the IR frequencies and  $^1\text{H}$  MAS NMR chemical shifts for each possible kind of hydroxyl, and in the experiments two samples with different crystal sizes are compared, but with a similar Si/Al ratio, to decipher the role of the external surface. Experimentally, Fourier self-deconvolution (FSD) of IR spectra is shown to shed new light on the various components of the composite spectra. Moreover, we report high field (800 MHz)  $^1\text{H}$  MAS and  $^1\text{H}$  double quantum (DQ) MAS NMR experiments for the first time for the investigation of zeolites. For the computational study, we take advantage of the surface models established recently<sup>27</sup> so as to refine the empirical assignment of infrared (in particular in the O-H stretching zone) and  $^1\text{H}$  MAS NMR spectra. As EFAl are invoked in the empirical assignment, we also model some mononuclear species of this kind (Figure 1-e),<sup>81-82</sup> to provide a more comprehensive assignment.

## 4.2. Experimental Methods and Computational Section

### 4.2.1. DFT calculations

Periodic DFT calculations were performed with the PBE (Perdew, Burke, and Ernzerhof) exchange-correlation functional<sup>83</sup> as implemented in VASP 5.4.1.<sup>84-85</sup> The projected augmented wave (PAW) method<sup>86</sup> was used to describe the core-electron interactions. Depending on the kind of calculations performed, the plane wave basis set was limited to a kinetic cutoff energy of 400-800 eV. A density dependent dispersion correction, dDsC,<sup>87</sup> was applied. The convergence criterion for the electronic self-consistent field relaxation was fixed to  $10^{-5}$  eV. All calculations were performed at the  $\Gamma$ -point. Full geometry optimizations were performed using a conjugate-gradient algorithm, with a convergence criterion on forces of  $0.02 \text{ eV \AA}^{-1}$ .

The bulk cell parameter and initial ionic positions of ZSM-5 (MFI) were obtained from the International Zeolite Association database<sup>88</sup> and then reoptimized in the purely siliceous form with an increased energy cutoff of 800 eV. The final values are (almost orthorhombic  $\alpha=89.99^\circ$ ,  $\beta=90.00^\circ$ ,  $\gamma=90.00^\circ$ ):  $a=20.009 \text{ \AA}$ ,  $b=19.901 \text{ \AA}$  and  $c=13.364 \text{ \AA}$ , in reasonable agreement with the experimental values<sup>89-90</sup> (orthorhombic:  $a=20.07\pm 0.01 \text{ \AA}$ ,  $b=19.92\pm 0.01 \text{ \AA}$  and  $c=13.42\pm 0.01 \text{ \AA}$ ). These values were then kept constant throughout the study. The bulk configuration exhibits 12 inequivalent T sites in the structure. The slab construction is performed following the methodology of our previous works.<sup>26-27</sup> The structure is cleaved along three different orientations ((100), (010), and (101)), which were determined to be the main surfaces observed experimentally for ZSM-5 crystals.<sup>9,91-92</sup> The thickness of the slab was set at two bulk units with a 25  $\text{\AA}$  vacuum layer. Finally, the surface was saturated with OH groups; hydrogen was added to monocoordinated O atoms and OH moieties saturated Si<sub>III</sub> atoms. The alumination of the bulk and surface structures was represented by the replacement of one silicon by an aluminum in one of these positions. H<sup>+</sup> was added as a compensation cation on one of the oxygen neighbors of aluminum.

Harmonic frequency calculations were performed with an energy cutoff of 400 eV on optimized structures under the same conditions, with a displacement of  $\pm 0.005 \text{ \AA}$  around the equilibrium atomic positions. For aluminated slabs, the atoms allowed to vibrate were the OH group containing the compensation cation, the Al/Si first neighbor, all O second neighbors, Si third neighbors, and O fourth neighbors.

Chemical shifts were calculated with the linear response approach, using the gauge including projector augmented wave (GIPAW) formalism.<sup>93-94</sup> The step size for the finite difference  $\mathbf{k}$ -space derivative was set to 0.003. First order finite difference stencil was used to calculate the magnetic susceptibility. The average of the isotropic chemical shielding ( $\sigma_{TMS}$ ) of each proton of a single tetramethylsilane in vacuum (20  $\text{\AA}^3$  box) was used as a reference to calculate the isotropic chemical shift  $\delta_{iso}$  of the various protons at the surface of ZSM-5, from their isotropic chemical shielding ( $\sigma_{iso}$ ):

$$\delta_{iso} = \sigma_{iso} - \sigma_{TMS} \quad \text{Eq. (1)}$$

#### 4.2.2. Samples and general characterization

The ZSM-5 zeolites were provided by Zeolyst and hereinafter referred as Z-22-Big and Z-25-Small. The zeolites were calcined before use for 2 hours at 873 K (5K/min ramp) under air flush. The overall Si/Al ratio of the zeolites was obtained by X Ray Fluorescence (XRF) using an ARL PERFORM'X Sequential X-Ray Fluorescence Spectrometer from ThermoFisher Scientific. The Si/Al ratio of the zeolites near the surface (up to 10 nm) were obtained by X Ray Photoelectron Spectroscopy (XPS) using an ESCA KRATOS Axis Supra Spectrometer. The textural properties of the zeolites were determined by physisorption of nitrogen associated with electron microscopy (Scanning Electron Microscopy: SEM, Nova NanoSEM<sup>TM</sup>, and Transmission Electron Microscopy: TEM, JEOL JEM-2100F, bright field). Microscopy images (SEM and TEM) make it possible to describe the morphology of the

crystals and estimate their theoretical external surfaces. A Micromeritics 2020 ASAP gas adsorption analyzer was used for nitrogen sorption measurements. Prior to analysis, the samples were outgassed for 1 hour at 373 K and for 4 hours at 723 K under secondary vacuum ( $1.10^{-5}$  mbar). Specific surface areas were determined from the BET equation. The total pore volume is the nitrogen volume adsorbed at  $P/P_0 = 0.99$ . The t-plot method was used to obtain the microporous volumes of the samples.

### 4.2.3. Infrared spectroscopy

The IR investigations were carried out using a Bruker Vertex 70 spectrometer at a spectral resolution of  $4\text{ cm}^{-1}$  and accumulating 64 scans. Self-supporting pellets ( $\approx 10\text{ mg cm}^{-2}$ ) were prepared by pressing sample powders at 0.5 tons and were treated under vacuum ( $<10^{-5}$  mbar) in a homemade IR glass cell. A spectrum of the sample was recorded at 298 K after thermal treatment under secondary vacuum ( $<10^{-5}$  mbar) every 50 K from 423 up to 673 K (the sample was left for 1h for each temperature step). Fourier self-deconvolution (FSD) of the IR spectra was performed on Thermo Omnic software in the  $4000 - 2500\text{ cm}^{-1}$  spectral range, using a line bandwidth of  $10\text{ cm}^{-1}$  (width of the contribution at the half-height) and an enhancement factor of 2 (ratio of the bandwidth before and after FSD treatment).

### 4.2.4. Nuclear Magnetic Resonance

Room temperature  $^{27}\text{Al}$  MAS NMR single pulse spectra were recorded on a Bruker Avance III 400 wide bore spectrometer operating at a static field of 9.4 T. The  $^{27}\text{Al}$  NMR frequency was 104.22 MHz. All samples were fully hydrated in a saturator for one night prior to measurements. Spectra were acquired in 4-mm zirconia rotors at a spinning rate of 12 kHz, a pulse length of  $1\text{ }\mu\text{s}$  ( $\pi/20$ ) and a pre-scan delay of 1 s, which ensured a quantitative analysis. The  $^{27}\text{Al}$  chemical shift was referred to a saturated  $\text{Al}(\text{NO}_3)_3$  solution.

$^1\text{H}$  MAS and  $^1\text{H}$  double quantum (DQ) MAS NMR experiments were performed at room temperature on a Bruker Avance III 800 narrow bore spectrometer operating at a magnetic field of 18.8 T (800 MHz  $^1\text{H}$  resonance frequency). Prior to  $^1\text{H}$  MAS and  $^1\text{H}$  DQ-MAS NMR measurements, samples were pretreated under secondary vacuum ( $<1.10^{-5}$  mbar) at 573 K for 10 hours and then sealed in a glass reactor. Dehydrated samples were packed into 2.5 mm zirconia rotors under inert conditions. All  $^1\text{H}$  spectra were acquired at a spinning rate of 30 kHz. One-dimensional  $^1\text{H}$  experiments were acquired using a DEPTH<sup>95-97</sup> pulse sequence, consisting of a  $\pi/2$  pulse of  $2.5\text{ }\mu\text{s}$  length followed by two  $\pi$  pulses by which probe background signals are suppressed. To ensure a quantitative analysis, a pre-scan delay of five times the  $^1\text{H}$  longitudinal relaxation time ( $T_1$ ) was applied. Spectral deconvolution was carried out using DMFit.<sup>98</sup> For  $^1\text{H}$  DQ-MAS NMR experiments, back-to-back (BABA) recoupling sequence<sup>99</sup> was chosen for excitation and reconversion of double quantum coherence. Experiments were recorded in 128 increments in the indirect dimension  $t_1$  with 32 scans each.  $\pi/2$  pulses of  $2.5\text{ }\mu\text{s}$  length were used and the pre-scan delay was set to 2 s. The  $^1\text{H}$  chemical shift was referred to adamantane.

## 4.3. Results and Discussion

### 4.3.1. Surface OH groups calculated by DFT

We investigate the properties of bulk sites and of surface sites modeled at different cleavages of ZSM-5 cut in the (100), (010) and (101) orientations (Figure S1 in Supporting information). We chose to investigate the sites of (010) and (101) orientations that are located on the most stable surfaces found under typical conditions of temperature and water pressure (cleavage 2 and cleavage 6 respectively, see ref. <sup>27</sup>). Conversely, all the stable surfaces appearing on the stability diagram in ref. <sup>27</sup> are considered for the (100) orientation (cleavages 1, 6 and 10).

In perfectly crystalline bulk models, only bridging Si-(OH)-Al groups are present. The nature of sites at the external surface can be different. We also found at the surface bridging groups Si-(OH)-Al. These surface Si-(OH)-Al groups are not all structurally equivalent, depending on the neighborhood of the oxygen linked to the Si and Al (first cationic coordination sphere, Figure 1-a). We show in the following that this may lead to subtle differences in the spectroscopic features of the corresponding Si-(OH)-Al groups. The neighbors may be: framework oxygen atom as in the bulk, hydroxyls linked to the aluminum or linked to the silicon atom of the bridging OH group.

We also found at the external surface water molecules adsorbed on aluminum with or without neighboring hydroxyl groups  $\text{Al}(\text{H}_2\text{O})(\text{OH})_n$  ( $n=0$  to 2, Figure 1-b).<sup>27</sup> Aluminols and silanols appear in structures depicted in Figure 1-a-b. For  $n=0$ , the dehydration of  $\text{Al}(\text{H}_2\text{O})$  was shown to generate  $\text{Al}_{\text{III}}$  sites.<sup>27</sup> The latter are close to Si-OH groups. In the case of the surface of mordenite, Bucko et al. proposed that a Si-(OH)-Al bridge can close upon bonding between the Si-OH and the  $\text{Al}_{\text{III}}$ .<sup>68</sup> This generates a 2MR (Figure 1-f and Figure 2-a), where the aluminum is linked to one of its silicon second neighbor by two oxygen atoms, including one linked to a proton. Such a situation was also shown to take place in the case of the (101) surface of ZSM-5.<sup>100</sup> In the present work, we evaluated this possibility at three locations (see terminology in ref. <sup>27</sup>): the Si59 site of the (100) surface cleavage 1, the Si87 site of the (100) surface cleavage 1 and the Si45 site of the (010) cleavage 2, and found that it corresponds to a reaction energy of 3.4 kJ/mol, 0.2 kJ/mol and -4.3 kJ/mol respectively. So, the two kinds of defects ( $\text{Al}_{\text{III}}$  versus 2MR) have very similar probability existence, in agreement with previous findings.<sup>68,100</sup>

Several kinds of environments exist for the many silanols existing at the surface (Figure 1-c). They may be terminal, vicinal or geminal, or three on the same silicon. Those linked to Al atoms via Si-O-Al bridges (Figure 1-d) are called Silanol-Al. They are called hydrogen-bond donor when the O-H...O non-covalent bond is smaller than 2.5 Å.

Monomeric extra-framework species represented in Figure 1-e were modeled (one monomer per simulation cell):  $\text{Al}(\text{OH})_3\text{H}_2\text{O}$  as alumina monomer and  $\text{Si}(\text{OH})_4$  (orthosilicic acid) as silica monomer. These monomers are studied in interaction with the bulk zeolite, and

with its external surface. A bulk and a surface cell (cleavage 1 of orientation (100)), following the terminology given in ref. <sup>27)</sup> of ZSM-5 with one T5 (IZA terminology) aluminated site is taken and the monomers are put into the structure in different ways to explore the different possible interactions. Each monomer can form various kinds of interactions with the zeolite. The spectroscopic calculation included each possible case of interaction modeled. EFAI and EFSi can form a covalent bond with a silicon or an aluminum atom, and this covalent bond can go along with a protonation of the zeolite structure or not. Therefore, the formation of a covalent bond between the zeolite structure and a monomer gather 16 different possibilities, which are all included in this study. The second possible interaction with the zeolite structure is a physisorption of the monomers, which can also go along with a protonation of the zeolite structure or not. Consequently, there are also 16 different possibilities for the physisorption interaction which are also included in this study.

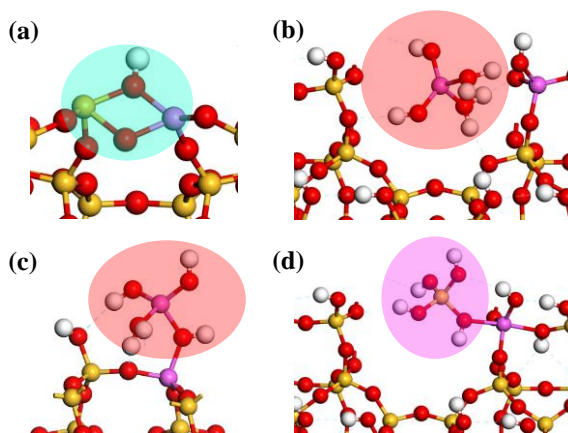


**Figure 2.** Examples of sites modeled by DFT calculations : (a) 2MR formed upon dehydration of the Si87 site of the (100) surface cleavage 1, (b) EFAI at the (100) surface of ZSM-5, after deprotonation of a close Al-(H<sub>2</sub>O) site, (c) EFAI at the (100) surface of ZSM-5, after formation of a O-Al covalent bond with a surface Al<sub>IV</sub> atom (d) EFSi at the (100) surface of ZSM-5, after formation of a O-Al covalent bond with a surface Al<sub>IV</sub> atom. Red: oxygen, purple: aluminum, yellow: silicon, white: hydrogen.

### 4.3.2. Main characteristics of the two zeolite samples

The physical-chemical properties of the two zeolites samples after calcination are summarized in Table 1. Z-22-Big has a type I isotherm, characteristic of purely microporous materials. In contrast, the nitrogen physisorption isotherm of Z-25-Small is type IV characteristic of a micro-mesoporous material (Supporting Information S2).

**Table 1.** Physical-chemical properties of the zeolite powders.

Sample	Z-22-Big	Z-25-Small
Na (ppm) <sup>a</sup>	209	230
Si/Al global (mol/mol) <sup>b</sup>	21.6 +/- 4.5	24.7 +/- 5.5
Si/Al surface (mol/mol) <sup>c</sup>	18.7 +/- 1.3	22.0 +/- 1.3
Crystal size (nm) <sup>d</sup>	2000 x 1000 x 400	40 x 40 x 40
V <sub>micro</sub> (cm <sup>3</sup> /g) <sup>e</sup>	0.177	0.159
V <sub>total</sub> (cm <sup>3</sup> /g) <sup>e</sup>	0.210	0.360
S <sub>BET</sub> (m <sup>2</sup> /g) <sup>e</sup>	410	410
S <sub>ext</sub> (m <sup>2</sup> /g) <sup>e</sup>	5	46
S <sub>ext</sub> (m <sup>2</sup> /g) <sup>f</sup>	4	88

<sup>a</sup> determined by AAS (atomic absorption spectrometry)

<sup>b</sup> determined by XRF (X Ray Fluorescence)

<sup>c</sup> determined by XPS (X-ray Photoelectron Spectroscopy)

<sup>d</sup> determined by SEM (Scanning Electron Microscopy)

<sup>e</sup> determined by nitrogen sorption analyses

<sup>f</sup> estimated from the crystal size (SEM)

The highest total pore volume for the sample Z-25-Small is due to the presence of intercrystalline mesopores generated by the stacking of small crystals as shown by SEM, but also to the presence of some intracrystalline mesopores as can be seen on the TEM images (Figure 3-a to c). The Z-22-Big zeolite presents the characteristic coffin shape of the ZSM-5 crystals, with approximate dimensions: 2 x 1 x 0.4  $\mu\text{m}$  (Figure 3-d). Starting from the crystal size obtained from the SEM images and considering that the crystals are very close in size, we can estimate their external surface area.<sup>101</sup> In our case considering the Z-25-Small as cubic crystals (40 x 40 x 40 nm) and the Z-22-Big as parallelepipedic crystals (2 x 1 x 0.4  $\mu\text{m}$ ), we obtain the corresponding external surface of 88 m<sup>2</sup>.g<sup>-1</sup> for Z-25-Small and 4 m<sup>2</sup>.g<sup>-1</sup> for Z-22-Big in good correlation with the values obtained from the nitrogen physisorption (46 and respectively 5 m<sup>2</sup>.g<sup>-1</sup>), although crystal agglomeration may explain the deviation obtained for Z-25-Small.

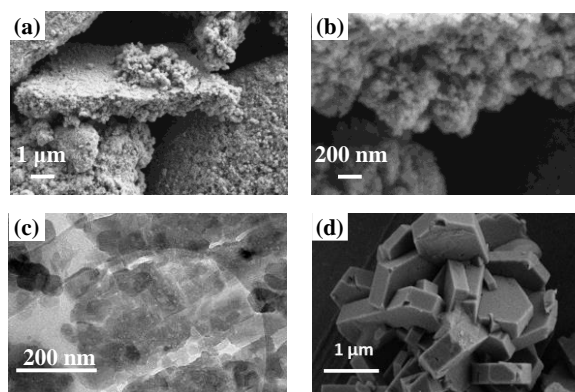


**Figure 3.** (a), (b) SEM and (c) TEM pictures of the Z-25-Small crystals. (d) SEM image of the Z-22-Big crystals.



By comparing the Si/Al ratio obtained by XRF (global) and XPS (near surface) we can estimate if there is a variation in the crystal composition (center *versus* near surface). The values obtained are present in Table 1. Considering the measurement error, we can estimate that only for the sample Z-22-Big we have a small variation in the Si/Al molar ratio, the center of the crystal exhibiting a higher Si/Al ratio than the surface.  $^{27}\text{Al}$  MAS NMR was performed on hydrated samples and shows that most aluminum species are tetrahedral, with negligible amount of octahedral species (Figure S2).

### 4.3.3. Infrared feature of surface groups

#### 4.3.3.1. General features

Infrared spectroscopy has been used in order to determine the evolution of the nature and concentration of the different hydroxyl groups present on the surface of the zeolite crystals upon thermal activation. Spectra of both zeolite samples report the conventional OH features of aluminum containing MFI framework (Figure 4-a and b) whatever the thermal treatment applied (423 – 673 K). Fourier self-deconvolution (FSD) of the interferograms has been done on IR spectra of Z-22-Big and Z-25-Small after thermal activation at 573 K, (Figure 5). FSD mathematical treatment applied on IR spectrum is close to the physical effect observed from NMR characterization of species with slow (solid) and fast (liquid state) relaxation times: the bandwidth of the contribution obtained after Fourier transformation decreases as function of the increase of the free induction decay. FSD treatment artificially enhances the exponential decay factor of the interferogram without the creation of an artificial IR component and consequently allows a “self-deconvolution” of the spectrum from the reduced bandwidth of each individual component.<sup>102</sup> The mathematical FSD treatment evidences the different spectral components present in the hydroxyl region, but it also corrects the baseline of the spectra due to scattering of the IR light on the zeolite crystals.

In Figure 5, the harmonic O-H stretching frequencies calculated by DFT are also reported. This spectral zone is well-known to be subjected to contributions due to anharmonicity. In the present work, they are not systematically estimated, assuming that they will not change the ranking between calculated frequencies. As we expect very low frequencies for hydrogen-bond donor groups,<sup>29,69,72,103-104</sup> we focused our analysis on free and hydrogen-bond acceptor OH groups.



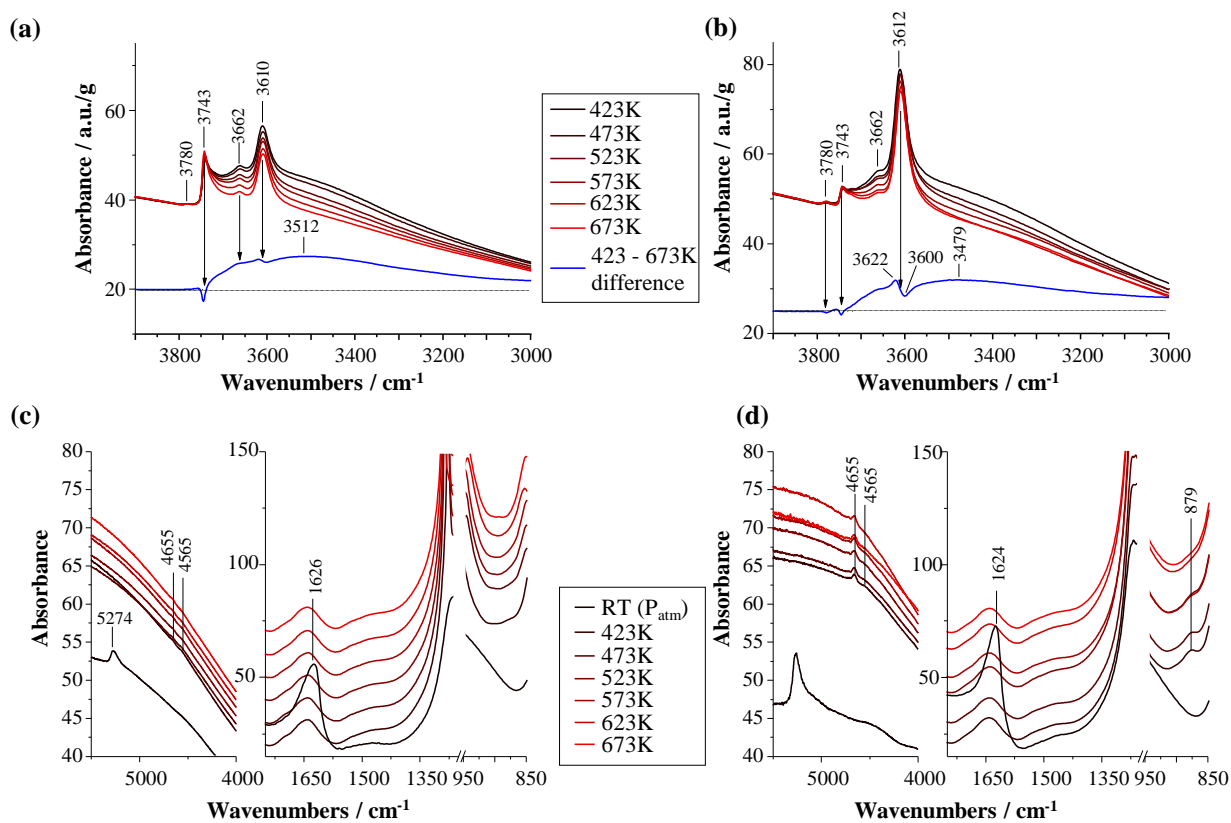


**Figure 4.** IR spectra of (a)-(c) Z-25-Small, (b)-(d) Z-22-Big, in the O-H stretching region (a)-(b), and in combination band plus bending zone (c)-(d). All spectra are acquired under secondary vacuum.

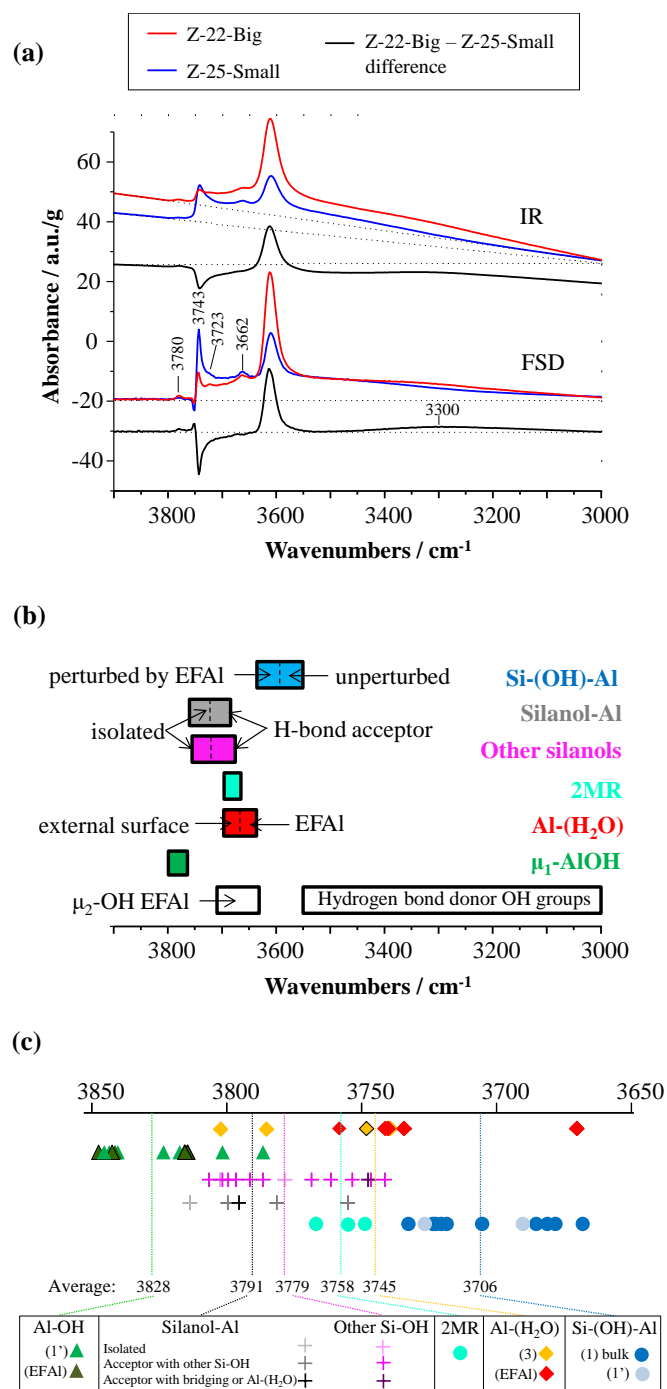


**Figure 5.** (a) IR spectra before (top) and after Fourier self-deconvolution (bottom) of the two samples activated at 573 K, and their difference. (b) Revised assignment of the IR spectra, from DFT calculations. (c) Harmonic O-H stretching frequencies calculated by DFT for a set of sites. The average for each family is also given. Symbols corresponding to isolated OH groups are circled in black.

#### 4.3.3.2. Contributions close to 3610 cm<sup>-1</sup>

At first, we observe a well resolved contribution located at 3610 cm<sup>-1</sup> due to the presence of bridging OH groups.<sup>31-42</sup> In DFT, bulk and surface Si-(OH)-Al have a harmonic contribution centered at 3706 cm<sup>-1</sup> in average (Figure 5-c). This means that the order of magnitude of the anharmonicity shift is close to 100 cm<sup>-1</sup> for these groups, at the present level of theory. Bulk and surface bridging OH groups do appear in similar spectral zones. The calculated values depend on the level of theory used. In the present work, they are higher than previous estimations.<sup>42,104</sup> Notably, bridging OH groups belonging to 2MR are not expected to vibrate in a similar spectral zone as other kinds of Si-(OH)-Al groups according to DFT, so that their situation will be described later (section 4.3.3.4).

The difference between spectra recorded after activation of Z-22-Big at 423 and 673 K show only slight differences in intensity between the two samples in this spectral zone. Maxima at 3622 cm<sup>-1</sup> and minima at 3600 cm<sup>-1</sup> appear (less significant for Z-25-Small). Because of the presence of an isosbestic point at 3610 cm<sup>-1</sup> (for all difference spectra obtained after subtraction of two consecutive spectra; not shown), we could discard the shift of the contribution at 3610 cm<sup>-1</sup> to lower wavenumbers upon thermal treatment. Moreover, all spectra have been recorded at the same temperature, so that temperature effect on the band width due to vibrational inhomogeneity of the zeolite lattice framework can also be discarded. Thus, the observation of maxima and minima at 3622 and 3600 cm<sup>-1</sup> instead of 3610 cm<sup>-1</sup> suggests that below the intense component centered at 3610 cm<sup>-1</sup>, at least two other contributions at 3600 and 3620 cm<sup>-1</sup> exist, which are related to a similar surface bridging hydroxyl. This correlates well with our DFT results: except one group that resonates close to the average value, other calculations lead to two groups of frequencies, separated by about 35 cm<sup>-1</sup>. From a structural point of view, the bridging hydroxyls vibrating below *versus* above average are very similar. The single classification resulting from our DFT calculations is that the signal appearing above average is dominated by bulk bridging OH groups that coexist with EFAls, whereas the one appearing below average corresponds to EFAls bulk bridging OH groups that are not coexisting with EFAls.

The two signals evolve upon temperature increase. The 3622 cm<sup>-1</sup> contribution decreases as the temperature increases. Following DFT observations, it can likely be assigned to bridging OH groups perturbed by EFAls (although not interacting chemically), that are thus shown to migrate outside the porosity as the temperature increases. The 3600 cm<sup>-1</sup> signal follows the opposite trend (Figure 4-b), supporting its DFT assignment to bridging OH groups that are not perturbed by EFAls, and which concentration increases as the mobility of EFAls increases.

#### 4.3.3.3. Contributions between 3750 and 3720 cm<sup>-1</sup>

At higher wavenumbers, in the 3750 – 3720 cm<sup>-1</sup> range, IR spectra exhibit a contribution centered at 3743 cm<sup>-1</sup> usually assigned to silanols. DFT results indicate a distribution of harmonic stretching frequencies of silanols (of all kinds) over the 3815-3740

$\text{cm}^{-1}$  interval. This latter interval is too large ( $75 \text{ cm}^{-1}$ ) to allow the assignment of the  $3720$  and  $3743 \text{ cm}^{-1}$  signals to the whole family of silanols considered in the computational study.

Isolated Si-OH groups resonate at higher frequencies than hydrogen-bond acceptor silanols in average, according to our DFT calculations (Table 2). Isolated Silanol-Al also appear at slightly higher frequency than other kinds of isolated silanols. Notably, we only have one example of isolated Silanol-Al in this study, all others are hydrogen-bond acceptors. This difference between Silanol-Al and other kinds of silanols disappears when these groups are hydrogen-bond acceptors with neighboring silanols. When the hydrogen-bond donor is a Si-(OH)-Al or a Al-(H<sub>2</sub>O) species, silanols are calculated to be strongly red-shifted ( $3749 \text{ cm}^{-1}$ ), in agreement with results reported on a DFT model of Amorphous Silica-Alumina.<sup>29</sup>

Thus, it is reasonable to assign the  $3720 \text{ cm}^{-1}$  contribution mainly to silanols and Silanol-Al that are hydrogen-bond acceptors with other silanols, whereas the  $3743 \text{ cm}^{-1}$  contribution is expected to correspond to isolated silanols, with a statistical majority of Si-OH different from Silanol-Al, the latter appearing with much lower intensity in this Si/Al range. Notably, the  $3720 \text{ cm}^{-1}$  resonance was previously assigned to internal silanols (in contrast with external silanols at  $3743 \text{ cm}^{-1}$ ), which is also likely, as internal silanols are expected to be more subjected to hydrogen bonds.<sup>43</sup> However, our work shows that this is not a sufficient assignment. Note also that Zecchina et al. anticipated that hydrogen-bond acceptors appear close to  $3730 \text{ cm}^{-1}$  on silicalite-1.<sup>37</sup> From our calculations, Silanol-Al that are hydrogen-bond acceptors with an Al-(H<sub>2</sub>O) are expected to appear at lower frequency (see section 3.3.4).

The difference between the spectra recorded after activation of the two samples at  $423$  and  $673 \text{ K}$  report a negative contribution at  $3743 \text{ cm}^{-1}$ , revealing an increase of Si-OH concentration upon temperature increase (Figure 4-a-b) that will be further discussed in section 3.3.8.

**Table 2.** Average vibrational frequency value and proton chemical shift for various kinds of silanols and Silanol-Al groups at the external surface as calculated by DFT.

Group	Data	Isolated	H-bond acceptor with another silanol	H-bond acceptor with Si-(OH)-Al or Al-(H <sub>2</sub> O)
Other kinds of Si-OH	$\nu_{\text{OH}} (\text{cm}^{-1})$	3792	3779	3749
	$\delta (\text{ppm})$	1.96	2.46	2.80
Silanol-Al	$\nu_{\text{OH}} (\text{cm}^{-1})$	3815	3780	3797
	$\delta (\text{ppm})$	1.63	2.29	3.03

#### 4.3.3.4. Contributions in the 3700 – 3660 cm<sup>-1</sup> range

In the interval 3690 – 3660 cm<sup>-1</sup>, between the Si-OH and Si-(OH)-Al stretching OH modes, fall the contributions that are, usually assigned to AlOH groups due to the presence of extraframework Al debris and/or Al partially attached to the framework.<sup>105-107</sup> Our DFT analysis refines and partially contradicts this assignment. Indeed, considering both Al-OH from the external surface and from monomeric EFAl (all  $\mu_1$ -OH), the vibration frequency is calculated to be higher than that of Si-OH. This is expected to correspond to the contribution discussed in section 3.3.5. We cannot exclude the presence of  $\mu_2$  aluminols on polymeric EFAls (not simulated here) that could give rise to signals in the 3690 – 3660 cm<sup>-1</sup> interval, similar to what was found on  $\gamma$ -Al<sub>2</sub>O<sub>3</sub> surface models.<sup>73,108</sup> Between silanols and bridging OH groups, DFT predicts that we have, by decreasing frequency order:

- Bridging OH groups belonging to 2MR cycles (Figure 2-a)
- silanols that are hydrogen-bond acceptors towards Al-(H<sub>2</sub>O) in particular (Table 2).
- Al-(H<sub>2</sub>O) species at the external surface, and belonging to EFAls at even lower frequency.

Thus, this spectral zone is the signature of the external surface combined with that of EFAls.

#### 4.3.3.5. Signal at 3780 cm<sup>-1</sup>

A weak contribution is observed at 3780 cm<sup>-1</sup> especially evidenced for Z-22-Big after high temperature treatment. It was assigned in the past to OH species of very low acidity and is generally enhanced with severe steaming conditions of HZSM-5 (and HBEA) zeolite at the expense of the acidic bridging OH sites.<sup>109-110</sup> From probe molecules (acid and base) interaction and looking at different spectral region (OH and T-O-T modes), Lavalley et al. proposed to assign this vibration to a basic hydroxy group on a tricoordinated Al atom partially attached to the framework.<sup>111</sup>

Our DFT investigations suggest that this signal is due to Al-OH groups ( $\mu_1$ -OH type) at the external surface and at EFAls. Here again, in average, isolated Al-OH appear at slightly higher frequency than hydrogen-bond acceptors. For the latter, the frequency domain is expected to overlap with that of isolated silanols: it is thus likely that the 3780 cm<sup>-1</sup> band is mainly due to isolated  $\mu_1$  Al-OH. This could explain why this band is observed mainly for the Z-22-Big sample, although it exhibits the lower external surface area, but due to a weaker hydrogen-bond network due to flatter surfaces with respect to Z-25-Small.

#### 4.3.3.6. Broad contribution between 3700 and 2800 cm<sup>-1</sup>

For both samples a very broad signal from 3700 to 2800 cm<sup>-1</sup> centered close to 3490 +/- 15 cm<sup>-1</sup> is evidenced in the difference spectra. It is due to hydrogen-bond donor OH groups, and possibly to the removal of neutral adsorbed water species. This will be confirmed in the next section by the disappearance of the contribution of  $\nu(\text{OH}\dots\text{O})_c$  mode.

#### 4.3.3.7. Combination modes and bending zone

At lower wavenumbers (Figure 4-(c)-(d)), a weak contribution located at  $880\text{ cm}^{-1}$  is evidenced after evacuation at 423 K for Z-22-Big due to the presence of residual  $\text{H}_2\text{O}$  neutral species.<sup>112</sup> This band does not occur on Z-25-Small, and may imply a stronger confinement of  $\text{H}_2\text{O}$  molecules and hence of the bridging OH groups on Z-22-Big in agreement with the larger size of the crystals. Spectra of both samples at atmospheric pressure and temperature do not report this specific contribution. In the latter condition, zeolite micropores are full of water molecules (see intense  $\delta(\text{H}_2\text{O})$  and  $\nu(\text{H}_2\text{O}) + \delta(\text{H}_2\text{O})$  combination modes at ca.  $1630$  and  $5274\text{ cm}^{-1}$  respectively), which lead to proton transfer with formation of  $\text{H}^+(\text{H}_2\text{O})_n$  species. The intensity of the band at  $5274\text{ cm}^{-1}$  is about 4 times higher on Z-22-Big than on Z-25-Small in agreement with the larger microporous volume.

The occurrence of the contribution at  $880\text{ cm}^{-1}$  due to  $\gamma(\text{OH}\dots\text{O})$  mode is generally accompanied with  $\nu(\text{OH}\dots\text{O})$  mode at ca.  $3696\text{ cm}^{-1}$ .<sup>112</sup> We may note however that the contribution at  $3696\text{ cm}^{-1}$  is not very sharp for Z-22-Big after activation at 423 K in agreement with the low intensity of the band found at  $880\text{ cm}^{-1}$ . Weak contributions at  $4655$  and  $4565\text{ cm}^{-1}$  are also observed for both zeolites due to  $(\nu + \delta)$  mode combination of Si-(OH)-Al and Si-OH groups respectively. The component at  $4655\text{ cm}^{-1}$  is more intense for Z-22-Big in agreement with the higher microporous volume and crystallinity, in line with the higher intensity of the  $3612\text{ cm}^{-1}$  band on this sample with respect to Z-25-Small.

#### 4.3.3.8. Quantitative analysis: impact of crystal size and of temperature

Considering the FSD spectra after activation at 573 K (Figure 5), quantitative comparison of both samples is easier due to the baseline correction. The main differences between the two samples concern the concentrations of Si-OH/Silanol-Al and Si-(OH)-Al species at  $3743$  and  $3610\text{ cm}^{-1}$ . Concentrations (determined from the net intensity measured on the FSD spectra), of Si-OH/Silanol-Al is 3 times higher on Z-25-Small, while concentration of acidic bridging sites is 2 times higher on Z-22-Big. This is in full agreement with the smaller size of Z-25-Small, inducing a higher external surface over crystallite volume ratio, even if the ratio of external surface between Z-22-Big and Z-25-Small is higher than 3 (table 1), but the latter data suffers from large uncertainties.

From the difference spectra (Z-22-Big – Z-25-Small, FSD) it is seen that the intensity of the contribution located at  $3663\text{ cm}^{-1}$  is almost the same for both samples. This was not expressed from the difference of conventional IR spectra, due to signal overlapping of the contribution with higher bandwidth.

After the FSD treatment, the Z-25-Small samples exhibit a more intense shoulder at  $3720\text{ cm}^{-1}$  than Z-22-Big. This band characterizes external mainly silanols and Silanol-Al that are hydrogen-bond acceptors with other silanols (section 3.3.3). Thus, Z-25-Small provides more abundant environment promoting hydrogen bonds, in agreement with the defects seen from TEM (Figure 3-c) and less flat surfaces with respect to Z-22-Big.

On the difference FSD spectrum, two contributions are evidenced at 3780 and 3300  $\text{cm}^{-1}$  due to a higher concentration of these species on Z-22-Big. The former could be interpreted by the fact that isolated  $\mu_1$ -Al-OH are more numerous on the flatter surfaces of Z-22-Big. While the latter could be due to the presence of residual  $\text{H}_2\text{O}$  neutral species, in agreement with the remaining contribution located at 880  $\text{cm}^{-1}$  at 573 K for Z-22-Big (Figure 4-d).

Peak intensities of the different resonances observed in the FSD-IR spectra have been followed as function of an increase of the activation temperature, 423 – 673 K (Figure 6). The spectra are reported in Figure S4. The evolution of the band at 880  $\text{cm}^{-1}$  has been obtained from the IR spectra reported in Figure 4. The concentration of bridging OH groups (3610  $\text{cm}^{-1}$ ) appears to be preserved upon the temperature increase up to 673 K, in line with the literature,<sup>32</sup> also a redistribution between the 3622 and 3600  $\text{cm}^{-1}$  resonances was mentioned in section 3.3.1 and explained by the thermally activated migration of EFAls from the structure. An enhancement of the band located at 3745  $\text{cm}^{-1}$  due to isolated external silanols concentration is observed as function of the temperature increase for the two samples. From DFT calculations, this increase can be assigned to the water desorption from Al-( $\text{H}_2\text{O}$ ) sites,<sup>27</sup> that affects the hydrogen-bond network and converts hydrogen-bond donor and acceptor silanols into isolated silanols. For small crystals, Z-25-Small, we also observe a small depletion of hydrogen-bond acceptor silanols (3722  $\text{cm}^{-1}$ ), and a more significant depletion of the 3450  $\text{cm}^{-1}$  band corresponding to hydrogen-bond donor OH groups. The fact that this is not observed on the Z-22-Big sample could be explained by the lower intensity of these signals (by a factor of more than two), making these less detectable.

The intensity of the contribution at 3663  $\text{cm}^{-1}$  decreases as a function of temperature for both samples. From DFT (section 3.3.4), it can be assigned to Al-( $\text{H}_2\text{O}$ ) species, Silanol-Al that are hydrogen-bond acceptors towards Al-( $\text{H}_2\text{O}$ ), 2MR bridging hydroxyls, and possibly  $\mu_2$ -OH from EFAls. The desorption of water from Al-( $\text{H}_2\text{O}$ ) is expected to induce the depletion of the two formers, but the appearance of 2MR sites on some of the Al atoms left dehydrated. The fact that two sites are lost for a third being gained, is consistent with the decrease of the intensity of this band as the temperature increases. Notably, the intensity of the 3660  $\text{cm}^{-1}$  band is quite similar for both samples (only slightly higher for Z-25-Small), whereas it is expected to be due at least in part to external surface species. This could be due to the lower surface Si/Al ratio of Z-22-Big, as shown by XPS (Table 1), at the origin of more numerous surface Al on big particles, counterbalancing (for this specific kind of sites) the effect of the lower external surface area.

For Z-22-Big, even if the concentration is low, IR spectra obtained show that the contribution at 3780  $\text{cm}^{-1}$  progressively increases as a function of the temperature. According to our DFT assignment, this reveals an increase of isolated  $\mu_1$ -Al-OH (section 3.3.5) concentration upon temperature increase, again consistently with the depletion of the hydrogen-bond network. This band is hardly detected for the Z-25-Small sample. As argued in section 3.3.5, this may be explained by a denser hydrogen-bond network on this sample.



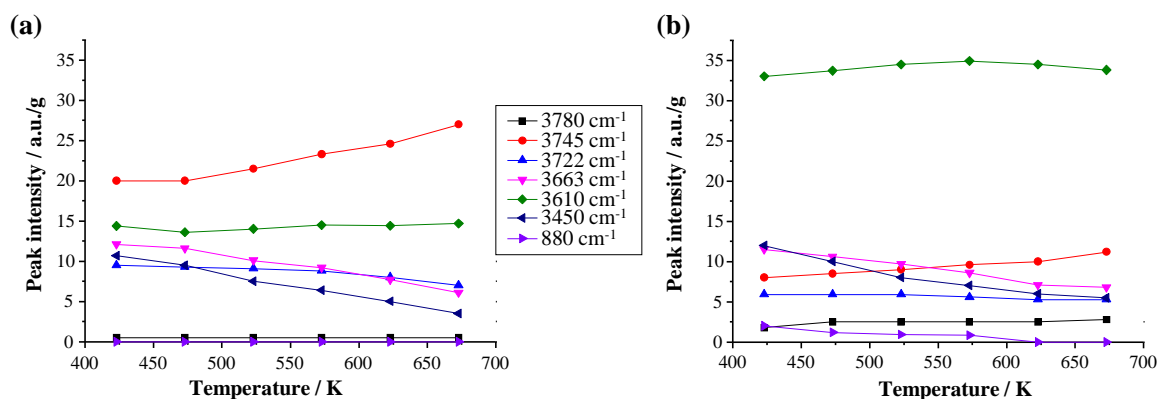


**Figure 6.** Evolution of the intensity of the different contribution observed in the hydroxyl region for a) Z-25-Small and b) Z-22-Big as function of the activation temperature.

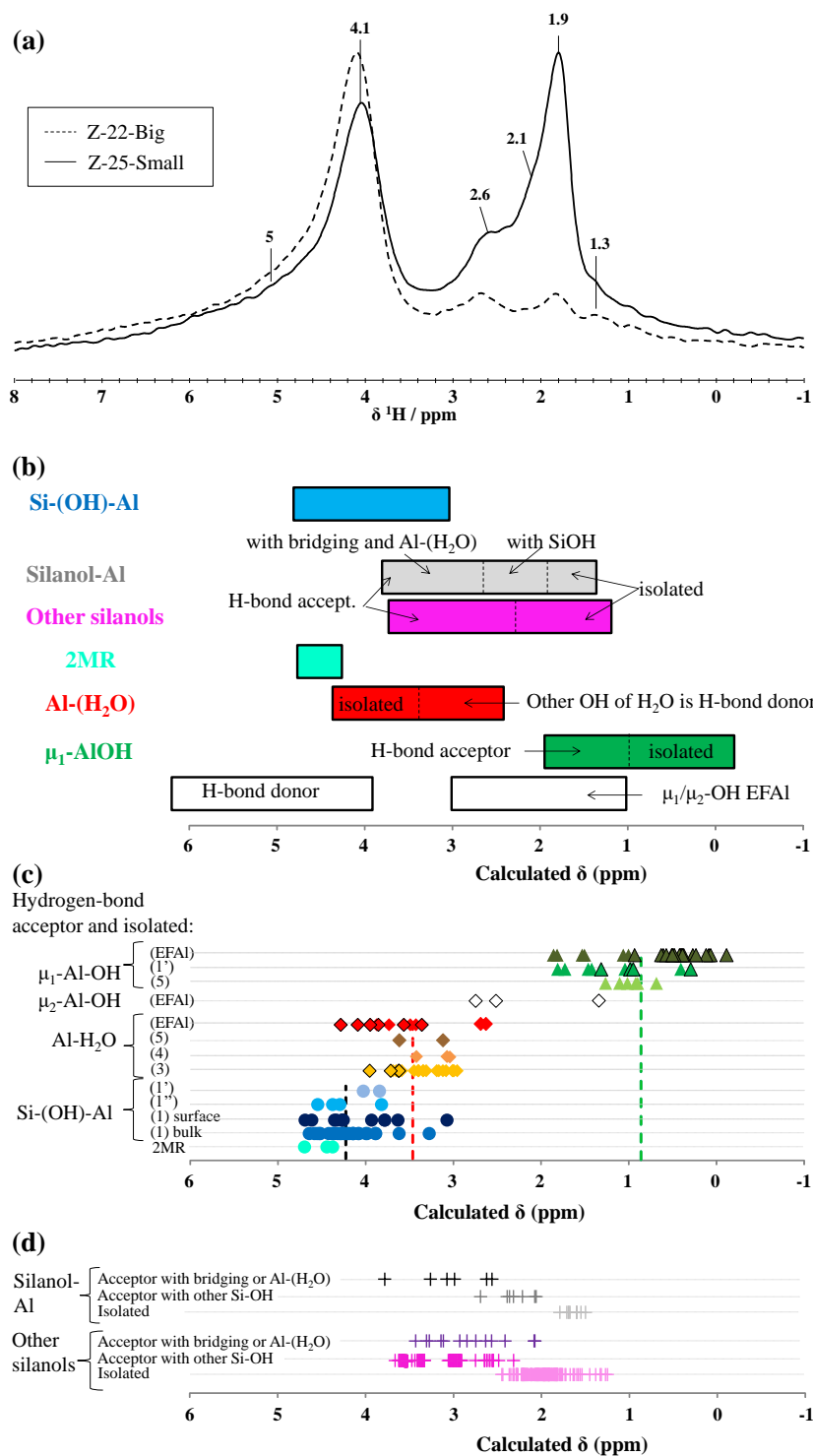
Thus, our experimental observations and DFT assignments appear to be fully consistent and make us able to explain the main spectral evolutions as a function of particle size and activation temperature. The lack of knowledge of extinction coefficients for the huge variety of groups, and the overlap between spectral zones characteristic of external surface sites invoked in our assignment, however, motivates the comparison of FTIR with  $^1\text{H}$  NMR.

#### 4.3.4. $^1\text{H}$ NMR feature of surface groups

##### 4.3.4.1. General feature

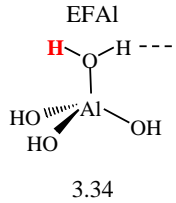
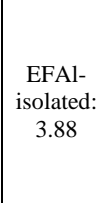
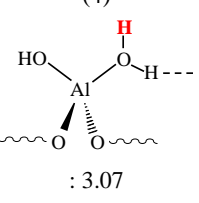
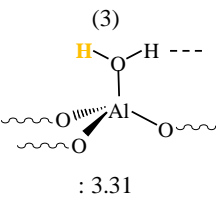
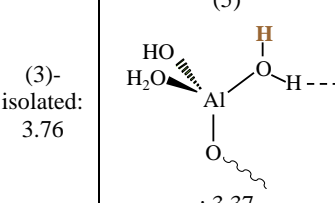
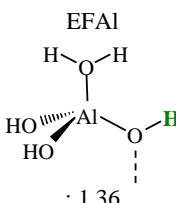
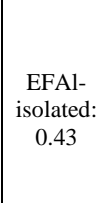
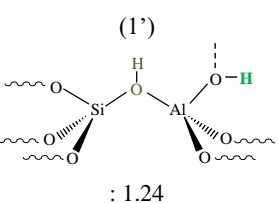
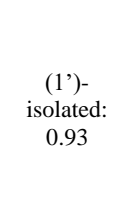
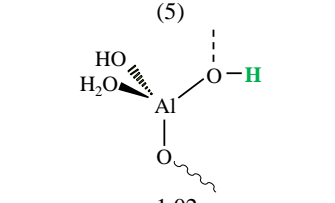
Figure 7 shows the  $^1\text{H}$  MAS NMR spectra obtained for Z-22-Big and Z-25-Small after activation at 573 K, together with the chemical shifts calculated by DFT. Being recorded at a high magnetic field of 18.8 T (800 MHz  $^1\text{H}$  resonance frequency), the spectra are highly resolved with respect to usual observations. Similarly to infrared, calculated chemical shifts are reported for protons which are not hydrogen bond donors. The latter exhibit very high shifts that are correlated with the hydrogen-bond length (Figure S4), in line with previous observations for other hydroxylated oxides.<sup>70-71,75</sup> However, the chemical shift of protons belonging to hydrogen bond acceptor hydroxyls are taken into account, as well as that of isolated OH groups. As for the DFT IR results, the calculated chemical shifts are separated in several families: average data for each family are given in Tables 2 and 3. Additional data for silanols are gathered in Supporting Information S4 (Figure S5 and Table S1).

Decomposition of the spectra are shown in Figure S6. Main lines are observed close to 4.1, 2.6, 1.9 (2.1 and 1.8 ppm for Z-25-Small) and 1.3 ppm, plus a broad contribution centered around 5.1 ppm. The following parts are devoted to the assignment of each of these lines thanks to our DFT calculations.



**Figure 7.** (a)  $^1\text{H}$  MAS NMR spectra normalized to the mass of the sample of Z-22-Big and Z-25-Small after activation at 573 K. (b) Simplified assignment proposed in the present work on the basis of DFT calculations.  $^1\text{H}$  NMR DFT calculated chemical shifts of: (c) Al-OH, Al- $\text{H}_2\text{O}$ , Bridging Si-(OH)-Al, and 2MR sites, (d) Silanol-Al and silanols. For (c), symbols corresponding to isolated Al-OH and Al- $\text{H}_2\text{O}$  are circled in black, and the numbers correspond to the terminology reported in Figure 1. Hydrogen-bond donor OH groups are fully excluded from the diagrams.

**Table 3.**  $^1\text{H}$  NMR DFT calculated chemical shifts by family and sub-families, of isolated and hydrogen-bond acceptor hydroxyls. The terminology corresponds to Figure 1. When necessary for the definition of the hydrogen-bond network, a refined structure is presented, the  $^1\text{H}$  under consideration being depicted with colors. Data corresponding to silanols and silanol-Al are given in Table 2.

Type of site	Total average (ppm)	Sub-family and average $^1\text{H}$ chemical shift per category (ppm)				
Si-(OH)-Al	4.20	(1'): 3.98	(1''): 4.30	(1)- surface: 4.12	(1)- bulk: 4.25	2MR: 4.55
Al-(H <sub>2</sub> O)	3.46	 EFAl 3.34	 EFAl-isolated: 3.88	 (4) : 3.07	 (3) : 3.31	 (5) : 3.37
Al-OH	0.86	 EFAl : 1.36	 EFAl-isolated: 0.43	 (1') : 1.24	 (1')-isolated: 0.93	 (5) : 1.02

#### 4.3.4.2. Signal close to 4 ppm

Signals ranging from 3.8 to 4 ppm are usually attributed to bridging Si-(OH)-Al groups, which our DFT calculations confirm. Indeed, for bulk bridging OH group, the calculated  $^1\text{H}$  chemical shift has an average value of 4.25 ppm. Bridging OH groups at the external surface of the zeolite exhibit a chemical shift average of 4.20 ppm. If second neighbors of the surface bridging OH groups are framework oxygen atom as in the bulk, their average chemical shift is 4.12 ppm. Hydroxyls groups can replace structural oxygen of ZSM-5 and be bounded to the aluminum of the bridging OH group, for an average chemical shift of 3.98 ppm, or to the silicon atom, for an average chemical shift of 4.30 ppm. All these values are rather close whereas the experimental signal is large: from 1D  $^1\text{H}$  MAS NMR, it does not seem easy to distinguish these various groups, as attested by the easy fitting of this part of the experimental spectra (Figure S5) by a single line.

Notably, bridging OH groups from 2MR sites are expected to appear at 4.55 ppm, thus in the upper chemical shift part of the bridging OH group family. This is different from FTIR, for which the 2MR signal is clearly differentiated from that of other bridging OH groups, and appears between the frequency of silanols and bridging groups. The trend in NMR is opposite, as 2MR sites are less shielded than other bridging and all silanols (see next sections).

However, DFT results suggest that Si-(OH)-Al groups are not the single species that resonate in this chemical shift range: water molecules belonging to Al(OH)<sub>n</sub>(H<sub>2</sub>O) species,

either from EFAl, either exposed at the zeolite outermost surface, also contribute (Figure 7-b and c). Those exhibiting the chemical shift closer to 4 ppm are isolated water molecules (no hydrogen-bond with the neighborhood), with an average chemical shift of 3.76 ppm for  $n=0$  at the external surface, and of 3.88 ppm in EFAls. Thus, contrary to previous thoughts, the signal close to 4 ppm is not due to bridging OH groups only, and likely holds part of the signal of Al-(H<sub>2</sub>O) species on EFAls and at the external surface.

#### 4.3.4.3. Signal close to 2.6 ppm

Peaks centering at 2.6 ppm are usually assigned to different types of AlOH groups associated with extra-framework species.<sup>50,59-60</sup> The DFT calculated chemical shifts that are the closer to this value are due to (i) water molecules belonging to Al(OH)<sub>n</sub>(H<sub>2</sub>O) species, either from EFAl, either exposed at the zeolite outermost surface, when one of the protons is hydrogen-bond donor, and (ii) hydrogen-bond acceptor silanols, either Silanol-Al or all other types, (iii)  $\mu_2$ -Al-OH, obtained when EFAl monomers bind covalently to surface Al atoms belonging to the zeolite outermost surface.

Regarding Al(OH)<sub>n</sub>(H<sub>2</sub>O) species at the external surface, for the water molecule, an average in chemical shift at 3.31 ppm ( $n=0$ ), 3.07 ppm ( $n=1$ ), and 3.37 ppm ( $n=2$ ) is observed for the non-hydrogen-bonded H, when the second is hydrogen-bond donor (Table 3). Thus, when the second hydrogen is donor the signal is shifted by -0.4 to -0.5 ppm with respect to isolated Al-(H<sub>2</sub>O) water molecules. The signals of protons of H<sub>2</sub>O adsorbed on alumina monomers (EFAl) were also modeled in similar configurations. The average of chemical shift signals are very similar to the surface Al(OH)<sub>n</sub>(H<sub>2</sub>O) surface species, with an average chemical shift of 3.34 ppm. The average values are higher than 2.7 ppm, but a significant proportion of the simulated sites give rise to signals lower than 3 ppm.

From Tables 2 and S1, it appears that the chemical shift of the surface Si-OH groups are not differentiated by the number of neighboring silanols but mainly by their isolated *versus* hydrogen bond acceptor nature. For the latter, the Silanol-Al nature does not impact much. A chemical shift average of 2.48 ppm is calculated, close to the experimental value of 2.6 ppm discussed here. Inside the hydrogen-bond acceptor Silanol-Al family, a rather clear ranking is observed as a function of the nature of the group that is hydrogen-bond donor. When this donor is a close Si-(OH)-Al or Al-(H<sub>2</sub>O), the Silanol-Al is characterized by a higher chemical shift (3.03 ppm) than when the donor is another silanol (2.29 ppm, which could rather correspond to the 2.2 ppm signal discussed in section 3.4.4). Isolated silanols (of Silanol-Al nature or other) appear at lower chemical shift, and do not contribute to the presently discussed spectral zone, but to the one discussed later in section 3.4.4.

While simulating the interaction of mononuclear EFAl with the external surface, in some configurations, covalent Al-O bonds were formed that result in the formation of  $\mu_2$ -Al-OH (in other terms, Al-(OH)-Al, as illustrated in Figure 2-c. Our DFT calculations show that they should appear between 1 and 3 ppm. Notably, on alumina surface and edge models, the same 1-3 ppm spectral zone was assigned to  $\mu_1$  and  $\mu_2$  OH groups, all linked to aluminum

atoms only.<sup>70</sup> Should polynuclear EFAl species be present, they may also participate to the signal close to 2.7 ppm, possibly also to lower chemical shift signals (see section 3.4.4).

Thus, our DFT investigation expands and refines the empirical assignment of this spectral region, usually considered coming from EFAl Al-OH only, by showing that it comes from Al-(H<sub>2</sub>O) groups from EFAls and from external surface sites, as well as from hydrogen-bond acceptor silanols, plus  $\mu_1$ -OH and  $\mu_2$ -OH groups from EFAls. This assignment is far less trivial than what is usually considered.

#### 4.3.4.4. Signals below 2.5 ppm

Several resonances within 1.3 and 2.1 ppm are observed experimentally (Figure 7-a) : peaks between 1.8 and 2.1 ppm are usually considered to arise from non-bridging SiOH groups, while minor peaks below 1.5 ppm have been attributed to Al-OH species.<sup>113</sup> According to our DFT calculations and by decreasing order of average chemical shift (Tables 2 and 3), the species likely to contribute in this zone are (Figure 7-b): (i) some hydrogen-bond acceptor Silanol-Al (when the donor is another silanol, 2.3 ppm), (ii) isolated silanols and Silanol-Al (1.96-1.63 ppm), (iii) hydrogen-bond acceptor  $\mu_1$ /  $\mu_2$ -Al-OH from EFAls (1.02-1.36 ppm). (i) and (ii) are likely assigned to the experimental 2.2 ppm contribution, whereas (iii) better fits with the 1.3 ppm signal.

Indeed, the free silanol groups exhibit a chemical shift average of 1.95 ppm. The chemical shift of isolated OH groups of EFSi adsorbed on the surface, Si(OH)<sub>4</sub>, are similar with an average of 1.92 ppm for free hydroxyl groups. Isolated Si-OH appear at higher chemical shifts with respect to Silanol-Al (1.96 *versus* 1.63 ppm). A clear ranking thus appears between Si-OH and Silanol-Al when these groups are isolated, which disappears (all features being mixed) when these groups are hydrogen-bond acceptors (section 3.4.3). This is very similar to observations made from infrared spectroscopy (section 3.3.3.).

Moreover, a difference is found between the signal of free *versus* hydrogen bond acceptor  $\mu_1$ -Al-OH groups. At the external surface, hydrogen-bond acceptor OH from Al(OH)<sub>2</sub>H<sub>2</sub>O species have an average chemical shift of 1.02 ppm. A signal at 1.24 ppm is found for hydroxyl groups neighboring a bridging group, HO-Al-(OH)-Si. For similar free Al-OH the signal is shifted to an average of 0.93 ppm. The calculated chemical shift of hydroxyl groups of EFAls exhibits similar trends, with average chemical shift of 1.36 and 0.43 ppm for hydrogen-bond donor and free Al-OH respectively. One isolated  $\mu_2$ -Al-OH from an EFAl connected to a surface Al atom appears at 1.34 ppm.

Notably, we do not experimentally observe intense resonances lower than 1 ppm, assigned to isolated  $\mu_1$ -Al-OH groups (from the external surface, from monomeric EFAls, but also from alumina edges<sup>70</sup>), which suggests that such configurations are not abundant on the investigated samples.

#### 4.3.4.5. Broad signal at higher chemical shifts

The broad signal observed at higher than 5 ppm are reported to correspond to strongly adsorbed residual water molecules.<sup>54,59,61</sup> According to our calculations, they shall also correspond to the a wide family of hydrogen-bond donor groups.

#### 4.3.4.6. Decomposition of the spectra, analysis of crystal size effects

The absolute and relative integrated peaks areas were obtained from spectral deconvolution (Figures S6 and S7). After treatment at 573 K, the integration of Z-25-Small leads to a smaller amount of protons with respect to Z-22-Big (10527 a.u./g<sub>zeolite</sub> for Z-25-Small versus 12658 in a.u./g<sub>zeolite</sub> for Z-22-Big). This is compatible with the ability of water molecules to desorb from Al-(H<sub>2</sub>O) upon thermal treatment, at variance with Si-(OH)-Al groups that are thermally stable. Al-(H<sub>2</sub>O) is indeed expected to be more abundant on the Z-25-Small sample due to its smaller particle size. Another explanation of the lower amount of integrated protons for Z-25-Small could also be the more important hydrogen-bond network (as also suggested by infrared, section 3.3.5.) leading to a more intense contribution of hydrogen-bond donors that may be merged with the contribution of the probe background.

With increasing crystal size, the intensity of the 1.9 ppm signal decreases from 31% of the total <sup>1</sup>H signal to 6%, which is coherent with a higher external surface area developed by Z-25-Small, as this signal is expected to be mainly due to external silanols. On the contrary, a higher proportion of the signal at about 4 ppm is observed for Z-22-Big (43% versus 25% for Z-25-Small). The ratio of the absolute number of these protons in each zeolite indicates that there are around twice more numerous in Z-22-Big (5467 a.u./g<sub>zeolite</sub>) as in Z-25-Small (2604 a.u./g<sub>zeolite</sub>) in agreement with IR results. This suggests that many aluminum atoms in Z-25-Small, possibly located at the outermost surface, do not form Si-(OH)-Al sites (important contributors to the 4 ppm signal), but rather AlOH groups, Al(H<sub>2</sub>O) species and Silanol-Al, as shown by the predominance of the 1-3 ppm signals for this sample.

#### 4.3.4.7. 2D NMR: assessing proximities

Two-dimensional <sup>1</sup>H DQ-MAS NMR spectra can provide direct information about proximities of different hydroxyl groups in zeolites (Figure 8). This technique allows one to identify dipolar interactions of two protons close in space at a maximum distance of a few Ångström.<sup>65</sup> Double Quantum frequency (DQ) in the indirect dimension corresponds to the sum of the two Single Quantum (SQ) frequencies in the direct dimension. Autocorrelation peaks appear as a single peak along the diagonal (2 $\delta_A$ ,  $\delta_A$ ), which correspond to dipolar coupling between equivalent protons (same chemical shift). Correlations between two different protons with different chemical shifts give rise to two off-diagonal peaks ( $\delta_A + \delta_B$ ,  $\delta_A$ ) and ( $\delta_A + \delta_B$ ,  $\delta_B$ ).<sup>64</sup> In the following, we discuss the correlation peaks observed experimentally on the basis of the DFT assignments. Notably, the distance between protons on a model containing two H per cell only has a minor impact on their chemical shifts (Figure S8) which makes it possible to assess proximities even if our models correspond to an effective Si/Al ratio of 96.

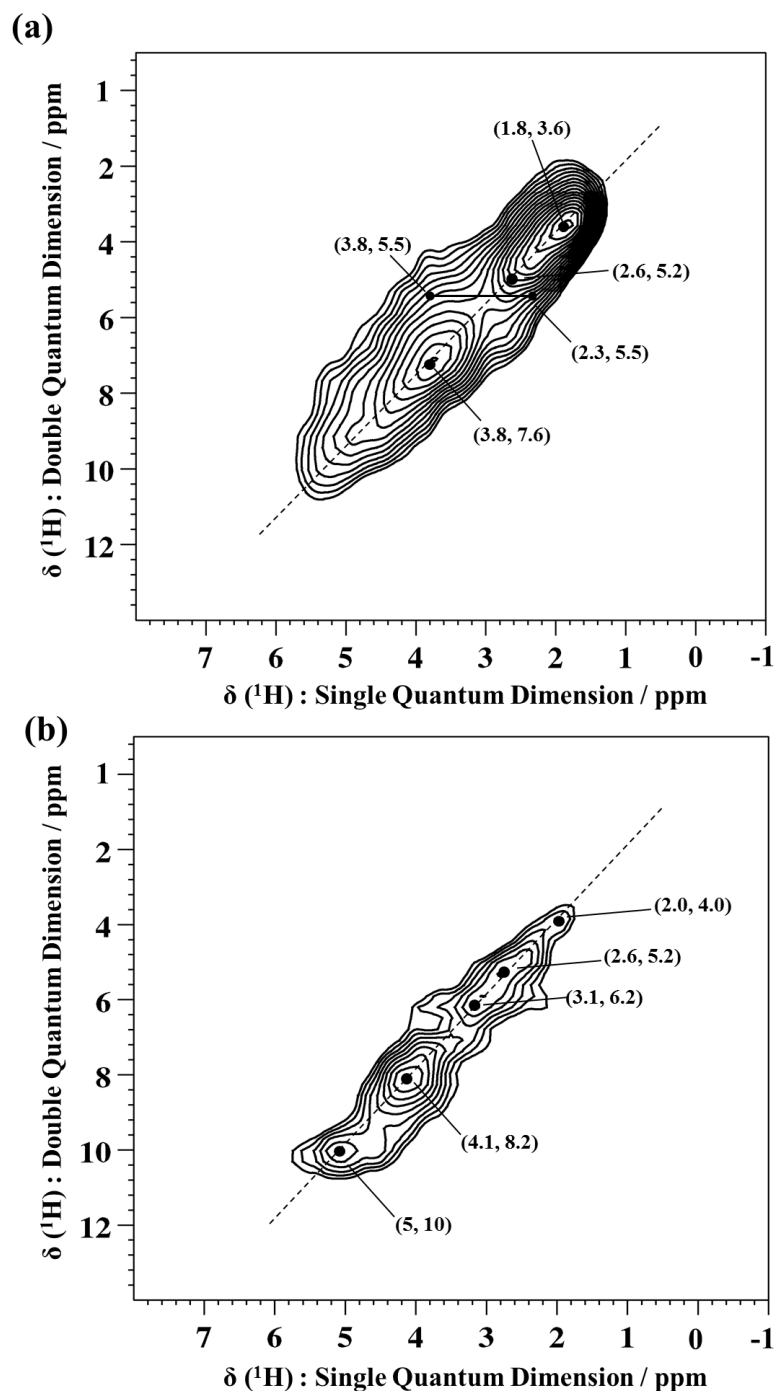


**Figure 8.** Two-dimensional  $^1\text{H}$  SQ-DQ NMR spectra (a) Z-25-Small and (b) Z-22-Big after activation at  $300^\circ\text{C}$ .

Figure 8-a shows the two-dimensional  $^1\text{H}$  correlation spectrum obtained for Z-25-Small. Three autocorrelation peaks along the diagonal of the spectrum are observed. A first one appears at 1.8 ppm (SQ) (3.6 ppm in DQ). We assigned this signal to isolated silanols and H-bond acceptor Silanol-Al (with donor SiOH). This indicates spatial proximity between



these groups. Basically, on the (101) surface model, isolated silanols are separated by less than 4 Å from other isolated or hydrogen-bond acceptor silanols.

Another autocorrelation peak appears at 2.6 ppm (SQ) (5.2 ppm in DQ), which can be ascribed to Al-(H<sub>2</sub>O) with one donor H (outermost surface and EFAl), most hydrogen-bond acceptor silanols (outermost surface and EFSi) and  $\mu_2$ -Al-OH (EFAl). Proximity of free protons Al-(H<sub>2</sub>O) between themselves when one proton is donor would require the proximity of two Al-(H<sub>2</sub>O) groups (two aluminum), which is not likely, due to the rather high Si/Al ratio. But the proximity of Al-(H<sub>2</sub>O) and H-bond acceptor Silanol-Al is highly likely in the configuration suggested in Figure 9. Notably, this configuration was shown to lead to particularly low O-H frequency in IR for the hydrogen-bond acceptor Silanol-Al (section 3.3.4). Also, several groups from EFAl are expected at 2.6 ppm, justifying per se the existence of the autocorrelation peak. Another indication from this autocorrelation peak is the possible proximity of EFAl with silanols and/or surface Al-(H<sub>2</sub>O), which some of our DFT models also confirm.

A third peak at 3.8 ppm (SQ) (7.6 ppm in DQ) is present. This chemical shift is somewhat lower than the 4.1 ppm peak observed in 1D <sup>1</sup>H NMR, assigned thanks to DFT to bridging Si-(OH)-Al and isolated Al-(H<sub>2</sub>O). In average (Table 3), isolated Al-(H<sub>2</sub>O) species are predicted at lower chemical shift (close to 3.8 ppm) with respect to bridging OH groups (close or above 4 ppm). Thus, the autocorrelation peak can be assigned, thanks to DFT, mostly to isolated Al-(H<sub>2</sub>O) species only, which is logical since each Al-(H<sub>2</sub>O) species contains two very proximate (about 1.6 Å) protons that correlate one with the other. 2D <sup>1</sup>H NMR is thus a powerful tool to evidence a species (isolated Al-(H<sub>2</sub>O)) within a group of sites (isolated Al-(H<sub>2</sub>O) plus bridging OH groups), whereas it was not possible in that case from 1D <sup>1</sup>H NMR.

Only one cross-correlation between different types of OH groups is observed at 2.3 ppm (SQ) / 3.8 ppm (SQ) (5.5. ppm in DQ). As already discussed, 3.8 ppm corresponds to isolated Al-(H<sub>2</sub>O) species. The 2.3 ppm signal in 2D corresponds to part of the 2.7 ppm signal in 1D. The latter was assigned to Al-(H<sub>2</sub>O) with one donor H, most hydrogen-bond acceptor silanols and  $\mu_2$ -Al-OH. The lowest part of it is expected from DFT to correspond to hydrogen-bond acceptor silanols and  $\mu_2$ -Al-OH. A proximity of Al-(H<sub>2</sub>O) and  $\mu_2$ -Al-OH is observed in practice in our models of EFAls connected to surface Al atoms (example in Figure 2-c), although on our models the corresponding Al-(H<sub>2</sub>O) species are hydrogen-bond donor. Another proximity between isolated Al-(H<sub>2</sub>O) and hydrogen-bond acceptor silanols is observed (depicted in Figure 9), that is also compatible with the observation of this cross-correlation. The projection shown in Figure S8 in the supporting information suggests, however, that the correlation pattern is rather broad: some Al-(H<sub>2</sub>O) are close to bridging OH groups, and to silanol groups as a whole, although no well-defined cross-correlation is observed.

For Z-22-Big (Figure 8-b), one difference is the absence of a clear 2.3 ppm (SQ) / 3.8 ppm (SQ) cross-correlation. This could be explained by the very low amount of Al-(H<sub>2</sub>O) species on that sample, due to its low external surface area. An autocorrelation peak at 4.1

ppm appears, whereas it was at 3.8 ppm for Z-25-Small: this suggests first that Al-(H<sub>2</sub>O) are in strong minority with respect to bridging OH groups (stronger than on the Z-25-Small sample, due to its lower external surface area), in agreement with the 1D <sup>1</sup>H MAS NMR spectra. Second, this indicates that some of the bridging OH groups are close one to the other, or close to Al-(H<sub>2</sub>O) species.

Notably, in many cases proximities between hydrogen-bond donor hydroxyls and other groups shall be seen, but their observation is not straightforward due to the width of the high chemical shifts signals of the former. Also, 2MR sites (expected at 4.55 ppm) do not show any proximity with other protons, or are too diluted to make this observation feasible.

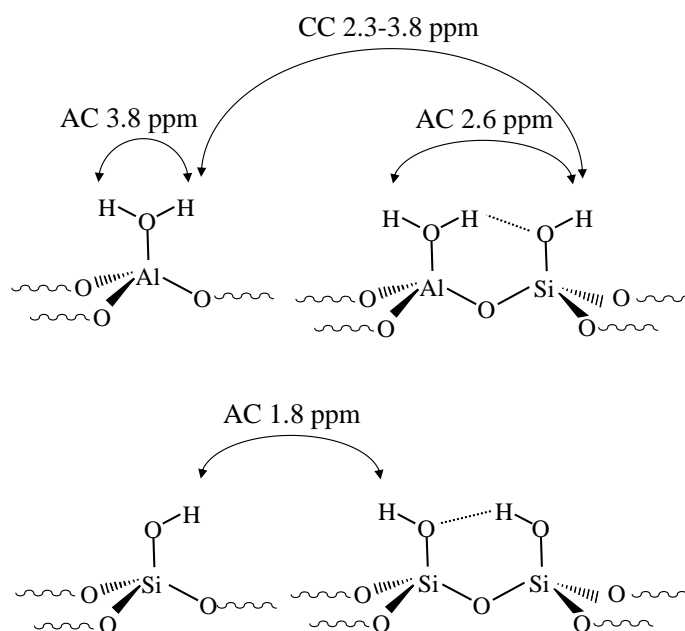


**Figure 9.** Simplified representation of the proximities observed by <sup>1</sup>H SQ-DQ NMR, for the sites that are specific to the external surface, as assigned by DFT. Extra-framework species are omitted for the sake of clarity, as well as bridging OH groups. AC: autocorrelation, CC: cross-correlation. AC with groups of the same nature are omitted (except within the isolated Al-(H<sub>2</sub>O)).

In the end, 2D <sup>1</sup>H MAS NMR appears to be a very insightful technique highly complementary to 1D <sup>1</sup>H MAS NMR when assigned in the light of DFT calculations, first to reveal sub-families of peaks within composite signals, then to analyze proximities. Thanks to DFT, autocorrelation peaks can also be assigned to correlations between several types of hydroxyl groups that appear at the same chemical shift. The spectroscopic expression of the external surface appears much more clearly thanks to our analysis, as well as the respective positions of the various surface sites, with particle size-dependent picture of the species in presence.

Notably, infrared and <sup>1</sup>H MAS NMR provide consistent but complementary insights. Figure S11 reports the evolution of the computed <sup>1</sup>H NMR chemical shift with the calculated O-H vibration frequency, for all the hydroxyl groups that have been investigated by both techniques. If a trend appears, it is rather approximate, showing that subtle structural effects

play a different role from one technique to another. Combining the two techniques is thus a way to detect differences between samples that cannot be seen with one technique only.

#### 4.4. Conclusion

The nature and spectroscopic expression of external surface sites of zeolites is a long-debated question, in particular for ZSM-5, one of the most popular zeolites, both from fundamental and industrial point of views. In the present work, we combine three cutting-edge complementary experimental and computational techniques (FTIR with Fourier self-deconvolution,  $^1\text{H}$  MAS NMR at 800 MHz – DEPTH and DQ-BABA, periodic DFT calculations of spectroscopic feature on up-to-date external surface models), analyzing the effect of crystallite size, so as to provide a description of the various kinds hydroxyl groups and of their proximities, with an unequaled level of detail. The effect of extra-framework is also discussed.

Computational and experimental observations appear to be fully consistent, leading to a refined assignment of the spectra. The complexity of the latter is revealed, at variance with oversimplified previous assignments. Behind a single line, very often several kinds of hydroxyls are hidden. FTIR and  $^1\text{H}$  MAS NMR appear to be strongly complementary in that respect. Even if the hydrogen-bond donor, acceptor or isolated nature of the hydroxyls is key for both spectroscopies, the peak distribution is not the same from one technique to the other when the chemical nature of the hydroxyl changes. Bridging Si-(OH)-Al groups and Al-(H<sub>2</sub>O) lead to overlapping signals in 1D  $^1\text{H}$  MAS NMR (but deciphered thanks to 2D  $^1\text{H}$  MAS NMR), whereas their resonances are strongly different in IR. Bridging OH groups belonging to 2MR sites appear in the same line as other bridging OH groups in NMR, whereas they exhibit a higher frequency in infrared. Thus, qualifying the hydroxyl groups is somewhat easier in infrared, whereas quantification and proximity assessment are obtained thanks to  $^1\text{H}$  NMR only.

On the basis of our DFT calculations, assignments are revisited with respect to previously published spectroscopic data. Whereas we confirm previous proposals with regard to silanols and Si-(OH)-Al bridging OH groups, we observe that other signals (between 3750 and 3600  $\text{cm}^{-1}$ , and between 1 and 4 ppm) are not only assigned to extra-framework species (which we confirm with dedicated models), but also enclose the signature of several types of sites exposed at the external surface of ZSM-5. In particular, Al-(H<sub>2</sub>O) species ( $\sim 3665$   $\text{cm}^{-1}$ , 3.8, 2.6 ppm) and Silanol-Al ( $\sim 3740$ , 3720, 3665  $\text{cm}^{-1}$ , 2.6, 2.2 ppm) contribute to several signals depending on their environment.  $\mu_1$ -Al-OH are also present at the external surface in low amount, with a 3780  $\text{cm}^{-1}$  signal in IR, and weak signals in the 0-2 ppm interval in  $^1\text{H}$  NMR.

This work provides a refined analysis of the external surface of ZSM-5, paving the way for the analysis of any zeolite and aluminosilicate, and opening the door to the investigation of structure-activity-reactivity relationships for the many hydroxyls groups present on such systems.

## References

- (1) Vermeiren, W.; Gilson, J. P., Impact of Zeolites on the Petroleum and Petrochemical Industry, *Topics Catal.* **2009**, *52*, 1131-1161.
- (2) Marcilly, C. *Acido-Basic Catalysis*; Technip: Paris, 2005.
- (3) Bertoni, F.; Bonduelle-Skrzypczak, A.; Francis, J.; Guillon, E., Hydrocracking, In *Catalysis by transition metal sulphides: from molecular theory to industrial applications*; Toulhoat, H., Raybaud, P., Eds.; Editions Technip: 2013, p 609-677.
- (4) Ennaert, T.; Van Aelst, J.; Dijkmans, J.; De Clercq, R.; Schutyser, W.; Dusselier, M.; Verboekend, D.; Sels, B. F., Potential and Challenges of Zeolite Chemistry in the Catalytic Conversion of Biomass, *Chem. Soc. Rev.* **2016**, *45*, 584-611.
- (5) Deka, U.; Lezcano-Gonzalez, I.; Weckhuysen, B. M.; Beale, A. M., Local Environment and Nature of Cu Active Sites in Zeolite-Based Catalysts for the Selective Catalytic Reduction of NO<sub>x</sub>, *ACS Catal.* **2013**, *3*, 413-427.
- (6) Borfecchia, E.; Beato, P.; Svelle, S.; Olsbye, U.; Lamberti, C.; Bordiga, S., Cu-CHA – A Model System for Applied Selective Redox Catalysis, *Chem. Soc. Rev.* **2018**, *47*, 8097-8133.
- (7) Argauer, R. J.; Landolt, G. R.; Mobil Oil Corporation: US 3702886, 1972.
- (8) Roeffaers, M. B. J.; Ameloot, R.; Bons, A.-J.; Mortier, W.; De Cremer, G.; de Kloe, R.; Hofkens, J.; De Vos, D. E.; Sels, B. F., Relating Pore Structure to Activity at the Subcrystal Level for ZSM-5: An Electron Backscattering Diffraction and Fluorescence Microscopy Study, *J. Am. Chem. Soc.* **2008**, *130*, 13516-13517.
- (9) Roeffaers, M. B. J.; Ameloot, R.; Baruah, M.; Uji-i, H.; Bulut, M.; De Cremer, G.; Müller, U.; Jacobs, P. A.; Hofkens, J.; Sels, B. F.; De Vos, D. E., Morphology of Large ZSM-5 Crystals Unraveled by Fluorescence Microscopy, *J. Am. Chem. Soc.* **2008**, *130*, 5763–5772.
- (10) Roeffaers, M. B. J.; Sels, B. F.; Uji-i, H.; Blanpain, B.; L'Hoëst, P.; Jacobs, P. A.; De Schryver, F. C.; Hofkens, J.; De Vos, D. E., Space- and Time-Resolved Visualization of Acid Catalysis in ZSM-5 Crystals by Fluorescence Microscopy, *Angew. Chem. Int. Ed.* **2007**, *46*, 1706-1709.
- (11) Karwacki, L.; de Winter, D. A. M.; Aramburo, L. R.; Lebbink, M. N.; Post, J. A.; Drury, M. R.; Weckhuysen, B. M., Architecture-Dependent Distribution of Mesopores in Steamed Zeolite Crystals as Visualized by FIB-SEM Tomography, *Angew. Chem. Int. Ed.* **2011**, *50*, 1294-1298.
- (12) Karwacki, L.; Kox, M. H. F.; Matthijs de Winter, D. A.; Drury, M. R.; Meeldijk, J. D.; Stavitski, E.; Schmidt, W.; Mertens, M.; Cubillas, P.; John, N.; Chan, A.; Kahn, N.; Bare, S. R.; Anderson, M.; Kornatowski, J.; Weckhuysen, B. M., Morphology-Dependent Zeolite Intergrowth Structures Leading to Distinct Internal and Outer-Surface Molecular Diffusion Barriers, *Nat. Mater.* **2009**, *8*, 959.
- (13) Choi, M.; Na, K.; Kim, J.; Sakamoto, Y.; Terasaki, O.; Ryoo, R., Stable Single-Unit-Cell Nanosheets of Zeolite MFI as Active and Long-Lived Catalysts, *Nature* **2009**, *461*, 246-249.
- (14) Varoon, K.; Zhang, X.; Elyassi, B.; Brewer, D. D.; Gettel, M.; Kumar, S.; Lee, J. A.; Maheshwari, S.; Mittal, A.; Sung, C.-Y.; Cococcioni, M.; Francis, L. F.; McCormick, A. V.; Mkhoyan, K. A.; Tsapatsis, M., Dispersible Exfoliated Zeolite Nanosheets and Their Application as a Selective Membrane, *Science* **2011**, *334*, 72.

- (15) Roth, W. J.; Nachtigall, P.; Morris, R. E.; Čejka, J., Two-Dimensional Zeolites: Current Status and Perspectives, *Chem. Rev.* **2014**, *114*, 4807-4837.
- (16) Grand, J.; Talapaneni, S. N.; Vicente, A.; Fernandez, C.; Dib, E.; Aleksandrov, H. A.; Vayssilov, G. N.; Retoux, R.; Boullay, P.; Gilson, J.-P.; Valtchev, V.; Mintova, S., One-Pot Synthesis of Silanol-Free Nanosized MFI Zeolite, *Nat. Mater.* **2017**, *16*, 1010-1015.
- (17) Mintova, S.; Jaber, M.; Valtchev, V., Nanosized Microporous Crystals: Emerging Applications, *Chem. Soc. Rev.* **2015**, *44*, 7207-7233.
- (18) Haw, K.-G.; Gilson, J.-P.; Nesterenko, N.; Akouche, M.; El Siblani, H.; Goupil, J.-M.; Rigaud, B.; Minoux, D.; Dath, J.-P.; Valtchev, V., Supported Embryonic Zeolites and their Use to Process Bulky Molecules, *ACS Catal.* **2018**, *8*, 8199-8212.
- (19) Haw, K.-G.; Goupil, J.-M.; Gilson, J.-P.; Nesterenko, N.; Minoux, D.; Dath, J.-P.; Valtchev, V., Embryonic ZSM-5 Zeolites: Zeolitic Materials with Superior Catalytic Activity in 1,3,5-Triisopropylbenzene Dealkylation, *New J. Chem.* **2016**, *40*, 4307-4313.
- (20) Martens, J. A.; Vanbutsele, G.; Jacobs, P. A.; Denayer, J.; Ocakoglu, R.; Baron, G.; Muñoz Arroyo, J. A.; Thybaut, J.; Marin, G. B., Evidences for Pore Mouth and Key-Lock Catalysis in Hydroisomerization of Long n-Alkanes over 10-Ring Tubular Pore Bifunctional Zeolites, *Catal. Today* **2001**, *65*, 111-116.
- (21) Martens, J. A.; Souverijns, W.; Verrelst, W.; Parton, R.; Froment, G. F.; Jacobs, P. A., Selective Isomerization of Hydrocarbon Chains on External Surfaces of Zeolite Crystals, *Angew. Chem. Int. Ed.* **1995**, *34*, 2528-2530.
- (22) Radhakrishnan, S.; Goossens, P. J.; Magusin, P. C.; Sree, S. P.; Detavernier, C.; Breynaert, E.; Martineau, C.; Taulelle, F.; Martens, J. A., In Situ Solid-State <sup>13</sup>C NMR Observation of Pore Mouth Catalysis in Etherification of beta-Citronellene with Ethanol on Zeolite Beta, *J. Am. Chem. Soc.* **2016**, *138*, 2802-2808.
- (23) Moreau, F.; Moreau, P.; Gnep, N. S.; Magnoux, P.; Lacombe, S.; Guisnet, M., Ethylbenzene Isomerization over Bifunctional Platinum Alumina-EUO Catalysts: Location of the Active Sites, *Microporous Mesoporous Mater.* **2006**, *90*, 327-338.
- (24) Zecevic, J.; Vanbutsele, G.; de Jong, K. P.; Martens, J. A., Nanoscale Intimacy in Bifunctional Catalysts for Selective Conversion of Hydrocarbons, *Nature* **2015**, *528*, 245-248.
- (25) Chizallet, C., Towards the Atomic Scale Simulation of Intricate Zeolitic Acidic Catalysts, *ACS Catal.* **2020**.
- (26) Rey, J.; Raybaud, P.; Chizallet, C., Ab Initio Simulation of the Acid Sites at the External Surface of Zeolite Beta, *ChemCatChem* **2017**, *9*, 2176-2185.
- (27) Treps, L.; Gomez, A.; De Bruin, T.; Chizallet, C., Environment, Stability and Acidity of External Surface Sites of Silicalite-1 and ZSM-5 Micro- and Nano-Slabs, -Sheets and -Crystals, *ACS Catal.* **2020**, *10*, 3297-3312.
- (28) Chizallet, C.; Raybaud, P., Acidity of Amorphous Silica-Alumina: From Coordination Promotion of Lewis Sites to Proton Transfer, *ChemPhysChem* **2010**, *11*, 105-108.
- (29) Leydier, F.; Chizallet, C.; Chaumonnot, A.; Digne, M.; Soyer, E.; Quoineaud, A. A.; Costa, D.; Raybaud, P., Brønsted Acidity of Amorphous Silica-Alumina: The Molecular Rules of Proton Transfer, *J. Catal.* **2011**, *284*, 215-229.

- (30) Hadjiivanov, K., Chapter Two - Identification and Characterization of Surface Hydroxyl Groups by Infrared Spectroscopy, In *Adv. Catal.*; Jentoft, F. C., Ed.; Academic Press: 2014; Vol. 57, p 99-318.
- (31) Bordiga, S.; Lamberti, C.; Bonino, F.; Travert, A.; Thibault-Starzyk, F., Probing Zeolites by Vibrational Spectroscopies, *Chem. Soc. Rev.* **2015**, *44*, 7262-7341.
- (32) Védrine, J. C.; Auroux, A.; Bolis, V.; Dejaifve, P.; Naccache, C.; Wierzchowski, P.; Derouane, E. G.; Nagy, J. B.; Gilson, J.-P.; van Hooff, J. H. C.; van den Berg, J. P.; Wolthuizen, J., Infrared, Microcalorimetric, and Electron Spin Resonance Investigations of the Acidic Properties of the H-ZSM-5 Zeolite, *J. Catal.* **1979**, *59*, 248-262.
- (33) Topsøe, N.-Y.; Pedersen, K.; Derouane, E. G., Infrared and Temperature-Programmed Desorption Study of the Acidic Properties of ZSM-5-Type Zeolites, *J. Catal.* **1981**, *70*, 41-52.
- (34) Jacobs, P. A.; Von Ballmoos, R., Framework Hydroxyl Groups of H-ZSM-5 Zeolites, *J. Phys. Chem.* **1982**, *86*, 3050-3052.
- (35) Datka, J.; Gil, B.; Baran, P., Heterogeneity of OH Groups in HZSM-5 Zeolites: Splitting of OH and OD Bands in Low-Temperature IR Spectra, *Microporous Mesoporous Mater.* **2003**, *58*, 291-294.
- (36) Armaroli, T.; Simon, L. J.; Digne, M.; Montanari, T.; Bevilacqua, M.; Valtchev, V.; Patarin, J.; Busca, G., Effects of Crystal Size and Si/Al Ratio on the Surface Properties of H-ZSM-5 Zeolites, *Appl. Catal. A* **2006**, *306*, 78-84.
- (37) Zecchina, A.; Bordiga, S.; Spoto, G.; Marchese, L.; Petrini, G.; Leofanti, G.; Padovan, M., Silicalite Characterization. 2. IR Spectroscopy of the Interaction of Carbon Monoxide with Internal and External Hydroxyl Groups, *J. Phys. Chem.* **1992**, *96*, 4991-4997.
- (38) Lonstad Bleken, B.-T.; Mino, L.; Giordanino, F.; Beato, P.; Svelle, S.; Lillerud, K. P.; Bordiga, S., Probing the Surface of Nanosheet H-ZSM-5 with FTIR Spectroscopy, *Phys. Chem. Chem. Phys.* **2013**, *15*, 13363-13370.
- (39) Holm, M. S.; Svelle, S. J. F.; Beato, P.; Christensen, C. H.; Bordiga, S.; Bjørgen, M., Assessing the Acid Properties of Desilicated ZSM-5 by FTIR using CO and 2,4,6-Trimethylpyridine (Collidine) as Molecular Probes, *Appl. Catal. A* **2009**, *356*, 23-30.
- (40) Brus, J.; Kobera, L.; Schoefberger, W.; Urbanova, M.; Klein, P.; Sazama, P.; Tabor, E.; Sklenak, S.; Fishchuk, A. V.; Dedecek, J., Structure of Framework Aluminum Lewis sites and Perturbed Aluminum atoms in Zeolites as Determined by  $^{27}\text{Al}\{^1\text{H}\}$  REDOR (3Q) MAS NMR Spectroscopy and DFT/Molecular Mechanics, *Angew. Chem. Int. Ed.* **2015**, *54*, 541-545.
- (41) Osuga, R.; Yokoi, T.; Doitomi, K.; Hirao, H.; Kondo, J. N., Infrared Investigation of Dynamic Behavior of Brønsted Acid Sites on Zeolites at High Temperatures, *J. Phys. Chem. C* **2017**, *121*, 25411-25420.
- (42) Losch, P.; Joshi, H. R.; Vozniuk, O.; Grunert, A.; Ochoa-Hernandez, C.; Jabraoui, H.; Badawi, M.; Schmidt, W., Proton Mobility, Intrinsic Acid Strength and Acid Site Location in Zeolites Revealed by VTIR and DFT Studies, *J. Am. Chem. Soc.* **2018**.
- (43) Hoffmann, P.; Lobo, J. A., Identification of Diverse Silanols on Protonated ZSM-5 Zeolites by Means of FTIR Spectroscopy, *Microporous Mesoporous Mater.* **2007**, *106*, 122-128.

- (44) Dessau, R. M.; Schmitt, K. D.; Kerr, G. T.; Woolery, G. L.; Alemany, L. B., On the Presence of Internal Silanol Groups in ZSM-5 and the Annealing of these Sites by Steaming, *J. Catal.* **1987**, *104*, 484-489.
- (45) Crépeau, G.; Montouillout, V.; Vimont, A.; Mariey, L.; Cseri, T.; Maugé, F., Nature, Structure and Strength of the Acidic Sites of Amorphous Silica Alumina: an IR and NMR Study, *J. Phys. Chem. B* **2006**, *110*, 15172-15185.
- (46) Zholobenko, V.; Freitas, C.; Jendrlin, M.; Bazin, P.; Travert, A.; Thibault-Starzyk, F., Probing the acid sites of zeolites with pyridine: Quantitative AGIR measurements of the molar absorption coefficients, *J. Catal.* **2020**, *385*, 52-60.
- (47) Freude, D.; Hunger, M.; Pfeifer, H.; Schwieger, W.,  $^1\text{H}$  MAS NMR Studies on the Acidity of Zeolites, *Chem. Phys. Lett.* **1986**, *128*, 62-66.
- (48) Engelhardt, G.; Jerschke, H. G.; Lohse, U.; Sarv, P.; Samoson, A.; Lippmaa, E., 500 MHz  $^1\text{H}$ -MAS N.M.R. Studies of Dealuminated HZSM-5 Zeolites, *Zeolites* **1987**, *7*, 289-292.
- (49) Beck, L. W.; White, J. L.; Haw, J. F.,  $^1\text{H}\{^{27}\text{Al}\}$  Double-Resonance Experiments in Solids: An Unexpected Observation in the  $^1\text{H}$  MAS Spectrum of Zeolite HZSM-5, *J. Am. Chem. Soc.* **1994**, *116*, 9657-9661.
- (50) Freude, D., Enhanced Resolution in the  $^1\text{H}$  NMR Spectra of Zeolite H-ZSM-5 by Heteronuclear Dipolar-Dephasing Spin-Echo MAS, *Chem. Phys. Lett.* **1995**, *235*, 69-75.
- (51) Hunger, M., Multinuclear Solid-State NMR Studies of Acidic and Non-Acidic Hydroxyl Protons in Zeolites, *Solid State Nucl. Magn. Reson.* **1996**, *6*, 1-29.
- (52) Brunner, E.; Beck, K.; Koch, M.; Heeribout, L.; Karge, H. G., Verification and Quantitative Determination of a New Type of Brønsted Acid Sites in H-ZSM-5 by  $^1\text{H}$  Magic-Angle Spinning Nuclear Magnetic Resonance Spectroscopy, *Micropor. Mater.* **1995**, *3*, 395-399.
- (53) Baba, T.; Ono, Y., Dynamic Properties of Protons in Solid Acids as Studied by Variable Temperature  $^1\text{H}$  MAS NMR, *Appl. Catal. A* **1999**, *181*, 227-238.
- (54) Huo, H.; Peng, L.; Grey, C. P., Low Temperature  $^1\text{H}$  MAS NMR Spectroscopy Studies of Proton Motion in Zeolite HZSM-5, *J. Phys. Chem. C* **2009**, *113*, 8211-8219.
- (55) Louis, B.; Vicente, A. I.; Fernandez, C.; Valtchev, V., Crystal Size–Acid Sites Relationship Study of Nano- and Micrometer-Sized Zeolite Crystals, *J. Phys. Chem. C* **2011**, *115*, 18603-18610.
- (56) Wang, M.; Jaegers, N. R.; Lee, M. S.; Wan, C.; Hu, J. Z.; Shi, H.; Mei, D.; Burton, S. D.; Camaioni, D. M.; Gutierrez, O. Y.; Glezakou, V. A.; Rousseau, R.; Wang, Y.; Lercher, J. A., Genesis and Stability of Hydronium Ions in Zeolite Channels, *J. Am. Chem. Soc.* **2019**, *141*, 3444-3455.
- (57) Poirier, M.; Millot, Y.; Silva Gomes, E.; Jaber, M.; Herledan, V.; Laugel, G.; Micoud, P.; Martin, F.; Lauron-Pernot, H.; Toulhoat, H., Complementarity of Density Functional Theory and Nuclear Magnetic Resonance Tools To Probe the Nano-Layered Silicates Surface Chemistry and Morphology, *J. Phys. Chem. C* **2019**, *124*, 267-286.
- (58) Hunger, M., Brønsted Acid Sites in Zeolites Characterized by Multinuclear Solid-State NMR Spectroscopy, *Catal. Rev.* **1997**, *39*, 345-393.
- (59) Deng, F.; Yue, Y.; Ye, C.,  $^1\text{H}/^{27}\text{Al}$  TRAPDOR NMR Studies on Aluminum Species in Dealuminated Zeolites, *Solid State Nucl. Magn. Reson.* **1998**, *10*, 151-160.



- (60) Seiler, M.; Wang, W.; Hunger, M., Local Structure of Framework Aluminum in Zeolite H-ZSM-5 during Conversion of Methanol Investigated by In Situ NMR Spectroscopy, *J. Phys. Chem. B* **2001**, *105*, 8143-8148.
- (61) Chen, K.; Abdolrhamani, M.; Sheets, E.; Freeman, J.; Ward, G.; White, J. L., Direct Detection of Multiple Acidic Proton Sites in Zeolite HZSM-5, *J. Am. Chem. Soc.* **2017**, *139*, 18698-18704.
- (62) Chen, K.; Horstmeier, S.; Nguyen, V. T.; Wang, B.; Crossley, S. P.; Pham, T.; Gan, Z.; Hung, I.; White, J. L., Structure and Catalytic Characterization of a Second Framework Al(IV) Site in Zeolite Catalysts Revealed by NMR at 35.2 T, *J. Am. Chem. Soc.* **2020**.
- (63) Paul, G.; Bisio, C.; Braschi, I.; Cossi, M.; Gatti, G.; Gianotti, E.; Marchese, L., Combined Solid-State NMR, FT-IR and Computational Studies on Layered and Porous Materials, *Chem. Soc. Rev.* **2018**, *47*, 5684-5739.
- (64) Brown, S. P.; Spiess, H. W., Advanced Solid-State NMR Methods for the Elucidation of Structure and Dynamics of Molecular, Macromolecular, and Supramolecular Systems, *Chem. Rev.* **2001**, *101*, 4125-4156.
- (65) Yu, Z.; Li, S.; Wang, Q.; Zheng, A.; Jun, X.; Chen, L.; Deng, F., Brønsted/Lewis Acid Synergy in H-ZSM-5 and H-MOR Zeolites Studied by  $^1\text{H}$  and  $^{27}\text{Al}$  DQ-MAS Solid-State NMR Spectroscopy, *J. Phys. Chem. C* **2011**, *115*, 22320-22327.
- (66) Xue, N.; Vjunov, A.; Schallmoser, S.; Fulton, J. L.; Sanchez-Sanchez, M.; Hu, J. Z.; Mei, D.; Lercher, J. A., Hydrolysis of Zeolite Framework Aluminum and its Impact on Acid Catalyzed Alkane Reactions, *J. Catal.* **2018**, *365*, 359-366.
- (67) Bonhomme, C.; Gervais, C.; Babonneau, F.; Coelho, C.; Pourpoint, F.; Azais, T.; Ashbrook, S. E.; Griffin, J. M.; Yates, J. R.; Mauri, F.; Pickard, C. J., First-Principles Calculation of NMR Parameters Using the Gauge Including Projector Augmented Wave Method: A Chemist's Point of View, *Chem Rev* **2012**, *112*, 5733-5779.
- (68) Bucko, T.; Benco, L.; Hafner, J., Defect Sites at the (001) Surface of Mordenite: An Ab Initio Study, *J. Chem. Phys.* **2003**, *118*, 8437-8445.
- (69) Bucko, T.; Benco, L.; Demuth, T.; Hafner, J., Ab Initio Density Functional Investigation of the (001) Surface of Mordenite, *J. Chem. Phys.* **2002**, *117*, 7295-7305.
- (70) Batista, A. T. F.; Wisser, D.; Pigeon, T.; Gajan, D.; Diehl, F.; Rivallan, M.; Catita, L.; Gay, A.-S.; Lesage, A.; Chizallet, C.; Raybaud, P., Beyond  $\gamma\text{-Al}_2\text{O}_3$  crystallite surfaces: The hidden features of edges revealed by solid-state  $^1\text{H}$  NMR and DFT calculations, *J. Catal.* **2019**, *378*, 140-143.
- (71) Chizallet, C.; Costentin, G.; Lauron-Pernot, H.; Che, M.; Bonhomme, C.; Maquet, J.; Delbecq, F.; Sautet, P., 1D and 2D  $^1\text{H}$  MAS NMR Structural Investigation of OH Groups on MgO by a Combination of Experiments and Theory, *J. Phys. Chem. C* **2007**, *111*, 18279-18287.
- (72) Chizallet, C.; Costentin, G.; Che, M.; Delbecq, F.; Sautet, P., Infra-Red Characterization of Hydroxyl Groups on MgO: a Periodic and Cluster DFT Study, *J. Am. Chem. Soc.* **2007**, *129*, 6442-6452.
- (73) Digne, M.; Sautet, P.; Raybaud, P.; Euzen, P.; Toulhoat, H., Use of DFT to Achieve a Rational Understanding of Acid-Basic Properties of Gamma-Alumina Surfaces, *J. Catal.* **2004**, *226*, 54-68.

- (74) Arrouvel, C.; Digne, M.; Breysse, M.; Toulhoat, H.; Raybaud, P., Effects of Morphology on Surface Hydroxyl Concentration: a DFT Comparison of Anatase-TiO<sub>2</sub> and  $\gamma$ -Alumina Catalytic Supports, *J. Catal.* **2004**, *222*, 152-166.
- (75) Tielens, F.; Gervais, C.; Lambert, J. F.; Mauri, F.; Costa, D., Ab Initio Study of the Hydroxylated Surface of Amorphous Silica: A Representative Model, *Chem. Mater.* **2008**, *20*, 3336-3344.
- (76) Sastre, G.; Katada, N.; Niwa, M., Computational Study of Brønsted Acidity of Mordenite. Effect of the Electric Field on the Infrared OH Stretching Frequencies, *J. Phys. Chem. C* **2010**, *114*, 15424-15431.
- (77) Islam, M. M.; Costa, D.; Calatayud, M.; Tielens, F., Characterization of Supported Vanadium Oxide Species on Silica: A Periodic DFT Investigation, *J. Phys. Chem. C* **2009**, *113*, 10740-10746.
- (78) Tosoni, S.; Pascale, F.; Ugliengo, P.; Orlando, R.; Saunders, V. R.; Dovesi, R., Quantum Mechanical Calculation of the OH Vibrational Frequency in Crystalline Solids, *Mol. Phys.* **2005**, *103*, 2549-2558.
- (79) Mortier, W. J.; Sauer, J.; Lercher, J. A.; Noller, H., Bridging and Terminal Hydroxyls. A Structural Chemical and Quantum Chemical Discussion, *J. Phys. Chem.* **1984**, *88*, 905-912.
- (80) Fleischer, U.; Kutzelnigg, W.; Bleiber, A.; Sauer, J., <sup>1</sup>H NMR Chemical Shift and Intrinsic Acidity of Hydroxyl Groups. Ab Initio Calculations on Catalytically Active Sites and Gas-Phase Molecules, *J. Am. Chem. Soc.* **1993**, *115*, 7833-7838.
- (81) Silaghi, M.-C.; Chizallet, C.; Raybaud, P., Challenges on Molecular Aspects of Dealumination and Desilication of Zeolites, *Microporous Mesoporous Mater.* **2014**, *191*, 82-96.
- (82) Silaghi, M.-C.; Chizallet, C.; Sauer, J.; Raybaud, P., Dealumination Mechanisms of Zeolites and Extra-Framework Aluminum Confinement, *J. Catal.* **2016**, *339*, 242-255.
- (83) Perdew, J.; Burke, K.; Ernzerhof, M., Generalized Gradient Approximation Made Simple, *Phys. Rev. Lett.* **1996**, *77*, 3865-3868.
- (84) Kresse, G.; Hafner, J., Ab Initio Molecular-Dynamics Simulation of the Liquid-Metal-Amorphous-Semiconductor Transition in Germanium, *Phys. Rev. B* **1994**, *49*, 14251-14269.
- (85) Kresse, G.; Furthmüller, J., Efficiency of Ab-Initio Total Energy Calculations for Metals and Semiconductors using a Plane-Wave Basis Set, *Comput. Mat. Sci.* **1996**, *6*, 15-50.
- (86) Kresse, G.; Joubert, D., From ultrasoft pseudopotentials to the projector augmented-wave method, *Phys. Rev. B* **1999**, *59*, 1758-1775.
- (87) Steinmann, S. N.; Corminboeuf, C., Comprehensive Benchmarking of a Density-Dependent Dispersion Correction, *J Chem Theory Comput* **2011**, *7*, 3567-3577.
- (88) Baerlocher, C.; McCusker, J. K., *Database of Zeolite Structures*: <http://www.iza-structure.org/databases/>.
- (89) Wu, E. L.; Lawton, S. L.; Olson, D. H.; Rohrman, A. C.; Kokotailo, G. T., ZSM-5-Type Materials. Factors Affecting Crystal Symmetry, *J. Phys. Chem.* **1979**, *83*, 2777-2781.
- (90) Olson, D. H.; Kokotailo, G. T.; Lawton, S. L.; Meier, W. M., Crystal Structure and Structure-Related Properties of ZSM-5, *J. Phys. Chem.* **1981**, *85*, 2238-2243.
- (91) Koegler, J. H.; van Bekkum, H.; Jansen, J. C., Growth Model of Oriented Crystals of Zeolite Si-ZSM-5, *Zeolites* **1997**, *19*, 262-269.

- (92) Zeng, G.; Chen, C.; Li, D.; Hou, B.; Sun, Y., Exposure of (001) Planes and (011) Planes in MFI Zeolite, *CrystEngComm* **2013**, *15*, 3521-3524.
- (93) Yates, J. R.; Pickard, C. J.; Mauri, F., Calculation of NMR Chemical Shifts for Extended Systems using Ultrasoft Pseudopotentials, *Phys. Rev. B* **2007**, *76*, 024401:024401-024411.
- (94) Pickard, C. J.; Mauri, F., All-Electron Magnetic Response with Pseudopotentials: NMR Chemical Shifts, *Phys. Rev. B* **2001**, *63*, 245101.
- (95) Robin Bendall, M.; Gordon, R. E., Depth and Refocusing Pulses Designed for Multipulse NMR with Surface Coils, *J. Magn. Reson.* **1983**, *53*, 365-385.
- (96) Bendall, M. R.; Pegg, D. T., Theoretical Description of Depth Pulse Sequences, On and Off Resonance, Including Improvements and Extensions Thereof, *Magn. Reson. Med.* **1985**, *2*, 91-113.
- (97) Cory, D. G.; Ritchey, W. M., Suppression of Signals from the Probe in Bloch Decay Spectra, *J. Magn. Reson.* **1988**, *80*, 128-132.
- (98) Massiot, D.; Fayon, F.; Capron, M.; King, I.; Le Calvé, S.; Alonso, B.; Durand, J. O.; Bujoli, B.; Gan, Z.; Hoatson, G., Modelling One- and Two-Dimensional Solid-State NMR Spectra, *Magn. Reson. Chem.* **2002**, *40*, 70-76.
- (99) Sommer, W.; Gottwald, J.; Demco, D. E.; Spiess, H. W., Dipolar Heteronuclear Multiple-Quantum NMR Spectroscopy in Rotating Solids, *J. Magn. Reson. A* **1995**, *113*, 131-134.
- (100) Hernandez-Tamargo, C. E.; Roldan, A.; de Leeuw, N. H., A Density Functional Theory Study of the Structure of Pure-Silica and Aluminium-Substituted MFI Nanosheets, *J. Solid State Chem.* **2016**, *237*, 192-203.
- (101) Song, W.; Justice, R. E.; Jones, C. A.; Grassian, V. H.; Larsen, S. C., Size-Dependent Properties of Nanocrystalline Silicalite Synthesized with Systematically Varied Crystal Sizes, *Langmuir* **2004**, *20*, 4696-4702.
- (102) Vazhnova, T.; Lukyanov, D. B., Fourier Self-Deconvolution of the IR Spectra as a Tool for Investigation of Distinct Functional Groups in Porous Materials: Brønsted Acid Sites in Zeolites, *Anal. Chem.* **2013**, *85*, 11291-11296.
- (103) Chizallet, C.; Digne, M.; Arrouvel, C.; Raybaud, P.; Delbecq, F.; Costentin, G.; Che, M.; Sautet, P.; Toulhoat, H., Insights into the Geometry, Stability and Vibrational Properties of OH Groups on  $\gamma$ -Al<sub>2</sub>O<sub>3</sub>, TiO<sub>2</sub>-Anatase and MgO from DFT Calculations, *Topics Catal.* **2009**, *52*, 1005-1016.
- (104) Jones, A. J.; Iglesia, E., The Strength of Brønsted Acid Sites in Microporous Aluminosilicates, *ACS Catal.* **2015**, *5*, 5741-5755.
- (105) Loeffler, E.; Lohse, U.; Peuker, C.; Oehlmann, G.; Kustov, L. M.; Zholobenko, V. L.; Kazansky, V. B., Study of Different States of Nonframework Aluminum in Hydrothermally Dealuminated HZSM-5 Zeolites using Diffuse Reflectance i.r. Spectroscopy, *Zeolites* **1990**, *10*, 266-271.
- (106) Jia, C.; Massiani, P.; Barthomeuf, D., Characterization by Infrared and Nuclear Magnetic Resonance Spectroscopies of Calcined Beta Zeolite, *J. Chem. Soc., Faraday Trans.* **1993**, *89*, 3659-3665.
- (107) Zecchina, A.; Bordiga, S.; Spoto, G.; Scarano, D.; Petrini, G.; Leofanti, G.; Padovan, M.; Areà, C. O., Low-Temperature Fourier-Transform Infrared Investigation of the

Interaction of CO with Nanosized ZSM5 and Silicalite, *J. Chem. Soc., Faraday Trans.* **1992**, *88*, 2959-2969.

(108) Digne, M.; Sautet, P.; Raybaud, P.; Euzen, P.; Toulhoat, H., Hydroxyl Groups on Gamma-Alumina Surfaces: a DFT Study, *J. Catal.* **2002**, *211*, 1-5.

(109) Zholobenko, V. L.; Kustov, L. M.; Kazansky, V. B.; Loeffler, E.; Lohser, U.; Peuker, C.; Oehlmann, G., On the Possible Nature of Sites Responsible for the Enhancement of Cracking Activity of HZSM-5 Zeolites Dealuminated under Mild Steaming Conditions, *Zeolites* **1990**, *10*, 304-306.

(110) Szanyi, J.; Paffett, M. T., The Adsorption of Carbon Monoxide on H-ZSM-5 and Hydrothermally Treated H-ZSM-5, *Micropor. Mater.* **1996**, *7*, 201-218.

(111) Vimont, A.; Lavalley, J. C.; Thibault-Starzyk, F., Infrared Spectroscopic Study of the Acidobasic Properties of Beta Zeolite, *J. Phys. Chem. B* **2000**, *104*, 286-291.

(112) Zecchina, A.; Geobaldo, F.; Spoto, G.; Bordiga, S.; Ricchiardi, G.; Buzzoni, R.; Petrini, G., FTIR Investigation of the Formation of Neutral and Ionic Hydrogen-Bonded Complexes by Interaction of H-ZSM-5 and H-Mordenite with CH<sub>3</sub>CN and H<sub>2</sub>O: Comparison with the H-NAFION Superacidic System, *J. Phys. Chem.* **1996**, *100*, 16584-16599.

(113) Jiao, J.; Altwasser, S.; Wang, W.; Weitkamp, J.; Hunger, M., State of Aluminum in Dealuminated, Nonhydrated Zeolites Y Investigated by Multinuclear Solid-State NMR Spectroscopy, *J. Phys. Chem. B* **2004**, *108*, 14305-14310.

## Chapter 5. Interaction of the acid sites with probe molecules and simple models of binder components

The previous chapters focused on the study of the external surface of H-ZSM-5. Preliminary results about the possible interactions of these surfaces with pyridine, that behaves as an acid/base probe molecule, were presented in Chapter 3. In Chapter 4, preliminary results dealing with the interaction with alumina or silica monomers was given, as well as the NMR and IR signals they produce. In this chapter, these interactions are going to be studied in detail. The acidic characteristics of the aluminated site are therein studied with the adsorption of pyridine, and 2,6-ditertbutylpyridine (DTBPy) at the external surface and in the bulk of the H-ZSM-5. As the acidity of the aluminated sites is defined, then the interaction with other components present in the shaping step are presented. The calculations, dealing with the interaction with sodium (present in silica binders), provide some clarifications on the experimental data generated by Demaret *et al.*<sup>1</sup> Then the interaction of H-ZSM-5 surface and bulk with monomers of binders,  $\text{Al}(\text{OH})_3\text{H}_2\text{O}$  and  $\text{Si}(\text{OH})_4$ , are studied in detail.

### 5.1. Acidity of the aluminated sites

The aluminated sites of zeolites generate acid sites with various strengths. The strength of these various acid sites was quantified by simulating the adsorption energy of pyridine and 2,6-ditertbutylpyridine (DTBPy) on Lewis Acid Sites (LAS) and Brønsted Acid Sites (BAS) according to three binding modes: formation of a N-Al bond (in an anti-position with respect to the BAS, as an example of LAS), protonation of the probe molecules and formation of hydrogen bonds (at BAS) (Figure 1). The formation of an hydrogen bond as in Figure 1 c is observed only once for pyridine adsorption in all the calculation configurations sampled and is not the most stable adsorption mode of pyridine. The two molecules are probes for the acid sites but the DTBPy is considered to be selective to the acid sites of the external surface due to the tertbutyl groups, which make this substituted pyridine too large to enter the pores inside the ZSM-5 crystals.<sup>2</sup>

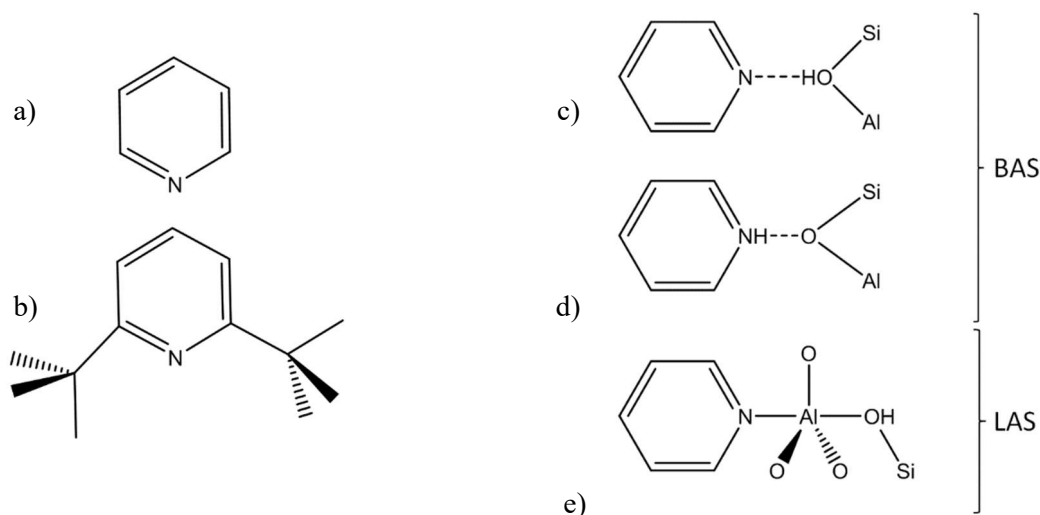


**Figure 1:** a) Pyridine; b) 2,6-ditertbutylpyridine; Adsorption modes on acid sites: c) formation of hydrogen bond (BAS); d) protonation of the probe molecule (BAS); e) formation of a N-Al bond (LAS) in an anti-position with respect to the bridging OH group.

The difference of strength between the different acid sites is quantified by calculating the adsorption energy of the probe molecules presented in Equation 1.

$$\Delta_{ads}U_{pyr} = U_{surf\_pyr} - U_{surf} - U_{pyr} \quad \text{Equation 1}$$

where  $\Delta_{ads}U_{pyr}$  is the pyridine (or the 2,6-ditertbutylpyridine) adsorption energy,  $U_{surf\_pyr}$  is the electronic free energy of the pyridine (or the 2,6-ditertbutylpyridine) adsorbed on the surface,  $U_{surf}$  is the electronic free energy of the surface and  $U_{pyr}$  is the electronic free energy of the pyridine (or the 2,6-ditertbutylpyridine) in vacuum (in a cubic cell of 30 Å side length). All electronic energies are calculated with VASP.

### 5.1.1. Brønsted Acid Sites

#### 5.1.1.1. Pyridine adsorption

The difference in strength between BAS can be determined firstly by the protonation of the pyridine. Only one adsorption configuration of pyridine was calculated with hydrogen bond (absence of proton transfer), it was observed on water adsorbed on aluminated site no. 59 of cleavage 1 of (100) orientation, see Chapter 3. It has an adsorption energy of  $-96 \text{ kJ mol}^{-1}$ , which is weak as compared to the adsorptions with pyridine protonation on the same surface site of  $-150 \text{ kJ mol}^{-1}$ . In comparison, the pyridine protonated but adsorbed on a silanol group neighboring this surface site (forming (OH)-Al-O-Si-(OH) surface group by cascade proton transfer<sup>3</sup>) has an adsorption energy of  $-125 \text{ kJ mol}^{-1}$ , which is even stronger than the adsorption with an hydrogen bond on the aluminated site.

The occurrence of protonation defines the most acidic Brønsted acid site. The most favorable positions of pyridine depend on the position of the aluminated sites. For a final position of pyridinium there are four possible initial positions of proton around the aluminum. The adsorption energy of pyridine is calculated against the most stable of these four positions. Pyridine molecule positions on BAS are explored around seventeen aluminum positions: in the bulk, and on three external surfaces cut along (100) (cleavage 1 and cleavage 6) and (010) (cleavage 2) orientations. Considering multiple aluminum positions should allow to highlight the most stable adsorption mode of pyridine between a stabilization in the bulk, in open micropore, at the outermost surface, or even on dehydrated aluminated surface sites. Figure 2 presents the most stable position of pyridine for each of these 17 aluminum positions, the adsorption energies are given in  $\text{kJ mol}^{-1}$  and separated into the dispersive part of the energy (orange, calculated with dDsC) and the non-dispersive part of the energy (grey, PBE component). To complete these information, the pyridine adsorption free energies are determined by evaluating the vibrational partition function of pyridine considered as an ideal gas, with the same method presented in Chapter 3. In Figure 2 the desorption temperature of pyridine is given in K for a partial pyridine pressure of  $10^{-4}$  bar. The associated values are given in Table 1 in section SI in the Supplementary Information of Chapter 5, together with more details about the name of the aluminated sites, the nature of the acid site before pyridine adsorption, the N-H bond length and the length of the H---O hydrogen bond.

The most favorable adsorption modes of pyridine have an adsorption energy below  $-200 \text{ kJ mol}^{-1}$ . In these cases, pyridine is protonated, and pyridinium is positioned in the zeolite bulk or at the pore-mouth of the external surface on bridging external surface site Si-OH-Al or HO-Si-OH-Al presented at the bottom of Figure 2. These molecules exhibit a desorption temperature above 600 K. A second category of adsorption modes with intermediate strength with adsorption energies between  $-200 \text{ kJ mol}^{-1}$  and  $-150 \text{ kJ mol}^{-1}$ , corresponding to a desorption temperature between 500 and 600 K. They correspond to pyridinium adsorbed in a pore-mouth on bridging Al-OH-Si or on bridging Al-OH-Si-OH. There is no clear distinction between the adsorption on these two bridging sites. Furthermore, if the most stable proton position is Al-OH-Si-OH, the pyridinium can get closer to another neighboring bridging group Al-O-Si with no hydroxyl groups on the silicon, and vice versa. This means that the information of the original location of the proton on the framework may be lost after proton transfer to pyridine.

The pyridine adsorption is also tested around aluminated sites of the  $\text{Al}(\text{OH})_n(\text{H}_2\text{O})$  type at the external surface sites. One can observe that even if it is by far the most stable aluminated site, the most stable way to adsorb pyridine on these sites includes the transfer of the protonated pyridine to a bridging oxygen between the aluminum and a silicon of the zeolite instead of staying close to the deprotonated Al-OH hydroxyl group, as represented at the bottom of Figure 2. This adsorption mode is not competitive compared to the previous ones, with adsorption energies higher than  $-150 \text{ kJ mol}^{-1}$  (lower in absolute value) and desorption temperatures below 500 K.

Similarly, pyridine is adsorbed on 2MR formed on dehydrated surface sites. These sites can be initially dehydrated  $\text{Al}(\text{OH})_n\text{H}_2\text{O}$  surface sites resulting into an  $\text{Al}_{\text{IV}}$  (as previously seen in Chapter 3), which are going to form a 2MR to adsorb pyridine as presented in bottom of Figure 2, in a similar way as what was observed for amorphous silica-alumina with Pseudo Bridging Silanols.<sup>3,4</sup> Or else, on some of these dehydrated site, 2MR form is already the most stable configuration and the pyridine deprotonate the 2MR to adsorb on one of its two oxygen atoms and form a similar adsorption mode. In both cases, if the pyridine adsorbs inside the zeolite structure as presented in Figure 2, it gives the best possible adsorption energies. Nevertheless, this adsorption mode is also in the last category (least favorable adsorption with respect to other sites). As it has been seen in Chapter 3 and showed again here, there are quite large variations in dispersive and the non-dispersive energy contributions, which makes that the stabilization of pyridine molecules has both van der Waals and electrostatic origins. It also confirms on other surfaces, like cleavage 6 cut along (100) orientation, or cleavage 2 cut along (010) orientation, that the confinement is a key factor in pyridine adsorption and that the adsorption of pyridine on Brønsted acid sites is most favorable inside the zeolitic network with respect to the external surface. To complete these data and to support the statements which are made, all the energies of local minima found around all the studied pyridine adsorbed close to aluminated surface sites are given in Figure 1 in section SI of the Supplementary Information of Chapter 5. This energetic analysis depends on the proton position around the aluminated sites.



Thus, in the end, we expect that with respect to pyridine as a probe molecule, larger crystal will exhibit higher Brønsted acidity with respect to small crystals for a given Si/Al ratio, as for the latter, the higher stability of Al(H<sub>2</sub>O) sites depletes the proton transfer ability with respect to more reactive bridging OH groups.

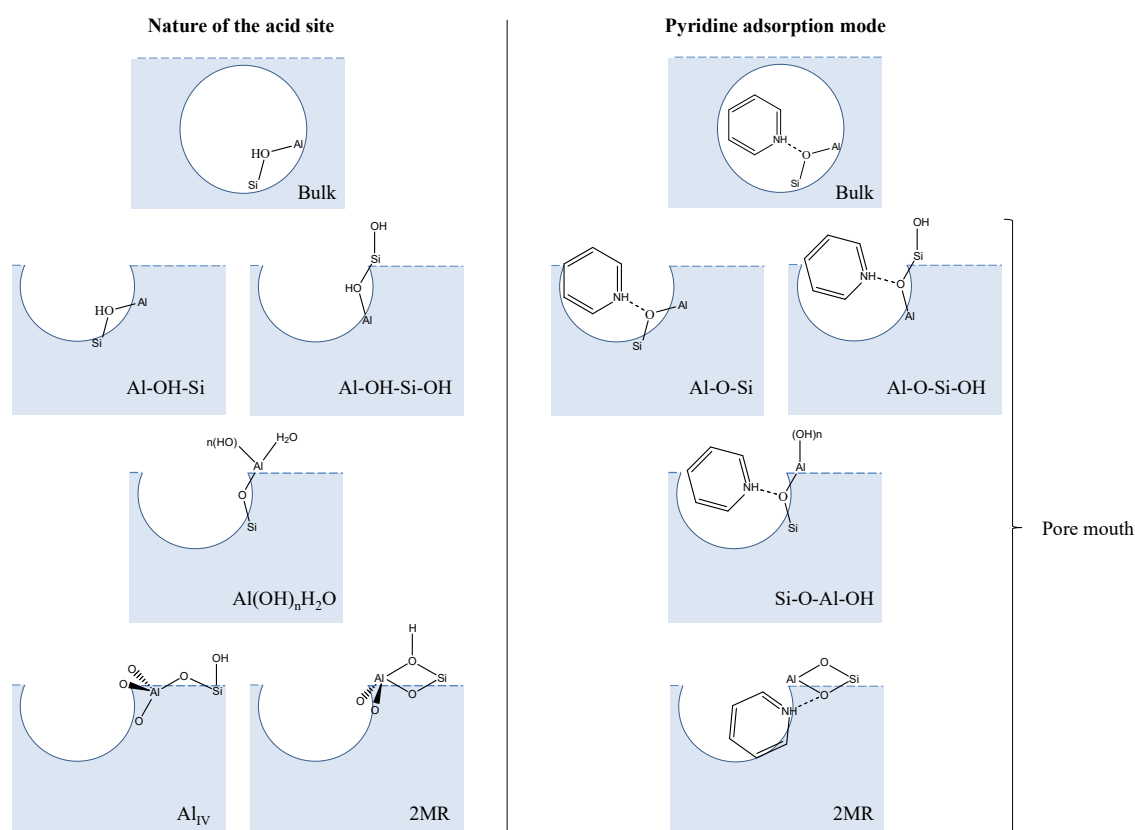
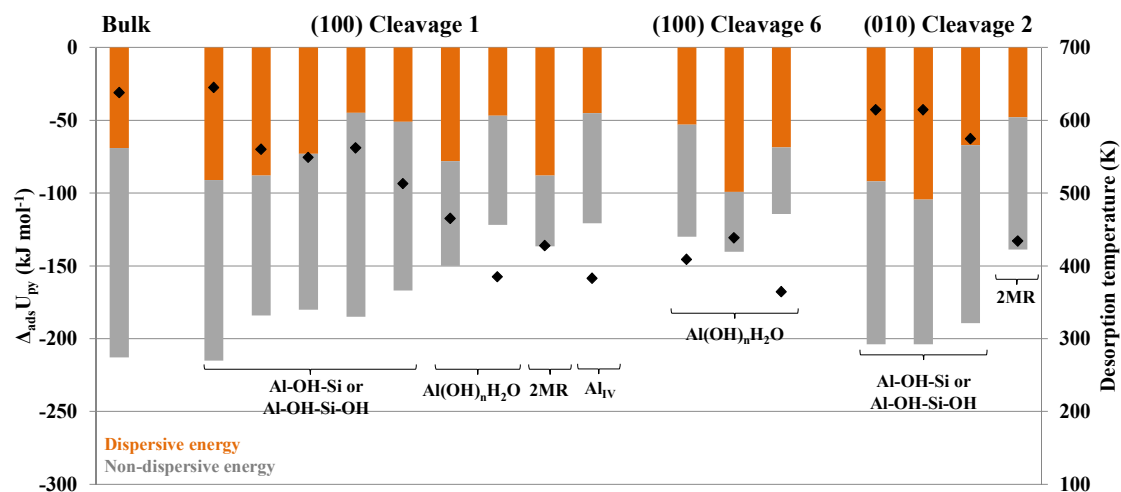


**Figure 2.** Adsorption energy of pyridine on BAS depending on the surrounding environment and the surface site in the H-ZSM-5 bulk, and on three external surfaces cut along (100) (cleavage 1 and cleavage 6) and (010) orientations (cleavage 2). Left: the pyridine adsorption value is decomposed into the dispersive (orange) and the non-dispersive (grey) parts of the energy in kJ mol<sup>-1</sup>. Right: Desorption temperature in K calculated with thermodynamic characteristics of pyridine for a partial pyridine pressure  $P_{\text{pyr}}=10^{-4}$  bar. Bottom: Schematic representation of pyridine position against its immediate surrounding and the nature of the initial aluminated surface site.

### 5.1.1.2. 2,6-ditertbutylpyridine adsorption

The 2,6-ditertbutylpyridine (DTBPy), in Figure 1 b), is also used as a probe experimentally for surface acid sites,<sup>2,5,6</sup> because it is considered that this molecule is too bulky to diffuse and adsorb in H-ZSM-5 pores. The molecule was modeled adsorbed in the bulk zeolite and at the external surface of zeolite. In the bulk, the T5 site is aluminated and 2,6-ditertbutylpyridine is adsorbed at the straight channel, at the sinusoidal channel, and at the intersection of straight and sinusoidal channels; the most stable adsorption mode corresponds to the intersection, and is shown in Figure 3 a). The proton is caught by the molecule (with a N-H covalent bond of 1.039 Å) while the molecule moves away because of the bulky tertbutyl groups leading to a hydrogen/oxygen distance of 1.961 Å. The total adsorption energy is equal to  $-217 \text{ kJ mol}^{-1}$ , where the dispersive adsorption energy contributes  $-268 \text{ kJ mol}^{-1}$ . It reveals that the adsorption of the DTBPy inside the zeolite network is essentially due to van der Waals interactions, while the electrostatics interactions hardly contribute to the adsorption of DTBPy inside the zeolite network. The dispersive adsorption energy is important enough to compensate the non-dispersive part of the energy to induce finally an important adsorption energy below  $-200 \text{ kJ mol}^{-1}$ , which correspond to the best range of energy for pyridine. However, in this stable mode, the protonated probe molecule is located at the intersection of straight and sinusoidal pores. While trying to localize the protonated probe molecule either in the straight or sinusoidal channel, one can see (Table 1) that it is strongly destabilized with respect to the intersection. This suggests that huge diffusion limitations will be encountered for the access of the molecule to the most stable adsorption site.

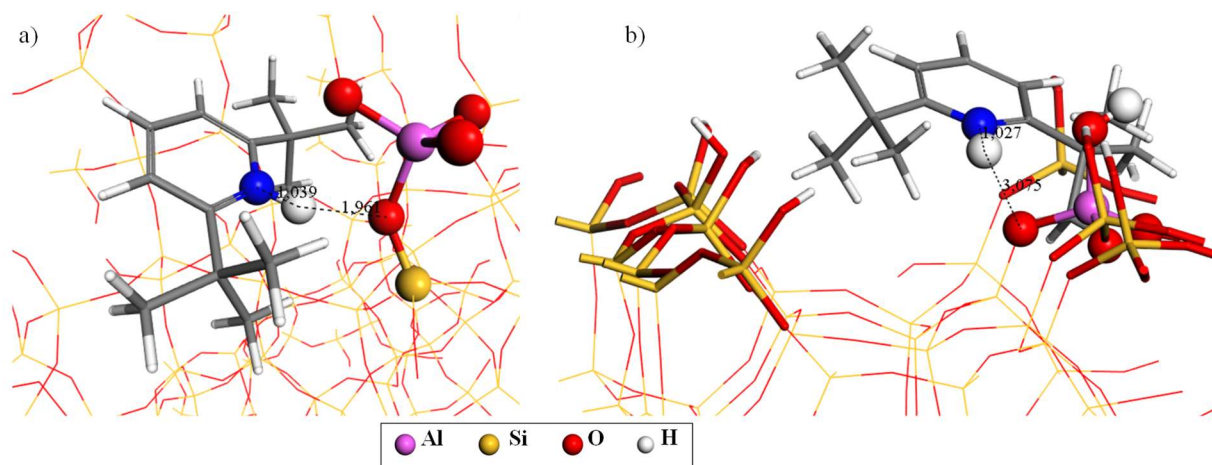


**Figure 3.** Most stable adsorption modes of 2,6-ditertbutylpyridine: a) in H-ZSM-5 bulk on T5 aluminated site; b) at the external surface cleavage 1 cut along (100) on Si59 aluminated site (equivalent of T5).

At the external surface of the zeolite the most stable DTBPy adsorption on aluminated site no. 59 on cleavage1 cut along (100) orientation, presented in Figure 3, has an adsorption energy equal to  $-148 \text{ kJ mol}^{-1}$ , as specified in Table 1. This is much weaker than at the bulk intersection site. The dispersive part of the adsorption energy is equal to  $-135 \text{ kJ mol}^{-1}$ , which reveals that the van der Waals interactions are mostly responsible of the adsorption of DTBPy while the electrostatic part is marginal. It also appears from the very long distance between the proton and the oxygen (3.075 Å).

Aluminated Site	Bulk			External Surface
	T5			Si_59
2,6-ditertbutylpyridine localization	Straight pores	Sinusoidal pores	Pores intersection	Pore mouth
Total adsorption energy (kJ mol <sup>-1</sup> )	561	6	- 217	- 148
Dispersive part of adsorption energy (kJ mol <sup>-1</sup> )	- 311	- 269	- 268	- 135

**Table 1.** Adsorption energies of 2,6-ditertbutylpyridine at the external surface of H-ZSM-5 and in the bulk

It can be concluded that the adsorption of the DTBPy is possible inside the zeolitic network of the H-ZSM-5. But seen the positive adsorption energies in the straight pores and sinusoidal pores which are positive, it can be concluded that the adsorption of DTBPy in the bulk must be limited by the diffusion inside the pores. Factually, the electronic part of the energy is shown not to be favorable to the adsorption of DTBPy on H-ZSM-5 in general so if the van der Waals interactions do not compensate its strength, like in straight or in sinusoidal pores, reaching the global minimum of adsorption can be very tough inside the pores. Finally, the fact that DTBPy is selective to the external surface is not driven by thermodynamics, but by diffusion limitations.

## 5.1.2. Lewis Acid Sites

### 5.1.2.1. Pyridine adsorption

The pyridine binding mode on Lewis acid sites corresponds to the formation of a N-Al bond as represented as an example the anti-approach with respect to the BAS in Figure 1 e. The approach can also be perpendicular against the BAS position. The most stable approach depends on the accessibility of the aluminum and the most stable position of the proton around aluminum. The possible structure surrounding these adsorption mode are represented at the bottom of Figure 4, they can be located in the bulk close to a bridging group Al-OH-Si or in the pore mouth at the external surface close to all the variety of Al-OH-Si, Al-OH-Si-OH, Si-OH-Al-OH, and Al(OH)<sub>n</sub>H<sub>2</sub>O (with n = 0 to 2) surface groups. The pyridine can also form a N-Al bond directly on dehydrated acid sites Al<sub>IV</sub> or Al<sub>III</sub> which can be LAS. The pyridine position can be inside the zeolite structure at the pore mouth or outside at the outermost surface.

The adsorption of LAS on these sites are studied in the bulk, and on three different surfaces: cleavage 1 cut along (100) orientation, cleavage 6 cut along (100) orientation, and cleavage 2 cut along (010) orientation. The adsorption energies on LAS close to bridging groups in the bulk and at the external surface are weak as compared to other LAS, as shown on Top of Figure 4, their adsorption energy values are between – 150 and – 100 kJ mol<sup>-1</sup>. The dispersive part of the energy can be important due to the confinement, but the non-dispersive part of the energy are higher than – 65 kJ mol<sup>-1</sup> which is also weak compared to the other

LAS. Indeed, the non-dispersive part of adsorption energies on dehydrated surface site are more important with values lower than  $-81 \text{ kJ mol}^{-1}$ . Except one case of adsorption on  $\text{Al}_{\text{III}}$  dehydrated on cleavage 2 cut along (010) orientation with a weak adsorption energy of  $-92 \text{ kJ mol}^{-1}$ , their adsorption energies are between  $-180$  and  $-260 \text{ kJ mol}^{-1}$ . The dispersive part of their energies is small when the pyridine is localized outside the zeolite structure, smaller than  $-33 \text{ kJ mol}^{-1}$ . While, when the pyridine is localized inside the zeolite structure this part of energy is around  $-80 \text{ kJ mol}^{-1}$ .

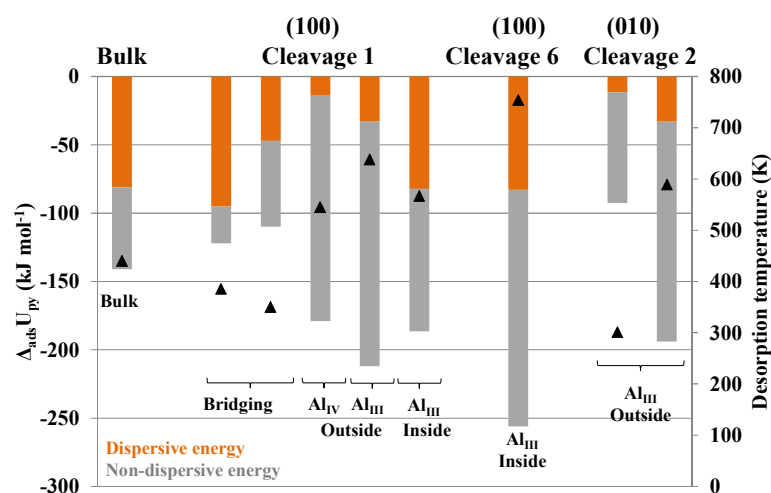


**Figure 4.** Adsorption energy of pyridine depending on the surrounding environment and the surface site in the H-ZSM-5 bulk, and on three external surfaces cut along (100) (cleavage 1 and cleavage 6) and (010) (cleavage 2) orientations. Left: the pyridine adsorption value is decomposed into the dispersive (orange) and the non-dispersive (grey) parts of the energy in  $\text{kJ mol}^{-1}$ . Right: Desorption temperature in K calculated with thermodynamic characteristics of pyridine for a partial pyridine pressure  $P_{\text{pyr}}=10^{-4}$  bar. Bottom: Schematic representation of pyridine position against its immediate surrounding and the nature of the initial aluminated surface site.

The strength of the LAS in the bulk and on the surface acid sites is not equivalent to BAS on the same sites except for  $\text{Al}(\text{OH})_n\text{H}_2\text{O}$  groups, for which the adsorption energy of pyridine is equivalent on LAS and on BAS. The strongest adsorption sites, which are comparable to the strongest BAS, are the dehydrated surface sites  $\text{Al}_{\text{III}}$  or  $\text{Al}_{\text{IV}}$ . It can be concluded that acid sites in the bulk or bridging acid sites at the external surface act preferentially like BAS. It remains more uncertain for  $\text{Al}(\text{OH})_n\text{H}_2\text{O}$  external surface sites, which have equivalent adsorption energies of pyridine, while acting like a BAS or like a LAS. But if the surface sites are dehydrated, the  $\text{Al}_{\text{III}}$  or  $\text{Al}_{\text{IV}}$  are clearly acting like LAS instead of BAS. One can observe that the desorption temperatures presented in Figure 4 of these dehydrated LAS are around 600 K and the most strongly adsorbed pyridine molecules desorb at 750 K, which is higher than for the most stable BAS found.

### 5.1.2.2. 2,6-ditertbutylpyridine adsorption

The DTBPy adsorption has also been tested on one LAS of the surface (no. 59 aluminated site of cleavage 1 cut along (100) orientation) and one LAS of the bulk of ZSM-5 (T5 aluminated in bulk). But most of the adsorption configurations are not stable. It is mostly due to the tertbutyl groups which are responsible of a high steric hindrance and which make the approach of the molecule to the aluminum site very difficult. Only two systems are found to be stable in our models: one surface site with an adsorption energy of  $-72 \text{ kJ mol}^{-1}$  and one bulk site with an adsorption energy of  $-45 \text{ kJ mol}^{-1}$ , which are shown in Figure S2 in section SI.2 of the Supplementary Information of Chapter 5. The adsorption energies of 2,6-ditertbutylpyridine are weak compared to the pyridine adsorption energies. The difficulties to find a DTBPy adsorbed on a LAS make us think that the DTBPy is more specific to BAS of the external surface.

### 5.1.3. Vibrational analysis of Brønsted and Lewis acid sites

The experimental analysis of BAS and LAS in the bulk and at the external surface can be studied with vibrational analysis as presented in Chapter 1 through the study of Akacem *et al.* in faujasite.<sup>7</sup> The analysis of 8a ( $1590\text{-}1614 \text{ cm}^{-1}$ ), 8b ( $1581\text{-}1590 \text{ cm}^{-1}$ ), 19a ( $1483\text{-}1486 \text{ cm}^{-1}$ ), and 19b ( $1438\text{-}1455 \text{ cm}^{-1}$ ) vibration modes' frequencies, which are the pyridine ring bending and stretching modes, give insight in the adsorption mode, which are represented by models of this simulation study. These modes are represented in Figure 29 and Figure 30 in section 1.3.1. in Chapter 1. Thus, the direct comparison of the calculated and experimental vibrational frequencies should give information on the presence of some of the proposed adsorption modes. The adsorption of pyridine on BAS induces changes for three of them: 8a ( $1600\text{-}1635 \text{ cm}^{-1}$ ), 8b ( $1605\text{-}1625 \text{ cm}^{-1}$ ), and 19b ( $1530\text{-}1550 \text{ cm}^{-1}$ ). While the adsorption on LAS induce changes on two of them: 8a ( $1630\text{-}1640 \text{ cm}^{-1}$ ), and 19b ( $1445\text{-}1465 \text{ cm}^{-1}$ ).

In the following Table 2 and Table 3, the frequencies are given depending on the adsorption mode of pyridine which are described in the previous paragraphs. The given references are the frequencies associated to an isolated pyridine into vacuum calculated by VASP (in a cubic cell of  $30 \text{ \AA}$  side length). The calculated frequencies of the modes are slightly under the reference data of the experiment. The vibrational analysis is made on

pyridine adsorbed on BAS and LAS in bulk and at the external surface, only on bridging sites. It can be observed that for pyridine adsorbed on BAS, in bulk and at the external surface, the increase of frequencies for 8a, 8b, and 19b vibration modes are slightly overestimated by our calculation but are of the same order of magnitude. On the contrary, the adsorption on LAS induces a translation of the frequencies of 8a, and 19b vibration mode, but the translation for 8a is slightly underestimated. Similarly to Leydier *et al.*, we observe that an inversion could be possible between 8a and 8b between the gas phase and the adsorbed phase.<sup>3</sup> Despite these small differences, it can be confirmed that the classical adsorption modes studied are confirmed by our analysis.

Surface	BULK							Calculated Reference
Aluminated site no.	T5							
Oxygen no.	162	146	145	162	146	145	155	
Pyridine adsorption mode	BAS in bulk			LAS in bulk				
<b>19b (cm<sup>-1</sup>)</b>	1552	1554	1562	1442	1448	1460	1451	1431
<b>19a (cm<sup>-1</sup>)</b>	1481	1480	1488	1475	1482	1495	1483	1468
<b>8b (cm<sup>-1</sup>)</b>	1637	1641	1654	1579	1580	1596	1582	1581
<b>8a (cm<sup>-1</sup>)</b>	1633	1628	1644	1606	1616	1641	1620	1583

**Table 2.** Vibrational analysis of pyridine ring bending and stretching mode of pyridine adsorbed on Brønsted and Lewis acid sites in H-ZSM-5 bulk.

Surface	Cleavage 1 cut along (100) orientation						
Aluminated site	59						
Oxygen no.	580	291	289	580	291	289	309
Pyridine adsorption mode	BAS Si-O-Al-OH			LAS Bridging			
<b>19b (cm<sup>-1</sup>)</b>	1555	1562	1573	1442	1444	1452	1447
<b>19a (cm<sup>-1</sup>)</b>	1484	1483	1489	1477	1481	1481	1480
<b>8b (cm<sup>-1</sup>)</b>	1639	1651	1671	1577	1581	1576	1579
<b>8a (cm<sup>-1</sup>)</b>	1635	1633	1643	1609	1615	1622	1614

**Table 3.** Vibrational analysis of pyridine ring bending and stretching mode of pyridine adsorbed on Brønsted and Lewis acid sites on H-ZSM-5 external surface.

#### 5.1.4. Comparison of calculated feature with respect to experiments from Demaret *et al.*

Experimentally, the adsorption of pyridine at the surface of H-ZSM-5 is observed and quantified thanks to the analysis of the 19a and 19b vibration modes.<sup>8-11</sup> The contribution of pyridine on BAS is highlighted with a peak around 1545 cm<sup>-1</sup> (19b vibrational mode of pyridinium). The adsorption on LAS is revealed by a peak at 1450 cm<sup>-1</sup> (19b vibrational mode of adsorbed pyridine). A peak at 1490 cm<sup>-1</sup> is considered as the contribution of pyridine adsorption on both acid sites according to their 19a vibration modes. The physisorbed



pyridine (hydrogen-bond mode, no proton transfer with acid site) have a frequency of  $1440\text{ cm}^{-1}$  for the 19b vibrational mode.

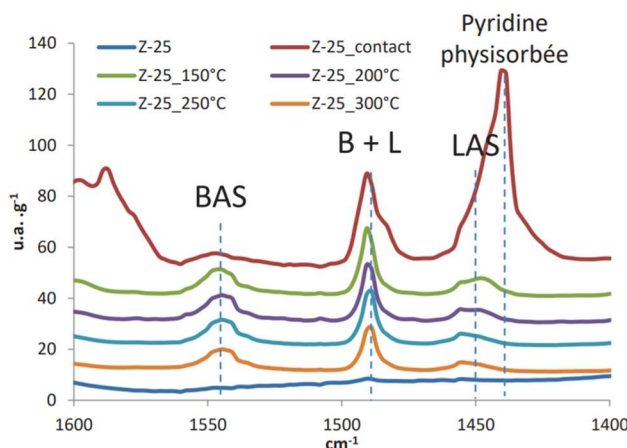


**Figure 5.** IR spectra of H-ZSM-5 crystals activated at  $300\text{ }^{\circ}\text{C}$  (named Z-25 in C. Demaret PhD work<sup>1</sup>) and IR spectra of pyridine thermodesorption on this crystals (Z-25\_ $x^{\circ}\text{C}$  where  $x$  is the temperature desorption). Z-25 correspond to Z-25-Small of Chapter 4.

Pyridine adsorption on zeolites crystals have been experimentally recorded by C. Demaret in her PhD work.<sup>1</sup> The sample two samples (small and large crystal sizes) already investigated in Chapter 4 have been analyzed. Figure 5 represents the IR spectra of zeolite pre-treated at  $300\text{ }^{\circ}\text{C}$  for 10 hours and the contact with pyridine is made at ambient temperature. The zeolites undergo different pyridine desorption steps ( $150\text{ }^{\circ}\text{C}$  for 2 hours,  $200$ ,  $250$ , and  $300\text{ }^{\circ}\text{C}$  for 1 hour). The number of BAS and LAS have been calculated and are shown in Figure S3 and S4 in section SI.3. of the Supplementary Information of Chapter 5. At the first desorption step at  $150\text{ }^{\circ}\text{C}$  ( $423\text{ K}$ ), obviously the physisorbed pyridine is eliminated from the surface of H-ZSM-5 crystals. But according to our theoretical results obtained in section 5.1.1. and 5.1.2. weak adsorption modes of BAS and LAS are also desorbed. Pyridine adsorbed on 2MR BAS, and some mild BAS on  $\text{Al}(\text{OH})_3(\text{H}_2\text{O})$  already desorb (Figure 2). Similarly, weak adsorption mode of pyridine on LAS have already desorbed notably LAS in bulk or on external surface bridging  $\text{Si}(\text{OH})\text{-Al}$  (Figure 4). Then pyridine desorbs gradually from LAS and BAS up to  $300\text{ }^{\circ}\text{C}$  ( $573\text{ K}$ ) but some pyridine molecules are maintained at the zeolite surface, in agreement with our calculation results. Pyridine adsorbed on dehydrated  $\text{Al}(\text{H}_2\text{O})$  external surface sites as LAS (Figure 4) and pyridine adsorbed on BAS of bridging  $\text{Al}(\text{OH})\text{-Si}$  groups in the bulk and at the external surface (Figure 2) are the only kind of adsorption maintained above  $300\text{ }^{\circ}\text{C}$ . Thus, our calculation gives an assignment to experimentally observed features in terms of nature and location of the probed acid sites. These assignments are reinforced upon comparison of the respective BAS and LAS concentrations estimated for the small and large crystals (Figures S2 and S3), that show a much higher concentration of BAS in large crystals, versus a higher amount of LAS on small crystals.



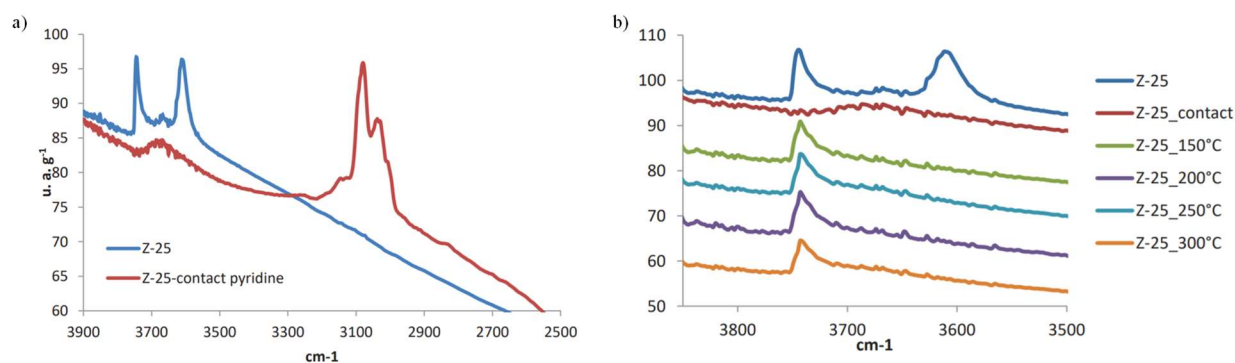


**Figure 6.** IR spectra of H-ZSM-5 crystals (named Z-25 in C. Demaret PhD work<sup>1</sup>); a) activated at 300 °C before and after contact with pyridine at ambient temperature; b) IR spectra of pyridine thermodesorption on this crystal (Z-25\_x°C where x is the temperature desorption). Z-25 correspond to Z-25-Small of chapter 4.

These conclusions can be confirmed with the IR spectra detailed at higher frequencies describing the surface of H-ZSM-5, obtained experimentally in the same PhD work<sup>1</sup> and presented in Figure 6. As confirmed in Chapter 4 by our theoretical calculations, the contribution at 3609 cm<sup>-1</sup> correspond to the O-H vibration of Al-(OH)-Si bridging surface site. All these sites are occupied by pyridine as soon as they are put in contact with it at ambient temperature as it is shown by the loss of the signal on Figure 6 a. These BAS are the strongest as it can be seen in Figure 6 b, where the contribution at 3609 cm<sup>-1</sup> is not restored even at 300 °C. The large signal between 3000 and 3100 cm<sup>-1</sup> (Figure 6-a) is experimentally attributed to the C-H vibration mode of pyridine<sup>9</sup> and its evolution is not followed according to the pyridine thermodesorption.

The signal between 3740 and 3720 cm<sup>-1</sup> has been attributed to silanol surface groups (isolated at 3743 cm<sup>-1</sup> and 3720 cm<sup>-1</sup> to silanols and silanol-Al that are hydrogen-bond acceptors with neighboring silanols). This signal disappears at ambient temperature due to the physisorbed pyridine but reappears as soon as the temperature is increased, suggesting that these surface sites are not strong BAS.

The signal between 3700 and 3660 cm<sup>-1</sup> has multiple attribution in Chapter 4: bridging OH groups belonging to 2MR cycles, silanols that are hydrogen-bond acceptor towards Al-(H<sub>2</sub>O), and Al-(H<sub>2</sub>O) species at the external surface. The contribution of these surface sites are more complicated to evaluate, experimentally due to the low signal, and theoretically due to the number of attribution. The pyridine adsorbed on 2MR and Al-(H<sub>2</sub>O) external surface groups desorb gradually between 25 and 300 °C. Besides the water molecules on Al-(H<sub>2</sub>O) external surface site desorb partially between this same range of temperature.

## 5.2. Sodium poisoning

Sodium cations were revealed to be poisoning the zeolite acid site.<sup>12</sup> The recent PhD work of C. Demaret suggests the migration of sodium from a silica binder to the zeolite by a  $\text{Na}^+/\text{H}^+$  exchange supposed to take place.<sup>1</sup> The acid properties of the catalyst decrease by 30% due to the presence of sodium. The impact of sodium on BAS is crucial. On the crystals used in her work, two possible scenarios for the sodium repartition in the ZSM-5 crystals are distinguished. Either the sodium will poison all the ZSM-5 crystal acid sites close to the surface on a limited thickness, or the entire crystal is homogeneously and partially poisoned by sodium to reduce the catalytic activity of 30%. A schematic representation of these two extreme scenarios is given in Figure 7. The first scenario was experimentally shown to be more realistic considering the impacts of sodium presence during catalytic reactions and the analysis of the acid properties of some ZSM-5 samples.

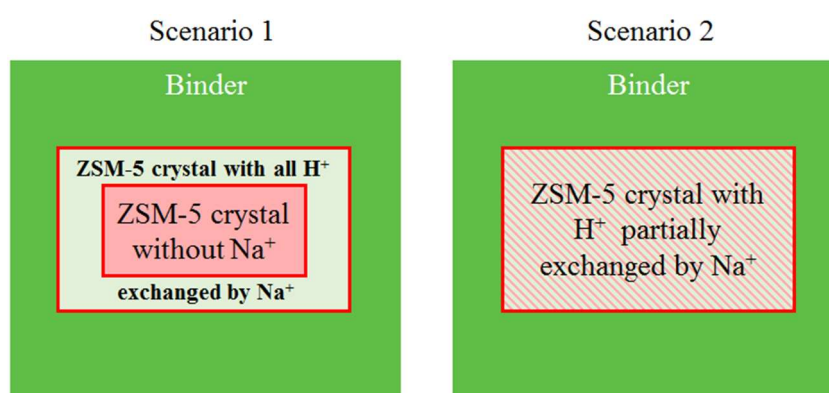
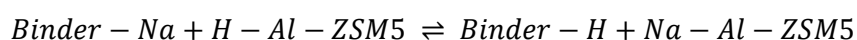


**Figure 7.** Two extreme scenarios for the  $\text{Na}^+/\text{H}^+$  exchange between ZSM-5 crystal and silica binders.<sup>1</sup>

Geometric models based on the respective impact of sodium on acidity and catalytic activity allowed to evaluate that the deepest sodium are situated between 1.5 and 9 nm under the surface depending on the samples. The explicit simulation of a large ZSM-5 crystal models would be too expensive (in computational costs) for DFT calculation. Later, reactive force field could be used to complete the following calculation. Thus, in the present study the exchange energy of sodium between some models of binder and the ZSM-5 bulk and external surface is evaluated. The reaction equation of sodium exchange between ZSM-5 and binder is written in Equation 2. The exchange energy is calculated by quantifying the energy of products and reactants of this reaction in separated simulations. If the result is positive the reaction is favorable to the reactant configurations, while a negative result indicate that the products configuration is the most favorable. The calculation between different binders configuration and ZSM-5 configuration allows to establish an order of preferential adsorption localization of the  $\text{Na}^+$ .



**Equation 2**

with *Binder – H* models of protonated binder and *Binder – Na* the models of same binders with one proton replaced with a  $\text{Na}^+$  cation. Similarly, *H – Al – ZSM5* represents H-

ZSM-5 models with an aluminated site and  $Na - Al - ZSM5$  the same model with the compensation proton replaced with a  $Na^+$  cation.

Three different models of binder are used for calculation the exchange energy. The first binder model is a model extracted from the study of Tielens *et al.* of the hydroxylated surface of amorphous silica,<sup>13</sup> with the following cell dimensions:  $a = 12.7745 \text{ \AA}$ ,  $b = 17.6362 \text{ \AA}$  and  $c = 25.1732 \text{ \AA}$ . This model is similar to an amorphous slab along  $a$  and  $b$  axes and is presented in Figure 8 a. The sodium cation is introduced in the model instead of an proton. The two other models presented in Figure 8 b-c are  $\gamma\text{-Al}_2\text{O}_3$  models developed at IFPEN which are slabs along  $a$  and  $b$  axes also presented in the same figure: alumina cut along the (110) orientation ( $a = 16.0670 \text{ \AA}$ ,  $b = 16.7790 \text{ \AA}$  and  $c = 23.0000$ ) and alumina cut along the (100) orientation ( $a = 11.1308 \text{ \AA}$ ,  $b = 16.7682 \text{ \AA}$  and  $c = 28.0000$ ) respectively.<sup>14-16</sup> Tielens' model has also been tested with one aluminated site presented in Figure 9 c. The ZSM-5 models used for the sodium exchange are the previous bulk model (with T5 as the silicon site substituted) and the surface model with the site no. 59 substituted presented in Figure 9 a-b.

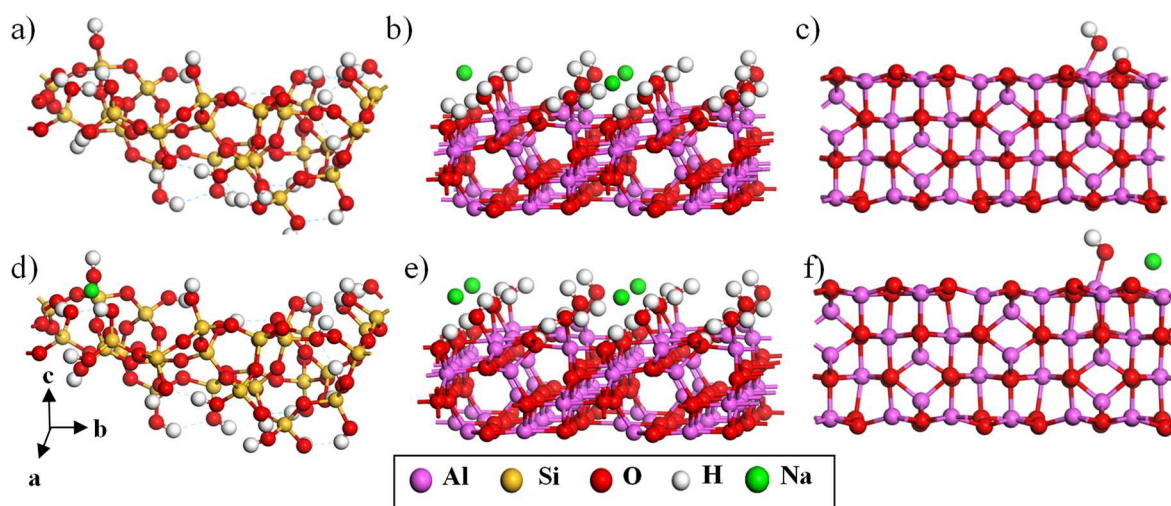


**Figure 8.** Binder models used for our calculations (a) Tielens' model<sup>13</sup> of amorphous silica, (d) exchanged with sodium in the present work. Digne's model of  $\gamma$ -Alumina (110) with 3 sodium (b) and 4 sodium (e)<sup>16</sup> and (100) (c)<sup>14</sup> surface, exchanged with sodium (f).

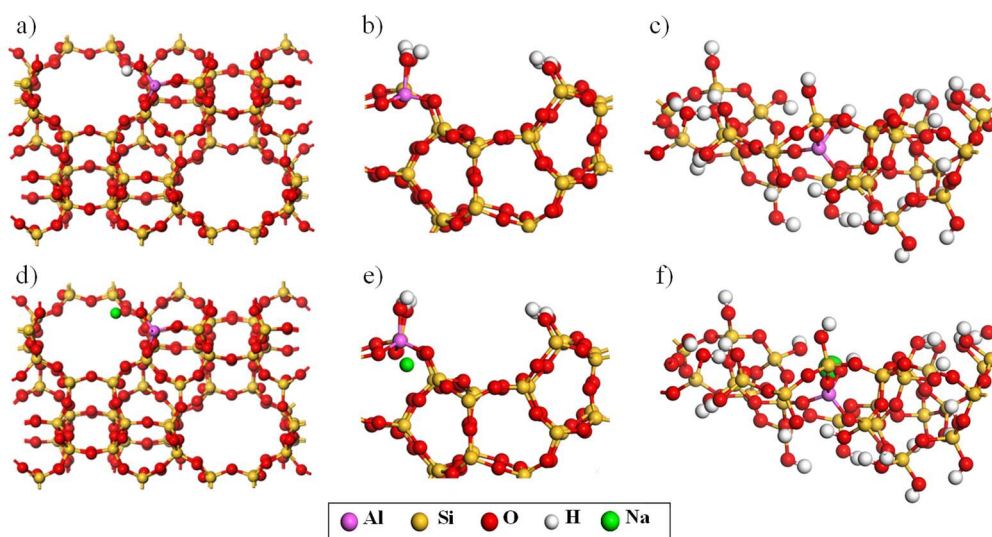


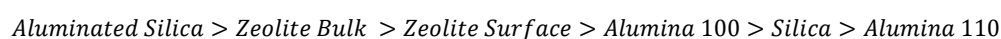
**Figure 9.** Aluminated surface models used for our calculations (a) aluminated H-ZSM-5 bulk, (d) proton exchanged with sodium; (b) aluminated site no. 59 on cleavage 1 of (100) orientation, (e) proton exchanged with sodium; (c) Tielens' model of amorphous silica with aluminated site, (f) proton exchanged with sodium.

The multiple configurations which are studied for the ZSM-5 models and the binders' model (different sodium positions) allow us to establish a statistic of the most stable thermodynamic adsorption of sodium. The consideration of only the most stable reactants and products give a thermodynamic order of stability.

The thermodynamic most stable configuration of binder with sodium are presented in Figure 8 a-c and the most stable configuration of aluminated surfaces with sodium are presented in Figure 9 a-c, and the corresponding energies are presented in Table 4. The calculations of the reaction of sodium exchange between all these configurations reveal that the sodium will preferably adsorb on the aluminated and hydroxylated silica, then on the aluminated site of the zeolite bulk as the order presented in Equation 3. The zeolite bulk is a better sodium absorber than the external surface of zeolite. And both are better than the pure hydroxylated silica. The detailed energy calculated for each result are given in section SII in the Supplementary Information of Chapter 5.

Zeolite model \ Binder model	Silica	Aluminated and hydroxylated of silica	Alumina (100)	Alumina (110)
ZSM-5 bulk	- 63.0	- 27.4	- 45.1	- 117.0
ZSM-5 external surface cleavage 1 (100) no. 59 substituted	- 27.2	8.4	- 9.3	- 81.2

**Table 4.** Exchange energies in  $\text{kJ mol}^{-1}$  between zeolite and binder models as presented in Equation 2. For one cation adsorbed on a model various position are explored and the most stable of these positions are included in the calculations, the detailed energies and the other explored positions are presented in section SII in the Supplementary Information of Chapter 5.



### Equation 3

The sodium will migrate from pure silica or from alumina to components presenting aluminosilicic environment sites like our models of zeolites or aluminated silica. Our theoretical results can complete the experimental ones by highlighting that an alumina binder will not be more favorable to the sodium adsorption than the ZSM-5. The comparison between the models of ZSM-5 external surface and bulk reveals that the bulk is more attractive for the sodium cation. This conclusion is in accordance with C. Demaret experimental results of partial poisoning of the ZSM-5 crystals. But our models do not allow us to evaluate a depth limit for sodium adsorption: diffusion limitations of sodium, rather than thermodynamic preference, is likely to explain the fact that the whole zeolite crystals are not homogeneously poisoned. A ReaxFF model, taking into account the dynamics of the sodium migration from the binder to the zeolite, would be a good complement to find an agreement with the scenario 1 previously exposed.

The model of aluminated and hydroxylated silica is one of the most sodium stabilizing surface with ZSM-5 models. It completes this study by confirming that sodium cation is more attracted by surfaces exposing silicon and aluminum than by pure silica or pure alumina models.

### 5.3. Interaction with monomers representative of the binders

Binders, as zeolites, can be formally decomposed into monomers. It is likely that during the shaping (in the presence of water and at  $\text{pH} \neq 7$ ), such monomers can be found in the medium, and may interact with the zeolite's surface, or even can migrate in the porosity. A preliminary approach of the interface between the binders and the zeolite consists in the understanding of the interaction of the monomers of the binders with H-ZSM-5. The two monomers studied here are  $\text{Al}(\text{OH})_3(\text{H}_2\text{O})$  ("alumina monomer") and  $\text{Si}(\text{OH})_4$  (silicic acid, "silica monomer") which are presented in Figure 10.

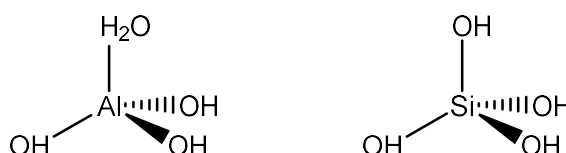


**Figure 10:** Schematic representation of monomers of binders (Left) Alumina monomer (Right) Silica monomer.

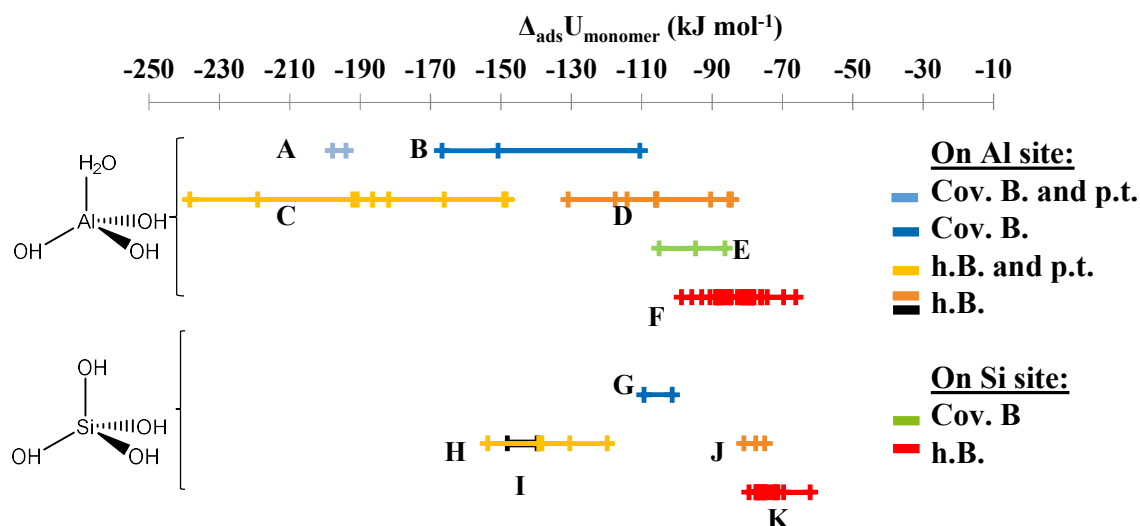
The two monomers interact in various way with the ZSM-5 crystals. Van der Waals and hydrogen bonding may result in non-covalent interaction, or they may form covalent and hydrogen bonds (due to the numerous hydroxyls on these monomers). They may also transfer a proton from the zeolite framework. The interactions of these monomers are studied in the aluminated bulk of H-ZSM-5 and at the H-ZSM-5 external surface (aluminated or not). Different adsorption sites are investigated. In bulk, T5 site is aluminated, when at the external surface the site no. 59 is aluminated on cleavage 1 cut along the (100) orientation. In some cases, the monomers are adsorbed on non-aluminated site equivalent in position to the aluminated one, to get information about the role of aluminium in a similar environment. The adsorption energies are calculated using Equation 4:

$$\Delta_{ads}U_{monomer} = U_{surf\_monomer} - U_{surf} - U_{monomer} \quad \text{Equation 4}$$

where  $\Delta_{ads}U_{monomer}$  is the monomer adsorption energy,  $U_{surf\_monomer}$  is the electronic free energy of the monomer adsorbed on the surface (bulk and external surface),  $U_{surf}$  is the electronic free energy of the surface (bulk and external surface) and  $U_{monomer}$  is the electronic free energy of the monomer in vacuum (in a cubic cell of 30 Å side length). All electronic energies are calculated by VASP.

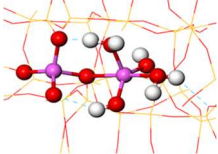
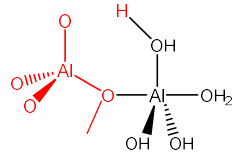
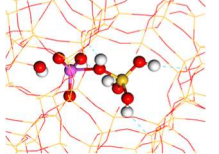
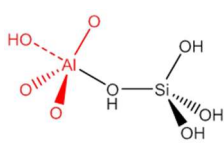
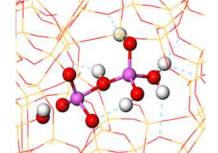
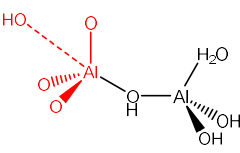
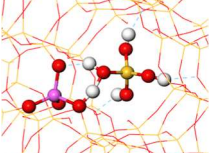
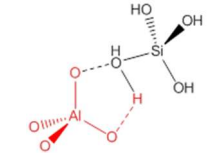
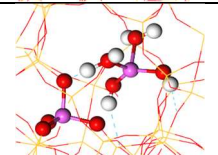
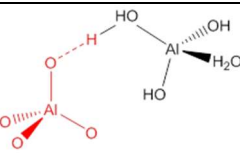
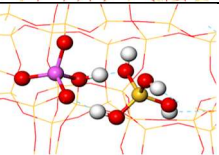
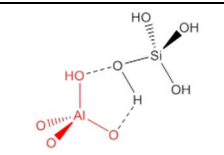
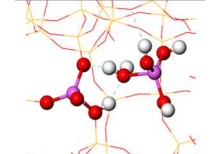
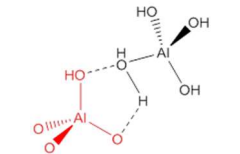
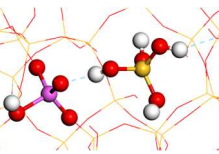
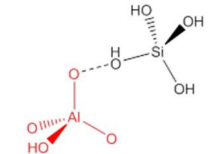
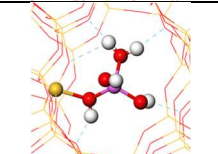
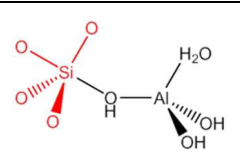
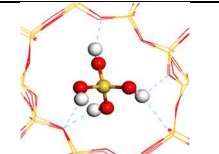
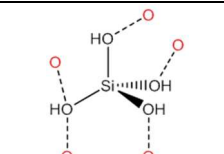
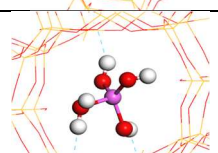
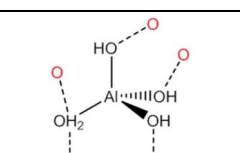
### 5.3.1. Monomer adsorption in bulk

The explored configurations are named with letters, adsorption A to F correspond to the adsorption of alumina monomers, adsorption G to K stand for the adsorption of silica monomer. The results obtained in the bulk are presented in Figure 11. The different configurations of monomers adsorption in the bulk are represented in Table 5.



**Figure 11.** Adsorption energies of alumina and silica monomers in  $\text{kJ mol}^{-1}$  in the bulk of ZSM-5. The interaction between monomers and zeolite are given by acronyms: Cov. B. = covalent bond, h.B. = hydrogen bond, p.t. = proton transfer, the detailed energies are given in Table S3 in section SIII.1 of the Supplementary Information of Chapter 5.



Name	Ball and stick view <sup>(a)</sup>	Schematic representation <sup>(b)</sup>	Name	Ball and stick view <sup>(a)</sup>	Schematic representation <sup>(b)</sup>
A			G		
B			H		
C			I		
D			J		
E			K		
F					

**Table 5.** Alumina and silica monomer adsorption representations in bulk of ZSM-5 depending on the nature of the monomer, the adsorption site and the bond formed. (a) Ball and stick representation of the monomer and the adsorption site (b) Schematic representation of the adsorption, atom originally from the zeolite network are represented in red, atoms originally from monomer are represented in black.

First it can be observed that for both silica and alumina monomers, the adsorption on or around silicon site in the bulk (represented in green and red in Figure 11) have weak adsorption energies compared to the adsorption on aluminated sites, higher than  $-90 \text{ kJ mol}^{-1}$  and  $-110 \text{ kJ mol}^{-1}$  respectively. Covalent bond formation between the monomers and the aluminated sites are better adsorption modes for both of them. For silica and alumina monomers the covalent bond formation modes lie around  $-110 \text{ kJ mol}^{-1}$ , and between  $-170$  and  $-100 \text{ kJ mol}^{-1}$  respectively, but it can be observed that the proton transfer from the acid site to the alumina monomer in addition with the covalent bond has an adsorption energy around  $-200 \text{ kJ mol}^{-1}$ . The covalent bond formation between monomers and external surface is clearly in favor of alumina monomers. Similarly, the adsorption of both monomers with hydrogen bonds is in favor of alumina monomer with an energy between  $-130$  and  $-80 \text{ kJ mol}^{-1}$  against around  $-80 \text{ kJ mol}^{-1}$  for silica without proton transfer. One specific group of adsorption with hydrogen bond only (the adsorption takes places further from the hydroxyl



group of the acid site but close to the aluminum see H & I configurations in Table 5) is observed for silica monomer between  $-150$  and  $-140$   $\text{kJ mol}^{-1}$ , which is included in the energy interval of adsorption of silica monomer with hydrogen bond and proton transfer (between  $-160$  and  $-120$   $\text{kJ mol}^{-1}$ ). The proton transfer stabilizes also the adsorption of alumina monomer with hydrogen bonding with energies between  $-240$  and  $-150$   $\text{kJ mol}^{-1}$ . There is a clear gap induced by the proton transfer which is in favor of the adsorption of both kinds of monomers. However, the best adsorption mode remains for both monomers the formation of hydrogen bond near aluminated sites instead of covalent bonds with the same sites.

The most stable adsorption configurations of silica (adsorption energy  $-153$   $\text{kJ mol}^{-1}$ ) and alumina (adsorption energy  $-238$   $\text{kJ mol}^{-1}$ ) monomers in bulk of ZSM-5 are represented as H and C in Table 5, respectively. The silica monomer is stabilized by five hydrogen bonds while only three hydrogen bonds are observed for alumina monomer adsorption. It can be guessed that the alumina must induce a very good interaction with the aluminated site to induce this better adsorption energy.

### 5.3.2. Monomer adsorption on the external surface of H-ZSM-5

The same simulations are conducted on the aluminated external surface models of H-ZSM-5 and at the purely silicic external surfaces of ZSM-5. The possibilities of interactions are more numerous than in the bulk. A selection of adsorption energies (best mode for each family of sites and modes) is given in Figure 12, the detailed various adsorption on both surfaces are given and shown in section SIII.2. in Supplementary Information of Chapter 5. This analysis reveals that the strongest interactions for both monomers is again the hydrogen bonding with proton transfer on an aluminated surface site. The adsorption energy for the alumina monomer goes down to  $-250$   $\text{kJ mol}^{-1}$  and the lowest energy adsorption for silica monomer is  $-128$   $\text{kJ mol}^{-1}$ . On the non-aluminated external surface of ZSM-5, the adsorption of monomers is also most favorable with hydrogen bonding ( $-150$   $\text{kJ mol}^{-1}$  for alumina monomer and  $-100$   $\text{kJ mol}^{-1}$  for silica monomer). The presence of aluminum on the external surface enhances the adsorption of the binder monomers.

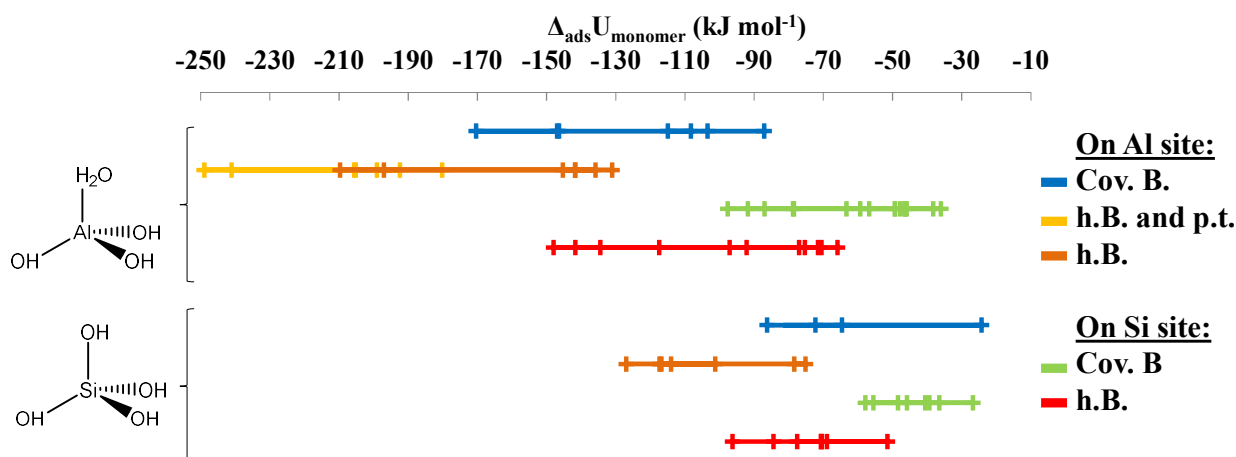


**Figure 12.** Adsorption energies of alumina and silica monomers in  $\text{kJ mol}^{-1}$  at external surface of H-ZSM-5 (aluminated and purely silicic surfaces). The interaction between monomers and zeolite are given by acronyms: Cov. B. = covalent bond, h.B. = hydrogen bond, p.t. = proton transfer.

The combination of all the results shows that the interaction of the zeolitic network is stronger with alumina monomers. The interaction of alumina may thus be stronger than the interaction with silica. The data show also that the alumina monomer is more attracted by the zone close to the aluminum of the zeolitic network than by silicon-rich zones. If the Si/Al ratio decrease, the number of aluminum atoms increase in the zeolite and the number interaction sites between zeolite and alumina type binder will increase.

A slight difference can be also highlighted by our study between the two monomers. The alumina monomers seem to be more attracted by the external surface aluminated sites whereas the silica monomers seem to prefer the bulk aluminated sites. But the differences in the adsorption energies are not high in both cases between surface and bulk (less than  $20 \text{ kJ mol}^{-1}$ ).

Referring to the Section 1.2. in Chapter 1 where the studies of Michels *et al.* are presented,<sup>17,18</sup> we can compare our theoretical models to their FT-IR spectra in Figure 22 of Chapter 1. They observed that with the shaping of ZSM-5 with silica, the signals attributed to Si-OH and the bridging Si-OH-Al almost disappear from the FT-IR spectra. So both kinds of sites are expected to vanish with silica. But for the interaction with attapulgite binder (clay composed of aluminum, silicon and magnesium cations) the spectra is mostly reduced for the bridging Si-OH-Al. It could be due to the strongest interaction of alumina monomer with aluminum of the zeolitic network compared to the silicon sites, in addition to the effect of the magnesium cations which are present in the mixture.

## 5.4. Conclusion

The aluminated sites of H-ZSM-5 surfaces in bulk and at external surface are shown to play a crucial role in the interaction with molecules. Their acidity can be quantified with the study of pyridine adsorption. It was shown that depending on the temperature conditions, and so the hydration level of the surface, the acidity of the outermost surface of H-ZSM-5 changes. In general, the bulk is characterized by its Brønsted acidity, as well as the hydrated external surfaces which expose strong BAS with bridging groups Si-(OH)-Al and mild BAS with Al(OH)<sub>n</sub>(H<sub>2</sub>O) groups (for n= 0 to 2). While, on dehydrated external surfaces, due to the exposition aluminum atom with lower oxidation numbers (Al<sup>III</sup>), the Lewis acidity is enhanced.

The calculation of sodium adsorption on surfaces of binders and aluminated surfaces (alumina, silica versus H-ZSM-5) showed a clear preference of sodium adsorption on aluminosilicic sites. The poisonous power of silica is highlighted in complement of experimental data. Combining the previous results about the key role of acid site, one can understand that it is crucial to avoid sodium in the mixture environment. The presence of sodium in the zeolite network would decrease its acidity.

Finally, our calculations reveal that the most favorable interaction between monomers and surfaces correspond mainly to the combination of hydrogen bonds and proton transfer; the monomers form hydrogen bonds with the acid site and some other atoms surrounding. The formation of covalent bond is less favorable for monomer adsorption. The covalent bond formation in bulk or at the external surface results into the deformation of the external surface site with atoms with higher valence (O, Si, or Al) or the break of a covalent bond. Dehydration of the external surfaces reduces the number of BAS while increasing the number of LAS. The interaction of monomers with LAS, resulting into covalent bonds, are less favorable and the interactions are weaker than interaction with BAS and with hydrogen bonds. The proton transfer, which is the favorite interaction, can induce changes in the zeolite acidity. Our calculations reveal that the silica and alumina monomers, used as binder models, are attracted by the aluminated site at the surface in the bulk and at the external surface. This could block all the acid sites which are the closest to the most external surface, which could itself result into decreasing accessibility to active acid site. Experimentally, the shaping of zeolite is made in a humid paste. It is complicated to evaluate the quantity of water in this mixture, but this study reveals that a controlled quantity of water could be essential to a good and strong interaction between zeolite and binder. However, the shaped zeolite/binder mixtures will undergo changes into their hydration levels during the multiple steps of the shaping (including thermal treatments), which can affect radically the interactions between zeolite and binder.

## References

- (1) Demaret, C. Mise en forme de zéolithes : Contrôle des propriétés acides des zéolithes et description de l'interface zéolithe / liant: Thèse de doctorat, IFPEN, 2019.
- (2) Góra-Marek, K.; Tarach, K.; Choi, M. 2,6-Di- tert- butylpyridine Sorption Approach to Quantify the External Acidity in Hierarchical Zeolites. *J. Phys. Chem. C* **2014**, *118*, 12266–12274.
- (3) Leydier, F.; Chizallet, C.; Chaumonnot, A.; Digne, M.; Soyer, E.; Quoineaud, A.-A.; Costa, D.; Raybaud, P. Brønsted acidity of amorphous silica–alumina: The molecular rules of proton transfer. *J. Catal.* **2011**, *284*, 215–229.
- (4) Chizallet, C.; Raybaud, P. Acidity of amorphous silica-alumina: From coordination promotion of Lewis sites to proton transfer. *Chem. Phys. Chem.* **2010**, *11*, 105–108.
- (5) Corma, A.; Fornés, V.; Forni, L.; Márquez, F.; Martínez-Triguero, J.; Moscotti, D. 2,6-Di-Tert-Butyl-Pyridine as a Probe Molecule to Measure External Acidity of Zeolites. *J. Catal.* **1998**, *179*, 451–458.
- (6) Weitkamp, J. Zeolites and related microporous materials: State of the art 1994 / proceedings of the 10th International Zeolite Conference, Garmisch-Partenkirchen, Germany, July 17-22, 1994 **1994**.
- (7) Akacem, Y.; Kassab, E. Vibrational Analysis of Pyridine Adsorption on the Brønsted Acid Sites of Zeolites Based on Density Functional Cluster Calculations. *J. Phys. Chem. C* **2008**, *112*, 19045–19054.
- (8) Topsoe, N. Infrared and temperature-programmed desorption study of the acidic properties of ZSM-5-type zeolites. *J. Catal.* **1981**, *70*, 41–52.
- (9) Buzzoni, R.; Bordiga, S.; Ricchiardi, G.; Lamberti, C.; Zecchina, A.; Bellussi, G. Interaction of Pyridine with Acidic (H-ZSM5, H- $\beta$ , H-MORD Zeolites) and Superacidic (H-Nafion Membrane) Systems: An IR Investigation. *Langmuir* **1996**, *12*, 930–940.
- (10) Freitas, C.; Barrow, N. S.; Zholobenko, V. Accessibility and Location of Acid Sites in Zeolites as Probed by Fourier Transform Infrared Spectroscopy and Magic Angle Spinning Nuclear Magnetic Resonance. *Johnson Matthey Tech.* **2018**, *62*, 279–290.
- (11) Zholobenko, V.; Freitas, C.; Jendrlin, M.; Bazin, P.; Travert, A.; Thibault-Starzyk, F. Probing the acid sites of zeolites with pyridine: Quantitative AGIR measurements of the molar absorption coefficients. *J. Catal.* **2020**, *385*, 52–60.
- (12) Kotrel, S.; Rosynek, M. P.; Lunsford, J. H. Quantification of Acid Sites in H-ZSM-5, H- $\beta$ , and H-Y Zeolites. *J. Catal.* **1998**, *182*, 278–281.
- (13) Tielens, F.; Gervais, C.; Lambert, J.-F.; Mauri, F.; Costa, D. Ab Initio Study of the Hydroxylated Surface of Amorphous Silica: A Representative Model. *Chem. Mater.* **2008**, *20*, 3336–3344.
- (14) Digne, M.; Sautet, P.; Raybaud, P.; Euzen, P.; Toulhoat, H. Hydroxyl Groups on  $\gamma$ -Alumina Surfaces: A DFT Study. *J. Catal.* **2002**, *211*, 1–5.
- (15) Digne, M.; Sautet, P.; Raybaud, P.; Euzen, P.; Toulhoat, H. Use of DFT to achieve a rational understanding of acid-basic properties of gamma-alumina surfaces. *J. Catal.* **2004**, *226*, 54–68.
- (16) Digne, M.; Raybaud, P.; Sautet, P.; Guillaume, D.; Toulhoat, H. Quantum chemical and vibrational investigation of sodium exchanged gamma-alumina surfaces. *Phys. Chem. Chem. Phys.* **2007**, *9*, 2577–2582.

(17) Michels, N.-L.; Mitchell, S.; Milina, M.; Kunze, K.; Krumeich, F.; Marone, F.; Erdmann, M.; Marti, N.; Pérez-Ramírez, J. Hierarchically Structured Zeolite Bodies: Assembling Micro-, Meso-, and Macroporosity Levels in Complex Materials with Enhanced Properties. *Adv. Funct. Mater.* **2012**, *22*, 2509–2518.

(18) Michels, N.-L.; Mitchell, S.; Pérez-Ramírez, J. Effects of Binders on the Performance of Shaped Hierarchical MFI Zeolites in Methanol-to-Hydrocarbons. *ACS Catal.* **2014**, *4*, 2409–2417.

## Chapter 6. Optimization of Reactive Force Fields for models of Interaction between ZSM-5 and binders

### 6.1. Introduction

The previous chapters have provided important information about the different surfaces of ZSM-5. The DFT calculations allowed studying the acidity thanks to adsorption of pyridine and ditertbutylpyridine probe molecules, and the interactions of these surfaces with small, individual species used as simplistic models of the binder, namely sodium, alumina and silica monomers. Knowledge of those interactions improves our understanding of the possible interactions of the ZSM-5 models with the binders' components. The interaction of zeolite bulk or zeolite external surface (cleavage 1 in (100) orientation) with alumina and silica monomers gave some preliminary insights (see Chapter 5) about the interactions that take place between zeolites and binders. However, more representative models are needed of both the zeolite and binder to take our comprehension to the next level. Consequently, three aspects need to be considered. Firstly, the presence of the water solvent. During the shaping the mixing of zeolite and binder occurs in water, forming a wet paste. However, the precise water quantity as a solvent is experimentally complicated to control. This will impact directly the water loading in the pores. Secondly, the use of one "simple" monomer does not necessarily represent well the binders. A first improvement would be the use of several alumina or silica monomers that interact with external zeolite surface model. Then a size increase of the binder model from a nanoparticle (an agglomerate of a dozen of monomers) to a small platelet (boehmite,  $\gamma$ -alumina, or amorphous silica) is to be envisaged. As a consequence of the larger binder models and the explicit addition of water, the zeolite external surface models need to be extended as well. So, the overall number of atoms increases rapidly by building such more representative models.

However, larger binder models that better represent the experimental system are currently too expensive in terms of computational resources for DFT calculations. As previously said, empirical force field methods are much less demanding and could therefore offer a good alternative. Yet, the force field parameters of the reactive force field (ReaxFF) are empirical parameters and must be validated before production calculations can be performed. The ideal force field can be applied to all possible systems, but in reality, they are applicable to a given family of systems. There is currently no force field available that correctly describes both zeolite systems<sup>1-3</sup> and alumina systems.<sup>4</sup> Therefore, a new ReaxFF force field needs to be optimized to describe our systems. To that end, the starting point of this study is formed by three existing force fields that are each reoptimized against a training set, which contains our reference data. Among the reactive force field devoted to H-ZSM-5, a first parameter set was developed by Pitman *et al.* to study the dynamic character of water and calcium cations confined into mesoporous regions.<sup>1</sup> A second interesting parameter set was developed by Joshi *et al.* to study the adsorption and diffusion of water molecules and their protonation inside the zeolite channels.<sup>2,5</sup> A third parameter set was constructed by Bai *et al.*

to simulate the Methanol to Olefins (MTO) reaction in MFI type zeolites.<sup>3</sup> These three parameter sets are detailed in section SI.1. in the Supporting Information of Chapter 6.

## 6.2. Methodology

### 6.2.1. Reactive force field

ReaxFF is a reactive force field that can model chemical reactions as it has been explained in section 2.4. in Chapter 2. It notably implies that during MD simulations bonds can be broken or formed on the fly. The description of interactions between atoms is a combination of bonding and non-bonding (electrostatic and Van der Waals) interactions making ReaxFF applicable to a large range of systems.<sup>6</sup> It is far from trivial to find the optimal parameters to describe a given system, because there are numerous parameters, creating a hyper dimensional surface where it is extremely difficult to find the global minimum. The latter corresponds to a set of parameters that describes best the data of a reference set (training set). It should, however, be noted that the optimized parameter set is not necessarily completely transferable and adjustments of the parameters may be needed even for systems of the same family.

### 6.2.2. Parameterization of ReaxFF

Originally, the initial method to optimize the parameters of a reactive force field is the successive one-parameter extrapolations (SOPPE),<sup>7</sup> but the numerical noises and the numerous local minima make SOPPE very laborious.<sup>8</sup> Many techniques were developed for ReaxFF parametrization or reparametrization: genetic algorithms GAs (good global optimization efficiency and automatized),<sup>9</sup> multi-objective evolutionary strategy,<sup>10</sup> a parallel local search algorithm,<sup>11</sup> Taguchi method-based optimization,<sup>12</sup> a Monte-Carlo FF (MCFF) optimizer,<sup>13</sup> and a covariance matrix adaptation evolutionary strategy (CMA-ES).<sup>14</sup> In the following study, the CMA-ES force field optimizer is used. Shchygol *et al.*<sup>15</sup> compared the GA optimizer to MCFF optimizer and to CMA-ES optimizer. The CMA-ES optimizer outperforms the MCFF optimizer at the same computational cost for a systematic comparison on three different training sets. Although CMA-ES is capable to find the most relevant reactive force field for three of these training sets, several runs are needed, due to the stochastic character within this algorithm. In the following work the CMA-ES optimizer is used as implemented in ADF2019.<sup>16,17</sup> CMA-ES is a stochastic algorithm for gradient-free numerical optimization of arbitrary functions. The detailed job file named `cma-es.run` is given in section SI.3. in the Supplementary Information of Chapter 6.

Two convergence criteria are used, and if one of them is reached, the optimization is stopped: MCFFIT and FFOTOL. The first defines the maximum number of iterations to reduce the total error. The second, is related to the step size and co-variance estimation. In our case, we applied the value of  $10^{-5}$  recommend by Shchygol *et al.*<sup>15</sup> and the ADF developers.<sup>17</sup> MCFFIT (here: 50000) needs to be sufficiently large, to assure that a minimum value for the total error is reached. It is to be noted that in our case we used the actual force field parameter values as an initial starting point, and we did not use a random guess.



The `mcrxdd` setting defines the width of the initial normal distribution of the parameter space. Small values start with a relatively broad initial distribution such that the algorithm explores a large portion of the parameter space before converging. Here we used `mcrxdd 25`, to turn CMA-ES into a more local optimizer with higher values since we already have good starting guess of the next step.

Due to the stochastic character of this algorithm several runs are needed to increase the chance to find the most performing reactive force field. Here, typically 15 to 20 runs were performed.

For those structures in the training set, that require a geometry optimization, we apply a maximum gradient of  $0.63 \text{ kcal mol}^{-1} \text{ \AA}^{-1}$  or a maximum number of iterations of 25 as a convergence criterion. With a relatively small number of geometry iterations, more “CMA-ES iterations” can be performed for a given amount of CPU time, while the final total error is not negatively impacted (see section SI.3. in the Supplementary Information of Chapter 6).

### 6.2.3. Parameters optimized

Generally, only those force field parameters, which are responsible for not accurately reproducing the correct chemical reactivity are selected to be “active” and thus to be optimized, in our case by the CMA-ES algorithm.

The parameter set of Joshi *et al.* or the parameter set of Pitman *et al.* have numerous activated parameters to adapt it to our systems. Activated parameters include both covalent and non-covalent bond interactions between Al-O, O-H, and bond angle parameters for Al-O-H, Al-O-O, Al-O-Al, O-Al-O, Al-Al-O, and Al-O-Si. The reader is referred to section SI.4. of the Supplementary Information of Chapter 6 through the reprography of the input “params” file for further details.

The Joshi force field,<sup>3</sup> is based on the original Si/Al/O/H force field by Joshi *et al.*<sup>5</sup> which in turn was trained against an extensive set of DFT data, including silicon/silicon oxide interfaces. To predict more accurately the strength of interaction and the potential energy surface between water molecules and the acidic protons of aluminosilicate models, a subset of parameters was refitted against DFT calculations.

The Pitman *et al.* force field essentially is a based on previously published works: H/O/Si<sup>18</sup> and H/O/Al<sup>19</sup> and extended with parameters for Ca/O and Ca/H.<sup>20</sup> The H/O/Si parameters were extracted from previous work of Van Duin *et al.*<sup>18,19,21</sup> where these parameters were optimized to fit to silicon and silicon oxide systems with quantum chemical calculations of small silicon clusters, condensed silica systems included in the training set. The Al/O/H parameters were trained against various phases of Al, Al<sub>2</sub>O<sub>3</sub>, and Al-O-H clusters. Finally, the Ca/O and Ca/H parameters were trained against calcium–water clusters, calcium oxide bulk and surface properties, calcium hydroxide, bcc and fcc Ca, and proton transfer reactions in the presence of calcium.

The reactive force field of Bai *et al.* is also inspired from the work of van Duin<sup>21</sup> and a previous study including  $\alpha$ -Al<sub>2</sub>O<sub>3</sub><sup>22</sup> for the Si, O, Al, H, and C atoms. The parameters are

extended to be representative of acidic zeolites. The goal of their work was to study the reactivity of these acid sites against MTO reaction. The previous studies extracted aluminum parameters from aluminum oxide, in their study they mostly changed parameters of aluminum to make them fit to their reactivity goals.

In the following, we will detail the training set and validation set that are used to optimize our reactive force field, using as three different starting points namely the force fields of Pitman *et al.*, Joshi *et al.* and Bai *et al.*

#### 6.2.4. Training set

Our training set is composed of geometries, charges and reaction energies. All these components were calculated with DFT with PBE functional, a plane wave basis and a dispersion correction dDsC as presented in a previous work (Chapter 3).<sup>23</sup> In the training sets, and later in the validation sets, the selected data can be *weighted* to reinforce the importance of some of them. The weight  $\sigma_i$  of a data  $i$  is implemented in the calculation of the objective function, such that small  $\sigma_i$  values give a high importance to data  $i$ . In our training sets and validation sets the following weights are used: 0.1 for distances, charges and energies, and 5.0 for angles.

Two training sets are made and will be distinguished by Tr.1 (training set n°1) and Tr.2 (training set n°2) in the following paragraphs. Both training sets are composed of surface models of H-ZSM-5. The cleavage 1 along (100) orientation (see the presentation of the external surfaces of ZSM-5 in Chapter 3) with its silicon number 59 changed by an aluminum (equivalent to the closest T5 site to the surface in IZA numeration system) and a compensating proton models (four possible position of compensating proton on an oxygen neighboring the aluminum, named H1, H2, H3, and H4) are taken. Emphasis is given on the bonds and the angles describing the active sites (Al-O, Al-O-Si, Al-O-H). The geometries of the hydration (named H1Hydration) and dehydration (named H1Deshydration) of the previous site forming an Al-H<sub>2</sub>O (named H1) surface site are added (similar bonds and angles), and the energies of these hydration ( $-16.1 \text{ kJ mol}^{-1}$ ) and dehydration ( $27.9 \text{ kJ mol}^{-1}$ ) reactions are also included in the training sets.

Secondly, the training sets are composed of alumina structures so the force field can describe as well binder models. In particular, geometrical features of the alumina monomer Al(OH)<sub>3</sub>(H<sub>2</sub>O) have been added together with the partial Hirshfeld charges of all the atoms. Details are found in trainset.in input files detailed in section SI.5. of the Supplementary Information of Chapter 6. Additionally, the energy curve of the water molecule desorption of a small cluster Al(H<sub>2</sub>O)[Si(OH)<sub>3</sub>]<sub>3</sub>, shown on Figure 8, calculated by DFT is added to the training sets.

The (100) and (110) surface orientations of the  $\gamma$ -Al<sub>2</sub>O<sub>3</sub> are added as well to both training sets, as they make part of the main surfaces exposed of  $\gamma$ -Al<sub>2</sub>O<sub>3</sub>.<sup>24</sup> The corresponding surface models were established by Digne *et al.*<sup>25,26</sup> and Wischert *et al.*<sup>27</sup> Each surface was studied at different hydration levels and some of them,  $\theta$  (in OH nm<sup>-2</sup>) values of 4.3, and 12.9 for the (100) surface and 3.0, 8.9, and 14.8 for the (110) surface, were selected for our training

sets. Details of their geometries are given geo input files in section SI.6. of the Supplementary Information of Chapter 6. The bulk cell of  $\gamma$ -Al<sub>2</sub>O<sub>3</sub> is also included in the training set.<sup>28</sup> Lastly,  $\gamma$ -Al<sub>2</sub>O<sub>3</sub> edge models are included, to build platelet for interface models. Edges models from Batista *et al.* are included in the training sets at different hydration levels. They are described by the number of water molecules adsorbed on the edge model and here are selected the models with 0, 3, and 6 water molecules adsorbed.<sup>29</sup> For all these alumina components many bonds and angles are implemented, details can be found in trainset.in in section SI.5. of the Supplementary Information of Chapter 6.

Both training sets also contain monomeric extra-framework species. These monomers were studied (Chapters 4-5, Al(OH)<sub>3</sub>H<sub>2</sub>O as alumina monomer and Si(OH)<sub>4</sub> as silica monomer) in interaction with the bulk zeolite and with its external surface. A bulk and a surface cell (cleavage 1 of orientation (100) following the terminology given in ref.<sup>23</sup>) of ZSM-5 with one T5 (IZA terminology) aluminated site is taken and the monomers are put into the structure in different ways to study the different possible interactions. Each monomer has various kinds of interactions with the zeolite. The training set is composed of bond and angles of the active sites of chosen models (details are found in section SI.5. in the Supplementary Information of Chapter 6). The chosen models include a) models interacting with the bulk; alumina monomer covalently bonded with the active site and proton transfer, alumina monomer covalently bonded with active sit, alumina monomer physisorbed at active site with proton transfer, alumina monomer physisorbed at active site, alumina monomer covalently bonded with a silicon of the zeolitic structure, alumina monomer physisorbed at the zeolite network, and silica monomer covalently bonded with the active site; b) models interacting with the active site at the external surface of zeolite; alumina monomer physisorbed with proton transfer, alumina monomer physisorbed, alumina monomer covalently bonded, a 2MR is formed between the monomer and the active site, alumina monomer covalently bonded on the dehydrated active site with or without protonation; c) models interacting with the silicon surface site at the external surface of zeolite; alumina monomer physisorbed in the zeolite network, alumina monomer physisorbed in the zeolite network on the dehydrated surface.

In Tr.2 additional emphasis (with respect to Tr.1) is given on the reproduction of water desorption from the zeolite external surface using desorption energy curves. Tr.2 is therefore extended by the different steps of hydration and dehydration of another surface's active site to strengthen the interaction of surface with water molecules. The site number 77 aluminated and forming an Al-H<sub>2</sub>O surface site from cleavage 6 along the (100) orientation is chosen, as it is the most stable in all the studied aluminated sites in Chapter 3. Several configurations are studied for each hydration and dehydration level and the most stable configuration are selected and shown in Figure S17 in the section SVII of the Supporting Information of Chapter 3. The most dehydrated surface exhibits 1.8 H<sub>2</sub>O nm<sup>-2</sup> and the most hydrated one presented on the stability diagram possess 2.8 H<sub>2</sub>O nm<sup>-2</sup>; their geometries are added to Tr.2 and the hydration energies from the most hydrated external surface to the most dehydrated one are also added.<sup>23</sup> Then, this external surface site is hydrated to form an octahedral site as shown in Figure 1 a-b which possess 3.0 H<sub>2</sub>O nm<sup>-2</sup>. The dehydration energy from 3.0 to 2.8

$\text{H}_2\text{O nm}^{-2}$  is added to the Tr.2. The bonds and angles of the active site (Al-O, Al-O-Si, Al-O-H) of these geometries are again added to Tr.2.

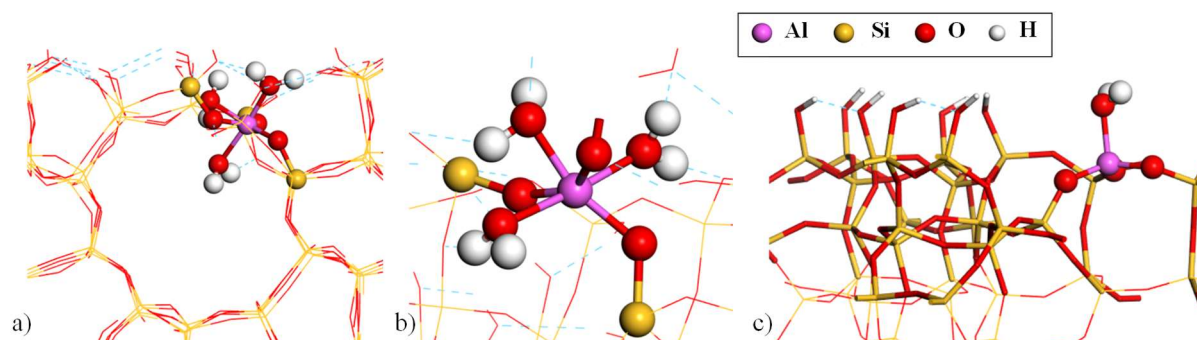


**Figure 1** Supplementary structures from the Tr.2; a-b) Octahedral structure of the aluminated site number 77 with  $3.0 \text{ H}_2\text{O nm}^{-2}$  at the external surface; c) Aluminated site number 121 on cleavage 2 of (010) orientation.

Tr.2 furthermore contains the desorption curve of water on the aluminated site number 121 on cleavage 2 of (010) orientation, shown in Figure 1c. The energy curve is calculated by DFT.

### 6.2.5. Validation set

The validation set is constructed to verify the predictive power of the generated reactive force fields.

Purely silicic surface are included in this set to give information about the ability of the reactive force field to reproduce the major external surfaces of H-ZSM-5, as studied in our previous work.<sup>23</sup> The two major surfaces of the stability diagrams presented in Figure 2 of Chapter 3 of each orientation (100), (010), and (101) presented in Figure 2 of Chapter 3 are selected, namely cleavage 1 ( $1.5 \text{ H}_2\text{O nm}^{-2}$ ), and 6 ( $4.1 \text{ H}_2\text{O nm}^{-2}$ ) for (100) orientation, cleavage 2 ( $1.5 \text{ H}_2\text{O nm}^{-2}$ ), and 6 ( $4.5 \text{ H}_2\text{O nm}^{-2}$ ) for (010) orientation, and cleavage 6 ( $1.9 \text{ H}_2\text{O nm}^{-2}$ ), and 7 ( $3.8 \text{ H}_2\text{O nm}^{-2}$ ) for (101) orientation.

One system with an aluminated site on each of these surfaces have been added, the aluinated sites no. 75 on cleavage 1 (100), no. 77 on cleavage 6 (100), no. 43 on cleavage 2 (010), no. 89 on cleavage 6 (010), no. 37 on cleavage 6 (101), and no. 57 on cleavage 9 (101). They have been also described in our previous work, in Chapter 3 and in section SVI.2. of Supplementary Information of Chapter 3, and they allow to check if the representation of the zeolites active site is correct.

The validation set also contains surfaces and edges of  $\gamma\text{-Al}_2\text{O}_3$  which are absent from the training set. They include (100)  $\gamma\text{-Al}_2\text{O}_3$  surfaces (for  $\theta$  values of 0.0, 8.8, and  $17.1 \text{ OH nm}^{-2}$ ), (110)  $\gamma\text{-Al}_2\text{O}_3$  surfaces (for  $\theta$  values of 0.0, 11.8, and  $17.8 \text{ OH nm}^{-2}$ ) and  $\gamma\text{-Al}_2\text{O}_3$  edges between (100) and (110) (2 and 7 adsorbed water molecules) surfaces. To complete the alumina representation, bulk and surfaces ((001), (010), and (101) orientations) of boehmite are added to the validation set.<sup>30,31</sup>

More atypical geometries are also included in the validation sets to challenge the reactive force field. The model of external surface of cleavage 1 of (100) orientation was aluminated with 4 aluminum atoms instead of one in our previous models, the aluminated sites can be all four close to the surface, or can be more homogeneously spread, as presented in Chapter 3 and shown in Table S14 in Supplementary Information of Chapter 3. Amorphous silica surface models from Tielens *et al.*<sup>32</sup> was aluminated to create disordered silica with a terminal Al-H<sub>2</sub>O or a bridging Al-OH-Si, also used in Chapter 5 for sodium adsorption. A model of thin layer of silica film on (100) surface of  $\gamma$ -Al<sub>2</sub>O<sub>3</sub> ( $\theta_{\text{Si}} = 6.4 \text{ Si nm}^{-2}$  and  $\theta_{\text{OH}} = 5.4 \text{ OH nm}^{-2}$ ) is modified, some nanoparticles of silica were added to the surface and added to the validation set.<sup>33</sup>

The sources of all the data being numerous, the geometries of the training and the validation sets are pre-optimized with the same DFT parameters which are used for the slabs in Chapter 3. Detailed information of each of the geometries in the validation set can be found in section SII of the Supplementary Information of Chapter 6.

## 6.3. Results

### 6.3.1. H-ZSM-5 cleavage 1 along (100) orientation

Preliminary tests are made on the three starting sets of parameters of Pitman, Joshi and Bai. The DFT-optimized geometries of the external surface of ZSM-5 (cleavage 1 along (100)) are used as a starting point for independent geometry optimizations performed with the three ReaxFF force fields (with Conjugate Gradient Algorithm with fixed cell parameters). The DFT-ReaxFF geometry agreement is quantified by the area of the pores of the zeolite. The area of the deep straight pores are calculated using the position of atoms; oxygen n°218 and silicon n°101, long side, oxygen n°435 and n°247, short side (straight pore 1 in Figure 2), silicon n°29 and oxygen n°438, long side, oxygen n°215 and n°378 (straight pore 2 in Figure 2) assuming the section of these pores are perfect ellipses. The area of the sinusoidal pore is also measured at the outermost surface with the positions of silicon n°77 and n°125, long side, and oxygen n° 565 and n°568, short side, using the same assumption. The detailed locations of these atoms are given in section SIII in the Supplementary Information of Chapter 6.

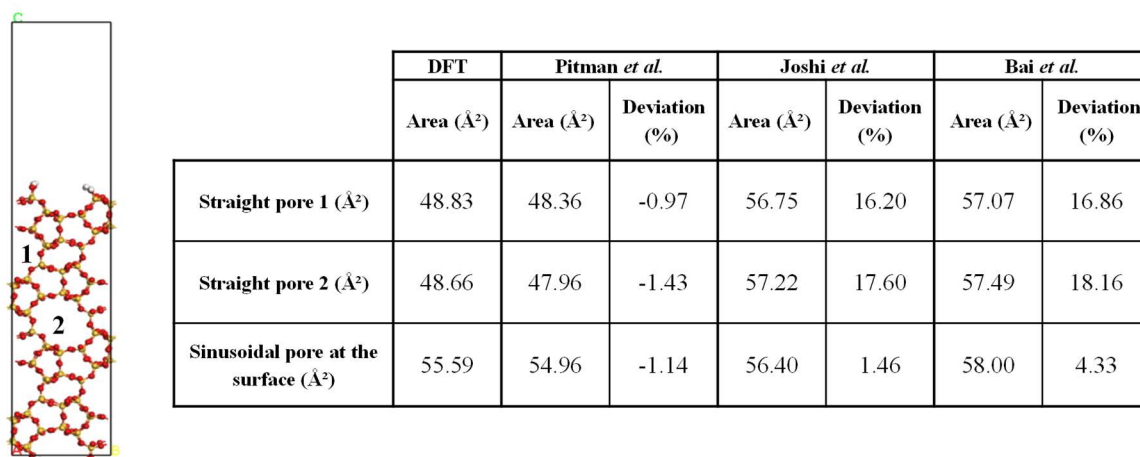


**Figure 2:** Preliminary tests of the reactive force fields of Pitman *et al.*,<sup>1</sup> Joshi *et al.*<sup>2,5</sup> and of Bai *et al.*<sup>3</sup> as compared to the DFT optimized structure of ZSM-5 external surface (cleavage 1 along (100)). (Left) Representation in ball and stick of the external surface model with the distinction on the straight pores by numbers 1 and 2 (Right) Table of the error with respect to the DFT data of the pores size depending on the modeling method used.

The results of geometry optimizations are presented in Figure 2 and compared to the optimized geometry obtained with DFT. Only the Pitman reactive force field conserves the ovoid shape of the straight pores while the Joshi and Bai force fields distort the structure to form a round shape for these pores. Consequently, the gap between the reference values and the ones generated by the Pitman force field is less than 2% of the area of every pores, while the two other reactive force fields generate an error between 16 and 19% for the straight pores areas (with a slightly less important deformation for the result generated by Joshi). For the sinusoidal pore, the Bai force field induces a deformation of more than 4% while the Joshi force field deformation value equals 1.46%. The reproduction of the DFT-optimized geometry is clearly better with the Pitman force field. But the general organization of the ZSM-5 crystal is conserved also by the two other reactive force fields. Since the Joshi and Bai force fields are very similar (similar parameters for Al, O, Si and H atoms and similar optimization ways which can be observed in section SI.1. of Supplementary Information of Chapter 6) only one of the two is selected for our reactive force field optimization. Beside the Pitman force field, the Joshi force field has been selected for further optimization, since it slightly better represents H-ZSM-5 and furthermore its parameter set contains additional chemical elements, that could also be exploited in a later stage (C/S/N/Na for Bai force field against C/S/N/Na/Ca/Cs/K/Sr/Mg for Joshi force field).

### 6.3.2. Selection of the initial reactive force field

The Pitman and Joshi reactive force fields have been trained against Tr.1 using the CMA-ES method, as described in Chapter 2, paragraph 2.4.3. The details of these optimizations can be found in paragraph 6.2.2.

The first way to check the efficiency of the improvement of the reactive force field is to observe if and how the total *weighted* error (Eq. 46 in Chapter 2), which is our objective function, diminishes as a function of the total number of iterations. An example of such a

RUN is shown in Figure 3. In total 15 exactly similar optimization RUNS were performed and Table 1 summarizes the final (best) total error for each RUN and each force field.

RUN	1	2	3	4	5	6	7	8	9	10	11	12	13	14	15
Pitman <i>et al.</i>	3220 6	2656 2	2392 3	2255 5	3573 0	1889 7	1389 2	1375 0	1586 5	1054 1	4334 5	6669 4	4624 3	6038 0	7107 6
Joshi <i>et al.</i>	7452	7828	7051	6008	8791	6324	5682	5483	4417	6594	1959 6	1389 3	8919	2771 8	1405 5

**Table 1.** Minimal value of the objective function obtained for 15 similar runs with the initial reactive force fields of Pitman *et al.* and Joshi *et al.* at the end of 48h CPU calculation on 4 nodes.

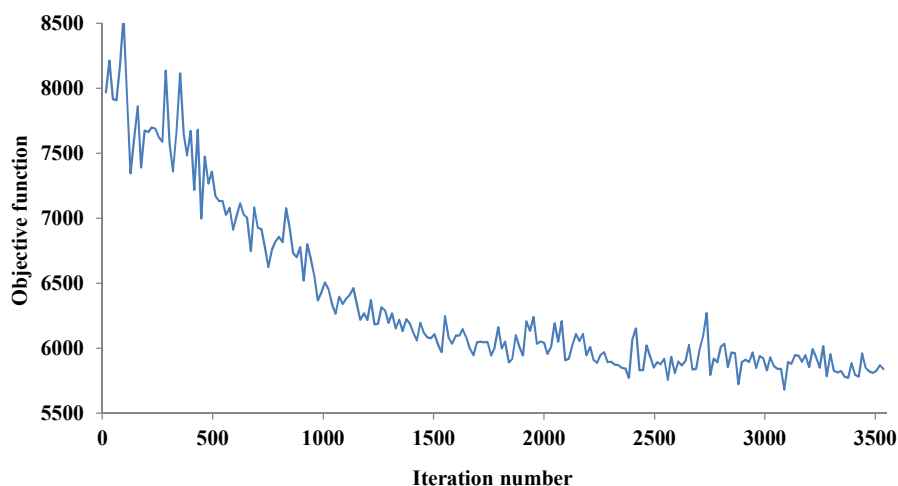


**Figure 3.** Optimization of Joshi's reactive force field with Tr.1 in RUN no.7 presented in Table 1

As detailed in the previous paragraph, multiple runs are needed with the CMA-ES method to increase the chance to converge to the global minimum, corresponding the best optimized parameter to describe Tr.1. In our case we used in total 15 runs. On the basis of the average total error value and the standard deviation (for each force field), this number seems quite reasonable.

The average and more importantly the minimum total error is significantly smaller, starting from the Joshi force field as compared to Pitman: respectively 4417 % and 10541 %. This suggests that the new force field optimized for the one of Joshi *et al.* should better describe our systems.

### 6.3.3. Objective function convergence and water desorption

Next, we reran 10 RUNS applied to Tr.1 and Tr.2 for the original Joshi force fields, but now with more iterations, including restarts. Based on the analysis of the objective functions, the desorption temperature of water molecule adsorbed on site no. 59 aluminated on cleavage 1 of (100) orientation (see Chapter 3) obtained with the Molecular Dynamic (MD) are presented in Table 2 and Table 3. One reactive force field from each training set will be selected. The molecular dynamics was run with a step size of 0.25 fs at a constant temperature of 0.01 K for 1000 steps. Then the temperature was linearly increased in 4 million steps up to



2500 K. The temperature of desorption depends on the water pressure as shown in the thermodynamic diagram (Figure 6a in Chapter 6), and the temperature desorption of this surface must be under 1000 K to approach a realistic model.

Tr.1	RUN	1	2	3	4	5	6	7	8	9	10
Start	Objective function	4327.83	3874.06	5172.42	2518.58	5659.94	3002.98	5118.56	3130.81	4181.32	4857.92
	Total number of iteration	57936	58064	57920	57264	57248	58352	57968	58528	59024	56528
	Desorption temperature	2000	no	1100	2400	2400	800	1200	2400	1300	no
Restart	Objective function after restart	3310.7	4090.48	3987.44	2494.44	5107.26	2845.43	4104.51	3360.16	3957.15	3702.96
	Total number of iteration	50336	50464	50144	50448	50592	50880	60384	58896	58528	60064
	Desorption temperature	no	2200	1450	1950	no	1800	2000	1500	2500	2200

**Table 2.** Reactive force fields characteristics from Tr.1 and initial reactive force field of Joshi *et al.* after a start and a restart: minimal value of the objective function, total number of iterations, and desorption temperature obtained with MD.

Tr.2	RUN	1	2	3	4	5	6	7	8	9	10
Start	Objective function	33942.7	56489.3	19835.6	86792.6	84041.2	70548.2	36824.4	62725.4	92692.7	131855
	Total number of iteration	30848	31152	27296	32448	31520	31744	31376	33712	33360	32832
	Desorption temperature	2050	2150	1750	no	2100	no	no	no	2200	2400
Restart	Objective function after restart	41224.9	54048.6	11960.3	58109.7	37825.8	48552.5	16207.4	62082.9	97433.6	43351.8
	Total number of iteration	27280	27488	144448	27776	26656	27920	27808	27728	27856	31968
	Desorption temperature	2000	2050	850	no	no	no	2500	1800	no	1700

**Table 3.** Reactive force fields characteristics from Tr.2 and initial reactive force field of Joshi *et al.* after a start and a restart: minimal value of the objective function, total number of iterations, and desorption temperature obtained with MD.

The training set that are going to be chosen should combine the smallest possible objective function and the most realistic possible water temperature desorption. From Tr.1, we selected the force field obtained with RUN 6 of the first start. This first reactive force field, named after Rff1, as an objective function equal to 3002 which is better than the initials tests made to choose between Pitman *et al.* and Joshi *et al.* as initial reactive force fields, but not from other RUN made on Tr.1. However, this force field has a water temperature desorption of 800 K which is closer to the DFT thermodynamic results than all the others. From Tr.2, we selected the force field obtained with RUN 3 of the restart. This second reactive force field, named after Rff2, as an objective function equal to 11960 which is better than all the objective function obtained with Tr.2 but worse than the ones obtained with Tr.1 due to the differences in their composition. Tr.2 is composed with supplementary energy input data, with a

relatively high weight. However, the water temperature desorption obtained is equal to 850 K which is similar to the result obtained with Rff1. The analysis of the two reactive force fields will however show (see next section) that the force field with the smallest error is not necessary the one to be selected. The detailed composition of Rff1 and Rff2 are given in section SIV of the Supplementary Information of Chapter 6.

### 6.3.4. Error distribution on the training sets for the two best force fields

#### 6.3.4.1. Distance and angle errors

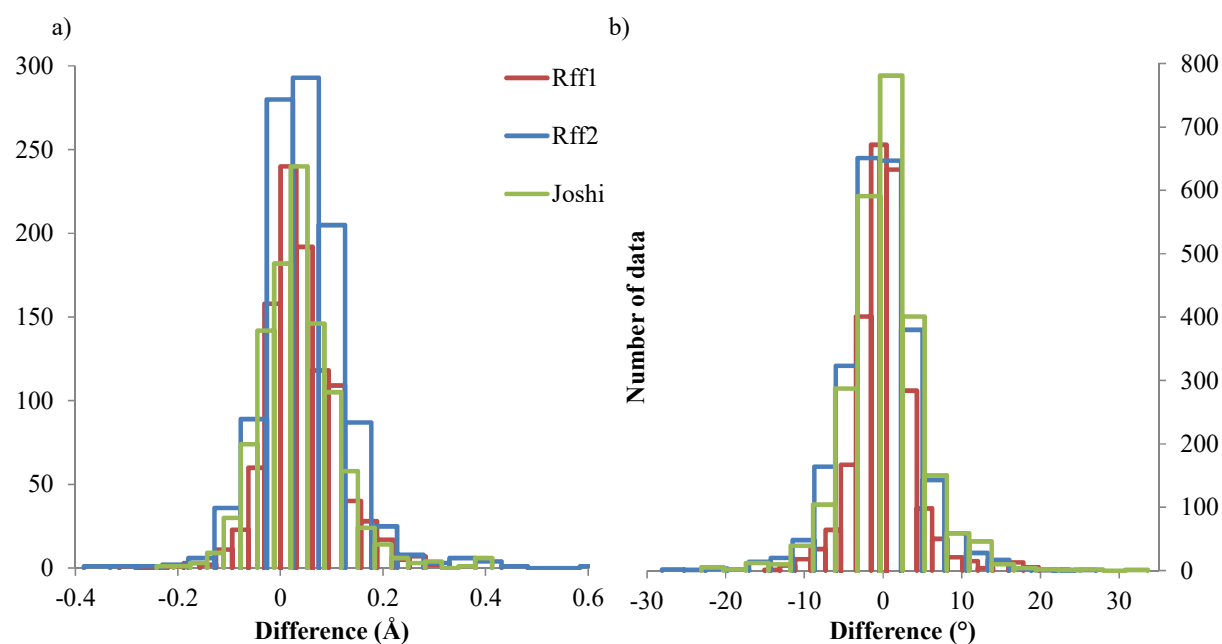


**Figure 4.** Error distribution of distances a) and angles b) obtained with the reactive force fields Rff1, Rff2, and Joshi's compared to the reference data obtained with DFT.

The overall error directly depends on the individual weights that are given for each data point in the training set. The chosen weight for the selected bond distances is 0.1, while the weight for angles is 5.0. The error distribution of the bond distances and bond angles are shown in Figure 4; it represents the number of data calculated by the two reactive force fields which are contained in the same interval of difference relatively to the reference data obtained with DFT. A large number of errors are concentrated around zero for the distances and the angles of both reactive force fields. In comparison, the error distributions of geometrical parameters of the initial Joshi *et al.* reactive force field is given on the same figure. One can observe that the error distribution is slightly improved for Rff1 compared to Joshi for distances and angles. Rff2 has errors up to 0.6 Å for the distances and up to 28° in absolute value for the angles which represent errors which are more important or equal to the performance of Joshi. An important distance difference will induce problems; water desorption from the surface, important modification of the acid sites, changes in a molecule adsorption mode. The weaknesses of Rff2 had to be controlled to verify that they are negligible and compared to the initial weaknesses of Joshi.

The maximum distance errors for Rff2 and Joshi concern a structural distance (Al-O) between aluminum in  $\gamma$ -alumina edge dehydrated. Joshi reactive force field generates elongation of two Al-O bonds inside the structure of 0.4 Å, while Rff2 induces height elongations between 0.4 to 0.6 Å of Al-O bonds. However, the general structure of the  $\gamma$ -alumina is well maintained as it can be seen in section SV.1 of Supplementary Information of Chapter 6.

The maximum distance errors concern also the distance between the oxygen of water molecules adsorbed on aluminum of (100)  $\gamma$ -alumina surface of 12.9 OH nm<sup>-2</sup>. This distance is increased of 0.4 Å by Joshi, while it is increased of 0.3 Å by Rff2 as is it shown in Figure 5. In comparison, Rff1 observes an elongation of 0.2 Å for these distances. The elongation is more reasonable for Rff1 and for Rff2 than for Joshi even if the difference is small. In comparison, the elongation of Al-(H<sub>2</sub>O) distance is more reasonable on (110)  $\gamma$ -alumina surface. It is equal to 0.3 Å for Joshi, while it is under 0.2 Å for Rff1 and Rff2 as shown in section SV.2 in the Supplementary Information of Chapter 6.

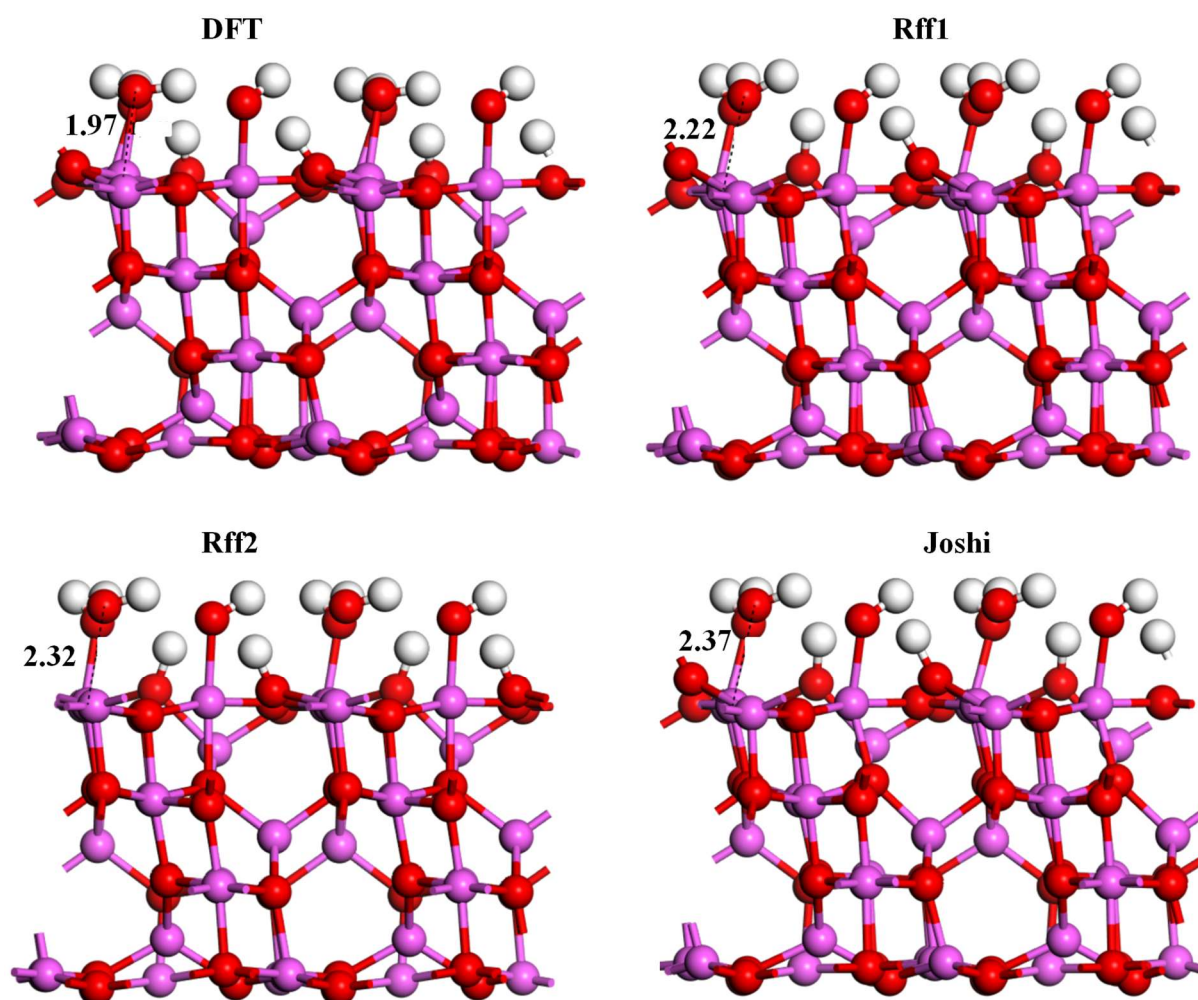


**Figure 5.** Results of geometry optimization of (100)  $\gamma$ -alumina surface of 12.9 OH nm<sup>-2</sup> calculated by DFT, Rff1, Rff2, and Joshi reactive force field.

The training set contains numerous structures of alumina monomer,  $\text{Al}(\text{OH})_3(\text{H}_2\text{O})$ , adsorbed on H-ZSM-5 surfaces in bulk and at the external surface. The distances and the angles of all these systems are not showing the highest errors. Meaning while these systems are optimized similarly to the reference data. The two most stable systems adsorption mode, hydrogen bonds and proton transfer, in bulk and at the external surface are presented in Figure 6. In bulk, the monomer is adsorbed on T5 aluminated site and the geometry optimization with Joshi, Rff1, and Rff2 observes no adsorption differences with the reference data obtained with DFT. The same adsorption mode at the external surface on aluminated site no. 59 on cleavage 1 of (100) orientation is presented in Figure 6. The geometry optimization with Joshi and Rff2 are equivalent to the reference data. Rff1 geometry optimization of this structure generate a difference which is surrounded with a black circle, the proton is transferred from the monomer to the acid site. The distance is not highlighted by the distance error distribution of Figure 4 because the transfer is not made on a long distance. However, the proton transfer is stabilizing the monomer at the surface as it has been shown in Chapter 5. Joshi initially represents well the adsorption, but Rff1 has lost this characteristic contrary to Rff2.

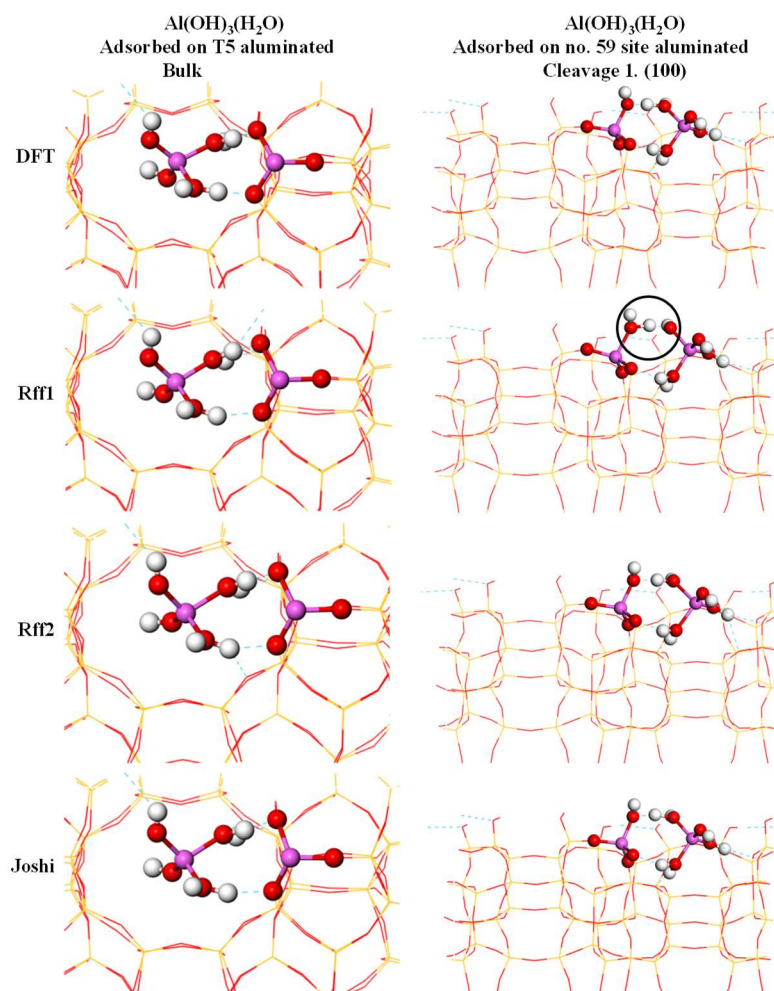


**Figure 6.** Results of geometry optimization of alumina monomer  $\text{Al}(\text{OH})_3(\text{H}_2\text{O})$  adsorbed on T5 aluminated site in bulk and aluminated site no. 50 at the external surface of cleavage 1 of (100) orientation with the most adsorption mode revealed in Chapter 5, hydrogen bonds and proton transfer, calculated by DFT, Rff1, Rff2, and Joshi reactive force field.

Joshi's reactive force field has already parameters adapted to the geometry optimization of our systems. The implementation of distance and angle in our case has two main objectives: first control and maintained the general performance of Joshi, and second try to improve the few localized errors which are lacking to Joshi. Rff1 fits to these two objectives when Rff2 enhances some errors. Rff1 and Rff2 can be considered as small improvement of Joshi reactive force field for the geometric aspects, but other aspects of the training set must also be controlled.

#### 6.3.4.2. Hirshfeld charge errors

The Hirshfeld net atomic charges of the alumina monomer are implemented in both training sets Tr.1 and Tr.2. The value of the net partial charges calculated by Rff1 and Rff2 are presented in Figure 7, where the reference values are given and also a representation of the alumina monomer with the atom numbers. The charges generated by the reactive force fields are higher in absolute value than the reference values, but they all have the correct plus/minus sign. An important difference is observed for the charge of O5, which has smallest negative charge of all oxygen atoms in the reference set, while it is the largest in Rff1 and Rff2. Similarly, the hydrogen H9 and H11 of the water molecule have the highest charge in the reference set, but are both smaller than H7, H8 and H10 in the hydroxyl groups in Rff1, whereas in Rff2 all hydrogen atoms have practically the same net atomic charge. The aluminum atom has an overestimated charge compared to the hydrogen for which the charge is already almost doubled. These aspects are similar to the results which are obtained with Joshi reactive force field. Rff1 and Rff2 are not improving the results of Joshi on the description of the Hirshfeld charges but maintain similar results.

The fact that both Rff1 and Rff2 overestimate the net atomic charge, might result in electrostatic interactions that become overestimated in the overall geometries.

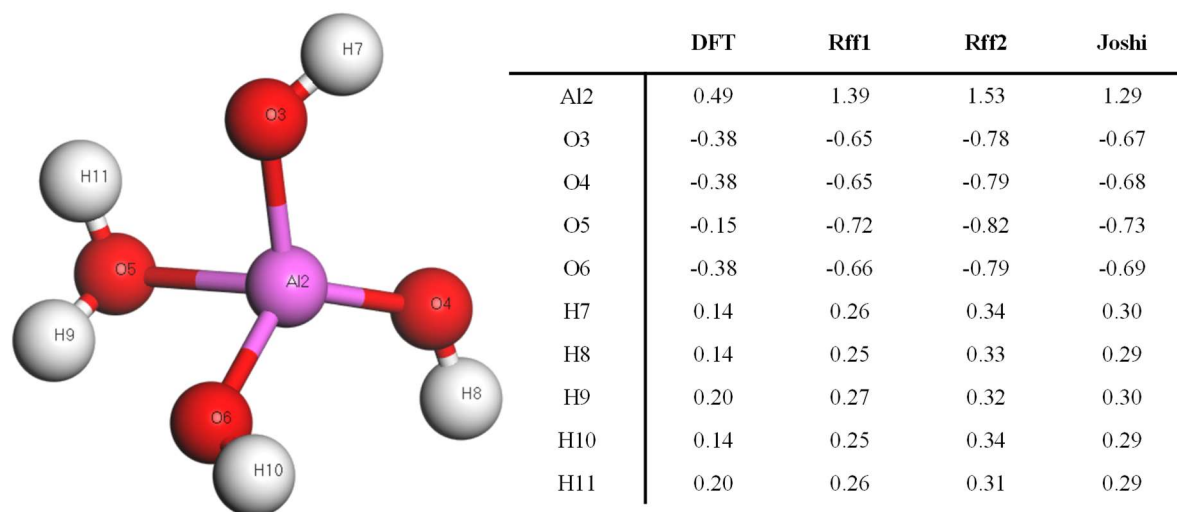


**Figure 7.** Hirshfeld charge distribution in alumina monomer calculated with the reference method DFT, with our two reactive force fields Rff1 and Rff2, and with Joshi's reactive force field.



### 6.3.4.1. Energy errors

The energy data in the training sets are given a relatively important weight. These energies are relative between two or three systems and can be considered as reaction energies. Figure 8 shows the energy curve for the water desorption of the cluster  $\text{Al}(\text{H}_2\text{O})[\text{Si}(\text{OH})_3]_3$  resulting from relaxed coordinate scans. The irregularities in the curves are mostly due to the dissociation path, which was chosen, being closely to the  $\text{Si}(\text{OH})_3$  groups generate hydrogen bonds which affects the energy curves. Both the Rff1 (red curve) and Rff2 (blue curve) reproduce well the black reference curve. It is to be noted that the desorption energy of this water molecule is influenced by the hydrogen bonds that are formed and broken upon the dissociation from the Al-center. This likely explains the differences between the reference data and those of Rff1 and Rff2 at the intermediate distances, as represented for 3.5 Å in section SV.3 of the Supplementary Information of Chapter 6, where hydrogen bonding plays an important role. The final desorption energy of the water molecule obtained with Rff1 (19.1 kcal mol<sup>-1</sup>) and Rff2 (22.0 kcal mol<sup>-1</sup>) are close to the reference value of 19.9 kcal mol<sup>-1</sup>. In comparison, Joshi reactive force field is farer from the references data. The training set gives here a more noticeable improvement.

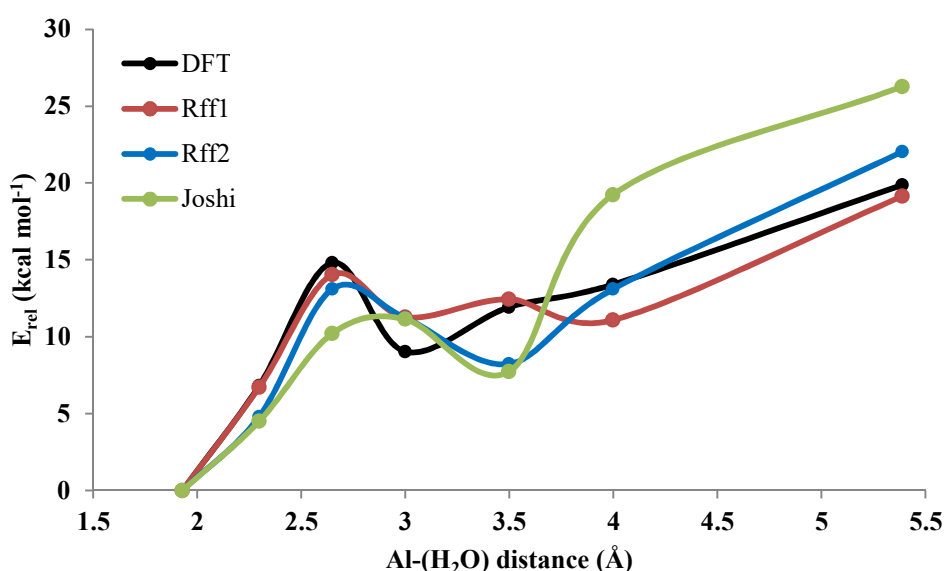


**Figure 8.** Energy desorption curve of the water molecule adsorbed on alumina and silicon cluster  $\text{Al}(\text{H}_2\text{O})[\text{Si}(\text{OH})_3]_3$  relative to the energy of the most stable adsorption position of water; calculated by DFT (black curve), Rff1 (red), Rff2 (blue), Joshi reactive force field (green).

Energies of the adsorption and desorption of water on the H-ZSM-5 external surfaces are also included in both training sets. The reference energies of hydration (from 1.7 to 2.1  $\text{H}_2\text{O nm}^{-2}$ ) and dehydration (from 1.7 to 1.3  $\text{H}_2\text{O nm}^{-2}$ ) of aluminated site no. 59 on cleavage 1 of (100), previously presented in Figure 6 in Chapter 3, orientation are equal to  $-16.1$  and  $27.9$  kcal mol<sup>-1</sup> respectively as presented in Table 4. Rff1 obtains for the same hydration and dehydration energies the values of  $-16.0$  and  $31.1$  kcal mol<sup>-1</sup> respectively, Rff1 represents very well the hydration and dehydration steps for this aluminated site no. 59. While Rff2 obtains  $-10.2$  and  $28.9$  kcal mol<sup>-1</sup> respectively. The dehydration is well reproduced by Rff2

but the hydration has an important difference of 6 kcal mol<sup>-1</sup> compared to the reference data. Again, the improvement from Joshi results is noticeable.

	DFT	Rff1	Rff2	Joshi
Dehydration	27.9	31.1	28.9	16.3
Hydration	-16.1	-16.0	-10.2	0.4

**Table 4.** Hydration and dehydration energies (kcal mol<sup>-1</sup>) of aluminated site no. 59 obtained with DFT (reference data) and with reactive force fields Rff1, Rff2, and Joshi's.

A second part of energy data is only implemented in Tr.2, but not in Tr.1. These energies have thus been used as a validation set for Rff1. The first set of supplementary energies in Tr.2 concerns the desorption of a water molecule from aluminated site no. 121 on cleavage 2 of H-ZSM-5 external surface cut along the (010) orientation. The reference desorption curve is represented by the black curve in Figure 9. The red curve represents the results obtained with Rff1 and the blue curve with Rff2. The equilibrium distance between the aluminum and the oxygen of the water molecule is around 2.04 Å for both force fields and overestimates the reference distance equal to 1.95 Å. Upon dissociation, the blue curve closely follows the black curve and the final desorption energy of 24.1 kcal mol<sup>-1</sup> obtained with Rff2 is in good agreement with the reference data of 26.8 kcal mol<sup>-1</sup>. Rff1 however underestimates this desorption energy (17.8 kcal mol<sup>-1</sup>), but was not specifically trained for it. However, it shows a radical improvement compared to Joshi force field which has a distorted representation of this desorption curve.

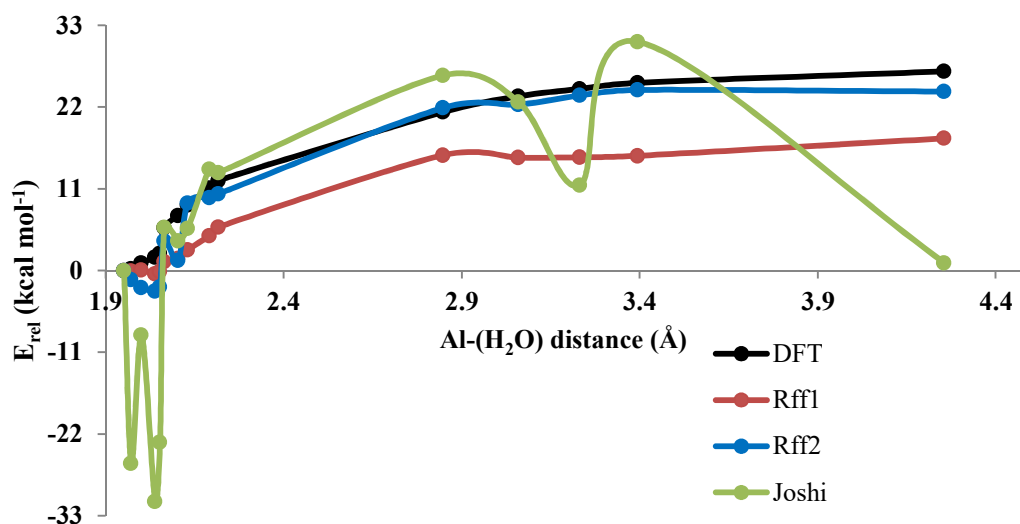


**Figure 9.** Desorption energy curve of water molecule adsorbed on (relative to the energy of the most stable adsorption position of water) aluminated site number 121 on cleavage 2 of (010) orientation; calculated by DFT (black), Rff1 (red), Rff2 (blue), and Joshi's reactive force field (green).

Tr.2 also contains the dehydration energies of the surface named cleavage 6 with aluminated site no. 77 cut along the orientation (100) from the hydrated surface with 3.0 H<sub>2</sub>O nm<sup>-2</sup> presented in Figure 1 a-b to the hydrated surface with 1.8 H<sub>2</sub>O nm<sup>-2</sup>, which are all presented in Figure S17 section SVII of Supplementary Information of Chapter 3. The desorption energies are presented in Table 5. As expected Rff2 yields better results than Rff1.



The desorption energy of 3.0 to 2.8 H<sub>2</sub>O nm<sup>-2</sup> is the most difficult energy to reproduce with a difference with the reference data of 6 kcal mol<sup>-1</sup> for Rff2 and 13.5 kcal mol<sup>-1</sup> for Rff1. For the other energies the differences with the reference data are below 3.3 kcal mol<sup>-1</sup> for Rff2, and the order of the energies is similar to the reference data. However, Rff1 have also important differences with the reference data for the desorptions 2.4 to 2.2 H<sub>2</sub>O nm<sup>-2</sup> and 2.0 to 1.8 H<sub>2</sub>O nm<sup>-2</sup>. It can be presumed that the octahedral form of aluminum present at 3.0 H<sub>2</sub>O nm<sup>-2</sup> is destabilized by Rff1 and Rff2. While the pentahedral and tetrahedral aluminum forms and the surface changes associated to the hydroxyl surface groups are better reproduced by Rff1 and Rff2. Finally, the energy of the Al<sub>III</sub> form is well reproduced by Rff2 while Rff1 seems to overestimate its stability compared to the tetrahedral form. The results obtain with Joshi force field are worse than the ones obtained with Rff1 and Rff2. There is an important improvement of the force field against these energies. The detailed Al-(H<sub>2</sub>O) distances of these active sites optimized by DFT and reactive force fields Rff1, Rff2, and Joshi are given in section SV.4 of the Supplementary Information of Chapter 6. These geometries are very close to the reference geometries, with a maximum elongation of the distance of 0.2 Å made by Rff2 on all the surfaces except 3.0 H<sub>2</sub>O nm<sup>-2</sup>, on which Rff1 that reflects the most the reference data while Rff2 and Joshi overestimate these distances going up to 0.4 Å.

	DFT	Rff1	Rff2	Joshi	Reaction
3.0 to 2.8 H <sub>2</sub> O nm <sup>-2</sup>	16.7	3.2	10.7	-95.6	
2.8 to 2.6 H <sub>2</sub> O nm <sup>-2</sup>	6.1	7.3	4.2	-3.8	
2.6 to 2.4 H <sub>2</sub> O nm <sup>-2</sup>	12.9	9.7	10.5	-1.4	
2.4 to 2.2 H <sub>2</sub> O nm <sup>-2</sup>	24	18.6	27.3	30.9	
2.2 to 2.0 H <sub>2</sub> O nm <sup>-2</sup>	39.1	40.3	41.4	70.1	
2.0 to 1.8 H <sub>2</sub> O nm <sup>-2</sup>	37.8	26.9	35.5	51.3	

**Table 5.** Water desorption energies in kcal mol<sup>-1</sup> from no. 77 aluminated site, on the surface named cleavage 6 cut along (100) orientation, from the hydrated surface with 3.0 H<sub>2</sub>O nm<sup>-2</sup> to the hydrated surface with 1.8 H<sub>2</sub>O nm<sup>-2</sup> obtained with DFT (reference data) and with reactive force fields Rff1, Rff2, and form Joshi et al.

With the selected force field parameters optimized with the CMA-ES algorithm two different force fields are obtained that generally well reproduce the data, especially the geometrical features like bond distances and bond angles, from their respective training sets. Initial reactive force field of Joshi has similar performances on geometrical feature. Accurate reproduction of the hydration/dehydration reaction energies sometimes appears to be more difficult. However, there is a clear improvement compared to Joshi force field. We thus conclude that from an “optimization” viewpoint, the CMA-ES is sufficiently accurate. However, the quality and quantity of the data in Tr.1 and Tr.2 to allow the optimized force field to predict the real systems needs to be confirmed. We therefore will now apply Rff1 and Rff2 to our predefined validation set.

### 6.3.5. Performance of the two optimized force fields on the validation set

The two reactive force fields Rff1 and Rff2 are applied to the validation sets presented in paragraph 6.2.5.

#### 6.3.5.1. Purely silicic surfaces and aluminated zeolite surfaces

The validation set is notably composed of purely silicic surfaces. The analysis of the errors on parameters at the external surface of silicalite are presented in Figure 10, the difference between reference data and the results obtained show very small differences. The maximum difference for distances is equal to 0.1 Å in absolute value, which is not significant. Similarly, the angle maximum difference is reasonable and tends to confirm that both Rff1 and Rff2, based on Joshi reactive force field, are very accurate for Si/O/H parameters for zeolite external surfaces.

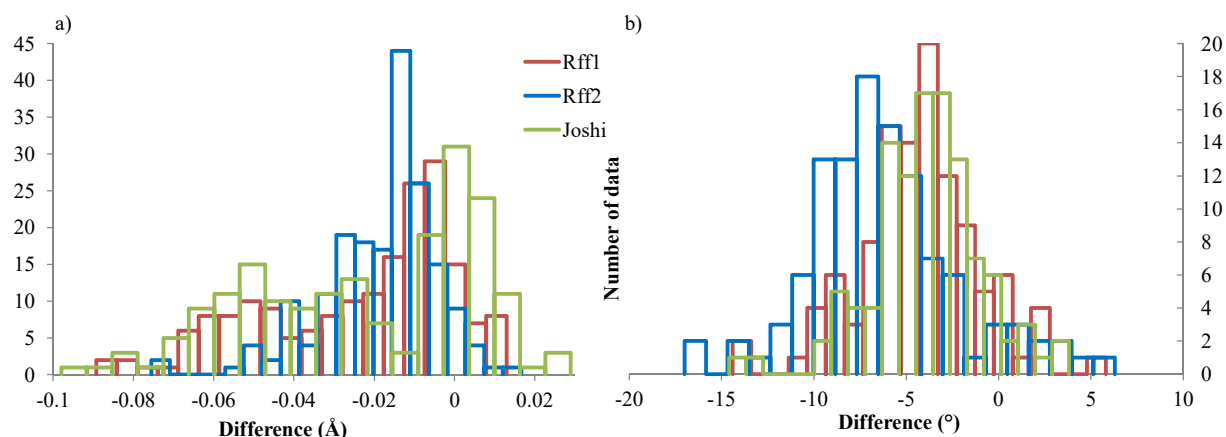


**Figure 10.** Error distribution of distances a) and angles b) obtained with the reactive force fields Rff1, Rff2, and Joshi compared to the reference data obtained with DFT on silicalite validation set.

Similar results are obtained with Rff1 and Rff2 on the aluminated external surfaces of zeolite validation set. The maximum distance error in absolute value is equal to 0.15 Å and the maximum angle error in absolute value is equal to 28°. These errors are very reasonable, even if it is not an improvement of Joshi, and show that both Rff1 and Rff2 force fields can predictively describe silicic and aluminated external surfaces accurately.

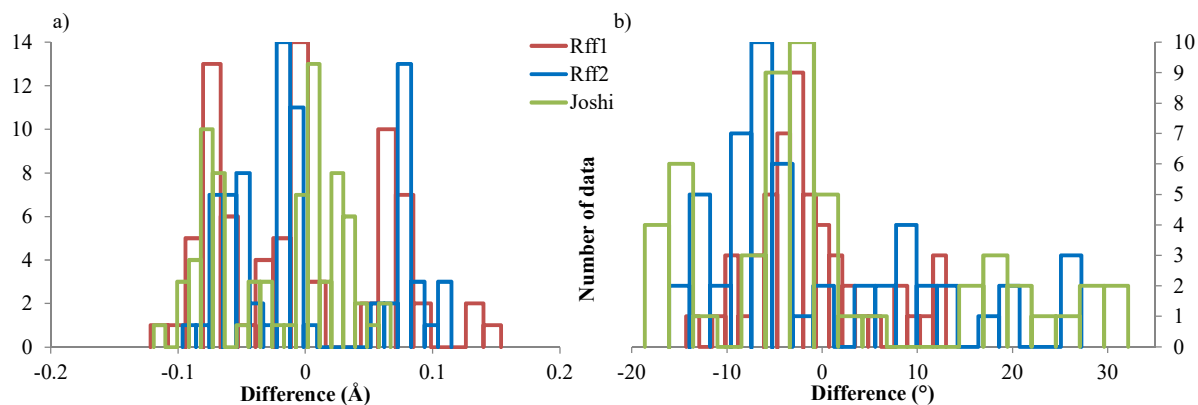


**Figure 11.** Error distribution of distances a) and angles b) obtained with the reactive force fields Rff1 and Rff2 compared to the reference data obtained with DFT on aluminated zeolite surface validation set.

### 6.3.5.2. $\gamma$ -alumina surfaces and edges

Next, we applied the two reactive force fields on  $\gamma$ -alumina and boehmite. The surface reorganizations are quantified and illustrated in Figure 12 where the bond distance and bond angle errors are plotted. Although the very large majority of the bond distances and bond angles have errors close to 0 Å respectively 0 degrees, some bond distances deviate up to 2.5 Å and these errors are analyzed in detail in the following paragraph.

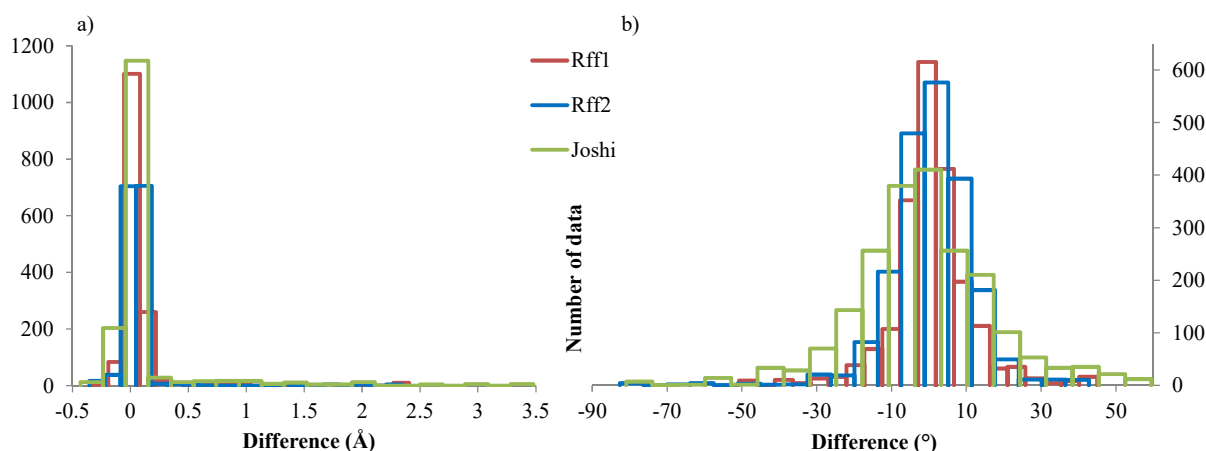


**Figure 12.** Error distribution of distances a) and angles b) obtained with the reactive force fields Rff1 and Rff2 compared to the reference data obtained with DFT on  $\gamma$ -alumina validation set.

The  $\gamma$ -alumina edges are well-optimized with both Rff1 and Rff2. There are small geometrical differences between reference data and both reactive force fields, Rff1 and Rff2, which can be observed in section SVI.1 of the Supplementary Information of Chapter 6. The geometries of (100)  $\gamma$ -alumina surface which are included in the validation set only show a small modification of the bulk structure as observed in Figure 13. But the hydrated surface show more marked differences for both Rff1 and Rff2. The geometry of the  $\gamma$ -alumina (100) surface of 8.8 OH nm<sup>-2</sup> shows a small surface deformation with Al-OH-Al bridges which are 20 to 25° above the surface and not parallel to the surface as in reference data. Which is accompanied by an increase in the distance between the hydroxyl group and another Al of the

surface from 2.2 Å (reference data) to 2.8 Å (Rff1) or 2.9 Å (Rff2). The same deformation can be observed on the more hydrated surface with 17.1 OH nm<sup>-2</sup>. For both surfaces, the distance between water molecules and surface aluminum is increased by Rff1 and Rff2; on 8.8 OH nm<sup>-2</sup> (100) surface from 2.0 Å to 2.2 Å (Rff1) or 3.6/3.4 Å (Rff2); on 17.1 OH nm<sup>-2</sup> (100) surface out from 2.0 Å to 2.3 Å (Rff1) or 3.6/3.7 Å (Rff2). But the orientation of the water molecules in the geometries resulting from Rff1 indicate that the Al-OH<sub>2</sub> bond is further stretched or that an interaction is maintained with the surface aluminum, see Figure 13. The water molecules in the optimized surfaces with Rff2 are completely reoriented and it seems that they are maintained at the surface only with hydrogen bond with the other surface groups.

The surface deformation of the (110)  $\gamma$ -alumina surface gets more pronounced, as can be seen from Figure 14. The dehydrated (110) surface with 0.0 OH nm<sup>-2</sup> is strongly corrugated with Rff1 (corresponding to distance errors from 2.3 Å to 4.7 Å), while it is slightly disorganized with Rff2 with smaller errors for both bond distances and angles, as it is surrounded in black on the Figure. The hydrated surfaces 11.8 and 17.8 OH nm<sup>-2</sup> undergo a reorganization of their surface groups, again with longer distances between the water molecules and aluminum of the surface: 2.0 Å (reference) and 2.2/2.3 Å (Rff1) and 3.6/3.7/3.8 Å (Rff2). It can be seen clearly on Figure 14 for the surface (110) with 11.8 OH nm<sup>-2</sup>, with the adapted representation it can be seen that the H<sub>2</sub>O molecule move off the aluminum atom of the structure with Rff1. The distance is even longer with Rff2, and the initial reactive force field of Joshi has even a longer distance, in addition of a disorganized bulk of the alumina. Furthermore, a reorientation of the water molecules is again observed with Rff2 and Joshi (molecule circled in orange in Figure 14) for the surface with 17.8 OH nm<sup>-2</sup>. It can be observed that the initial reactive force field of Joshi is highly less relevant than Rff1 or Rff2 for (110)  $\gamma$ -alumina surfaces.

On the basis of the above-mentioned observations, it is seen that Rff2 reproduces correctly both the (100) and (110) dry surfaces, while Rff1 better reproduces the (partially) hydrated surfaces, although still substantial deviations are observed with respect to the reference data.

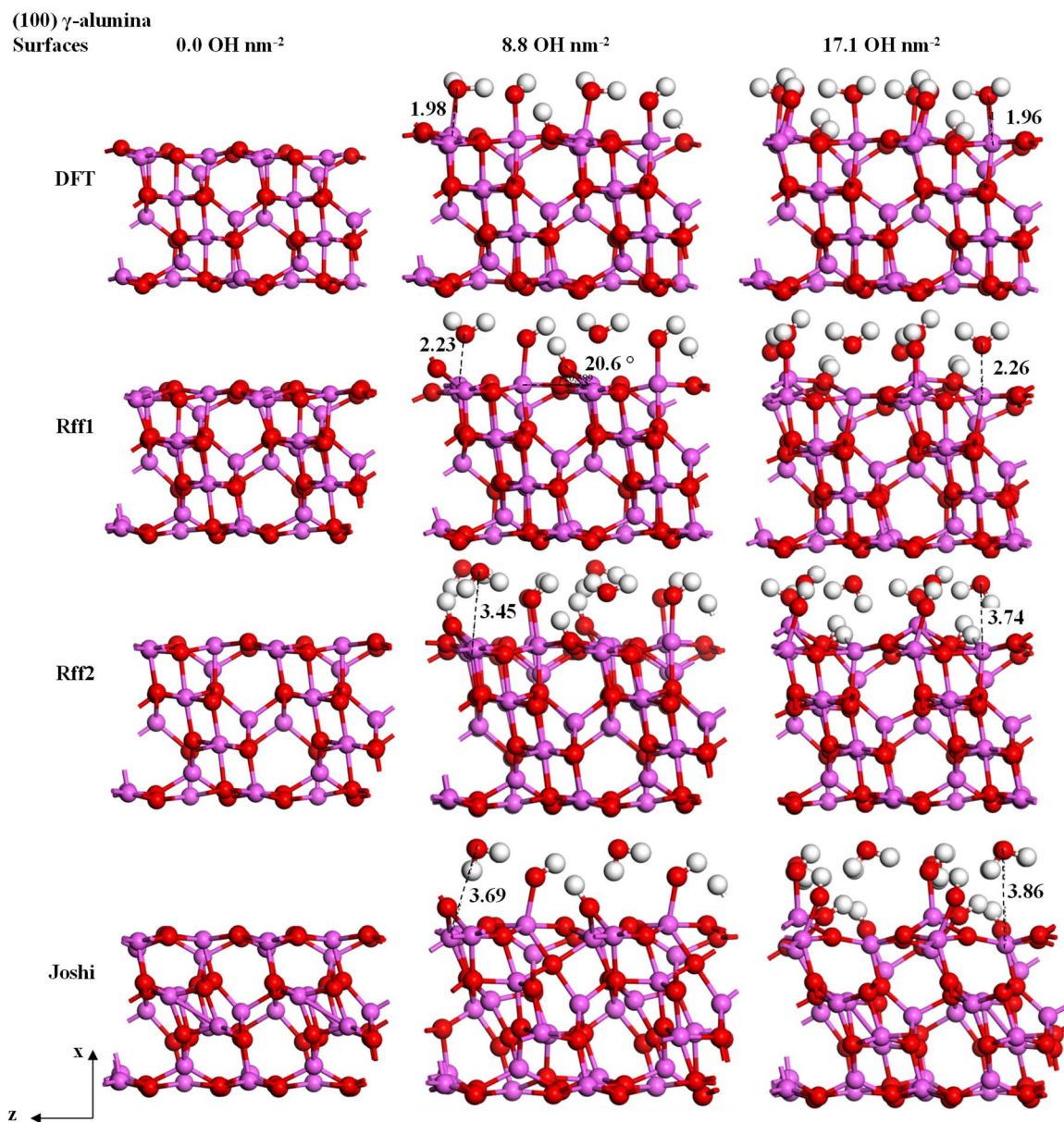


**Figure 13.** Geometry optimizations of (100)  $\gamma$ -alumina surfaces with different hydration level; with the reference method (DFT) and with the two developed reactive force fields of this study Rff1 and Rff2.

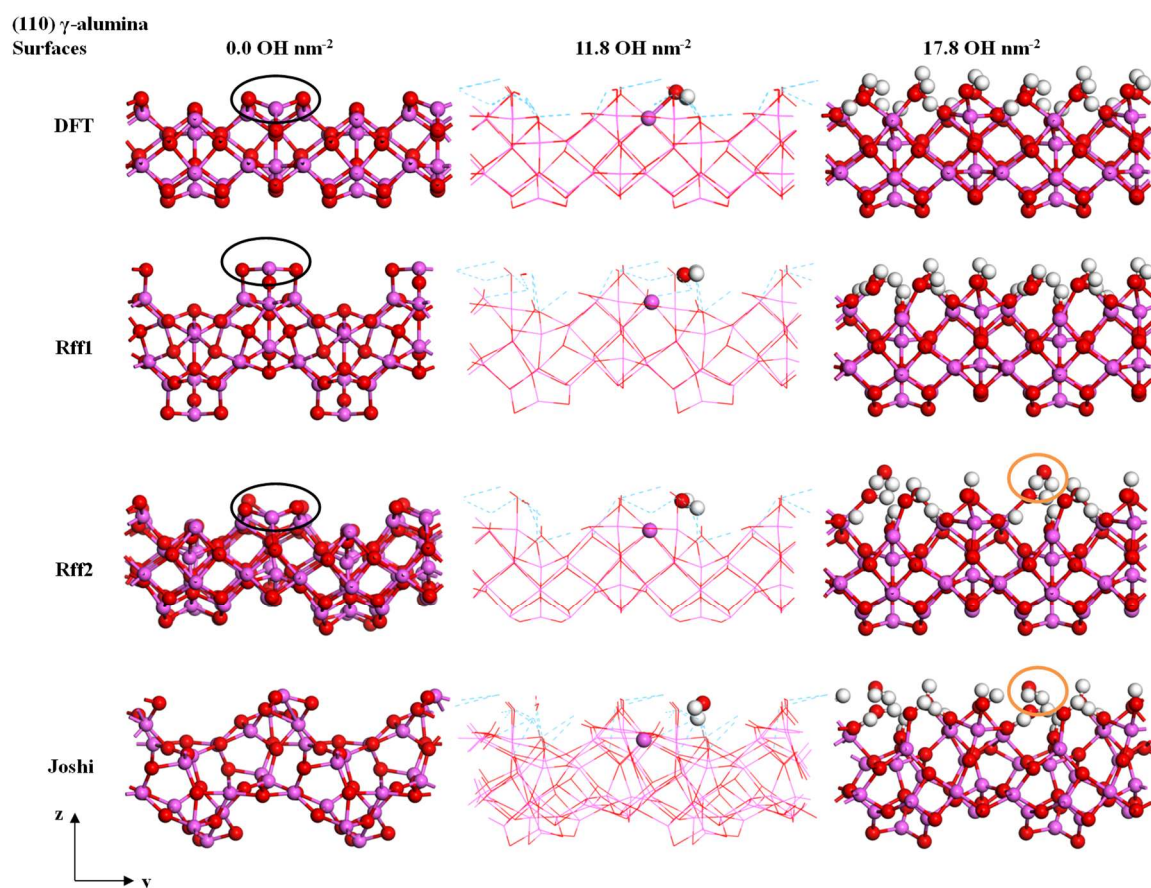


**Figure 14.** Geometry optimizations of (110)  $\gamma$ -alumina surfaces with different hydration level; with the reference method (DFT) and with the two developed reactive force fields of this study Rff1 and Rff2.

### 6.3.5.3. Boehmite surfaces

The performance difference between Rff1 and Rff2 is also observed for the boehmite structure as can be seen from Figure 15 and Figure 16. For example, the number of bond distances with error around 0.7 Å is larger with Rff1 than with Rff2. The important angles errors are mainly due to rotation of the hydroxyl surface groups. In contrast to the hydrated  $\gamma$ -alumina surfaces, Rff1 performs worse, as compared to Rff2, for the hydrated (101) boehmite surface, where water desorption is seen between the sheets with Rff1. The reference structure is, however, better maintained with Rff2, where the Al-O distance is only slightly longer: 2.1 Å with respect to 1.9 Å (reference data).



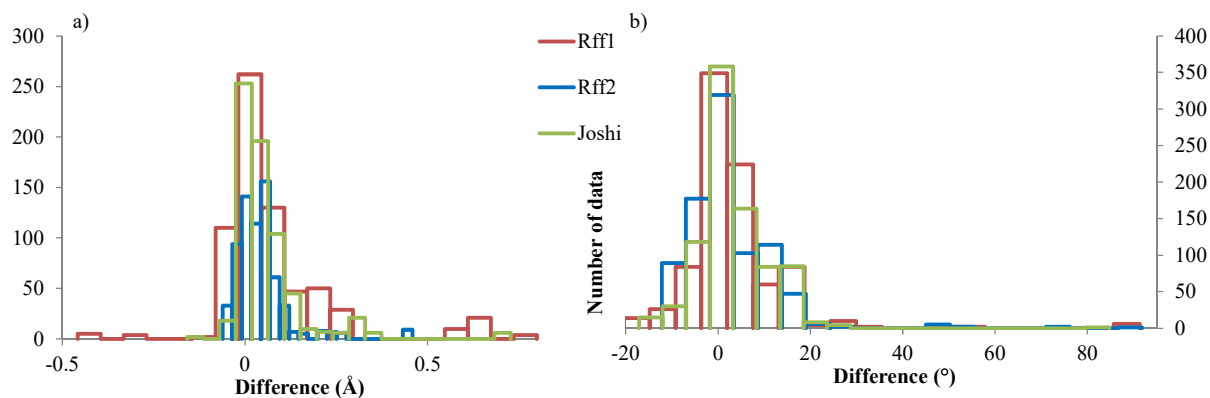


**Figure 15.** Error distribution of distances a) and angles b) obtained with the reactive force fields Rff1 and Rff2 compared to the reference data obtained with (DFT) on boehmite validation set.

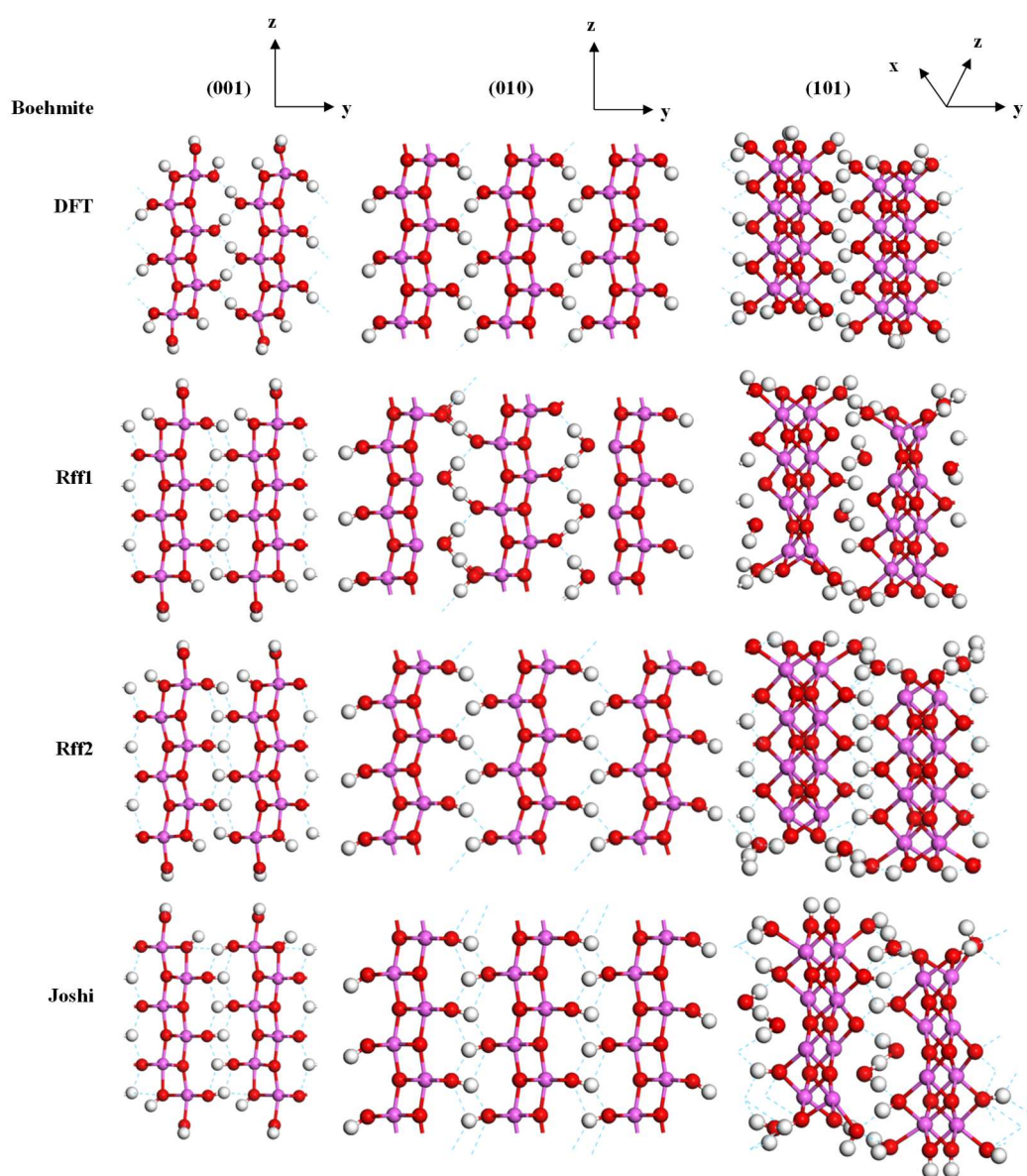


**Figure 16.** Geometry optimizations of (001), (010), and (101) boehmite surfaces with the reference method (DFT) and with the two developed reactive force fields of this study Rff1 and Rff2.



### 6.3.5.4. Various alumino-silicate structures

Our validation set is also composed of relevant mixed alumino-silicate structures. Here, both Rff1 and Rff2 perform well, as can be seen from the small errors for the bond distances and bond angles Figure 17. The only significant error that could be highlighted is made by Rff2 on geometries of (100) cleavage 1 surface with 4 aluminated sites, where the most external surface site, again of the aluminated site of no. 59 site of cleavage 1 in (100) cut orientation, is distorted. These surface site are bridging Al-OH-Si groups and the covalent bond between aluminum and oxygen is elongated by 0.37 Å, as shown on Figure 18, This elongation is only observed for the groups at the external surface, while the geometry is better reproduced for such groups within the bulk structure. However, this elongation does not break the covalent Al-O bond in the external surface groups implemented in Tr.1 and Tr.2 (systems named H2, and H3) which are equivalent surface groups but implemented with only one aluminated site in the structure.

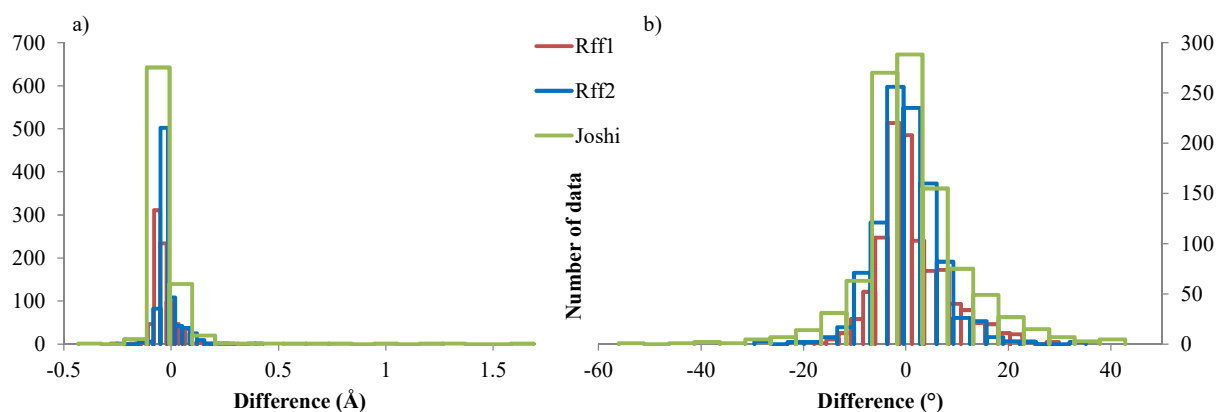


**Figure 17.** Error distribution of distances a) and angles b) obtained with the reactive force fields Rff1 and Rff2 compared to the reference data obtained with (DFT) on aluminosilicate geometries validation set.

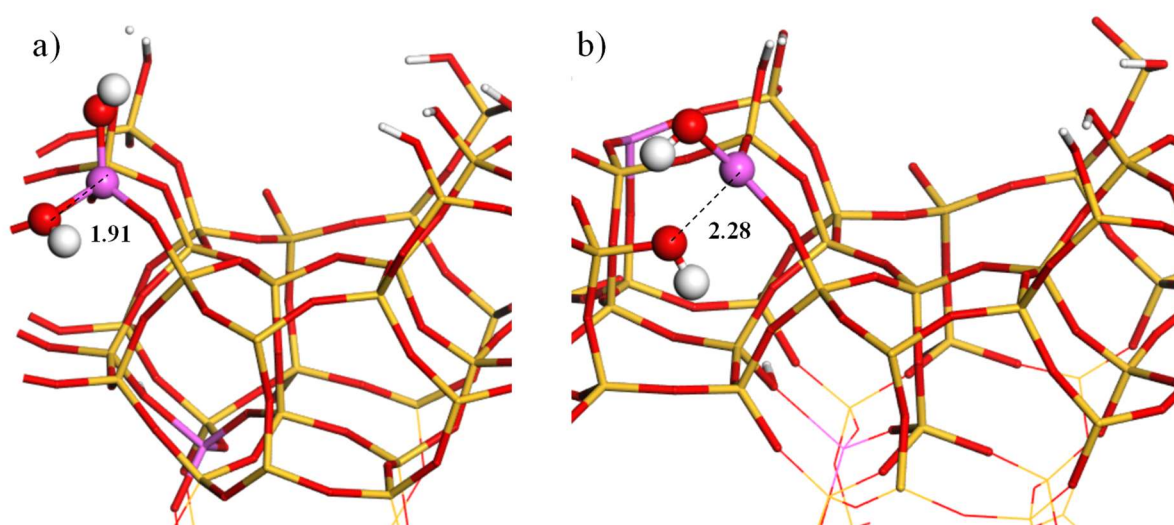


**Figure 18.** Geometry of the 4Alz system composed of four aluminated sites including three Al-OH-Si bridging groups at the most external surface and one deeper in the structure optimized with a) DFT and b) Rff2

## 6.4. Conclusion

Two force fields have been optimized with the objective to describe both zeolitic and binder models. Starting with two well-established force fields,<sup>1,2</sup> the CMAS-ES algorithm has been applied to train those force fields against two training sets and they were validated against a validation set containing representative structures.

To avoid that the optimization algorithm got trapped in a local minimum, several optimization runs were performed. The optimized force fields were classified by considering the total overall error, errors in bond distances and bond angles, net atomic charges and reaction energies.

The best force field (Rff1), issue from training set 1, and the best force field (Rff2) issue from training set 2 (which envelopes the data in training set 1, but is extended with data on the water desorption) have been applied to a common validation set.

It follows that Rff2 presents advantages in geometries representations. The resulting geometries of dehydrated  $\gamma$ -alumina and boehmite are closer to the reference data than Rff1 resulting ones. Yet, the reproduction of the properties of  $\gamma$ -alumina component is a decent performance with Rff1, for hydrated surfaces, while Rff2 could be used preferably for dehydrated surfaces. The geometry optimization of boehmite surfaces is clearly in favor of Rff2, which respect better the geometries and the chemistry between two sheets of boehmite. Furthermore, Rff1 and Rff2 are equivalent for the representation of H-ZSM-5 including: bulk, external surfaces, aluminated sites, interaction with monomers. The validation sets have confirmed our conclusions about the very satisfying performances of both reactive force fields to reproduce the structural properties of H-ZSM-5 and interactions of water with H-ZSM-5. Rff2 has a small advantage in describing the desorption curves and hydration/dehydration energies calculations. Even though this small benefit is not clearly expressed in the molecular dynamics simulation to determine the water desorption temperature.

At this moment it is difficult to conclude that either Rff1 or Rff2 is clearly superior to the other. Both reactive force fields may be used for H-ZSM-5 interactions in hydrated or dehydrated environment. Probably the best way to continue is to the apply both force fields in molecular dynamics simulations and carefully observe the structural changes of the zeolite and the reactivity between the zeolite and binder models. Once suspicious reactions or solid-deformations occur, these (elementary) reactions need to be recalculated with DFT to verify if they are indeed thermodynamically feasible. If not, they need to be added to the training set and the force field need parameters to be reoptimized. Using this iterative process, the force field parameters should convergence to values that adequately and precisely describe our systems.

## References

- (1) Pitman, M. C.; Duin, A. C. T. van. Dynamics of confined reactive water in smectite clay-zeolite composites. *J. Am. Chem. Soc.* **2012**, *134*, 3042–3053.
- (2) Joshi, K. L.; Psfogiannakis, G.; van Duin, A. C. T.; Raman, S. Reactive molecular simulations of protonation of water clusters and depletion of acidity in H-ZSM-5 zeolite. *Phys. Chem. Chem. Phys.* **2014**, *16*, 18433–18441.
- (3) Bai, C.; Liu, L.; Sun, H. Molecular Dynamics Simulations of Methanol to Olefin Reactions in HZSM-5 Zeolite Using a ReaxFF Force Field. *J. Phys. Chem. C* **2012**, *116*, 7029–7039.
- (4) Shin, Y. K.; Kwak, H.; Vasenkov, A. V.; Sengupta, D.; van Duin, A. C. T. Development of a ReaxFF Reactive Force Field for Fe/Cr/O/S and Application to Oxidation of Butane over a Pyrite-Covered Cr<sub>2</sub>O<sub>3</sub> Catalyst. *ACS Catal.* **2015**, *5*, 7226–7236.
- (5) Joshi, K. L.; van Duin, A. C. T. Molecular Dynamics Study on the Influence of Additives on the High-Temperature Structural and Acidic Properties of ZSM-5 Zeolite. *Energy Fuels* **2013**, *27*, 4481–4488.
- (6) Senftle, T. P.; Hong, S.; Islam, M. M.; Kylasa, S. B.; Zheng, Y.; Shin, Y. K.; Junkermeier, C.; Engel-Herbert, R.; Janik, M. J.; Aktulga, H. M. *et al.* The ReaxFF reactive force-field: Development, applications and future directions. *npj Comput Mater* **2016**, *2*, 9396.
- (7) Duin, A. C. T. van; Baas, J. M. A.; van de Graaf, B. Delft Molecular Mechanics: A New Approach to Hydrocarbon Force Fields: Inclusion of a Geometry-dependent Charge Calculation. *J. Am. Chem. Soc.* **1994**, *90*, 2881–2895.
- (8) Iype, E.; Hütter, M.; Jansen, A. P. J.; Nedeia, S. V.; Rindt, C. C. M. Parameterization of a reactive force field using a Monte Carlo algorithm. *J. Comput. Chem.* **2013**, *34*, 1143–1154.
- (9) Dittner, M.; Müller, J.; Aktulga, H. M.; Hartke, B. Efficient global optimization of reactive force-field parameters. *J. Comput. Chem.* **2015**, *36*, 1550–1561.
- (10) Rice, B. M.; Larentzos, J. P.; Byrd, E. F. C.; Weingarten, N. S. Parameterizing complex reactive force fields using multiple objective evolutionary strategies (MOES): Part 2: transferability of ReaxFF models to C-H-N-O energetic materials. *J. Chem. Theory Comput.* **2015**, *11*, 392–405.
- (11) Deetz, J. D.; Faller, R. Parallel optimization of a reactive force field for polycondensation of alkoxy silanes. *J. Phys. Chem. B* **2014**, *118*, 10966–10978.
- (12) Hu, X.; Schuster, J.; Schulz, S. E. Multiparameter and Parallel Optimization of ReaxFF Reactive Force Field for Modeling the Atomic Layer Deposition of Copper. *J. Phys. Chem. C* **2017**, *121*, 28077–28089.
- (13) Kirkpatrick, S.; Gelatt, C. D., JR.; Vecchi, M. P. Optimization by Simulated Annealing. *Science* **1983**, *220*, 671–680.
- (14) Trnka, T.; Tvaroška, I.; Koča, J. Automated Training of ReaxFF Reactive Force Fields for Energetics of Enzymatic Reactions. *J. Chem. Theory Comput.* **2018**, *14*, 291–302.
- (15) Shchygol, G.; Yakovlev, A.; Trnka, T.; van Duin, A. C. T.; Verstraelen, T. ReaxFF Parameter Optimization with Monte-Carlo and Evolutionary Algorithms: Guidelines and Insights. *J. Chem. Theory Comput.* **2019**, *15*, 6799–6812.
- (16) Velde, G. t.; Bickelhaupt, F. M.; Baerends, E. J.; Fonseca Guerra, C.; Gisbergen, S. J. A. van; Snijders, J. G.; Ziegler, T. Chemistry with ADF. *J. Comput. Chem.* **2001**, *22*, 931–967.

- (17) A.C.T. van Duin, W.A. Goddard, M.M. Islam, H. van Schoot, T. Trnka, A.L. Yakovlev. *ReaxFF 2019.3, SCM*; Theoretical Chemistry, Vrije Universiteit, Amsterdam, The Netherlands.
- (18) Fogarty, J. C.; Aktulga, H. M.; Grama, A. Y.; van Duin, A. C. T.; Pandit, S. A. A reactive molecular dynamics simulation of the silica-water interface. *J. Chem. Phys.* **2010**, *132*, 174704.
- (19) Russo, M. F.; Li, R.; Mench, M.; van Duin, A. C.T. Molecular dynamic simulation of aluminum–water reactions using the ReaxFF reactive force field. *Int. J. Hydrogen Energy* **2011**, *36*, 5828–5835.
- (20) Manzano, H.; Pellenq, R. J. M.; Ulm, F.-J.; Buehler, M. J.; van Duin, A. C. T. Hydration of calcium oxide surface predicted by reactive force field molecular dynamics. *Langmuir* **2012**, *28*, 4187–4197.
- (21) van Duin, A. C. T.; Strachan, A.; Stewman, S.; Zhang, Q.; Xu, X.; Goddard, W. A. ReaxFF SiO Reactive Force Field for Silicon and Silicon Oxide Systems. *J. Phys. Chem. A* **2003**, *107*, 3803–3811.
- (22) Zhang, Q.; Qi, Y.; Hector, L. G.; Çağın, T.; Goddard, W. A. Atomic simulations of kinetic friction and its velocity dependence at Al/Al and  $\alpha$ -Al<sub>2</sub>O<sub>3</sub>/ $\alpha$ -Al<sub>2</sub>O<sub>3</sub> interfaces. *Phys. Rev. B* **2005**, *72*, 890.
- (23) Treps, L.; Gomez, A.; Bruin, T. d.; Chizallet, C. Environment, Stability and Acidity of External Surface Sites of Silicalite-1 and ZSM-5 Micro and Nano Slabs, Sheets, and Crystals. *ACS Catal.* **2020**, *10*, 3297–3312.
- (24) Nortier, P.; Fourre, P.; Mohammed, A. B.; Saur, O.; Lavalley, J. C. Effects of Crystallinity and Morphology on the Surface Properties of Alumina. *Appl. Catal.* **1990**, *61*, 141–160.
- (25) Digne, M.; Sautet, P.; Raybaud, P.; EUZEN, P.; Toulhoat, H. Hydroxyl Groups on  $\gamma$ -Alumina Surfaces: A DFT Study. *Journal of Catalysis* **2002**, *211*, 1–5.
- (26) Digne, M. Use of DFT to achieve a rational understanding of acid?: Basic properties of  $\gamma$ -alumina surfaces. *Journal of Catalysis* **2004**, *226*, 54–68.
- (27) Wischert, R.; Laurent, P.; Copéret, C.; Delbecq, F.; Sautet, P.  $\gamma$ -Alumina: The essential and unexpected role of water for the structure, stability, and reactivity of "defect" sites. *J. Am. Chem. Soc.* **2012**, *134*, 14430–14449.
- (28) Krokidis, X.; Raybaud, P.; Gobichon, A.-E.; Rebours, B.; Euzen, P.; Toulhoat, H. Theoretical Study of the Dehydration Process of Boehmite to  $\gamma$ -Alumina. *J. Phys. Chem. B* **2001**, *105*, 5121–5130.
- (29) Batista, A. T.F.; Wisser, D.; Pigeon, T.; Gajan, D.; Diehl, F.; Rivallan, M.; Catita, L.; Gay, A.-S.; Lesage, A.; Chizallet, C. *et al.* Beyond  $\gamma$ -Al<sub>2</sub>O<sub>3</sub> crystallite surfaces: The hidden features of edges revealed by solid-state <sup>1</sup>H NMR and DFT calculations. *J. Catal.* **2019**, *378*, 140–143.
- (30) Raybaud, P.; Digne, M.; Iftimie, R.; Wellens, W.; EUZEN, P.; Toulhoat, H. Morphology and Surface Properties of Boehmite ( $\gamma$ -AlOOH): A Density Functional Theory Study. *J. Catal.* **2001**, *201*, 236–246.
- (31) Chiche, D.; Chizallet, C.; Durupthy, O.; Chanéac, C.; Revel, R.; Raybaud, P.; Jolivet, J.-P. Growth of boehmite particles in the presence of xylitol: Morphology oriented by the nest effect of hydrogen bonding. *Phys. Chem. Chem. Phys.* **2009**, *11*, 11310–11323.

(32) Tielens, F.; Gervais, C.; Lambert, J.-F.; Mauri, F.; Costa, D. Ab Initio Study of the Hydroxylated Surface of Amorphous Silica: A Representative Model. *Chem. Mater.* **2008**, *20*, 3336–3344.

(33) Chizallet, C.; Raybaud, P. Pseudo-bridging silanols as versatile Brønsted acid sites of amorphous aluminosilicate surfaces. *Angew. Chem. Int. Ed.* **2009**, *48*, 2891–2893.

## General Conclusions and Perspectives

During these three years of PhD, a theoretical study has been undertaken on the structure and acidity of the external surface of H-ZSM-5, and its interaction with binder models, to better understand the shaping mechanism at the nanometer scale.

The present study has been conducted at two different levels of theory method: periodic Density Functional Theory calculations have been performed in first place to study physical chemical properties of H-ZSM-5 bulk and external surfaces with a high accuracy on relatively small (up to hundreds of atoms). Secondly these data were used to parametrize an empirical reactive force field to be able to simulate larger and more representative H-ZSM-5/binder models. nanometer scale.

For this purpose, we also have relied on experimental data provided by the PhD work of Coralie Demaret (2016-2019) which is a detailed study of zeolite shaping with silica and alumina binder in different operating conditions to be able to evaluate their impact on physical and chemical zeolite properties.

The study of external surfaces of H-ZSM-5 has resulted into a purely computational article published in *ACS Catalysis* entitled: “Environment, Stability, and Acidity of External Surface Sites of Silicalite-1 and ZSM-5 Micro and Nano Slabs, Sheets, and Crystals” (doi: 10.1021/acscatal.9b05103 and written by L. Treps, A. Gomez, T. de Bruin, and C. Chizallet). Thanks to this study, detailed models of external surfaces of silicalite-1 and H-ZSM-5 zeolites have been obtained for relevant orientations ((100), (010), and (101)). Combining the thermodynamic study of these surfaces and crystal growth approaches (Si<sub>33</sub> building block, or microscopy pictures of H-ZSM-5 crystals), it has been shown that the formation of the zeolites surfaces is not purely thermodynamically driven, but that kinetic aspects also play a key role. A detailed description of H-ZSM-5 acid site is also provided, stating for their localization in the zeolite network, their strength, their stability, and their behavior in hydrated or dehydrated environment.

In the bulk and at the pore mouth of zeolite, the bridging groups Al-OH-Si have been shown to be the strongest Brønsted acid sites (BAS) which can be found on H-ZSM-5. At the outermost surface, the Al(OH)<sub>n</sub>H<sub>2</sub>O groups are the most stable surface sites which induces that they only behave as mild BAS. But the desorption of the water molecule upon heating reveals surface aluminums which behave like strong Lewis acid sites (LAS). In classical condition of temperature and pressure of reactions (water partial pressure of 10<sup>-4</sup> and temperature between 500 and 700 K), it has been highlighted that all these acid sites are coexisting on H-ZSM-5 surface. These results provide a complementary understanding of former experimental data.

In addition to this analysis, a second article close to be submitted has been written with the contribution of spectroscopy groups, and is entitled: “Spectroscopic Expression of the External Surface Sites of H-ZSM-5” (written by L.Treps, C. Demaret, D. Wisser, B. Harbuzaru, A. Méthivier, E. Guillon, D. Benedis, A. Gomez, T. de Bruin, M. Rivallan, L. Catita, A. Lesage, and C. Chizallet). In this article, the FT-IR and <sup>1</sup>H NMR experimental

characterizations are completed and revisited thanks to our computed spectroscopic data. The nanometer scale of the theoretical study of surface sites has allowed the access to a more detailed overview of the specificities of these sites. That is the reason why in some case it has been necessary to revisit the “classical” signal attributions made in literature. The key role of the nature of the hydroxyl groups (isolated, hydrogen-bond donor, or hydrogen-bond acceptor) have been highlighted for both FT-IR and  $^1\text{H}$  NMR, even if the impact is not similar for both spectroscopy techniques.  $^1\text{H}$  NMR signals of bridging Si-(OH)-Al groups and Al-(H<sub>2</sub>O) have a common interval which is not the case for FT-IR signals. In general, it has been concluded that the NMR signals are mainly useful for the quantification and proximity assessment while FT-IR appears to be more useful to identify the nature of the hydroxyl groups.

As a preliminary study of the interaction between zeolite and binders, the interaction between H-ZSM-5 with some small elements of binders (like cation or monomers) has been studied. In correlation with the experimental observation, the Na<sup>+</sup> cation has been revealed to be more attracted by the zeolite acid sites than by pure silica. It is also observed that alumina monomers have a stronger interaction with the zeolitic network than silica monomers and are more particularly attracted by the ZSM-5 framework aluminum-rich zones. This could eventually explain some pore blockage observed experimentally with alumina-based binders. The strong interaction between monomer and BAS compared to the interaction between monomer and LAS (of dehydrated surfaces) could also explain the importance of the presence of water during shaping.

These high-precision DFT data have generated, were then used to train the reactive empirical force field, ReaxFF, with the objective to describe larger and more representative atomistic zeolite/binder models that are too expensive for DFT calculations. The optimization of the reactive force field has been conducted with previously published force field as starting points. The reactive force fields have been trained with a large set of data composed of H-ZSM-5 aluminated surfaces geometries, atomistic partial charges, water desorption energies from some of these surfaces, models of monomer adsorption, and models of  $\gamma$ -alumina. The best obtained force fields have been applied to a validation set composed of new models of  $\gamma$ -alumina, models of boehmite, silicalite-1 surfaces (MFI type), and aluminated surfaces of H-ZSM-5. Finally, two reactive force fields have emerged that both seem to have the potential describe zeolite/binder interactions.

These two force fields need to be further tested and will applied to bigger systems of zeolite/binder interactions. The size of the binder could be progressively increased, from nanoparticles, to binder platelet, and finally a surface to surface contact. The reactive force fields which have been obtained can be tested on these future models and eventually re-optimized if some defaults are noticed in their applications.

In parallel, the external surface sites of H-ZSM-5 would deserve complement in their analysis. The reactivity of acid sites in the bulk and at the external surface of H-ZSM-5 could be studied as a parallel of the experimental results obtained in xylene isomerization to answer if the weak or middle acid sites have a catalytic activity. The mono or the bimolecular



mechanisms which are proposed by the literature for these reactions could be boosted by one or the other sites. The diffusion of molecules is also an essential point that should be studied to analyze the limitations and the accessibility of the acid sites.

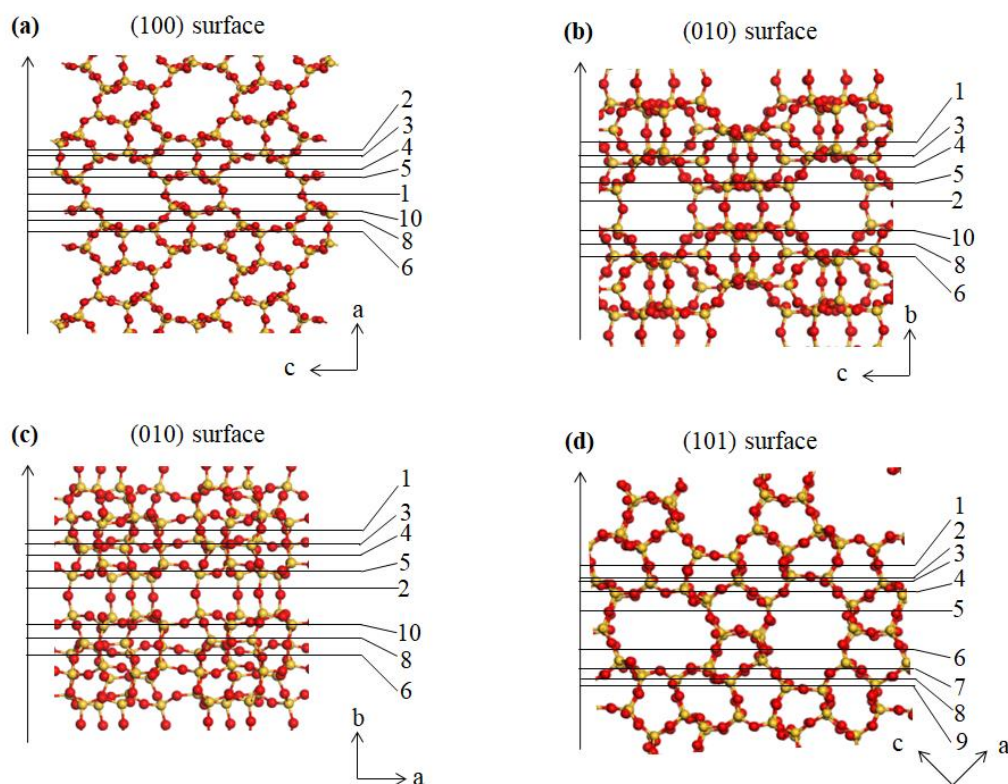
The defects which can be present in the zeolite structure, after dealumination for example, could also be studied to know more about their formation and their influence on the acidity of the bulk and of the external surface of zeolites.

Finally, the  $^{27}\text{Al}$  NMR could be a good complement which can be parallelized with the experimental data on ZSM-5.

## Chapter 3: Supplementary Information

### SI. Variation of the cleavage height for each surface orientation

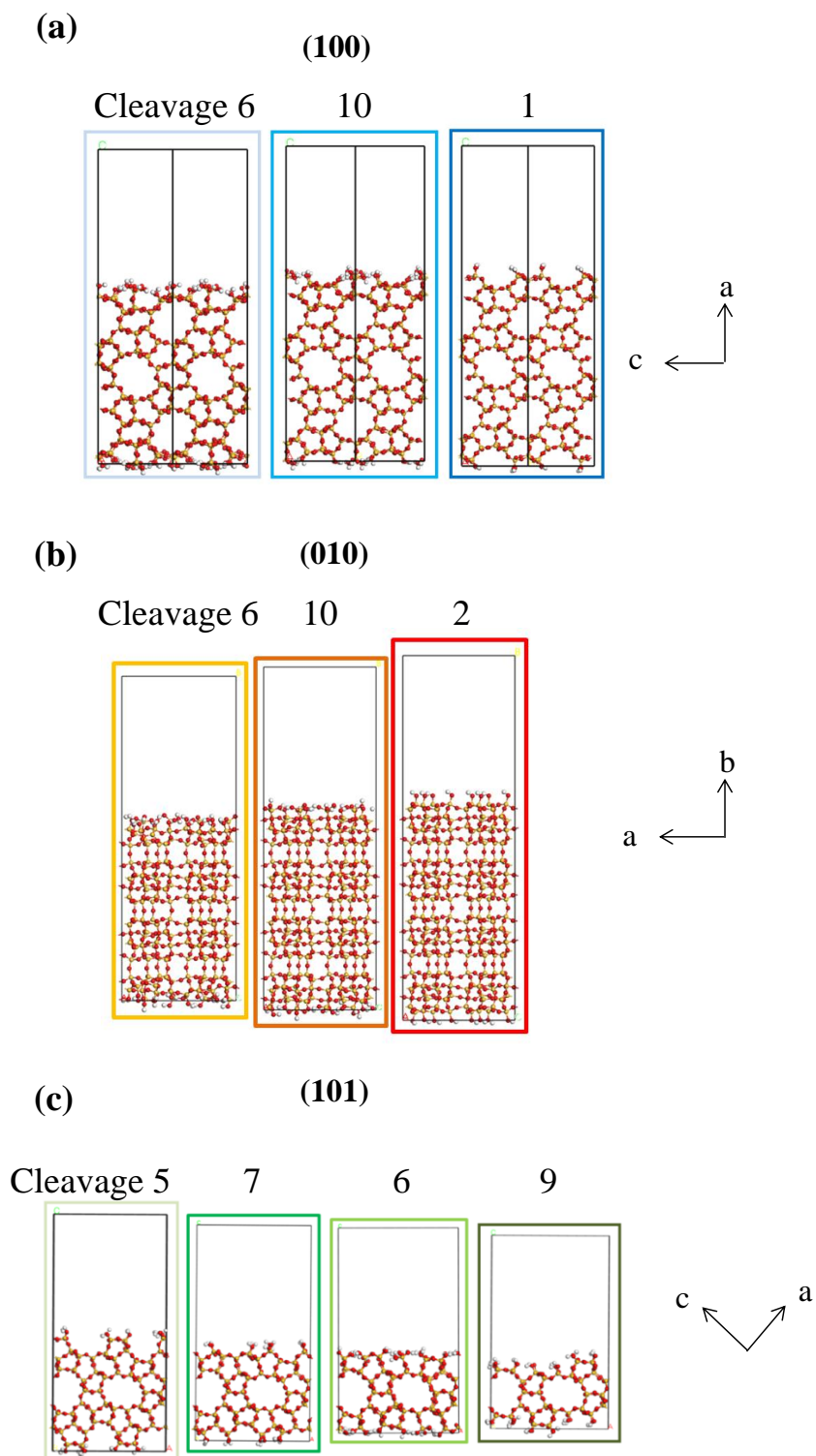
For each investigated cleavage direction, a set of cleavage height was studied as illustrated in Figure S1.



**Figure S1.** Different heights of cleavage along the (a) (100), (b) (010) and (c) (101) directions and their names (red: oxygen atoms; yellow: silicon atoms).

For the (100) surface orientation, cleavage 1 and 2 can generate a cell with a fractional thickness of 2 bulk units (see section SII) with symmetric surfaces. The others are non-symmetric for the same fractional thickness, it generates a cell with two different surfaces with the following association: 3/6, 4/8 and 5/10. To generate a symmetric cell with these last cleavages, the thickness was set smaller than 2. Figure S2 depicts side views of most important cleavages for each surface orientations.

The surface energies generated by the two methods are almost the same (Table S1) but the symmetric cell allows to calculate the individual surface energies. There is no substantial difference in energy when a dipolar correction is added (Table S1), so that such corrections were not applied in the following. For the (010) orientation, the same kind of approach led to asymmetric slabs in the 6/3, 8/4 and 10/5 cases. For the (101) surface orientation, the thickness is limited to a single cell for cleavage 1, because in this orientation the lateral dimensions of the cell are larger than for the two other surface orientations. The other cleavages are made symmetric by adjusting the thickness.

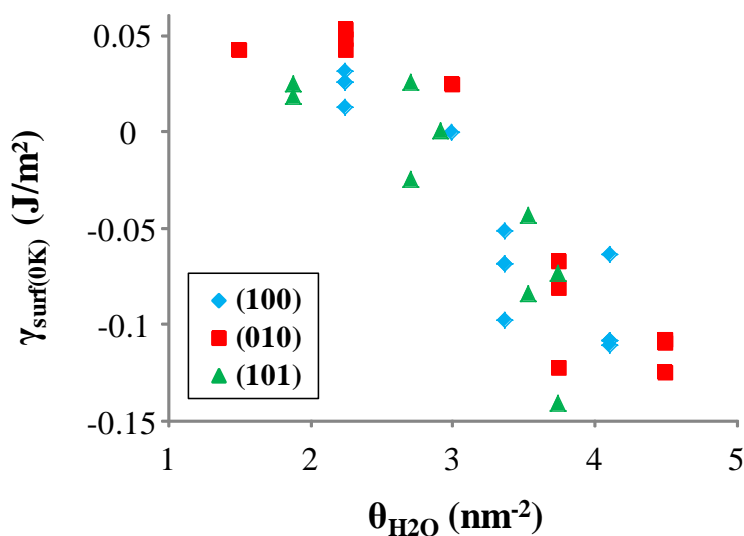


**Figure S2.** Side views of the simulation cells for the (a) (100), (b) (010) and (c) (101) surface orientations, at various cleavages.

**Table S1.** Surface free energies at 0 K for cleavages (CLV) along different surfaces: (100), (010) and (101). The most stable terminations according to the thermodynamic analysis are reported in bold.

(100)	$\theta_{\text{H}_2\text{O}}$ ( $\text{nm}^{-2}$ )	$\gamma_{\text{surf}}$ ( $\text{J}\cdot\text{m}^{-2}$ )	(010)	$\theta_{\text{H}_2\text{O}}$ ( $\text{nm}^{-2}$ )	$\gamma_{\text{surf}}$ ( $\text{J}\cdot\text{m}^{-2}$ )	(101)	$\theta_{\text{H}_2\text{O}}$ ( $\text{nm}^{-2}$ )	$\gamma_{\text{surf}}$ ( $\text{J}\cdot\text{m}^{-2}$ )
<b>CLV1</b>	<b>1.50</b>	<b>0.037</b>	CLV1	3.01	0.0239	CLV1	2,92	0.0001
CLV2	3.00	-0.001	<b>CLV2</b>	<b>1.50</b>	<b>0.0412</b>	CLV2	2.71	0.0257
CLV3	4.11	-0.064	CLV3	4.51	-0.1091	CLV3	3.54	-0.0438
CLV4	2.25	0.031	CLV4	2.26	0.0469	CLV4	3.75	-0.0735
CLV5	3.37	-0.052	CLV5	3.76	-0.0680	CLV5	1.88	0.0241
CLV6	4.11	-0.111	CLV6	4.51	-0.1258	<b>CLV6</b>	<b>1.88</b>	<b>0.0178</b>
CLV8	2.25	0.012	CLV8	2.26	0.0414	CLV7	3.75	-0.1412
CLV10	3.37	-0.098	CLV10	3.76	-0.1237	CLV8	3.54	-0.0841
CLV6/3	4.11	-0.109	CLV6/3	4.51	-0.1105	CLV9	2.71	-0.0252
CLV8/4	2.25	0.025	CLV8/4	2.26	0.0521			
CLV10/5	3.37	-0.069	CLV10/5	3.76	-0.0820			
CLV6/3 correction dipolaire	4.11	-0.109						
CLV8/4 correction dipolaire	2.25	0.025						
CLV10/5 correction dipolaire	3.37	-0.069						

The surface energy variations are very low from one surface to the other, and mainly depends on the water coverage (water being in the form of Si-OH groups) (Figure S2).

**Figure S3.** Evolution of the surface energy calculated at 0K function of the water coverage on each surface termination.

## SII. Convergence of the calculated properties as a function of the slab thickness

The choice of the thickness of the slab model employed throughout the study is made thanks to a set of simulations for several thickness presented in Figure S4.

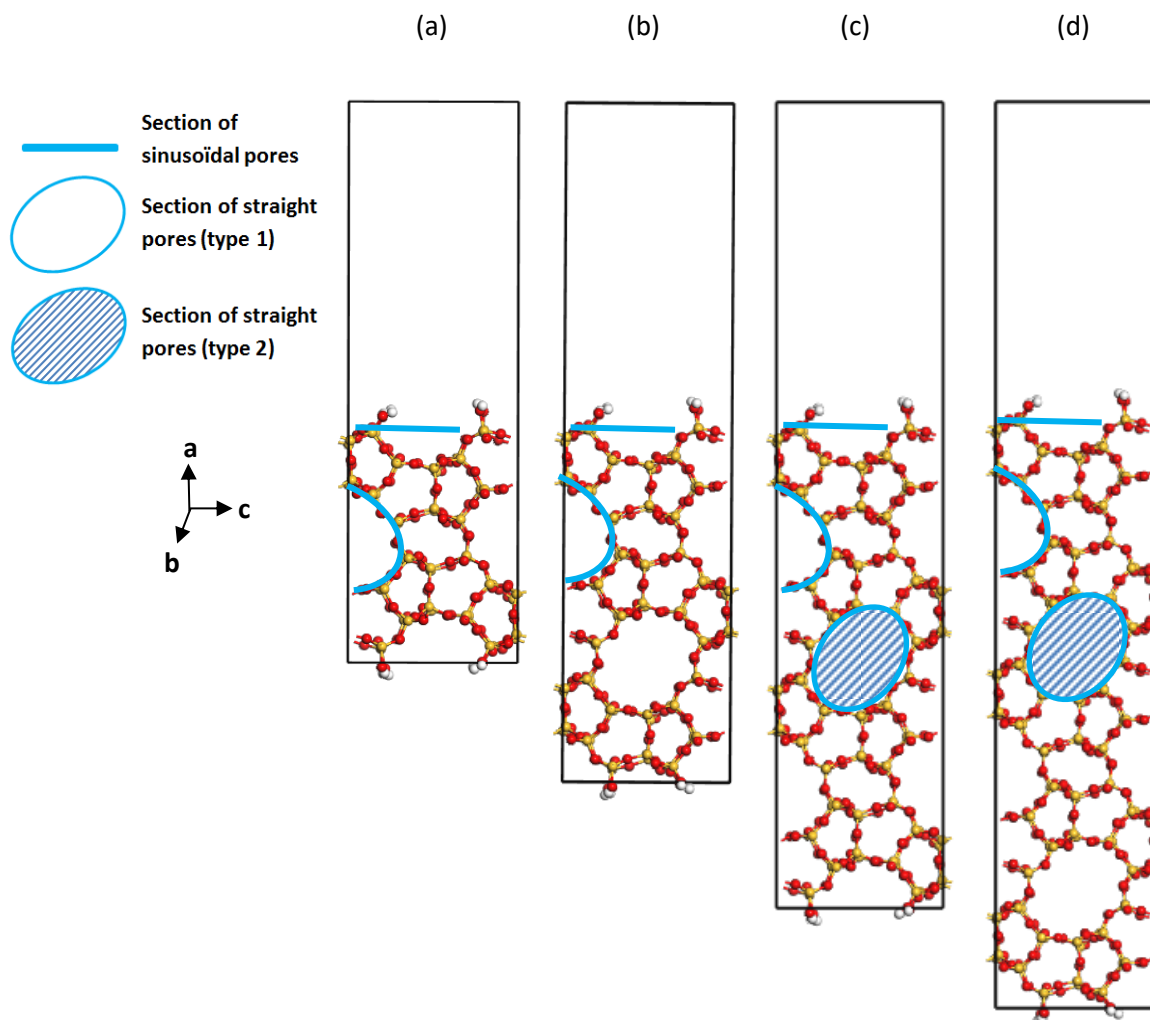


**Figure S4.** Side view of the investigated silicic slabs (cleavage (100)) at different height (bulk unit) along the a axis. Highlight of the measurement of the section area of the pores, the sinusoidal pore section is measured at the external surface whereas the straight pore sections are measured depending on the depth of the pore (type 1 close to the surface, type 2 deeper). Ellipse: straight pores along the b axis, green and black: sinusoidal pores along the a axis.

The dimensions of the pores are measured at the surface and in the layer (Figures S4 and S5). The dimensions of the pore in the middle of the cell should be as similar as possible as that of the bulk. A thickness of 2 bulk units in the a direction is a satisfactory compromise between accuracy and computational cost.

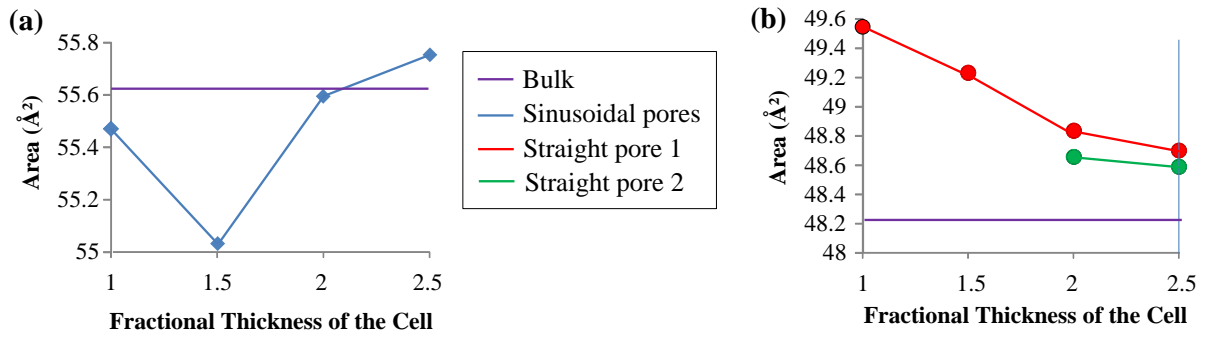


**Figure S5.** Area of the section of the (a) sinusoidal and (b) straight pores at the surface depending on the thickness of the model and compared to the similar pore of the bulk.

### SIII. Surface free energies for the various surfaces as a function of temperature

#### SIII.1. (100) orientation

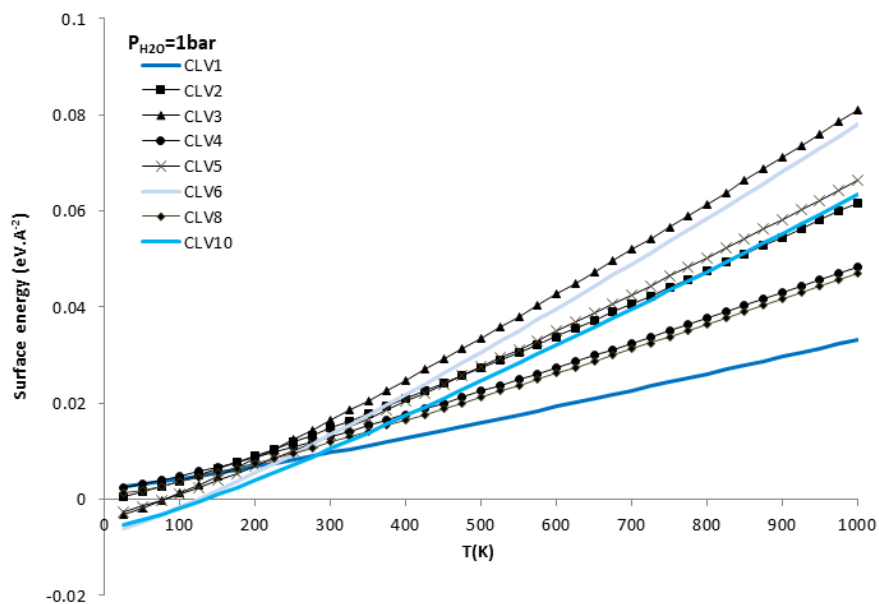


**Figure S6.** Evolution of the surface free energy as a function of the temperature for a water pressure of 1 bar, for all cleavage heights investigated in the (100) orientation, including those that do not appear in the final thermodynamic diagram (Figure 2 in the manuscript).

#### SIII.2. (010) orientation

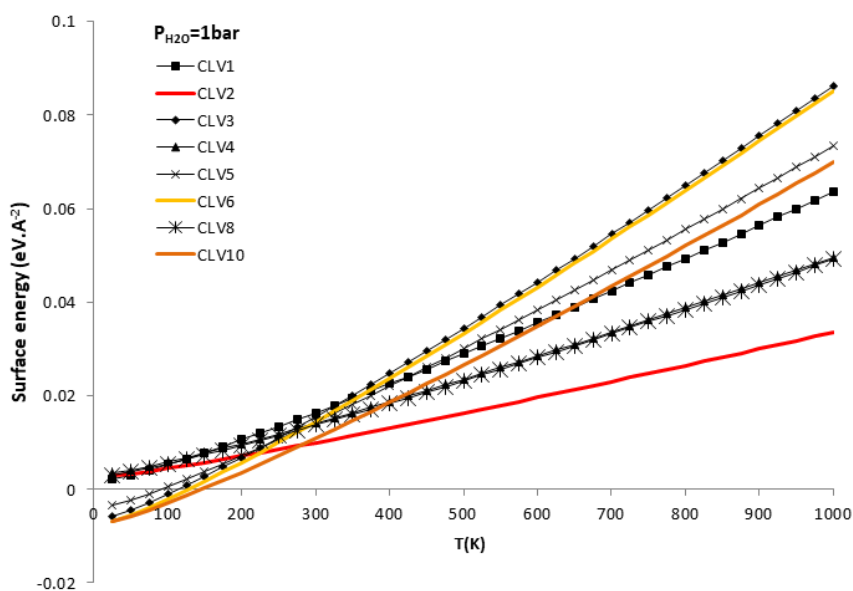


**Figure S7.** Evolution of the surface free energy as a function of the temperature for a water pressure of 1 bar, for all cleavage heights investigated in the (010) orientation, including those that do not appear in the final thermodynamic diagram (Figure 2 in the manuscript).



### SI.3. (101) orientation

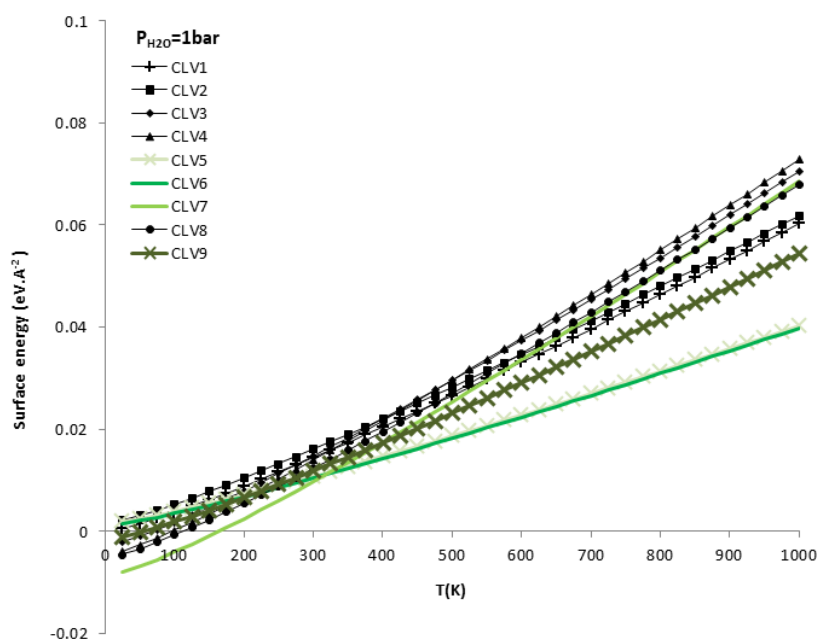


**Figure S8.** Evolution of the surface free energy as a function of the temperature for a water pressure of 1 bar, for all cleavage heights investigated in the (101) orientation, including those that do not appear in the final thermodynamic diagram (Figure 2 in the manuscript).

### SI.4. Comparison of surface free energies for the various surfaces as a function of temperature

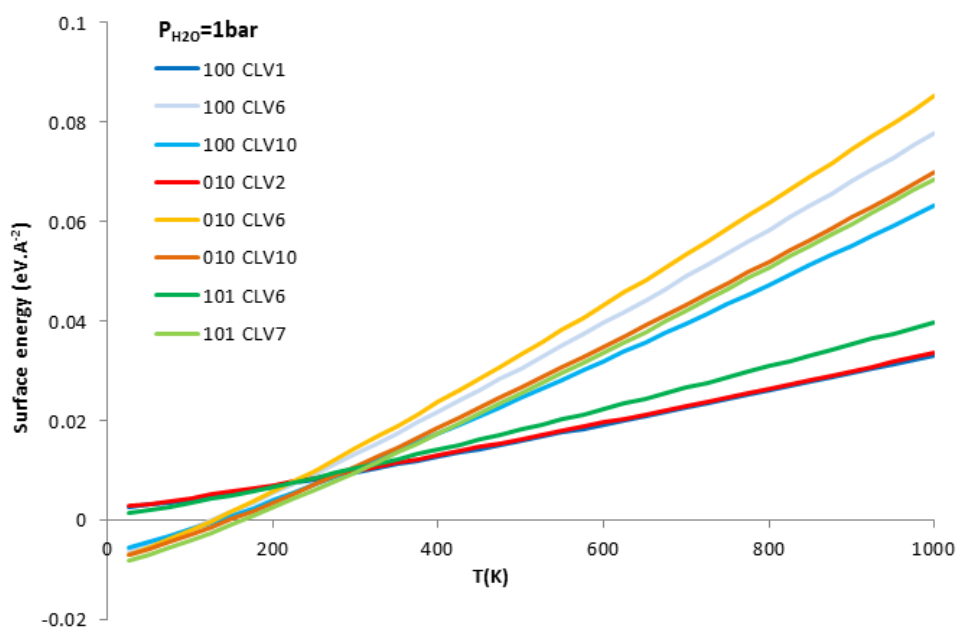


**Figure S9.** Evolution of the surface free energy as a function of the temperature for a water pressure of 1 bar, for the relevant cleavage heights appearing on the thermodynamic diagram (Figure 2 in the manuscript) of all surface orientations.

## SIV. Morphology constructions and comparison with experiments <sup>1</sup>

Gruene *et al.* performed (inter alia) TEM measurements for small monocrystalline silicalite-1 samples.<sup>1</sup> The reported dimensions were completed by other measurements (on the pictures, Figure S10), to allow a better comparison with our thermodynamic predictions (Figure 3).

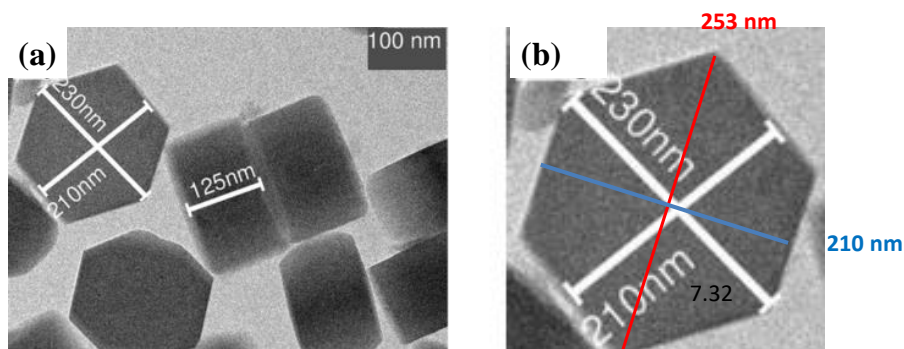


**Figure S10.** (a) TEM images of silicalite-1 crystals from ref.<sup>1</sup>, (b) zoom on the particle analyzed for the measurements of the dimensions along the hexagonal projection. The colored dimensions were deduced from measurements on the screen. In red: longer dimension and blue: shorter dimension.

## SV. Construction of surface model from the $\text{Si}_{33}$ precursor species

Similarities between the models obtained by cleavage of the bulk structure and that obtained by assemblies of  $\text{Si}_{33}$  precursors are pointed out in Figure S11.

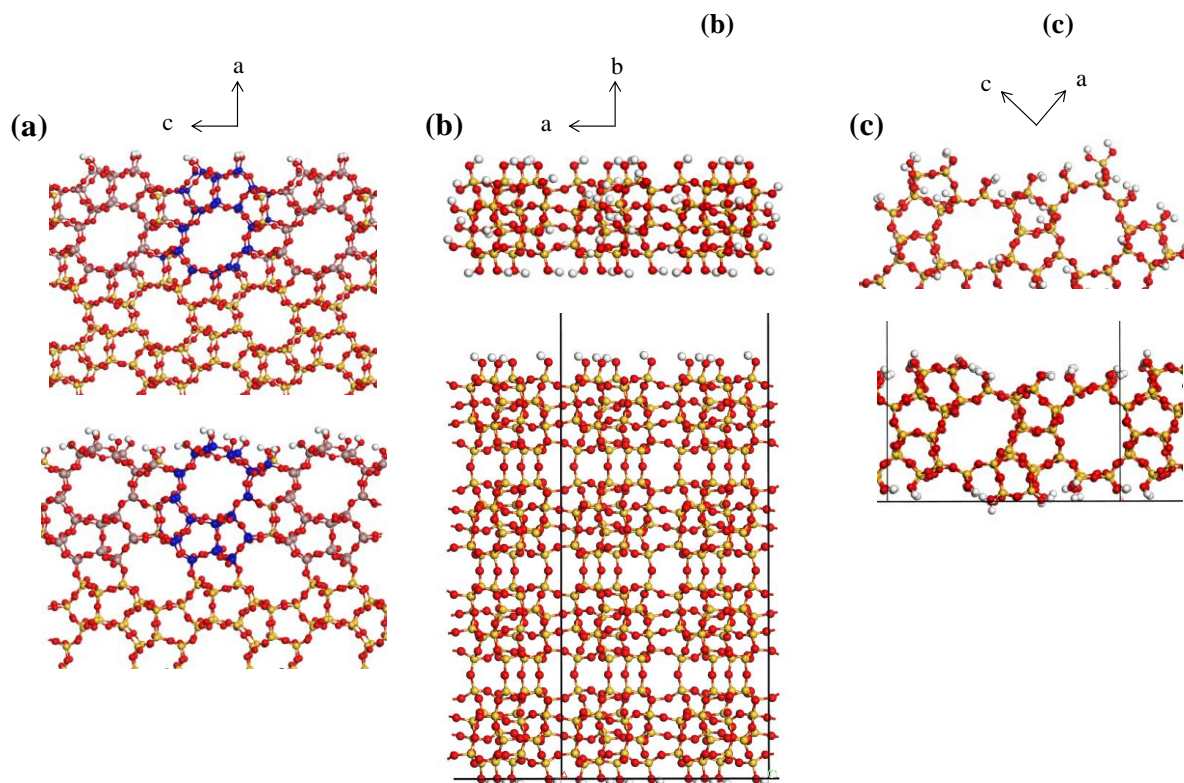


**Figure S11.** (a) Cleavage n°1 (top) and n°2 (bottom) for the (100) orientation, built by bulk cleavage. The Si atoms of the elementary  $\text{Si}_{33}$  units are emphasized in blue and grey for better visualization. (b) Analogy between the lateral view of a portion of the type 1 double nanoslab (top) and cleavage n°2 of the (010) surface (bottom). (c) approximate analogy between one of the lateral surface of the type 1 double nanoslab (top) and cleavage n°9 of the (101) surface (bottom).

## SVI. Aluminations energies

### SVI.1. Aluminations of the bulk sites

**Table S2.** Aluminations energies ( $\text{kJ}\cdot\text{mol}^{-1}$ ) for bulk sites of the ZSM-5 T-sites. The terminology of the sites follows the one of IZA. Color code: Sinusoidal channel ; Straight channel ; Intersection.

Al position	O position	$\Delta_r U_{alum}$ ( $\text{kJ}\cdot\text{mol}^{-1}$ )	Al position	O position	$\Delta_r U_{alum}$ ( $\text{kJ}\cdot\text{mol}^{-1}$ )
T1	O1	-22	T7	O16	-18
T1	O2	-24	T7	O18	-13
T1	O3	-26	T7	O11	-29
T1	O4	-11	T7	O17	-34
T2	O2	-22	T8	O17	-40
T2	O6	-32	T8	O19	-33
T2	O5	-27	T8	O6	-31
T2	O7	-31	T8	O20	-17
T3	O10	-44	T9	O15	-23
T3	O5	-26	T9	O21	-20
T3	O8	-29	T9	O19	-27
T3	O9	-9	T9	O22	-8
T4	O12	-28	T10	O24	-37
T4	O11	-37	T10	O3	-22
T4	O4	-19	T10	O23	-20
T4	O9	-8	T10	O22	-25
T5	O1	-18	T11	O16	-26
T5	O13	-28	T11	O25	-24
T5	O12	-13	T11	O14	-18
T5	O14	-19	T11	O24	-34
T6	O13	-24	T12	O25	-34
T6	O15	-14	T12	O8	-29
T6	O10	-26	T12	O26	-23
T6	O7	-18	T12	O20	-27

Li *et al.* also used DFT calculations to investigate the most stable T sites positions on the ZSM-5 bulk.<sup>3</sup> The relative energies of the T-sites of the bulk for a ratio of Si/Al=95 has been constructed to be compared to their model (Figure S12). Both sets of data are rather similar, the energies are in a  $20 \text{ kJ}\cdot\text{mol}^{-1}$  interval, so the difference of stabilization for this Si/Al is not significant. Both studies find that the T-sites in the sinusoidal and straight pore are among the most stable sites. But we disagree on the order of stability for the T-site in the intersection. However, the energy difference is so weak that the differences could be included in the uncertainty of the DFT methods we use.

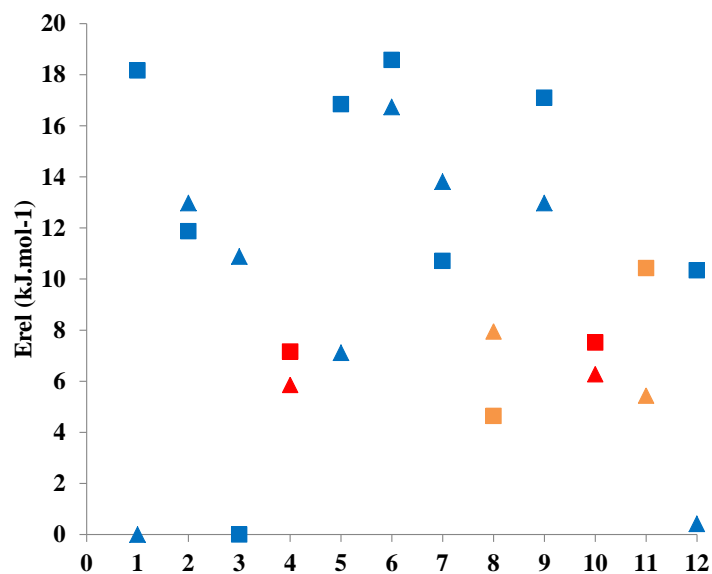


**Figure S12.** Relative aluminations energies (kJ.mol<sup>-1</sup>) of the different T-sites of the ZSM-5 bulk for Si/Al=95. T-sites at channel intersections are plotted in blue, whereas red and orange symbols correspond to T-sites within the sinusoidal and the straight channels respectively. T-sites are indicated by numbers corresponding the IZA attribution. Squares correspond to the results obtained in the present study whereas triangles correspond to the study of Li *et al.*<sup>3</sup>

### SVI.2. Aluminations of the surface sites

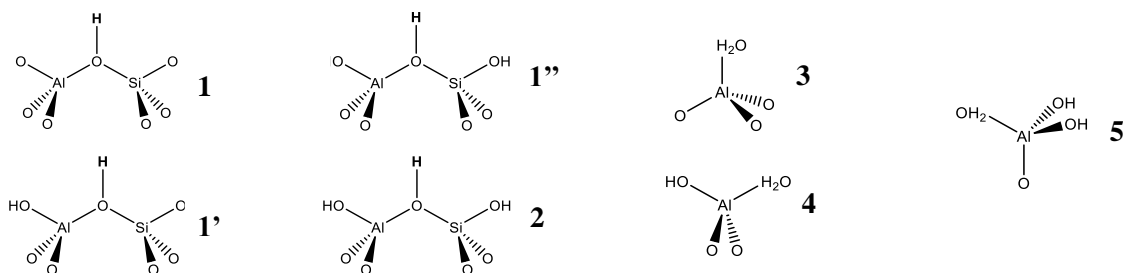


**Figure S13.** Nature of the surface acid sites associated to numbers for the legend of the following tables: Bridging Si-OH-Al, possibly close to Si-OH and/or Al-OH (1, 1', 1'' and 2), water molecules adsorbed on the aluminum, possibly close to Al-OH groups (3, 4 and 5).

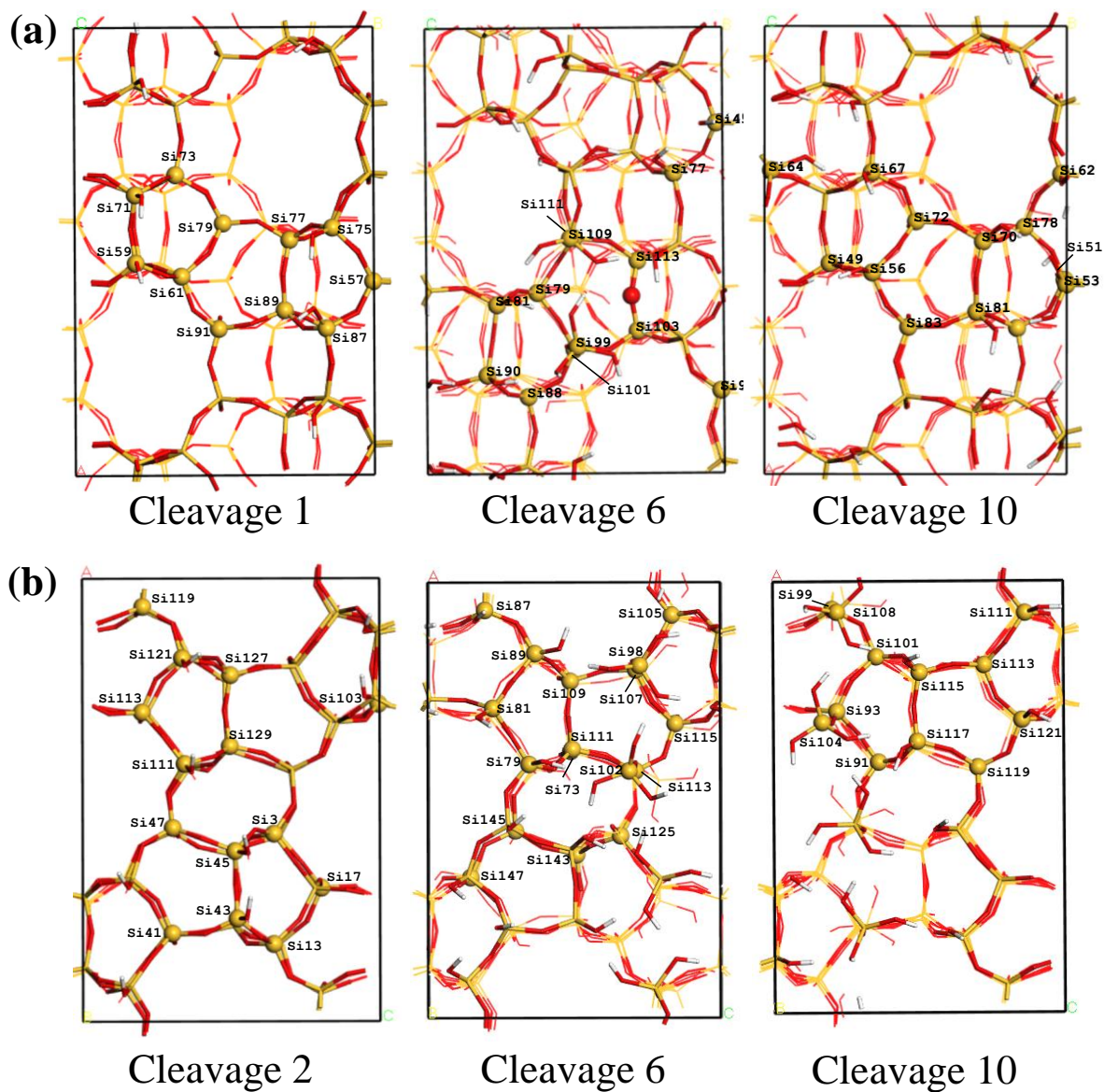


**Figure S14.** Top views of the most important surface cleavages, showing the numbering of the silicon atoms, on the (a) (100) and (b) (010) orientations.



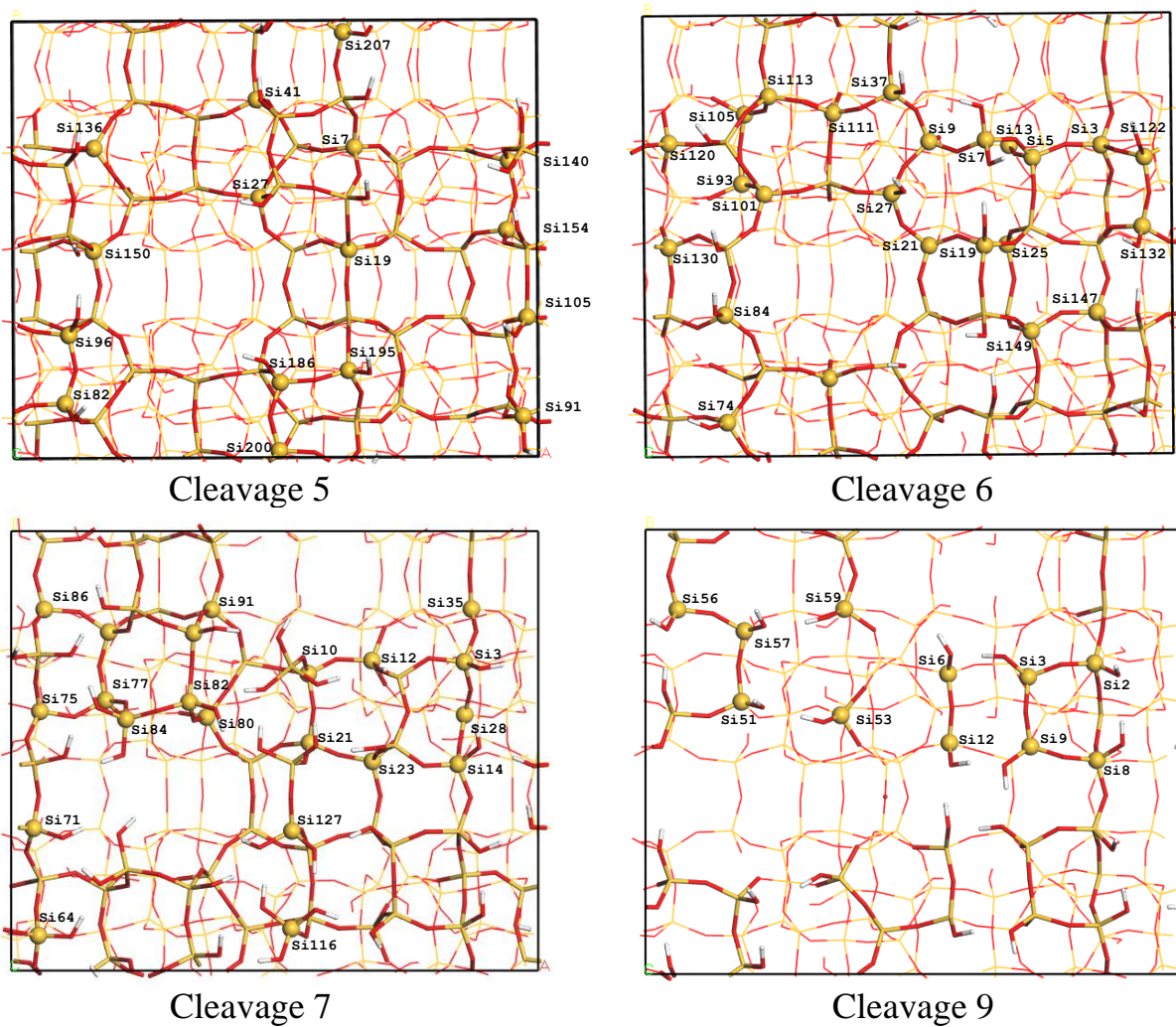


**Figure S15.** Top views of the most important surface cleavages, showing the numbering of the silicon atoms, on the (101) orientation.



**Table S3.** Aluminatation energy ( $\text{kJ}\cdot\text{mol}^{-1}$ ) for the slab model corresponding to cleavage 1 along (100). The types of site are defined in Figure S13. The aluminum position is shown in Figure S14. The same aluminum name can appear for different proton position due to the four oxygen surrounding the aluminum which could be studied here.

Type of site	Al position	$\Delta_r U_{alum}$ ( $\text{kJ}\cdot\text{mol}^{-1}$ )
Bridging Si-OH-Al (Type 1)	Si_87	-52
	Si_79	-49
	Si_89	-46
	Si_89	-38
	Si_77	-37
	Si_61	-37
	Si_79	-35
	Si_77	-35
	Si_91	-34
	Si_79	-33
	Si_87	-33
	Si_73	-32
	Si_73	-30
	Si_69	-27
	Si_91	-27
	Si_77	-25
	Si_73	-25
	Si_91	-25
	Si_61	-23
	Si_61	-23
	Si_69	-20
	Si_89	-20
Si_91	-15	
Si_79	-15	
Si_57	-15	
Bridging Si-OH-Al (Type 1')	Si_75	-34
	Si_71	-23
	Si_71	-22
	Si_75	-22
	Si_59	-17
	Si_75	-14
	Si_59	-12
Bridging Si-OH-Al (Type 1'')	Si_89	-51
	Si_69	-49
	Si_57	-46
	Si_73	-39
	Si_69	-39
	Si_77	-35
	Si_57	-33
	Si_57	-22
	Si_61	-21
Bridging Si-OH-Al (Type 2)	Si_59	-38
	Si_87	-25
	Si_71	-19
Al-H <sub>2</sub> O (Type 3)	Si_75	-75
	Si_87	-68
	Si_71	-68
	Si_59	-57

**Table S4.** Alumination energy ( $\text{kJ}\cdot\text{mol}^{-1}$ ) for the slab model corresponding to cleavage 6 along (100). The types of site are defined in Figure S13. The aluminum position is shown in Figure S14.

Type of site	Al position	$\Delta_r U_{alum}$ ( $\text{kJ}\cdot\text{mol}^{-1}$ )
Bridging Si-OH-Al (Type 1)	Si_101	-52
	Si_103	-43
	Si_79	-36
	Si_101	-36
	Si_101	-36
	Si_111	-35
	Si_103	-33
	Si_88	-33
	Si_88	-33
	Si_79	-32
	Si_113	-31
	Si_113	-29
	Si_111	-28
	Si_113	-27
	Si_103	-26
	Si_88	-25
Si_111	-24	
Si_79	-19	
Bridging Si-OH-Al (Type 1')	Si_77	-42
	Si_81	-33
	Si_90	-29
	Si_105	-23
	Si_109	-14
Bridging Si-OH-Al (Type 1'')	Si_103	-41
	Si_111	-50
	Si_113	-38
	Si_79	-47
	Si_88	-48
	Si_101	-21
Bridging Si-OH-Al (Type 2)	Si_45	-69
	Si_45	-58
	Si_77	-55
	Si_105	-52
	Si_92	-46
	Si_109	-44
	Si_105	-38
	Si_45	-38
	Si_81	-38
	Si_81	-37
	Si_90	-37
	Si_77	-30
	Si_99	-29
	Si_92	-23
Si_92	-18	
Si_90	-13	
Al-H <sub>2</sub> O (Type 3)	Si_77	-141
	Si_45	-127
	Si_92	-114
	Si_90	-101
	Si_81	-62
Si_105	-57	
Al-H <sub>2</sub> O (Type 4)	Si_109	-79
	Si_109	-74
Al-H <sub>2</sub> O (Type 5)	Si_99	-105
	Si_99	-82
	Si_99	-69

**Table S5.** Aluminatation energy ( $\text{kJ}\cdot\text{mol}^{-1}$ ) for the slab model corresponding to cleavage 10 along (100). The types of site are defined in Figure S13. The aluminum position is shown in Figure S14.

Type of site	Al position	$\Delta_r U_{alum}$ ( $\text{kJ}\cdot\text{mol}^{-1}$ )
Bridging Si-OH-Al (Type 1)	Si_49	-56
	Si_51	-53
	Si_62	-45
	Si_49	-41
	Si_49	-41
	Si_62	-40
	Si_83	-33
	Si_83	-29
	Si_51	-26
	Si_78	-23
	Si_78	-19
	Si_62	-17
	Si_51	-17
	Si_72	-17
	Si_78	-16
Bridging Si-OH-Al (Type 1')	Si_67	-81
	Si_56	-59
	Si_70	-51
	Si_67	-36
	Si_56	-32
	Si_81	-31
	Si_70	-27
	Si_81	-22
	Si_64	-20
	Si_56	-16
Si_53	1	
Bridging Si-OH-Al (Type 1'')	Si_62	-85
	Si_78	-47
	Si_49	-40
	Si_72	-40
	Si_72	-40
	Si_83	-39
	Si_72	-35
	Si_51	-24
	Si_83	-22
Bridging Si-OH-Al (Type 2)	Si_67	-35
	Si_81	-18
	Si_64	-5
	Si_70	1
Al-H <sub>2</sub> O (Type 3)	Si_67	-102
	Si_70	-99
	Si_56	-84
	Si_81	-54
Al-H <sub>2</sub> O (Type 4)	Si_64	-96
	Si_64	-71
Al-H <sub>2</sub> O (Type 5)	Si_53	-86
	Si_53	-70
	Si_53	-33

**Table S6.** Alumination energy ( $\text{kJ}\cdot\text{mol}^{-1}$ ) for the slab model corresponding to cleavage 2 along (010). The types of site are defined in Figure S13. The aluminum position is shown in Figure S14.

Type of site	Al position	$\Delta_r U_{alum}$ ( $\text{kJ}\cdot\text{mol}^{-1}$ )
Bridging Si-OH-Al (Type 1)	Si_103	-46
	Si_17	-42
	Si_127	-39
	Si_17	-32
	Si_113	-32
	Si_41	-32
	Si_17	-31
	Si_13	-27
	Si_47	-26
	Si_103	-26
	Si_3	-26
	Si_103	-25
	Si_129	-25
	Si_119	-25
	Si_17	-22
	Si_13	-20
	Si_127	-19
	Si_129	-19
	Si_3	-18
	Si_3	-14
Si_103	-11	
Si_13	-9	
Si_129	-9	
Si_127	-8	
Bridging Si-OH-Al (Type 1')	Si_45	-22
	Si_121	-18
	Si_111	-17
	Si_45	-16
	Si_121	-15
	Si_121	-14
	Si_111	-13
	Si_111	-9
	Si_43	-3
Si_43	-1	
Bridging Si-OH-Al (Type 1'')	Si_113	-42
	Si_41	-36
	Si_47	-35
	Si_113	-34
	Si_119 / T5	-34
	Si_129 / T3	-34
	Si_119	-30
	Si_47 / T11	-29
	Si_41	-28
	Si_41 / T8	-27
	Si_113 / T2	-26
	Si_3 / T1	-24
	Si_119	-23
	Si_127 / T4	-22
Si_47	-22	
Si_13 / T6	-17	
Bridging Si-OH-Al (Type 2)	Si_43	-26
	Si_45	-21
Al-H <sub>2</sub> O (Type 3)	Si_43 / T9	-59
	Si_45 / T10	-58
	Si_111 / T7	-43
	Si_121 / T12	-35

**Table S7.** Alumination energy ( $\text{kJ}\cdot\text{mol}^{-1}$ ) for the slab model corresponding to cleavage 6 along (010). The types of site are defined in Figure S13. The aluminum position is shown in Figure S14.

Type of site	Al position	$\Delta_r U_{alum}$ ( $\text{kJ}\cdot\text{mol}^{-1}$ )
Bridging Si-OH-Al (Type 1)	Si_111	-48
	Si_73	-44
	Si_111	-42
	Si_125	-41
	Si_143	-40
	Si_73	-39
	Si_125	-34
	Si_73	-34
	Si_73	-33
	Si_145	-32
	Si_143	-32
	Si_111	-30
	Si_125	-29
	Si_147	-27
	Si_125	-26
	Si_147	-25
	Si_143	-23
	Si_145	-23
	Si_147	-23
	Si_145	-22
	Si_145	-22
Si_147	-17	
Si_143	-10	
Bridging Si-OH-Al (Type 1')	Si_98	-42
	Si_89	-39
	Si_102	-17
	Si_79	-16
Bridging Si-OH-Al (Type 1'')	Si_107	-68
	Si_113	-57
	Si_111	-52
	Si_109	-39
	Si_105	-29
	Si_115	-22
Bridging Si-OH-Al (Type 2)	Si_87	-55
	Si_81	-47
	Si_87	-45
	Si_81	-40
	Si_79	-32
	Si_89	-27
	Si_89	-26
	Si_87	-21
	Si_81	-18
	Si_79	-17
Al-H <sub>2</sub> O (Type 3)	Si_89	-113
	Si_79	-97
	Si_81	-73
	Si_87	-64
Al-H <sub>2</sub> O (Type 5)	Si_102	-90
	Si_98	-80
	Si_98	-75
	Si_98	-73
	Si_102	-32
	Si_102	9

**Table S8.** Aluminatation energy ( $\text{kJ}\cdot\text{mol}^{-1}$ ) for the slab model corresponding to cleavage 10 along (010). The types of site are defined in Figure S13. The aluminum position is shown in Figure S14.

Type of site	Al position	$\Delta_r U_{alum}$ ( $\text{kJ}\cdot\text{mol}^{-1}$ )
Bridging Si-OH-Al (Type 1)	Si_93	-41
	Si_91	-36
	Si_101	-36
	Si_93	-32
	Si_101	-32
	Si_93	-27
	Si_99	-26
	Si_91	-25
	Si_99	-22
	Si_101	-22
	Si_91	-21
	Si_119	-21
	Si_99	-19
	Si_113	-11
Bridging Si-OH-Al (Type 1')	Si_111	-44
	Si_115	-33
	Si_115	-31
	Si_121	-20
	Si_117	-17
	Si_117	-16
	Si_108	-9
	Si_111	-9
	Si_121	-7
	Si_104	-4
	Si_121	-4
	Si_111	9
Bridging Si-OH-Al (Type 1'')	Si_113	-52
	Si_99	-43
	Si_119	-43
	Si_119	-43
	Si_113	-41
	Si_93	-24
	Si_101	-16
	Si_91	-14
	Si_119	-8
	Si_113	-4
	Bridging Si-OH-Al (Type 2)	Si_115
Si_117		2
Al-H <sub>2</sub> O (Type 3)	Si_111	-100
	Si_117	-89
	Si_121	-87
	Si_115	-4
Al-H <sub>2</sub> O (Type 5)	Si_104	-104
	Si_104	-99
	Si_108	-94
	Si_108	-47
	Si_108	-42
	Si_104	-30

**Table S9.** Aluminations energy ( $\text{kJ}\cdot\text{mol}^{-1}$ ) for the slab model corresponding to cleavage 5 along (101). The types of site are defined in Figure S13. The aluminum position is shown in Figure S15.

Type of site	Al position	$\Delta_r U_{alum}$ ( $\text{kJ}\cdot\text{mol}^{-1}$ )
Bridging Si-OH-Al (Type 1)	Si_136	-48
	Si_150	-40
	Si_19	-39
	Si_27	-38
	Si_140	-38
	Si_7	-38
	Si_41	-36
	Si_7	-33
	Si_154	-29
Bridging Si-OH-Al (Type 1')	Si_200	-55
	Si_105	-43
	Si_195	-38
	Si_195	-35
	Si_207	-33
	Si_186	-32
	Si_96	-24
	Si_82	-23
	Si_91	0
Bridging Si-OH-Al (Type 1'')	Si_7	-60
	Si_41	-56
	Si_7	-53
	Si_19	-52
	Si_154	-46
	Si_27	-44
	Si_136	-34
	Si_140	-33
	Si_150	-10
Bridging Si-OH-Al (Type 2)	Si_82	-70
	Si_105	-59
	Si_200	-54
	Si_207	-52
	Si_96	-43
	Si_200	-43
	Si_186	-41
	Si_105	-35
	Si_82	-34
	Si_195	-31
	Si_186	-28
	Si_96	-25
	Si_207	-24
Si_91	2	
Al-H <sub>2</sub> O (Type 3)	Si_207	-91
	Si_96	-87
	Si_200	-87
	Si_105	-82
	Si_186	-69
	Si_82	-64
	Si_195	-63
Al-H <sub>2</sub> O (Type 4)	Si_91	-71
	Si_91	-45



**Table S10.** Aluminations energy (kJ.mol<sup>-1</sup>) for the slab model corresponding to cleavage 6 along (101). The types of site are defined in Figure S13. The aluminum position is shown in Figure S15.

Type of site	Al position	$\Delta_r U_{alum}$ (kJ.mol <sup>-1</sup> )
Bridging Si-OH-Al (Type 1)	Si_5	-61
	Si_149	-55
	Si_55	-54
	Si_13	-53
	Si_25 / T12	-53
	Si_55	-52
	Si_149 / T8	-50
	Si_111 / T11	-44
	Si_149	-44
	Si_5	-44
	Si_147	-42
	Si_3	-41
	Si_120	-40
	Si_105	-38
	Si_105	-38
	Si_93	-38
	Si_3	-37
	Si_105 / T8	-36
	Si_55 / T5	-35
	Si_147	-35
	Si_93 / T2	-34
	Si_3 / T1	-33
	Si_111	-33
	Si_25 / T12	-32
	Si_13 / T6	-32
	Si_113 / T12	-32
	Si_93	-31
	Si_130	-31
	Si_113	-31
	Si_130 / T10	-30
	Si_101 / T6	-29
	Si_111	-28
	Si_25	-28
	Si_113	-27
	Si_25	-26
	Si_9	-26
	Si_93	-25
	Si_5 / T2	-25
	Si_21	-25
	Si_120 / T4	-24
Si_105	-23	
Si_21	-22	
Si_13	-22	
Si_147	-21	
Si_13	-21	
Si_101 / T6	-20	
Bridging Si-OH-Al (Type 1')	Si_37	-52
	Si_132	-40
	Si_7	-36
	Si_122	-32
	Si_37	-31
	Si_132	-31
	Si_74	-28
Si_122	-23	

	Si_84	-21
	Si_74	-18
	Si_19	-16
	Si_84	-15
	Si_7	-13
	Si_27	-11
	Si_27	-11
	Si_27	-5
	Si_74	-4
	Si_19	32
Bridging Si-OH-Al (Type 1'')	Si_21 / T10	-45
	Si_5	-42
	Si_149	-41
	Si_120	-39
	Si_9 / T4	-38
	Si_147 / T7	-34
	Si_130	-33
	Si_113	-32
	Si_9	-30
	Si_130	-29
	Si_55	-28
	Si_3	-28
	Si_9	-27
	Si_111	-26
	Si_120	-22
	Si_21	-21
	Si_101	-20
Si_101 / T6	-19	
Bridging Si-OH-Al (Type 2)	Si_37	-33
	Si_132	-19
	Si_122	-18
	Si_19	-7
	Si_84	-5
Al-H <sub>2</sub> O (Type 3)	Si_37 / T7	-75
	Si_132 / T5	-75
	Si_84 / T9	-72
	Si_19 / T9	-71
	Si_74 / T3	-59
	Si_122 / T11	-55
	Si_27 / T1	-48
Al-H <sub>2</sub> O (Type 4)	Si_7 / T3	-57
	Si_7	-54

**Table S11.** Alumination energy ( $\text{kJ}\cdot\text{mol}^{-1}$ ) for the slab model corresponding to cleavage 7 along (101). The types of site are defined in Figure S13. The aluminum position is shown in Figure S15.

Type of site	Al position	$\Delta_r U_{alum}$ ( $\text{kJ}\cdot\text{mol}^{-1}$ )
Bridging Si-OH-Al (Type 1)	Si_80	-73
	Si_35	-51
	Si_28	-49
	Si_75	-42
	Si_23	-38
	Si_75	-35
	Si_12	-34
	Si_88	-34
	Si_91	-31
	Si_21	-29
	Si_77	-27
	Si_10	-25
	Si_86	-22
	Si_28	-8
Bridging Si-OH-Al (Type 1')	Si_127	-55
	Si_82	-49
	Si_14	-44
	Si_3	-39
	Si_93	-19
	Si_71	-18
	Si_84	-10
	Si_3	-9
	Si_116	-6
	Si_64	-3
	Si_64	18
Bridging Si-OH-Al (Type 1'')	Si_77	-64
	Si_21	-63
	Si_80	-56
	Si_23	-55
	Si_88	-55
	Si_35	-47
	Si_28	-41
	Si_75	-40
	Si_12	-35
	Si_28	-34
	Si_91	-34
	Si_86	-30
	Si_10	-24
	Si_75	-16
Bridging Si-OH-Al (Type 2)	Si_14	-90
	Si_82	-48
	Si_93	-45
	Si_82	-40
	Si_71	-38
	Si_127	-35
	Si_14	-33
	Si_3	-29
	Si_93	-14
	Si_84	-5
Al-H <sub>2</sub> O (Type 3)	Si_82	-102
	Si_3	-95
	Si_93	-75
	Si_14	-34

Al-H <sub>2</sub> O (Type 4)	Si_127	-98
	Si_64	-87
	Si_127	-72
	Si_84	-70
	Si_71	-63
	Si_71	-57
	Si_84	-40
	Si_64	-37
Al-H <sub>2</sub> O (Type 5)	Si_116	-59
	Si_116	-45
	Si_116	-35

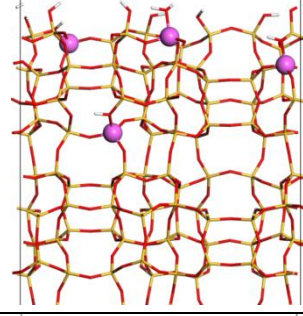
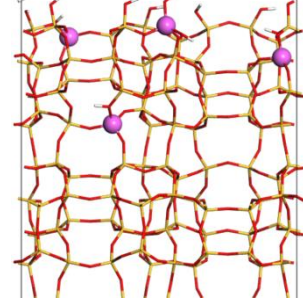
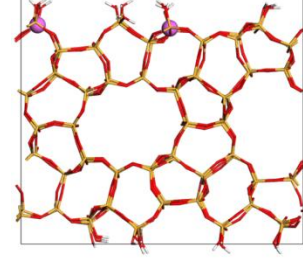
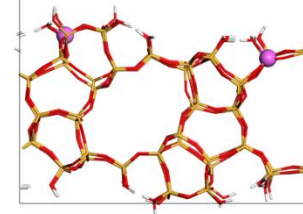
**Table S12.** Aluminatation energy (kJ.mol<sup>-1</sup>) for the slab model corresponding to cleavage 9 along (101). The types of site are defined in Figure S13. The aluminum position is shown in Figure S15.

Type of site	Al position	$\Delta_r U_{alum}$ (kJ.mol <sup>-1</sup> )
Al-H <sub>2</sub> O (Type 3)	Si_57	-110
	Si_59	-108
	Si_51	-91
	Si_8	-89
	Si_3	-88
	Si_53	-82
	Si_56	-79
	Si_2	-75
	Si_12	-66
	Si_9	-63
	Si_6	-60

**Table S13.** Comparison of the nature and stability of the most stable sites in bulk aluminated structures, when exposed on the three considered dominant surface orientations.

Most stable T-sites in the bulk	$\Delta_r U_{Al}$ (kJ.mol <sup>-1</sup> ) in the bulk	Rank among (100) most stable surface sites (cleavage 1) / Nature of the site	Rank among (010) most stable surface sites (cleavage 2) / Nature of the site	Rank among (101) most stable surface sites (cleavage 6) / Nature of the site
T3	-44	9 / Al-OH-Si	13 / Al-OH-Si-OH	7 / Al-(H <sub>2</sub> O)(OH) 6 / Al-H <sub>2</sub> O
T8	-40	7 / Al-OH-Si-OH	8 / Al-OH-Si-OH	8 / Al-OH-Si
T4	-37	10 / Al-OH-Si-OH	7 / Al-OH-Si	26 / Al-OH-Si
T10	-37	8 / Al-OH-Si-OH	2 / Al-H <sub>2</sub> O	18 / Al-OH-Si-OH

**Table S14.** Aluminations energies obtained by decreasing the surface Si/Al ratio.\* The surface Si/Al ratio is defined for the surface layer which depth corresponds to one bulk unit.

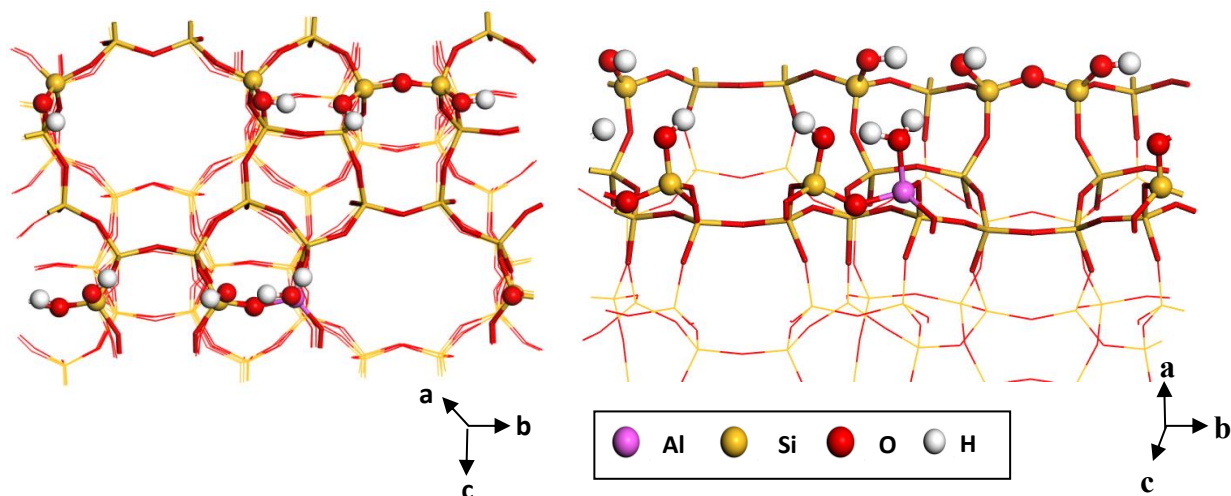
Surface Si/Al	Surface	Aluminated sites	Type of site	Illustration	$\Delta_r U_{al\_tot}$ (kJ.mol <sup>-1</sup> )	$\Delta_r U_{al\_theo}$ (kJ.mol <sup>-1</sup> )
23	(100) cleavage 1	Si_59 Si_63 Si_109 Si_117	Al-H <sub>2</sub> O / 3 Al-OH-Si / 1 Al-OH-Si-OH / 1'' Al-OH-Si-OH / 1''		-138	-158
23	(100) cleavage 1	Si_59 Si_63 Si_109 Si_117	OH-Al-OH-Si / 1' Al-OH-Si / 1 Al-OH-Si-OH / 1'' Al-OH-Si-OH / 1''		-100	-113
43	(101) cleavage 6	Si_37 Si_132	Al-H <sub>2</sub> O / 3 Al-H <sub>2</sub> O / 3		-144	-150
55	(101) cleavage 9	Si_57 Si_8	Al-H <sub>2</sub> O / 3 Al-H <sub>2</sub> O / 3		-205	-199

$$* \Delta_r U_{al\_tot} = (U_{slab\_n\_Al} + nU_{Si(OH)_4} - U_{slab} - nU_{Al(OH)_3H_2O})$$

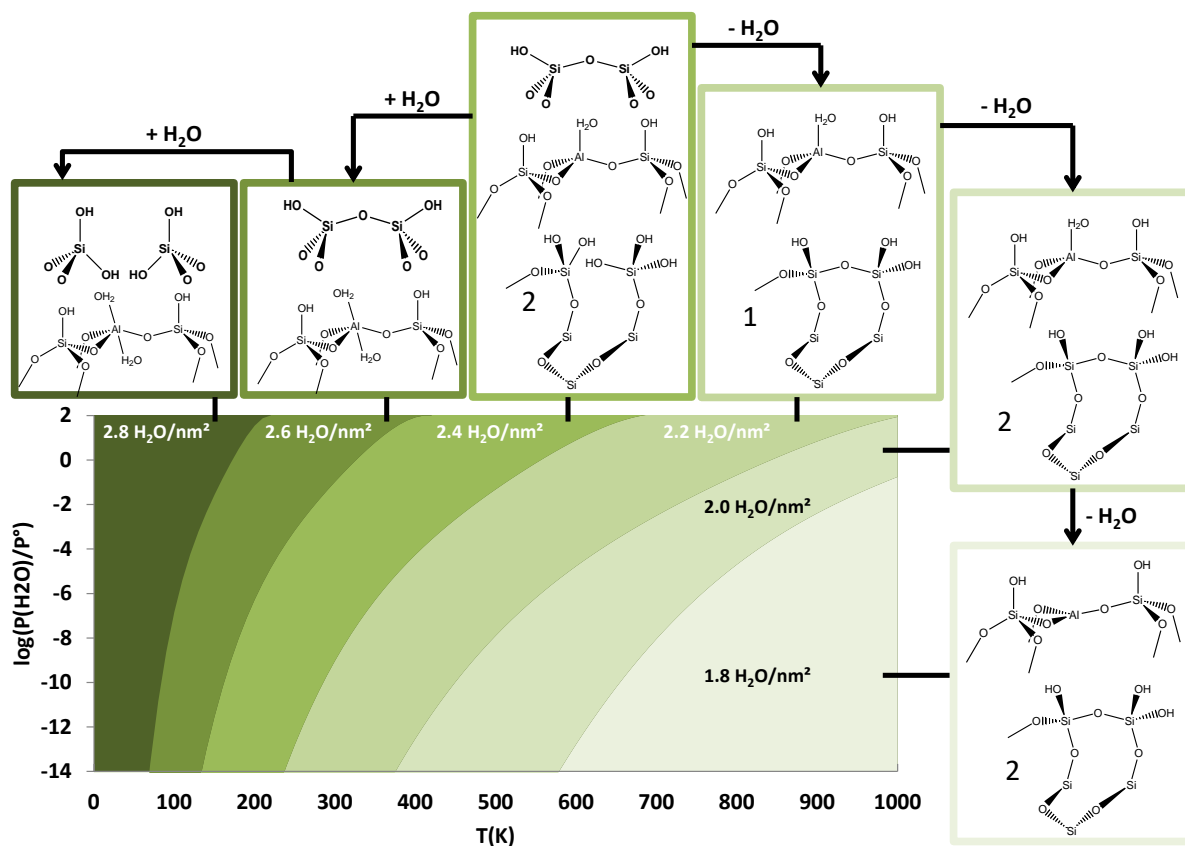
$$\Delta_r U_{al\_theo} = \sum_i \Delta_r U_{Si_i}$$

with  $n$  the number of aluminated sites per unit cell,  $U_{slab\_n\_Al}$  the energy of the surface with  $n$  aluminated sites,  $U_{slab}$  the similar but purely silicic surface and  $\Delta_r U_{Si_i}$  the aluminations energy defined in Eq. 2 of the silicon number  $n$ , this value can differ depending on the position of the proton.

## SVII. Surface hydration/dehydration reactions

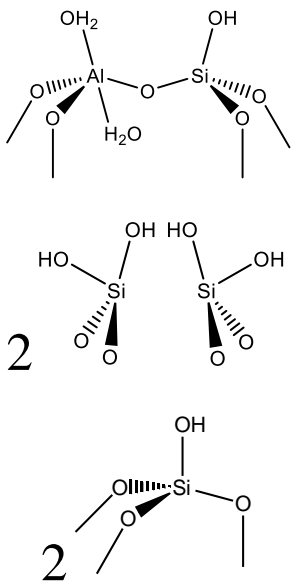
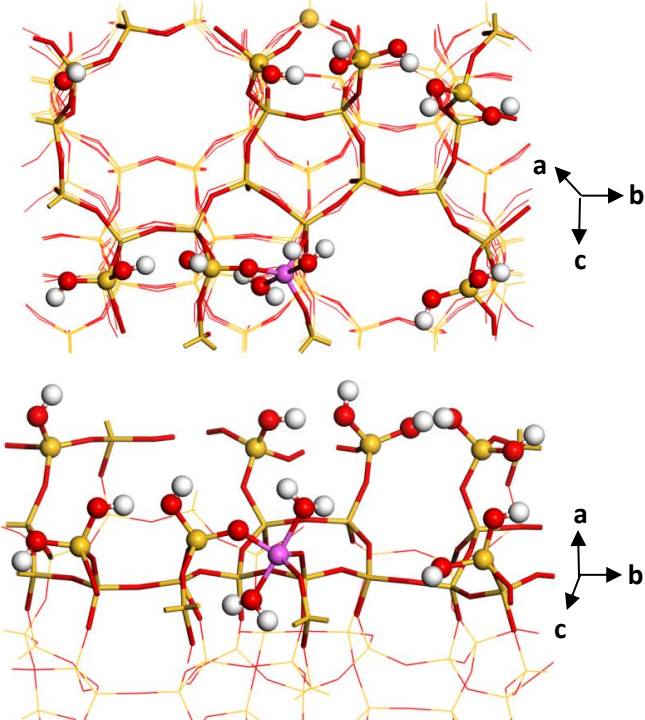
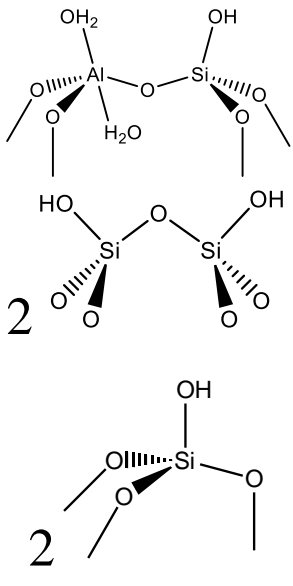
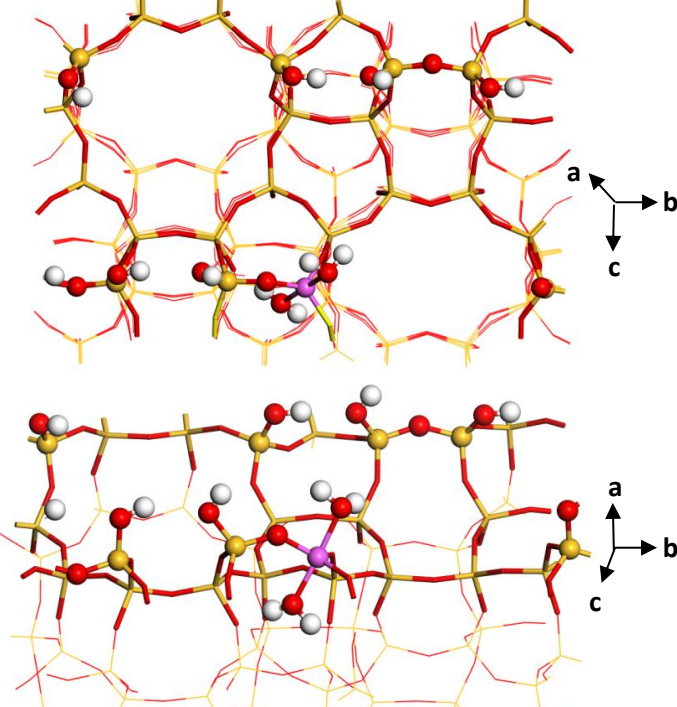


**Figure S16.** Surface of the initial surface for hydration and dehydration with  $1.7 \text{ H}_2\text{O}/\text{nm}^2$  (Left) Top view (Right) Side view. This surface exhibits 7 Si-OH groups and one Al-H<sub>2</sub>O. The two pairs of Si-OH groups are close neighbors and form at the surface a HO-Si-O-Si-OH bridges.

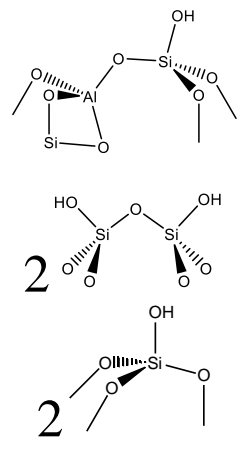
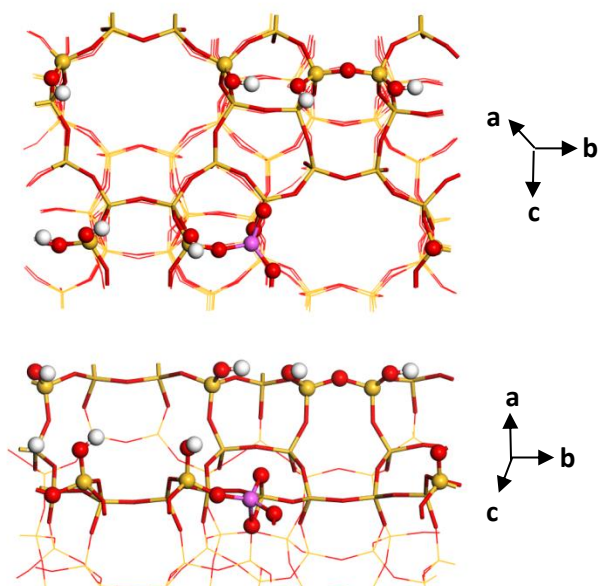
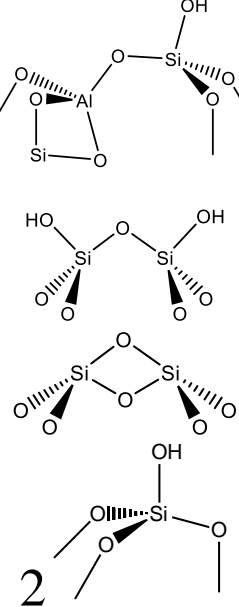
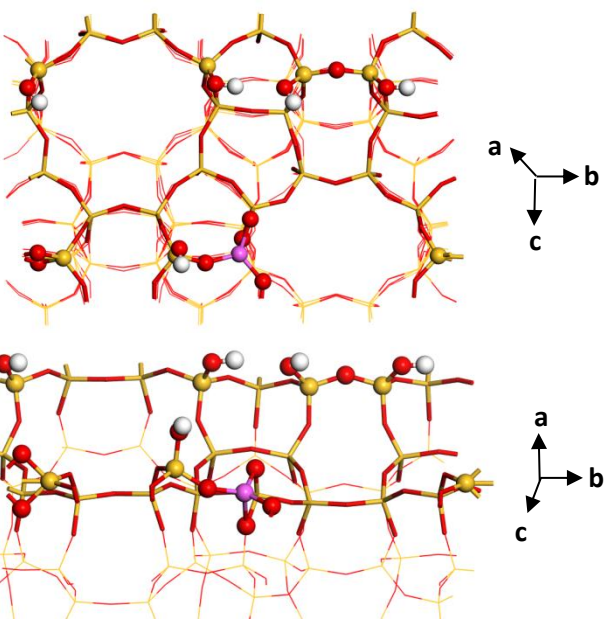
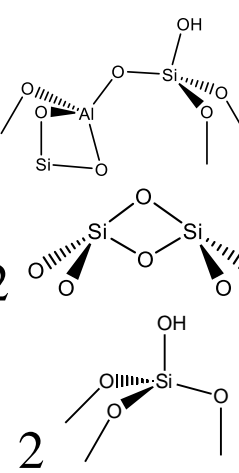
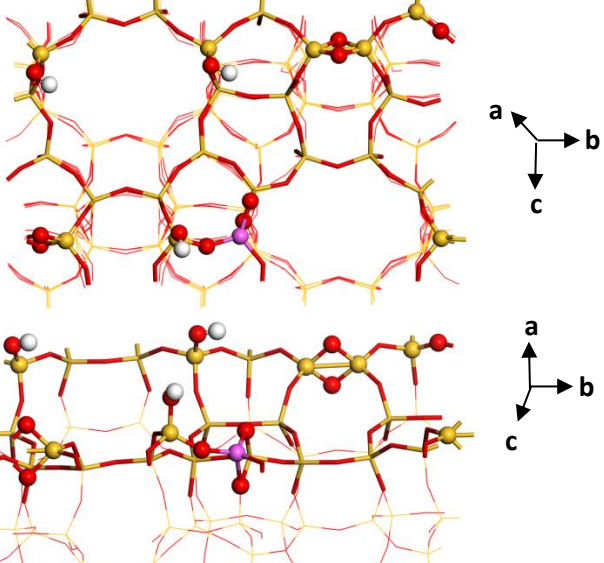


**Figure S17.** Surface hydration thermodynamic diagram for Al-(H<sub>2</sub>O) site n°77 belonging to the cleavage 6 of (100) surface of ZSM-5

**Table S15.** Structures (Schematic view, top view and side view) of the systems invoked in Figure 6-a in the manuscript.

Hydration level ( $\text{H}_2\text{O}\cdot\text{nm}^{-2}$ )	Schematic hydroxyl and aluminum groups	Surface	$\Delta_r U_{hyd}$ ( $\text{kJ}\cdot\text{mol}^{-1}$ )
2.8			-95
2.1			-56



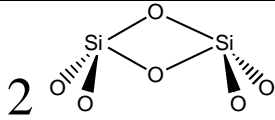
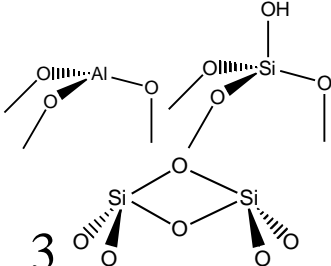
1.3			128
0.9			293
0.6			454

The electronic adsorption or desorption energy of each water molecule was calculated according to **Equation S1** and using the surface hydrated at  $1.7 \text{ H}_2\text{O}\cdot\text{nm}^{-2}$ .

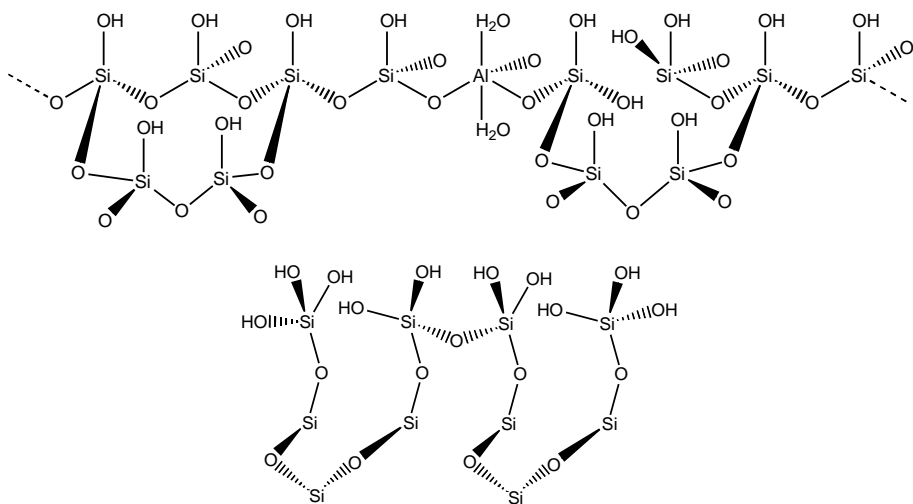
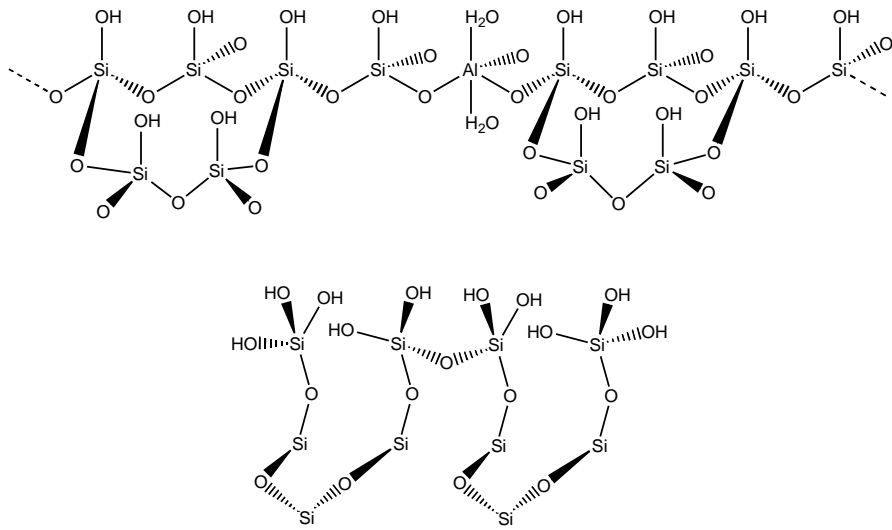
$$\Delta_r U_{hyd} = U_{hydrated\_slab} - U_{slab} -/+ n_{\text{H}_2\text{O}} U_{\text{H}_2\text{O}}$$

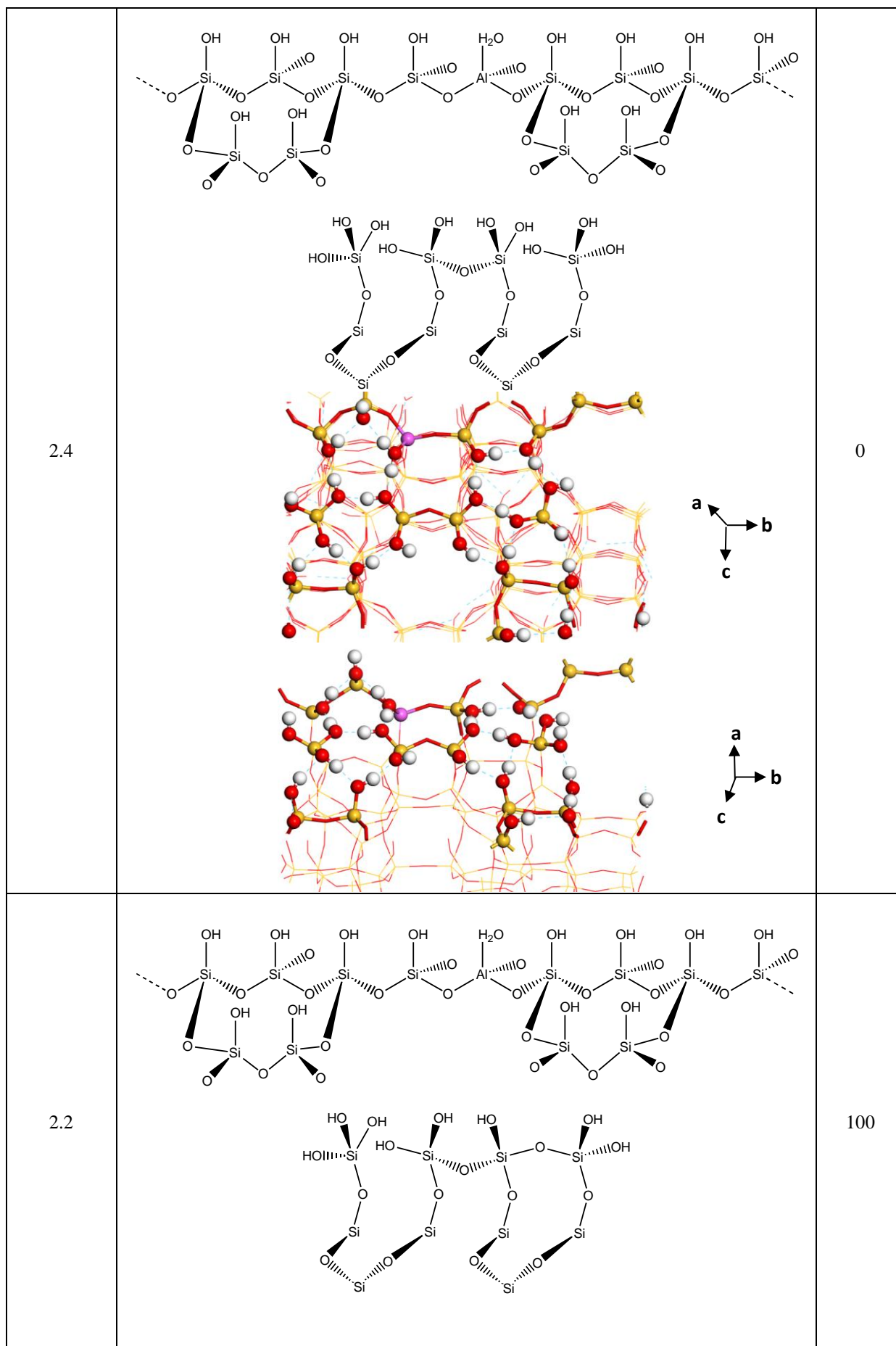
**Equation S1****Table S16.** Structures (Schematic view) of the systems invoked in Figure 6-b.

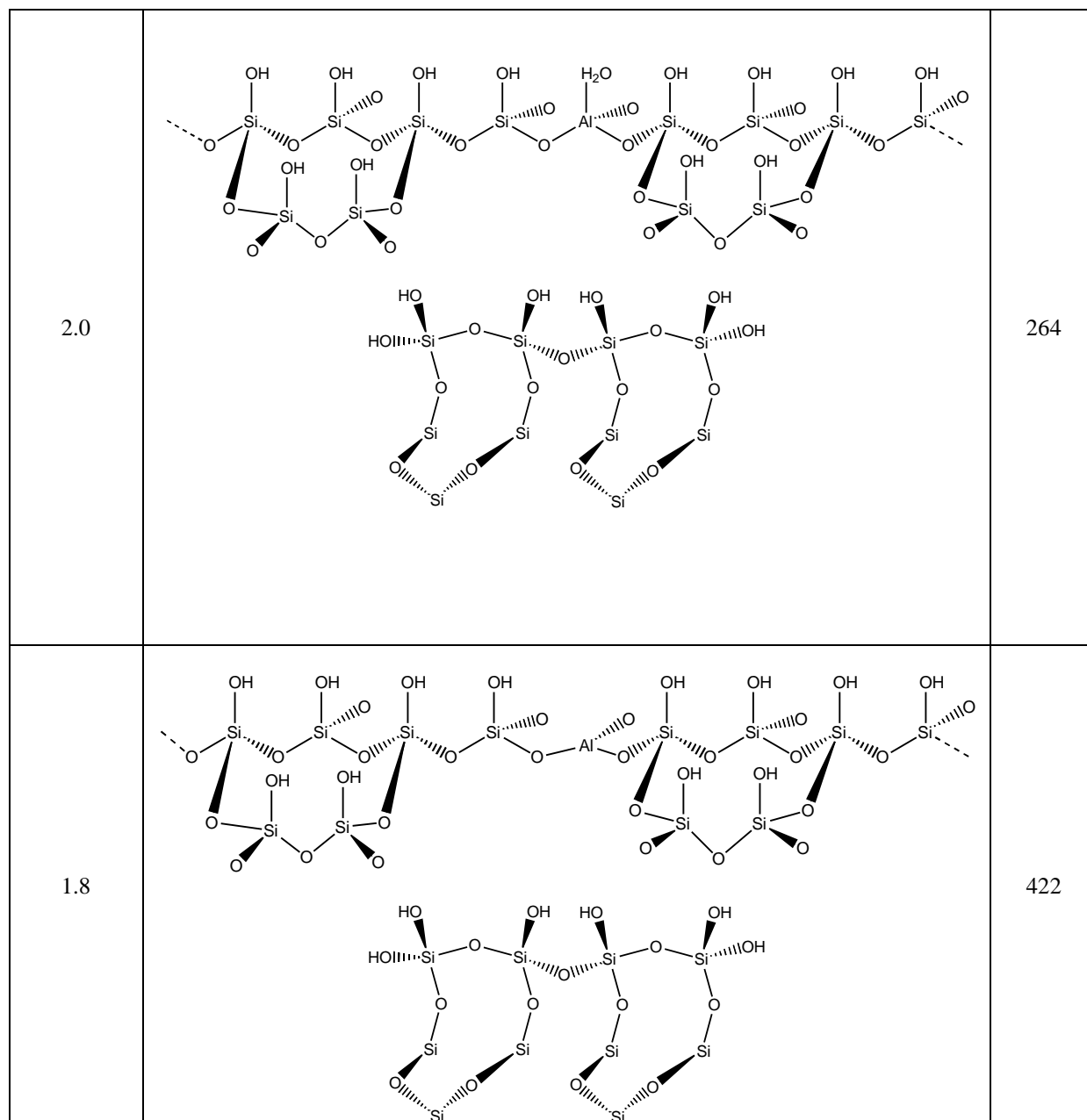
Hydration level ( $\text{H}_2\text{O}\cdot\text{nm}^{-2}$ )	Schematic hydroxyl and aluminum groups	$\Delta_r U_{hyd}$ ( $\text{kJ}\cdot\text{mol}^{-1}$ )
2.1		-13
1.7		0
0.9		320
0.6		497

		
0.2		894

**Table S17.** Structures (Schematic view) of the systems invoked in Figure S17.

Hydration level ( $\text{H}_2\text{O}\cdot\text{nm}^{-2}$ )	Schematic hydroxyl and aluminum groups	$\Delta_r U_{hyd}$ ( $\text{kJ}\cdot\text{mol}^{-1}$ )
2.8		-80
2.6		-54





## References

- (1) Gruene, T.; Li, T.; van Genderen, E.; Pinar, A. B.; van Bokhoven, J. A., Characterization at the Level of Individual Crystals: Single-Crystal MFI Type Zeolite Grains, *Chem. Eur. J.* **2018**, *24*, 2384-2388.
- (2) Zhai, D.; Liu, Y.; Zheng, H.; Zhao, L.; Gao, J.; Xu, C.; Shen, B., A First-Principles Evaluation of the Stability, Accessibility, and Strength of Brønsted Acid Sites in Zeolites, *J. Catal.* **2017**, *352*, 627-637.
- (3) Li, C.; Vidal-Moya, A.; Miguel, P. J.; Dedecek, J.; Boronat, M.; Corma, A., Selective Introduction of Acid Sites in Different Confined Positions in ZSM-5 and Its Catalytic Implications, *ACS Catal.* **2018**, *8*, 7688-7697.

## Chapter 4: Supplementary Information

### S1. Additional structural DFT data

#### S1.1. Surface orientations considered

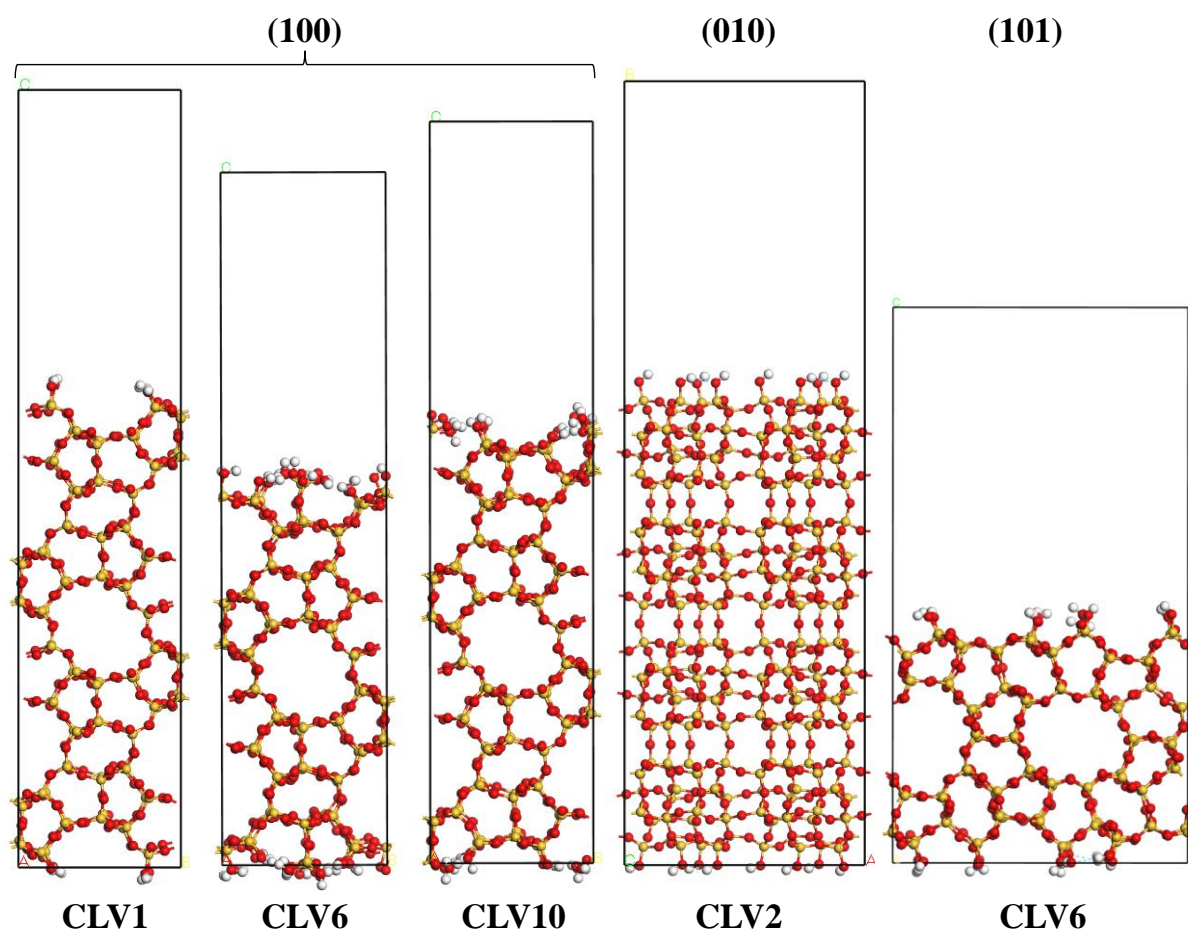


**Figure S1.** Side views of the surface model used as a basis for the simulation of the external surface of ZSM-5: (a) (100) orientation, according to cleavages 1, 6 and 10 (see ref. <sup>1</sup>), (b) (010) orientation, (101) orientation.



## S2. Main characteristics of the two zeolite samples

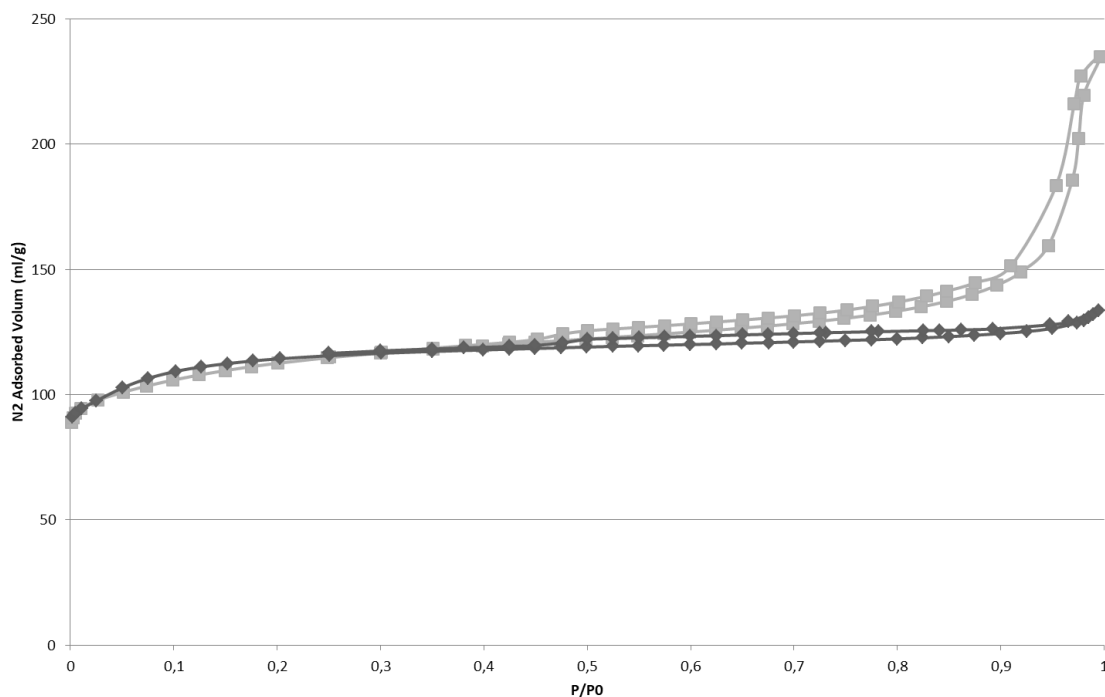


**Figure S2.** Nitrogen adsorption isotherm for the Z-22-Big (rhombus) and Z-25-Small (squares) samples.

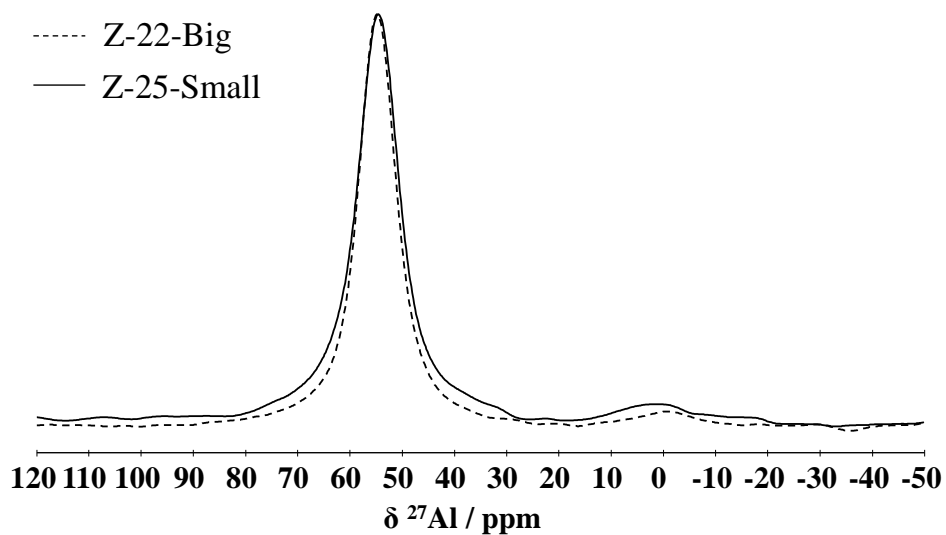


**Figure S3.**  $^{27}\text{Al}$  NMR spectra of the two hydrated zeolite samples.

## S3. Additional Infrared data

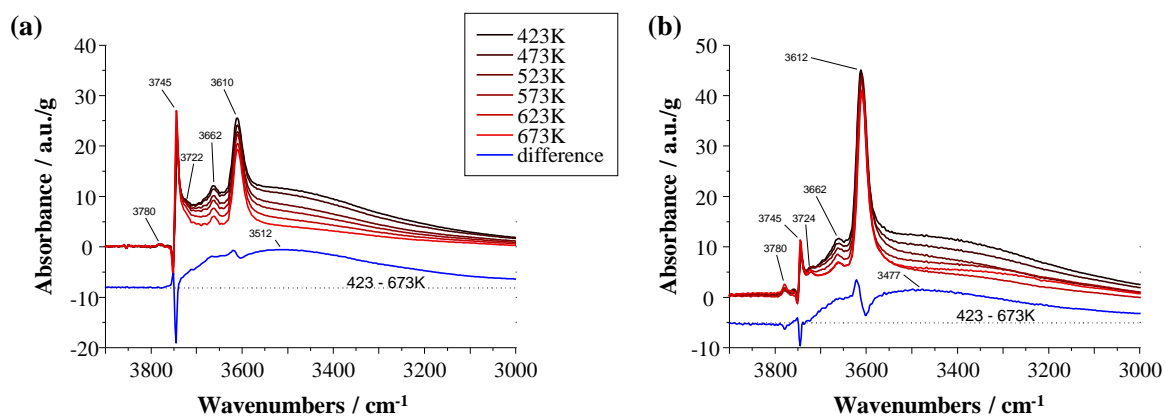


**Figure S4.** FSD-IR spectra of a) Z-25-Small and b) Z-22-Big after activation at different temperatures under secondary vacuum from 423 to 723 K. In blue, difference spectrum between spectra of the sample activated at 423 and 673 K.

## S4. Additional $^1\text{H}$ NMR data

- Calculated chemical shift of protons belonging to hydrogen-bond donor groups

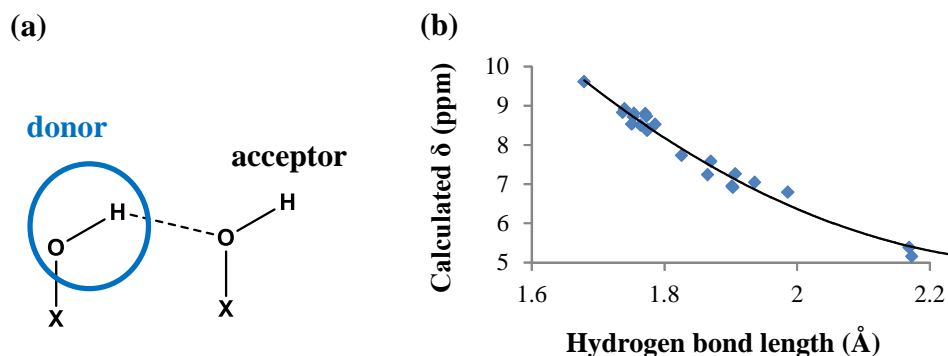


**Figure S4.** (a) Scheme of hydroxyl groups involved in a hydrogen bond as donor or acceptor. (b) Relation between the DFT calculated chemical shift and the hydrogen bond length for hydrogen bond donor groups, for bulk Si-(OH)-Al sites.

- Calculated chemical shifts of silanols ranked in terms of neighborhood with other silanols

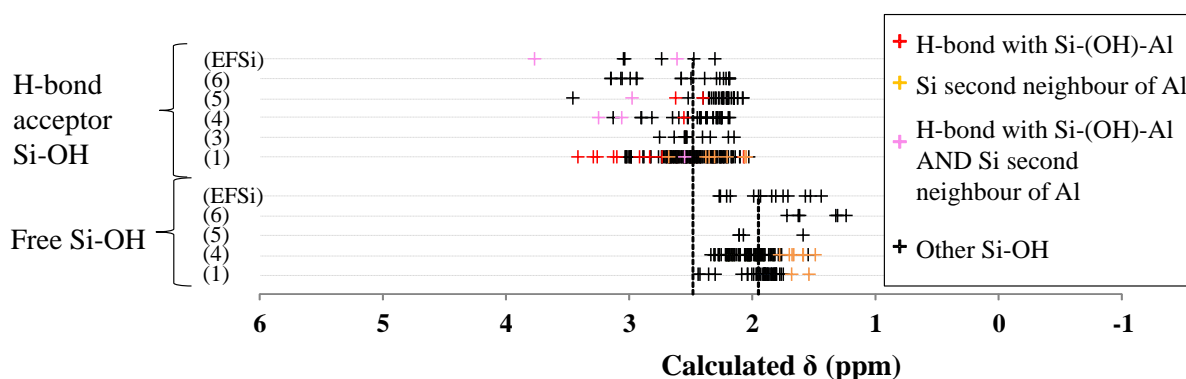


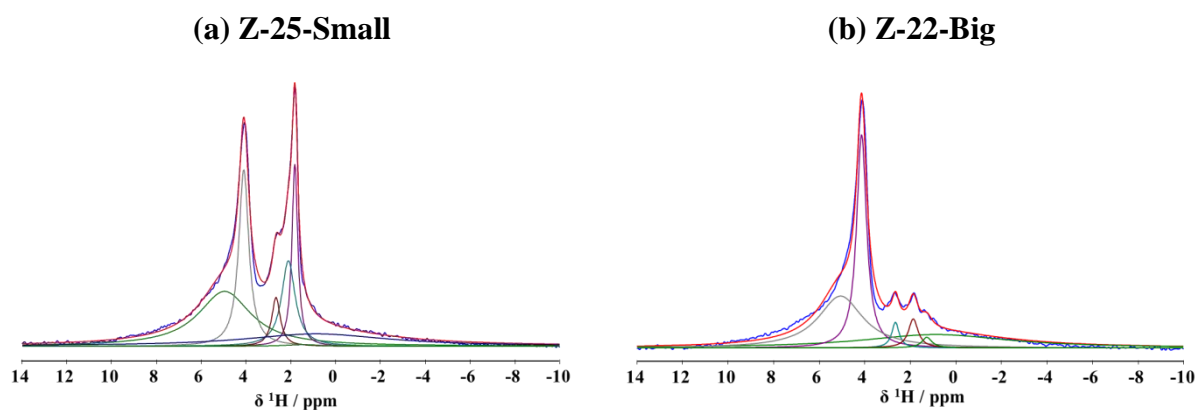
**Figure S5.**  $^1\text{H}$  NMR DFT calculated chemical shifts of silanols classified according to their neighborhood with other silanols, see Table S1 for terminology.

**Table S1.**  $^1\text{H}$  NMR DFT calculated average chemical shifts of silanols classified according to their neighborhood with other silanols.

	Total Average (ppm)	1	2	3	4	5	6	EFSi
Isolated	1.95	1.91	No Data	No Data	2.00	1.97	1.47	1.92
H-bond acceptor	2.48	2.51	No Data	2.48	2.48	2.29	2.56	2.85

- **Effect of crystal size : Z-22-Big vs. Z-25-Small**

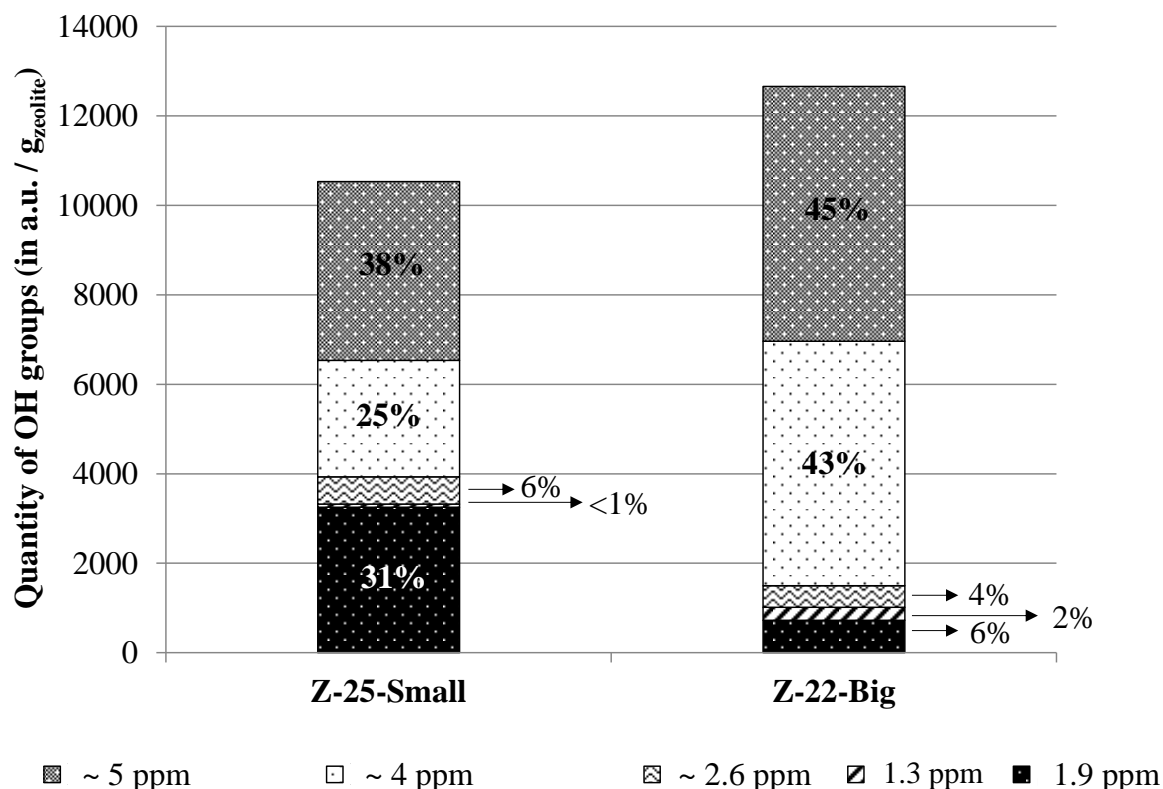
$^1\text{H}$  NMR spectral deconvolution was done using DMFit as illustrated in Figure S6. The  $^1\text{H}$  chemical shifts obtained through spectral deconvolution gathered in Table S2. The absolute and relative integrated peaks areas obtained are reported in Figure S7. Prior to  $^1\text{H}$  MAS measurements, all samples were pretreated under secondary vacuum at  $300^\circ\text{C}$  for 10 hours and then sealed in a glass reactor.



**Figure S6.** Deconvolution of spectral components of  $^1\text{H}$  MAS NMR spectra using DMFit (in blue : experimental spectrum; in red - best fitted model). For both samples, peaks were fitted using Lorentzian curves. Despite the use of the  $^1\text{H}$  DEPTH sequence, a very large and weak signal can be observed around 0.9 ppm, which can be attributed to probe background signal. The intensity, width and position of this signal were kept constant for spectral deconvolution in both cases.

**Table S2.**  $^1\text{H}$  chemical shifts obtained from  $^1\text{H}$  MAS NMR spectral deconvolution using DMFit for Z-22-Big and Z-25-Small samples.

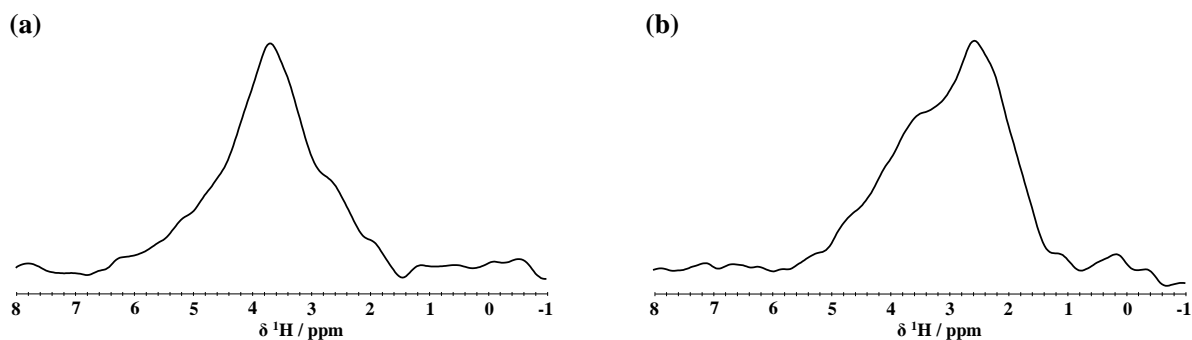
OH group	Z-22-Big	Z-25-Small
	$\delta (^1\text{H}) / \text{ppm}$	$\delta (^1\text{H}) / \text{ppm}$
H-bond acceptor $\mu_1/\mu_2\text{-Al-OH}$	1.3	1.4
Isolated SiOH, H-bond acceptor Silanol-Al (with other SiOH)	1.9	1.8
	-	2.1
Al-( $\text{H}_2\text{O}$ ) with one donor H, most hydrogen-bond acceptor silanols and $\mu_2\text{-Al-OH}$	2.6	2.7
Bridging Si-(OH)-Al and isolated Al-( $\text{H}_2\text{O}$ )	4.1	4.1
H-bond donors	5.1	4.9



**Figure S7.** Relative peak intensity contributions obtained from deconvolution of  $^1\text{H}$  MAS NMR spectra using DMFit. Note that these values have an estimated uncertainty of 10% and values below 5% are not precise.<sup>2</sup> The intensity of the peak at 0.9 ppm (probe background) was not taken into account in these calculations.

Spectral deconvolution indicates that Z-22-Big has 7.5 times more bridging SiOHAl groups than silanols, whereas in the case of Z-25-Small, there are only 0.8 bridging sites for one silanol group. Concerning AlOH and Al(H<sub>2</sub>O) species, Z-22-Big has 1.1 times more aluminols and Al(H<sub>2</sub>O) than Z-25-Small. Despite the close Si/Al ratio, Figure 2 indicates a much higher number of hydroxyl groups bonded to aluminum atoms (*i.e.*, protons involved in bridging SiOHAl, AlOH and Al(H<sub>2</sub>O) groups) in Z-22-Big (6238 in a.u./g<sub>zeolite</sub>) than in Z-25-Small (3284 in a.u./g<sub>zeolite</sub>). This difference can be explained due to H-bond donors species ( $\delta(^1\text{H}) > 5\text{ppm}$ ). Indeed, some of these protons might be attached to surface aluminum atoms, however their proportion is difficult to determine. This discrepancy may also arise from aluminum atoms that are not bonded to a hydroxyl, which is unlikely in the zeolite lattice, but possible in extra-framework positions.

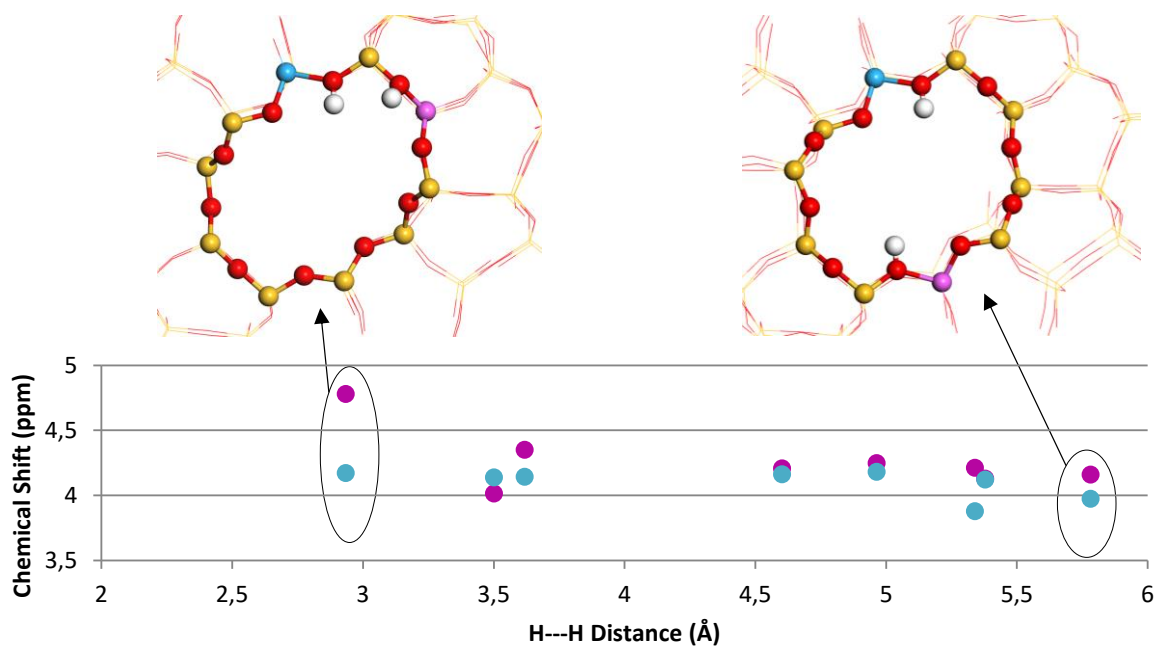
- **Projections of 2D NMR**



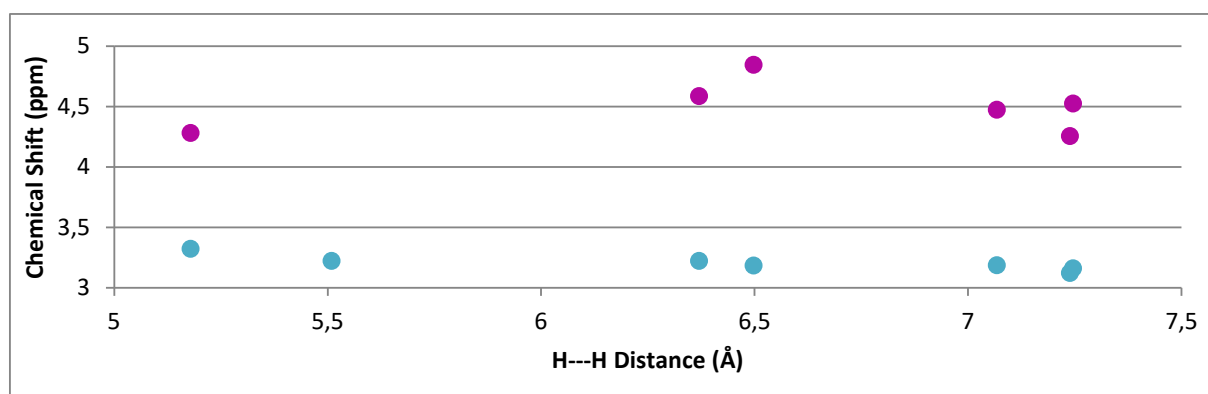
**Figure S8.** Projection along F1 dimension of 1H SQ-DQ spectra for the Z-25-Small sample, at a position of (a) 7.6 ppm, (b) 5.5 ppm in F1.

- **Effect of proton proximity in the DFT models**

The common Si/Al surface ratio in the models is 96. It was shown in ref. <sup>1</sup> that these models are relevant regardless of the differences in Si/Al ratios, in terms of stability. In Figure S9 the chemical shifts are reported for two protons of two aluminated sites with an increasing distance between them. One proton does not change its position between the different calculations (in the bulk model Figure S9; T5 site is aluminated and the proton is adsorbed on oxygen number 162; and in the external surface model Figure S10; Si59 external surface site is aluminated and the proton form a water molecule adsorbed on the aluminum; they are represented in blue in the Material Studio representation and on the graphics). Conversely, the position of the second one is changing (together with the position of the aluminum atom represented in purple in Figure S8 and S9), which changes the distance between the two protons. The aluminated sites have a bridging nature Si-(OH)-Al in the bulk. One observes that the proximity of the second proton has a minor impact on the value of the chemical shift of the fixed proton and the variable proton (less than 0.4 ppm), except for the first point for which the distance between the two hydrogen is under 3 Å). The same results are observed with calculations at the external surface of the zeolite, where the nature of the surface sites remain bridging Si-OH-Al. Here the fixed proton is part of a water molecule adsorbed on an aluminum while the nature of the changing second proton can vary. The fixed proton has a signal variation under 0.2 ppm and the changing one has a signal variation under 0.6 ppm which should be mainly due to changes in their environment.

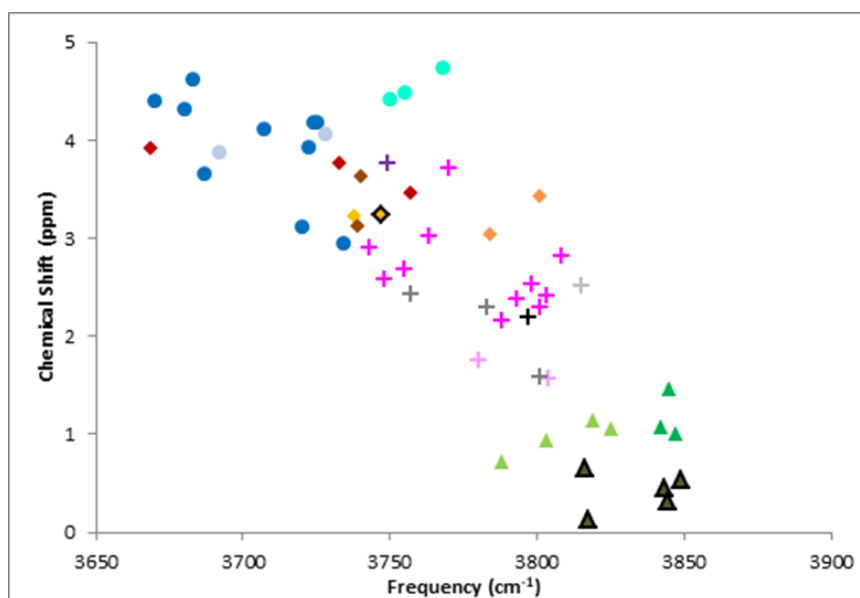


**Figure S9.** Chemical shift of protons depending on the distance between them in the bulk of H-ZSM-5. The blue dots represent a proton which does not change its position whereas the purple is not attached to the same oxygen atom.



**Figure S10.** Chemical shift of protons depending on the distance between them at the external surface of H-ZSM-5. The blue dots represent a proton which does not change its position whereas the purple is not attached to the same oxygen atom.



**S5. Correlation between IR and NMR computational data**

**Figure S11.** Correlation between computed proton chemical shifts and O-H vibration frequency for the same OH groups. The colour code is the same as in Figures 5 and 7.

## References

- (1) Treps, L.; Gomez, A.; De Bruin, T.; Chizallet, C., Environment, Stability and Acidity of External Surface Sites of Silicalite-1 and ZSM-5 Micro- and Nano-Slabs, -Sheets and -Crystals, *ACS Catal.* 2020, *10*, 3297–3312.
- (2) Batista, A. T. F.; Wisser, D.; Pigeon, T.; Gajan, D.; Diehl, F.; Rivallan, M.; Catita, L.; Gay, A.-S.; Lesage, A.; Chizallet, C.; Raybaud, P., Beyond  $\gamma$ -Al<sub>2</sub>O<sub>3</sub> crystallite surfaces: The hidden features of edges revealed by solid-state <sup>1</sup>H NMR and DFT calculations, *J. Catal.* 2019, *378*, 140-143.

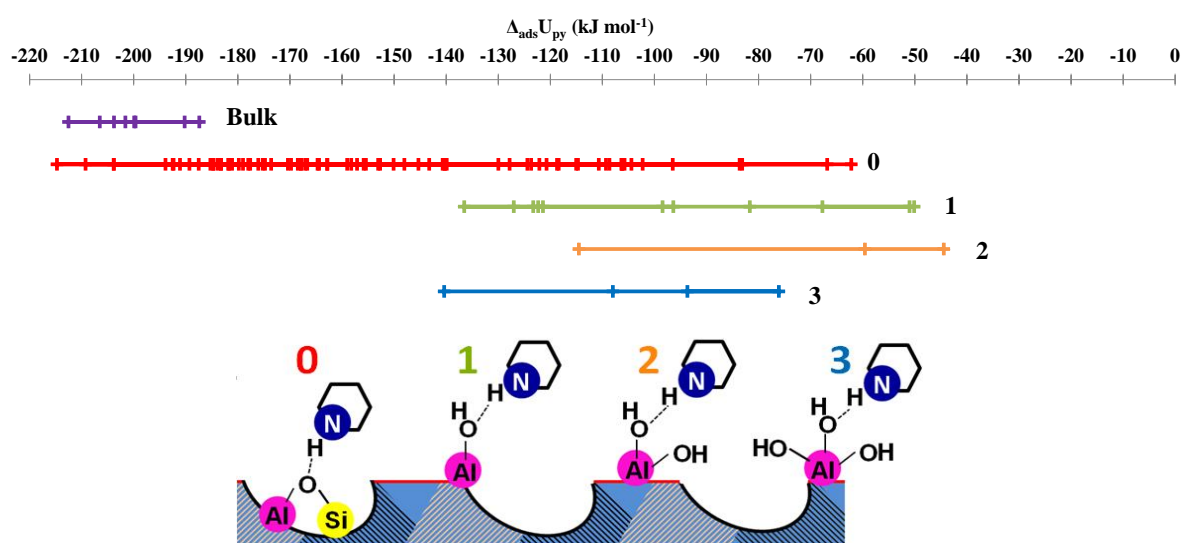
# Chapter 5: Supplementary Information

## SI. Pyridine adsorption

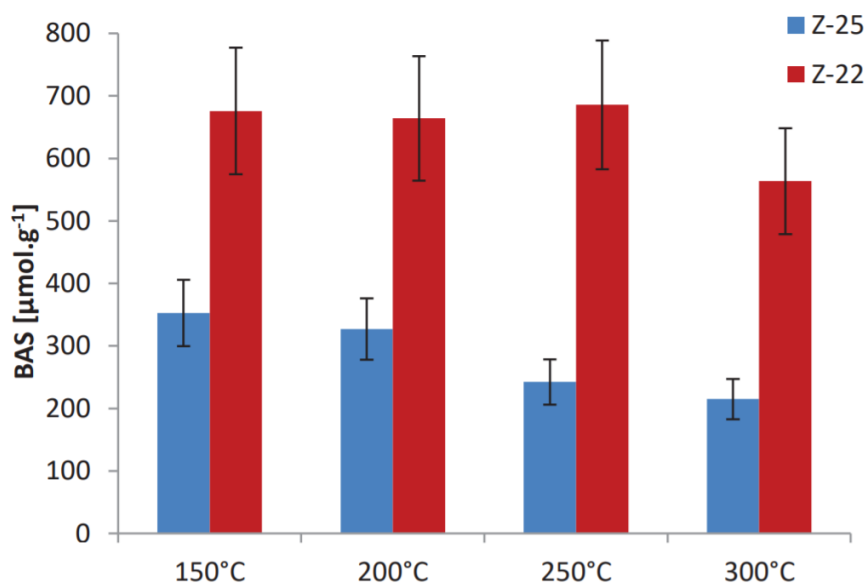
### SI.1. Pyridine adsorption on Brønsted Acid Sites

Surface orientation	Bulk	(100)										(010)					
Cleavage	none	1										6					
Aluminated Site	T5	Si_91	Si_79	Si_57	Si_69	Si_89	Si_59	Si_75	Si_87 dehydrated	Si_59 dehydrated	Si_77	Si_99	Si_109	Si_113	Si_127	Si_41	Si_45 dehydrated
Acid Site Configuration	Al-OH-Si	Al-OH-Si	Al-OH-Si	Al-OH-Si-OH	Al-OH-Si-OH	Al-OH-Si-OH	Al-H <sub>2</sub> O	Al-H <sub>2</sub> O	2MR	Al <sub>iv</sub>	Al-H <sub>2</sub> O	Al(OH) <sub>2</sub> H <sub>2</sub> O	Al(OH)H <sub>2</sub> O	Al-OH-Si-OH	Al-OH-Si	Al-OH-Si-OH	2MR
$\Delta_{ads}U_{py}$ (kJ.mol <sup>-1</sup> )	-213	-215	-184	-180	-185	-167	-150	-122	-137	-121	-130	-140	-114	-204	-204	-189	-139
$\Delta_{asp}U_{py}$ (kJ.mol <sup>-1</sup> )	-69	-91	-88	-73	-45	-51	-78	-47	-88	-45	-53	-99	-69	-92	-105	-67	-48
$\Delta_{non\_dir}U_{py}$ (kJ.mol <sup>-1</sup> )	-144	-124	-96	-107	-140	-116	-72	-75	-49	-76	-77	-41	-46	-112	-99	-122	-91
$T_{des-py}$ (K)	638	645	560	549	562	513	465	385	428	383	409	438	365	614	614	575	198
Adsorption mode	Bulk	Pore mouth															
N-H (Å)	1.06	1.07	1.07	1.08	1.07	1.07	1.07	1.20	1.10	1.10	1.08	1.05	1.14	1.06	1.06	1.08	1.11
O...H (Å)	1.73	1.59	1.59	1.56	1.68	1.65	1.53	1.29	1.49	1.49	1.57	1.81	1.39	1.71	1.68	1.58	1.48

**Table S1.** Complementary details about adsorption mode of pyridine on BAS depending on the surrounding environment and the surface site in the H-ZSM-5 bulk, and on three external surfaces cut along (100) (cleavage 1 and cleavage 6) and (010) orientations (cleavage 2) presented in Figure 2 of Chapter 5.



**Figure S1.** Pyridine adsorption energy  $\Delta_r U_{ads\_pyr}$  (kJ.mol<sup>-1</sup>) on the different Brønsted acid sites of H-ZSM-5: Bulk (purple) – bridging Al-OH-Si; 0 (red) – bridging Al-OH-Si in open micropores; 1 (green) – H<sub>2</sub>O adsorbed on aluminum; 2 (orange) - H<sub>2</sub>O adsorbed on aluminum with one hydroxyl group; 3 (blue) - H<sub>2</sub>O adsorbed on aluminum with two hydroxyl groups. 1, 2, 3 are at the outermost surface.

**SI.2. Experimental results of pyridine adsorption**

**Figure S2.** BAS concentration obtained with adsorption/desorption of pyridine at different temperatures (from C. Demaret PhD work)<sup>1</sup>. Z-22 and Z-25 correspond to Z-22-Big and Z-25-Small of chapter 4.

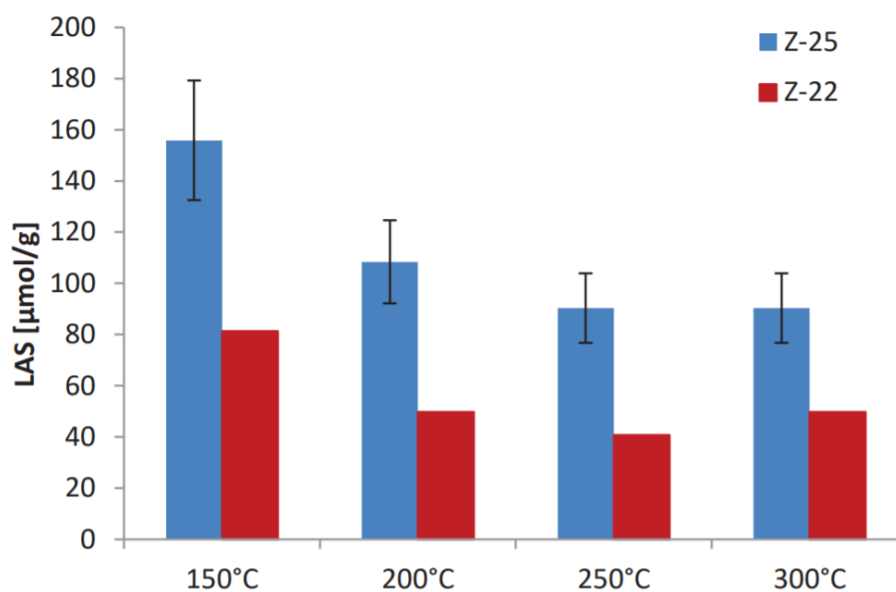


**Figure S3.** LAS concentration obtained with adsorption/desorption of pyridine at different temperatures (from C. Demaret PhD work)<sup>1</sup>. Z-22 and Z-25 correspond to Z-22-Big and Z-25-Small of chapter 4.

### SII. Exchange energy of sodium

Model	Exchange cation	Energy (eV)
Aluminated and hydroxylated Tielens' model <sup>2</sup> of silica	Na <sup>+</sup>	-834.56
		<u>-834.64</u>
		-834.48
	H <sup>+</sup>	-834.21
		-834.33
		<u>-834.93</u>
		-834.28
ZSM-5 bulk	Na <sup>+</sup>	-834.22
		-2306.05
		-2306.94
		<u>-2306.12</u>
	H <sup>+</sup>	-2306.85
		-2306.93
		<u>-2306.13</u>
ZSM-5 external surface cleavage 1 (100) site no. 59 substituted	Na <sup>+</sup>	-2306.03
		-2306.98
		-2306.04
		<u>-4723.20</u>
	H <sup>+</sup>	-4722.89
		-4722.98
		-4723.11
Alumina (100)	Na <sup>+</sup>	<u>-4723.11</u>
	H <sup>+</sup>	<u>-4723.57</u>
Hydroxylated Tielens' model <sup>2</sup> of silica	Na <sup>+</sup>	-4723.16
		-4723.10
		-4723.37
		<u>-1206.48</u>
		<u>-1206.96</u>
	H <sup>+</sup>	<u>-831.20</u>
Alumina (110)	Na <sup>+</sup>	<u>-831.43</u>
	H <sup>+</sup>	<u>-831.43</u>
Hydroxylated Tielens' model <sup>2</sup> of silica	Na <sup>+</sup>	-831.38
		<u>-831.68</u>
		-831.53
		<u>-832.34</u>
	H <sup>+</sup>	<u>-1396.20</u>
Alumina (110)	Na <sup>+</sup>	<u>-1397.41</u>
	H <sup>+</sup>	<u>-1397.41</u>

**Table S2.** Energies of the different model with sodium cation and proton. For one cation adsorbed on a model various position are explored and the most stable of these position are underlined (in blue for sodium positions and in yellow for hydrogen positions).

### SIII. Monomer adsorption

#### SIII.1. Monomer adsorption in bulk

Monomer	Zeolite site	Bond	Proton transfer	Site name	$\Delta_{ads}U_{monomer}$ (kJ mol <sup>-1</sup> )
Al	Al	Covalent	Yes	A	-194
					-198
			No	B	-151
					-111
					-167
					-186
		-182			
		-192			
		Hydrogen bond	Yes	C	-219
					-148
					-166
					-149
					-191
					-238
			No	D	-106
					-131
					-90
					-117
	-106				
	-85				
	Si	Covalent	No	E	-106
					-85
					-114
					-85
					-95
					-105
		Hydrogen bond	No	F	-86
					-92
					-88
					-99
					-80
					-89
					-81
					-88
					-78
					-89
-80					
-93					
-79					
-91					
-70					
-74					
-88					
-85					
-81					
-66					
-82					
-96					
-85					
-76					
-81					
-80					
-86					
-76					
-89					
-79					

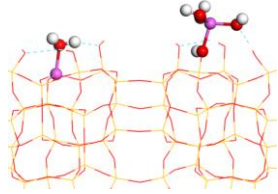
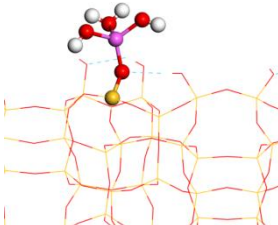
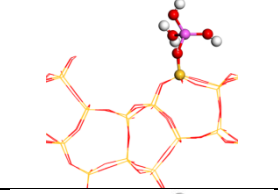
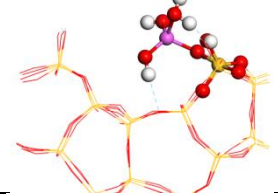
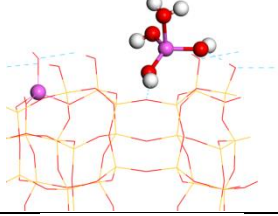
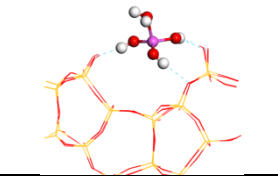
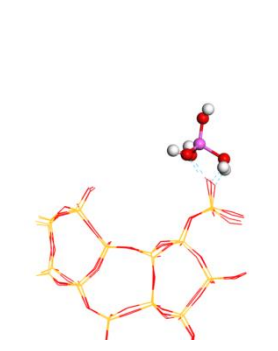
					-83
					-79
					-87
					-78
					-85
Si	Al	Covalent	No	G	-101
		Hydrogen bond	Yes	H	-109
					-140
			No	I	-148
					-120
					-154
				-138	
				-139	
				-130	
			J	-75	
	-81				
	-78				
	-76				
	Si	Hydrogen bond	No	K	-75
					-72
					-74
					-76
					-75
					-62
					-72
-71					
-72					
-75					
-70					
-77					
-77					
-77					
-77					
-80					
-77					

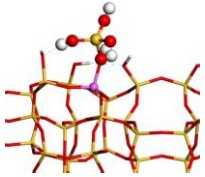
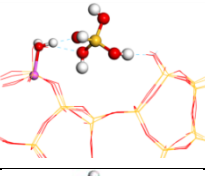
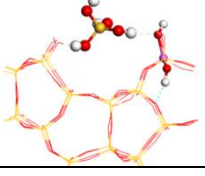
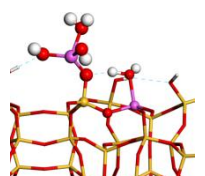
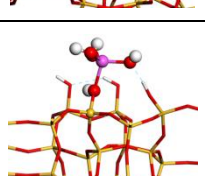
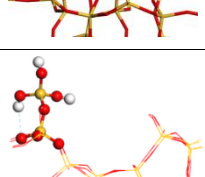
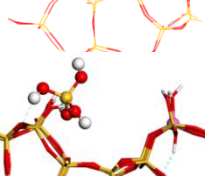
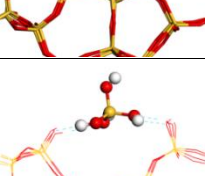
**Table S3.** Adsorption energies of the alumina and silica monomers in ZSM-5 bulk in  $\text{kJ mol}^{-1}$ .

## SIII.2. Monomer adsorption at the external surface

Monomer	Category presented in Figure 12 of Chapter 5	External surface aluminated site	Ball and stick view <sup>(a)</sup>	Description of the adsorption modes	$\Delta_{ads}U_{monomer}$ (kJ mol <sup>-1</sup> ) <sup>(b)</sup>	
Al(OH) <sub>3</sub> (H <sub>2</sub> O)	Covalent Bond with aluminated site	No. 59 Al(H <sub>2</sub> O)		Covalent bond, Si-OH-Al break	-147.0	
				Covalent bond, Si-OH-Al break	-170.3	
				2MR with two aluminum atoms <sup>(c)</sup>	-146.4	
				Covalent bond, hydrogen bond with the water molecule <sup>(c)</sup>	-108.3	
				Covalent bond, hydrogen bond with the water molecule <sup>(c)</sup>	-115.0	
				Covalent bond, hydrogen bond with the water molecule <sup>(c)</sup>	-103.5	
				Covalent bond, no hydrogen bond with the water molecule <sup>(c)</sup>	-87.1	
				Covalent bond, no hydrogen bond with the water molecule <sup>(c)</sup>	-87.1	
	Hydrogen Bond and proton transfer, with aluminated site				Hydrogen Bond and proton transfer	-241.0
					Hydrogen Bond and proton transfer	-192.5
					Hydrogen Bond and proton transfer	-205.2
					Hydrogen Bond and proton transfer	-199.1
					Hydrogen Bond and proton transfer	-249.0
					Hydrogen Bond and proton transfer	-205.6
		Hydrogen Bond and proton transfer	-180.2			
	Hydrogen Bond with aluminated site		No. 59 Al(H <sub>2</sub> O)		Surface site: Al(H <sub>2</sub> O)	-141.7
					Surface site: Al(H <sub>2</sub> O)	-197.0
					Surface site: Al(H <sub>2</sub> O)	-209.7
					Surface site: proton transferred to a Si-O-Al bridge	-135.9
					Surface site: proton transferred to a Si-O-Al bridge	-141.8
				Surface site: proton transferred to a Si-O-Al bridge	-145.3	
	Surface site: proton transferred to a Si-O-Al bridge	-131.0				



Al(OH) <sub>3</sub> (H <sub>2</sub> O)	Covalent Bond	No. 59 Al(H <sub>2</sub> O)		(c)	-78.8
					-87.0
					-97.7
		-56.7			
		-46.6			
		-36.1			
		-47.8			
		-38.3			
		-78.8			
	No		(c)	-63.3	
				-49.4	
				-46.3	
	Hydrogen bonds with water <sup>(c)</sup>		Hydrogen bonds with water <sup>(c)</sup>	-91.8	
				-78.5	
	Si pentavalent		Si pentavalent	-81.4	
	Hydrogen Bond	No. 59 Al(H <sub>2</sub> O)			-75.4
					-71.5
-77.0					
No				-70.5	
				-92.2	
Hydrogen bonds with water			Hydrogen bonds with water	-97.1	
				-117.4	
				-148.0	
				-141.7	
-134.5					
-65.9					

Si(OH) <sub>4</sub>	Covalent Bond with aluminated site	No. 59 Al(H <sub>2</sub> O)		(c)	<u>-86.3</u>			
					-24.2			
					-64.6			
					-72.3			
	Hydrogen Bond with aluminated site	No. 59 Al(H <sub>2</sub> O)		Surface site: Al(H <sub>2</sub> O)	<u>-127.0</u>			
					-116.8			
					-114.0			
					-101.3			
	Hydrogen Bond with aluminated site	No. 59 Al(H <sub>2</sub> O)		Surface site: proton transferred to a Si-O-Al bridge	-75.1			
					<u>-78.3</u>			
	Covalent Bond	No. 59 Al(H <sub>2</sub> O)		Covalent bond on Si second neighbor of aluminated site <sup>(c)</sup>	-45.9			
					<u>-55.6</u>			
					No		Covalent bond not neighboring the aluminated site <sup>(c)</sup>	-26.8
								<u>-36.5</u>
		No	No		(c)	-39.3		
						-48.4		
						<u>-57.9</u>		
						-40.5		
	Hydrogen Bond	No. 59 Al(H <sub>2</sub> O)			-70.5			
					<u>-70.7</u>			
-70.5								
-69.0								
No		No			-77.6			
					-51.5			
					-84.4			
					<u>-96.3</u>			

**Table S4.** Alumina and silica monomer adsorption representations in bulk of ZSM-5 depending on the nature of the monomer, the adsorption site and the bond formed. (a) Ball and stick representation of the most stable monomer and the adsorption site (b) Adsorption energies of the alumina and silica monomers in ZSM-5 bulk in kJ mol<sup>-1</sup>, the position corresponding to the ball and stick view is underlined (c) On these structures, the adsorption reaction is a condensation reaction, the adsorption energy is calculated using Equation 1.

$$\Delta_{ads}U_{monomer} = U_{surf\_monomer} + U_{water} - U_{surf} - U_{monomer}$$

**Equation 1**

## References

- (1) Demaret, C. Mise en forme de zéolithes : Contrôle des propriétés acides des zéolithes et description de l'interface zéolithe / liant: Thèse de doctorat, IFPEN, 2019.
- (2) Tielens, F.; Gervais, C.; Lambert, J.-F.; Mauri, F.; Costa, D. Ab Initio Study of the Hydroxylated Surface of Amorphous Silica: A Representative Model. *Chem. Mater.* **2008**, *20*, 3336–3344.

# Chapter 6: Supplementary Information

## SI. Inputs for ReaxFF optimization with CMA-ES optimizer

### SI.1. Starting force fields

Considering the large amount of data contained in reactive force field files, these files are directly supplied as supplementary material under the names Joshi\_ffield, Pitman\_ffield and Bai\_ffield for Joshi's, Pitman's and Bai's reactive force fields respectively.

### SI.2. Cma-es.run for CMA-ES optimizers

```
#!/bin/sh
# =====
#   REMOVE OLD OUTPUT FILE
# =====
if test -f MCFFOptimizer.log ; then rm MCFFoptimizer.log; fi
# =====
#   CONTROL SETTINGS
# =====
cat > control <<eor
# General parameters
  1 tors13   Use 2013 formula for torsions
  0 itrans
  1 icobo
  1 icentr  0: off, 1: put center of mass at center of cube, 2: put com at origin
  1 imetho  Normal MD-run 1: Energy minimisation
  1 igeofo  0:xyz-input geometry 1: Biograf input geometry 2: xmol-input geometry
100.0 axis1  a cell axis
100.0 axis2  b cell axis
100.0 axis3  c cell axis
90.000 angle1  cell angles
90.000 angle2  cell angles
90.000 angle3  cell angles
  25 irecon  Frequency of reading control-file
  0 isurpr  1: Surpress lots of output 2: Read in all geometries at the same time
  5 ixmolo  xmolout 0: xyz only, 1: xyz + vels + molnr, 2: xyz + mol.nr, 5: xyz + bonds
  1 ichupd  Charge update frequency
  4 icharg  always 4: Full system EEM
298.00 mdtemp  MD-temperature (K), unless tregime file is present
100.0 tdamp1  1st Berendsen/Anderson temperature damping constant (fs)
  0 nrstep
# MD-parameters
  1 imdmet  MD-method. 1:Velocity Verlet+Berendsen 2:Hoover-Nose (again NVT); 3:NVE 4:NPT
0.250 tstep  MD-time step (fs)
0.00 mdpres  MD-pressure (GPa)
500.0 pdamp1  Berendsen pressure damping constant (fs)
  0 inpt    0: Change all cell parameters in NPT-run  1: fixed x 2: fixed y 3: fixed z
40000 nmdit  Number of MD-iterations
1000000 iout1  Output frequency to unit 71 and unit 73
1000000 iout2  Save coordinates (xmolout, moldyn.vel, Molfra)
  1 iout3  Create moldyn.xxx files (0: yes, 1: no)
  0 ivels  0: Use velocities from vels restart-file; 1: Zero initial velocities
2000 iout6  Frequency of molsav.xxxx restart file creation (xyz, vels and accel)
  50 iout7  Frequency of reaxout.kf writing
  25 irten  Frequency of removal of rotational and translational motions
  0 npreit  Nr. of iterations in previous runs
0.00 range  range for back-translation of atoms outside periodic box
# MM-parameters
1.000 endmm  End point criterium for MM energy minimisation (force)
  0 imaxmo  0: conjugate gradient, 1: L-BFGS
30000 imaxit  Maximum number of iterations
  1 iout4  Frequency of structure output during minimisation
  0 icelop  0 : no cell opt, 1: numerical cell opt
1.00010 celopt  Cell parameter change factor
  0 icelo2  0: Cubic cell optimization; 1/2/3: only a/b/c; 4: c/a ratio
#CMA-ES parameters
50000 mcffit
0.00001 ffitol
  25 mcrxdd
  0 fort99
eor
```

```

cat > iopt <<eor
7
eor
# =====
#   Nr. of cores
# =====
$ADFBIN/reaxff > cma-es.out

```

### SI.3. Tests on MAXIT criteria

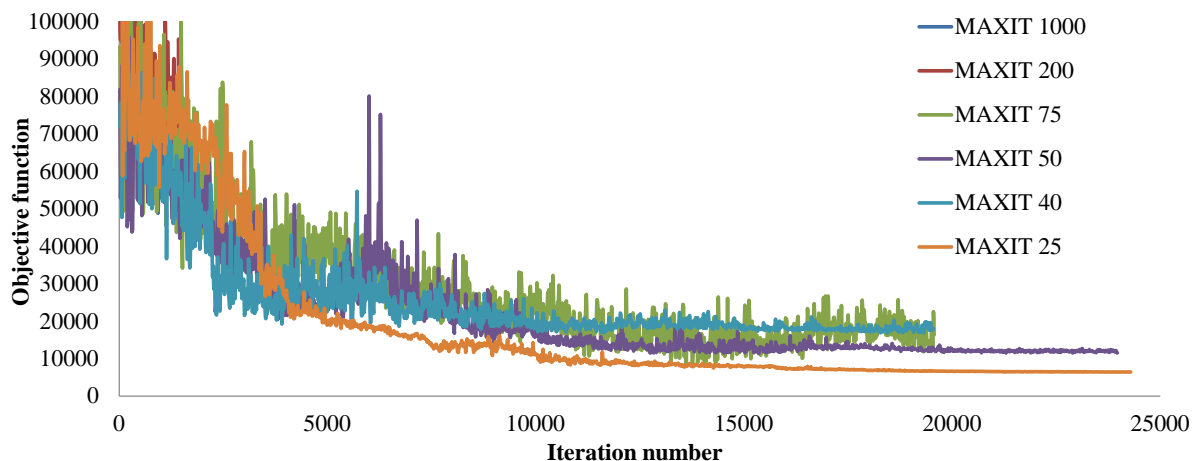


**Figure S1.** Analysis of the MAXIT criteria influence on reactive force field optimization (Tr.1 with a random initial guess).

For the optimization of a random initial guess using Tr.1, the MAXIT criteria used for the geometry optimizations is tested. The convergence of the objective function is observed for MAXIT values from 1000 to 25 in Figure S1. It is enhanced that the MAXIT 25 allows to do faster iteration which conduct to a lower objective function compared to higher MAXIT values for a given number of CPU cores.

### SI.4. Params for CMA-ES optimizers

Pitman's params						Joshi's params					
#	Key	delta	min	max	comment	#	Key	delta	min	max	comment
2	2 14	0.029920	2.0000	5.0000	# H:14 EEM chi	2	2 14	0.029920	3.0000	6.5362	# H:14 EEM chi
2	2 15	0.043817	8.0000	12.0000	# H:15 EEM eta	2	2 15	0.043817	6.2079	12.0000	# H:15 EEM eta
2	3 14	0.005297	7.9703	9.0000	# O:14 EEM chi	2	3 14	0.005297	7.9703	10.0000	# O:14 EEM chi
2	3 15	0.020404	6.9585	10.0000	# O:15 EEM eta	2	3 15	0.020404	6.9585	10.0000	# O:15 EEM eta
2	7 1	0.003583	1.5000	3.0000	# Al:1 R(sigma)	2	13 1	0.003583	1.0000	3.5550	# Al:1 R(sigma)
2	7 4	0.004067	1.9671	4.0000	# Al:4 R(VdW)	2	13 4	0.004067	1.9671	4.0000	# Al:4 R(VdW)
2	7 5	0.000898	0.1430	0.5000	# Al:5 E(VdW)	2	13 5	0.000898	0.1430	0.5000	# Al:5 E(VdW)
2	7 6	0.005856	0.1000	0.7000	# Al:6 EEM Gamma	2	13 6	0.005856	0.2000	1.0121	# Al:6 EEM Gamma
2	7 7	0.026836	-3.0000	0.0000	# Al:7 R(pi)	2	13 7	0.026836	-3.0000	1.0000	# Al:7 R(pi)
2	7 9	0.026395	7.0000	12.0397	# Al:9 Alpha(VdW)	2	13 9	0.026395	8.0000	12.0397	# Al:9 Alpha(VdW)
2	7 10	0.147131	0.0000	20.0000	# Al:10 Gamma VdW shld	2	13 10	0.147131	1.6831	20.0000	# Al:10 Gamma VdW shld
2	7 12	0.005000	0.0000	0.5076	# Al:12 p(ovun5)	2	13 12	0.005000	0.0000	0.5076	# Al:12 p(ovun5)
2	7 13	0.005000	15.0000	17.0151	# Al:13 p_xel2 (ereax)	2	13 13	0.005000	15.0000	17.0151	# Al:13 p_xel2 (ereax)
2	7 14	0.033420	-0.7626	2.5794	# Al:14 EEM chi	2	13 14	0.033420	-3.0000	2.5794	# Al:14 EEM chi
2	7 15	0.014258	5.4061	7.0000	# Al:15 EEM eta	2	13 15	0.014258	5.4061	8.0000	# Al:15 EEM eta
2	7 19	0.109217	67.5458	100.0000	# Al:19 HeatForm term	2	13 19	0.109217	67.5458	90.0000	# Al:19 HeatForm term
2	7 20	1.179671	0.0000	137.9671	# Al:20 p_boc4 part	2	13 20	1.179671	15.0000	137.9671	# Al:20 p_boc4 part
2	7 21	0.000860	0.1640	0.5000	# Al:21 p_boc3 part	2	13 21	0.000860	0.1000	0.4000	# Al:21 p_boc3 part
2	7 25	0.193396	-30.0000	-3.8430	# Al:25 p_ovun2	2	13 25	0.193396	-30.0000	-3.8430	# Al:25 p_ovun2
2	7 26	0.015000	0.0000	3.0000	# Al:26 p_val3	2	13 26	0.015000	0.0000	3.0000	# Al:26 p_val3
3	6 1	1.223076	102.0000	224.3076	# b%HO:1 E(Sigma)	3	9 1	1.223076	102.0000	224.3076	# b%HO:1 E(Sigma)
3	6 4	0.004971	-0.9126	-0.4155	# b%HO:4 p_be1	3	9 4	0.004971	-0.9126	-0.4155	# b%HO:4 p_be1
3	6 8	0.006393	0.3607	1.0000	# b%HO:8 p_ovun1	3	9 8	0.006393	0.3607	1.0000	# b%HO:8 p_ovun1
3	6 9	0.038900	0.0000	5.0050	# b%HO:9 p_be2	3	9 9	0.038900	0.5000	5.0050	# b%HO:9 p_be2
3	6 13	0.001343	-0.1788	-0.0445	# b%HO:13 p_bo1	3	9 13	0.001343	-0.1788	-0.0445	# b%HO:13 p_bo1

3	6	14	0.023430	3.6021	5.9451	# b%HO:14 p_bo2	3	9	14	0.023430	3.6021	7.0000	# b%HO:14 p_bo2
3	21	1	2.500000	180.0000	250.0000	# b%AlO:1 E(Sigma)	3	59	1	1.008315	127.6561	228.4876	# b%AlO:1 E(Sigma)
3	21	4	0.100000	-1.5000	-0.1000	# b%AlO:4 p_be1	3	59	4	0.009080	-2.0000	-0.0100	# b%AlO:4 p_be1
3	21	8	0.004462	0.0100	0.4562	# b%AlO:8 p_ovun1	3	59	8	0.004462	0.0100	0.4562	# b%AlO:8 p_ovun1
3	21	9	0.050000	0.0000	1.0000	# b%AlO:9 p_be2	3	59	9	0.009268	0.0000	0.9278	# b%AlO:9 p_be2
3	21	13	0.050000	-0.5000	-0.0500	# b%AlO:13 p_bo1	3	59	13	0.001260	-0.5000	-0.0740	# b%AlO:13 p_bo1
3	21	14	0.014929	4.6533	6.1462	# b%AlO:14 p_bo2	3	59	14	0.014929	4.6533	7.0000	# b%AlO:14 p_bo2
4	2	1	0.000842	0.0000	0.1125	# o%HO:1 E(VdW)	4	2	1	0.000842	0.0100	0.1125	# o%HO:1 E(VdW)
4	2	2	0.007145	0.0000	3.0000	# o%HO:2 R(VdW)	4	2	2	0.007145	0.0000	1.9998	# o%HO:2 R(VdW)
4	2	3	0.021662	8.7528	15.0000	# o%HO:3 Alpha(VdW)	4	2	3	0.021662	8.7528	14.0000	# o%HO:3 Alpha(VdW)
4	2	4	0.002116	0.5000	1.0929	# o%HO:4 R(sigma)	4	2	4	0.002116	0.8813	1.0929	# o%HO:4 R(sigma)
4	15	1	0.002661	0.1084	0.3745	# o%AlO:1 E(VdW)	4	36	1	0.002661	0.1084	0.3745	# o%AlO:1 E(VdW)
4	15	2	0.001821	0.0000	3.0000	# o%AlO:2 R(VdW)	4	36	2	0.001821	0.5000	2.0000	# o%AlO:2 R(VdW)
4	15	3	0.019534	9.6284	15.0000	# o%AlO:3 Alpha(VdW)	4	36	3	0.019534	9.6284	13.0000	# o%AlO:3 Alpha(VdW)
4	15	4	0.001979	1.4030	1.6009	# o%AlO:4 R(sigma)	4	36	4	0.001979	1.4030	1.8000	# o%AlO:4 R(sigma)
5	54	1	0.253803	45.0000	100.0000	# v%AlOH:1 Theta0	5	118	1	0.253803	64.6197	90.0000	# v%AlOH:1 Theta0
5	54	2	0.138307	5.9184	19.7491	# v%AlOH:2 p_val1	5	118	2	0.138307	5.9184	19.7491	# v%AlOH:2 p_val1
5	54	3	0.084932	0.5000	5.0000	# v%AlOH:3 p_val2	5	118	3	0.084932	0.0000	10.0000	# v%AlOH:3 p_val2
5	54	5	0.026324	0.3676	5.0000	# v%AlOH:5 p_val7	5	118	5	0.026324	0.3676	4.0000	# v%AlOH:5 p_val7
5	54	7	0.020000	0.0000	2.0000	# v%AlOH:7 p_val4	5	118	7	0.020000	0.5000	3.0000	# v%AlOH:7 p_val4
5	56	1	0.506933	13.8580	64.5513	# v%AlOAl:1 Theta0	5	119	1	0.840000	1.0000	85.0000	# v%AlOAl:1 Theta0
5	56	2	0.294013	10.5987	40.0000	# v%AlOAl:2 p_val1	5	119	2	0.289250	11.0750	40.0000	# v%AlOAl:2 p_val1
5	56	3	0.094418	0.5527	9.9945	# v%AlOAl:3 p_val2	5	119	3	0.030155	4.2820	7.2975	# v%AlOAl:3 p_val2
5	56	5	0.023381	0.0000	3.0000	# v%AlOAl:5 p_val7	5	119	5	0.020000	1.0000	3.0000	# v%AlOAl:5 p_val7
5	56	7	0.018092	1.1908	3.0000	# v%AlOAl:7 p_val4	5	119	7	0.007041	1.0100	3.0000	# v%AlOAl:7 p_val4
5	59	1	0.376940	20.0000	84.7469	# v%OAlO:1 Theta0	5	120	1	0.506933	10.0000	64.5513	# v%AlOAl:1 Theta0
5	59	2	0.326074	7.3926	40.0000	# v%OAlO:2 p_val1	5	120	2	0.294013	7.0000	40.0000	# v%AlOAl:2 p_val1
5	59	3	0.027550	1.2450	4.0000	# v%OAlO:3 p_val2	5	120	3	0.094418	0.5527	9.9945	# v%AlOAl:3 p_val2
5	59	5	0.029000	0.1000	5.0000	# v%OAlO:5 p_val7	5	120	5	0.023381	0.0000	3.0000	# v%AlOAl:5 p_val7
5	59	7	0.019877	0.0000	7.0000	# v%OAlO:7 p_val4	5	120	7	0.018092	0.0000	3.0000	# v%AlOAl:7 p_val4
5	62	1	0.599900	5.0000	64.9900	# v%AlOSi:1 Theta0	5	123	1	0.376940	47.0529	84.7469	# v%OAlO:1 Theta0
5	62	2	0.119191	0.0000	11.9291	# v%AlOSi:2 p_val1	5	123	2	0.326074	7.3926	40.0000	# v%OAlO:2 p_val1
5	62	3	0.012973	1.0000	4.0000	# v%AlOSi:3 p_val2	5	123	3	0.027550	1.2450	5.0000	# v%OAlO:3 p_val2
5	62	5	0.002052	0.0000	1.2052	# v%AlOSi:5 p_val7	5	123	5	0.029000	0.1000	4.0000	# v%OAlO:5 p_val7
5	62	7	0.024258	0.5000	3.4258	# v%AlOSi:7 p_val4	5	123	7	0.019877	1.0123	3.0000	# v%OAlO:7 p_val4
5	63	1	0.882703	0.0000	100.0000	# v%AlSiO:1 Theta0	5	124	1	0.567483	0.0000	56.7483	# v%AlAlO:1 Theta0
5	63	2	0.049840	0.0050	5.3794	# v%AlSiO:2 p_val1	5	124	2	0.143267	0.0009	14.3276	# v%AlAlO:2 p_val1
5	63	3	0.007500	0.0000	1.0000	# v%AlSiO:3 p_val2	5	124	3	0.068621	0.1000	6.9621	# v%AlAlO:3 p_val2
5	63	5	0.005000	0.0000	1.0000	# v%AlSiO:5 p_val7	5	124	5	0.021153	0.5000	2.7047	# v%AlAlO:5 p_val7
5	63	7	0.003434	1.7626	3.0000	# v%AlSiO:7 p_val4	5	124	7	0.019860	1.0000	3.0000	# v%AlAlO:7 p_val4
5	64	1	0.838306	0.0000	100.0000	# v%OAlSi:1 Theta0	5	127	1	0.599900	5.0000	64.9900	# v%AlOSi:1 Theta0
5	64	2	0.046777	0.0005	5.0489	# v%OAlSi:2 p_val1	5	127	2	0.119191	0.0100	15.0000	# v%AlOSi:2 p_val1
5	64	3	0.002500	-1.0000	0.5000	# v%OAlSi:3 p_val2	5	127	3	0.012973	2.7027	4.0000	# v%AlOSi:3 p_val2
5	64	5	0.005000	0.0000	1.0000	# v%OAlSi:5 p_val7	5	127	5	0.002052	0.5000	1.2052	# v%AlOSi:5 p_val7
5	64	7	0.007265	0.5000	3.0000	# v%OAlSi:7 p_val4	5	127	7	0.024258	1.0000	4.0000	# v%AlOSi:7 p_val4
7	1	1	0.008017	1.4000	3.0000	# h%OHO:1 R(hb)	7	1	1	0.008017	1.4000	3.0000	# h%OHO:1 R(hb)
7	1	2	0.071638	-8.0000	0.0000	# h%OHO:2 E(hb)	7	1	2	0.071638	-7.1638	0.0000	# h%OHO:2 E(hb)
7	1	3	0.034576	1.3000	6.0000	# h%OHO:3 p_hb2	7	1	3	0.034576	1.0000	6.0000	# h%OHO:3 p_hb2
7	1	4	0.262985	1.7032	28.0017	# h%OHO:4 p_hb3	7	1	4	0.262985	1.7032	28.0017	# h%OHO:4 p_hb3

### SI.5. Trainset.in for CMA-ES optimizers

Considering the large amount of data contained in trainset.in input files, these files are directly supplied as supplementary material under the names trainsetTr1.in, and trainsetTr2.in for Tr.1 and Tr.2 respectively.

### SI.6. Geo file for Tr.1 and Tr.2 CMA-ES optimizers

Considering the large amount of data contained in geo input files, these files are directly supplied as supplementary material under the names geo\_Tr1, geo\_Tr2 for Tr.1 and Tr.2 respectively.

## **SII. Inputs for Validation Sets with CMA-ES optimizer**

Considering the large amount of data contained in input files, these files are directly supplied as supplementary material under the names `geox`, and `trainsetx.in` (with  $x$  = name of the validation set). The validation set are named as following: `alumina` (validation set with  $\gamma$ -alumina structures), `boehmite` (validation set with boehmite structures), `silicalite` (validation set with purely silicic external surface of H-ZSM-5), `alsurf` (validation set with one aluminated site at the external surface of H-ZSM-5), and `mix` (validation set with aluminated amorphous silica, pseudo-normal model, and four aluminated sites at the external surface of H-ZSM-5).

## **SIII. Analysis of H-ZSM-5 pores' area**

Considering the large amount of data contained in POSCAR, this file is directly supplied as supplementary material under the name of `POSCAR_clv1_100`.

## **SIV. Rff1 and Rff2 compositions**

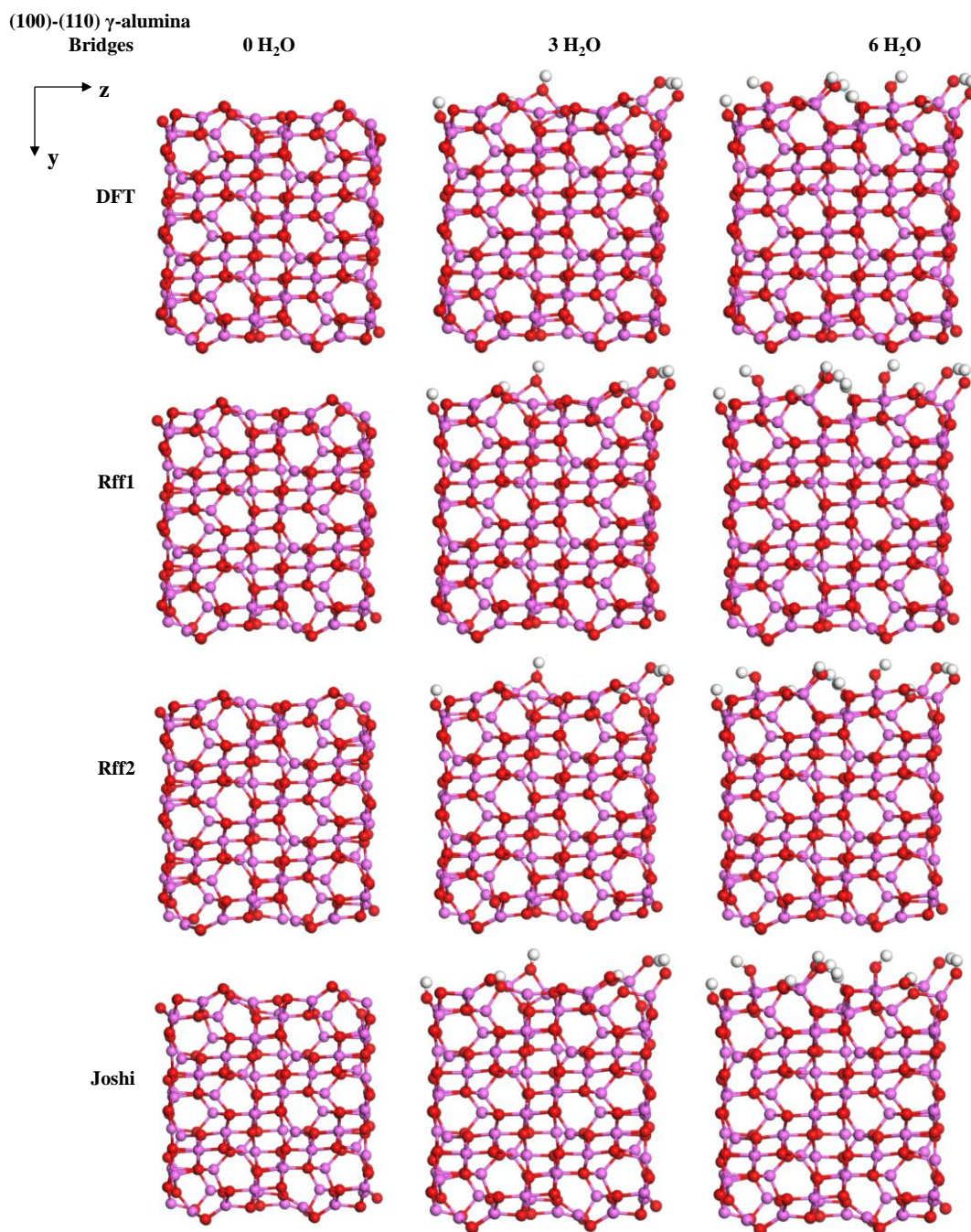
### **SIV.1. Rff1**

Considering the large amount of data contained in reactive force field files, this file is directly supplied as supplementary material under the names `Rff1_fffield`.

### **SIV.2. Rff2**

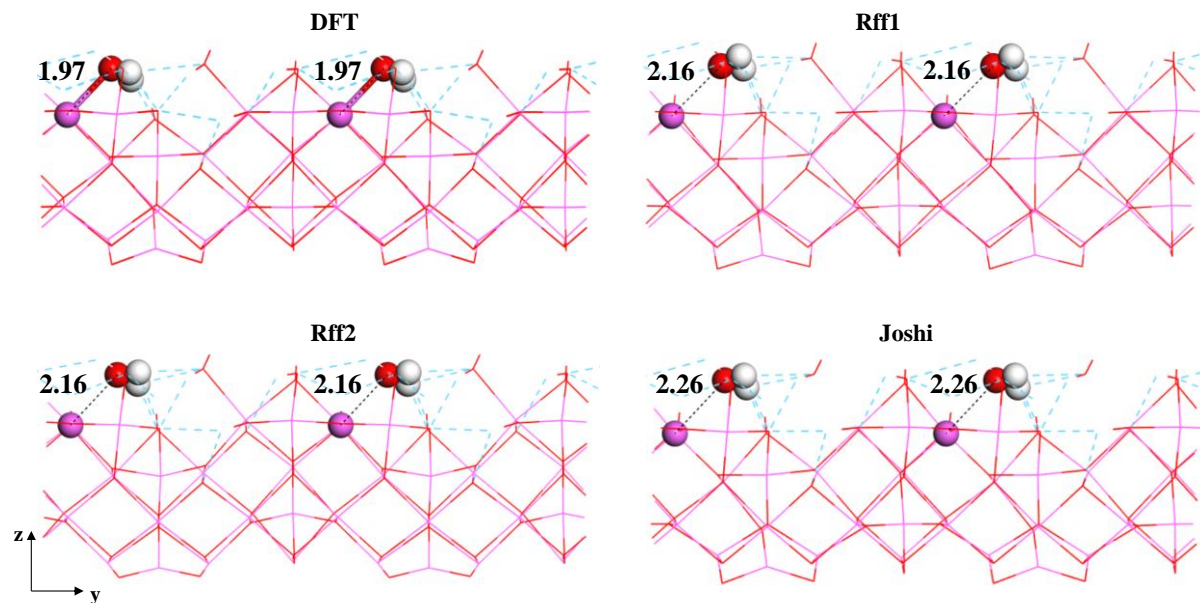
Considering the large amount of data contained in reactive force field files, this file is directly supplied as supplementary material under the names `Rff2_fffield`.



**SV. Error distribution on the training sets for the two best force fields****SV.1.  $\gamma$ -alumina edges**

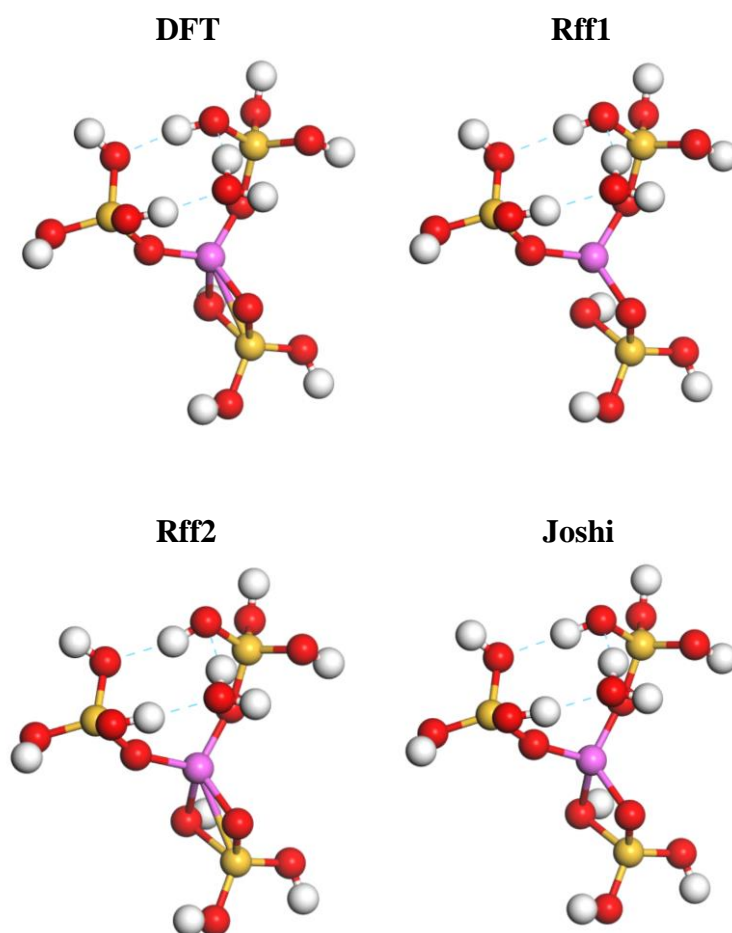
**Figure S2.** Results of geometry optimization of (110)-(100)  $\gamma$ -alumina edges with 0, 3, and 6 water molecules calculated by DFT, Rff1, Rff2, and Joshi reactive force field.



SV.2. (110)  $\gamma$ -alumina surface

**Figure S3.** Results of geometry optimization of (110)  $\gamma$ -alumina surface of  $14.8 \text{ OH nm}^{-2}$  calculated by DFT, Rff1, Rff2, and Joshi reactive force field.

The hydrated surface of (110)  $\gamma$ -alumina with  $3.0$ , and  $8.9 \text{ OH nm}^{-2}$  do not present water molecules adsorbed on the surface contrary to the one with  $14.8 \text{ OH nm}^{-2}$  which possess height water molecules adsorbed on its surface.

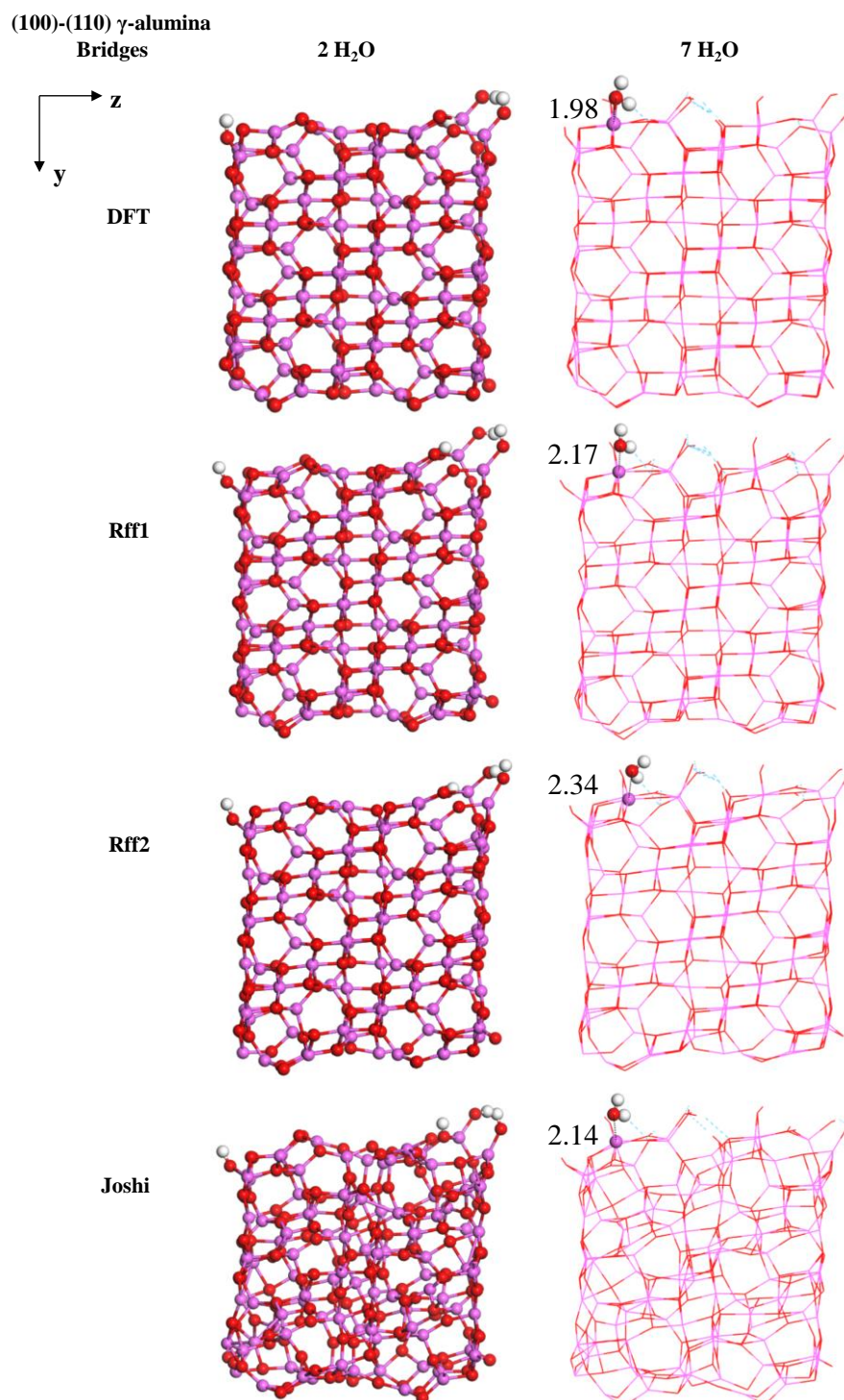
SV.3. Water molecule desorption on alumina and silicon cluster  $\text{Al}(\text{H}_2\text{O})[\text{Si}(\text{OH})_3]_3$ 

**Figure S4.** Results of geometry optimization of  $\text{Al}(\text{H}_2\text{O})[\text{Si}(\text{OH})_3]_3$  for a fixed distance between Al atom and  $\text{H}_2\text{O}$  molecule of 3.5 Å calculated by DFT, Rff1, Rff2, and Joshi reactive force field.

**SV.4. Water molecule desorption on aluminated site no. 77 on cleavage 6 of (100) orientation**

	DFT	Rff1	Rff2	Joshi	Structure of the acid site
3.0 H <sub>2</sub> O nm <sup>-2</sup>	1.96 1.91 2.10	2.10 2.09 2.10	2.21 2.33 2.23	2.15 2.22 2.14	
2.8 H <sub>2</sub> O nm <sup>-2</sup>	1.96 2.10	2.06 2.02	2.10 2.12	2.09 2.08	
2.6 H <sub>2</sub> O nm <sup>-2</sup>	1.96 2.09	2.04 2.02	2.12 2.13	2.09 2.09	
2.4 H <sub>2</sub> O nm <sup>-2</sup>	1.87	2.03	1.98	2.04	
2.2 H <sub>2</sub> O nm <sup>-2</sup>	1.91	2.00	1.98	1.98	
2.0 H <sub>2</sub> O nm <sup>-2</sup>	1.91	2.02	2.00	1.94	

**Table S1.** Water to aluminum distances obtained on aluminated site no. 77, on the surface named cleavage 6 cut along (100) orientation, from the hydrated surface with 3.0 H<sub>2</sub>O nm<sup>-2</sup> to the hydrated surface with 1.8 H<sub>2</sub>O nm<sup>-2</sup> obtained with DFT (reference data) and with reactive force fields Rff1, Rff2, and Joshi's.

**SVI. Error distribution  $\gamma$ -alumina edges of the alumina validation sets for the two best force fields**

**Figure S5.** Results of geometry optimization of (110)-(100)  $\gamma$ -alumina edges with 0, 3, and 6 water molecules calculated by DFT, Rff1, Rff2, and Joshi reactive force field.

## References

- (1) Gruene, T.; Li, T.; van Genderen, E.; Pinar, A. B.; van Bokhoven, J. A., Characterization at the Level of Individual Crystals: Single-Crystal MFI Type Zeolite Grains, *Chem. Eur. J.* **2018**, *24*, 2384-2388.
- (2) Zhai, D.; Liu, Y.; Zheng, H.; Zhao, L.; Gao, J.; Xu, C.; Shen, B., A First-Principles Evaluation of the Stability, Accessibility, and Strength of Brønsted Acid Sites in Zeolites, *J. Catal.* **2017**, *352*, 627-637.
- (3) Li, C.; Vidal-Moya, A.; Miguel, P. J.; Dedecek, J.; Boronat, M.; Corma, A., Selective Introduction of Acid Sites in Different Confined Positions in ZSM-5 and Its Catalytic Implications, *ACS Catal.* **2018**, *8*, 7688-7697.